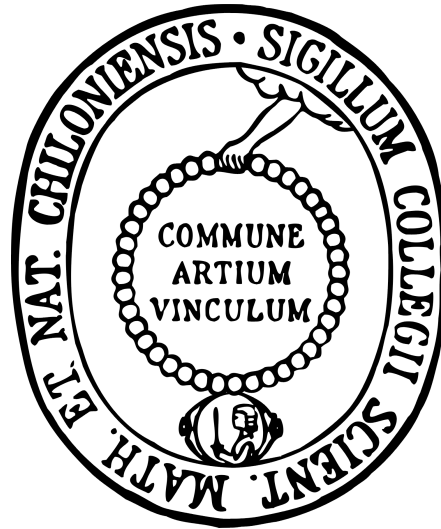


**THE EARLY TOARCIAN ENVIRONMENTAL CRISIS:
MECHANISMS AND CONSEQUENCES OF AN ICEHOUSE-
GREENHOUSE TRANSITION**



- DISSERTATION -

zur Erlangung des Doktorgades
der Mathematisch-Naturwissenschaftlichen Fakultät
der Christian-Albrechts-Universität zu Kiel

vorgelegt von
(Dipl. Geol. Wolfgang Rübsam)

Kiel, 2015

Erster Gutachter: Prof. Dr. Lorenz Schwark
Zeiter Gutachter: Prof. Dr. Volker Thiel
Dritter Gutachter Prof. Dr. Ulrich Heimhofer

Tag der mündlichen Prüfung: 10.2.2016
zum Druck genehmigt: 10.2.2016

Danksagung

Ich danke allen Personen, die Anteil am Gelingen meiner Promotion hatten. Allen voran danke ich meinen Eltern, welche mich während meines Studiums der Geologie in Köln als auch während meiner Promotionszeit in Kiel fortwährend unterstützt haben. Ihnen gilt mein besonderer Dank!

Meiner lieben Freundin Ramona danke ich für die Geduld und das Verständnis, welches Sie mir entgegengebracht hat.

Ebenso bedanke ich mich bei meinen geschätzten Kollegen, insbesondere bei Martin Stockhausen und Wolf Tilmann Pfeiffer, die immer offen waren für fachliche Diskussionen.

Besonderer Dank richtet sich auch an meinen Betreuer und Mentor Prof. Dr. Lorenz Schwark, der mich stets dazu angeregt hat über den Tellerrand zu blicken und meinen fachlichen Horizont zu erweitern. Stets stand er Ideen offen gegenüber und hat die Arbeit weit über das erforderliche Maß unterstützt. Die konstruktiven Diskussionen mit Prof. Dr. L. Schwark haben maßgeblich dazu beigetragen, dass das in der Arbeit behandelte Thema in dem hier vorliegenden Umfang und der fachlichen Tiefe behandelt werden konnte.

Des Weiteren bedanke ich mich bei Prof. Dr. Volker Thiel und Prof. Dr. Ulrich Heimhofer für die Begutachtung der Arbeit und bei den Professoren Dr. Martin Frank und Prof. Dr. Romain Bousquet, welche neben Prof. Dr. Lorenz Schwark und Prof. Dr. Volker Thiel dem Prüfungskomitee angehörten.

Zu guter Letzt möchte ich mich natürlich auch bei allen Angehörigen der Arbeitsgruppe Organische Geochemie des Geowissenschaftlichen Institutes der Universität zu Kiel bedanken. Ohne die Unterstützung des technischen Personals wäre es nicht möglich gewesen einen so hochwertigen und umfangreichen Datensatz zu erzeugen. Hier sind insbesondere Frau Petra Fiedler, Frau Eyke Kirchhoff, Marieke Sieverding und Vanessa Grote zu nennen.

Eidesstattliche Erklärung

Wolfgang Rübsam
Von-der-Horst Str. 3
24118 Kiel

Ich versichere an Eides statt durch meine eigenhändige Unterschrift, dass ich die vorgelegte Dissertation mit dem Thema: "THE EARLY TOARCIAN ENVIRONMENTAL CRISIS: MECHANISMS AND CONSEQUENCES OF AN ICEHOUSE-GREENHOUSE TRANSITION" selbstständig und ohne nicht offengelegte Hilfe Dritter verfasst und keine anderen als die angegebenen Quellen und Hilfsmittel genutzt habe.

Alle Stellen, die wörtlich oder dem Sinne nach auf Publikationen oder Vorträgen anderer Autoren beruhen, sind als solche in korrekter Zitierung kenntlich gemacht.

Die Dissertation in der vorgelegten oder einer ähnlichen Fassung noch nicht zu einem früheren Zeitpunkt an der Christian-Albrechts-Universität zu Kiel oder einer anderen in- oder ausländischen Hochschule als Dissertation eingereicht worden ist.

Ich versichere zudem, dass die Arbeit unter Einhaltung der Regeln guter wissenschaftlicher Praxis der Deutschen Forschungsgemeinschaft entstanden ist.

Meine Anteile an etwaigen Publikationen zu dieser Dissertation entsprechen denen, die in der untenstehenden gemeinsamen Erklärung mit dem Betreuer, angegeben sind.

Die Bedeutung dieser eidesstattlichen Versicherung und die strafrechtlichen Folgen einer unwahren eidesstattlichen Versicherung (§156,161 des Strafgesetzbuches) sind mir bekannt und bewusst.

Kiel, 20.12.2015

(Ort, Datum)



(Unterschrift Doktorand)

Thesis abstract

Mechanisms triggering the Early Toarcian global warming (Early Jurassic; ~183 Ma BP) and the associated environmental perturbation, comprising ocean acidification, sea level rise, expansion of marine oxygen minimum zones, black shale deposition and diversity loss in marine ecosystems are debated controversially. Environmental changes were accompanied by a major perturbation of the global carbon cycle, expressed by a striking negative carbon isotope excursion that reflects the injection of isotopically-light carbon into the Earth's ocean and atmosphere system. Carbon sources and mechanisms of carbon release remain unknown. Moreover, a precise timescale of the Early Toarcian environmental crisis and the carbon cycle perturbation is under debate. This thesis applies an integrated geochemical approach, comprising inorganic, organic and isotope geochemical proxies to single sediment sequence to reveal mechanisms of the global warming and environmental change during the Early Toarcian. Geochemical data were combined with continuous core scanning techniques that allowed to establish a floating chronology and a precise timescale. Results of this thesis allow to propose a new and unifying model that explains the key-features of the Early Toarcian and links them into a coherent Earth system concept.

The key features of the Early Toarcian can be explained by the response of the Earth's sensitive cryosphere (polar ice caps and cryosphere-stored carbon) towards a moderate global warming. The formation of a persistent cryosphere during the late Pliensbachian cold phase was associated with an increase of the cryosphere-stored carbon pool and with the formation of persistent polar ice caps. The cryosphere became destabilized by a rise in global temperature that was initiated by the emplacement of the Karoo-Ferrar LIP during the Early Toarcian. Melting of polar ice caps during global warming can explain the rapid sea level rise that occurred synchronically with the increase in SST. Moreover, the demise of cryosphere-stored carbon and the release of ^{12}C -enriched carbon into the Earth's ocean-atmosphere system can explain the Toarcian carbon cycle perturbation. Global warming, sea level rise and carbon release occurred synchronically in discrete steps and were paced by changes in the Earth's solar orbit. Release of greenhouse gases from the cryosphere caused a positive feedback and drove the Earth's climate into an extreme greenhouse phase. The rise in global temperatures by about 6°C occurred within <0.5 Myr, whereas the carbon cycle perturbation lasted for about 0.9 Myr. The stepwise nature of this event can be associated with single hyperthermals, whereby each hyperthermal was connected with an individual methane gun of less than 100 kyr in duration. A stepwise change in environmental conditions over a period of >0.5 Myr may explain the low extinction rates documented for nektonic ecosystems. Different durations previously calculated can be attributed to highly variable sedimentation rates in the different basins on the Western Tethyan shelf.

Black shale deposition on the Western Tethyan shelf, attributed to the T-OAE, reflect the local response of a shelf environment towards global warming, acceleration of the hydrological cycle, increased nutrient fluxes and the associated eutrophication of the shelf sea. Paleogeographic features of the Western Tethyan shelf, comprising hydrodynamic restriction and connection with the Arctic Ocean via the Viking Corridor that allowed the inflow of Arctic freshwater, further contributed to the establishment of water column stratification and prolonged bottom water euxinia.

Zusammenfassung (German thesis abstract)

Mechanismen und Prozesse, welche der globalen Erwärmung während des unteren Toarciums (Früher Jura; ~183 Ma BP) und den damit einhergehenden Umweltveränderungen, wie Ozeanversauerung, Meeresspiegelanstieg, Ausdehnung mariner Sauerstoffminimumzonen, Akkumulation bituminöser Sedimente, Verringerung des Artenreichtums und das Aussterben zahlreicher mariner Organismengruppen zu Grunde liegen werden kontrovers diskutiert. Diese Umweltveränderungen wurden von einer massiven Störung des globalen Kohlenstoffkreislaufs begleitet, welche sich in einer negativen Isotopenexkursion des Kohlenstoffs ausdrückt, die einen verstärkten Eintrag isotopisch leichten Kohlenstoffs in die Atmosphäre und Ozeane anzeigt. Mögliche Kohlenstoff-Reservoirs als auch Prozesse die zu dessen Freisetzung führten sind weitestgehend unbekannt. Darüber hinaus gibt es keine Einigkeit über den Zeitraum, in welchem sich die Klima und Umweltveränderungen abliefen. Im Rahmen dieser Arbeit wurden verschiedene geologische und geochemische Arbeitsansätze kombiniert und hier zum ersten Mal auf eine einzelne Sedimentabfolge angewendet, um Einblicke in die den Umweltveränderungen während des unterem Toarciums zu Grunde liegenden Prozesse zu erlangen. Geochemische Daten wurden mit kontinuierlichen Messverfahren kombiniert, welche die Erarbeitung einer relativen Zeitskala ermöglichten. Die Ergebnisse der Arbeit erlaubten die Entwicklung eines neuen konzeptionellen Modells, welches die wichtigsten Beobachtungen erklären kann und in einem vereinheitlichenden Erdsystem zusammenführt.

Die Umweltveränderungen während des unteren Toarciums können mit der Reaktion der Kryosphäre (polare Eiskappen und in der Kryosphäre gespeicherter Kohlenstoff) auf eine extern ausgelöste moderate globale Erwärmungsphase erklärt werden. Die Bildung einer ausgedehnten Kryosphäre während einer Kaltphase im späten Pliensbachium führe zu einem starken Anwachsen des an die Kryosphäre gebundenen Kohlenstoffpools und ermöglichte zudem die Bildung ausgedehnter polarer Eiskappen. Die Eruption der Karoo-Ferrar Flutbasaltprovinz im frühen Toarcium leitete eine globale Erwärmungsphase ein die zur Destabilisierung der Kryosphäre führte. Das durch die Erwärmung ausgelöste Abschmelzen der polaren Eiskappen erlaubt es das rasche Meeresspiegelanstieg zu erklären der mit einem Anstieg der Temperatur des Meerwassers einherging. Die Destabilisierung der an die Kryosphäre gebundenen Kohlenstoff-Reservoirs und die damit verbundene Freisetzung von Treibhausgasen, für die eine leichte Isotopensignatur des Kohlenstoffs angenommen werden kann, stellt einen plausiblen Mechanismus dar um den globalen Kohlenstoffkreislauf nachhaltig zu beeinflussen als auch um die negative Isotopenexkursion des Kohlenstoffs zu erklären. Globale Erwärmung, Meeresspiegelanstieg und die Freisetzung von Treibhausgasen liefen Zeitgleich ab und erfolgte in diskreten Events in Abhängigkeit von Änderungen der Erdbahnparameter. Die Freisetzung von Treibhausgasen hatte eine positive Rückkopplung zur Folge, welche die globale Erwärmung verstärkte und die Erde in ein extremes Treibhausklima führte. Der Anstieg der globalen Temperaturen erfolgte in weniger als 0.5 Myr, wobei sich die Störung des Kohlenstoffkreislaufs über einen Zeitraum von etwa 0.9 Myr erstreckte. Der mehrstufige Charakter kann mit einzelnen rapiden Erwärmungsphasen erklärt werden, wobei jede Erwärmungsphase von der Freisetzung zusätzliche Treibhausgase begleitet wurde und sich über

einen Zeitraum von etwa 100 kyr erstreckte. Die schrittweise ablaufende Erderwärmung über einen Zeitraum von etwa 0.5 Myr liefert eine mögliche Erklärung für das relative moderate Artensterben liefern. Unterschiedliche Angaben bezüglich der Dauer, die für dieses Ereignis berechnet wurden, können mit hoch-variablen Sedimentationsraten in den einzelnen Teilbecken des West-Tethys Schelfs erklärt werden.

Die Ablagerung bituminöser Sedimente auf dem West-Tethys Schelf, die das Ozeanische Anoxische Ereignisse im Toarcium definieren, kann als der lokale Ausdruck dieses Schelfmeeres auf die globale Erwärmung, verstärkte Verwitterungsprozesse, erhöhten Nährstoffeintrag und das daraus resultierende Nährstoffüberangebot gewertet werden. Die verbesserte Erhaltung organischen Materials wurde zudem durch die speziellen paleogeographischen Gegebenheiten dieses Ablagerungsraumes begünstigt. Der Zustrom arktischen Frischwassers auf den West-Tethys Schelf über den Viking Korridor begünstigte eine stabile Dichteschichtung des Wasserkörpers, welche in Verbindung mit einer stark eingeschränkten Wasserzirkulation und einer hydrodynamischen Restriktion die Bildung andauernder euxinischer Bedingungen im Tiefenwasser erlaubte.

INDEX OF CONTENTS

Index of Contents	I
List of Abbreviations	V
List of Figures	VI
List of Tables	XI
Chapter One: Introduction and Synopsis	1
1.1. General Introduction	2
1.1.1. Early Jurassic Stratigraphy and Timescale	3
1.1.2. Sea Level Evolution and Eustatic Sequences	6
1.1.3. Paleogeography of the Western Tethyan Shelf	8
1.2. The Early Toarcian Environmental Crisis	11
1.2.1. Toarcian biotic crisis	12
1.2.2. Toarcian Carbon Cycle perturbation	14
1.2.3. Toarcian climate evolution and climate zones	17
1.2.4. Role and timing of the Karoo-Ferrar volcanism	21
1.2.5. Toarcian black shales and anoxia	23
1.3. Motivation and objectives	25
Chapter Two: Chronology of the Early Toarcian environmental crisis	27
2.1. Introduction	29
2.2. Periodicity in sediments of Core FR-210-078	30
2.3. Discussion	36
2.3.1. Astronomical and sea level controls on sedimentary cycles	36
2.3.2. Towards the 405 kyr cycles in the Lorraine record	39
2.3.3. Duration of ammonite zones and subzones	39
2.3.4. Durations of the Toarcian carbon cycle perturbations	41
2.3.5. Correlation with other sections	42
2.4. Conclusions	44
Chapter Three: Astronomically-forced cryosphere demise during the Early Toarcian	45
3.1. Introduction	47
3.2. Pattern, pacing and periodicity of the Toa-CIE	49
3.2.1. Pattern and pacing of the Toa-CIE	49
3.2.2. Periodicity of the Toa-CIE and inferred mechanisms	50

Index of Contents

3.3. Carbon sources and reservoirs	52
3.4. Indices for a persistent cryosphere during the Early Jurassic	52
3.5. Cryosphere demise during astronomically forced hyperthermals	53
3.6. Conclusions	56
Chapter Four: Glacio-eustatic sea level and salinity changes during the Early Toarcian	57
4.1. Introduction	59
4.2. Sediment composition and characterization	61
4.2.1. Sediment composition and sedimentation structure	61
4.2.2. Characterization of the siliciclastic sediment fraction	64
4.2.3. Composition of the carbonate fraction	66
4.2.4. Characterization of the organic matter fraction	70
4.3. Salinity proxies	74
4.3.1. Oxygen isotope values of the carbonate fraction	74
4.3.2. Distribution of methyltrimethyltridecylchromans	75
4.3.3. Abundance of C ₃₀ -steroids	75
4.4. Discussion	77
4.4.1. Sequence stratigraphic framework and sea level evolution	77
4.4.2. Evolution of sea surface salinity	83
4.4.3. Controls on sea level and salinity changes	88
4.4.4. Sea level and salinity changes during the Toa-CIE	94
4.4.5. Ocean circulation pattern on the Western Tethyan shelf	97
4.5. Conclusions	100
Chapter Five: Controls on redox conditions in the Lorraine Sub-Basin during the Early Toarcian	102
5.1. Introduction	104
5.2. Background – tracing anoxia and euxinia in ancient sediments	105
5.2.1. Sedimentological evidence	105
5.2.2. TOC-TS-Fe systematic	105
5.2.3. Trace elements	106
5.2.4. Biomarker proxies	107
5.2.5. Isotope systems ($\delta^{34}\text{S}$ and $\delta^{98/95}\text{Mo}$)	108
5.3. Results	110
5.3.1. Lithological observations, OM and pyrite burial	110
5.3.2. Trace element-based proxies	111

Index of Contents

5.3.3. Biomarker-based proxies	113
5.3.4. Sulfur and molybdenum isotopes	116
5.4. Discussion	118
5.4.1. Assessing the redox facies	118
5.4.2. Evolution of redox conditions	129
5.4.3. Insights into the hydrological regime and extent of shelf sea anoxia	132
5.4.4. Controls on redox conditions and PZE	137
5.4.5. Redox fluctuations during the upper <i>H. elegantulum</i> subzone	140
5.4.6. Evolution of redox conditions during the Toa-CIE	142
5.5. Conclusions	144
Chapter Six: Phytoplankton community dynamics during the Early Toarcian	146
6.1. Introduction	148
6.2. Background: Biomarkers as indicators of marine phytoplankton	150
6.3. Results	152
6.3.1. Molecular composition of the aliphatic hydrocarbon fraction	152
6.3.2. Eukaryotic and prokaryotic contributions	153
6.3.3. Distribution of steroidal compounds	154
6.4. Discussion	157
6.4.1. Assessing the steroid sources	157
6.4.2. Changes in the phytoplankton community structure	164
6.4.3. Phytoplankton response towards the Toa-CIE	167
6.4.4. Phytoplankton community dynamics during the upper <i>H. elegantulum</i> subzone	170
6.5. Conclusions	172
Chapter Seven: Concluding discussion and summary	173
7.1. Environmental and biotic changes during the Toarcian: A unifying model	174
7.2. Facies model for the Lorraine Sub-Basin	176
7.3. Outlook	181
Appendix and Supplementary Information	182
A1. Study Site and Stratigraphy	183
A1.1. Geology of the Paris Basin	183
A1.2. Study site and drill locations	183
A1.3. Biostratigraphy and core correlation	184
A1.4. Lithology of Core FR-210-078	186
A2. Paleogeographic reconstruction of the Western Tethyan Shelf	189

Index of Contents

A3. Methodology and analytical procedures	192
A3.1. Continuous measurements	193
A3.1.1. Magnetic Susceptibility (MagS) measurement	193
A3.1.2. Spectrophotometry (sediment color)	193
A3.2. Discrete sample analysis	194
A3.2.1. Bulk Geochemistry	195
A3.2.2. Element concentrations (ICP-OES; Fusion glass disc WDX)	196
A3.2.3. Isotope Geochemistry	196
A3.2.4. Molecular Geochemistry	198
A3.3. Organic petrology and microscopy of thin sections	199
A3.4. Spectral Analysis	199
A4. GC-MS traces	201
Supplementary information	206
S1. Supplementary information: Chapter One	206
S2. Supplementary information: Chapter Two	208
S3. Supplementary information: Chapter Three	210
S4. Supplementary information: Chapter Four	213
S5. Supplementary information: Chapter Five	217
S6. Supplementary information: Chapter Six	220
Information onto the digital data sheet	224
References	225

List of Abbreviations

BSR	b acterial s ulfate r eductions
CIE	C arbon I sotope E xcursion
CSC	C ryosphere s tored c arbon
DBT	D ibenzothi p hene
$\delta^{13}\text{C}_{\text{org}}$	stable carbon isotope composition of organic matter
$\delta^{13}\text{C}_{\text{carb}}$	stable carbon isotope composition of the bulk carbonate fraction
$\delta^{98/95}\text{Mo}$	isotopic ratio of ^{98}Mo and ^{95}Mo
$\delta^{98/95}\text{Mo}_{\text{SW}}$	isotopic ratio of ^{98}Mo and ^{95}Mo in seawater
$\delta^{98/95}\text{Mo}_{\text{SED}}$	isotopic ratio of ^{98}Mo and ^{95}Mo in sediment
$\delta^{18}\text{O}_{\text{carb}}$	stable oxygen isotope composition of the bulk carbonate fraction
$\delta^{34}\text{S}_{\text{bulk}}$	sulfur isotope composition of the bulk sediments
FSST	f alling stage s ystems t ract
GC-MS	G as chromatography m ass spectrometry
HC	h ydrocarbon
HST	h ighstand s ystems t ract
LST	l owstand s ystems t ract
MagS	M agnetic S usceptibility
MFZ	m aximum f looding z one (stage of highest sea level)
MRS	m aximum r egressive s urface (stage of lowest sea level)
m/z	mass-charge-ratio
OAE	O ceanic A noxic E vent
Phen	Phenanthrene
Phy	phytane
PI	Pliensbachian
PP	p rimary p roduction
Pr	pristane
PZE	p hotic z one e uxinia
SSS	s ea s urface s alinity
SST	s ea s urface t emperature
TE	t race e lement
TIC	t otal i norganic c arbon
Toa	Toarican
T-OAE	T oarican O ceanic A noxic E vent
Toa-CIE	T oarican c arbon i sotope e xcursion
TOC	t otal o rganic c arbon
TOC_{cf}	t otal o rganic c arbon calculated on c arbonate- f ree base
TS	t otal s ulfur
TS_{cf}	t otal s ulfur calculated on c arbonate- f ree base
TST	t ransgressive s ystems t ract

List of Figures

Chapter 1

Figure 1-1:	Inter-correlation of upmost Pliensbachian and Lower Toarcian ammonite zones and subzones throughout the Arctic and European Realms.	4
Figure 1-2:	Stratigraphy and astronomical timescale (AST) of the Lower Jurassic.	5
Figure 1-3:	Toarcian sequence stratigraphy and sea level evolution.	7
Figure 1-4:	Global paleogeographic reconstruction during the Toarcian.	8
Figure 1-5:	Detailed paleogeographic reconstruction of the western Tethyan shelf.	9
Figure 1-6:	A volcanic greenhouse scenario.	11
Figure 1-7:	Evolution of invertebrate macrofauna species ranges and calcareous nannofossils during the Late Pliensbachian and Early Toarcian.	13
Figure 1-8:	Generalized carbon isotope stratigraphy for the upper Pliensbachian and lower Toarcian.	15
Figure 1-9:	High-resolution $\delta^{13}\text{C}$ records from the Cleveland Basin and the Paris Basin.	16
Figure 1-10:	Late Pliensbachian and Early Toarcian climate evolution.	17
Figure 1-11:	Evolution of faunal and floral realms.	18
Figure 1-12:	Paleogeographic distribution of climate sensitive sediments during the Pliensbachian and the Early Toarcian.	20
Figure 1-13:	Radiometric dates for the emplacement of igneous rocks associated with the Karoo-Ferrar-LIP.	22
Figure 1-14:	Stratigraphic and spatial distribution of the Toarcian bituminous facies.	23

Chapter 2

Figure 2-1:	Stratigraphic evolution of sediment color (a^*) and magnetic susceptibility.	31
Figure 2-2:	2π -MTM power spectrums for Intervals 1 to 4.	33
Figure 2-3:	Filter output for sediment color (a^*) and magnetic susceptibility.	33
Figure 2-4:	Filter output for ultra high-resolution sediment color (a^*) of the basal Schistes Carton Fm (Interval 3).	34
Figure 2-5:	MTM power spectra for the tuned a^* -series compared with the astronomical model La2004.	35
Figure 2-6:	Tuned a^* -time series and filter output for eccentricity, obliquity and precession components.	40
Figure 2-7:	Compared floating chronologies for the pelagic Sakahogi section, the Peniche section in the Mediterranean realm for the Lorraine Sub-Basin.	43

Chapter 3

Figure 3-1:	Evolution of the climate system and the carbon cycle throughout the Late Pliensbachian and the Early Toarcian.	48
Figure 3-2:	Filter outputs for statistically significant frequency peaks in the organic carbon isotope records from the Lorraine Sub-Basin and the Cleveland Basin.	51
Figure 3-3:	Chronology of the Toarcian carbon cycle perturbation and inferred mechanisms.	54

List of Figures

Chapter 4

Figure 4-1:	Evolution of climate system, carbon cycle and sea level throughout the Late Pliensbachian and the Early Toarican.	60
Figure 4-2:	Sediment composition and sedimentation style of Core FR-210-078.	63
Figure 4-3:	Stratigraphic evolution of proxies that reflect changes in the composition of the siliciclastic sediment fraction.	65
Figure 4-4:	Stratigraphic evolution of carbonate content and composition of the carbonate fraction.	69
Figure 4-5:	The OI-HI and the TAR-HI plots, reflecting changes in the organic matter composition (marine versus terrestrial sources) and preservation.	71
Figure 4-6:	Representative microphotographs (in incident light fluorescence mode) from polished blocks for 4 different facies types identified in Core FR-210-078.	73
Figure 4-7:	Evolution of proxies proposed to reflect changes in the sea surface salinity (SSS), comprising MTTCs, C ₃₀ steroids and δ ¹⁸ O values.	76
Figure 4-8:	Evolution of Si/Al ratio, TAR and the Al/K ratio and inferred changes in the sea level.	82
Figure 4-9:	Evolution of salinity-related proxies and inferred changes in the SSS.	86
Figure 4-10:	Cross-plots of the tri-/di-MTTC ratio with the TAR and the Si/Al ratio reflect the relation of sea level changes and changes in the SSS.	88
Figure 4-11:	Evolution of climate, sea level and sea surface salinity during the Late Pliensbachian and Early Toarcian as well as inferred control mechanisms.	91
Figure 4-12:	Detailed view towards the evolution of the sea level and the SSS throughout the upper <i>H. elegantulum</i> subzone that exhibits a pronounced variability that can be attributed to astronomically forced glacial/interglacial cycles.	93
Figure 4-13:	Cross-plots of δ ¹³ C ^{org} values with TAR and tri-/di-MTTC showing that lowest carbon isotope values, reflecting the Toa-CIE, were bounded to a high sea level and significantly reduced SSS.	94
Figure 4-14:	Detailed view towards the evolution of the sea level and the SSS during the Early Toarcian Carbon cycle perturbation.	96
Figure 4-15:	Evolution of ocean currents on the Western Tethyan shelf during the Early Toarcian.	99

Chapter 5

Figure 5-1:	Stratigraphic evolution of TOC, TS values (as well as TOC _{cf} and TS _{cf}) and the TS/Fe ratio.	110
Figure 5-2:	Stratigraphic evolution of selected redox-sensitive trace elements, expressed as TE/Al ratio.	113
Figure 5-3:	Stratigraphic evolution of biomarker-based redox proxies Pr/Phy, HHI*, C ₃₂ /C ₃₁ hopanes and the ratio of DBT/Phen.	115
Figure 5-4:	Stratigraphic evolution of isorenieratane concentrations, δ ³⁴ S and δ ^{98/95} Mo data.	117
Figure 5-5:	Cross-plots of TOC _{cf} with Ni/Al, Cu/Al, V/Al and Mo/Al ratios.	121
Figure 5-6:	Cross-plots of TS _{cf} with Ni/Al, Cu/Al, V/Al and Mo/Al ratios.	124

List of Figures

Figure 5-7:	Cross-plots of TOC with TS and of Fe with TS concentrations.	126
Figure 5-8:	Hughes plot allowing to assess the degree of S-incorporation into OM and the cross-plot of sulfur isotope values with the DBT/Phen ratio.	126
Figure 5-9:	Cross-plot of Pr/Pyh with the HHI* and cross plot of HHI* with the C ₃₂ /C ₃₁ hopane ratio.	128
Figure 5-10:	Evolution of inorganic and organic geochemical redox proxies and inferred changes in the redox regime and the extent of PZE.	131
Figure 5-11:	Stratigraphic evolution of Mo/TOC trends for different basins situated on the Western Tethyan shelf.	133
Figure 5-12:	Cross-plot of 1/Mo with $\delta^{98/95}\text{Mo}$ values and a mechanistic model illustrating processes that affect the isotopic signature of sedimentary molybdenum.	135
Figure 5-13:	Evolution of Mo/TOC and $\delta^{98/95}\text{Mo}$ values in the Lorraine Sub-Basin and the Cleveland Basin as well as inferred changes in the areal extent of shelf sea anoxia and the hydrodynamic regime.	136
Figure 5-14:	Cross-plots of V/Al with the tri/di-MTTC ratio and the Si/Al ratio.	137
Figure 5-15:	Cross-plot of isorenieratane concentrations with the tri/di-MTTC ratio and the Mo/TOC ratio.	138
Figure 5-16:	Evolution of redox conditions the extent of PZE in relation with changes in the hydrodynamic regime, changes in SSS and sea level changes.	139
Figure 5-17:	Redox fluctuations throughout the upper <i>H. elegantulum subzone</i> .	141
Figure 5-18:	The evolution of redox conditions during the Toa-CIE.	143
 Chapter 6		
Figure 6-1:	Biotic response towards changes in climate and oceanographic conditions during the Early Toarcian.	149
Figure 6-2:	Composition of the aliphatic hydrocarbon fraction and evolution of the TAR and the steroid/hopanoid ratio.	153
Figure 6-3:	Stratigraphic evolution of steroid.	156
Figure 6-4:	Ternary-plot for steroids in the range from C ₂₇ to C ₂₉ .	157
Figure 6-5:	Cross-plots of steroids (C ₂₇ to C ₂₉) with the TAR and the tri-/di-MTTC ratio.	160
Figure 6-6:	The cross-plot of C ₃₀ steroids with the TAR and the ratio of tri-/di-MTTCs.	161
Figure 6-7:	The evolution of marine phytoplankton during the Early Toarcian.	166
Figure 6-8:	The evolution and values of the steroid/hopanoid ratio during the carbon cycle perturbation.	168
Figure 6-9:	The evolution of C ₂₈ /C ₂₇ and the C ₂₇ /C ₂₉ steroid ratios during the carbon cycle perturbation.	169
Figure 6-10:	Fluctuations of steroid ratios throughout the upper <i>H. elegantulum subzone</i> .	171
 Chapter 7		
Figure 7-1:	Chronology of the Early Toarcian environmental crisis and the associated OAE.	175
Figure 7-2:	Facies model for the upmost <i>P. spinatum</i> and the lower <i>D. tenuicostatum zones</i> .	177

List of Figures

Figure 7-3:	Facies model for the upmost <i>D. tenuicostatum</i> zone and the lower <i>H. elegantulum</i> subzone.	178
Figure 7-4:	Facies model for the upper <i>H. elegantulum</i> subzone.	179
Figure 7-5:	Facies model for the <i>H. falciferum</i> subzone.	180
Appendix		
Figure A1:	Geological map of the Paris Basin and the a location maps of the drill sites	184
Figure A2:	Biostratigraphic framework and core correlation	185
Figure A3:	Lithology of Core FR-210-078.	187
Figure A4:	Photographs of thin sections.	188
Figure A5:	Paleogeographic map of the Western Tetyhan shelf.	190
Figure A6:	Detailed construction of he Western Tethyan shelf and shelf morphology.	191
Figure A7:	Generalized analytical flow chart.	192
Figure A8:	Sampling scheme used to obtain discrete samples.	194
Figure A9:	Total ion current chromatogram of an aliphatic fraction.	201
Figure A10:	Ion chromatograms (m/z 85) of an aliphatic hydrocarbon fraction showing the distribution of <i>n</i> -alkanes.	201
Figure A11:	Ion chromatograms m/z 191, 369, 367 of an aliphatic hydrocarbon fraction showing the distribution of regular hopanes and hopenes.	202
Figure A12:	Ion chromatogram m/z 217 of an aliphatic hydrocarbon fraction showing the distribution of regular steranes.	202
Figure A13:	Ion chromatogram m/z 257 and m/z 271 of an aliphatic hydrocarbon fraction showing the distribution of diasterenes and 4Me-diasterenes.	203
Figure A14:	Ion chromatograms m/z 121, 135 and 149 of an aromatic hydrocarbon fraction showing the distribution of mono-, di, and tri-MTTCs.	204
Figure A15:	Ion chromatograms of m/z 178 and of m/z 184 of an aromatic hydrocarbon fraction showing Phen and DBT.	204
Figure A16:	Ion chromatograms m/z 133 of a aromatic hydrocarbon fraction showing the distribution aryl isoprenoids and aromatic carotenoid biomarkers.	205
Supplementary: Chapter Two		
Figure S2-1:	Cross-plots of carbonate content with MagS-values and of TOC _{cf} with a*- values.	208
Figure S2-2:	2 π -MTM power spectrum for Intervals 1+2 and for Interval 4.	208
Figure S2-3:	Filter output for a*-, b*- and MagS-values.	209
Supplementary: Chapter Three		
Figure S3-1:	Late Pliensbachian and Early Toarcian $\delta^{13}\text{C}$ stratigraphy for the Cleveland, the Lusitanian and the Paris Basin as well as for the Lorraine Sub-Basin.	210
Figure S3-2:	$\delta^{13}\text{C}_{\text{org}}$ values corrected for variable OM sources.	211
Figure S3-3:	MTM power spectrums for tuned a*-values and $\delta^{13}\text{C}_{\text{org}}$ data sets from the Lorraine Sub-Basin and the Cleveland Basin compared with the astronomical model La2004.	212

List of Figures

Supplementary: Chapter Four

- Figure S4-1:** Stratigraphic evolution of $\delta^{18}\text{O}$ data from location situated at different latitudes. 213
- Figure S4-2:** Cross-plots of carbonate content with siliciclastics and of Si with Al contents. 214
- Figure S4-3:** Cross-plots of carbonate content with Ca and Sr concentrations. 214
- Figure S4-4:** Stratigraphic evolution of TOC and carbonate content as well as of Ni/Al, Cu/Al and Sr/Ca ratios. 215
- Figure S4-5:** Stratigraphic evolution of TAR, CPI and T_{max} values. 216
- Figure S4-6:** The cross-plot of bulk carbonate $\delta^{18}\text{O}$ with $\delta^{13}\text{C}$ values. 216

Supplementary: Chapter Five

- Figure S5-1:** Cross-plots of Al with Ni, Cu, V and Mo concentrations. 217
- Figure S5-2:** The cross-plot of isorenieratane concentration with HHI* values. 218
- Figure S5-3:** The cross-plots of $\delta^{98/95}\text{Mo}$ values with Mn/Ca and isorenieratane concentrations. 218
- Figure S5-4:** Evolution of redox conditions and PZE for different basins throughout the Western Tethyan Shelf. 219

Supplementary: Chapter Six

- Figure S6-1:** Marine extinction throughout from the Ordovician to the Neogene in comparison with the evolution of the Earth climate. 220
- Figure S6-2:** Cross-plots of regular steranes with diasterenes from C_{27} to C_{30} . 221
- Figure S6-3:** Stratigraphic evolution of 4Me-diasterenes. 222
- Figure S6-4:** Stratigraphic evolution of steroid ratios throughout Core FR-210-078. 223

List of Tables

List of Tables

Chapter 5

Table 5-1:	Geochemical data about selected redox-sensitive trace element.	106
-------------------	--	-----

Chapter 6

Table 6-1:	Sterol distribution in microalgae, bacteria and fungi and habitats of the different microalgae.	151
-------------------	---	-----

Table 6-2:	Changes in the steroid sources.	163
-------------------	---------------------------------	-----

Supplementary: Chapter One

Table S1-1:	Summary of magnitudes documented for the Toa-CIE.	206
--------------------	---	-----

Table S1-2:	Oxygen isotope data available for the Pliensbachian and Toarcian.	207
--------------------	---	-----

Chapter One:

Introduction and Synopsis

1.1. General Introduction

During distinctive periods in Earth history Earth's environment and climatic system experienced drastic changes and perturbations, which resulted in extinctions events of variable extent. In some cases such periods coincide with large volcanic eruptions or celestial bolide impacts that have the potential to affect the climate and the environment at a global scale and thus have been attributed to be possible triggers and/or causes of the changes in question (e.g. [Bond & Wignall, 2014](#)). However, whether such events are rather triggering mechanisms than the cause itself is less constrained. Thus, understanding environmental dynamics of the system during periods of profound environmental changes and biodiversity loss, so-called "Events in Earth History", is of major importance in order to be able to evaluate the response of the Earth's system towards externally triggered climate change. Studying such periods in Earth's history might further provide substantial information in the understanding of past, recent and future climate changes and can help predicting the anthropogenic impact in recent climate change ([Hulme et al., 1999](#); [Trenberth et al., 2015](#)) and biodiversity loss ([Ceballos et al., 2015](#)).

The Early Toarcian (Early Jurassic, ~183 Ma BP) is in the focus of ongoing research as this period coincides with pronounced global events, including mass extinction ([Hallam, 1986](#)), global warming ([Dera et al., 2011a](#)), rapid high-amplitude sea level rise ([Pittet et al., 2014](#)), rise in atmospheric CO₂ ([McElwain et al., 2005](#)), carbon cycle perturbation ([Hesselbo et al., 2000a](#)) and expansion of death zones throughout shelf seas ([Jenkyns et al., 2001](#)), with the latter being accompanied by enhanced accumulation of organic carbon in marine sediments (e.g. [Baudin et al., 1990](#); [Jenkyns et al., 2001](#)) resulting in the so-called Toarcian Oceanic Anoxic Event ([Jenkyns, 1988](#)). This profound environmental crisis concurred with the emplacement of the Karoo-Ferrar Large Igneous province (K-F-LIP; [Bond & Wignall, 2014](#); [Burgess et al., 2015](#)), indicating a temporal and causal relationship between both events. However, the impact of the K-F-LIP emplacement and the response of the Earth's system is debated controversially and fundamental questions about causes and causal relationships between volcanism, climate change, biodiversity loss and carbon cycle dynamics are still less constrained.

This Chapter gives an overview on the current state of knowledge concerning the Early Toarcian times period, paleogeography, climate evolution, carbon cycle dynamics, extinction events and shelf sea anoxia.

1.1.1. Toarcian Stratigraphy and Timescale

The Toarcian was introduced by d'Orbigny (1842 – 1851, 1852) at Vrines quarry, near the city of Thouars (Toarcium in Latin) in central western France, and represents the uppermost stage of the Lower Jurassic (Liassic) series following the Pliensbachian. The subdivision of the Toarcian stage is commonly based on ammonite faunas allowing to differentiate 8 distinctive ammonite zones that can be further subdivided into several ammonite subzones (e.g. Gabilly, 1976; Howarth, 1992a, 1992b; Elmi et al., 1994; 1997). The European ammonite zones serve as global standard for the entire Jurassic and other biostratigraphic and chemostratigraphic data are commonly calibrated to it. A comprehensive stratigraphic overview as well as some historical background is given by Page (2003).

The base of the Toarcian stage

In northwest Europe the base of the Toarcian is marked by a changeover from Pliensbachian *Pleuroceras* faunas to Toarcian *Dactyloceras* faunas. In its name giving region in France the base of the Toarcian stage corresponds to the *Dactyloceras tenuicostatum* chronozone, whose type locality is located on the coast of northern England (Buckman, 1910). However, the upper Pliensbachian and the lowermost Toarcian sediment successions are characterized by numerous depositional hiatuses and condensed intervals resulting from rapid sea level changes that can be traced throughout northwest Europe (e.g. Pittet et al., 2014 and references therein). The ensuing major unconformity, expressed by the partial absence of the ammonite zones or subzones, as well as the limited correlation potential of subboreal ammonite faunas exclude the northwestern European sector from being a suitable candidate for a global boundary stratotype. Therefore, the base of the Toarcian is defined by the first occurrence of a diversified *Eodactylites* ammonite fauna (Goy et al., 1996) at sections in the Mediterranean realm where gaps are less pronounced (Elmi, 1999). The *Eodactylites* ammonite fauna can be correlated with the base of the *Dactyloceras tenuicostatum* ammonite zone (*Protogrammoceras paltus* horizon). Suggested candidates for a Global Stratotype Section and Point (GSSP) of the Toarcian are the Ponto do Trovao section (Peniche, Portugal; Elmi, 2006) and the Almonacid de la Cuba section in the Iberian Range (Comas-Rengifo et al., 2010).

Toarcian ammonite stratigraphy, provincialism and correlative schemes

Throughout Europe the Early Toarcian as well as the Late Pliensbachian ammonite faunas can be grouped into the different faunal provinces that can be attributed to a latitudinal climate gradient (e.g. Page, 2003; 2008). While the faunal provincialism was most pronounced during the Late Pliensbachian it was diminished during the Early Toarcian while at the same time intensive faunal mixing occurred resulting in a more cosmopolitan fauna (Enay, 1980; Dera et al., 2011b). Different zonal schemes have been established for these provinces, whereby a cross-correlation at subzone scale is limited by the high degree of faunal differentiation. Commonly a **Boreal**, **Subboreal**, **Submediterranean** and **Mediterranean Province** can be distinguished (Fig. 1-1). The **Boreal Province**, characterized by *Tiltoniceras*, *Elegantuliceras*, *Ovaticeras* and *Pseudolioceras*

Introduction and Synopsis

faunas (Knyazev et al., 2003; Nikitenko et al., 2008 and references therein) is restricted to the Arctic realm, extending into the southern Viking corridor and during certain periods in time also further south to northern England and Scotland (Page, 2003). The **Subboreal Province** is restricted to northern England, Scotland and parts of the North Sea sector and is most significant when faunas were dominated by *Dactyloiceras*. Towards southern England a shift to a more Submediterranean faunal character has been observed (Howarth, 1992a, 199b; Page, 2003). The **Submediterranean Province** comprises the areas of southern England, France, Germany and northern Spain. Faunas of this province are commonly richer in *Hildocerataceae*, sometimes to the virtual exclusion of *Dactyloiceratidae*. Chronozonal schemes of the **Subboreal** and **Submediterranean Provinces** show a similar zonal scheme but differ at the subzonal scale (Gabilly, 1976; Elmi et al., 1994; 1997). However, strong similarities exist between these provinces allowing a detailed correlation of the two (Page, 2003). The **Mediterranean Province** mainly comprises Italy, Austria, southern Spain, Portugal and northern Africa (Page, 2003; 2008). The high degree of faunal differentiation between the Mediterranean and the other provinces necessitates the development of a separate zonal scheme as summarized by Elmi et al. (1997).

Stage	Substage	Arctic Realm		European Realm					
		boreal		subboreal	submediterranean	mediterranean			
Toarcian	middle	<i>Dactyloiceras commune</i>	?	<i>Hildoceras bifrons</i>	<i>D. commune</i>	<i>Hildoceras bifrons</i>	<i>H. sublevsoni</i>	<i>Hildoceras bifrons</i>	<i>H. sublevsoni</i>
	lower	<i>Harpoceras falciferum</i>	<i>H. falciferum</i>	<i>Harpoceras serpentinum</i>	<i>H. falciferum</i>	<i>Harpoceras serpentinum</i>	<i>H. falciferum</i>	<i>Harpoceras levsoni</i>	<i>H. falciferum?</i>
			<i>E. elegantulum</i>		<i>C. exaratum</i>		<i>E. elegantulum</i>		<i>H. levsoni</i>
upper	<i>Tiltoniceras antiquum</i>	?	<i>Dactyloiceras tenuicostatum</i>	<i>D. semicelatum (i)</i>	<i>Dactyloiceras tenuicostatum</i>	<i>D. semicelatum (ii)</i>	<i>Dactyloiceras polymorphum</i>	<i>D. semicelatum (ii)</i>	
				<i>D. tenuicostatum</i>				<i>D. mirabile</i>	
<i>D. clevelandicum</i>									
<i>P. paltum</i>									
	<i>Amaltheus villegaensis</i>	?	<i>Pleuroceras spinatum</i>	<i>P. hawskerense</i>	<i>Pleuroceras spinatum</i>	<i>P. hawskerense</i>	<i>Emaciatoceras emaciatum</i>	<i>C. elisa</i>	

Figure 1-1: Inter-correlation of uppermost Pliensbachian and Lower Toarcian ammonite zones and subzones throughout the Arctic and European Realms (after Elmi et al., 1997; Macchioni, 2002; Page, 2003; Knyazev et al., 2003; Nikitenko et al., 2008).

Pliensbachian-Toarcian Boundary Date

The dating of the Pliensbachian-Toarcian transition is debated controversially. The Geological Timescale 2012 (Gradstein et al., 2012) sets the boundary at 182.7±0.7 Ma BP. However, this date mainly based on radiometric dating of Karro sills (e.g. Svensen et al., 2007) that cannot be precisely correlated with sediment successions elsewhere, e.g. Europe. More recently, precise U-Pb dating of an ash layer in the *D. tenuicostatum* zone from a sediment succession in South America yielded an age of 183.2±0.3 Ma BP, resulting in a minimum age of 183.5 Ma BP for the Pliensbachian-Toarcian boundary (Sell et al., 2014). Furthermore, the Pliensbachian-Toarcian boundary is bracketed by ash layer dates from North America between 184.0+6/-1 and 183.2±0.7 Ma BP, supporting a dating of about 183.6 Ma BP (Pálffy et al., 2002). Interestingly, the same age is also indicated by an astronomical timescale (ATS) established for a pelagic Panthalassa section spanning the entire Early Jurassic (Ikeda & Hori, 2014). It is therefore likely that the age of the Pliensbachian-Toarcian boundary as proposed by Gradstein et al. (2012) is affected by some uncertainties. Recent studies provided new radiometric dates indicating that the boundary date is most likely 183.6 Ma BP as originally proposed by Pálffy et al. (2000). This is further supported by new floating chronologies from a continuous pelagic section (Fig. 1-2). It is therefore reasonable to use the more recent results that differ from the data given in the Geological Timescale 2012 (Gradstein et al., 2012).

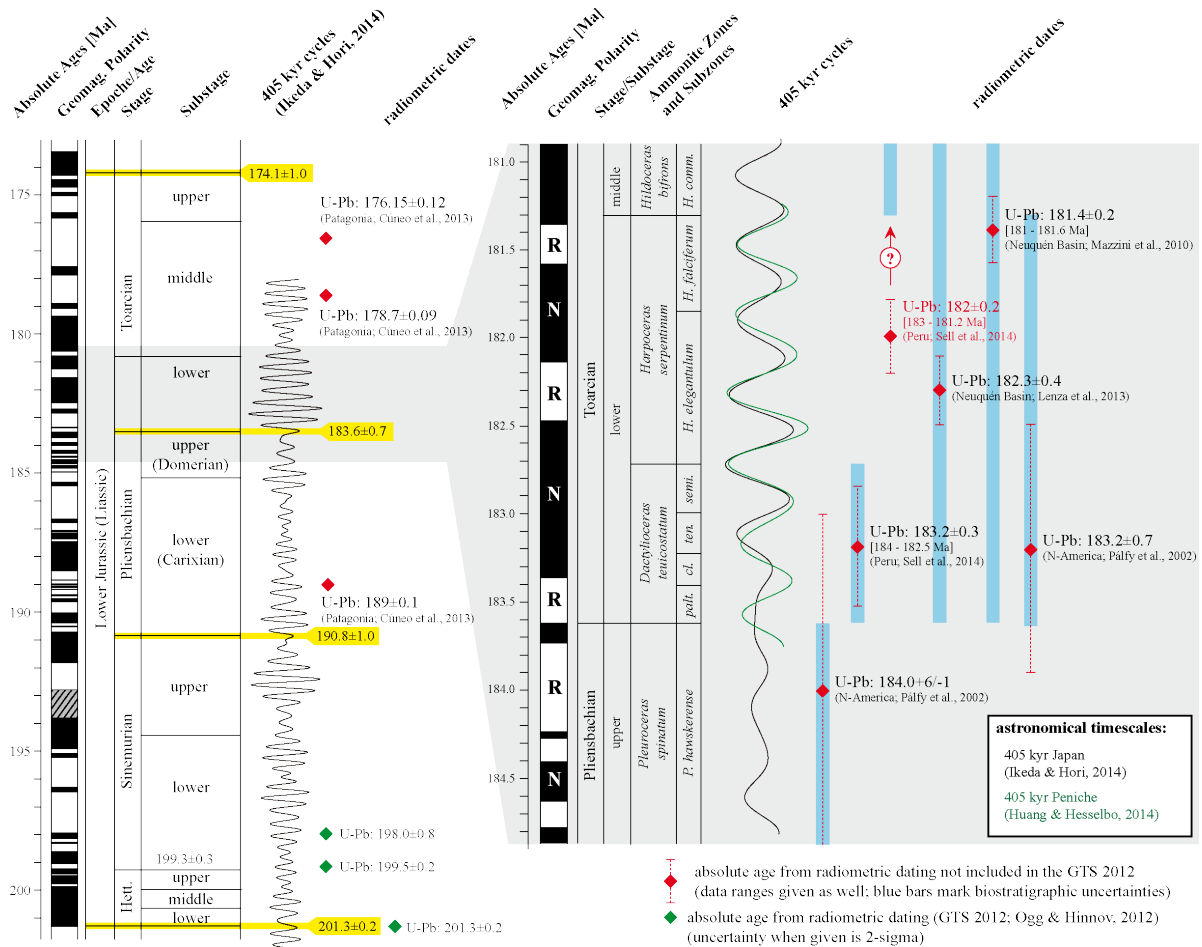


Figure 1-2: Stratigraphy and astronomical timescale (AST) of the Lower Jurassic. The AST based on findings by Ikeda & Hori (2014) and match well with absolute dates available from U-Pb dating. Floating chronologies and absolute ages result in a boundary age of about 183.6 Ma BP for the Pliensbachian-Toarcian boundary.

Duration of Ammonite Zones

The lower Jurassic timescale is still under ongoing research and durations calculated for ammonite zones are mainly based on floating chronologies (Fig. 1-2). Cyclostratigraphic investigations indicate a duration of about 0.8 to 1.0 Myr for the *D. polymorphum* zone (Suan et al., 2008; Bodin et al., 2010; Huang & Hesselbo, 2014), which coincides with the *D. tenuicostatum* zone (Elmi et al., 1997; Macchioni, 2002). The duration of the *H. levsioni* zone, which concurs with the *H. serpentinum/H. falciferum* zone (Elmi et al., 1997; Macchioni, 2002), has been calculated to about 1.4 to 1.6 Myr (Suan et al., 2008a; Huang & Hesselbo, 2014). The durations of ammonite subzones are less well constrained. Strontium isotope trends from the Cleveland Basin indicate spans of about 1 Myr and 0.3 Myr for the *C. exaratum* and *E. falciferum* subzones, respectively (McArthur et al., 2000). A minimum duration of 0.6 Myr for the *C. exaratum/E. elegantulum* subzone is also supported by cyclostratigraphic investigations carried out on a core from the Southern German Basin (Suan et al., 2008a).

1.1.2. Sea Level Evolution and Eustatic Sequences

The lower Jurassic (Liassic) covers a major transgressive-regressive cycle (Carnian-Toarcian cycle), which can be subdivided into four minor 2nd order, tectonoeustacy-originated, transgressive-regressive facies cycles (Vail et al., 1991; Hardenbol et al., 1998). The uppermost 2nd order cycle corresponds to the Toarcian stage. The lower Toarcian records a transgressive phase, whereas a regressive trend is documented throughout the middle and upper Toarcian (Fig. 1-3). The 2nd order Toarcian cycle comprises of six complete (Toa1-Toa2, Toa2-Toa3, Toa3-Toa4, Toa4-Toa5, Toa5-Toa6, Toa6-Toa7) and two incomplete (Pl8-Toa1 and Toa7-Aa1) eustatic sequences (3rd and 4th order cycles, Fig. 1-3). These sequences are clearly documented throughout the Boreal and Tethyan realms (Hardenbol et al., 1998; Gély & Lorenz, 2006) and might be of glacio-eustatic origin, possibly related to long eccentricity changes (Boulila et al., 2011). A potential control of glacio-eustic mechanisms towards Late Pliensbachian and Early Toarcian on sea level changes is also indicated by the strong coupling of climate and sea level changes that has been documented for this period (Brandt, 1986; Suan et al., 2010; Korte & Hesselbo, 2011; also see 1.2.3.). Throughout the Western Tethyan shelf these rapid high-amplitude sea level changes resulted in numerous depositional hiatuses upon regressive stages and condensation upon rapid transgressive stages (Pittet et al., 2014 and references therein).

Following a regressive trend during the Late Pliensbachian that might be related to global cooling and a possible glaciation (e.g. Price, 1999; Rosales et al., 2004; Silva & Duarte, 2015) the Early Toarcian records a rapid sea level rise, whereby the amplitude has been estimated to about 30 to 90 m (Hallam, 1997; 2001; Hesselbo & Jenkyns, 1998). The Pl8-Toa1 sequence corresponds to the *D. tenuicostatum* zone, with the Toa1 sequence boundary being placed within the upper *D. tenuicostatum* zone or possibly within the *D. semicelatum* subzone (Gély & Lorenz, 2006; Pittet et al., 2014). The transgressive part can be strongly condensed, whereas the uppermost regressive stage can result in

Introduction and Synopsis

hiatuses (Pittet et al., 2014). The Toa1-Toa2 sequence corresponds to the uppermost *D. tenuicostatum* zone (*D. semicelatum* zone) and the lower part of the *H. serpentinum* zone (*H. elegantulum* subzone). The basal part of the sequence can be extremely condensed, with the maximum flooding zone being placed in the lowermost *H. elegantulum* subzone (Howarth, 1980; Pittet et al., 2014). In many basins of the Western Tethyan Shelf this sequence is characterized by the deposition of organic-rich facies corresponding to the Schistes Carton, Posidonia Shale, Jet Rock or equivalents (Ponsot, 1994; Hesselbo & Jenkyns, 1998). The Toa2 boundary is recognized by a lithological change (e.g. Rey & Cubaynes, 1991; de Graciansky et al. 1993) or by a hiatus (Ponsot, 1994). In the case of a hiatus the sequence Toa1-Toa2 can be missing (Ponsot, 1994). The Toa2-Toa3 sequence corresponds to the *H. falciferum* subzone, whereby the maximum flooding surface is placed at the uppermost *H. serpentinum* zone close to the *H. serpentinum*-*H. bifrons* boundary. The Toa3 boundary can be placed within the lower *H. bifrons* zone. The Toa1 and Toa3 boundaries are only minor boundaries. Therefore, and with respect to Hardenbol et al. (1998), the sequences Toa1-Toa2 and Toa2-Toa3 are considered as 4th order cycles (Fig. 1-3).

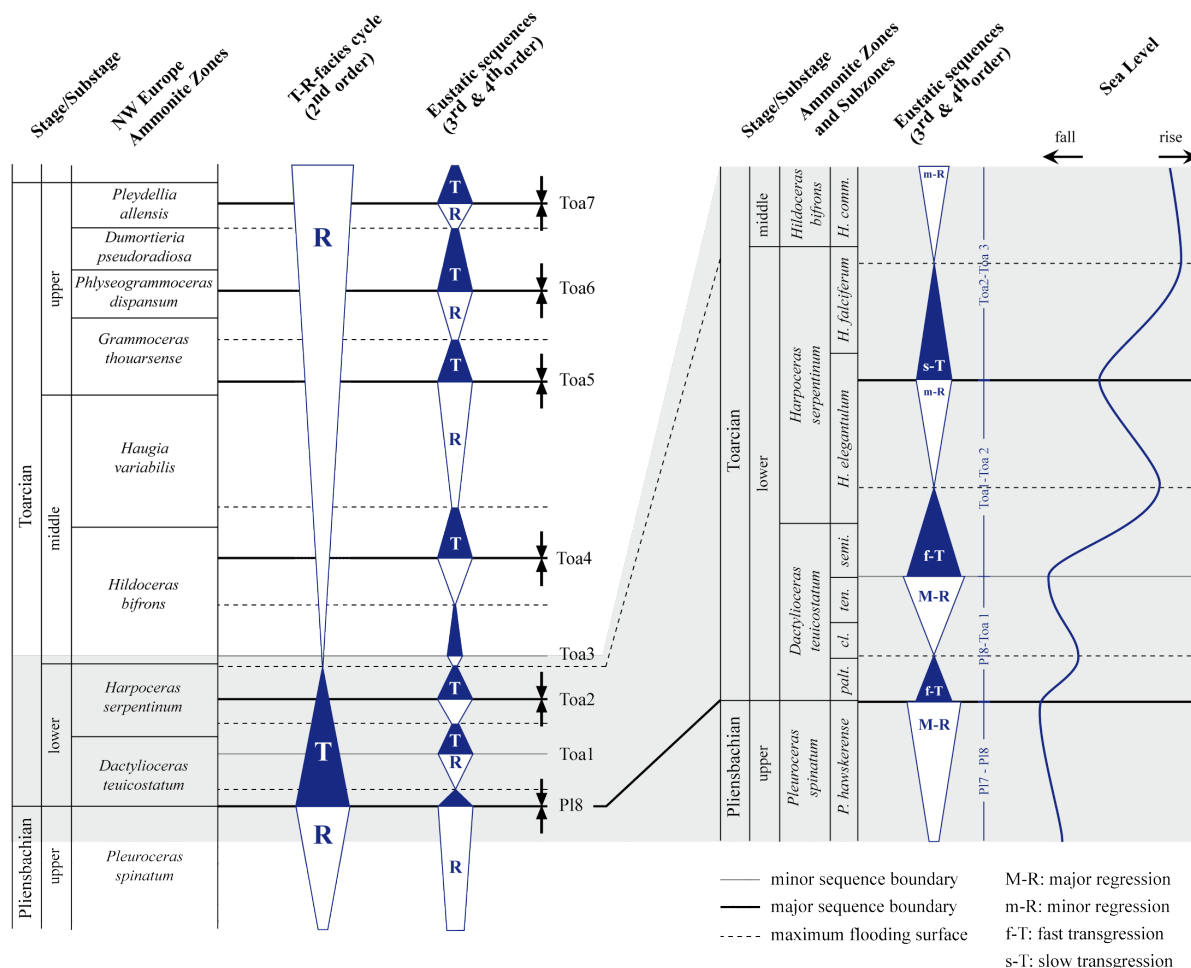


Figure 1-3: Toarcian sequence stratigraphy and sea level evolution (Hardenbol et al., 1998; Gély & Lorenz, 2006). Major T-R facies cycles correspond to 2nd order cycles (5 – 50 Myr), minor eustatic sequences correspond to 3rd order (0.2 – 5 Myr) and 4th order (0.1 – 0.2 Myr) sea level cycles (Vail et al., 1991). Rapid high-amplitude sea level fluctuations during the Late Pliensbachian and Early Toarcian resulted in numerous depositional hiatuses and condensed sediment intervals (e.g. Pittet et al., 2014 and references therein).

1.1.3. Palaeogeography

At the beginning of the Jurassic the entire landmass was combined in the supercontinent Pangaea that originated from the collision of Gondwana and Laurussia in the Late Paleozoic (Ziegler, 1990). The landmass was centered at the equator, surrounded by the Panthalassa Ocean and enclosing the wedge-shaped Tethyan Ocean to the east (Golonka, 2007; Scotese, 2014; Fig. 1-4). The beginning break-up of Pangaea in the Late Triassic and Early Jurassic was marked by an increased spreading activity and the emplacement of large igneous provinces, like the Central Atlantic Magmatic Province in the Late Triassic (Schlische et al., 2003; Marzoli et al., 2004) and the Karoo-Ferrar Large Igneous Province in the Early Toarcian (Encarnación et al., 1996; Burgess et al., 2015 also see 1.2.4.).

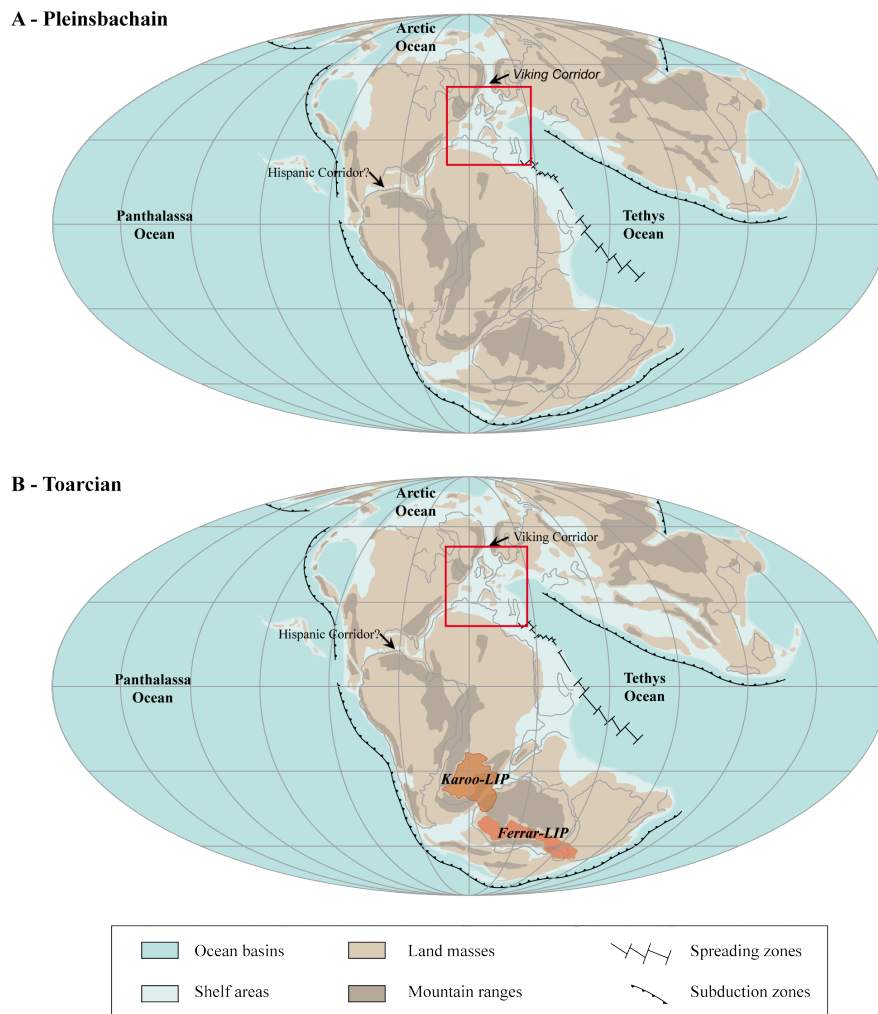


Figure 1-4: Global paleogeographic reconstruction during the **A)** Pliensbachian and **B)** Toarcian (modified from Golonka, 2007; Scotese, 2014). A major transgression during the Early Toarcian resulted in the flooding of wide continental areas and further allowed a water exchange between Arctic Ocean and Western Tethyan shelf via the Viking Corridor (shift in the position of global coastlines and distribution of orogenic highs after Smith et al., 1994; Golonka, 2007; Scotese, 2014). Whether a persistent connection between the Western Tethyan shelf the Panthalassa Ocean via the Hispanic Corridor existed during the Early Toarcian is debated controversially. Distribution of Karoo and Ferrar lavas is from Hasti et al. (2014), whereby the exact extent and distribution of Ferrar lavas is unknown due to the Antarctic ice cover. The position of the Western Tethyan Shelf is marked by the red square.

On the northern hemisphere the increased rifting activity led to the southwards propagation of the Norwegian-Greenland rift into the Central Atlantic and the westward propagation of the Tethyan rift. These processes established an extensional tectonic regime that formed a shallow epicontinental shelf (Western Tethyan shelf) between 10° and 50° on the northern hemisphere that opened into the Tethyan Ocean towards the southeast (Fig. 1-4) (Ziegler, 1990; Bassoulet et al., 1993; Thierry et al., 2000). The opening of the Viking Corridor during the Sinemurian (Surlyk, 1991; Scott and Turton, 2001) established a connection between the Arctic and Tethyan Ocean and further allowed the inflow of low saline Arctic waters onto the Western Tethyan shelf (Bjerrum et al., 2001; Dera et al., 2015). Whether a persistent connection between Tethyan and Panthalassa Ocean via the Hispanic Corridor existed during the Early Jurassic is debated controversially. However, recent works indicate that at least during global sea level high stand water exchange via the Hispanic corridor was possible and established faunal migration routes between the Tethyan and the Panthalassa Ocean (Aberhan, 2001; Arias, 2006; Mancenido, 2002).

The Western Tethyan shelf (Fig. 1-5A) was heavily structured into several sub-basins (e.g. Cleveland Basin, Northern and Southern Germany Basin, Paris Basin), separated by shallow sills and swells (Fig. 1-5B) (Ziegler, 1990; Bassoulet et al., 1993). The development of these paleogeographic features was mainly related to the regional tectonic subsidence controlled by extensional faulting (Guillocheau et al., 2001; Pienkowski et al., 2008). In the Northern German Basin the onset of halokinetic movement during the Late Triassic further promoted the formation of several troughs and highs (Pienkowski et al., 2008).

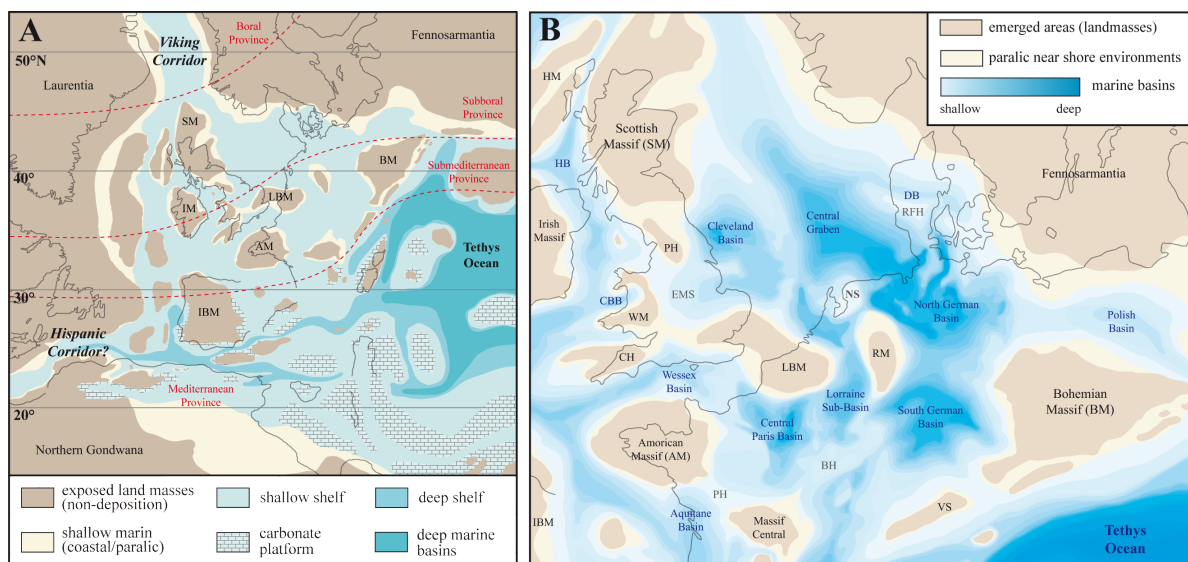


Figure 1-5: A) Paleogeography of the western Tethyan shelf area (modified after Ziegler, 1990; Bassoulet et al., 1993 and Thierry et al., 2000). Ammonite faunal provinces, introduced in chapter 1.1.1. are shown in red (Page et al., 2003, 2008). **B)** Detailed reconstruction of the Western Tethyan shelf and proposed shelf morphology (see appendix A2 for details and references). (HM: Herbrides Massif; PH: Pennine High; WM: Welsh Massif; CH: Cornubia High; RH: Rhenish Massif; LBM: London-Brabant-Massif; VS: Vindelician Swell; EMS: East Midland Shelf; NS: Netherlands Swell; RFH: Ringkobing-Fyn High; BH: Burgundy high; PH: Poitou High; HB: Herbrides Basin; DB: Danish Basin; CBB: Cardigan Bay Basin; IBM: Iberian Massif)

The shallow epicontinental shelf area was surrounded by marginal marine areas in the southeast and lowlands in the west, north and northeast (Fig. 1-5A). In addition to the fresh water inflow from the Arctic Ocean (Bjerrum et al., 2001; Dera et al., 2015) river influx from the surrounding landmasses as well as from the numerous large islands located in shelf area resulted in decreased seawater salinities (Röhl et al., 2001; Dera et al., 2009b). Spatial differences in seawater salinities, documented throughout the Western Tethyan shelf (McArthur et al., 2000; Bailey et al., 2003; Dera & Donnadieu, 2012), in combination with a latitudinal climate gradient is expressed by a faunal provincialism as introduced in chapter 1.1.1. (Fig. 1-5A).

1.2. The Early Toarcian Environmental Crisis

The Early Toarcian environmental crisis comprises a profound biodiversity loss, drastic global warming, perturbation of the carbon cycle and widespread shelf sea anoxia expressed by elevated rates of organic matter burial. Environmental changes were accompanied by the eruption of the Karoo-Ferrar Large Igneous Province, indicating a temporal and causal relation between both events (e.g. [Bond & Wignall, 2014](#)). Large volcanic eruptions can initiate a cascade of events as summarized by the “Volcanic Greenhouse Scenario” by [Wignall \(2001; 2005\)](#) illustrated in figure 1-6. In this scenario enhanced volcanic CO₂ emissions trigger global warming, resulting in an acceleration of the hydrological cycle, shelf sea eutrophication, anoxia and mass extinctions. Furthermore, volcanic warming can trigger the release of additional carbon from climate sensitive reservoirs like gas hydrates or permafrost. Additionally, prolonged volcanic activity, accompanied by the injection of SO₂, aerosols and ash particles into atmosphere and stratosphere, can affect the climate and the carbon cycle during the time span of emplacement and can furthermore enhance CO₂ introduced warming subsequent to cooling events (e.g. [Robock, 2000](#); [Self et al., 2014](#); [Mussard et al., 2014](#)). For a detailed discussion of all processes and events reference is made to the corresponding literature, especially the works by [Wignall \(2001; 2005\)](#), [Bond & Wignall, \(2014\)](#) and [Caruthers et al. \(2014\)](#).

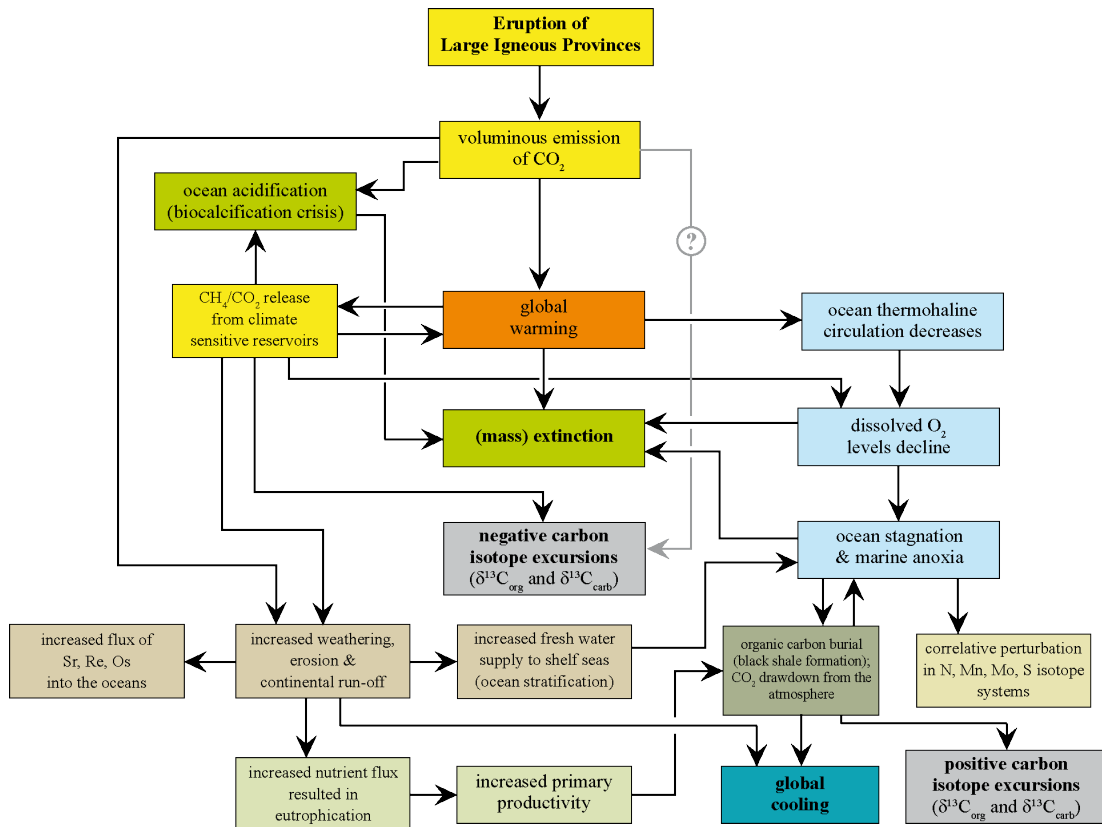


Figure 1-6: The volcanic greenhouse scenario illustrating cause-and-effect relationships of the earth system towards volcanic triggered global warming (modified after [Wignall, 2001, 2005](#); [Bond & Wignall, 2014](#)). Not all systems must necessarily be affected during enhanced volcanic activity. Furthermore, global cooling during explosive volcanic event is not illustrated. Weather volcanic CO₂ emissions can be responsible for large negative carbon isotope excursion is questionable due to the isotopic composition of carbon of volcanic gas emissions ($\delta^{13}\text{C}_{\text{volcanic}}$ about -6 to -14‰).

1.2.1. Toarcian biotic crisis

The Late Pliensbachian and Early Toarcian periods record several periodically recurring multi-phased extinctions events, which are thought to be of global significance and affected marine and terrestrial organisms (Benton, 1995; Little & Benton, 1995; Caruthers et al., 2014). A major extinction phase can be placed at the Pliensbachian-Toarcian boundary. This extinction primarily affected brachiopodes, ostracod faunas, benthic foraminifera and bivalvs, whereby ammonites and belemnites experienced a drastic turnover (Little & Benton, 1995; Harries & Little, 1999; Caswell et al., 2009). However, the magnitude of the extinction seems to be a regional phenomena (Hallam, 1986). The Pliensbachian-Toarcian extinction was followed by a second extinction phase at the *D. tenuicostatum*-*H. serpentinum* boundary that primarily affected benthic invertebrates, such as bivalvs, brachiopodes, ostracodes and foraminifera and coincides with widespread anoxia on the Western Tethyan shelf (Riegraf, 1985; Little & Benton, 1995; Danise et al., 2013). This second extinction phase was more pronounced in areas with bituminous facies but is also evident from other settings (Riegraf, 1985). Differences in the dynamics of these extinction events hint at episodes of elevated ecological stress due to climate and/or sea level fluctuations (Dera et al., 2010). Evolution of marine invertebrate macrofauna throughout the Late Pliensbachian and Early Toarcian is shown in figure 1-7.

Extinction events that affected marine invertebrates were accompanied by major changes in the community structure of marine phytoplankton. Dinoflagellates that experienced a strong radiation during the upper Pliensbachian and the lowermost Toarcian (*lower D. tenuicostatum zone*) were abruptly replaced by opportunistic faunas, like prasinophytes, during the *H. elegantulum subzone* (e.g. Bucefalo Palliani et al., 2002; van de Schootbrugge et al., 2005a).

Additionally, a biocalcification crisis is evident from the near disappearance of shallow-water carbonate platforms (Dromart et al., 1996; Trecalli et al., 2012) and a drastic decrease in abundance and size-reduction of the major pelagic carbonate producer *Schizosphaerella punctuata* (Erba, 2004; Mattioli and Pittet, 2004; Tremolada et al., 2005; Mattioli et al., 2009; Suan et al., 2010). The nanofossil crisis can be placed in the upper *D. tenuicostatum* and lower *H. serpentinum zone* and is assumed to be the result of global warming and ocean acidification (Fraguas et al., 2012; Trecalli et al., 2012; Clémence, 2014; Clémence et al., 2015) (Fig. 1-7). The effect of rising seawater temperatures is well expressed in nanofossil assemblages from Spain, where a shift from cold water loving *Calcevascularis jansae* and *Schizosphaerella punctuata* dominated fauna to a temperate-loving *Biscutum spp.* dominated fauna has been clearly documented across the Pliensbachian-Toarcian boundary. The lower *H. serpentinum zone* is dominated by the opportunistic taxa *Crepidolithus* and *Lotharingius* (Fraguas et al., 2012). The demise of *Schizosphaerella punctuata* is also documented from the Paris Basin and was accompanied by a pelagic sedimentation blackout (Hermoso et al., 2012). However, *Crepidolithus* was not documented in the interval corresponding to the biocalcification crisis. In the Paris Basin, as well as in other basins of the Western Tethyan shelf, the strongly depleted nanofossil assemblage of the uppermost *D. tenuicostatum* and lower *H. serpentinum zones* was dominated by *Calyculus*, which is known to be tolerant to low saline and low

nitrate waters (Mattioli et al., 2008; Hermoso et al., 2009b). The spatial differences highlight the role of local water mass conditions and thus the local character of the Early Toarcian extinction events.

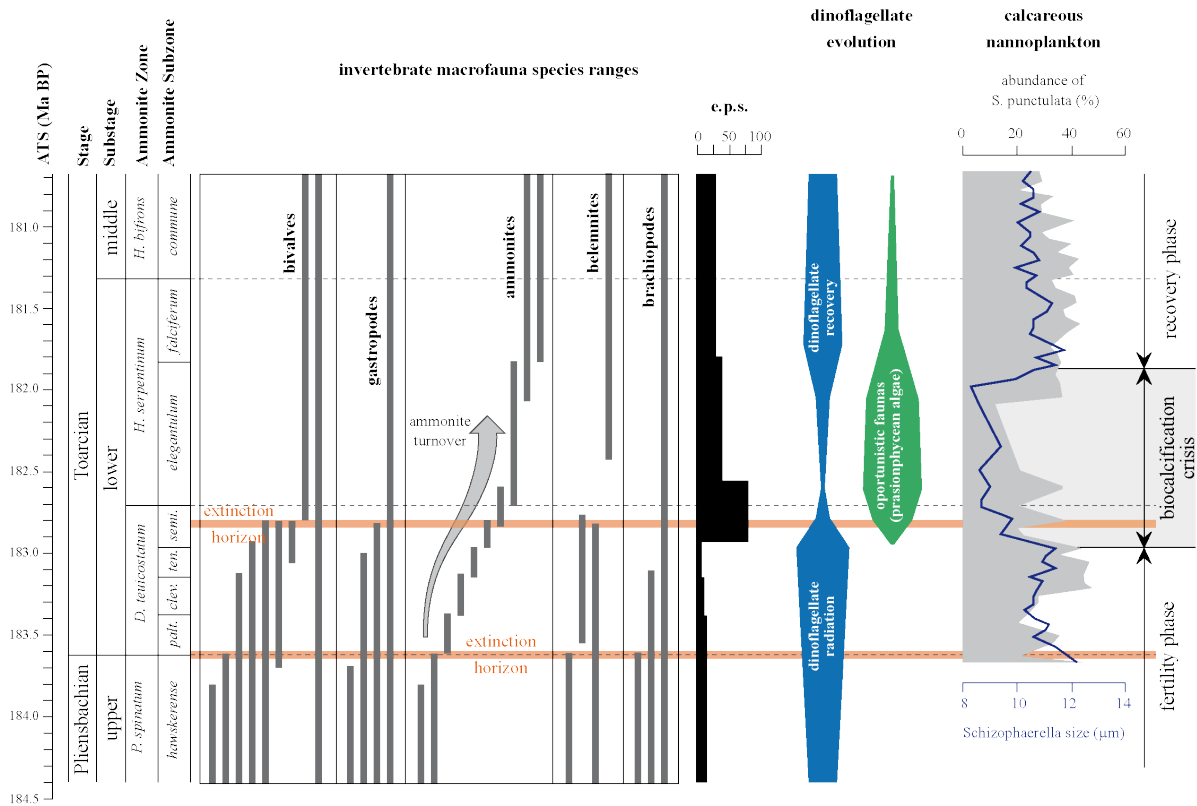


Figure 1-7: Simplified evolution of invertebrate macrofauna species ranges during the Late Pliensbachian and Early Toarcian (e.p.s. = extinction per subzone) (modified from Little & Brenton, 1995). The extinction interval at the Pliensbachian-Toarcian boundary is of global significance, whereas the extinction interval in the uppermost *D. tenuicostatum* zone primarily affected benthic taxa. The upper *D. tenuicostatum* and lower *H. serpentinum* zones are further highlighted by a drastic biocalcification crisis that resulted from the acidification of the oceans (e.g. Clémence, 2014) and by a replacement of dinoflagellates by opportunistic faunas, like prasinophytes (e.g. Bucefalo Palliani et al., 2002).

1.2.2. Toarcian Carbon Cycle perturbation

The Early Toarcian carbon isotope record shows an increasing trend, which resulted from increased rates of organic carbon burial associated with the selective removal of isotopically-light carbon from the oceans during a time of widespread black shale deposition (Jenkyns, 1988; Kump & Arthur, 1999). This positive trend was interrupted by a striking negative carbon isotope excursion (CIE) that is assumed to reflect the largest carbon cycle perturbation during the Mesozoic. The Early Toarcian carbon isotope excursion (Toa-CIE) has been documented in marine organic matter and carbonate (e.g. Jenkyns & Clayton, 1997; Jenkyns, 1988; Hesselbo et al., 2000a; Röhl et al., 2001; Kemp et al., 2005; Hermoso et al., 2012) as well as in terrestrial organic matter (Hesselbo et al., 2000; 2007; Hesselbo & Pieńkowski, 2011) spanning the uppermost *D. tenuicostatum* zone and lower *H. serpentinum/H. falciferum* zone (Fig. 1-8). Additionally, a minor negative CIE documented from the Western Tethyan shelf (e.g. Hesselbo et al., 2007; Littler et al., 2010) can be placed at the Pliensbachian-Toarcian boundary (Pl-Toa-CIE). The major Toa-CIE has been documented at numerous locations on the Western Tethyan shelf (see abovementioned references) as well as at several locations outside Europe:

- Arctic: [Suan et al., 2011a](#)
- North America: [Caruthers et al., 2011](#)
- Japan: [Gröcke et al., 2011](#); [Kemp & Izumi, 2014](#)
- North Africa: [Bodin et al., 2010](#); [Krencker et al., 2015](#)
- South America: [Al-Surwaidi et al., 2010](#); [Guex et al., 2012](#) (incomplete records).

The Toa-CIE is evident in different depositional environments and is not limited to the anoxic or euxinic basins of the Western Tethyan shelf (e.g. Hesselbo et al., 2007, Hesselbo & Pieńkowski, 2011; Sabatino et al., 2013). Thus, recycling of isotopically light CO₂ in a stratified water column as previously proposed by Küspert (1982) fail to explain the Toa-CIE. Additional evidence for a global atmospheric signal comes from $\delta^{13}\text{C}$ -data of fossil wood documenting the negative Pl-Toa-CIE and Toa-CIE (Hesselbo et al., 2000a; 2007; Hesselbo & Pieńkowski, 2011). It can therefore be inferred that the negative carbon isotope excursion reflects a global perturbation of the carbon cycle, which affected all exchangeable reservoirs and occurred simultaneously. The variable magnitude of -4 to -7‰ documented in the $\delta^{13}\text{C}_{\text{org}}$ shift of the Toa-CIE (table S1-1) can be explained by different organic matter sources. Values corrected for variable organic matter sources result in a magnitude of about -3 to -4‰ (Suan et al., 2015; Montero-Serrano et al., 2015), which is comparable with the magnitude of about -3‰ documented for $\delta^{13}\text{C}_{\text{carb}}$ values. Higher amplitudes in the $\delta^{13}\text{C}_{\text{carb}}$ excursions were mainly documented for organic-rich facies (table S1-1) and might result from diagenetic effects under the influence of organic matter (e.g. Lavastre et al., 2001 and references therein).

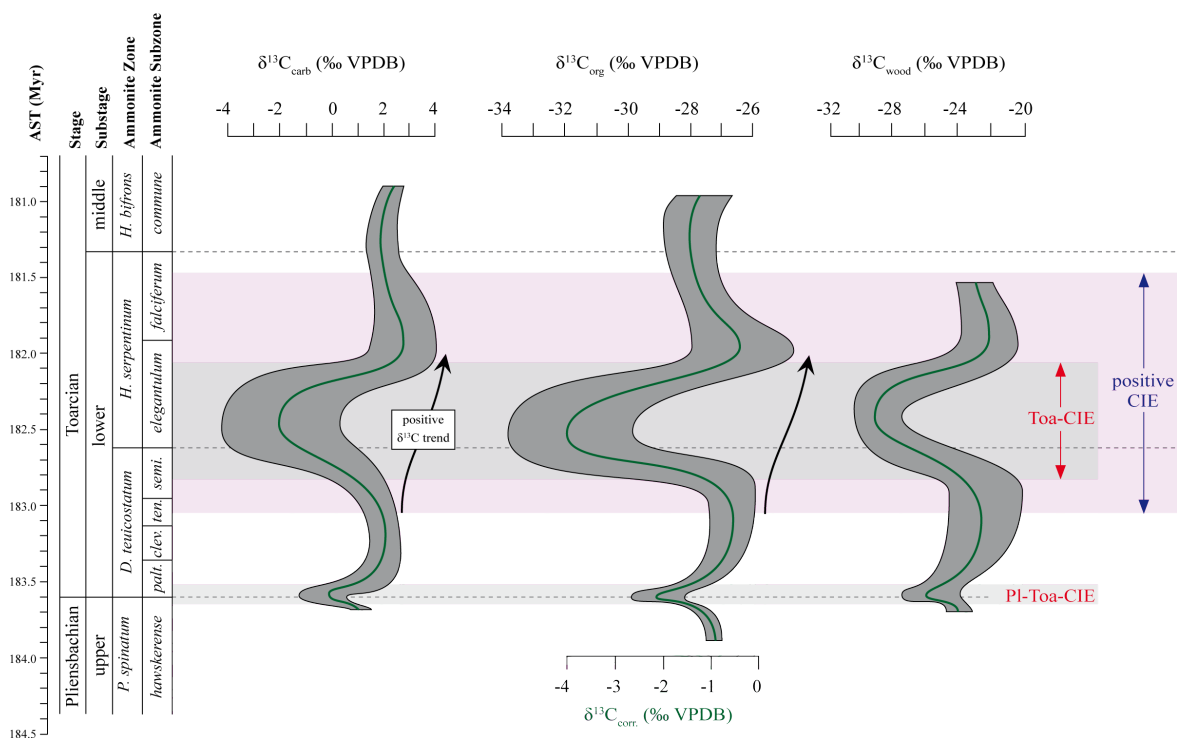


Figure 1-8: Generalized carbon isotope stratigraphy for the upper Pliensbachian and lower Toarcian (modified from Kemp et al., 2011 and references therein). The carbon isotope record shows two negative excursions at the Pliensbachian-Toarcian boundary (PI-Toa-CIE) and within the uppermost *D. tenuicostatum* zone and *H. elegantulum* subzone (Toa-CIE), respectively. The magnitude of the main Toa-CIE varies between -3 and -7‰, whereby values corrected for different organic matter sources result in a magnitude of about -3 to -4‰ (Suan et al., 2015; Montero-Serrano et al., 2015). The positive CIE spans the upper *H. elegantulum* and lower *H. falciferum* subzones.

High-resolution $\delta^{13}\text{C}$ -records with sufficient sample resolution have shown that the shift to lower isotope values occurred in discrete steps that might reflect single carbon injections into the earth ocean-atmosphere system (Kemp et al., 2005; Hesselbo & Pieńkowski, 2011; Hermoso et al., 2012). Five shifts can be distinguished. Shift 1 and 2 correspond to the pre-excursion interval, whereas shift 3 to 5 can be attributed to the main Toa-CIE (Fig. 1-9). According to Kemp et al. (2005, 2011) these distinct pulses reflect astronomically forcing carbon injections. Durations calculated for the Toa-CIE by cyclostratigraphy range from ~0.2 to ~0.9 Myr (Kemp et al., 2005, 2011; Suan et al., 2008; Sabatino et al., 2009; Huang & Hesselbo, 2014), whereby Sr-isotope trends indicate a duration of roughly 0.5 Myr (McArthur et al., 2000). The release of ^{13}C -depleted carbon from gas hydrates has been taken into account as a possible carbon source (e.g. Hesselbo & Pieńkowski, 2011; Hesselbo et al., 2000, 2007; Kemp et al., 2005). This however raises questions about gas hydrate storage and mechanisms of carbon release and is further difficult to reconcile with a duration longer than 0.2 Myr. Other authors suggested the release of ^{12}C -enriched CH_4 from magmatic intrusions into organic-rich sediments during the emplacement of the Karoo Large Igneous Province (McElwain et al., 2005; Svensen et al., 2007). Alternatively it has been suggested that the Toa-CIE resulted from the emission of CO_2 from the Karoo-Ferrar volcanism (e.g. Suan et al., 2008; Brazier et al., 2015). However, volcanic carbon emissions fail to explain the astronomically forced periodicity documented in the Toa-CIE pattern (Kemp et al., 2005, 2011; Huang & Hesselbo, 2014).

Introduction and Synopsis

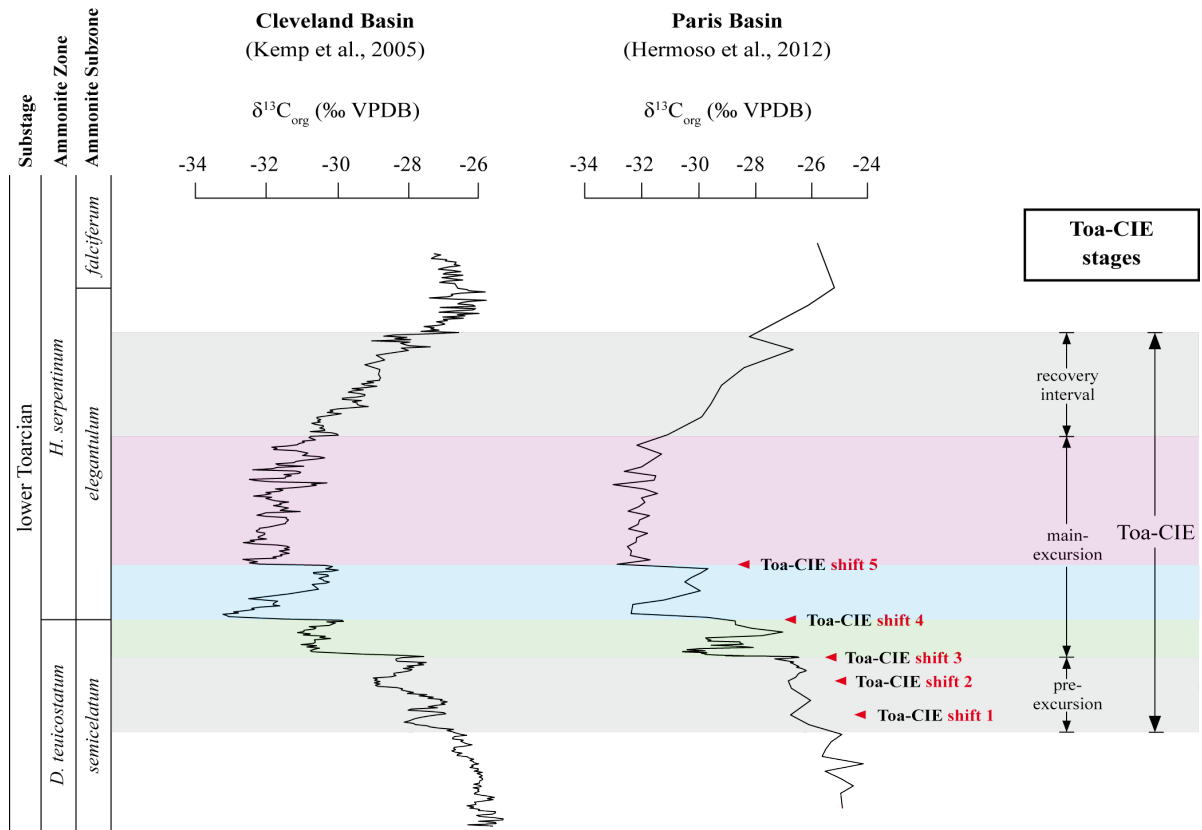


Figure 1-9: High-resolution carbon isotope records from the Cleveland and the Paris Basin exhibit strong similarities in pattern and pacing of the Toa-CIE. The tripartite nature, proposed by Kemp et al. (2005) is also evident from the Paris Basin (Hermoso et al., 2012). Calculated durations vary strongly and range from ~0.2 to ~0.9 Myr (see text for discussion).

1.2.3. Toarcian climate evolution and climate zones

Pliensbachian-Toarcian climate evolution

The Toarcian climate (as well as the Jurassic climate) is subject of controversial discussion and in the focus of ongoing research. Originally, the Jurassic has been attributed to a greenhouse period without significant changes throughout the period. The equator-pole gradient is assumed to have low and the existence of persistent polar ice has been ruled out (e.g. Frakes et al., 1992; Hallam, 1994). This view has been changed fundamentally by recent works showing drastic climate changes during the Jurassic, comprising icehouse, greenhouse as well as extreme hothouse periods (Vaughan, 2007; Dera et al., 2011a). These works provide strong evidence that the late Pliensbachian correspond to cold stage (icehouse) prior to a rapid global warming of about 7°C that occurred in the Lower Toarcian within less than 0.5 Myr (Dera et al., 2011a). The rapid warming event in the Lower Toarcian can be inferred from the evolution of oxygen isotope data (e.g. Rosales et al., 2004; Suan et al., 2010) and stomata analysis indicating a drastic rise in $p\text{CO}_2$ (McElwain et al., 2005). Changes in the distribution of clay mineral assemblages (e.g. Dera et al., 2009a; Branski, 2012) indicate an increase in humidity resulting in enhanced continental leaching (Cohen et al., 2004) (Fig. 1-10).

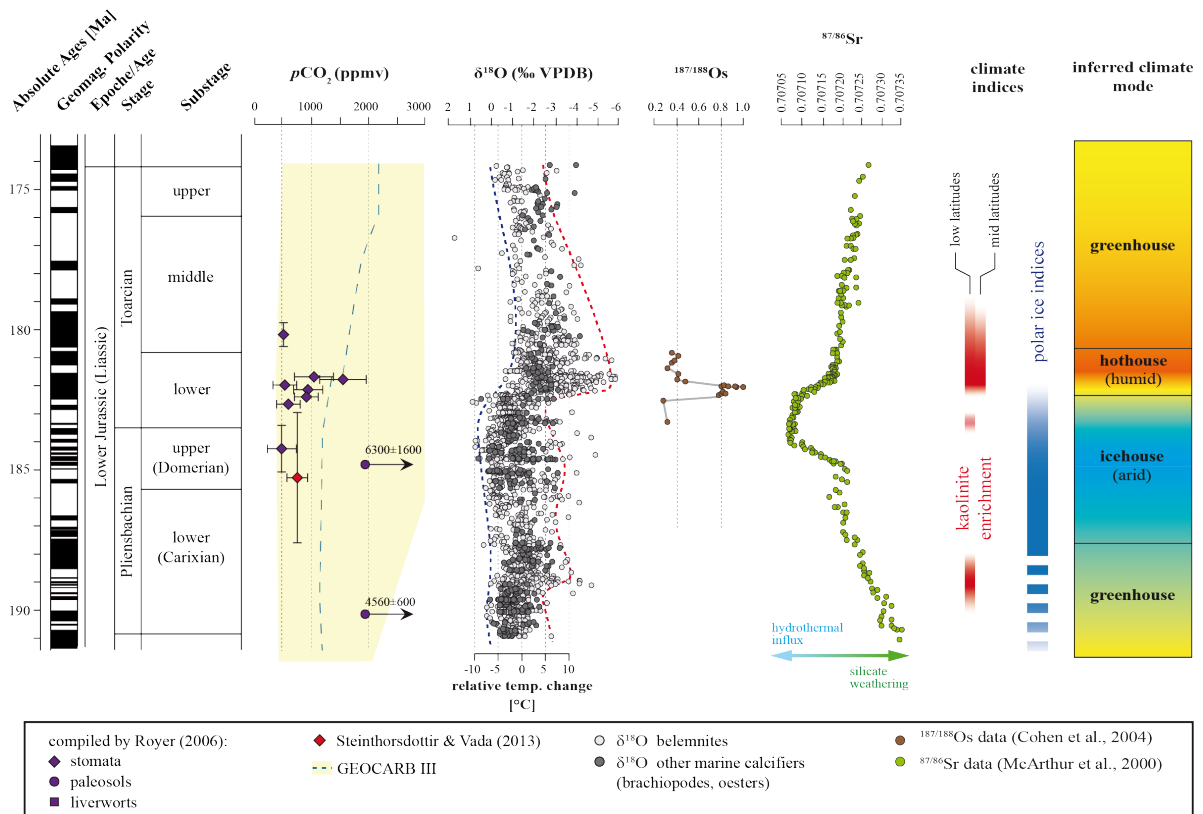


Figure 1-10: The Pliensbachian and Toarcian climate evolution deduced from sedimentological and geochemical parameters. Several lines of evidence hint to cold climate conditions (icehouse) during the late Pliensbachian prior to a global warming that occurred during the early Toarcian. The rapid warming that occurred during the Early Toarcian resulted in hothouse conditions (also see Dera et al., 2011a; Silva & Duarte, 2015). Oxygen isotope data were collected from numerous sources (see table S1-2).

The Late Pliensbachian-Early Toarcian climate evolution is also expressed in the evolution of faunal and floral realms. The Late Pliensbachian cooling is evident from the southward migration of cold-loving marine taxa (e.g. Taylor et al., 1984; van de Schootbrugge et al., 2005; Arp & Seppelt, 2011; Dera et al., 2011b; Damborenea et al., 2013), whereas the development of an endemic Arctic fauna during the Pliensbachian indicates strong latitudinal contrasts in climate and oceanographic conditions (Dera et al., 2011b). The global warming during the Early Toarcian resulted in a northward migration of warm-loving Mediterranean taxa and was accompanied by a profound reorganization of faunal provinces (Fig. 1-11). The strong provincialism documented for the Pliensbachian disappeared during the Early Toarcian and was replaced by a cosmopolitan fauna (Dera et al., 2011b).

The cold climate conditions during the Pliensbachian are also indicated by the absence of warm-loving vegetation at high latitudes in pre-Toarcian strata, whereas the Early Toarcian warming is expressed by northward migration of thermophilic vegetation and an increase in the abundance of *Classopollis* associated with warm-loving *Cheirolepidiaceae* (Vakhrameev, 1991; Wang et al., 2005; Wade-Murphy et al., 2006) (Fig. 1-11). Abovementioned environmental changes occurred simultaneously within the upper *D. tenuicostatum* and lower *H. serpentinum* zone.

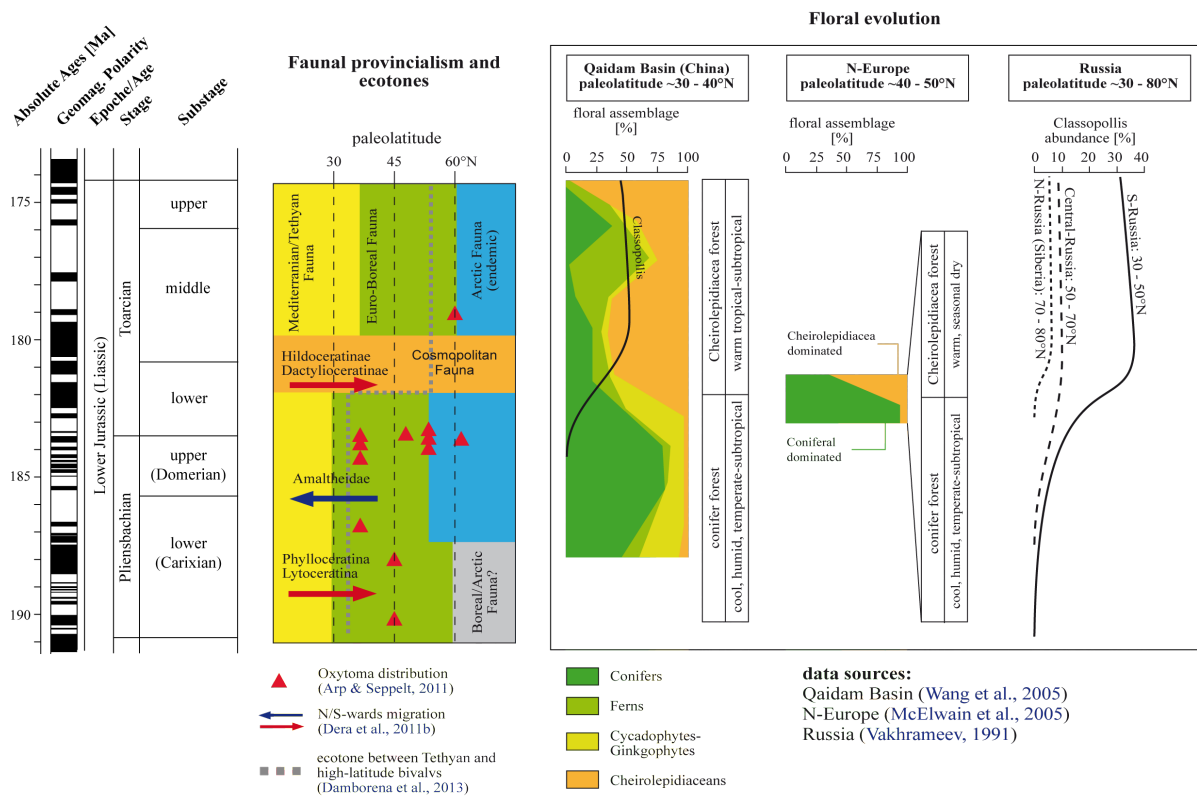


Figure 1-11: Evolution of faunal and floral realms throughout the Late Pliensbachian and Early Toarcian indicate drastic environmental changes that occurred during the uppermost *D. tenuicostatum* zone. The formation of an endemic Arctic fauna during the Late Pliensbachian is associated with a southwards expansion of Euro-Boreal faunas towards lower latitudes. The demise of the Arctic fauna during the Early Toarcian (uppermost *D. tenuicostatum* zone) was accompanied by the northwards migration of Mediterranean faunas and is also expressed by distribution of the coldwater-loving *Oxytoma*. A warming of high-latitudes expressed by the shift in faunal provinces is also reflected by a significant northwards shift of *Classopollis* associated with warm-loving *Cheirolepidiaceae*.

Glacially derived deposits and evidence for polar ice

During the Late Pliensbachian cold climates at high latitudes are indicated by the occurrence of glacially derived deposits including diamictites, tillites, exotic boulder rocks and glendonites that were reported from Siberia (Epshteyn, 1978; Kaplan, 1978; Price, 1999; Suan et al., 2013a). More recently glendonites, documented in Late Pliensbachian sediments from northern Germany corresponding to a paleolatitude of about 45°N (Teichert & Luppold, 2012), indicate that cold climates might have extended to mid-latitudes (Fig. 1-12). The occurrence of these glendonites has been debated controversially and was rather attributed to methane seeps than to cold climates (Teichert & Luppold, 2012). However, glacially derived deposits in combination with fossil plants diagnostic for cold climates were documented in Late Pliensbachian/Early Toarcian sediments from similar paleolatitudes (Tchoumatchencoet al., 2008). Furthermore, it is interesting to note that recent methane seeps were documented most frequently along permafrost boundaries boundary (Anthony et al., 2012). Thus it can be argued that glendonites from N-Germany were formed at methane seeps at water temperatures below 7°C, which has been assumed as the temperature limit for ikaite formation (Buchardt et al., 1997; Rickaby et al., 2006).

The existence of polar ice is also indicated by a significant coupling of climate and sea level changes during the Pliensbachian and Early Toarcian (Brandt, 1986; Suan et al., 2010; Korte & Hesselbo, 2011; Pittet et al., 2014), whereby the Early Toarcian warming event can be associated with a rapid sea level rise of about 30 to 90 m (Hallam, 1997). According to the timescale proposed for the Early Toarcian the climate change and sea level rise occurred rapidly and cannot be explained by tectonic processes or thermal expansion of ocean water (e.g. Pitman & Golovchenko, 1983). Furthermore, rapid high-amplitude sea level fluctuations during the Lower Toarcian indicate glacio-eustatic mechanisms as driving factors for sea level changes (Pittet et al., 2014).

Distribution of climate-sensitive sediments and inferred climate belts

The distribution patterns of climate sensitive sediments (e.g. like coals, evaporites, desert sands) and vegetation realms are common tools to reconstruct past climate belts (e.g. Parrisch et al., 1982; Ziegler et al., 1994; Rees et al., 2000; Ziegler et al., 2003). Several attempts that use the distribution patterns of fossil vegetation have been undertaken to reconstruct Jurassic climate belts. As a result of poor stratigraphic control of terrestrial paleovegetation, only Early, Middle and Late Jurassic epochs can be distinguished (Ziegler et al., 1994; Rees et al., 2000). The poor temporal resolution (5 – 20 Myr) does not allow the identification of periods reflecting contrasting climates or rapid climate changes within a single epoch (Dera et al., 2011a). In the case of the Early Jurassic it must be assumed that floral realms and inferred climate belts, proposed by Ziegler et al. (1994) or Rees et al. (2000), represent only an average view and sum up data from the cooler Sinemurian/Pliensbachian and the warmer Hettangian and Toarcian. Thus, it can be assumed that the northern limit of paleovegetation documented for the Early Jurassic reflects the warm climate extreme of these epochs (Hettangian, Toarcian) and is thus not representative for the extent of climate belts during cold stages (Sinemurian, Pliensbachian). Additionally, it has been confirmed that the Early Jurassic records a pronounced equator-pole zoning, with the boundary between warm

and cool temperate floras situated at about 45°N (Ziegler et al., 1994; Rees et al., 2000). The northwards extent of Early Jurassic vegetation and coal was mainly limited to latitudes between 60 and 70°N, whereas coal deposits attributed to the Pliensbachian stage show a southward shift with a maximum of coal formation at about 50°N (Parrish et al., 1982). The northern limit of Jurassic coal deposits and vegetation shows a similar latitudinal extent of to that Holocene peat (Markwick, 2007), indicating similar climate conditions at these latitudes. It is further interesting to note that the present day tree line is situated at about 70°N (Brown et al., 1997). It can therefore be assumed that the tree line during the Pliensbachian was situated at similar latitudes.

These data indicate that the Pliensbachian was characterized by a strong equator-pole gradient. This gradient is well expressed by the distribution of climate sensitive sediments (e.g. Parrish et al., 1982) and by the extent of vegetation realms (Ziegler et al., 1994; Rees et al., 2000). Reconstructed surface temperatures estimated from climate models for the Early Jurassic exhibit a similar pattern (Fig. 1-12), whereby extreme cold temperatures were reconstructed for mid and high latitudes of northern Pangaea (Chandler et al., 1992; Golonka et al., 1994).

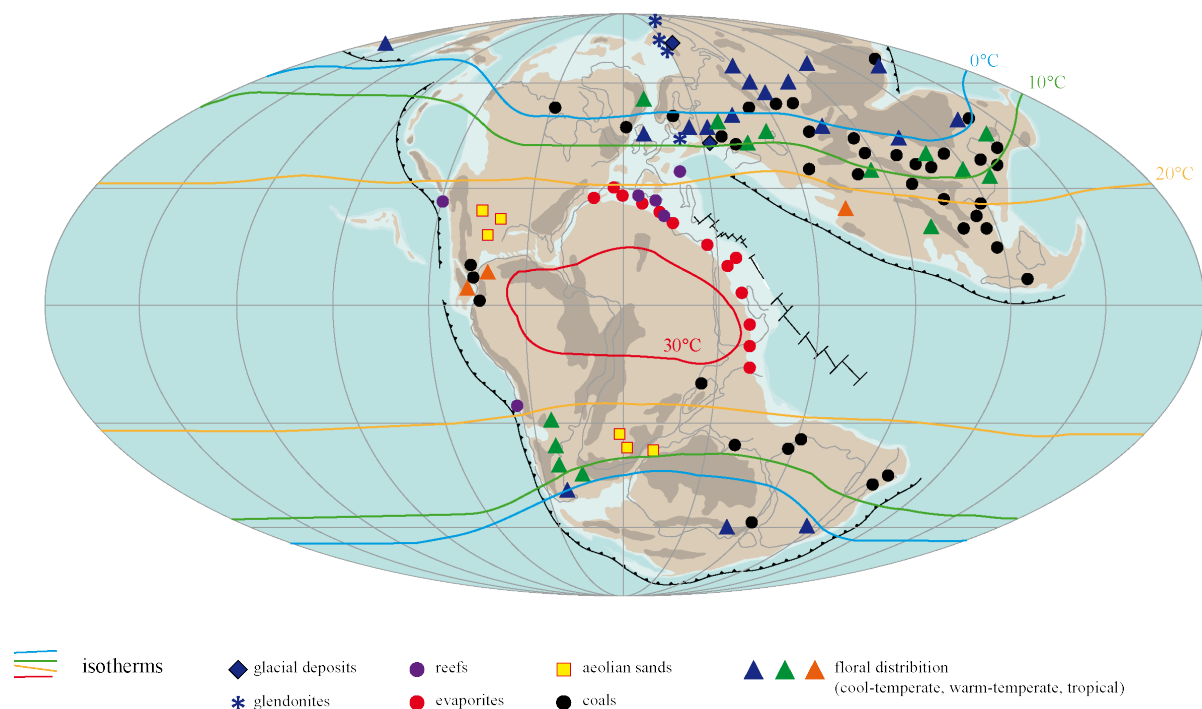


Figure 1-12: Distribution of climate sensitive sediments (glacial deposits, coals, aeolian sands, evaporites) and floral realms. The overall distribution of climate sensitive sediments is in good agreement with modeling results that propose a strong equator-pole gradient, whereby cold climate conditions prevailed at latitudes above 60°. However, this map provides only an averaged view of the Early Jurassic, an epoch comprising strongly contrasting climate conditions, including icehouse as well as greenhouse periods (see text for references and detailed discussion).

1.2.4. Role and timing of the Karoo-Ferrar volcanism

Eruptions of large igneous provinces have assumed to be a major trigger for environmental instabilities and mass extinctions (e.g. [Bond & Wignall, 2014](#)). An example being the causal and temporal connection between the emplacement of the Karoo-Ferrar Large Igneous Province (K-F-LIP) and the Toarcian environmental crisis, which is indicated by several lines of evidence (e.g. [Pálffy & Smith, 2000](#); [Caruthers et al., 2014](#)). The emplacement of the K-F-LIP in southern Africa, Antarctica, southern Australasia and Tasmania can be linked to breakup of Gondwana that started in the Late Pliensbachian to Early Toarcian period ([Encarnación et al., 1996](#); [Riley & Knight, 2001](#)). Both magmatic provinces consist of large basalt lava flows, dike swarms and sill complexes that were emplaced nearly simultaneously during distinct short-term events ([Jourdan et al., 2007, 2008](#); [Moulin et al., 2011](#); [Svensen et al., 2012](#)) within a period of about 5 Myr between 185 and 180 Ma BP (e.g. [Encarnación et al., 1996](#); [Riley et al., 2006](#); [Jourdan et al., 2008](#)). The Ferrar LIP is represented by the Kirkpatrick Basalt, the Dufek layered mafic intrusion and numerous sills that were emplaced within a period of about 350 kyr, with the onset of magmatic activity being dated to 182.8 Ma BP using high-precision U-Pb techniques ([Burgess et al., 2015](#)). The geomagnetic polarity of the Kirkpatrick Basalt is exclusively of normal polarity and thus supports rapid emplacement ([Bachtadse & Rolf, 2012](#); [Lemna et al., 2015](#)). The age of the Karoo-LIP is less constrained. Absolute ages (mainly K/Ar and $\text{Ar}^{40}/\text{Ar}^{39}$) indicate that the entire province was emplaced in a period of 8 – 10 Myr with an activity peak occurring between 185 and 180 Ma BP (e.g. [Jourdan et al., 2007, 2008](#)). Precise U-Pb dating of sills and dykes resulted in ages of 183.7 ± 0.6 ([Encarnación et al., 1996](#)), 182.5 ± 0.4 ([Svensen et al., 2007](#)), 183.0 ± 0.5 to 182.3 ± 0.6 ([Svensen et al., 2012](#)), 183.0 ± 0.1 to 181.0 ± 0.2 ([Sell et al., 2014](#)) and 182.3 ± 0.1 ([Burgess et al., 2015](#)) for the intrusive magmatism in the Karoo province. These dates are in good agreement with ages calculated for the Ferrar province, while a slightly older date (~ 500 kyr) has been calculated for the onset of the Karoo volcanism ([Burgess et al., 2015](#)). Extrusive magmatism in the Karoo province occurred in two major phases ([Moulin et al., 2011](#); [Moulin et al., 2012](#); [Gourtillet & Fluteau, 2014](#)), an older volumetrically minor one (basal Lesotho Basalt, Letaba River Basalt) and a younger volumetrically major one (upper Lesotho Basalt, Sabi River Basalt, Botswana Basalt). Basalts belonging to the initial stage are of reverse magnetic polarity ([Hargreaves et al., 1997](#); [Moulin et al., 2011](#); [Gourtillet & Fluteau, 2014](#)). K/Ar (and $\text{Ar}^{40}/\text{Ar}^{39}$) datings of the basalts indicate an age of $\sim 184 \pm 2$ My BP ([Duncan et al., 1997](#); [Jourdan et al., 2007, 2008](#); [Moulin et al., 2011](#)). Basalts attributed to the main extrusive phase are exclusively of normal magnetic polarity ([Hargreaves et al., 1997](#); [Moulin et al., 2011](#); [Gourtillet & Fluteau, 2014](#)) and were emplaced between 181 ± 2 and 183 ± 2 Ma BP ([Duncan et al., 1997](#); [Jourdan et al., 2007, 2008](#); [Moulin et al., 2011](#)). Despite of the large error bars, geomagnetic data support a rapid emplacement of the Karoo basalts within brief events ([Hargreaves et al., 1997](#); [Moulin et al., 2011](#); [Moulin et al., 2012](#); [Gourtillet & Fluteau, 2014](#)). A detailed comparison of these ages with ages from U-Pb dating is problematic due to a possible miscalibration of the ^{40}K decay constant resulting in a $\sim 1\%$ shift of K/Ar (and $\text{Ar}^{40}/\text{Ar}^{39}$) ages towards younger values (review in [Jourdan et al., 2008](#); [Mundil et al., 2006](#); [Pálffy, 2008](#)). However, synthesis of

geomagnetic information and available data on absolute ages indicate that the Karoo-Ferrar volcanism started in the uppermost Pliensbachian and continued into the lower Toarcian, with the peak activity occurring during the *tenuicostatum* zone (Fig. 1-13). The initial magmatic activity in the Karoo province is represented by several intrusions as well as by the emplacement of the basal Lesotho and Letaba River basalts (both are mainly of reverse magnetic polarity). This initial stage might be responsible for the minor Pl-Toa-CIE observed at the Pliensbachian-Toarcian boundary. Based on geomagnetic and stratigraphic data, the main activity phase of the Karoo province, characterized by the rapid emplacement of the upper Lesotho, Sabi River and Botswana Basalt as well as by intrusive magmatism occurred simultaneously with the Ferrar magmatism (e.g. Encarnación et al., 1996; Riley et al., 2006).

The peak activity of the Karoo-Ferrar volcanisms took place between 184 to 182 Myr BP, while the emplacement of the voluminous flood basalts occurred between 183.3 and 182.4 Ma, corresponding to the *D. tenuicostatum* zone. The chronology proposed for the emplacement of the Karoo-Ferrar-LIP clearly hint at a temporal connection between volcanic activity and environmental instabilities. Thus, the K-F-LIP can be assumed to be the major trigger of the Early Toarcian Environmental Crisis.

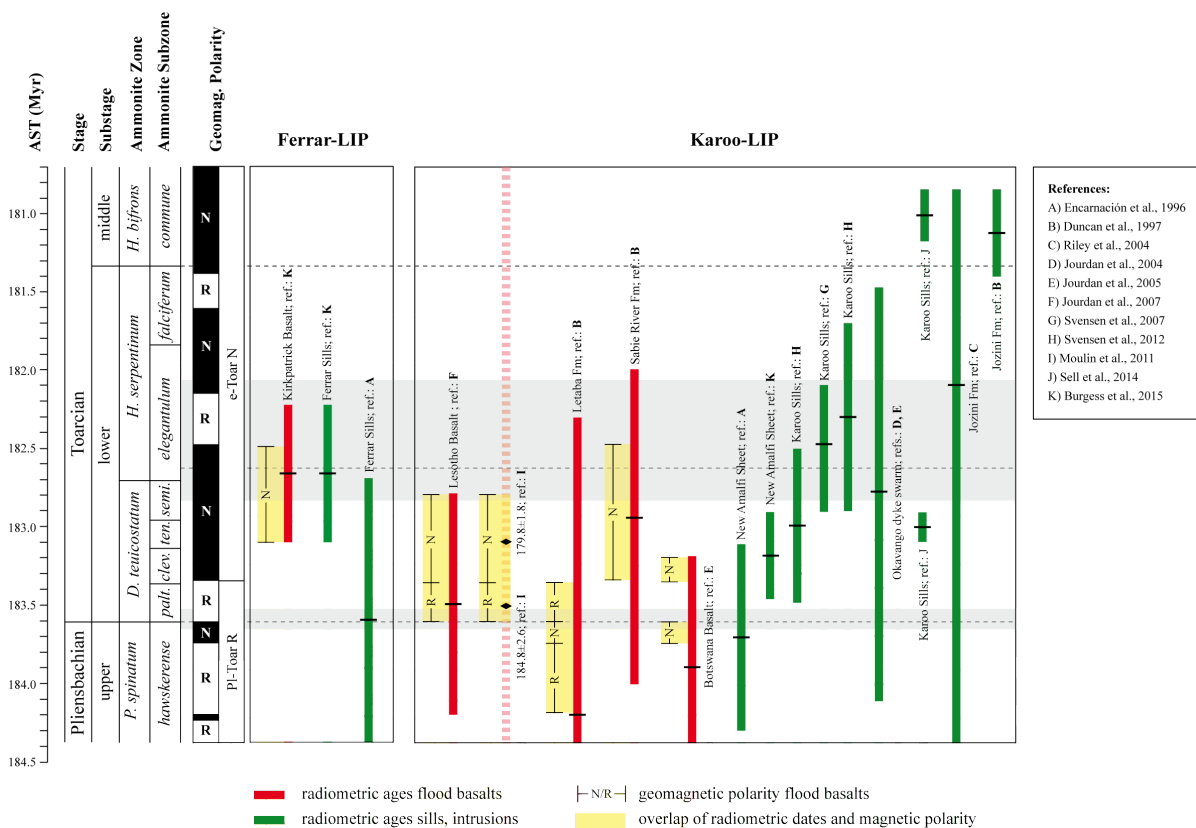


Figure 1-13: Summary of radiometric dates for the emplacement of igneous rocks associated with the Karoo-Ferrar-LIP. Radiometric dates in combination with geomagnetic information available for flood basalts allow to correlate the peak activity of the Karoo-Ferrar volcanism with Toarcian environmental crisis.

1.2.5. Toarcian black shales and anoxia

Organic-rich sediments (black shales, see Wignall, 1994) of Early Toarcian age are widely distributed throughout northwestern Europe and the Mediterranean (Fig. 1-14B) (e.g. Farrimond et al., 1988; 1994; Jenkyns, 1988; Baudin et al., 1990; Bassoulet & Baudin, 1994). Contemporaneous bituminous facies have also been documented from Canada, Alaska, Argentina, Madagascar, Japan and Australia (Jenkyns, 1988). The widespread occurrence of Early Toarcian bituminous deposits that are limited to oxygen depleted environments let to the assumptions that they correspond to a Toarcian Oceanic Anoxic Event (T-OAE) (Jenkyns, 1985). In stratigraphically well constrained sections throughout Europe, Early Toarcian black shales mainly correlate to the upper *D. tenuicostatum* zone and the *H. serpentinum*/*H. falciferum* zone, whereby onset and stratigraphic extent can differ strongly (Fig. 1-14A) highlighting the role of local controls towards organic matter accumulation (Wignall et al., 2005; McArthur, 2007; McArthur et al., 2008a, 2008b). Black shale deposition occurred during a phase of rapid sea level rise (Röhl et al., 2001; Hermoso et al., 2013) and global warming (Dera et al., 2011a) leading to an intensification of continental weathering rates (Cohen et al., 2004) which in turn stimulated the primary productivity and water column stratification (Hermoso et al., 2013). Differences in onset and stratigraphic extent of black shale deposition reflect different paleogeographic settings and hydrodynamical regimes (Hermoso et al., 2013).

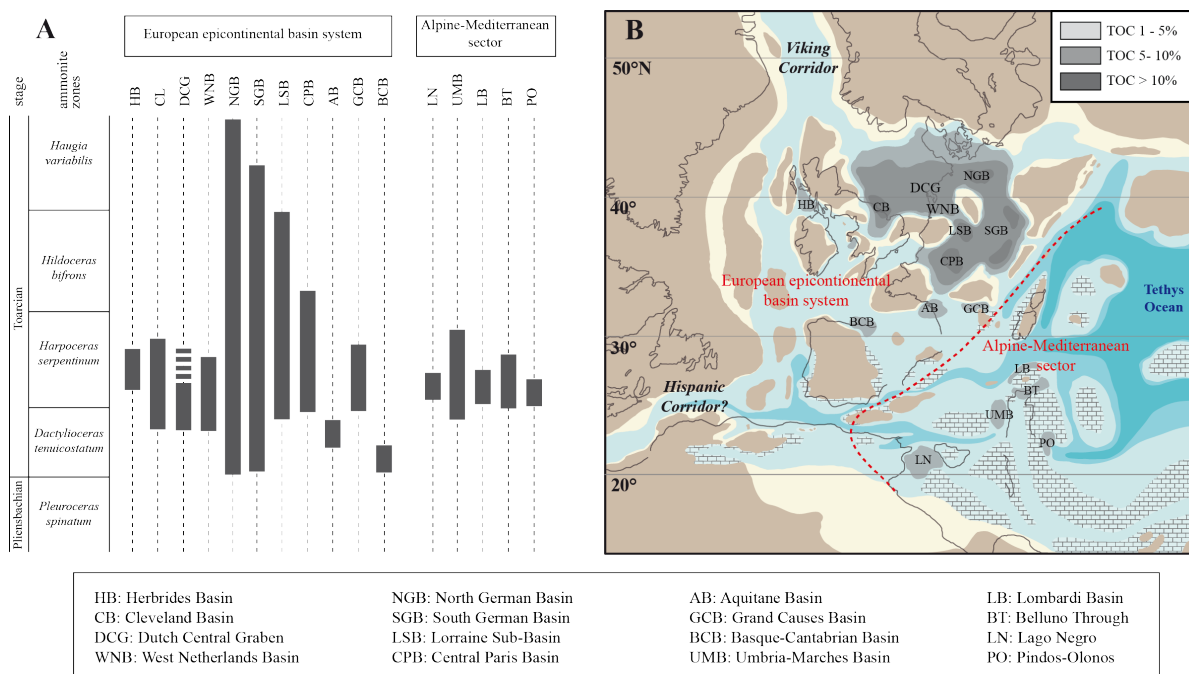


Figure 1-14: A) Stratigraphic distribution of bituminous facies throughout the latest Pliensbachian and early Toarcian throughout the European epicontinental shelf and the Alpine-Mediterranean sector (Riegraf, 1985; Fleet et al., 1987). **B)** Spatial distribution of bituminous facies corresponding to the Early Toarcian Oceanic Anoxic Event, deposited during the upper *D. tenuicostatum* zone and the *H. serpentinum* zone (Baudin et al., 1990).

Throughout Europe bituminous sediments were accumulated in two different paleogeographic regimes, one being alongside the margins of the Tethyan Ocean (Alpine-Mediterranean region) and the other one being within the epicontinental basin system of the northwestern shelf area (northern Europe) (Fig. 1-14B) (Jenkyns, 1988; Farrimond et al., 1988). Black shales are wide spread throughout the European epicontinental basin and show a high organic matter content (TOC > 5 wt.%) that can be attributed to kerogen type II (Baudin et al., 1990). Black shales of the Mediterranean-Alpine sector show a lower organic matter content (TOC < 2 wt.%) and are limited to restricted basins. Organic matter from these basins is also of kerogen type II but is in general less well preserved.

1.3. Motivation and objectives

Despite of numerous studies spanning the fields of paleontology, sedimentology and geochemistry, major questions concerning the underlying mechanisms that lead to the profound environmental changes documented during the Early Toarcian remain unsolved. Thus, no model exists that links the different observations into a coherent Earth system concept. An exceptionally well-preserved core (FR-210-078) from southern Luxembourg, spanning from the Late Pliensbachian to the Early Toarcian, offered the possibility to study the Early Toarcian environmental changes on a remarkable temporal resolution and in a very high detail. Additional information about the study site is given in the appendix (see appendix A1).

The work presented is based on the combined use of high-resolution continuous core analysis and discrete sample analysis, comprising organic, inorganic and isotope geochemical approaches. It is anticipated that this approach allows to discuss environmental dynamics on different timescales and to distinguish long-term trends and events. An overview on the conducted analytical procedures and methodology is given in the appendix (see appendix A3).

The following major objectives are addressed in this study:

(1) Timescale and chronology of the Early Toarcian environmental crisis and the associated carbon cycle perturbation are still discussed controversially (e.g. [Suan et al., 2008](#); [Huang & Hesselbo, 2014](#); [Boulila et al., 2014](#)). However, a robust timescale is essential for the understanding of processes and mechanisms that led to the profound environmental changes documented for this time. One purpose of this study is to develop a cyclostratigraphy-based chronology for Core FR-210-078 by analyzing high-resolution data obtained from continuous core scanning of sediment color and magnetic susceptibility. The resulting robust timescale will allow the discussion of relevant processes and underlying mechanisms that resulted in the major Toa-CIE.

(2) There is strong evidence that the Western Tethyan shelf was affected by enhanced fresh water inflow resulting in brackish surface waters, at least during certain periods e.g. [Röhl et al., 2001](#); [Bailey et al., 2003](#); [Hermoso et al., 2009b](#); [Dera et al., 2009b](#); [2015](#)). However, evolution of sea surface salinity as well as possible sources of fresh water are less well constrained. This study aims to reconstruct changes in sea surface salinities and gain information on fresh water sources and water mass dynamics on the Western Tethyan shelf. This knowledge can be useful for a better understanding of the mechanisms controlling the fresh water supply. Furthermore, identifying freshwater sources might allow to draw conclusions about environmental and climatic conditions.

(3) Water column stratification, rise in sea level and eutrophication have been assumed to drive organic matter accumulation on the Western Tethyan shelf (e.g. [Röhl et al., 2001](#); [Hermoso et al., 2013](#)). A purpose of this study is to reconstruct the dynamics of shelf sea anoxia and photic zone euxinia and their implication on inorganic, organic and isotope geochemical parameters. Particular attention is paid to factors controlling the proposed restriction of the Western Tethyan shelf sea and the water exchanges with the Arctic and Tethyan Oceans (e.g. [McArthur et al., 2008a](#)).

(4) Studying dynamics of marine primary producer communities during periods of enhanced ecological stress are of major importance for our understanding of marine ecosystems and can help evaluating the impact of global warming and rising atmospheric CO₂ concentration on community structures. Numerous works focused on the evolution calcareous nannofossils (e.g. [Mattioli et al., 2008](#); [Fraguas et al., 2012](#)) or organic-walled phytoplankton ([van de Schootbrugge et al., 2005](#)) during the Late Pliensbachian and Early Toarcian. However, these groups represent only a minor part of the overall marine primary producer communities. The response of primary producers without hard-fossil structures or skeletons, representing the majority of marine primary producers, has not been investigated with a sufficient resolution. It is anticipated that the detailed analysis of steroid biomarkers will provide insights into to response of marine phytoplankton to the Early Toarcian environmental changes.

Answering these questions will enhance our understanding of past climate and environmental changes and can provide vital insights in the underlying mechanisms. This knowledge might also help understanding recent and future climate changes and may allow to predict the impact of anthropogenic-introduced global warming.

Chapter Two:

Chronology of the Early Toarcian environmental crisis

Abstract

Early Toarcian (Jurassic; ~183 Ma) sediments recorded profound environmental changes, including mass extinction, global warming, marine transgression as well as widespread bottom water anoxia and organic matter accumulation on the Western Tethyan shelf. Enhanced organic matter accumulation was accompanied by a positive carbon isotope excursion (CIE) in pelagic carbonate, which marks the Toarcian Oceanic Anoxic Event. These environmental changes were accompanied by a major perturbation of the global carbon cycle, expressed by negative CIE, interrupting the positive trend. The duration of the carbon cycle perturbation is still debated, with estimates for the negative CIE range from ~200 to ~600 kyr. Here we present ultra high-resolution (<1kyr) measurements of magnetic susceptibility and sediment color from a marine section located in the Lorraine Sub-Basin (NE Paris Basin) documenting Milankovitch-controlled fluctuations in depositional conditions that occurred superimposed onto the overall sea level evolution. Differences in the wavelength of the sedimentary cycles indicate variable sediment accumulation rates that mainly resulted from rapid sea level fluctuations. The most pronounced sea level rise that took place within the uppermost *D. tenuicostatum* zone resulted in a strong condensation of the basal Schistes Carton formation. Strong condensation can explain the discrepancy between durations previously calculated for the CIE placed at this stratigraphic interval. Our data support durations of ~900 kyr and ~600 kyr for the positive and negative CIE, respectively. The cyclostratigraphy-based timescale further proposes a duration of >555 kyr for the *D. tenuicostatum* zone and ~1300 kyr for the *H. serpentinum* zone. The durations of the *H. elegantulum* and *H. falciferum* subzones can be estimated to ~790 kyr and ~520 kyr, respectively. A change in the orbital response from eccentricity- to obliquity-forcing, evident from other locations, is well-expressed in the Lorraine Basin and occurred within the CIE interval. The strong impact of the obliquity component in post-event deposits hints to processes most effective at high latitudes, such as the waxing and waning of polar ice. Paleogeographic features of the Western Tethyan shelf supported the tele-connection of higher to lower latitude processes via water exchange through the Viking corridor.

2.1. Introduction

The Early Toarcian (Early Jurassic, ~183 Ma BP) is highlighted by its event-character including mass extinctions at the Pliensbachian-Toarican boundary and at the *D. tenuicostatum*-*H. serpentinum* boundary (Harries & Little, 1999; Caswell et al., 2009). Both extinction intervals are marked by pronounced negative shift in carbon isotope values recorded in organic matter and carbonate, which indicate (global) perturbations of the carbon cycle (Hesselbo et al., 2000; 2007; Suan et al., 2008; Littler et al., 2010; Kemp et al., 2005; 2011). Extinction events and carbon cycle perturbations occurred during a period of rapid global warming that may mark the transition from an icehouse to a greenhouse world (e.g. Suan et al., 2008; Dera et al., 2011a; Silva & Duarte, 2015 and references therein). Global warming caused an acceleration of the hydrological cycle (Cohen et al., 2004) and led to an eutrophication of the Tethyan shelf seas that contributed to the widespread deposition of organic-rich sediments (Baudin et al., 1990), which are attributed to the Toarcian Oceanic Anoxic Event (T-OAE) (Jenkyns, 1988). A fundamental reorganization of the global climate system that resulted in changes in the water storage is documented by a shift from eccentricity- and precession- to obliquity-dominant orbital forcing as evident from cyclostratigraphic investigations at locations across the Western Tethyan shelf (Hinnov and Park, 1999, Suan et al., 2008; Huang & Hesselbo, 2014). Furthermore, rapid high-amplitude (glacio-eustatic) sea level fluctuations, superimposed on the 2nd order transgression that occurred throughout the *D. tenuicostatum* and *H. serpentinum* zones (Hardenbol et al., 1998 and Gély and Lorenz, 2006), resulted in highly fluctuating depositional conditions and led to the formation of depositional hiatuses and condensed stratigraphic intervals that are documented for the upper Pliensbachian and lowermost Toarcian (e.g. Röhl & Schmidt-Röhl, 2005, Léonide et al., 2012 and Pittet et al., 2014).

Due to the event character of this period a robust timescale is of major importance for the understanding of triggering mechanisms, especially for those causing the pronounced carbon cycle perturbation that is closely related to the T-OAE (Hinnov & Park, 1999; Suan et al., 2008; Kemp et al., 2011; Huang & Hesselbo, 2014; Boulila et al., 2014). Timescale and chronology of the Early Toarican environmental crisis and carbon cycle perturbation are topic of ongoing controversial discussion, whereby durations of ammonite zones and the carbon cycle perturbation mainly base on floating chronologies as discrete time lines (e.g. tephra layers, intrusions, etc.) are not available for biostratigraphic and chemostratigraphic well-constrained sections. However, floating chronologies based on cyclostratigraphy are subject to contrasting interpretation and discussion as exemplified for the Early Toarcian by previous contributions that calculated durations between ~200 and ~900 for the Toarican carbon cycle perturbation (e.g. Suan et al., 2008; Kemp et al., 2011; Boulila et al., 2014; Huang and Hesselbo, 2014). This chapter presents a timescale at the ammonite subzone scale deduced from spectral analysis. Results highlight the importance of changes in astronomical forcing superimposed onto the general sea level evolution and reveal that changes in sea level and sediment supply result in strongly differing sediment accumulation rates that are well expressed by cyclostratigraphy. Changes in sediment accumulation rates have the potential to explain the different durations calculated for the Toarcian negative carbon isotope excursion.

2.2. Periodicity in sediments of Core FR-210-078

Sediments of Core FR-210-078, represented by the Grés médioliasiques Fm and by the Schistes Carton Fm, correspond the Late Pliensbachian (*P. spinatum zone*) and to the Early Toarican (*D. tenuicostatum zone* and *H. serpentinum zone*). Details on the biostratigraphic framework are given in the appendix A1.3 (Fig. A2). The Early Toarican carbon cycle perturbation expressed by a negative CIE in the upmost *D. tenuicostatum zone* (e.g. Hesselbol et al., 2000a; Kemp et al., 2005; Hermoso et al., 2012) is well expressed at a similar stratigraphic position in sediments corresponding the basal Schistes Carton Fm. The overall evolution of $\delta^{13}\text{C}_{\text{carbonate}}$ -data (see appendix 3.2.3 for methodology) reveals a pronounced positive excursion of about +3‰ covering the uppermost *D. tenuicostatum zone* and lower *H. serpentinum zone* (mainly *H. elegantulum subzone*), which can be associated with Early Toarican Oceanic Anoxic Event (e.g. Jenkyns & Clayton, 1997; Hesselbo et al., 2000a; also see Chapter 1.2.2.). This positive trend is interrupted by a pronounced negative carbon isotope excursion of about -5‰ at the base of the Schistes Carton Fm, represented by Interval 3 (Fig. 2-1). The initial shift to more negative values can be placed in the uppermost *D. tenuicostatum zone*, whereas the main body of the CIE as well as a subsequent gradual recovery phase can be placed in the lower *H. elegantulum subzone*. In addition, two negative spikes of -1 and -2‰, respectively, were observed within the uppermost *H. elegantulum subzone* (Fig. 2-1). Furthermore, a less pronounced negative shift of -1‰ occurs close to the Pliensbachian-Toarican boundary.

The striking negative Toa-CIE further aligns with a major facies changes marking the transition between Grés médioliasiques Fm and Schistes Carton Fm. Both formations strongly differ in their lithological characteristics, which are described in detail in the appendix A1.4.. Sediments corresponding the Grés médioliasiques Fm consist of homogenous light-grey to grey bioturbated claystones, with a mainly low carbonate content. The Schistes Carton Fm is composed of laminated grey to dark-grey bituminous marls, with exception of the basal part that consists of a bituminous claystone. However, a remarkable variability has been observed in sediments of the Schistes Carton Fm, indicating profound fluctuations in depositional conditions. Results from high-resolution measurements obtained from continuous measurements of magnetic susceptibility and sediment color (review appendix A3.1 for methodology) show a strong correlation with lithological changes and reveal a significant cyclicity that is well defined in the *H. elegantulum subzone*, less so in the *H. falciferum subzone* and seems to be absent in the Grés médioliasiques Fm. High MagS-values and low a*-values are limited to the Grés médioliasiques Fm and to the horizons within the Schistes Carton Fm that show an indistinct lamination. In contrast, laminated sediments of the Schistes Carton Fm are characterized by elevated a*- and low MagS-values (Fig. 2-1). Changes in parameter obtained from continuous core measurements can be associated with changes in the sediment compositions, whereby variations in carbonate and organic matter content obtained from bulk geochemical analysis (see appendix 3.2.1 for methodology) have the highest impact towards magnetic susceptibility and sediment color. A good positive correlation observed between total organic carbon content and a*-values indicates that changes in organic matter abundance strongly

affect this parameter (Fig. S2-1). Throughout the Schistes Carton Fm a robust negative correlation is observed between MagS-values and carbonate content, as a negative correlation is observed throughout the Grès médioliasiques Fm (Fig. S2-1).

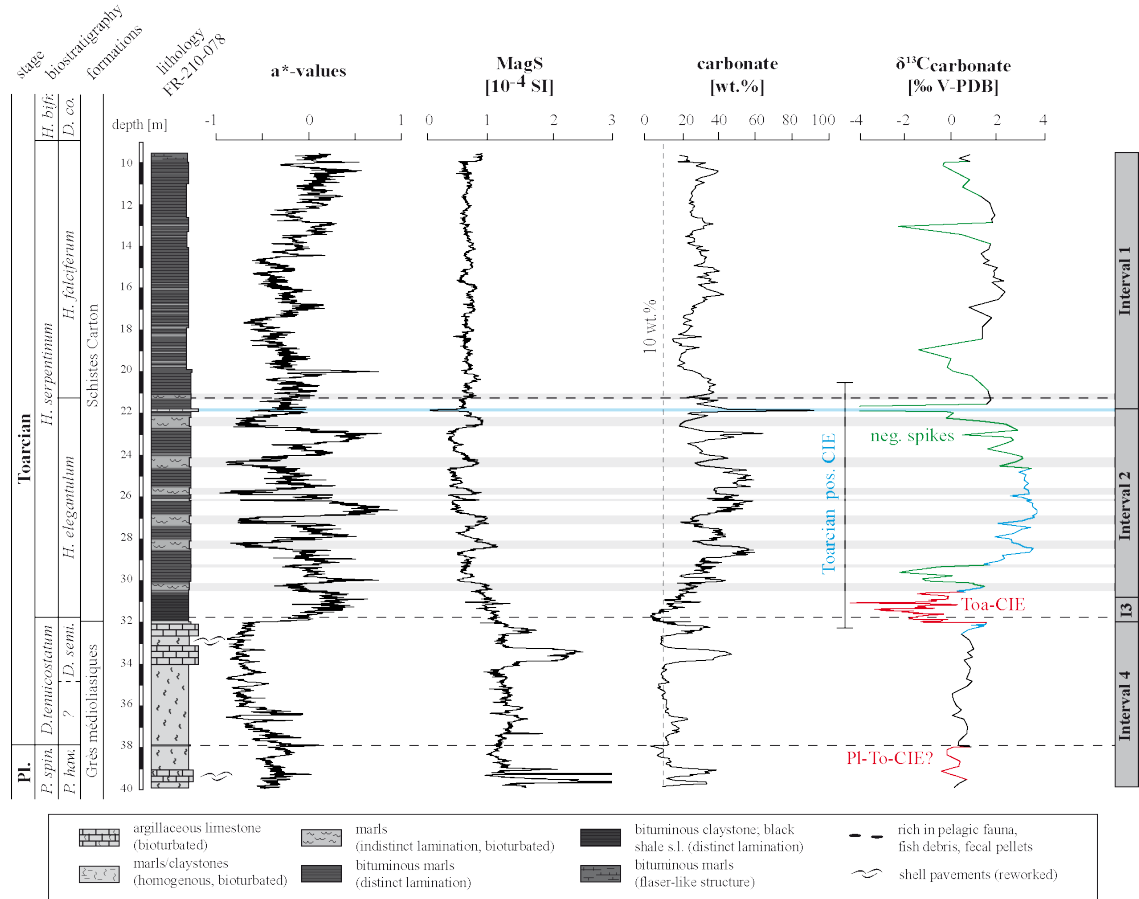


Figure 2-1: Down-core plots showing the evolution of sediment color a^* (L^* - and b^* -values not shown here), magnetic susceptibility (MagS), variations in carbonate content and $\delta^{13}\text{C}_{\text{carbonate}}$ data. Intervals 1 to 4 are distinguished on the basis of sedimentological and geochemical criteria. Indistinct-laminated intercalations identified within Interval 2 (upper *H. elegantulum* subzone) are highlighted grey, the blue mark indicates a brief carbonate-rich interval. The stratigraphic interval that corresponds to the Toarcian Oceanic Anoxic Event is well expressed by a positive carbon isotope excursion (highlighted in blue). Negative shifts in carbon isotope values are highlighted in red, the most pronounced -5% shift occurred within Interval 3 (upmost *D. tenuicostatum* zone and lower *H. elegantulum* subzone) and could be assigned to the Toarcian carbon cycle perturbation. The negative carbon isotope excursion associated with the Pliensbachian-Toarcian boundary is indicated but is not expressed very clear. Several negative spikes observed throughout the profile might result from diagenesis under the influence of organic matter (Lavastre et al., 2011; see Fig. S4-6 in the appendix) and are also documented in $\delta^{13}\text{C}_{\text{carbonate}}$ data from other location (e.g. Röhl et al., 2001; Hermoso & Pellenard, 2014). (Pl. = Pliensbachian; *P. spin.* = *P. spinatum* zone; *H. bifr.* = *H. bifrons* zone; I3 = Interval 3.)

On the base of lithological observations (e.g. sedimentation style) and bulk geochemical data four intervals (Interval 1- 4) can be distinguished in Core FR-210-078. Within the Grès médioliasiques Fm (Interval 4; 39.92 – 31.97 m) carbonate content is relatively low and varies between 10 and 20 wt.%. High carbonate content that exceeds 20 wt.% is limited to narrow horizons in the uppermost *P. spinatum* and *D. tenuicostatum* zones (Fig. 2-1). The basal Schistes Carton Fm (Interval 3; 30.75 – 31.97 m) is characterized by the lowest carbonate content (mainly <10 wt.%). The lowest values (<5 wt.%) occur at the base of this interval, as an increasing trend characterizes the upper part of Interval 3. Elevated carbonate values (>10 wt.%) within Interval 3 are restricted to narrow horizons (Fig. 2-1). Highest and most variable carbonate content is observed in Interval 2 (30.75 – 22.00 m) where values vary between ~20 and ~60 wt.%. High carbonate concentrations occur mainly in the marls that show a distinct lamination and low concentrations in the more homogenous horizons that show an indistinct lamination. A thin horizon from 21.88 to 21.79 m reaches a carbonate content of 90 wt.%. The carbonate content throughout Interval 1 (22.00 – 9.55 m) is less variable and mainly ranges from ~20 to ~40 wt.% (Fig. 2).

Throughout the Intervals 1 - 4, distinguished by sedimentological criteria, the presence of regular cycles is confirmed by spectral analysis. In Interval 1 the presence of three significant frequency peaks that correspond to wavelengths of 2.90 m, 1.05 m and 0.60 m is confirmed by spectral analysis. Hierarchy of the cycles allowed to attribute those to eccentricity (100 kyr), obliquity (35 kyr) and precession (21 kyr) forced cycles (Fig. 2-2). The presence of regular cycles with mean wavelengths of 1.10 m, 0.65 m and 0.45 m is confirmed for Interval 2. Cycle hierarchy allowed to attribute these cycles to obliquity (35 kyr) and precession (21 kyr and 15 kyr) cycles. Another frequency peak, representing a periodicity with a mean wavelength of about 3.00 m, is present in the MTM power spectrum for Interval 2 but does not reach the 90% confidence level (Fig. 2-2). This cycle most likely represents the short eccentricity component. However, due to the short sampling interval the eccentricity component was not well expressed, but appeared clearly when analyzing the entire sediment succession from 9.55 to 30.75 m (Intervals 1 + 2; Fig. S2-2; S2-3). Interval 3, representing the black shale interval (sensu lato), reveals evidence for the presence of two regular cycles with a mean wavelength of 0.20 m and 0.07 m. The wavelength ratio hints to cycles matching with those of eccentricity (100 kyr) and obliquity (35 kyr) (Fig. 2-4). Spectral analysis of the ultra-high resolution a*-data confirmed this cyclicity and further revealed evidence for the presence of a regular cyclicity with a mean wavelength of 0.04 m and 0.03 m that can be attributed to the 21 kyr and 15 kyr precession index (Fig. 2-4). Throughout Interval 4 the presence of regular cycles corresponding to wavelengths of 1.15 m, 0.50 m and 0.30 m is confirmed for the a*-data (Fig. 2-2). Cycle hierarchy allowed to attribute these cycles to 100 kyr, 35 kyr and 21 kyr orbital cycles. A strong frequency peak corresponding to a 0.50 m cycle is also evidenced in the MagS data, whereas a frequency peak corresponding to the 1.15 m cycle is indicated but didn't reach the 90% confidence level. Interestingly no frequency peak reflecting the precession parameter is observed in the MagS-data. Shifts in the cycle's wavelengths observed between the intervals reflect significant differences in the sediment accumulation rate.

Chapter Two: Chronology of the Early Toarcian environmental crisis

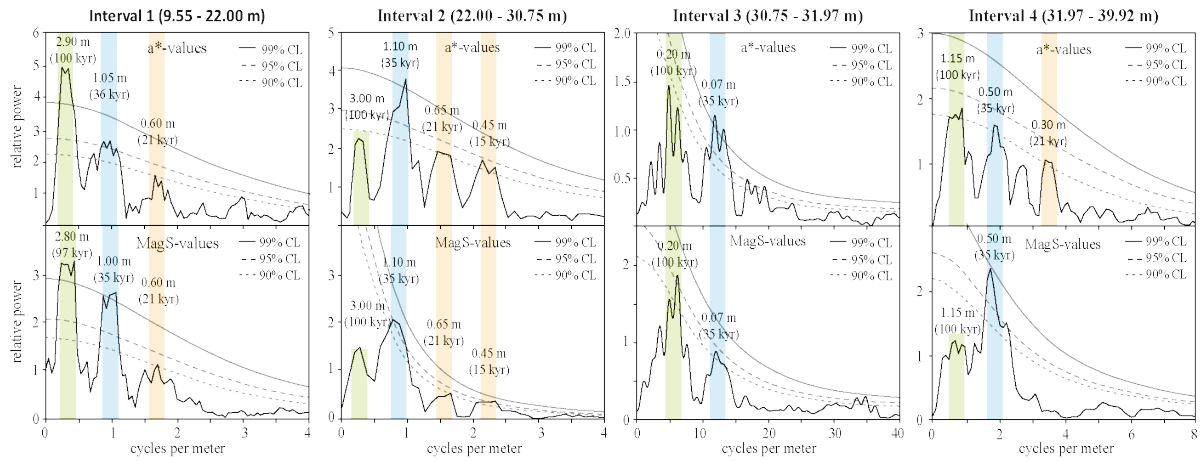


Figure 2-2: The 2π -MTM power spectrum for Intervals 1 – 4 of a^* - and MagS-core depth series (CL: confidence levels). Hierarchy of significant spectral peaks may be attributed to Milankovitch cycles. Spectral peaks attributed to eccentricity cycles (100 kyr) are marked in green, obliquity cycles (35 kyr) are marked in blue and precession cycles (21 kyr and 15 kyr) are marked in orange. The presence of a regular cyclicality within Interval 3 is confirmed by spectral analysis for the ultra-high resolution a^* -core depth series (Fig. 2-4).

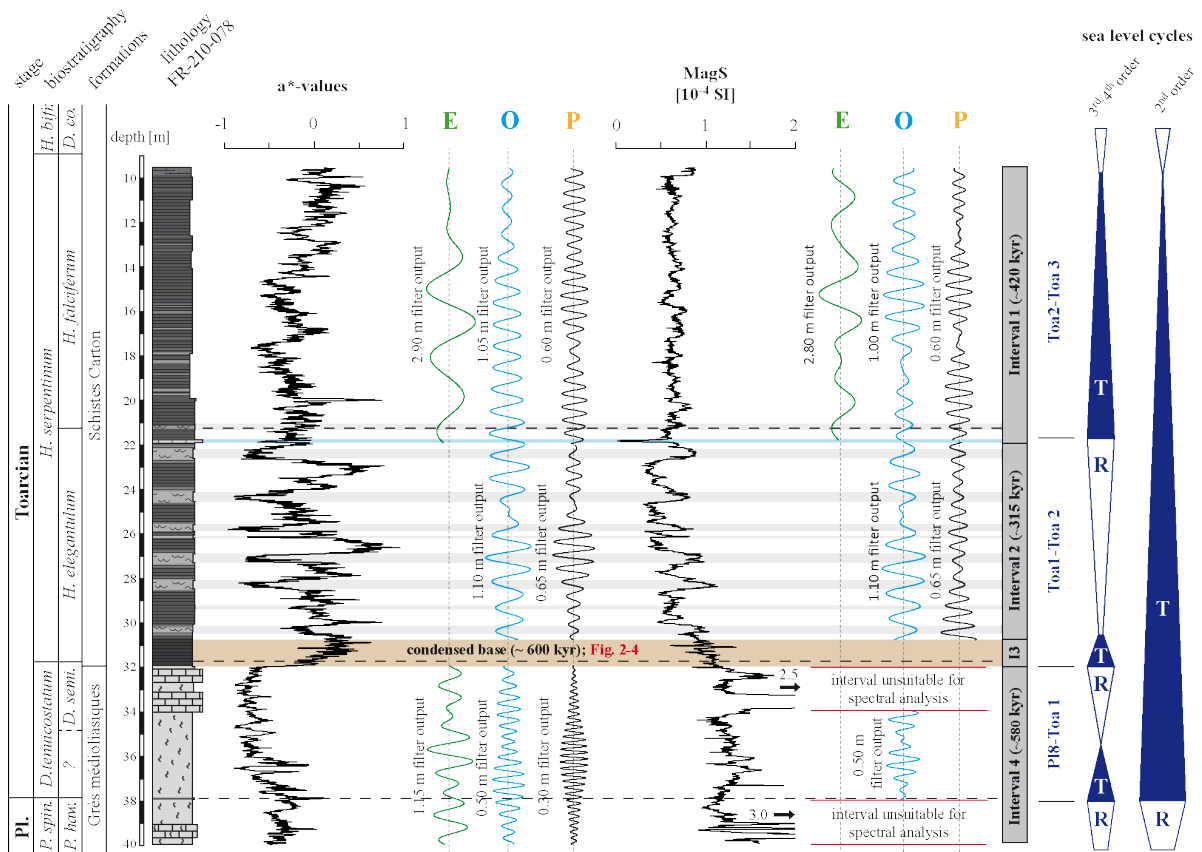


Figure 2-3: Stratigraphic and lithological chart of Core FR-210-078. Lithological changes are well expressed by sediment color and MagS-data and show a strong cyclic pattern. The periodicity closely resembles Milankovitch cycles, allowing deduction of a time scale at the ammonite subzone level (E: short eccentricity; O: obliquity; P: precession). Cycles were extracted using the Gaussian filter with a bandwidth of 0.2 for Intervals 1 and 2. A bandwidth of 0.25 was used to extract cycles in the Interval 4. Evolution of the sea level is adapted from Hardenbol et al. (1998) (also see Chapter 1.1.2). Details on the biostratigraphic framework are given in the appendix A1.3..

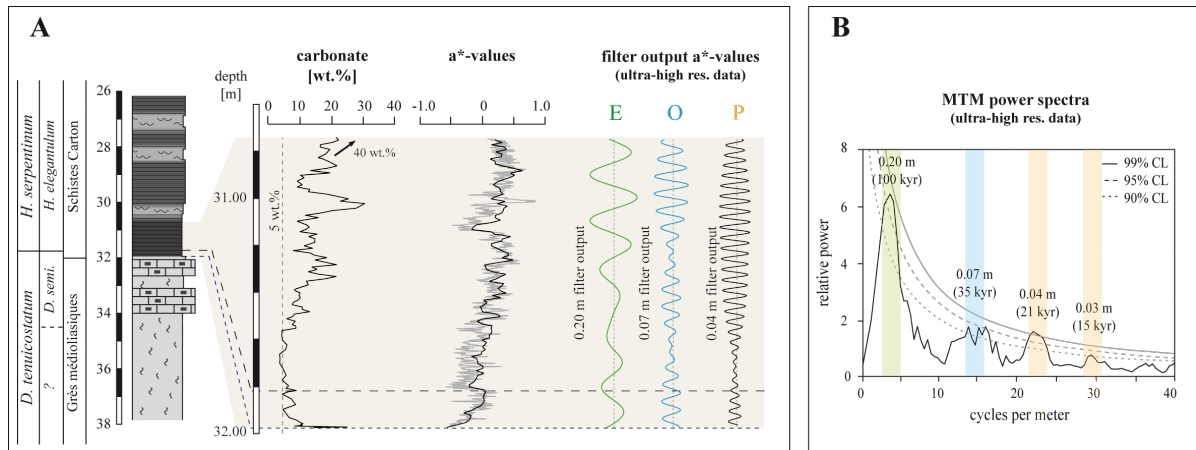


Figure 2-4: **A)** Stratigraphic and lithological chart of the basal Schistes Carton Fm (Interval 3; 30.75–31.97 m). Interval 3 is characterized by strongly reduced carbonate content (generally <10 wt.%), as the lower black shale interval is characterized by the most severe carbonate depletion (<5 wt.%). The overall trend observed within the 1 cm-scaled a*-values (black curve) shows a good fit with ultra-high resolution a*-data (re-sampled to 1 mm) obtained from line camera scanning. The presence of regular cycles that can be attributed to 100 kyr eccentricity, 35 kyr obliquity and 21 kyr precession-forced orbital cycles indicate a strong condensation, which is corroborated by sedimentological findings. Cycles within Interval 3 were extracted using the Gaussian filter with a bandwidth of 4. **B)** The 2π-MTM power spectrum of the ultra-high resolution a*-data (rescaled to 1 mm) for the black shale interval (Interval 3; 30.75–31.97 m) confirms the presence of regular cycles with mean wavelengths of 0.20 m, 0.07 m, 0.04 m and around 0.03 m. Hierarchy of these cycles match well with those of Milankovitch cycles and confirmed the cyclicity observed in the 1 cm-scaled data sets (CL: confidence levels).

The 1 cm scaled a*-data (Intervals 1, 2, 4) and 1 mm scaled a*-data (Interval 3) were transformed from a depth to a time domain by performing orbital tuning for each interval separately. Orbital tuning was performed by calibrating cycles attributed to the obliquity term in the original data to a 35 kyr periodicity. We used the 35 kyr obliquity component as this parameter was well-expressed throughout all intervals (Figs. 2-3, 2-4). Afterwards the 1 cm scaled a*-data for Intervals 1, 2 and 4 were combined with the 1 mm scaled a*-data set for Interval 3 and the entire tuned a*-data series was interpolated, even-scaled to 0.5 kyr and subjected to spectral analysis. The MTM power spectrum for the entire tuned a*-data showed significant periodicities at ~100 kyr, 55 kyr, 43 kyr, 36 kyr, 33 kyr, ~26 kyr, 21 kyr, 19 kyr, 18 kyr and 14 kyr and, thus, showed an excellent fit with the astronomical model of La2004 (Fig. 2-5). According to Berger & Loutre (1994) and the La2004 astronomical model (Laskar et al., 2004) the cycle hierarchies match excellent with those for the Early Jurassic Period.

Chapter Two: Chronology of the Early Toarican environmental crisis

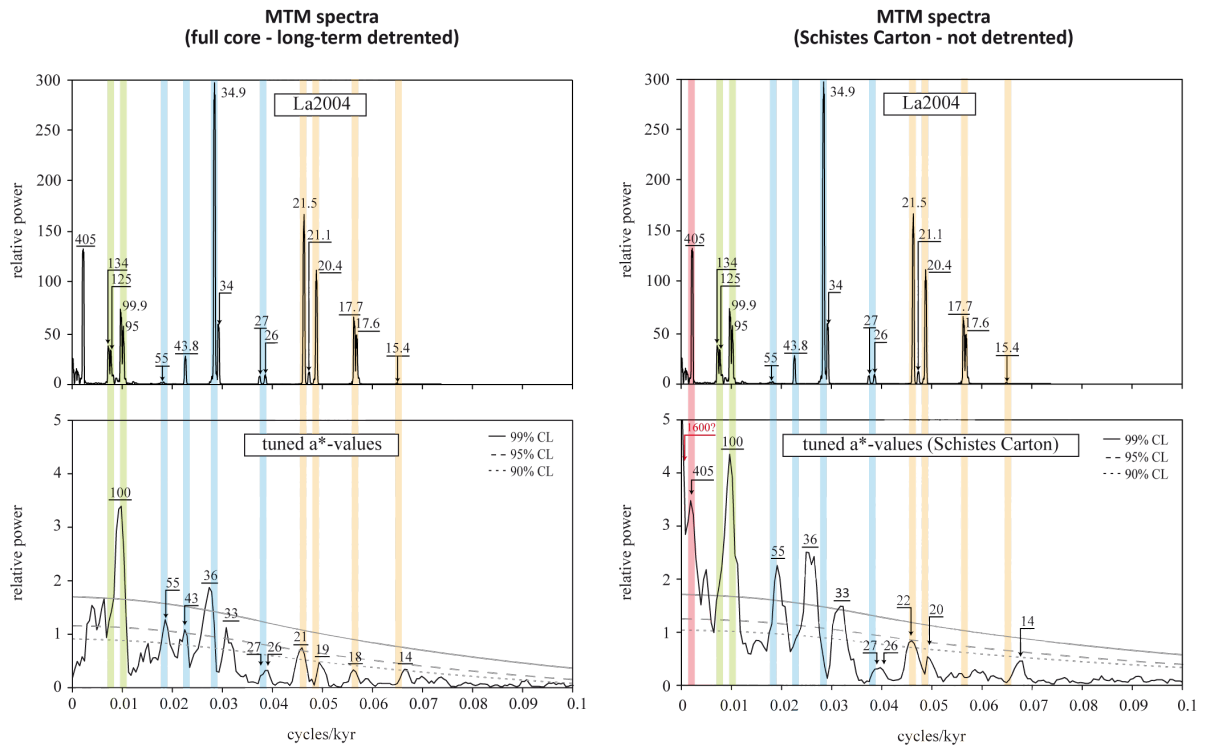


Figure 2-5: MTM power spectra for the tuned a^* -series compared with the astronomical model La2004 (Laskar et al., 2004). All major predicted frequencies are present in our tuned a^* -series, whereby only low-frequencies (e.g. 405 kyr period) are not present, which might result from the detrending procedure that mainly affect those frequencies (power spectra on the left). However, a frequency peak matching the 405 kyr cycle clearly appears when analyzing only the data from the Schistes Carton Fm and detrending procedures were not applied (spectra on the right).

2.3. Discussion

2.3.1. Astronomical and sea level controls on sedimentary cycles

Throughout the investigated section changes in lithology are well documented by the evolution of sediment color and MagS-values. Changes in sediment color are controlled by several factors, including organic matter and carbonate content as well as mineral assemblage (e.g. [Zhao et al., 2011](#)). As in Core FR-210-078 high a*-values and b*-values (Fig. 2-1) are associated with the dark-grey laminated horizons of the Schistes Carton Fm, organic matter content is assumed to have been the major contributing factor. A strong relation between organic matter content and a*-chromaticity is confirmed by a positive regression that is observed between these parameters (Fig. S2-1). Changes in MagS-values could be mainly attributed to variable dilution of terrigenous-derived minerals by marine derived carbonate (e.g. [Ellwood et al., 2000](#)). A negative correlation that is observed between MagS-values and carbonate content throughout the Schistes Carton Fm supports this interpretation (Fig. S2-1).

The long-term 2nd order sea level rise proposed by [Hardenbol et al. \(1998\)](#) (see also [Gély & Lorenz, 2006](#) for the Paris Basin) is well expressed by decreasing MagS-values observed throughout the sediment succession (Fig. 2-3). Furthermore, deposition in a shallow marine and high energetic environment during the Grès médioliasiques Fm is corroborated by homogenous and bioturbated sediments as well as by a low carbonate content and the occurrence of minor contributions of silt. In contrast, laminated sediments of the Schistes Carton Fm indicate deposition in a low-energy deposition environment below wave and storm base during a stage of higher sea level ([Wignall, 1994](#)).

Throughout the Grès médioliasiques Fm all Milankovitch cycles are well expressed by fluctuations in sediment color (Interval 4; Fig. 2-3). In particular, obliquity and precession components appear well defined in a*- and b*-values. A strong eccentricity component is also present but a slightly differing number of cycles is observed in a*- and b*-values (Figs. S2-2, S2-3). This discrepancy can be attributed to the incomplete removal of preferentially long-wavelength cycles by erosional events ([Weedon, 2003](#)). MagS-data of Interval 4 were only analyzed from 34.00 to 38.00 m as data below and above show strong positive peaks attributed to single events and thus are not suitable for spectral analysis. Results hint to the presence of eccentricity and obliquity components, although the spectral peak corresponding to the eccentricity cycle does not reach the 90% confidence level. Interestingly, no spectral peak matching with those of the precession index is found in the MagS-series. A combination of eccentricity, obliquity and precession signals in sediments corresponding to the *D. tenuicostatum* zone was also documented in the Peniche ([Suan et al., 2008](#)) and Colle di Sogno ([Hinnov and Park, 1999](#); [Hinnov et al., 2000](#)) sections. During the deposition of the Grès médioliasiques Fm a generally low and fluctuating sea level strongly affected sedimentation in the Lorraine Sub-Basin, whereby short-lived sea level fluctuations led to formation of hiatuses and condensed intervals that are well-documented for the upper Pliensbachian and lower Toarican across the Tethyan shelf area (e.g. [Röhl & Schmidt-Röhl, 2005](#); [Léonide et al., 2012](#)).

These short-lived sea level changes were most likely climate-controlled and may indicate glacio-eustatic sea level fluctuations (Pittet et al., 2014). Iron-bearing, dolomitic horizons characterized by elevated MagS-values and the occurrence of reworked shell fragments are observed within the uppermost *P. spinatum* zone and upper *D. tenuicostatum* zone (Figs. 2-1, 2-3) and may indicate erosion and/or condensation. Dolomitic intercalations in the uppermost *D. tenuicostatum* zone were also observed in the Sancerre core (Hermoso et al., 2103) and could correspond to the D2 discontinuity (see figure 5 in Pittet et al., 2014). A carbonate-rich intercalation in the uppermost *P. spinatum* zone that is marked by elevated MagS-values may correspond to the stage of lowest sea level in the uppermost Pliensbachian. A thin intercalation of dark-grey, laminated bituminous sediments marks the sea level rise, taking place at the Pliensbachian-Toarician boundary (Pl8-Toa1 cycle; Fig. 2-3) and resulting in a stage of condensation that may correspond to the D1 condensed interval in the Lusitanian Basin (Pittet et al., 2014).

In the Lorraine Sub-Basin as well as in the central Paris Basin the Schistes Carton Fm mainly consists of bituminous marls represented by Intervals 1 and 2 (9.55 – 30.75 m), whereas the basal part (Interval 3, 30.75 – 31.97 m) represents a bituminous claystone (black shale, *sensu lato*) deposited during a stage of rapid sea level rise (Figs. 2-3, 2-4). Within this interval results from spectral analysis of $\delta^{13}C$ - and MagS-data indicate the presence of regular cycles with mean wavelengths of 20 and 7 cm. On the base of their frequency ratios these cycles were attributed to 100 kyr eccentricity and 35 kyr obliquity cycles (Fig. 2-2). This finding was confirmed by the results from spectral analysis of the ultra-high-resolution $\delta^{13}C$ -data, obtained from image analysis, that also indicated the presence of a strong 100 kyr eccentricity- and 35 kyr obliquity-forced cyclicity. Furthermore, 21 kyr precession based cycles were clearly present in the ultra-high resolution data (Fig. 2-4). The dominance of eccentricity forcing in sediments from Peniche/Portugal, corresponding to the lowermost *H. serpentinum* zone, was corroborated by Suan et al. (2008) and Huang & Hesselbo (2014). Results attest a strongly reduced wavelength for the sedimentary cycles observed within Interval 3, when compared with intervals below and above (Figs. 2-3, 2-4). It is thus inferred that the 1.22 m of strata attributed to Interval 3 represents a stage of extreme condensation and covers about 600 kyr. Strong condensation can occur as the result of a rapid sea level rise, accompanied by retrograding coastlines, decreased terrigenous input and thus sediment starvation (Coe, 2003). Extremely slow sediment accumulation rates resulting in strong condensation are documented for several black shale deposits deposited during transgressive phases (Wignall, 1994). Extreme condensation around the *D. tenuicostatum*-*H. serpentinum* boundary is also documented by the D3 condensed interval for the Lusitanian Basin (Pittet et al., 2014). Furthermore, Interval 3 sediments are characterized by strongly decreased carbonate contents (4 to 10 times lower) than in the marls of Intervals 1 and 2 (Fig. 2-1). Low carbonate contents at the basal Schistes Carton Fm and isochronous deposits across the Tethyan shelf have been attributed to a biocalcification crisis that led to a sharp decline in calcareous nanoplankton due to harsh environmental conditions (Mattioli et al., 2009). The decline of calcareous primary productivity might further have contributed to decreased sediment accumulation rates. Sediment starvation in the siliciclastic-dominated environments of the northern Paris Basin most likely resulted from a rapid sea level rise. Condensation originating from a

biocalcification crisis might be more important in carbonate-dominated environments that were located further south in the Mediterranean realm (Mattioli & Pittet, 2002; Léonide et al., 2012). Thereby, the degree of condensation in isochronous deposits within various European Basins (Cleveland Basin, South German Basin, Paris Basin, Lusitanian Basin, Lombardy Basin) can differ strongly. Furthermore, strong condensation of the *D. tenuicostatum* zone in the Sancerre core highlights the spatial variability of the depositional conditions in the Paris Basin during this period. These highly variable depositional conditions in a shallow shelf sea can result in strongly differing sediment accumulation rates.

Following a rapid sea level rise, reflected by Interval 3, the Intervals 1 and 2 represent a period of generally high sea level, which is indicated by high carbonate content and decreased MagS-values (Fig. 2-1). In detail, however, sediments corresponding to Interval 2 show frequent intercalations of horizons with indistinct lamination and partly homogenous sedimentation style. The alternations between distinct laminated and indistinct laminated horizons are well expressed in MagS-data and sediment color and could indicate short-lived sea level fluctuations, which can be clearly attributed to obliquity-forced cycles (Figs. 2-2, 2-3). Similar observations were made by Hinnov & Park (1999) and Suan et al. (2008), who inferred that sedimentary cycles during the *H. serpentinum* zone (or time-equivalent chronozones) show a very strong obliquity component. The dominant influence of the obliquity parameter might indicate processes most effective at high latitudes (Berger & Loutre, 1994; Laepple & Lohmann, 2009). Furthermore, Interval 2 could represent the highstand system tract of the Toa1-Toa2 sea level cycle (Fig. 2-3). A less rapid sea level rise or stagnation, resulting in a progradation of the coastline (Coe, 2003), as well as elevated weathering rates (Cohen et al., 2004), would have led to an increase in sediment supply and to a steady accommodation space. This setting was very sensitive towards short-lived fluctuations in sea level, which may have been controlled by high-latitude processes, such as the waxing and waning of polar ice. As the Tethyan shelf was connected with the Arctic Ocean via the Viking Corridor (see Fig. 1-4 in Chapter 1.1.3.), processes at high latitudes could be tele-connected to low latitudes via the water exchange between the Arctic and Tethyan Oceans (Bjerrum et al., 2001).

Interval 1 corresponds to the stage of the highest sea level, as the maximum flooding zone of the 2nd order sea level cycles can be placed somewhere within the uppermost *H. serpentinum* zone, which is confirmed by Gély & Lorenz (2006) for the Paris Basin (Fig. 2-3). The periodicity observed in sediment color and MagS-data reveals an amalgamated eccentricity, obliquity and precession signal (Figs. 2-2, 2-3). The reduced strength of the obliquity parameter indicates that high latitude processes were no longer the major controlling factor on sedimentation or sedimentation processes and that the Lorraine Basin during this period was less sensitive to short-lived sea level variations due to a generally high sea level.

2.3.2. Towards the 405 kyr cycles in the Lorraine record

The identification of 405 kyr cycles in the original data is problematic due to strongly fluctuating sedimentation rates. Low frequency cycles are also not expressed in the tuned a*-data series (Fig. 2-5), as a result of the detrending procedure that was applied to the tuned a*-data. Furthermore, low frequency cycles might be obscured by erosional surfaces in the *D. tenuicostatum* zone, resulting in partially missing strata and thus the partial removal of those cycles. However, analyzing the tuned a*-data for the Schistes Carton Fm. does not require removal of long-term trends and consequently low frequency cycles are not affected by any detrending artefacts (e.g. [Vaughan et al., 2014](#)). Following this approach and analyzing the tuned a*-data for the Schistes Carton Fm. allows identification of a frequency matching with the 405 kyr period. In addition, a long-term trend in the dataset might reflect the 1.6 Myr period. Hence, it can be stated that a 405 kyr (and the 1.6 Myr) period though not very prominent is indicated in our data set (Figs. 2-5, 2-6). In summary, the *H. serpentinum* zone according to our analysis covers about 3 to 4 405 kyr cycles, matching findings from the Peniche section ([Huang & Hesselbo, 2014](#)).

2.3.3. Duration of the ammonite zones and subzones

A timescale for the sediment succession and thus for the ammonite zones and subzone was inferred from the tuned a*-time series (Fig. 2-6). The *D. tenuicostatum* zone spans from 37.90 m to 31.82 m, the *D. tenuicostatum*-*H. serpentinum* boundary is placed within the lowermost Schistes Carton Fm (Fig. 2-3). The *D. tenuicostatum* zone covers 5.5 short eccentricity (100 kyr), about 16 obliquity (35 kyr) and 27 (21 kyr) precession cycles identified in interval 4 and approximately one additional short eccentricity cycle identified in Interval 3 (Figs. 2-4, 2-6). Counting these cycles resulted in a duration of 550 to 560 kyr. Here we suggest that the sediment succession corresponding to the *D. tenuicostatum* zone represents ~555 kyr of sediment accumulation. This duration is only a minimum estimation as erosional events during this stage are most likely. Our results are in agreement with the timescale of [Gradstein et al. \(2012\)](#), which lists a duration of 800 - 1000 kyr for the *D. tenuicostatum* zone. Differences to the findings of [Boulila et al. \(2014\)](#), who calculated a duration of less than 100 kyr can be attributed to uncertainties in biostratigraphic framework and unrecognized changes in sediment accumulation rate and/or erosional events in the Sancerre core.

The *H. serpentinum* zone includes the Intervals 1 – 3; the lowermost part of Interval 3 corresponds to the *D. tenuicostatum* zone (Figs. 2-4, 2-6). Approximately 12 short eccentricity (100 kyr), 35 obliquity (35 kyr) and about 60 precession-based (21 kyr) astronomical cycles are attributed to the *H. serpentinum* zone, resulting in a duration of 1200 to 1260 kyr (Fig. 2-6). However, the *H. serpentinum*-*H. bifrons* boundary is not recovered in Core FR-210-078 but would be placed at a depth of around 6 to 7 m (see appendix A1.3.) based on parallelization with core FR-207-142 ([Guérin-Franiatte et al., 2010](#)). Assuming no significant changes in sediment accumulation rate, the missing sediment interval of around 2.5 m covers another 100 kyr. Cumulatively, a minimum

duration of 1300 to 1360 kyr can thus be estimated for the *H. serpentinum* zone. The duration of the *H. elegantulum* subzone can be estimated to at least 790 kyr and the duration of the *H. falciferum* subzone to a minimum of 520 kyr (Fig. 2-6). Despite all uncertainties the duration of the *H. serpentinum* zone as proposed here is in good agreement with durations calculated by [Suan et al. \(2008\)](#) or [Huang & Hesselbo \(2014\)](#), who suggested a duration ranging from 1.1 Myr to 1.6 Myr. Furthermore, our results match well with the Geological Timescale 2012 that proposes a cyclostratigraphy-based duration of about 1.3 Myr for the *H. serpentinum* zone (see [Gradstein et al., 2012](#) and references therein). In addition, strontium isotope data from the Cleveland Basin assigns durations of about 1 Myr and 0.3 Myr, for the *H. elegantulum* and *H. falciferum* subzones, respectively ([McArthur et al., 2000](#)), which slightly differs from the 0.8 Myr and 0.5 Myr estimated by this study. However, the total 1.3 Myr duration calculated for the *H. serpentinum* zone is in good agreement with the Sr-isotope profile based duration of about ~Myr ([McArthur et al., 2000](#)). Differences in the durations calculated for the ammonite subzones might result from uncertainties of biostratigraphic boundaries.

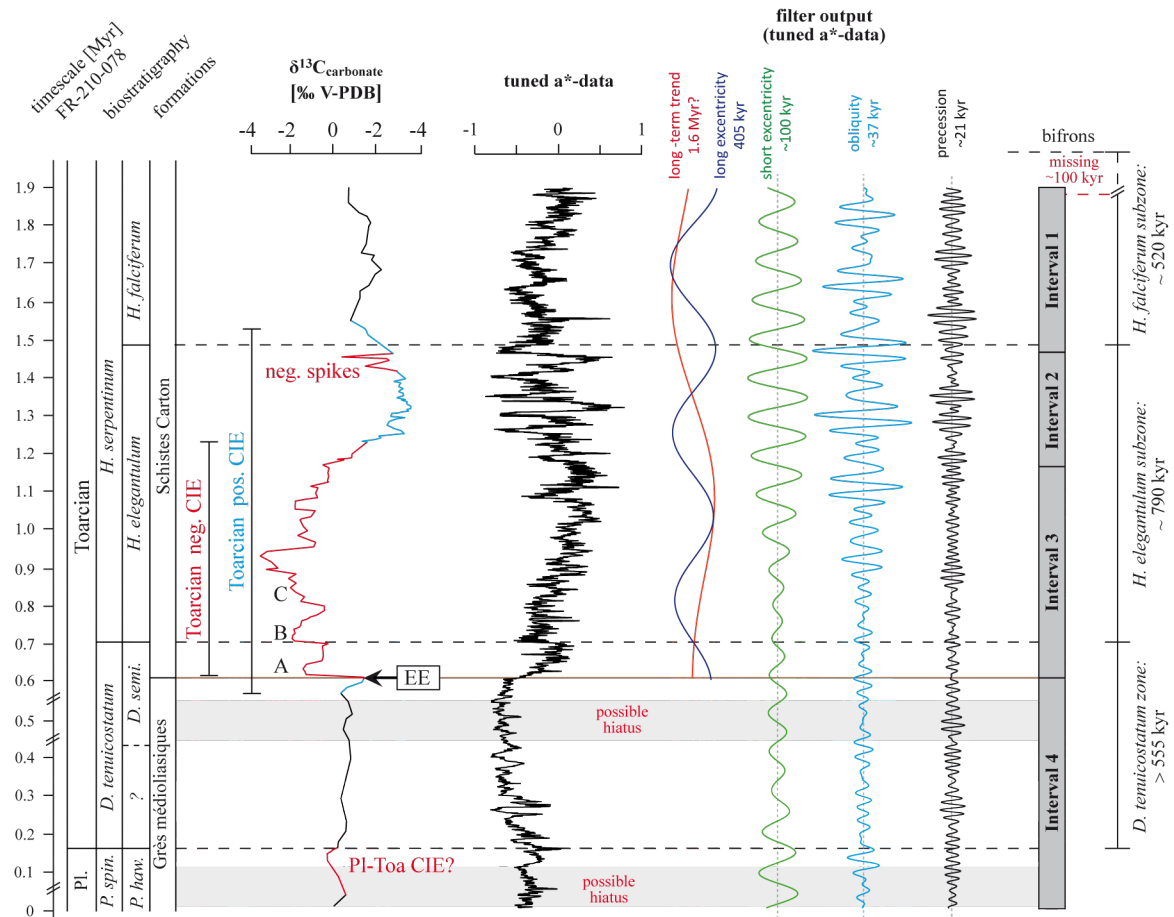


Figure 2-6: Tuned a*-time series plotted against the stratigraphic column and corresponding filter output for eccentricity, obliquity and precession components. The resulting timescale for the entire *H. serpentinum* zone is in agreement with findings from the Peniche section ([Suan et al., 2008](#); [Huang & Hesselbo, 2014](#)). The duration of ~555 kyr for the *D. tenuicostatum* zone is only a minimum estimation as Interval 4 is most likely affected by erosional events. The duration for the *H. serpentinum* zone can be estimated to ~1.31 Myr, the *H. elegantulum* subzone lasted ~790 kyr and the *H. falciferum* subzone lasted ~520 kyr. On the base of the timescale proposed here, the positive Toarcian CIE lasted for 900 to 1000 kyr and the negative Toarcian CIE lasted for ~600 kyr.

2.3.4. Duration of the Toarcian carbon cycle perturbations

A pronounced positive shift in $\delta^{13}\text{C}_{\text{carbonate}}$ -values of about +3‰, that spans the uppermost *D. tenuicostatum* zone and lower *H. serpentinum* zone (mainly *H. elegantulum* subzone) that is commonly associated with the Toarcian Oceanic Anoxic Crisis (e.g. Jenkyns, 1988), is well expressed in our data (Figs. 2-1, 2-6). This positive shift is interrupted by a striking negative CIE, which is documented from several time-equivalent sections across the Western Tethyan shelf (e.g. Röhl et al., 2001; Suan et al., 2008, 2011; Sabatino et al., 2009; Kemp et al., 2011; Hermoso et al., 2013, 2014). The negative CIE is commonly attributed to reflect a perturbation of the global carbon cycle that occurred at the *D. tenuicostatum*-*H. serpentinum* transition (Suan et al., 2008; Huang & Hesselbo, 2014). The stratigraphic position of the negative CIE confirms the biostratigraphic boundary between *D. tenuicostatum* zone and *H. serpentinum* zone (Figs. 2-1, 2-6). Furthermore, a slightly negative shift of -1‰ might correspond to the negative CIE documented from the Pliensbachian-Toarcian boundary (Suan et al., 2008; Littler et al., 2010; Pittet et al., 2014). However, this negative shift is less pronounced, which might result from the relative low sample resolution in this interval. Two additional brief negative excursions of -1 and -2‰ were observed within the upper *H. elegantulum* subzone (Figs. 2-1, 2-6). These negative spikes were also reported from the northern Paris Basin at a similar stratigraphic position (Hermoso et al., 2014) but were not documented elsewhere and, thus, most likely reflect local mechanisms. However, the overall evolution of the carbon isotope values matches well with the proposed carbon isotope stratigraphy of the lower Toarcian allowing a correlation of the Lorraine Sub-Basin with other distant sections.

The durations of the positive and negative Toarcian carbon isotope excursions are still debated. Most recently, a duration of ~600 kyr for the main body of the negative Toarcian CIE has been proposed (McArthur et al., 2000; Suan et al., 2008, 2011; Sabatino et al., 2009; Huang & Hesselbo, 2014) and a duration of ~900 kyr for the positive CIE (Suan et al., 2011b). In contrast, cyclostratigraphic investigations from the southern Paris Basin (Sancerre Core, Boulila et al., 2014) calculated a duration of ~200 and ~400 kyr for the negative and positive CIE, respectively. The timescale for Core FR-210-078 proposed here clearly support durations of ~600 and ~900 kyr for the negative and positive CIE, respectively. The main body of negative Toarcian CIE corresponds to the condensed Interval 3 and covers 6 cycles that were attributed to 100 kyr eccentricity cycles, which exactly fits with the number of cycles evident from other locations (Suan et al., 2008, 2011; Huang & Hesselbo, 2014).

Furthermore, the interval between isotope shifts A and B (Fig. 2-6) covers one 100 kyr eccentricity cycle, which agrees with results from other locations at the Western Tethyan shelf (Suan et al., 2008; Huang & Hesselbo, 2014). Differences in sediment thickness of this interval clearly reflect different sediment accumulation rates. The positive Toarcian CIE that mainly spans the Intervals 2 and 3 covers about 9 cycles attributed to 100 kyr eccentricity, which supports findings from Dotternhausen (southern Germany, Suan et al., 2011b). This exact fit of the timescale proposed here and the resulting durations of the carbon isotope excursions with other sections indicates extreme condensation in the basal Schistes Carton Fm (Interval 3) and further provides an

explanation for the discrepancy between the duration of the carbon cycle perturbation in the Paris Basin (Boulila et al., 2014) and other Basins (Suan et al., 2008; 2011b; Sabatino et al., 2009; Huang & Hesselbo, 2014).

2.3.4. Correlation with other Sections

The timescale developed here, in combination with the robust biostratigraphy at ammonite subzone scale, allow to compare our results with data from other locations. One of the most complete and intensively studied locations is located in the Lusitanian Basin (Peniche, Portugal). A high-resolution carbon isotope stratigraphy has been elaborated by Hesselbo et al. (2007) and a floating chronology has been constructed by Suan et al. (2008) and Huang & Hesselbo (2014). In the Lorraine Sub-Basin as well as in the Lusitanian Basin the *H. serpentinum/H. levsoni* zone spans 3 to 4 long (405 kyr) eccentricity cycles, whereby the Toa-CIE interval spans about 1.5 405 kyr cycles (Fig. 2-7). A correlation on ammonite subzone scale is prevented by the missing identification of those zones in the Lusitanian Basin.

In the Lusitanian Basin the *D. polymorphum* zone, which corresponds to the *D. tenuicostatum* zone, covers about two 405 kyr cycles, resulting in a duration of about 0.8 to 0.9 Myr. On the contrary, in the Lorraine Sub-Basin the *D. tenuicostatum* zone represents only 0.5 Myr. This discrepancy can be explained by highly condensed intervals and hiatuses that are documented throughout the northwestern Tethyan shelf (Buckman, 1910; Röhl & Schmidt-Röhl, 2005; Léonide et al., 2012) and most likely resulted from rapid sea level fluctuations (Pittet et al., 2014). Condensation and hiatuses are less pronounced in the Mediterranean as indicated by the longer timespan represented by *D. polymorphum* zone in the Lusitanian Basin (Fig. 2-7).

It is interesting to note that a similar periodicity has been documented from the pelagic Sakahogi section (Inuyama area, Japan, Ikeda & Hori, 2014). Unfortunately, the poor biostratigraphy and missing carbon isotope data complicate a detailed comparison with sections on the Western Tethyan Shelf. Carbon isotope data are, however, available from the Katsuyama section (Gröcke et al., 2011), also located in the Inuyama area (Japan). Correlation of both section allow to estimate the approximate stratigraphic position of the Toa-CIE within the Sakahogi section (see figures 3, 4 in Ikeda & Hori, 2014). The resulting position of the Toa-CIE interval in the Sakahogi section appear at a similar stratigraphic interval like in sections on the Western Tethyna Shelf (Fig. 2-7), supporting the synchronicity and similar duration of the Toa-CIE.

Chapter Two: Chronology of the Early Toarcian environmental crisis

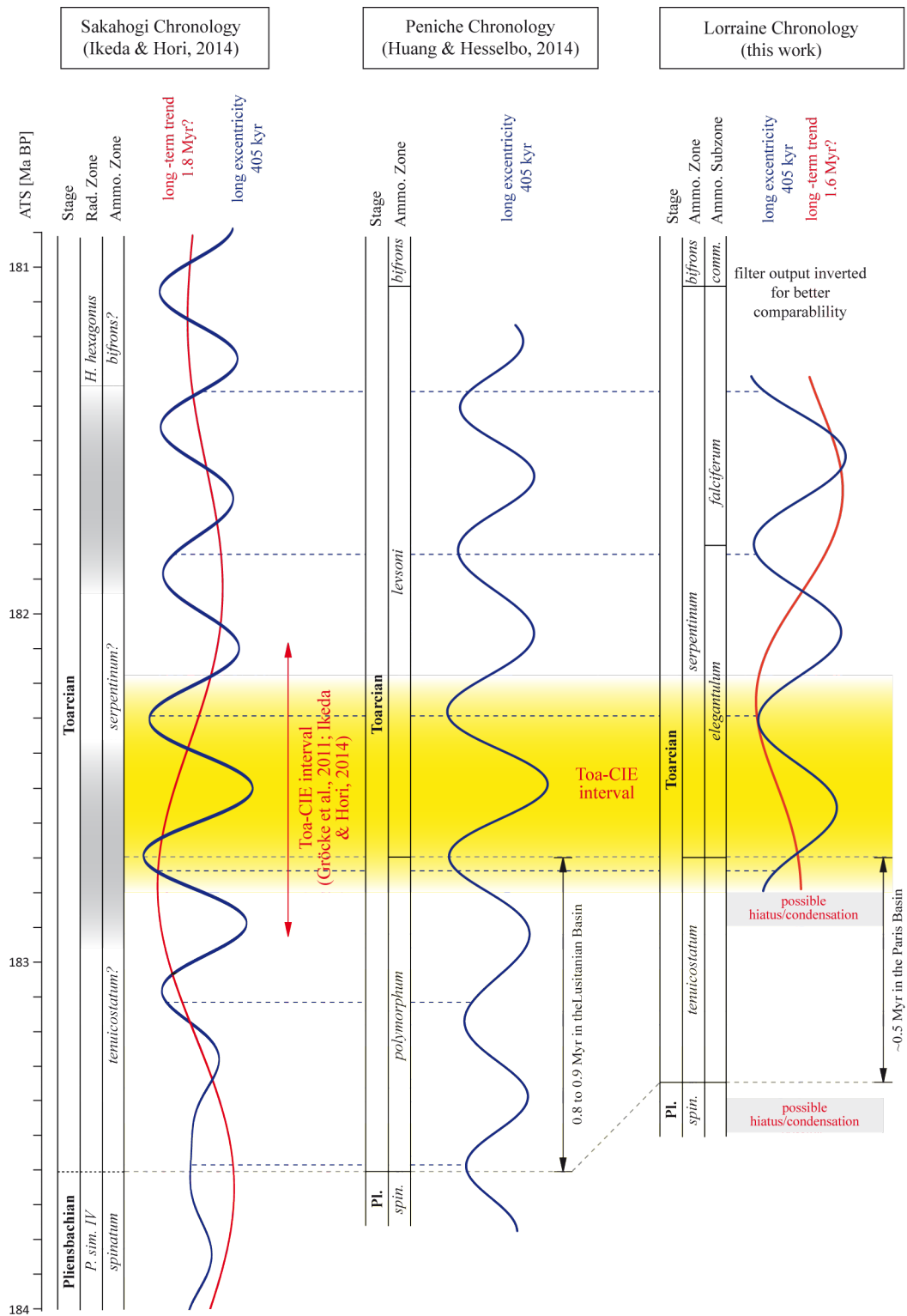


Figure 2-7: Floating chronologies for the pelagic Sakahogi section (Japan, Ikeda & Hori, 2014), the Peniche section in the Mediterranean realm (Huang & Hesselbo, 2014) and for the Lorraine Sub-Basin (this study) exhibit a similar periodicity of the 405 kyr eccentricity cycles. Offsets in cycle minima and maxima result from the different parameters subjected to spectral analysis. The short time interval represented by the Lorraine record might also affect the filter output. However, despite these uncertainties all sections show a similar periodicity, which allows a detailed comparison of these sections. Unfortunately no carbon isotope data exists for the Sakahogi section. Furthermore, the biostratigraphy of this section is affected by large uncertainties. For a better comparability the filter output for the Lorraine Sub-Basin is shown reverse.

2.4. Conclusions

The sedimentation regime during the lower Toarcian in the Lorraine Sub-Basin was controlled by a cyclic forcing mechanism with Milankovitch frequencies. The relative impact of the astronomical forcing parameters changed throughout the sediment succession. Obliquity exerted the most dominant impact especially during the upper *H. elegantulum subzone*, an observation that has been confirmed in stratigraphy across the western Tethyan shelf and the Mediterranean Tethyan province. The strong impact of obliquity forcing may indicate that processes at high latitudes affected the sedimentation on the Western Tethyan shelf, favored by water exchange between Arctic and Tethyan Oceans via the Viking Corridor. Spectral analysis of distinctive intervals defined by lithological and geochemical characteristics allows to identify drastic variations in sedimentation rates, where our results indicate a strong condensation of the basal Schistes Carton Fm (uppermost *D. tenuicostatum zone* and lower *H. serpentinum zone*). Condensation occurred as the result of a rapid sea level rise and might further have been exacerbated by a drastic decrease in carbonate production due to a biocalcification crisis. These abrupt changes might be obscured when spectrally analyzing only the complete sediment succession, and thus explain the discrepancy between interpretations by [Boulila et al. \(2014\)](#) versus [Suan et al. \(2008\)](#) or [Huang & Hesselbo \(2014\)](#). Our results allow to deduce a minimum timescale for each ammonite subzone: *D. tenuicostatum zone* (>555 kyr); *H. elegantulum subzone* (~790 kyr); *H. falciferum subzone* (~520 kyr) and hence resulting in a minimum duration of the *H. serpentinum zone* of ~1.31 Myr. The duration of the negative carbon isotope excursion can be estimated to ~600 kyr, the overall positive carbon isotope excursion lasted for ~900 kyr. Comparison of the Lorraine chronology with chronologies established for the Lusitanian Basin and the pelagic Sakahogi section exhibit a similar periodicity and thus highlighting the global nature of the Toarcian carbon cycle perturbation.

Chapter Three:

Astronomically-forced cryosphere demise during the Early Toarcian

Abstract

The Early Toarcian (Early Jurassic; ~183 Ma BP) records a drastic global warming of about 5 to 7°C, a threefold increase in atmospheric CO₂ concentration as well as a rapid high-amplitude sea level rise. Environmental changes were further accompanied by the most striking perturbation of the global carbon cycle recorded in the Mesozoic. The carbon cycle perturbation, documented by a negative carbon-isotope excursion of about -3‰, affected all biospheric reservoirs and reflects a injection of huge amounts of ¹²C-enriched carbon into the Earth's ocean-atmosphere system. Carbon cycle perturbation and environmental changes occurred synchronously within less than 0.5 Myr. Chronology, mechanisms as well as carbon sources contributing to the carbon cycle perturbation and to the environmental crisis remain controversial. This chapter presents a conceptual model, which shows that astronomically-forced demise of the Earth cryosphere, during an icehouse-greenhouse transition, has the potential to explain the main key-features of the Early Toarcian environmental changes, including global warming, sea level rise and carbon cycle perturbation. Findings allow explaining the cyclic pattern as well as the duration of about 900 kyr calculated for the carbon cycle perturbation. The orbital control towards the CIE pattern cannot be explained by volcanogenic mechanisms, whereas the dissociation of shelf gas hydrates alone fails to explain the duration and further raises questions about gas hydrate storage. The Toa-CIE can be explained by a series of high-frequency and high-amplitude hyperthermals that were controlled by changes in Earth's solar orbit. The shift in the astronomical forcing from eccentricity to obliquity resulted from changes in the internal feedback mechanisms of the Earth cryosphere during global warming. Global warming was initiated by the Karoo-Ferrar volcanism that released large amounts of CO₂ into the Earth atmosphere and caused an initial global warming.

Findings support the existence of a Late Pliensbachian cryosphere that stored large amounts of carbon formed during former warm climates and transferred into the cryosphere during the Late Pliensbachian cooling. Results further highlight the role of cryosphere-stored carbon and the amplification of climate dynamics during stages of rapid global warming triggered by external processes, like volcanism or anthropogenic greenhouse gas emissions.

3.1. Introduction

Recent paleoclimatic investigations challenged former views of an equal Early Jurassic climate (e.g. [Frakes et al., 1992](#)) and indicated that during the Early Toarcian (Early Jurassic; ~183 Ma BP) the Earth experienced a drastic global warming as expressed by a rise in SST of about 5 to 8°C ([Dera et al., 2011](#); [Silva & Duarte, 2015](#); [Gómez et al., 2015](#)), a threefold increase in atmospheric CO₂ concentrations ([McElwain et al., 2005](#)) and a northwards shift of warm-climate loving flora by as much as 1500 to 2000 km ([Vakhrameev, 1991](#)). Progressive global warming was accompanied by a rapid rise in sea level, probably as the result of melting ice polar ice sheets ([Suan et al., 2010](#); [Pittet et al., 2014](#)).

Environmental changes were accompanied by the largest carbon isotope excursion documented in sedimentary records during the Mesozoic, expressed by a marked carbon isotope excursion for both carbonate and organic carbon of -3 to -4‰ ([Suan et al., 2015](#)) documented in all exchangeable biospheric reservoirs ([Hesselbo et al., 2000a; 2007](#); [Kemp et al., 2005](#); [Hermoso et al., 2012](#)). The Toarcian carbon isotope excursion (Toa-CIE) reflects a massive injection of ¹²C-enriched carbon into the ocean-atmosphere system lasting for a period of about 0.6 to 0.9 Myr ([Suan et al., 2008a](#); [Huang & Hesselbo, 2014](#); [Ruebsam et al., 2014; 2015](#)) (Fig. 3-1).

Carbon sources and release mechanisms causing the Toa-CIE have been discussed controversially, including volcanic CO₂ emission ([Suan et al., 2008a](#); [Brazier et al., 2015](#)), igneous intrusions into organic-rich sediments ([McElwain et al., 2005](#); [Svensen et al., 2007](#)) and the destabilization of marine methane hydrates ([Hesselbo et al., 2000a](#); [Kemp et al., 2005](#)). Recent works reinforced a causal and temporal link between carbon cycle perturbation and the emplacement of the Karoo-Ferrar Large Igneous Province (e.g. [Ikeda & Hori, 2014](#); [Burgess et al., 2015](#)). However, it has been demonstrated that the Toa-CIE has an astronomically-forced periodicity, which volcanism as a main controlling mechanisms fails to explain ([Kemp et al., 2005](#); [Huang & Hesselbo, 2014](#)). Also, the injection of ¹²C-enriched carbon from marine gas hydrates into the atmosphere-ocean system is difficult to reconcile with the Toa-CIE duration of about 0.6 to 0.9 Myr ([Dickens, 1999](#); [Beerling & Brental, 2007](#)). Moreover, neither volcanic activity, nor methane dissociation from marine gas hydrates can explain the rapid high-amplitude sea level rise of about 30 to 90 m within less than 0.5 Myr accompanying the Toa-CIE ([Hallam, 1997](#); [Pittet et al., 2014](#)). Thus, mechanisms of carbon release, carbon sources as well as triggering mechanisms contributing to the Toarcian carbon cycle perturbation and associated environmental changes remain controversial. Thus, mechanisms of carbon release, carbon sources as well as triggering mechanisms contributing to the massive Toarcian carbon cycle perturbation and associated environmental changes remain controversial.

In this chapter, a novel and unifying explanation for the extensive and rapid climate change observed during the Early Toarcian is presented that links for the first time all observed environmental responses and the astronomically forced patterns in the environmental records. This conceptual model shows that cryosphere stored carbon (CSC), released during externally triggered global warming, has the potential to explain the key features of the Early Toarcian carbon cycle

perturbation. This carbon reservoir formed during the Late Pliensbachian icehouse and expanded toward lower latitudes where it became most sensitive towards minor climate changes. Karoo-Ferrar volcanism alone fails to explain pattern, pacing as well as magnitude of the Toa-CIE but provides a suitable triggering mechanism (Palfly & Smith, 2000; Burgess et al., 2015) for an initial CO₂ increase and global warming that in dependency of the Earth's orbital cycles resulted in the periodically crossing of climate thresholds controlling the release of carbon from the cryosphere. This model allows the linking of previous isolated observations in a coherent Earth System concept that explains earth atmosphere interaction and climate change during the Toarcian and further highlights the role of cryosphere stored carbon as a major driver of past and recent climate change (Schoor et al., 2015).

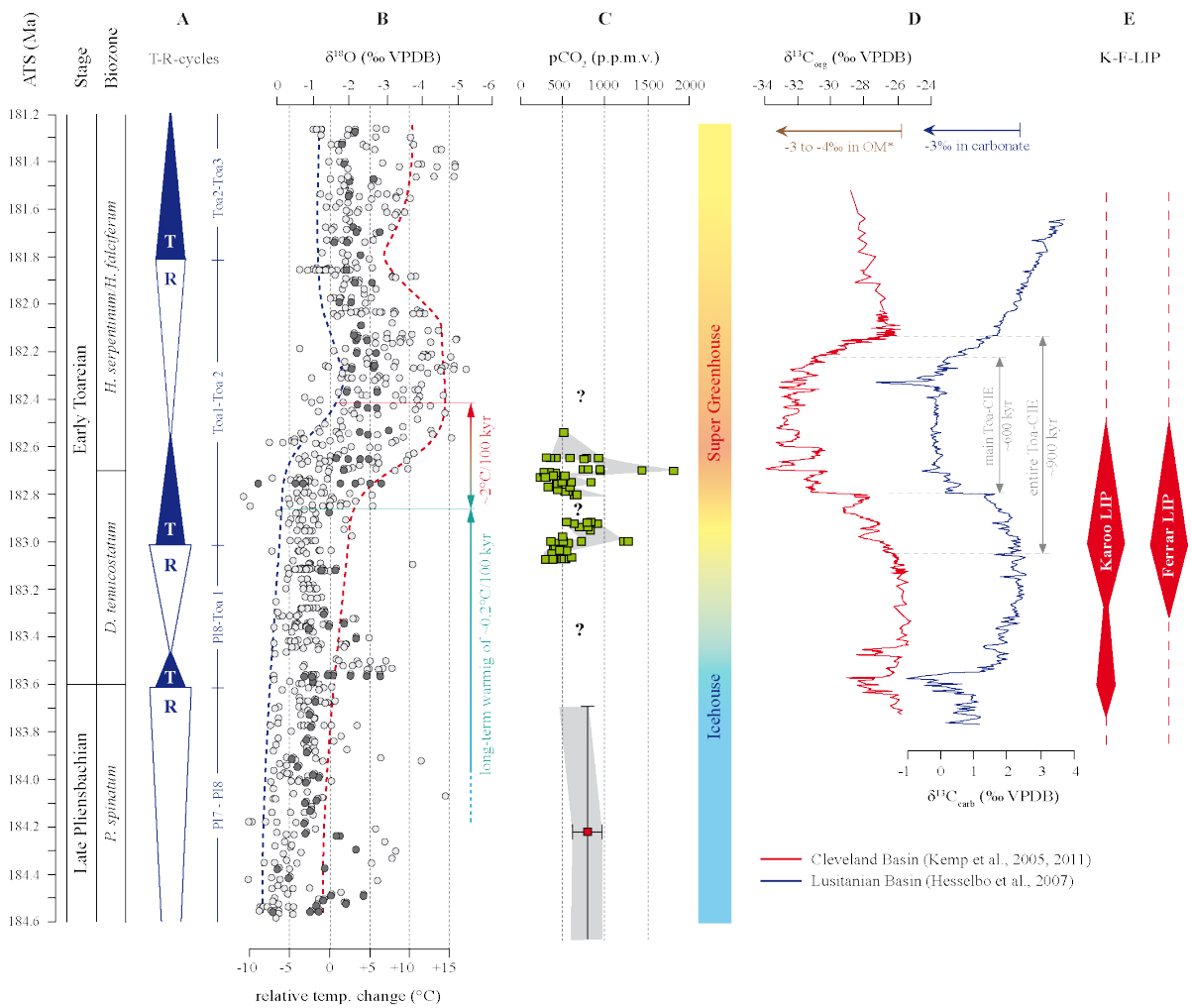


Figure 3-1: Overview of environmental changes taking place during the Early Toarcian at the *D. tenuicostatum*-*H. serpentinum* zone transition. The Toarcian carbon cycle perturbation (D) was accompanied by rapid sea level rise (A), a rise in sea surface temperatures (B) and increasing atmospheric CO₂ concentrations (C). Environmental changes occurred concomitant to the emplacement of the Karoo-Ferrar LIP (E), indicating a causal and temporal relation between environmental changes and volcanic activity (see Chapter 1.2.4.). Environmental changes were calibrated to the astronomical timescale proposed in Chapter 2. The Pliensbachian-Toarcian boundary date is set to 183.6 Ma BP (see Chapter 1.1.1.). *The negative shift documented in δ¹³C_{org} varies strongly between different locations (-7 to -4‰). Calibration the carbon isotope data to different OM sources result in a -3‰ shift (Montero-Serrano et al., 2015; Suan et al., 2015; Fig. S3-2).

3.2. Pattern, pacing and periodicity of the Toa-CIE

3.2.1. Pattern and pacing of the Toa-CIE

To investigate changes in the global carbon cycle during the Early Toarcian a new high-resolution organic carbon isotope record has been generated for Core FR-210-078 (see appendix A3.2.3. for methodology). The Toa-CIE is well expressed in the $\delta^{13}\text{C}_{\text{org}}$ -record from the Lorraine Sub-Basin by a -7‰ shift that spans the uppermost *D. tenuicostatum zone* and the lower *H. elegantulum subzone* (Fig. 3-1), whereby the shift from background values of -26‰ to more negative values of about -33‰ within the Toa-CIE occurred in three discrete steps. The $\delta^{13}\text{C}_{\text{org}}$ values remain low throughout the lower part of the *H. elegantulum subzone*, before values return to pre-excursion values of about -26‰ (Fig. 3-1). The absolute magnitude of the Toa-CIE is of local phenomena and varies in dependency of the substrate. Normalization of $\delta^{13}\text{C}_{\text{org}}$ data to specific organic matter sources and maturities resulted in a magnitude of about -3 to -4‰ (Fig. S3-2), which match findings of studies by [Suan et al. \(2015\)](#) and [Montero-Serrano et al. \(2105\)](#).

Stratigraphic position as well as pattern and pacing of the Lorraine $\delta^{13}\text{C}_{\text{org}}$ -record match with the $\delta^{13}\text{C}_{\text{org}}$ -record from the Cleveland Basin ([Kemp et al., 2005](#)), confirming the trans-regional nature of the carbon cycle perturbation. Comparison of the high-resolution $\delta^{13}\text{C}_{\text{org}}$ -records from the Cleveland Basin ([Kemp et al., 2005](#)) and the Lorraine Sub-Basin (this work) allows to establish a detailed carbon isotope stratigraphy for the Toarcian carbon cycle perturbation, with identification of four main stages (I - IV) (Fig. 3-3). Toa-CIE stage I comprised the initial decrease in carbon isotope composition from $\delta^{13}\text{C}$ values of about -26‰ to values near -28‰ that occurred between 183.0 and 182.8 Ma BP. Superimposed on the steady $\delta^{13}\text{C}$ decrease are two minor negative shifts (I-A & I-B) reported from the Cleveland Basin ([Kemp et al., 2005](#)). This interval is not covered in the Lorraine Sub-Basin, where the upmost *D. tenuicostatum zone* is affected by an erosive event and/or strong condensation ([Ruebsam et al., 2014; 2015; also see Pittet et al., 2014](#)) (Fig. S3-1). Toa-CIE stage II, spanning the period from 182.8 to 182.6 Ma BP, records the most pronounced negative $\delta^{13}\text{C}$ trend by -7‰ (about -3 to -4‰ corrected for different OM sources), pinpointed by three major pulses (II-A, II-B, II-C), which coincide with those noted in the Cleveland Basin ([Kemp et al., 2005](#)). Pulses II-A and B exhibit the highest $\delta^{13}\text{C}$ amplitudes of -5 to -4‰, respectively, whereby each negative shift is followed by a recovery phase. Each pulse represents a single event, whereby the partial lack of stage I in the Lorraine Sub-Basin causes a different amplitude for isotope shift II-A (Fig. 3-3; S3-1). The third step II-C with about -2‰ is less pronounced and marks the transition to Toa-CIE stage III. This stage spans the time from 182.6 to 182.2 Ma BP and is characterized by repeated $\delta^{13}\text{C}$ variations of about $\pm 1\%$ (Fig. 3-2). During stage IV, $\delta^{13}\text{C}$ values of organic C rapidly return from -32 to -26‰ within less than 100,000 yrs of sedimentation. The agreement between the $\delta^{13}\text{C}$ record from the Lorraine Sub-Basin and that of [Kemp et al. \(2005\)](#) is astounding and minor differences in the amplitude of the entire Toa-CIE as well as amplitudes of individual negative $\delta^{13}\text{C}$ shifts may be attributed to differences in organic matter composition.

3.2.2. Periodicity of the Toa-CIE and inferred mechanisms

The $\delta^{13}\text{C}_{\text{org}}$ -data, fitted to the timescale proposed in Chapter 2, were subjected to spectral analysis. Additionally, $\delta^{13}\text{C}_{\text{org}}$ -data from the Cleveland Basin (Kemp et al., 2005) were analyzed as well to compare periodicities that might be present in both records as previously shown by Huang & Hesselbo, (2014). A description of the methodology is given in the appendix A3.4.. Furthermore, significant changes in sediment accumulation rates have been confirmed for the Lorraine Sub-Basin and are also indicated for the Early Toarcian of the Cleveland Basin (McArthur et al., 2000; Huang & Hesselbo, 2014). Therefore, only $\delta^{13}\text{C}_{\text{org}}$ -data corresponding the main Toa-CIE interval, which shows no significant litho-facies changes, were subjected to spectral analysis (Fig. 3-2).

Spectral analysis of $\delta^{13}\text{C}_{\text{org}}$ -data from the Lorraine Sub-Basin and the Cleveland Basin confirms the presence of a similar periodicity in both organic carbon isotope records that match with those of Milankovitch frequencies and further align with the astronomical model La2004 (Laskar et al., 2004). The initial Toa-CIE stage I displays two ~ 100 kyr eccentricity cycles, while the main Toa-CIE (stages II and III) is composed of six ~ 100 kyr eccentricity cycles and an additional cycle is associated with the recovery interval, resulting in a duration of ~ 600 kyr and ~ 900 kyr for the main Toa-CIE interval and the entire Toa-CIE, respectively (Fig. 3-2). During Toa-CIE stage I variations in $\delta^{13}\text{C}_{\text{org}}$ data match with eccentricity periods, stage II documents a mixed signal with a strengthening of the obliquity component (~ 38 kyr), while $\delta^{13}\text{C}$ variations within stage III are increasingly dominated by obliquity cycles (Fig. 3-2). A similar periodicity as well as a shift in the astronomical response from eccentricity to obliquity dominated signals has been documented in sediment characteristics of Core FR-210-078 (Ruebsam et al., 2014, 2015; also see chapter 2) and is also evident from other locations throughout the Western Tethyan shelf (Hinnov & Park, 1999; Suan et al., 2008a; Huang & Hesselbo, 2014). The coevolution of astronomical-forced periodicities in sedimentological proxies, reflecting oceanographic and/or environmental changes, and $\delta^{13}\text{C}_{\text{org}}$ values indicate a direct coupling of carbon cycle and environmental changes possibly related to climate fluctuations (Fig. S3-3). Shifts in astronomical forcing, documented in periodicity of sedimentological parameters (Hinnov & Park, 1999; Suan et al., 2008a), have been ascribed to reorganization of global water and ice storage (Hinnov & Park, 1999). According to these authors, dominant eccentricity/precession forcing has been associated with water/ice storage at mid-latitudes due to integrated annual insolation at these latitudes controlling hydrology (Berger & Loutre, 1994). Dominant obliquity forcing indicates water/ice storage at high latitudes, where integrated annual insolation is controlled by changes in obliquity (Berger & Loutre, 1994). Alternatively, the shift from eccentricity to obliquity forcing can also be explained by internal feedback mechanisms of polar ice sheets during a long-term global warming, whereby eccentricity periods dominate during cold climate stages and obliquity periods during warm climate stages (Ruddiman, 2006). In both cases eccentricity forcing dominated during icehouse conditions with an expanded cryosphere, whereas obliquity forcing dominated during greenhouse stages with a reduced cryosphere extent. Concerning this relation, the eccentricity-obliquity shift, documented in carbon isotope data, can be attributed to an astronomically forced injection of ^{12}C -enriched carbon from climate-sensitive

reservoirs that has been destabilized after climate thresholds were crossed during long-term global warming.

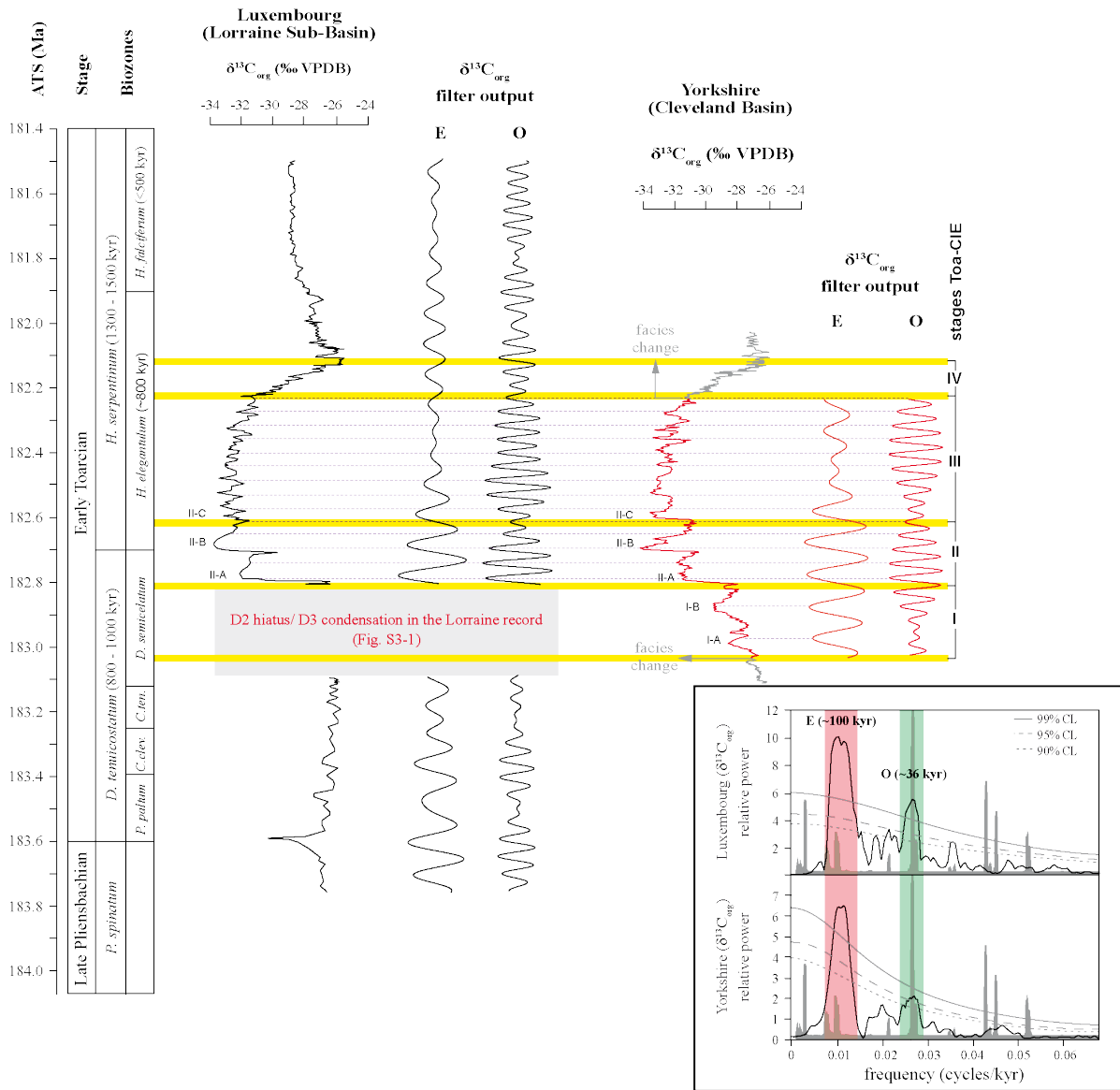


Figure 3-2: Filter outputs for statistically significant frequency peaks in the organic carbon isotope records from the Lorraine Sub-Basin and the Cleveland Basin (data from Kemp et al., 2005). The timescale based on findings of Chapter 2. The MTM power spectra for both $\delta^{13}C_{org}$ records are shown as well. On the base of the frequency ratios peaks can be attributed to ~100 kyr eccentricity and ~36 kyr obliquity periods. MTM spectrums further match with the astronomical model La2004 (Laskar et al., 2004).

3.3. Inferred carbon reservoirs

Observations support previous findings suggesting astronomically-pulsed injections of ^{12}C -enriched carbon from climate sensitive reservoirs, since the observation of astronomically driven $\delta^{13}\text{C}$ variations cannot be explained by volcanogenic mechanisms (Hesselbo et al., 2000a; Kemp et al., 2005; Huang & Hesselbo, 2014). Moreover, pattern, pacing and periodicity hint to an astronomically forced carbon injection from climate-sensitive associated with the Earth cryosphere that became destabilized during long-term global warming. The only suitable reservoir of ^{12}C enriched carbon that can explain these observations is cryosphere-stored-carbon (CSC) in marine and terrestrial settings (Majorowicz et al., 2014), comprising marine gas hydrates ($\delta^{13}\text{C}$ on average -60‰; Anthony et al., 2012), permafrost soil carbon ($\delta^{13}\text{C} \approx -25$ to -35 ‰; Anthony et al., 2012; Vonk et al., 2014), and cryosphere capped methane reservoirs ($\delta^{13}\text{C} \approx -60$ to -90 ‰; Anthony et al., 2012; Wadham et al., 2012). Cryosphere stored carbon composed of CO_2 and CH_4 comprises a major uncertainty in the understanding of Earth's carbon cycle and climate system as reservoir sizes as well as their response towards global warming are poorly understood. Release of carbon from these climate-sensitive reservoirs, in form of CH_4 and CO_2 , can substantially promote and accelerate global warming (e.g. Schuur et al., 2015). Furthermore, release of ^{12}C -enriched carbon is prone to cause major perturbation of the global carbon cycles that would be expressed in a negative CIE (e.g. Dickens, 1999; Majorowicz et al., 2014), as repeatedly observed in this study (Fig. 3-1).

3.4. Indices for a persistent cryosphere during the Early Jurassic

The CSC-model proposed here requires a widespread and persistent cryosphere in polar regions during a period that dominantly has been attributed to a greenhouse mode (Frakes et al., 1992). The view of an overall ice-free Jurassic resulted from poorly dated occurrences of glacially derived deposits and floral distribution patterns in the fossil record of the entire Early Jurassic (see Chapter 1.2.3.). Improved chronologies and higher temporal resolution of oxygen isotope records challenge this view and provide strong evidence for a dramatic cold snap during the Late Pliensbachian, preceding the Toarcian environmental crisis (Vaughan, 2007; Korte & Hesselbo, 2011; Dera et al., 2011a; Silva & Duarte, 2015; Gómez et al., 2015). Occurrence of glendonites and glacially derived deposits at mid- and high latitudes (Fig. 3-3; also see Chapter 1.2.3.) corroborate geochemical proxies (Dera et al., 2011a). The size of the Late Pliensbachian cryosphere carbon pool required to explain the here described Toa-CIE and its astronomically forced variations is difficult to estimate. Former warm climates preceding the Late Pliensbachian resulted in an expansion of the biosphere to high latitudes and promoted the formation of a huge mid- and high-latitude biosphere carbon pool. This biosphere carbon pool was transferred into the cryosphere during the Late Pliensbachian icehouse that lasted for about 3 Myr (Dera et al., 2011a; Silva & Duarte, 2015), a timescale similar to the Pleistocene glaciation (e.g. Knies et al., 2009).

3.5. Cryosphere demise during astronomically forced hyperthermals

Pattern, pacing as well as astronomically forced periodicity documented in the carbon isotope data from the Lorraine Sub-Basin and the Cleveland Basin document a pulsed injection of ^{12}C -enriched carbon into the earth atmosphere during single hyperthermals. The causal and temporal link between the early Toarcian carbon cycle perturbation and the eruption of the K-F-LIP is well constrained (Chapter 1.2.4.) and provided a reasonable triggering mechanism for a global warming initiated cryosphere demise (e.g. [Burgess et al., 2015](#)). The long-term decrease documented in $\delta^{13}\text{C}$ -values might reflect CO_2 emissions from volcanic sources ($\delta^{13}\text{C}_{\text{volcanic}} \approx -6$ to -14‰ ; [Brazier et al., 2015](#)) but might also reflect changes in organic matter composition due to sea level variations ([Montero-Serrano et al., 2015](#); [Suan et al., 2015](#)) (Figs. 3-1, 3-3).

Cryosphere demise and release of ^{12}C -enriched carbon from CSC occurred in several steps in dependence of the sensitivity and stability of the carbon reservoirs and thus has been linked to single “methane guns” ([Dickens, 1999](#)). Carbon release from labile reservoirs, including near surface terrestrial permafrost at mid-latitudes and cryosphere-capped methane reservoirs and methane hydrate at shallow shelf settings ([Majorowicz et al., 2014](#)) was controlled by eccentricity/precession forced insolation changes ([Berger & Loutre, 1994](#); [Hinnov & Park, 1999](#)) and is expressed by the negative $\delta^{13}\text{C}$ excursions within Toa-CIE stages I and II (Fig. 2). The increase in $\delta^{13}\text{C}_{\text{org}}$, subsequent to the negative pulses I-A, I-B, II-A and II-B, reflects brief recovery phases of the cryosphere associated with cooling, decreasing atmospheric CO_2 concentration ([McElwain et al., 2005](#)) and a recovery of the cryosphere associated carbon pool due to CO_2 sequestration by enhanced continental weathering ([Cohen et al., 2004](#)) and organic carbon burial ([Silva & Duarte, 2015](#)). Thus, negative $\delta^{13}\text{C}$ shifts within stages I and II can be attributed to single hyperthermals followed by a subsequent cooling phase that lasted for about 100 kyr, which is in agreement with mass balance calculations proposed for such “methane guns” ([Dickens, 1999](#); [Beerling & Brentnall, 2007](#); [Majorowicz et al., 2014](#)). Ongoing warming, accelerated by the volcanic-triggered release of greenhouse gases, promoted the subsequent demise of more stable cryosphere carbon reservoirs, mainly comprising terrestrial CSC at high latitudes ([Majorowicz et al., 2014](#)). Thawing of high-latitude cryosphere of reduced extent was paced by obliquity periods and is expressed by the $\delta^{13}\text{C}$ fluctuations within stage III (Fig. 3-3). Demise of persistent high-latitude cryosphere occurred over a period of about 400 kyr (stage III), which is in agreement with model results that proposed a total CSC demise 400 kyr after deglaciation ([Majorowicz et al., 2014](#)). The exact amplitude of each single negative $\delta^{13}\text{C}_{\text{org}}$ shift might not exceed -1‰ , when assuming an absolute amplitude of about -3 to -4‰ for the Toa-CIE ([Montero-Serrano et al., 2015](#); [Suan et al., 2015](#)), which is similar to the amplitude documented for the PETM and subsequent smaller hyperthermals ([DeConto et al., 2012](#); [Kirtland Turner et al., 2014](#)). It is interesting to note that the hyperthermals of the Early Eocene are associated with a global warming that occurred within a period of about 5 Myr with an estimated warming of about $0.9^\circ\text{C}/\text{Myr}$ ([Kirtland Turner et al., 2014](#)). The warming of about $2^\circ\text{C}/\text{Myr}$ estimated for the Early Toarcian resulted in a more rapid carbon release and a higher frequency of hyperthermals.

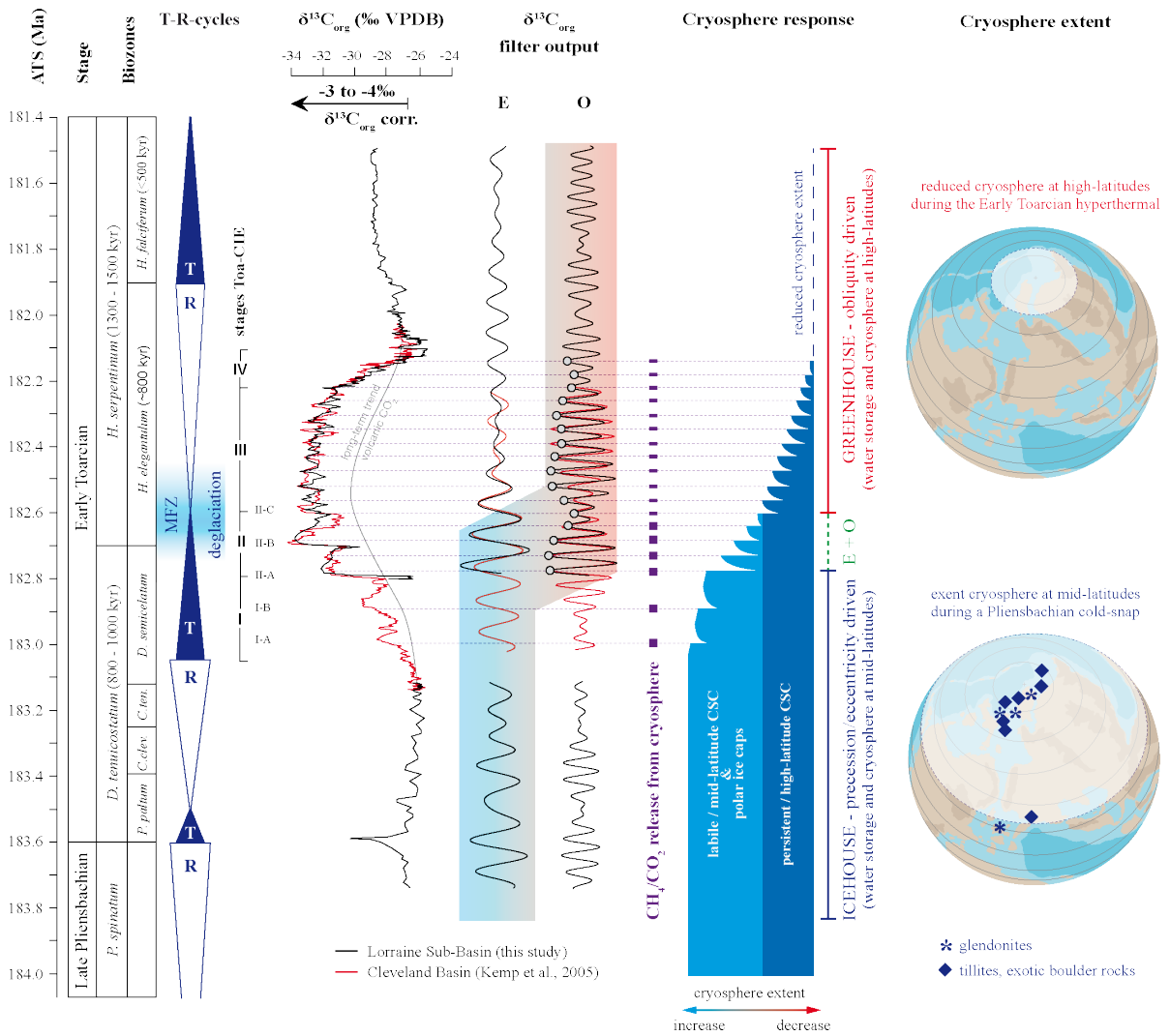


Figure 3-3: Chronology of the Toarcian carbon cycle perturbation and inferred mechanisms. Toa-CIE steps I-A, I-B, II-A, II-B, II-C as well as fluctuations within Toa-CIE stage III can be attributed to individual hyperthermal that were accompanied by carbon release from climate sensitive reservoirs as indicated by the astronomical controlled periodicity of these events. Initial carbon release was externally triggered and stimulated by volcanism of the K-F-LIP. The shift in the astronomical response from eccentricity to obliquity documents carbon injection from mid- and high-latitudinal reservoirs that occurred after exceeding of climate thresholds during long-term global warming.

Moreover, this release of CSC caused an expeditious deglaciation that resulted in a rapid sea level rise, whereby the highest sea level indicating a near-total demise of polar ice is placed in the climax of the Toa-CIE interval (Pittet et al., 2014). The coupling of climate system and carbon cycle is well documented and highlight the role of the cryosphere during the Early Toarcian environmental crisis (Suan et al., 2010; Pittet et al., 2014). The recovery phase (stage IV), following the main Toa-CIE, indicates a depletion of the CSC pool. A gentle cooling occurring within the uppermost *H. elegantulum* subzone coincides with a sea level fall (Pittet et al., 2014) and might have resulted from enhanced silicate weathering (Cohen et al., 2004) and organic matter burial rates (Silva & Duarte, 2015). Moreover, the demise of polar ice that resulted from global warming caused a collapse of the thermohaline circulation that transported warm water masses towards higher latitudes. A sluggish ocean circulation is supported by a modeling approach (Dera & Donnadieu, 2012) and may have promoted the formation of polar ice caps in the upper *H. elegantulum* subzone.

Astronomically forced demise of the cryosphere, including loss of CSC and thawing of polar ice caps, triggered by the emplacement of the K-F-LIP emplacement can explain simultaneous response and coupling of carbon cycle, climate system and sea level changes that have been indicated for the Early Toarcian by a similar evolution of astronomically forced periodicities expressed in sedimentological proxies and carbon isotope data (Hinnov & Park, 1999; Kemp et al., 2005; 2011; Suan et al., 2008a; Huang & Hesselbo, 2014; Ruebsam et al., 2014; 2015). A shift in astronomical response has been postulated for the Pleistocene cooling, whereby obliquity dominated during the warm Pliocene and eccentricity/precession during the cold Pleistocene (Patterson et al., 2014). Thus, it can be inferred that eccentricity-obliquity shift during the Early Toarcian warming can be linked to global warming and possibly to a transition from an icehouse to a greenhouse world.

These results highlight the role of the cryosphere during past and recent global warming, triggered by external mechanisms such as volcanism or anthropogenic greenhouse gas emissions. The timescale of such hyperthermals seems to relate to the triggering mechanisms and the rate of global warming. Rapid warming results in a more frequent overrun of tipping points causing a rapid response of Earth's cryosphere. Results show that the Early Toarcian environmental crisis that occurred over a period of about 900 kyr represents a highly dynamic event, comprising a relatively rapid transition from icehouse to greenhouse conditions, punctuated by brief hothouse events.

3.6. Conclusions

The conceptual model proposed here allows for the first time the linking of many previously isolated observations, including carbon cycle perturbation, global warming and sea level rise, in a coherent Earth System that explains earth atmosphere interactions and climate change during the Early Toarcian. Results confirm an astronomical control on the single carbon injections into the ocean-atmosphere system, whereby the shift in the astronomical response from eccentricity to obliquity forcing, documented in sedimentological parameters (e.g. [Suan et al., 2008a](#); [Ruebsam et al., 2014](#); [2015](#)) as well as in ^{13}C -records can be linked to the displacement of the cryosphere from mid- to high-latitudes during global warming. Observations can be explained by a near-simultaneous demise of polar ice and CSC, resulting in a rapid glacio-eustatic sea level rise and carbon release from ^{13}C -depleted reservoirs, respectively. Cryosphere demise was triggered by the Karoo-Ferrar volcanism that alone fails to explain the Toa-CIE and associated environmental changes, but provides a suitable external triggering mechanism that has the potential to destabilize labile cryosphere after exceeding a thermodynamic threshold. The demise of the cryosphere and release of ^{13}C -depleted carbon was then paced by changes in Earth's solar cycles that repeatedly initiated further passings of climate thresholds. Larger amplitudes during the initial Toa-CIE stages (I, II) resulted from lower frequencies between the single "methane guns" ([Dickens, 1999](#)) and thus longer recover phases that allowed a replenishment of the carbon reservoirs. On the contrary, higher frequencies of "methane guns" during Toa-CIE stage III resulted in lower amplitudes due to shorter replenishment phases.

These results highlight the role of the cryosphere during past and recent global warming, triggered by external mechanisms such as volcanism or anthropogenic greenhouse gas emissions. The timescale of such hyperthermals seems to be related to the triggering mechanisms and the rate of global warming. Rapid warming results in a more frequent overrun of tipping points causing a rapid response of the Earth's cryosphere. The Early Toarcian environmental crisis occurred over a period of about 900 kyr, thus representing rather a hothouse stage than a single brief hyperthermal event. Within the Toarcian hothouse stage several individual hyperthermals indicate the astronomical forced response of the Earth's climate system during rapid global warming.

Chapter Four:

**Glacio-eustatic sea level and salinity cycles during
the Early Toarcian –
Inferred mechanisms and implications for water
mass conditions on the Western Tethyan Shelf**

Abstract

Global warming during the Early Toarcian was accompanied by a rapid high amplitude 3rd order sea level rise that occurred superimposed onto the long-term 2nd order Liassic transgression. The latter was most likely controlled by tectonic processes, whereas the origin of the 3rd order sea level changes remains controversial. Glacio-eustatic mechanisms have been previously invoked as a possible driver, but have not been proven so far. Identifying the underlying mechanisms of Early Toarcian sea level changes is however of paramount importance as oceanographic changes, including widespread black shale deposition throughout the Western Tethyan shelf, were controlled by sea level evolution. Moreover, formation of anoxic bottom waters throughout the Western Tethyan shelf has been associated with a massive freshwater discharge onto the shelf sea that promoted the formation of a stable pycnocline. However, freshwater sources as well as mechanisms controlling the discharge of low-saline waters to the shelf sea remain controversial.

Long-term 2nd order as well as superimposed 3rd order sea level cycles proposed for the Early Toarcian are well expressed in sediments of Core FR-210-078 and can be inferred from changes in sedimentological and geochemical characteristics. Stratigraphic position as well as extent match with the sequence stratigraphy proposed for the Early Toarcian. A rapid transgression in the upmost *D. tenuicostatum* zone can be associated with the major facies change and resulted in a strong condensation of the basal Schistes Carton Fm. Moreover, this high-amplitude sea level rise occurred synchronically with the Early Toarcian carbon cycle perturbation and a drastic global warming, confirming a coupling of climate system, carbon cycle and sea level changes.

Results of this chapter indicate that ice sheet dynamics controlled by 405 kyr astronomical cycles affected the oceanographic conditions throughout the Western Tethyan epicontinental shelf and were the main driver of sea level and salinity changes. Moreover, the coupling of sea level and salinity changes can be explained by the waxing and waning of polar ice caps, which confirm a glacio-eustatic origin of 3rd and 4th order sea level cycles and further identify polar ice as the major freshwater source. Rising global temperatures resulted in the melting of polar ice caps, which initiated a glacio-eustatic sea level rise and an enhanced freshwater discharge to the Western Tethyan shelf. The strong impact of Arctic-derived freshwater on the oceanographic conditions throughout the Western Tethyan shelf resulted from paleogeographic features, comprising a severe restriction of the shelf sea and its connection with the Arctic Ocean via the Viking Corridor. Freshwater discharge to the Western Tethyan shelf can be assumed to have been most efficient during stages of high sea level, when the Viking Corridor reached its widest extent. The impact of Arctic derived fresh water contributions onto the Western Tethyan shelf is expressed by the geographical gradient documented in oxygen isotope data, whereby lower isotope values have been documented from northernmost latitudes in proximity to the Viking Corridor.

4.1. Introduction

Numerous recent paleoclimatic studies, based on oxygen isotope data from belemnites, brachiopods and oysters as well as on the investigation of floral and faunal characteristics and dynamics (see Chapter 1.2.3.), indicate a major global warming during the Early Toarcian that occurred subsequent to a Late Pliensbachian cold climate stage (e.g. Korte & Hesselbo, 2010; Dera et al., 2011a; Silva & Duarte, 2015; Gómez et al., 2015). These works challenged former views of a monotonous Early Jurassic greenhouse climate, with temperatures 5 – 10°C warmer than present day, a low equator-pole temperature gradient and without polar ice caps (e.g. Chandler et al., 1992; Frakes et al., 1992; Hallam, 1994). Moreover, evidence for polar ice during the Late Pliensbachian is provided by the occurrence of glacially derived deposits and glendonites at high- and mid-latitudes (Tchoumatchenco et al., 2008; Suan et al., 2011a; 2013a; Teichert & Luppold, 2013). Therefore, the Early Toarcian warming might reflect a transition from an icehouse to a greenhouse world. Global warming occurred synchronically with a perturbation of the carbon cycle as well as with a rapid high-amplitude 3rd order sea level rise of about 30 – 90 m (e.g. Hardenbol et al., 1998; Hallam, 2001; Immenhauser, 2001; also see Chapter 1.1.2.). Coupling of climate system and sea level changes led to the assumption that glacio-eustatic mechanisms were the main driver of Early Toarcian sea level changes (e.g. Suan et al., 2010; Pittet et al., 2014), which however remains to be confirmed.

Beside a drastic rise in SST, oxygen isotope data from different latitudes across the Western Tethyan shelf expose a strong geographical north-south gradient, with a higher amplitude of about 2 to 3‰, and lower absolute $\delta^{18}\text{O}$ values in locations situated at high latitudes (Figs. 4-1; S4-1). If exclusively linked to temperature changes, the isotopic difference would indicate SST for locations at high latitudes exceeding those at lower latitudes by about 10°C, which is not plausible. It has been therefore assumed that the isotopic difference in $\delta^{18}\text{O}$ values between the locations at mid- and high-latitudes result from significantly lowered sea surface salinity throughout the Western Tethyan shelf (Saelen et al., 1996; Röhl et al., 2001; Dera & Donnadieu, 2012). Mechanisms of shelf water freshening as well as freshwater sources have been discussed controversial and comprise increased riverine freshwater discharge due to intensification of the monsoonal circulation during global warming (Röhl et al., 2001; Bailey et al., 2003; Bour et al., 2007), the inflow of low saline Arctic freshwater (Bjerrum et al., 2001; van de Schootbrugge et al., 2005) that possibly resulted from the demise of polar ice caps (Suan et al., 2010; Dera et al., 2015).

An acceleration of the hydrological cycle and thus and intensification of the continental runoff is indicated by changes in clay mineral assemblages (Dera et al., 2009a; Branski, 2012) as well as by other geochemical proxies (Cohen et al., 2004; Montero-Serrano et al., 2015). Furthermore, intensification of monsoonal circulation during the Early Toarcian has been indicated by sedimentological observations (Suan et al., 2013b; Krencker et al., 2015). On the contrary, an Arctic freshwater source is supported by modeling results (Bjerrum et al., 2001; Dera & Donnadieu, 2012) as well as by the N-S gradient, observed in $\delta^{18}\text{O}$ data, whereby lowest values are documented from northernmost locations in proximity to the Viking Corridor (Fig. S4-1).

Chapter Four: Glacio-eustatic sea level and salinity cycles during the Early Toarcian

Sea level evolution as well as changes in oceanographic conditions strongly affected the hydrodynamic regime and organic matter accumulation throughout the Western Tethyan shelf (Röhl et al., 2001; Frimmel et al., 2004; Hermoso et al., 2013). Therefore, understanding underlying mechanism controlling sea level and salinity changes on the Western Tethyan shelf can provide important insights into superior earth system processes. This chapter examines timing as well as evolution of sea level and changes in sea surface salinity, in the Lorraine Sub-Basin during the Early Toarcian environmental crisis by using inorganic, organic and isotope geochemical proxies as well as sedimentological characteristics. The detailed reconstruction of sea level and sea surface salinity evolution will help to unravel mechanisms governing their fluctuations.

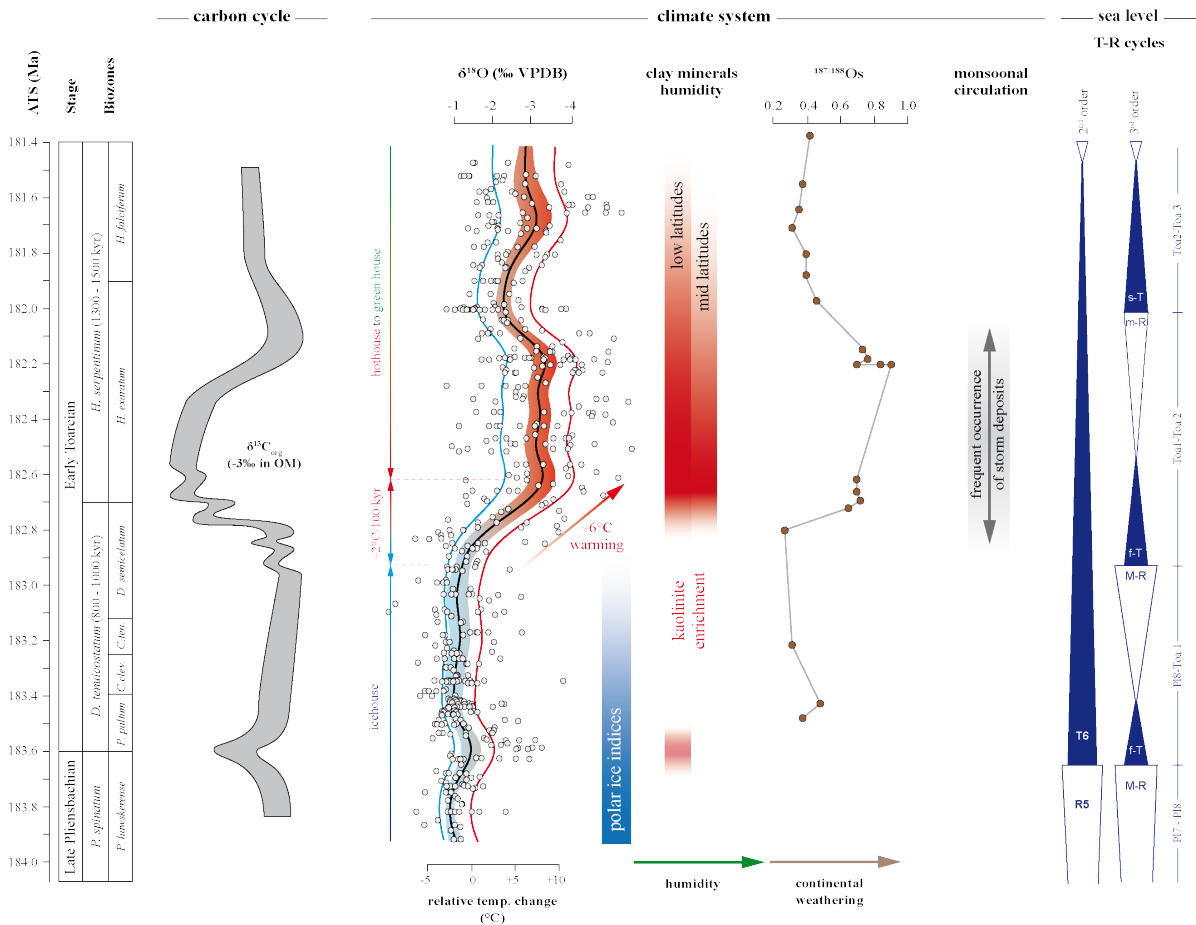


Figure 4-1: The Early Toarcian carbon cycle perturbation was accompanied by drastic environmental changes, comprising a major global warming of about 6°C (Dera et al., 2011a) and an increase in humidity, resulting in the intensification of continental weathering (Cohen et al., 2004; Dera et al., 2009a; Branski et al., 2012). Global warming further caused an intensification of the monsoonal circulation as indicated by the frequent occurrence of storm deposits (Krencker et al., 2015). Moreover, paleoclimatic changes were accompanied by significant changes in sea level that occurred superimposed onto the log-term 2nd order Liassic transgression (e.g. Hardenbol et al., 198; Pittet et al., 2014). The timing of these environmental changes implies a common trigger mechanism.

4.2. Sediment composition and characterization

4.2.1. Sediment composition and sedimentation structure

Sediments of Core FR-210-078 can be described as a four-component system, consisting of a siliciclastic, a carbonate, an organic matter and a pyrite/sulfide fraction (Fig. 4-2). Amounts of the different sediment constituents were calculated following the approach of Röhl et al. (2001). Carbonate, organic matter and sulfide contents were calculated from elemental analysis of TOC, TIC and TS and were expressed as weight percentage (see appendix 3.2.1. for methodology). The siliciclastic content is calculated by the equation:

$$\text{siliciclastics (wt.\%)} = 100 \text{ (wt.\%)} - \text{carbonate (wt.\%)} - \text{OM (wt.\%)} - \text{pyrite/sulfides (wt.\%)}$$

The inverse relation between carbonate and siliciclastic contributions (Fig. S4-2A in the appendix) indicate variable contributions of allochthonous detrital input and autochthonous marine carbonates, preferentially derived from calcareous nannoplankton, like *coccolithophorids* and *schizosphaerelles* (e.g. Röhl et al., 2001, Mattioli et al., 2008; Hermoso et al., 2009b, 2009b). Thus, variations between siliciclastics and carbonates can be attributed to changes in terrigenous contributions and changes in the abundance of calcareous nannoplankton. The former is controlled by sea level changes and continental run off (e.g. Coe, 2003), whereby changes in the abundance of marine biocalcifiers can be related to nutrient availability and environmental conditions, like seawater chemistry, CO₂ concentration or temperature (e.g. Melinte, 2004 and references therein).

Interval 4: Sediments of Interval 4, corresponding to the upper *P. spinatum* zone and lower *D. tenuicostatum* zone, are dominated by siliciclastics (78.3 wt.% on average), whereas the carbonate content stays below 20 wt.% (17.8 wt.% on average). The concentration of organic matter is low and do not exceed 2 wt.% (1.2 wt.% on average), except for some thin horizons were they reach ~3 wt.%. Concentrations of sulfides are low (2.7 wt.% on average), but show a high variability (between 1.3 and 10.6 wt.%). However, high sulfide concentrations are bound to horizons enriched in euhedral pyrite clasts that are most likely of diagenetic origin (Rickard, 2012). The matrix of sediments in Intervals 4 has a preferentially homogenous character, indicating intensive sediment reworking by benthic organisms that resulted in the destruction of former sedimentation structures (Fig. A3). Allochthonous clasts are rather rare but occur at certain horizons. However, coarse sandy contributions and high energy sedimentation structures, like wave ripples or cross stratification were not observed, indicating deposition in an intermediate water depth below the wave base in a certain distance from the coastline (Sahagian et al., 1996; Immenhauser, 2005). Two thin horizons within the upmost *P. spinatum* zone and the upper *D. tenuicostatum* zone show increased carbonate concentrations accompanied by decreased concentrations of siliciclastics. These horizons are further highlighted by the occurrence of reworked shell pavements, indicating an increased impact of wave action towards sedimentation (Fig. 4-2). Sediments corresponding to the Pliensbachian-Toarcian

boundary interval show a contrasting sedimentation style. Sediments are laminated and significantly enriched in OM and framboidal pyrite, indicating a temporary deepening of the depositional environment accompanied by enhanced OM accumulation. Deposition most likely occurred below the wave and storm base, whereby sediments were not affected by benthic reworking processes.

Interval 3: Sediment of Interval 3, corresponding to the uppermost *D. tenuicostatum* zone and lower *H. elegantulum* subzone, are significantly enriched in OM, whose concentration exceed 10 wt.% (10.2 wt.% on average). High OM concentrations are accompanied by high sulfide concentrations that reaches 6.8 wt.%. This interval shows the lowest carbonate content (on average 12.7 wt.%), whereby a slightly increasing trend is observed throughout this interval. Accordingly, siliciclastic contributions (on average 70.3 wt.%) dominate the sediment composition. Sediments show a distinct parallel texture and are strongly enriched in pelagic fauna, like ammonites and fish debris (Fig. A4). Furthermore, fecal pellets and lenses of solid bitumen were observed at certain horizons. The laminated sedimentation style indicates deposition below the wave and storm base and implies that sediment supply occurred by hemipelagic settling and frequent suspension currents. Furthermore, the significant enrichment of pelagic fauna indicates sediment starvation (Figs. 4-2, A3, A4).

Interval 2: Sediments within Interval 2, representing the upper *H. elegantulum* subzone, are characterized by fluctuating contributions of carbonate and siliciclastics, whereby the highest carbonate concentrations are observed in this interval (38.6 wt.% on average). Accordingly, concentrations of siliciclastics are significantly decreased (48 wt.% on average). Sediments are enriched in OM (8.5 wt.% on average) and sulfides (5.0 wt.% on average). This interval shows a remarkable variability in the sediment composition and sedimentation style. Two main types can be distinguished: I) horizons showing a distinct lamination with high carbonate, OM and sulfide concentrations, and II) horizons showing indistinctly laminated (partly homogenous) sediments with lower carbonate, OM and sulfide concentrations (Figs. A3, A4). The prevailing sedimentation process can be ascribed to suspension and turbidity currents (Fig. 4-2). Sedimentation occurred in a low energetic environment, below the wave and storm base. However, the removal of sediment structured in homogenous sediment horizons can be attributed to enhanced benthic activity during certain periods of deposition. Variability of sediment composition as well as sedimentation style indicates that the depositional environment was extremely sensitive towards fluctuations in environmental and oceanographic conditions.

Interval 1: Composition of sediments within Interval 1, corresponding to the *H. falciferum* subzone, show slightly increased concentrations of siliciclastics (59.3 wt.% on average) and reduced carbonate concentrations (29.7 wt.% on average). Furthermore, slightly reduced OM and sulfide contributions of 7.6 and 4.6 wt.%, respectively, are documented within this interval (Fig. 4-2). The sediment structure throughout this interval is less variable, when compared with Interval 2. However, lamination of the sediment is less persistent indicating that sedimentation was affected by re-deposition processes (e.g. winnowing), which most likely resulted from contour currents as significant bioturbation traces were not observed (Figs. A3, A4). Sedimentation was most likely controlled by turbidity currents and temporarily altered by bottom currents (Fig. 4-2).

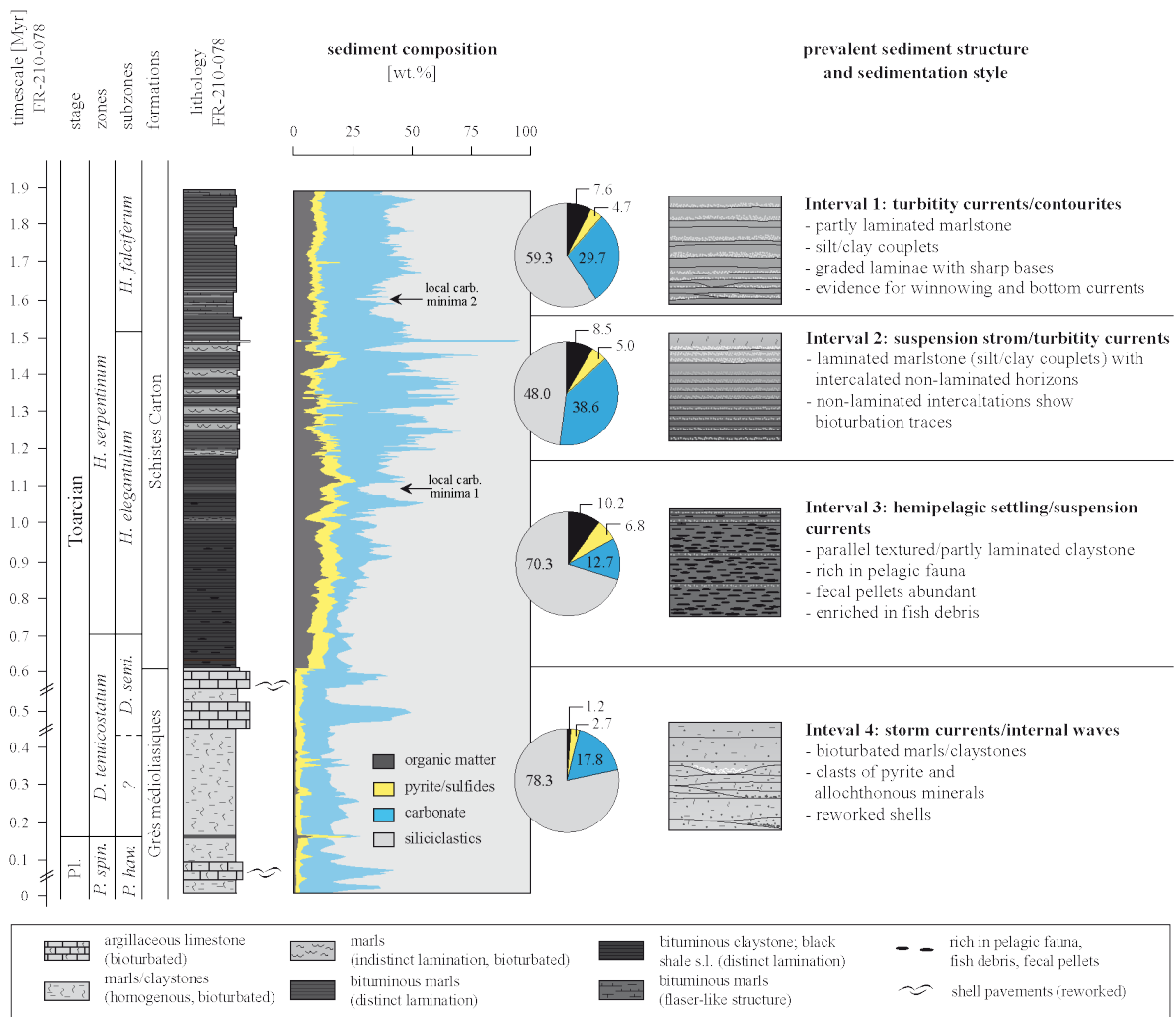


Figure 4-2: Sediment composition and sedimentation style of Core FR-210-078 expressed as a four-phase system, consisting of organic matter, pyrite (sulfides), carbonated and siliciclastic components. Prevailing sediment structures follow the nomenclature of Wignall (1994) and are shown for the different intervals that were distinguished on the base of lithological observations (introduced in Chapter 2; Figs. A3, A4 in the appendix). Changes in lithology, sediment composition and sedimentation style are plotted versus the timescale proposed for Core FR-210-078 (see Chapter 2).

4.2.2. Characterization of the siliciclastic sediment fraction

Changes in the composition of the detrital siliciclastic sediment fraction can be inferred from relative changes in the distribution of elements such as Si, Al, Zr, Ti, K, or Na (e.g. Calvert & Pedersen, 2007). Variations in the relative abundance of Si, Zr and Ti can be associated with changes in the grain-size of the detrital sediment fraction (silt/sand versus clay; *sensu lato*) as these elements are commonly associated with minerals, like quartz (SiO_2), zirconium (ZrSiO_4) or rutile (FeTiO_3), transported with the silt/sand-sized fraction. Changes in the composition of clay mineral assemblages can be inferred from the relative abundance of Al, K and Na and result from changes in continental weathering conditions, changes in the source area or sea level changes (e.g. Nesbitt & Young, 1982; Yarincik et al., 2000a; Pellenard & Deconinck, 2006). Clay assemblages with high Al concentration are characteristic for a kaolinite dominance, whereby the relative enrichment of K and Na can be linked to clay mineral assemblages dominated by illites and smectites, respectively (e.g. Calvert & Pedersen, 2007). Change in the clay mineral assemblages that can be linked to changes in the weathering regime were expressed as Al/K and $\ln(\text{Al}/\text{Na})$ ratios as suggested for sediments with variable carbonate concentration (von Eynatten et al., 2003; Goldberg & Humayun, 2010).

Interval 4, comprising the upper *P. spinatum* and the lower *D. tenuicostatum* zones, documents the highest Si/Al and Zr/Al ratios, indicating high contributions of silt-sized siliciclastics (Fig. S4-2B), whereas sand-sized contributions can be ruled out on the base of sedimentological observations. Highest ratios were documented for a horizon within the uppermost *P. spinatum* zone, whereas the Pliensbachian-Toarcian boundary is marked by a short-term decrease in the ratios. Variable, but low Al/K and $\ln(\text{Al}/\text{Na})$ indicate that clay mineral assemblages in this interval are dominated by relative high, but variable illite and smectite contributions (Fig. 4-3). The uppermost *D. tenuicostatum* zone and the lower *H. elegantulum* subzone, represented by Interval 3, show an abrupt decrease in Si/Al and Zr/Al ratios, implying that the siliciclastic fraction within this interval is dominated by clay minerals. An increase in the ratios, documented in the upper part of this interval, indicate increased contributions of silt-sized siliciclastics. The Al/K and $\ln(\text{Al}/\text{Na})$ ratios show different trends throughout this interval. Preferentially low Al/K ratios reflect increased contributions of illite relative to kaolinite, whereby slightly increased $\ln(\text{Al}/\text{Na})$ ratios indicate reduced smectite contributions relative to kaolinite (Fig. 4-3). Elevated contributions of silt-sized siliciclastic throughout Interval 2 (upper *H. elegantulum* subzone) are indicated by slightly elevated Si/Al and Zr/Al ratios, whereas both ratios shown a decreasing trend throughout this interval. Slightly increased in Al/K and $\ln(\text{Al}/\text{Na})$ ratios can be attributed to elevated kaolinite contribution relative to illite and smectite (Fig. 4-3). A local maximum in Si/Al and Zr/Al ratios at the base of Interval 1 (*H. falciferum* subzone) indicate elevated silt-sized contributions, followed by a decreasing trend in both proxies that indicates an enhancement in contributions of clay-sized detritus. High Al/K and Al/Na ratios confirm that the clay mineral assemblage in this interval is dominated by kaolinite relative to illite and smectite (Fig. 4-3).

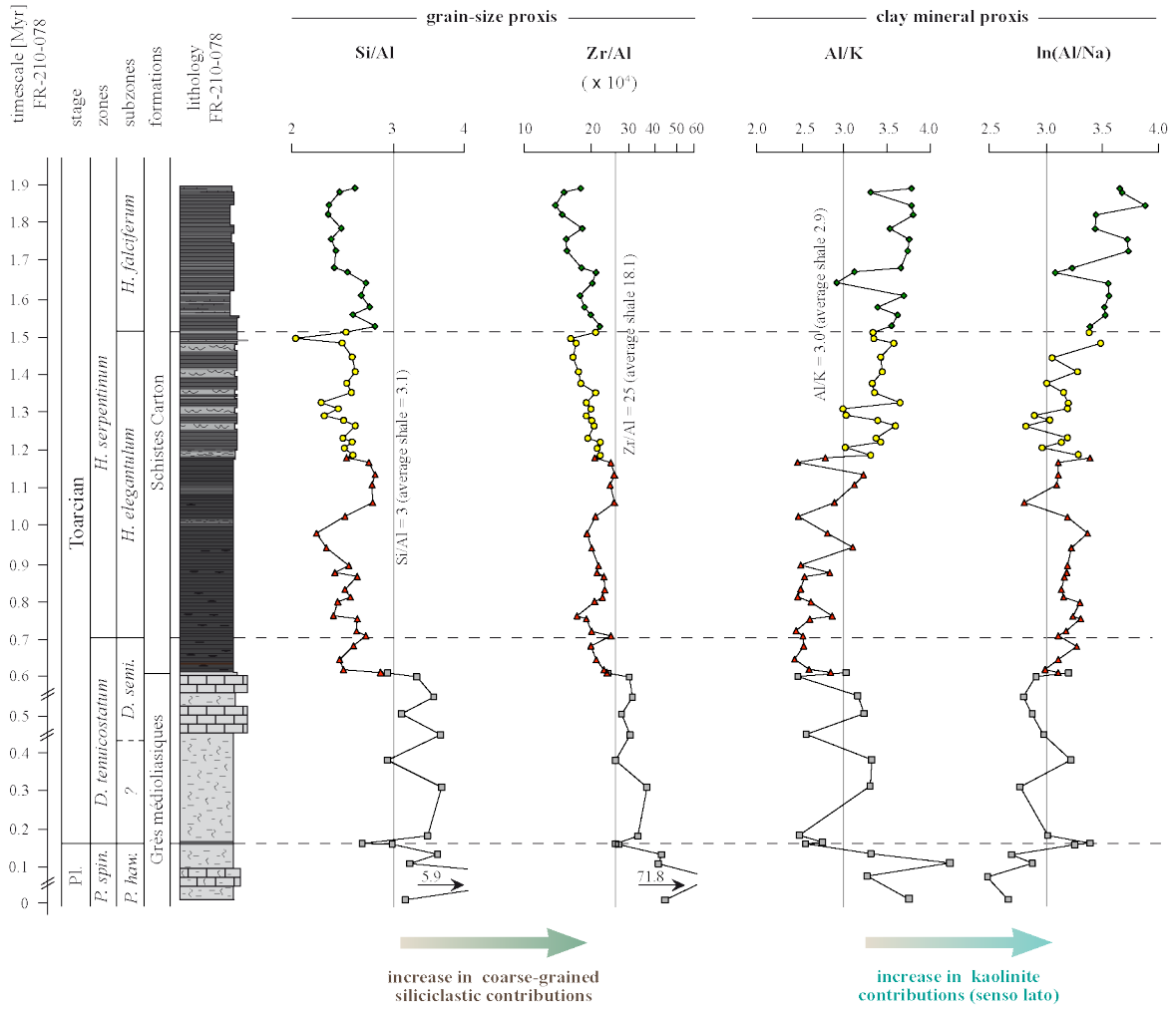


Figure 4-3: Stratigraphic evolution of proxies that allow to detect changes in the composition of the siliclastic sediment fraction. The Si/Al and Zr/Al ratios (logarithmically scaled) represent changes in grain size (silt versus clay; senso lato), whereby Al/K and ln(Al/Na) ratios reflect changes in the clay mineralogy (kaolinite versus illite and smectite; senso lato) (Calvert & Pedersen, 2007). (Si/Al and Zr/Al plotted on a logarithmic scale)

4.2.3. Composition of the carbonate fraction

Previous works carried out in the Central Paris Basin and adjacent areas confirmed that changes in carbonate content of contemporaneous sediments are bound to the abundance of calcareous nannoplankton, which varied as a function of productivity and dilution by terrigenous contributions (Röhl et al., 2001; Mattioli et al., 2008; Hermoso et al., 2009b; Lézin et al., 2012). Furthermore, changes in abundance and composition of the biogenic carbonates were controlled by environmental conditions, whereby the Lower Toarcian is marked by a pronounced biocalcification crisis accompanying the Toarcian carbon cycle perturbation (Erba, 2004; Mattioli et al., 2004; 2008; 2009; Tremolada et al., 2005; Hermoso et al., 2012; Clémence et al., 2015). A drastic demise in marine biocalcifying organisms is well expressed in sediments of Core FR-210-078 by a drastic drop in the carbonate concentration synchronically to the negative Toa-CIE within the upmost *D. tenuicostatum* zone and the lower *H. elegantulum* subzone (Interval 3) (Fig. 4-4; Fig. S4-3A). However, the biocalcification crisis does not result in an overall break down of primary productivity and thus rather represents a shift in the primary producing community structure that culminate in a decoupling of primary productivity and carbonate production (Jenkyns et al., 2001; Bucefalo Palliani et al., 2002; Hermoso et al., 2009b). A high primary productivity and a decoupling of OM and carbonate production during the Toa-CIE interval (Interval 3) is confirmed by a low carbonate concentrations accompanied by high TOC values as well as high Cu/Al and Ni/Al ratios that can be linked to the OM flux and thus to the primary productivity (Fig. S4-4) (Algeo & Maynard, 2004; Tribouillard et al., 2006).

Changes in the composition of the carbonate fraction and the incorporation of elements like Mg, Mn and Sr can provide information about the community structure of marine biocalcifiers (Li et al., 2012; 2013; Hermoso et al., 2009b), changes in the primary productivity (Stoll & Schrag, 2001) and in oceanographic conditions (Vincent et al., 2006), but can also reflect diagenetic and sedimentological processes (e.g. Huckriede & Meischner, 1996; Jarvis et al., 2001). Distinguishing between biological and sedimentologic/diagenetic controls on the carbonate composition is not unambiguous when using element/calcite ratios obtained from bulk geochemical analysis, as the ratio of biogenic versus diagenetic/micritic carbonate is unknown. However, it can be assumed that in intervals with high carbonate concentrations changes in the element/calcite ratio reflect changes in the biogenic carbonate fraction that can be linked to changes in the community structure of biocalcifying organisms. On the contrary, carbonate poor intervals might carry a mixed signal with a strengthened impact of diagenetic processes (Hermoso et al., 2009b; 2012).

Magnesium and manganese incorporation

Controls on Mg and Mn incorporation into biogenic carbonates have been debated controversially, whereby a SST or SSS control on the incorporation of Mg and Mn in the carbonate lattice cannot be confirmed. Moreover, the Mg/Ca and Mn/Ca ratio of biogenic carbonates might be related to changes in the community structure of biocalcifiers (Li et al., 2012; 2013). Incorporation of Mg and Mn into the carbonate fraction can further result from early diagenetic processes in

relation to redox conditions and sea level changes associated with organic matter flux and detrital input (Jarvis et al., 2001). Mg-incorporation is favored by low sulfate concentrations in pore waters, as SO_4^{2-} can preclude dolomite formation by forming Mg- SO_4 bonds (Irwin et al., 1977). The incorporation of Mn into the carbonate lattice is also affected by redox conditions. Under anoxic conditions manganese is present in seawater as dissolved Mn^{2+} . Re-oxygenation events result in the oxidation of reduced Mn^{2+} species to $\text{Mn}^{3+/4+}$, which form insoluble Mn-oxides that congregate in bottom waters close to the water-sediment interface. Furthermore, Mn^{2+} concentrations in bottom waters can be significantly increased by enhanced Mn scavenging on organic matter particles that act as an efficient Mn pump (Jarvis et al., 2001 and references therein). Reestablishment of anoxia again forms dissolved Mn^{2+} , which in combination with increased alkalinity (due to the activity of sulfate reducing bacteria) can lead to the precipitation of rhodochrosite (Huckriede & Meischner, 1996).

Mg/Ca and Mn/Ca ratios show identical trends throughout the studied sediment section, implying that similar mechanisms controlled the accumulation of these elements into the sediment. Relative high Mg/Ca and Mn/Ca ratios, varying around 1.1 and 105, respectively, were documented in samples from Interval 4. However, no significant trend has been documented throughout this interval (Fig. 4-4). Increased Mg/Ca and Mn/Ca ratios reaching values of about 1 and 400, respectively, were documented for the PI-Toa boundary black shale (Fig. 4-4). As carbonate concentrations are always low throughout Interval 4, variations in the ratios most likely reflect a diagenetic signal possibly related to changes in redox condition and/or pore water chemistry. Following a drastic rise in both ratios at the base of Interval 3 (Mg/Ca up to 1; Mn/Ca up to 300) an overall decreasing trend to Mg/Ca and Mn/Ca ratios of about 0.1 and 50, respectively, is documented throughout the upper part of the interval (Fig. 4-4). The maximum at the base of Interval 3 marks the onset of black shale deposition represented by the Schistes Carton Fm. Furthermore, two positive spikes were documented from the upper part of the interval, where Mg/Ca and Mn/Ca ratios show a brief increase to values of about 0.7 and 200, respectively. Horizons, showing increased Mg/Ca and Mn/Ca ratios are highlighted by the lowest carbonate content documented throughout this interval. The overall decreasing trend that started in Interval 3 continues throughout Interval 2, whereby ratios exhibit a significant variability that is better manifested in the Mn/Ca ratios. Throughout this interval Mg/Ca ratios vary between 0.01 and 0.1, whereas Mn/Ca ratios range from 20 to 70 (Fig. 4-4). Both ratios remain low and less variable throughout Interval 1, where Mg/Ca ratios of about 0.7 and Mn/Ca ratios of about 20 were recorded (Fig. 4-4).

Strontium incorporation

The Sr incorporation into biogenic carbonates varies as a function of PP rates of marine calcifiers, whereby elevated Sr concentrations reflect increased PP rates (e.g. Stoll & Schrag, 2001; Wien et al., 2005). Furthermore, changes in SSS have been confirmed to affect the Sr incorporation into the carbonate fraction, whereby freshwater carbonates typically show lower Sr concentrations as freshwater is depleted in Sr^{2+} compared with normal marine seawater (e.g. Vincent et al., 2006). Additionally, different rates of Sr incorporation in the biogenic carbonate lattice have been

documented on taxon level (e.g. [Hermoso et al., 2009b](#)). Early Toarcian sediments from the Western Tethyan shelf show highly contrasting Sr-concentrations, whereby certain stratigraphic intervals are strongly depleted, while others are highly enriched. It has been shown that the variable rates of Sr incorporation into the biogenic carbonate fraction can be attributed to changes in the abundance and community structure of calcareous nannoplankton that represent the main carbonate-producing organisms during this period (e.g. [Hermoso et al., 2009a, 2009b](#); [Minoletti et al., 2009](#); [Lézin et al., 2012](#)). Intervals characterized by low Sr incorporation rates (low Sr/Ca ratios) are dominated by the coccolithophorid *Calyculus*, which has been confirmed to mineralize coccospheres from brackish low-nitrate waters ([Mattioli et al., 2008](#); [Hermosos et al., 2009b](#)). An increase in the Sr incorporation (high Sr/Ca ratios) can be associated with an increased abundance of the coccolithophorid *Crepidolithus* (e.g. [Bour et al., 2007](#); [Hermoso et al., 2009b, 2012](#); [Lézin et al., 2012](#)), a deep dwelling coccolithophorid that have been proven to be strongly enriched in Sr (e.g. [Hermoso & Minoletti, 2008](#); [Minoletti et al., 2009](#)).

In sediments from the Schistes Carton Fm (Intervals 1 - 3) Sr is preferentially bound to the carbonate fraction as indicated by the correlation of Ca with Sr, whereby different slopes of regression lines, indicate variable rates of Sr incorporation into the biogenic carbonate fraction (Fig. S4-3B). Significant amounts of Sr bound to clay minerals can be excluded for samples from the Schistes Carton Fm (Intervals 3, 2, and 1). Thus, the Sr/Ca ratios reflect the degree of Sr incorporation into the carbonate lattice. Evolution of carbonate and Sr concentrations match excellent with observations from the Sancerre Core in the southern Central Paris Basin ([Hermoso et al., 2009b](#)), indicating that similar “basin-wide” processes controlled Sr incorporation into the carbonate lattice.

Moderate ratios between 20 and 80 were documented in sediments corresponding to Interval 4 (upmost *P. spinatum* and lower *D. tenuicostatum* zones), whereby the Pliensbachian-Toarcian boundary and a horizon in the middle part of the *D. tenuicostatum* zone show higher ratios up to 150 and 180, respectively. Increased ratios of about 140 were also documented in the basal and the upper part of Interval 3 (upmost *D. tenuicostatum* zone and lower *H. elegantulum* subzone) that are further highlighted by high Mg/Ca and Mn/Ca ratios, which support a diagenetic origin of this signal (Fig. 4-4). With exception of the high ratios in the carbonate-depleted basal part of Interval 3, Sr/Ca ratios are low through this interval and do not exceed ratio of 70, indicating a drastic Sr depletion of the carbonate fraction. The lower part of Interval 2 (upper *H. elegantulum* subzone) is marked by a significant increase culminating in the middle part of this profile were the highest Sr/Ca ratios of about 150 to 200 were observed. This rapid increasing is followed by a drop in the upper part of Interval 2, were ratios decrease to about values of about 70 (Fig. 4-4). Superimposed to this long-term trend, Sr/Ca ratios show a remarkable variability throughout Interval 2 that roughly aligns with lithological changes. Following a minimum in Sr/Ca ratios of about 50 that marked the base of Interval 1 (*H. falciferum* subzone) ratios show an increasing trend throughout the lower half of this interval, culminating in an maximum of about 120. On the contrary, a steady decrease from ratios of about 120 to 50 is documented throughout the upper part of the profile (Fig. 4-4).

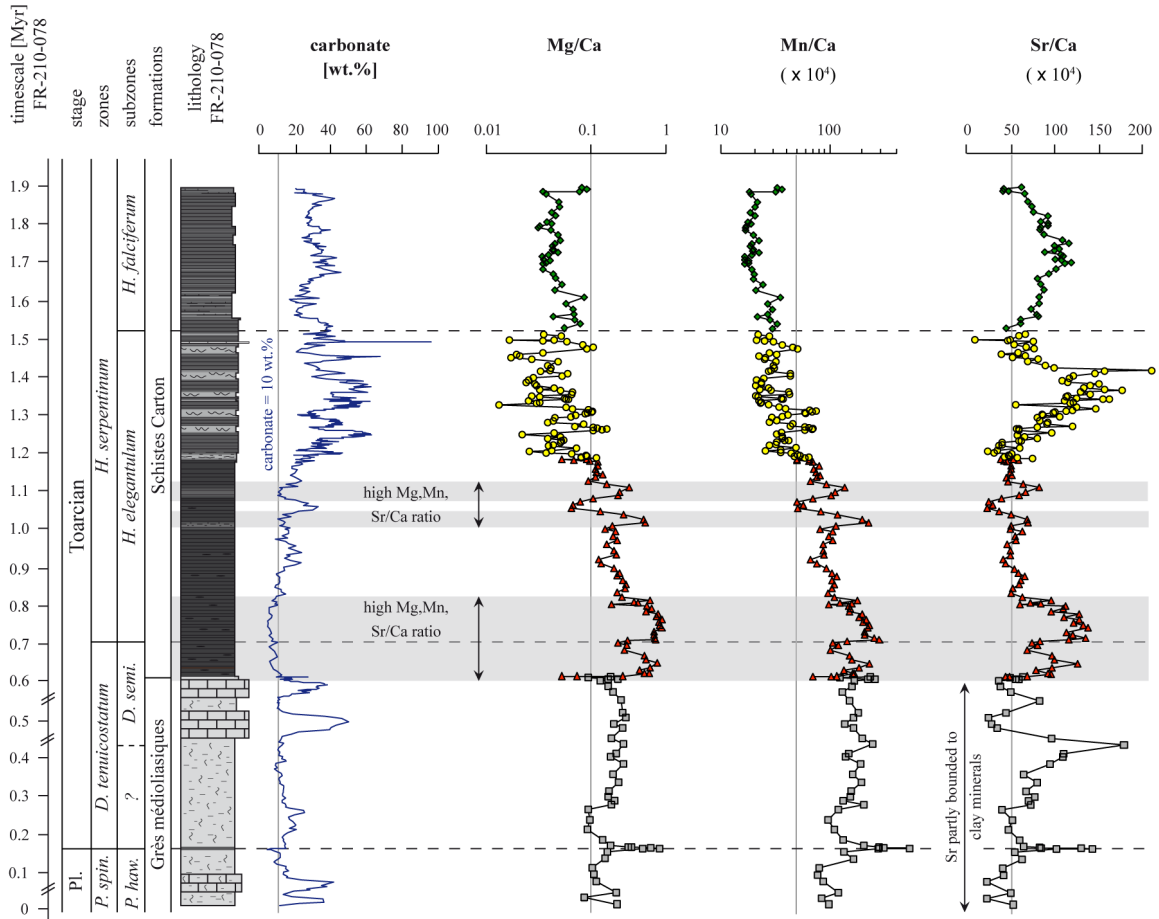


Figure 4-4: Stratigraphic evolution of carbonate content and composition of the carbonate fraction, expressed as Mg/Ca, Mn/Ca and Sr/Ca ratios (Mg/Ca and Mn/Ca ratios are scaled logarithmically). Changes in ratios can reflect shifts in the community structure of biocalcifying organisms (Li et al., 2012; 2013), but can also result from early diagenetic processes. High incorporations rates of Mg and Mn can result from oxygen depletion and can be further characteristic for condensed sediment intervals and thus represent early diagenetic processes. Strontium is preferentially bound to biogenic carbonates produced by calcareous nannoplankton (Hermoso et al., 2009b), whereas Sr/Ca ration in the grey highlighted intervals might also represent a diagenetic signal as a significant proportion of the carbonate fraction is represented by non-biogenic protodolomite. Additionally, the weak correlation of carbonate with Sr in samples from the Grès médioliasiques Fm imply that certain amounts of Sr might be associated with allochthonously derived clay minerals (Fig. S4-2B).

4.2.4. Characterization of the organic matter fraction

Information about composition and preservation of sedimentary organic matter can be obtained from the HI and OI values that allow to distinguish between terrigenous and marine organic matter sources. Furthermore, the maturity state of the sedimentary OM can be inferred from the T_{\max} value (e.g. Bordenave et al., 1993). Marine OM is characterized by low OI and high HI values, while land plant derived OM exhibit an opposite pattern. Furthermore, enhanced organic matter degradation can result in a decrease of the HI values. Additionally, the distribution pattern of odd-numbered *n*-alkanes can provide information about variations in the contribution of terrigenous and marine originated OM. The *n*-alkanes, present in the aliphatic hydrocarbon fraction, were quantified by using the mass fragment m/z 85. Representative ion chromatograms for Intervals 1 to 4 are shown in the appendix (Fig. A10). Contributions of long-chain odd-numbered *n*-alkanes (>20 carbon atoms) are originated in land plants (Eglinton & Hamilton, 1967; Cranwell et al., 1987), while *n*-alkanes from aquatic sources are dominated by odd-numbered *n*-alkanes with chain lengths of <20 carbon atoms (Cranwell, 1973; Cranwell et al., 1987; Meyers, 2003). Changes in relative contributions of terrigenous-originated long-chain *n*-alkanes versus marine originated short-chain *n*-alkanes are expressed by the TAR (terrestrial-aquatic-ratio; Bourbonniere & Meyers, 1997), which is defined as:

$$TAR = \frac{C_{25} + C_{27} + C_{29}}{C_{15} + C_{17} + C_{19}}$$

Additionally, the carbon preference index (CPI; Bray & Evans, 1961) provides information about *n*-alkane sources (even-numbered diagenetic versus odd-numbered biologic):

$$CPI = \frac{1}{2} \times \left[\frac{(C_{25} + C_{27} + C_{29} + C_{31} + C_{33})}{(C_{24} + C_{26} + C_{28} + C_{30} + C_{32})} + \frac{(C_{25} + C_{27} + C_{29} + C_{31} + C_{33})}{(C_{26} + C_{28} + C_{30} + C_{32} + C_{34})} \right]$$

Furthermore, the composition of marine sedimentary organic matter can be strongly affected by the preservation conditions that vary in dependence on OM burial efficiency and redox condition (Burdige, 2007; Zonneveld et al., 2010) but is also affected by differences in the stability and degradability of more labile marine versus refractory terrestrially derived OM (Meyers & Ishiwatari, 1993). Thus, a predominance of refractory land plant derived OM in marine sediments can also result from the poor preservation of more labile marine OM due to enhanced biodegradation.

A low thermal maturity of the OM has been established by previous works (Ruebsam, 2010; Wagner, 2010) and is also confirmed for Core FR-210-078 by low T_{\max} values ranging from 422 to 428°C for the Grés médioliasiques Fm (Interval 4) and from 416 to 423°C for the Schistes Carton Fm (Intervals 1 - 3) (Fig. S4-3). Variations in T_{\max} values between the different facies types can be attributed to specific kerogen types (Bordenave et al., 1993). Due to the low thermal maturity

changes in the TAR and the CPI can be attributed to changes in OM sources, which is supported by the similar trend exhibited in both parameters (Fig. S4-5).

Organic matter of Interval 4 (upper *P. spinatum* and lower *D. tenuicostatum* zones) is characterized by variable OI values (~20 and ~80 mgCO₂/gTOC) and low HI values (<300 mgHC/gTOC). Thus, OM can be attributed to kerogen types II/III (Fig. 4-5A), representing significant terrestrial contributions into a shallow marine environment. Marine OM in this interval is affected by enhanced reworking as indicated by low HI values. The distribution pattern of *n*-alkanes, expressed as TAR, supports this interpretation and confirms significant land plant derived OM contributions (TAR > 0.8; Fig. 4-5B), whereby a clear odd-over-even predominance is indicated by high CPI values ranging between 2 and 3 (Fig. S4-5). Organic matter corresponding to the Pliensbachian-Toarcian boundary black shale differs from this trend. Elevated HI values (up to 530 mgHC/gTOC), low OI values (<20 mgCO₂/gTOC) as well as low TAR values (<0.7) indicate that OM within the Pl-Toa boundary interval is dominated by well-preserved marine OM contributions and can be attributed to kerogen type II.

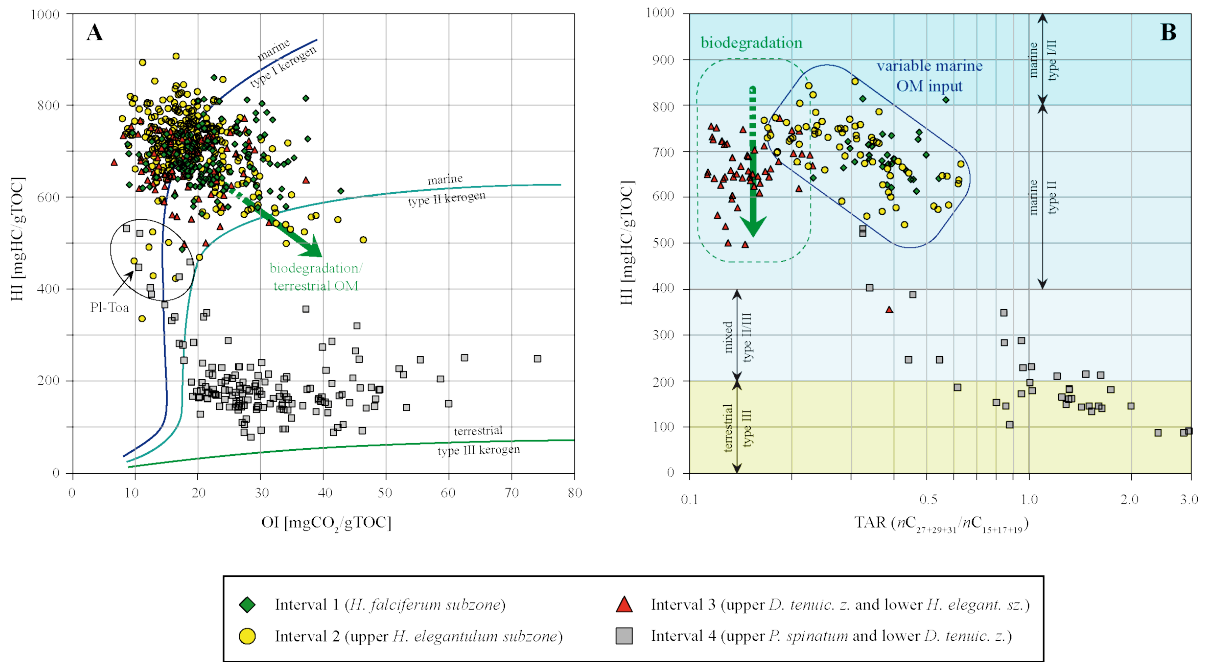


Figure 4-5: A) HI-OI plot indicates increased contributions of terrestrial derived OM for the Grés médioliasiques Fm. On contrast the Pl-Toa boundary is highlighted by increased marine OM input. Samples from the Schistes Carton Fm plot in fields corresponding to kerogen types I-II, indicating well-preserved OM of preferentially marine origin. Samples that show increased OI and lowered HI values indicate that increased contributions and/or enhanced OM reworking affected the composition of the sedimentary OM. HI values exceeding 800 mgHC/gTOC might indicate phases of monospecific algal blooms resulting in increased contributions of H-rich lipids. B) The TAR versus HI plot allows distinguishing between marine and terrestrial OM contributions as well as between differences in the state of OM preservation. The lowest TAR is documented in samples of the basal Schistes Carton Fm. Slightly reduced HI values might indicate enhanced OM degradation due to extremely slow burial rates during a stage of drastic sediment starvation.

Organic matter in sediments corresponding to the Schistes Carton Fm (Intervals 1- 3) can be, on the base of high HI (> 400 mgHC/gTOC) and low but variable OI values (8 – 50 mgCO₂/gTOC), attributed to kerogen types I/II that indicate dominantly marine OM sources (Fig. 4-5A). Preferentially marine OM sources are also confirmed by low TAR values that do not exceed 0.7 (Fig. 4-5B) and by low CPI values that range from 1.2 to 2.0. Lowest TAR values accompanied by slightly decreased HI values are observed in Interval 3 (upmost *D. tenuicostatum* zone and lower *H. elegantulum* subzone), which might result from enhanced OM degradation processes within this interval. A weak covariation of TAR with HI values is observed for OM from Intervals 1 and 2 (upper *H. elegantulum* and *H. falciferum* subzones), indicating variable amounts of land plant derived OM into a marine depositional environment. Moreover, variable degrees of marine OM preservation might also contribute to this pattern (Fig. 4-5B).

Additional information about the composition of sedimentary organic matter and the microlithotype can be obtained from petrographic inspection of polished blocks. Samples from distinct laminated and parallel-textured bituminous intervals show a high abundance of alginites that frequently occur in form of mats or are enriched in distinct horizons, confirming a preferentially autochthonous marine organic matter sources (Fig. 4-7A, B). Telalginites preferentially occur in form of *Tasmanales* but are restricted to samples from the upmost *D. tenuicostatum* zone (lower part of Interval 3) and to the distinctly laminated horizons in the upper *H. elegantulum* subzone (Interval 2) and in the *H. falciferum* subzone (Interval 1). The abundant occurrence of *Tasmanales* in contemporaneous sediments has been previously documented (e.g. [Littke et al., 1988](#)). *Tasmanales* has been associated with transgressive black shales (see [Tyson, 1995](#) pp. 305), whereby other authors suggest a relation to brackish or to cold water environments (e.g. [Filho et al., 2012](#)), which can, however, not be unequivocally confirmed (see discussion by [Tyson, 1995](#), pp. 299 – 308 and references therein).

Sediments from the upmost *D. tenuicostatum* zone and the lower *H. elegantulum* subzone (Interval 3) are further highlighted by an extremely high abundance of small framboidal pyrite (typically <10 μm in diameter). Furthermore, these sediments show no distinct lamination, indicating deposition under extreme stagnant conditions, which match other sedimentological observations (see 4.2.1.). Similar observations were made for a parallel core studied by [Song et al. \(2014\)](#). Samples from indistinct and bioturbated intervals, identified within the upper *H. elegantulum* subzone (Interval 2), show a significantly reduced abundance of disperse alginites. These horizons are highlighted by a frequent occurrence of sporinites (Fig. 4-7C, D), indicating higher contributions of allochthonous organic matter. Furthermore, framboidal pyrites are less abundant in these horizons.

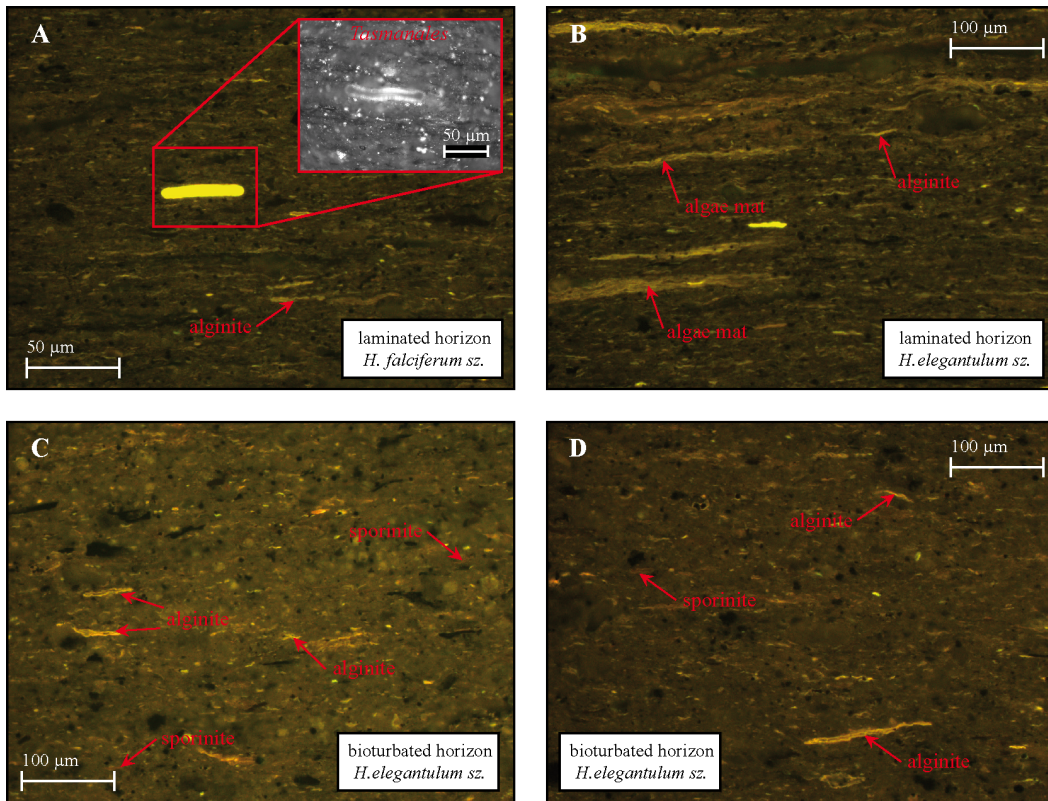


Figure 4-6: Representative microphotographs (in incident light fluorescence mode) from polished blocks for 4 different facies types identified in Core FR-210-078. Samples from bituminous intervals (**A**, **B**) contain high concentrations of alginite, which can occur as algal mats. Large telalginites (*Tasmaniales*) occur in the upmost *D. tenuicostatum* zone and the *H. falciferum* subzone (Intervals 3 and 1; **A**). Samples from indistinctly laminated and bioturbated horizons within the upper *H. elegantulum* subzone (Interval 2) show a significantly lower abundance of alginites but are enriched in sporinites (**C**, **D**).

4.3. Salinity proxies

4.3.1. Oxygen isotope values of the carbonate fraction

Oxygen isotope values of authigenic carbonates vary as a function of the temperature, precipitation and the $\delta^{18}\text{O}$ value of the seawater, whereby the $\delta^{18}\text{O}$ value of the seawater is controlled by the extent of polar ice and/or by riverine freshwater discharge into a marine environment (e.g. Grossmann, 2012 and references therein). Storage of ^{18}O -depleted water in form of polar ice and glaciers results in the ^{18}O enrichment of the seawater and consequently of marine authigenic minerals. This trend is reinforced by lower SST during glacial periods (Lea et al., 2000). The dual dependence of the $\delta^{18}\text{O}$ -values can amplify the signal and thus can be clearly attributed to a climate signal.

A drastic decrease in $\delta^{18}\text{O}$ values of about -1.5 to -3.5‰ at the *D. tenuicostatum*- *H. serpentinum* transition is documented from several locations throughout the Western Tethyan shelf and the Mediterranean and is commonly interpreted as a rise in global sea surface temperatures (e.g. Dera et al., 2011a and references therein). The magnitude of the $\delta^{18}\text{O}$ drop exhibits a strong geographical gradient, whereby the higher amplitudes were documented from the NE part of the shelf. Amplitudes decrease towards the SE, whereby lowest amplitudes were recorded from locations in the Mediterranean realm (e.g. Dera & Donnadieu, 2012; Fig. S4-1). This gradient reflects rather a salinity signal than a temperature signal as an increase in SST temperatures of about 10°C towards higher latitudes is most unlikely (e.g. McArthur et al., 2000; Bailey et al., 2003; Dera & Donnadieu, 2012).

Throughout the studied interval oxygen isotope data of the bulk carbonate fraction vary between -7 and -3.5‰. Rhythmic fluctuations between -6 and -4.5‰ were documented for sediments from Interval 4 (upmost *P. spinatum* and lower *D. tenuicostatum* zones). Values drastically increase to about -3.5‰ in sediments corresponding to the basal Interval 3 (upmost *D. tenuicostatum* zone and lower *H. elegantulum* subzone). In the following values show a decreasing trend throughout this interval. Lowest values of about -7‰ were documented in samples from the upper part of the interval. Moreover, very low oxygen isotope values might result from diagenetic processes under the influence of organic matter (Fig. S4-6). Slightly higher $\delta^{18}\text{O}$ values that range from -6.2‰ to -4.3‰ are documented in samples from Interval 2 (upper *H. elegantulum* subzone). Throughout this interval $\delta^{18}\text{O}$ values rhythmically, whereby lower values are documented in samples from distinctly laminated horizons and higher values from the indistinctly laminated horizons (Fig. 4-7). Oxygen isotope data in samples from Interval 1 (*H. falciferum* subzone) range from -6.4 to -4.8, whereby no significant trend can be observed (Fig. 4-7).

4.3.2. Distribution of methyltrimethyltridecylchromans

The distribution of methyltrimethyltridecylchromans (MTTCs) has been successfully applied as surface seawater salinity parameter (e.g. Bechtel et al., 2007; Wang et al., 2011; Tulipani et al., 2015), whereby the origin of these compounds is still debated. A biosynthetic origin from phytoplanktonic organisms has been proposed by Sinnighe Damsté et al. (1993), although MTTCs or appropriate diagenetic precursor molecules have never been found in living organisms. Alternatively, an early diagenetic origin by condensation reactions of phenol and alkylphenoles (Li et al., 1995; Tulipani et al., 2013), or by cyclization of alkylphenols (Barakat & Rullkötter, 1993) has been proposed. Mono-, di- and tri-methyl substituted MTTCs are present in all samples in the aromatic hydrocarbon fraction, whereby only traces of mono-MTTCs have been detected. Therefore, the relative distribution of MTTCs is expressed as tri-/di-MTTC ratio. Characteristic ion chromatograms are shown in the appendix (Fig. A14). High ratios, indicating a dominance of 5,7,8-trimethyl-MTTC, reflect diminish surface salinities, whereas low ratios indicate increased concentrations of 5,8 and 7,8-dimethyl-MTTCs reflect more saline conditions.

Low and less variable ratios between 3 and 5 are documented throughout Interval 4 (upmost *P. spinatum* and lower *D. tenuicostatum* zones), whereas the Pliensbachian-Toarcian boundary black shale is highlighted by a shift to ratios of about 14 (Fig. 4-7). A significant increase in the ratio is also documented within the lower part of Interval 3 (upmost *D. tenuicostatum* zone and lower *H. elegantulum* subzone), whereby values remain very high (~10 on average) throughout this interval. Lower ratios that vary between 5 and 10 are noted within Interval 2 (upper *H. elegantulum* subzone), whereby periodically fluctuation follows lithological changes. High ratios are documented for distinctly laminated sediments, whereas low ratios are documented for horizons showing an indistinct lamination. Subsequently an increasing trend in tri-/di-MTTC ratios is observed throughout Interval 1 (*H. falciferum* subzone) (Fig. 4-7).

4.3.3. Abundance of C₃₀ steroids

The occurrence of C₃₀-4-desmethylsteroids (C₃₀ steroids) is highly diagnostic for marine environments as these compounds are biosynthesized by marine *Pelagophyte* algae, like *Sarcinochrysis marina* and *Nematochryopsis roscoffensis* (Volkman, 2003), which are intolerant towards enhanced freshwater input and thus lower SSS (Peters et al., 2005). These algae were originally assigned to the *Chrysophyceae* but have been reclassified into *Pelagophyceae* (see Volkman, 2003 and references therein). The C₃₀ steroids, present in the aliphatic hydrocarbon fraction, were identified using m/z 217 for the regular steranes and m/z 257 for the dia-sterenes in combination with their molecular masses. Characteristic ion chromatograms are shown in the appendix (Figs. A12, A13A). The amount of C₃₀ steroids is expressed as the sum of regular C₃₀ steroids and C₃₀ dia-sterenes, as both compounds derive from in a C₃₀ sterol precursor (Mackenzie et al., 1982).

Low concentrations of C_{30} steroids of $\sim 6.5\%$ on average are found in samples from Intervals 4 and 3 (upmost *P. spinatum* and *D. tenuicostatum* zone, lower *H. elegantulum* subzone), whereby the Pliensbachian-Toarcian boundary is marked by a significant 2.5% drop in the abundance of C_{30} steroids (Fig. 4-6). A slight increase in the concentration of C_{30} steroids is documented in the middle part of Interval 3 (lower *H. elegantulum* subzone) and is followed by a significantly decreasing trend culminating in a minimum of about 4.7% within the uppermost part of this interval (Fig. 4-6). Samples from Interval 2 (upper *H. elegantulum* subzone) are substantially enriched in C_{30} steroids ($\sim 7.5\%$ on average), whereby values are highly variable (6 – 12%) and show periodically fluctuations throughout his interval. Average concentrations of about 7.5% in samples from Interval 1 (*H. falciferum* subzone) are comparable to the concentrations reported in samples from the Interval 2, but exhibit a much lower variability (Fig. 4-7).

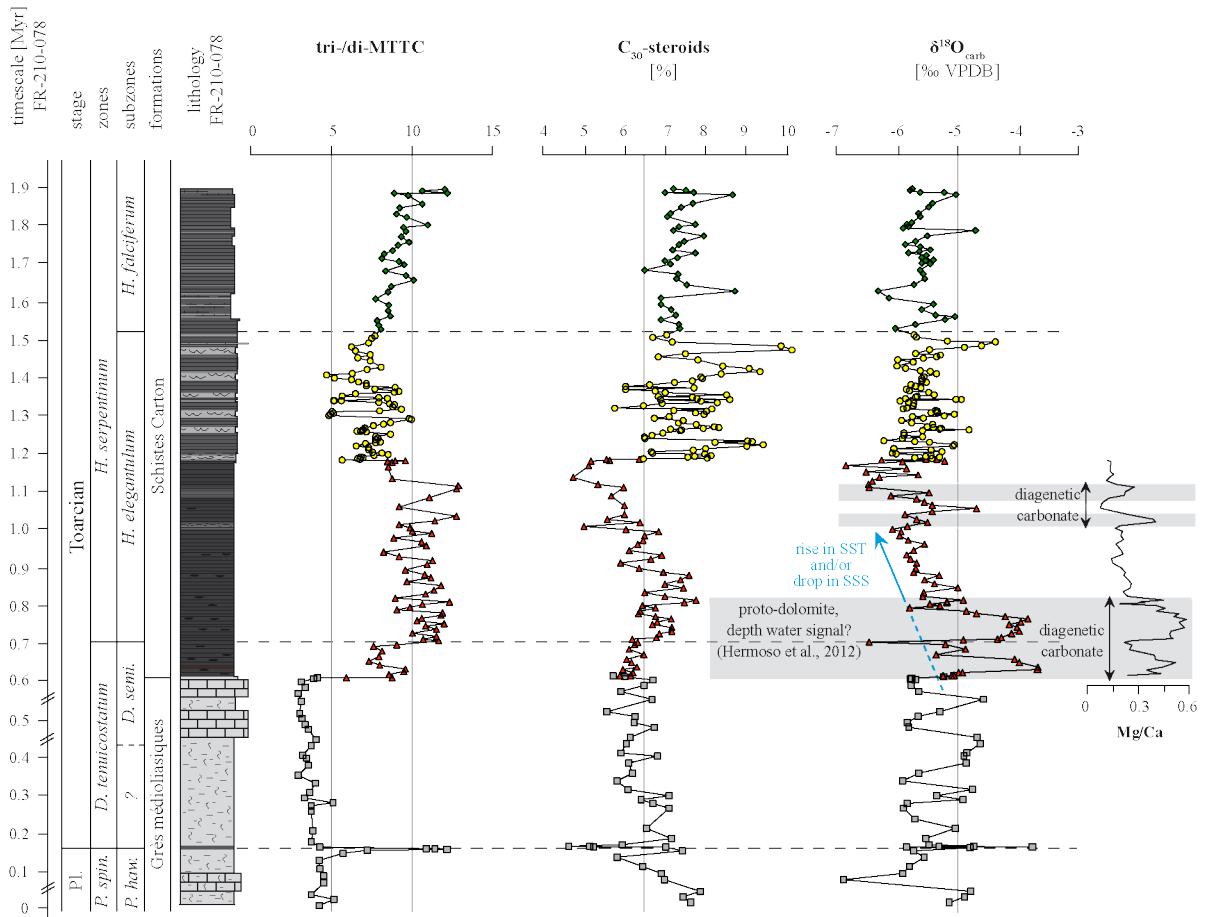


Figure 4-7: Evolution of proxies proposed to reflect changes in the sea surface salinity (SSS), comprising MTTCs, C_{30} steroids and $\delta^{18}O$ values. The drastic increase in tri-/di-MTTC ratios attest a drop in SSS that aligns with a major facies change at the base of the Schistes Carton Fm. Lowest SSS can be assumed for the upmost *D. tenuicostatum* zone and the lower *H. elegantulum* subzone. The low abundance of C_{30} steroids further indicates conditions differing from normal marine environments. A return to more normal marine conditions, with increased SSS, occurred in the upper *H. elegantulum* subzone and is evident from both proxies. The evolution of SSS can be also inferred from $\delta^{18}O$ values, whereas some horizons were possibly affected by diagenetic alteration as indicated by the significant coevolution of $\delta^{18}O$ values with Mg/Ca ratios. Furthermore, the upmost *D. tenuicostatum* zone is associated with a rise in sea surface temperatures (SST) of about $6^{\circ}C$, also contributing to a decrease in $\delta^{18}O$ values.

4.4. Discussion

4.4.1. Sequence stratigraphic framework and sea level evolution

The evolution of the sea level can be inferred from changes in sediment composition as well as from changes in the composition of the different sediment constituents. Transgressive phases can be expressed by an increase in autochthonous marine carbonate contributions, a decrease in the grain size of the clastic sediment fraction (low Si/Al, Zr/Al; Williams et al., 2001; Coe, 2003) and a decrease in terrestrially originated organic matter contributions (e.g. high HI, low OI and TAR). However, changes in sediment composition in highly dynamic shallow marine shelf settings can also result from climate changes that affected the intensity of continental run off and thus the sediment supply from continents. Furthermore, changes in current systems can result in changes in the source area from which sediments were delivered.

Long-term sea level evolution (the 2nd order Liassic transgression)

The Early Toarcian is marked by a long-term 2nd order tectonoeustacy-driven transgression (T6; Liassic transgression) following a Late Pliensbachian regressive phase (R5) that led to the formation of hiatuses and sedimentation gaps in contemporaneous strata across the Western Tethyan shelf (Hardenbol et al., 1998; Pittet et al., 2014). The base of the Liassic transgression, the P18 maximum regressive surface (MRS), can be placed in the upper *P. spinatum* zone (upmost Pliensbachian). In Core FR-210-078 this MRS corresponds to a horizon strongly enriched in reworked shell fragments that further shows high Si/Al, Zr/Al as well as high TAR values, indicating significant contributions of coarse quartz-rich silt-sized siliciclastics and terrestrially contributed organic matter (Fig. 4-8). The sediment structure is characteristic for a shallow marine environment, where deposition is affected by wave action as indicated by reworked shell material. A similar position of the P18 MRS has also been documented in the southern Central Paris Basin (Gély & Lorenz, 2006; Hermoso et al., 2013).

The Liassic transgression is well expressed by a long-term decrease in Si/Al and Zr/Al ratios throughout the *D. tenuicostatum* and *H. serpentinum* zones, indicating a decrease in coarse-grained quartz-rich siliciclastics due to retrograding coastlines that resulted in reduced contributions from the continents (Coe, 2003). According to Hardenbol et al. (1998) and Gély & Lorenz (2006) the maximum flooding surface (MFS) is placed somewhere within the uppermost *H. serpentinum* zone, close to the *H. serpentinum*-*H. bifrons* boundary. In the Sancerre Core this stratigraphic interval is marked by the lowest input of coarse siliciclastics, accompanied by the lowest Si/Al and Zr/Al ratios (Hermoso et al., 2013). The *H. serpentinum*-*H. bifrons* boundary is not recovered in Core FR-210-078, however, lowest Si/Al and Zr/Al ratios are also documented for the upper *H. falciferum* subzone. Results further match with the findings from the Southern German Basin, where the MFS of the Liassic transgression is also placed in the upper *H. falciferum* subzone and characterized by a condensed sediment interval (Röhl et al., 2001).

Short-term sea level evolution (3rd order eustatic cycles)

Subsequent to the 2nd order transgression the Early Toarcian records several rapid high-amplitude sea level fluctuations that were attributed to 3rd order cycles, namely the P18-Toa1; Toa1-Toa2; Toa2-Toa3 cycles (review Chapter 1.1.2.; also see [Hardenbol et al., 1998](#); [Gély & Lorenz, 2006](#)), which are possibly of glacio-eustatic origin (e.g. [Hallam, 1997, 2001](#); [Pittet et al., 2014](#)).

P18-Toa1 cycle. The P18-Toa1 cycle covers the uppermost *P. spinatum* zone and the major part of the *D. tenuicostatum* zone ([Hardenbol et al., 1998](#); [Gély & Lorenz, 2006](#)). A rapid, but short-lived transgressive phase, which started in the uppermost *P. spinatum* zone, is well expressed in Core FR-210-078 by a laminated bituminous claystone that highlights the Pliensbachian-Toarcian boundary (Pl-Toa boundary black shale). The sedimentation style indicates that deposition occurred below the wave and storm base and allochthonous contributions were transported via turbidity currents. A decrease in silt-sized siliciclastic contributions is documented by low Si/Al ratios (<3). Reduced input from the continental sources has been also confirmed by decreased TAR values (<1) and increased HI values (>500 mgHC/gTOC), indicating that OM in this horizon is of dominantly marine origin. The transgressive phase, marking the lower part of the P18-Toa1 cycle, might have led to strongly reduced sediment accumulation rates, resulting in the condensation of the Pliensbachian-Toarcian boundary section. Reduced input of siliciclastic contribution relative to the organic matter flux might be indicated by elevated Mn/Ca ratios (>300), supporting reduced sediment accumulation rates ([Jarvis et al., 2001](#)). A drop in Al/K ratios to values of about 2.5 indicates a reduced kaolinite contribution, which can reflect a decrease in chemical weathering or a rapid transgression as kaolinite is preferentially deposited in proximity to shore lines ([Yarincik et al., 2000a](#); [Pellenard & Deconinck, 2006](#)). With respect to lithological observations and other geochemical data, a sea level-driven control of the Al/K ratio is more likely. Furthermore, an increase in kaolinite contributions to the shelf sea that resulted from a short-lived warming at the Pl-Toa boundary has been documented from contemporaneous sediments of adjacent basins ([Suan et al., 2008b, 2010](#); [Dera et al., 2009a; 2011a](#); [Branski, 2012](#)). Condensation of the Pliensbachian-Toarcian boundary interval has also been documented for other locations (D1 condensation; [Pittet et al., 2014](#)) and might result in a shorter duration of the *D. tenuicostatum* zone in sections on the Western Tethyan shelf when compared with the Mediterranean realm (compare [Suan et al., 2008a](#) and [Ruebsam et al., 2014, 2105](#)). Following the sea level rise in the lowermost *D. tenuicostatum* zone, the upper part of this interval represents a steady regressive phase. Sediments are dominated by silt-sized siliciclastic contributions as indicated by high Si/Al that vary between 3 and 4 and Zr/Al ratios that scatter around 30 (Fig. S4-2B). Elevated organic matter contributions from the continents are also indicated by high TAR values >1 and low HI values that tend to remain below 300 mgHC/gTOC. Furthermore, periodically fluctuations in the geochemical proxies discussed can be attributed to high-frequency sea level fluctuations. The Toa1 MRS can be placed in the uppermost *D. tenuicostatum* zone and is marked by a sediment interval enriched in reworked shells that is characterized by high Si/Al (~3.8), Zr/Al (~30) and TAR values of about 1.5 (Fig. 4-8). This sequence boundary is not recognized in the Sancerre Core, where the uppermost *D. tenuicostatum* zone has been attributed to the MFS of the P18-Toa1 cycle ([Hermoso et al., 2013](#)). A similar conclusion was reached by [Ponsot \(1994\)](#), who

attributed the P18-Toa1 cycle to the *D. tenuicostatum* zone and to the *H. exaratum* subzone. Interpretation by Ponsot (1994) and Hermoso et al. (2013) might result from the fact that the P18-Toa1 cycle can be missing partly due to erosion and/or strong condensation. However, Gély & Lorenz (2006) identified the Toa1 MRS within the uppermost *D. tenuicostatum* zone. A regressive trend in the upper *D. tenuicostatum* zone is also evident from the Southern German Basin (Reisdorf, 2001; Röhl et al., 2001; Montero-Serrano et al., 2015), from the British Islands (e.g. Hesselbo, 2008) as well as from the Lusitanian Basin (e.g. Pittet et al., 2014). In the Lusitanian Basin the regressive phase in the upper *D. tenuicostatum* zone is expressed by the D2 hiatus (Pittet et al., 2014). A sea level fall resulting in the removal of sediments corresponding to the *D. tenuicostatum* zone is also reported from some settings from the Paris Basin (van Breugel et al., 2006).

Toa1-Toa2 cycle. The 3rd order Toa1-Toa2 cycle covers the upmost *D. tenuicostatum* zone (*D. semicelatum* subzone) and the *H. elegantulum* subzone, represented by Intervals 3 and 2. The transgressive phase of this cycle is well expressed by a significant change in the lithology, marking the boundary between the Grés médioliasiques Fm and the Schistes Carton Fm. Sediments show a distinctive parallel textured and partly laminated sedimentation style and are highly enriched in OM, indicating that deposits were unaffected by wave and storm action or benthic reworking processes in a deep basin under extremely stagnant conditions. Extreme stagnant conditions are also indicated by the microstructure of sediments that show no distinct lamination. The high content of siliciclastics (70.3 wt.% on average), characterized by low Si/Al (~2.4) and Zr/Al (~20) ratios, indicate, in combination with sediment structures, that sediment supply was dominated by fine-grained mud and was transported via hemipelagic settling and periodically reoccurring suspension currents. Sediments are significantly enriched in pelagic fauna, fecal pellets and *Tasmanales* remains (telalginites), indicating strongly reduced sediment accumulation rates that resulted from rapidly retrograding coastlines (Coe, 2003). A significant retrogradation of the coastlines during the Toa1-Toa2 transgression is also indicated by low Al/K ratios of ~2.5 that indicate drastically reduced abundances in kaolinite (Yarincik et al., 2000a; Pellenard & Deconinck, 2006). Similar observations have been reported from the Sancerre Core, where the basal Schistes Carton Fm and thus the Toa-CIE interval is also highlighted by low abundances in kaolinite (Hermoso & Pellenard, 2014). Low kaolinite concentration in sediments from the Paris Basin cannot be explained by climate-driven processes, as this stratigraphic interval represents a period of drastic global warming (Dera et al., 2011a), increase in $p\text{CO}_2$ (McElwain et al., 2005) and enhanced continental weathering (Cohen et al., 2004; Montero-Serrano et al., 2015) that resulted in an increased kaolinite contributions to the shelf seas (Dera et al., 2009a; Branski, 2012). Thus, low kaolinite concentrations clearly support a rapid sea level rise, taking place during this time. Low sediment accumulation rates further resulted in only minor dilution of the OM fraction as expressed by high OM concentrations. The nearly total absence of terrigenous contributions is also indicated by very low TAR values (0.1 to 0.2) that confirm predominantly marine OM sources (alginites and telalginites). However, extremely slow burial rates resulted in enhanced degradation processes, expressed by slightly lowered HI values (Fig. 4-5B). Additionally, the biocalcification crisis, accompanying the Toarcian carbon cycle perturbation, resulted in only minor contributions of autochthonous marine carbonate (12.7 wt.% on average),

which further contributed to a sediment starvation. These observations are in agreement with elevated Mn incorporation rates into the carbonate fraction ($Mn/Ca = 100$ to 300) that can be characteristic for condensed sediment intervals (Jarvis et al., 2001). Condensation of contemporaneous strata has also been documented from the Lusitanian Basin (D3 condensation; Pittet et al., 2014) as well as from the Cleveland Basin (McArthur et al., 2000; McArthur & Wignall, 2007 and references therein). The MFS of the Toa1-Toa2 cycle is not easy to identify, but might be located somewhere within the lower *H. elegantulum* subzone, which is in agreement with findings from the Lusitanian Basin (Pittet et al., 2014). The upper *H. elegantulum* subzone (Interval 2) can be attributed to a regressive phase (FSST). An increase in silt-sized detrital contribution is clearly expressed by increased Si/Al (2.4 to 2.8) and Zr/Al (15 to 22) ratios. A strengthening of continental derived contributions is also evident from an increase in the TAR (0.2 to 0.6), indicating enhanced delivery of land plant derived OM (Fig. 4-8). This sea level fall was accompanied by a drastic increase in sediment accumulation rates resulting from progradating coastlines (Coe, 2003) as well as from re-deposited sediments eroded at shallow marine settings that become sensitive towards winnowing processes (Macquacker & Howell, 1999; Trabucho-Alexandre, 2014). The sensitivity of the environment towards fluctuations in sea level and/or environmental changes is clearly expressed by the lithological variability that has been documented in the upper *H. elegantulum* zone (Interval 2). The exact position of the Toa2-MRS is not unambiguous but can be placed somewhere within the lowermost *H. falciferum* subzone as high Si/Al values (~ 2.8) and Zr/Al values (~ 22), accompanied by increased concentrations of siliciclastic as well as increased TAR values (~ 0.6), are documented for this interval (Fig. 4-8). The steady increase in autochthonous carbonate, observed throughout the upper *H. elegantulum* zone, resulted from a recovery phase of marine nannoplankton following a biocalcification crisis (e.g. Mattioli et al., 2009; Hermoso et al., 2009b; Clémence et al., 2015). Changes in sediment accumulation rates accompanying the sea level changes within the 3rd order Toa1-Toa2 cycle are also evident from cyclostratigraphy (Ruebsam et al., 2014; 2015) and strontium isotope trends (McArthur et al., 2000; McArthur & Wignall, 2007).

An additional 4th order cycle can be identified within the FSST of the Toa1-Toa2 cycle. The cycle is bordered by two local maxima in Si/Al and Zr/Al ratios and in TAR values marking the MRS. The lower Toa1a MRS is placed in the uppermost part of Interval 3, whereby the upper MRS matches the Toa2 MRS in the lowermost part of Interval 1 (lowermost *H. falciferum* subzone) (Fig. 4-8). The Toa1a MRS further roughly matches the D4 hiatus identified in the Lusitanian Basin at a similar stratigraphic position (Pittet et al., 2014). The MFS can be placed within the uppermost *H. elegantulum* subzone and is marked by a drop in the TAR values. As mentioned above, sediments within this interval show a remarkable variability that is expressed by periodical facies changes aligning with changes in sediment composition and geochemical proxies. Horizons showing a distinctively laminated sediment structure are characterized by high OM (preferentially alginites) and carbonate contents as well as by low TAR values (< 0.3). On the contrary, sediments showing an indistinctively laminated and a partly bioturbated sediment structure are characterized by low OM and carbonate contents, accompanied by increased siliciclastic contributions and elevated TAR values (> 0.3). Organic matter in these horizons is of mixed autochthonous and allochthonous origin

as testified by the occurrence of alginites and sporinites (Fig. 4-6B, C, D). These facies changes can be interpreted as short-term sea level fluctuations, whereby a high sea level is manifested in laminated OM rich facies and a low sea level in a bioturbated OM poor facies.

Interestingly, facies changes are not well expressed in the Si/Al and Zr/Al ratios, indicating that sea level changes did not cause significant changes in the ratio of clay versus silt-sized detritus. Thus it can be assumed that sea level changes were not accompanied by significant shifts in the coastline and distal settings did not experience drastic changes in continental derived siliciclastics. Moreover, it can be assumed that drops in sea level initiated an intensification of erosive events and winnowing processes in shallow marine settings, in particular in near shore environments or on top of sills and swells. Mud previously deposited in these settings during the Toa1-Toa2 transgression became more prone to erosion and was transported via ocean currents to local depressions (e.g. Fraugères & Stow, 1993; Macquacker & Howell, 1999; Trabucho-Alexandre, 2014). Thus, consequences of sea level fluctuations towards sedimentation were bound to the local paleogeographic setting and resulted in the formation of several hiatuses at shallow settings (van Breugel et al., 2006), whilst local depression received increased rates of sediment supply. The higher variability expressed in the TAR might result from differences in the transport mechanisms of terrigenous organic matter and siliciclastics (Nitttrour, 1981; Wakeham & Lee, 1993).

Toa2-Toa3 cycle. The 3rd order Toa2-Toa3 cycle covers the *H. falciferum* subzone and the lower *H. bifrons* zone, whereby the MFS is placed at the *H. serpentinum* - *H. bifrons* boundary (Ponsot, 1994; Hardenbol et al., 1998; Gély & Lorenz, 2006). Only the TST of this cycle is covered in Core FR-210-078 and is indicated by a decrease in Si/Al ratios (~2.4) and Zr/Al ratios (~17). The overall trend matches with findings from the Central Paris Basin (Hermoso et al., 2013) as well as with the overall sequence stratigraphy established for the Early Toarcian (e.g. Hardenbol et al., 1998; Gély & Lorenz, 2006). However, sediments of the *H. falciferum* subzone show increased contributions of siliciclastics, whereby carbonate concentrations are slightly reduced. This can result from a reduced abundance of marine biocalcifiers due to a decrease in the primary productivity or from increased siliciclastic input due to enhanced continental weathering and increased riverine discharge (Cohen et al., 2004). Additionally, OM from the *H. falciferum* subzone shows elevated TAR values that vary between 0.3 and 0.5, indicating enhanced contributions from terrestrial sources. Microscopic observations confirm the presence of a few sporinites, however, sedimentary organic matter is clearly dominated by alginites (Fig. 4-7A).

These observations are not fully in accordance with the proposed sea level evolution that attributes the *H. falciferum* subzone to the stage of the highest sea level that should show the lowest concentrations of terrigenous derived contributions (Hardenbol et al., 1998; Gély & Lorenz, 2006; Hermoso et al., 2013). However, this problem can be overcome when assuming an acceleration of the hydrological cycle that resulted in enhanced chemical weathering and an increase in continental run off, which is indicated by elevated Al/K and ln(Al/Na) ratios (Fig. 4-8), and which is further supported by previous works (e.g. McArthur et al., 2000; Cohen et al., 2004; Dera et al., 2009a). The different trend documented in the siliciclastic and organic matter fraction can be explained by different transport mechanisms for the different fractions. Silt-sized siliciclastics were deposited in

proximity to coastlines (e.g. Nittrour, 1981), whereas OM can be easily transported to distal settings (e.g. Wakeham & Lee, 1993). These mechanisms also resulted in a higher variability of the TAR within the upper *H. elegantulum* subzone.

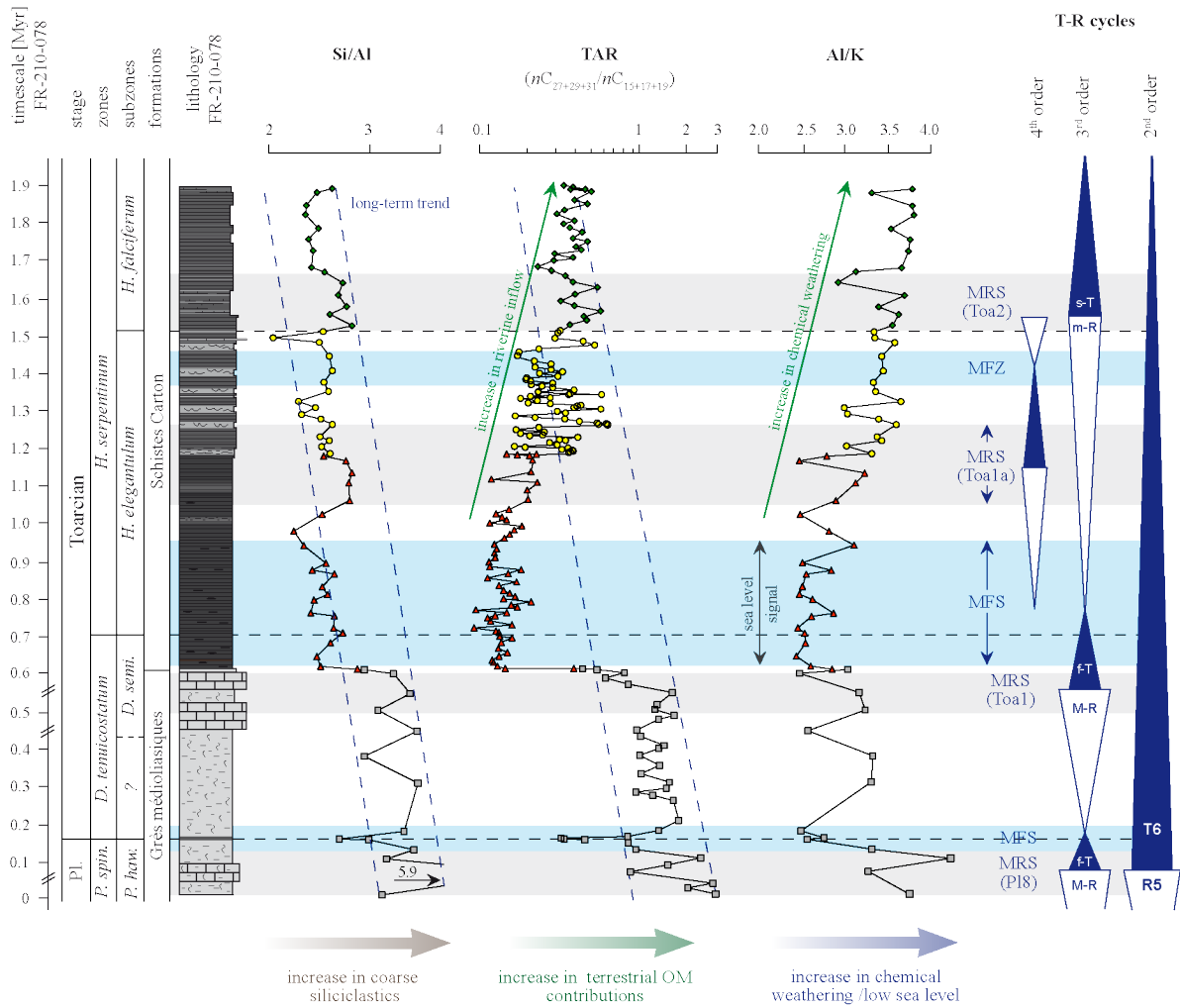


Figure 4-8: Changes in composition of siliciclastics and sedimentary organic matter allow to reconstruct the sea level evolution, whereby changes in geochemical proxies are aligned with facies changes. The long-term 2nd order Liassic transgression is well expressed in all parameters by significant decrease in Si/Al ratios and the TAR (Si/Al and TAR are scaled logarithmically). The divergent trends observed between Si/Al and TAR in the upper *H. elegantulum* and *H. falciferum* subzones reflect different transport mechanisms for siliciclastic and terrestrial OM. Coarse-grained siliciclastics marked by high Si/Al ratios are preferentially stored in proximity to the shore line. Terrestrial OM can be transported to distal locations by surface current systems. Elevated amounts of terrestrial OM can also result from elevated continental run off. An increase in humidity accompanied by enhanced chemical weathering and continental run off can be inferred from the steady increase of the Al/K ratio. Low Al/K ratios in Interval 3 can be explained by rapidly retrograding coastlines that resulted in a kaolinite depletion in distal areas. Superimposed 3rd order cycles were identified within the *D. tenuicostatum* zone as well as within the *H. elegantulum* and *H. falciferum* subzones. Additionally the upper part of the *H. elegantulum* subzone might cover another 4th order sea level cycle.

4.4.2. Evolution of sea surface salinity

The Early Toarcian records a drastic decrease in $\delta^{18}\text{O}$ values measured in the calcite of marine invertebrates, which has been attributed to reflect a drastic rise in SST that started in the upmost *D. tenuicostatum* zone (e.g. [Dera et al., 2011a](#) and references therein; also see Chapter 1.2.3.). The decrease in $\delta^{18}\text{O}$ values is evident from different basins throughout the Western Tethyan shelf situated at different latitudes between ~ 10 and $\sim 45^\circ\text{N}$, where significant differences have been documented in the amplitude of the oxygen isotope decrease. Highest amplitudes (about -3‰ on average), resulting in the most negative $\delta^{18}\text{O}$ values, were documented from basins situated at high latitudes (above $>30^\circ\text{N}$), whereas basins located at lower latitudes (below 30°N) show a lower amplitude of about -1.5‰ (Fig. S4-1) (e.g. [Saalen et al., 1996](#); [Bailey et al., 2003](#); [van de Schootbrugge et al., 2005a](#); [Dera & Donnadieu, 2012](#)). Significant latitudinally dependent differences were also expressed in $\delta^{18}\text{O}$ values measured on the bulk carbonate fraction, whereby data from the Lorraine Sub-Basin (this study) and the southern Paris Basin (e.g. [Hermoso et al., 2009b](#)) show a -3‰ offset when compared with data from the Mediterranean realm (Fig. 4-9) (also see [Röhl et al., 2001](#)).

When interpreting the geographical $\delta^{18}\text{O}$ data pattern in terms of differences in SST, temperatures in the submediterranean and subboreal realms would exceed those of the mediterranean realm by 5 to 10°C (also see [Dera & Donnadieu, 2012](#)). Such a latitudinal gradient is unrealistic as SST temperatures commonly decline with increasing latitude. Therefore, additional factors must be taken into account to explain the geographical differences in $\delta^{18}\text{O}$ data. Lower $\delta^{18}\text{O}$ data in NE areas of the Western Tethyan shelf might have resulted from a shift of the habitat of marine biocalcifiers from cold bottom waters to warm surface waters due to the formation of anoxic bottom waters during the Toarcian Oceanic Anoxic Event ([Ullmann et al., 2014](#)). However, bottom water anoxia alone cannot fully explain latitudinal differences in $\delta^{18}\text{O}$ data as these are also documented between different anoxic basins on the NW shelf (Fig. S4-1).

Alternatively, enhanced freshwater discharge onto the NE part of the Western Tethyan shelf has been suggested to explain the oxygen isotope data, whereby proposed freshwater sources comprise enhanced rainfall and fluvial freshwater discharge that resulted from global warming and the intensification of monsoonal circulation pattern ([Röhl et al., 2001](#); [Bailey et al., 2003](#); [Krencker et al., 2015](#)), the inflow of low saline Arctic water masses (e.g. [Bjerrum et al., 2001](#); [Hesselbo et al., 2000](#)), or the melting of polar ice that also promote a southwards discharge of low saline Arctic waters (e.g. [Suan et al., 2010](#); [Dera & Donnadieu, 2012](#)). Despite all uncertainties concerning freshwater sources it seems to be approved that SSS of the northwestern Western Tethyan Shelf strongly differed from those in the SE part of the shelf in proximity to the Tethyan Ocean. Reduced SSS were for example also indicted by the community structure of calcareous nannoplankton that records preferentially brackish surface water conditions at least during the T-OAE (e.g. [Mattioli et al., 2008](#); [Hermoso et al., 2009b](#)).

According to [Li et al. \(2013\)](#) a difference in $\delta^{18}\text{O}$ values of about -2 to -3‰ can be attributed to a salinity decrease of about 20 psu. Surface salinities in the present day world oceans vary between 31 and 39 psu, whereby high salinities are recorded at 30° north and south ([Antonov et al., 2010](#)). On the contrary, 17 psu are recorded for the Black Sea ([Mertens et al., 2012](#)), whereas SSS in the Baltic Sea range from 13 to 1 psu ([Meier et al., 2006](#)). Assuming relatively high salinities of about 35 psu in the shelf seas at about 20 to 30°N (Mediterranean realm), like the Lusitanian Basin or the Basque-Cantabrian Basin, the -3‰ offset in $\delta^{18}\text{O}$ values indicate SSS of about 15 psu for the northeastern part of the Western Tethyan shelf. With respect to present day observations a salinity difference of about 20 psu between the open Tethyan Ocean and the restricted Western Tethyan shelf is not unrealistic as similar SSS were documented for the Black Sea or the Baltic Sea. However, [Saelen et al. \(1996\)](#) proposed a salinity decrease of only 5 psu for the Cleveland Basin.

To understand mechanisms controlling changes in SSS throughout the Western Tethyan shelf it is of major interest to reconstruct the evolution of SSS during the Early Toarcian. As abovementioned, previous studies by [Mattioli et al. \(2008\)](#) and [Hermoso et al. \(2009b\)](#) have shown that surface water conditions directly affected the community structure of calcareous nannoplankton, whereby shift in the community structure are expressed by the evolution of Sr/Ca ratios of biogenic carbonate. The high variability of Sr/Ca ratios attest strongly contrasting conditions in surface waters and further indicate significantly reduced SSS during certain periods of the Early Toarcian (Fig. 3A in [Hermoso et al., 2009b](#)). The evolution of the Sr/Ca ratios in the Lorraine Sub-Basin shows strong similarities with observations from the southern Central Paris Basin indicating at least basin wide changes in SSS (Fig. 4-9; also see Fig. 3A in [Hermoso et al., 2009b](#)). On the base of these observations and in combination with biomarker and isotope geochemical proxies the evolution of SSS during the Early Toarcian in the Lorraine Sub-Basin can be assessed.

Overall low tri-/di-MTTC ratios (<5) indicate normal marine to semi-saline SSS throughout the upper *P. spinatum* and the lower *D. tenuicostatum* zones, whereby a slightly increasing trend might be associated with a steady increase in SSS. This trend was interrupted by a drastic shift towards higher tri-/di-MTTC values (up to 13), indicating a drop in SSS at the Pliensbachian-Toarcian boundary. This interpretation is supported by a drastic decrease in the concentrations of C_{30} steroids that indicates reduced abundance of marine algae due to decreased SSS ([Peters, 2005](#)) (Fig. 4-9). The interpretation of Sr/Ca ratios and $\delta^{18}\text{O}$ values in terms of salinity changes is more complicated as both proxies show no clear trend throughout this interval. It can be assumed that the overall low abundance of biogenic carbonate throughout the upper *P. spinatum* and the lower *D. tenuicostatum* zones (17.8 wt.% on average, but preferentially below 10 wt.%) results in a relative high impact of diagenetic processes affecting the carbonate geochemistry. Furthermore, certain amounts of Sr throughout this interval might be associated with clay minerals (Fig. S4-3B). Thus an unambiguous interpretation of Sr/Ca ratios as well as of $\delta^{18}\text{O}$ data is not possible. Interestingly, oxygen isotope values from bulk carbonate of contemporaneous sediments from the southern Central Paris Basin, where higher carbonate contents are documented (~30 wt.% on average), show relative constant values of about -4‰, which is about 1.5‰ heavier than in the Lorraine Sub-Basin ([Hermoso et al., 2009b](#)).

Lower $\delta^{18}\text{O}$ values in the Lorraine Sub-Basin can result from riverine freshwater discharge, which is however not reflected in the tri-/di-MTTC ratios. Thus, a stronger impact of a diagenetic signal onto the carbonate geochemistry in sediments from the Lorraine Sub-Basin that resulted from the overall lower contribution of biogenic carbonates offers the best explanation for the differences in oxygen isotope values. Indeed, tri-/di-MTTC ratios from the Lorraine Sub-Basin match well with the $\delta^{18}\text{O}$ data from the southern Central Paris Basin (Hermoso et al., 2009b), which allow to deduce normal marine to semi-marine salinities during the *P. spinatum* and the lower *D. tenuicostatum* zones in the Paris Basin. However, an offset of about -1 to -2‰ between the more open marine Mediterranean realm and the Paris Basin already persisted during the *P. spinatum* and *D. tenuicostatum* zones, indicating lower SSS in the Paris Basin than in the Mediterranean realm (Fig. 4-9). A rapid increase in the tri-/di-MTTC ratio to values >10 that is documented in the upmost *D. tenuicostatum* zone and indicates a shift from semi-saline SSS to preferentially brackish conditions that persisted throughout the upmost *D. tenuicostatum* zone and the lower *H. elegantulum* subzone. No significant response is documented in the concentrations of C_{30} steroids, which indicate that the Toa-1-Toa2 transgression placed in this interval was not associated with a radiation of marine *Pelagophyte* algae (Peters et al., 2005). However, a slightly increase in the C_{30} steroids can be correlated with the proposed MFS and is followed by a decreasing trend that can be associated with a regressive phase (Fig. 4-9). The Sr/Ca ratios and the $\delta^{18}\text{O}$ values from the upper *D. tenuicostatum* zone and the lowermost *H. elegantulum* zone again contain a strong diagenetic signal that prohibits a detailed reconstruction of salinity changes on the base of these data. Similar observations were made in sediments from southern Central Paris Basin, where a mixed biogenic/diagenetic signal has been proposed for contemporaneous sediments (Hermoso et al., 2009b; 2012). The strong impact of diagenetic processes onto Sr/Ca and $\delta^{18}\text{O}$ values in the Lorraine Sub-Basin might again have resulted from the overall lower content of biogenic carbonate in this area when compared with data from the Central Paris Basin (carbonate content Toa-CIE interval: ~20 wt.% at Sancerre; <10 wt.% at FR-210-078). Excluding the horizons, which potentially contain a strong diagenetic signal, the remaining trends in Sr/Ca ratios and the $\delta^{18}\text{O}$ values allow to infer oceanographic conditions, whereby trends match findings from the southern Central Paris Basin (Hermoso et al., 2009b).

Throughout the lower *H. elegantulum* zone very low Sr/Ca ratios can, with respect to findings by Mattioli et al., (2008) and Hermoso et al. (2009b), be associated with calcareous nannoplankton assemblages dominated by coccolithophorid *Calyculus* that mineralize from brackish low-nitrate waters and thus support biomarker data. Further evidence for enhanced freshwater contributions is provided by the frequent occurrence of *Tasmanales* that can be indicative for freshwater environments by might also result from sediment starvation or sediment bypassing (Tyson, 1995), which is also indicated for this interval. Additionally, a decrease in $\delta^{18}\text{O}$ values can reflect elevated fresh water contributions, but might also contain a temperature signal that is associated with global warming taking place during the upmost *D. tenuicostatum* zone and the lower *H. elegantulum* subzone (Dera et al., 2011a). However, a significant offset between $\delta^{18}\text{O}$ values from the Mediterranean and the NW Tethyan shelf can be attributed to a latitudinal salinity gradient that is expressed in bulk $\delta^{18}\text{O}$ values as well as in $\delta^{18}\text{O}$ values of belemnites (Fig. 4-9, S4-1).

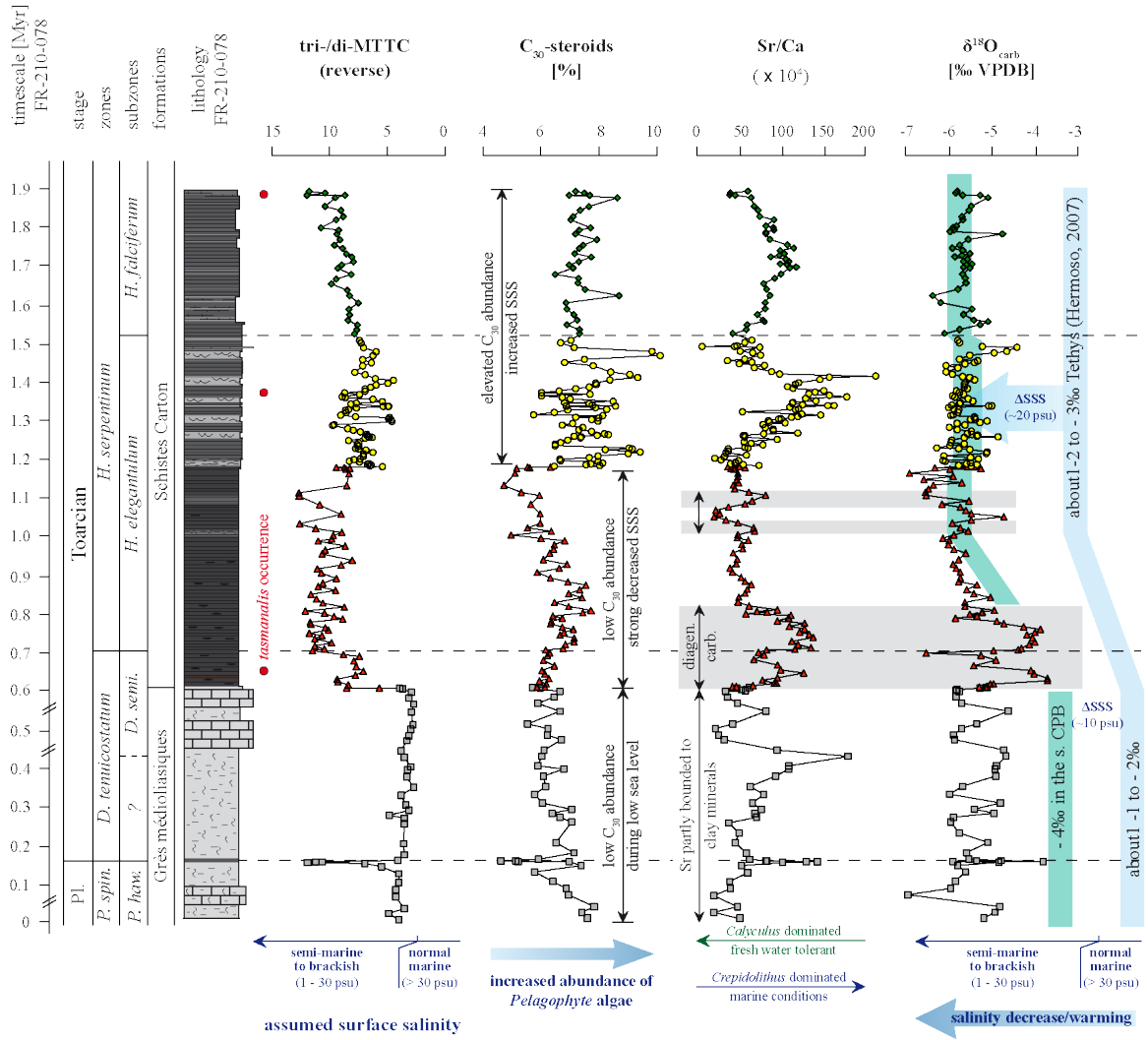


Figure 4-9: Evolution of salinity-related proxies, comprising MTTCs, C_{30} -steroid concentrations, Sr/Ca ratios and $\delta^{18}O$ data allows to reconstruct the evolution of SSS during the Early Toarcian (Sr/Ca and $\delta^{18}O$ values within horizons highlighted in grey most likely reflect diagenetic processes). All proxies confirm a massive freshwater surge that occurred during the upmost *D. tenuicostatum* zone and lower *H. elegantulum* subzone (for better comparison tri-/di MTTC ratios are plotted reverse). The overall offset between oxygen isotope values from the Mediterranean (Valdorbia section, Italy; see Hermoso, 2007) and the European Basin System clearly confirm a pronounced latitudinal salinity gradient. Data from the southern Central Paris Basin (southern Paris Basin Hermoso et al., 2009b) show heavier $\delta^{18}O$ values in sediment of the *P. spinatum* and *D. tenuicostatum* zones. This offset might result from early diagenetic processes in the Core FR-210-078, as fluctuations in Sr/Ca ratios and $\delta^{18}O$ values are not confirmed by tri-/di-MTTC ratios. Absolute values of the tri-/di-MTTC ratios indicate that SSS in the Paris Basin were generally lower than in the open Tethyan Ocean (MTTC calibrated to the scale proposed by Schwark et al., 1998).

The upper *H. elegantulum subzone* records a decrease in tri-/di-MTTC ratio to values that vary between 5 and 10, indicating a return to more semi-marine SSS. Increased SSS are also indicated by the rapid increase in concentrations of C₃₀ steroids documenting elevated contributions from marine *Pelagophyte* algae that are diagnostic for marine environments (Volkman, 2003; Peters et al., 2005) (Fig. 4-9). This interval further shows a drastic increase in Sr/Ca ratios that has been associated with an increase in the abundance of the coccolithophorid *Crepidolithus*, a deep dweller common in normal marine environments (Hermoso & Minoletti, 2008; Minoletti et al., 2008; 2009). An increase in SSS is also supported by an increase in $\delta^{18}\text{O}$ values. Additionally, all salinity parameters show a strong periodicity within the upper *H. elegantulum subzone* that is also expressed in the lithology as well as in sea level related proxies. Higher SSS (low tri-/di-MTTC) are indicated for horizons that show only an indistinct lamination and evidence for increased continental contributions thus representing a lower sea level. On the contrary, lower SSS (high tri-/di-MTTC) are indicated for horizons with distinct lamination deposited during a higher sea level.

An steady increase in the tri-/di-MTTC ratios from values of about 7 to 10 is documented throughout the *H. falciferum subzone* and indicate a slightly decrease in SSS, whereby values indicate preferentially semi-brackish conditions. A rapid increase in the ratio in the upmost part of the profile indicates another fresh water surge. This horizon is also highlighted by the occurrence of *Tasmanales*. Relative high concentrations of C₃₀ steroids indicate at least temporarily marine conditions (Peters et al., 2005) that however differed from full marine conditions, as indicated by $\delta^{18}\text{O}$ values that remain low throughout the *H. falciferum subzone* (Fig. 4-9). Sr/Ca ratios throughout this interval show a maximum in the middle part of the *H. falciferum subzone* that might indicate an increase in *Crepidolithus* abundance. The proposed fresh water surge in the uppermost part of the *H. falciferum subzone* was accompanied by a drop in Sr/Ca ratios, indicating another shift in the community structure of calcareous nannoplankton to assemblages dominated by *Calyculus* (Mattioli et al., 2008; Hermoso et al., 2009b).

4.4.3. Controls on sea level and salinity changes

The sea level evolution proposed for the Early Toarcian, including the 2nd order Liassic transgression as well as the 3rd and 4th order Pl8-Toa1, Toa1-Toa1a, Toa1a-Toa2 and Toa2-Toa3 cycles, is well-expressed by sedimentological features and geochemical data from the Lorraine Sub-Basin. Furthermore, stratigraphic position of transgressive and regressive stages match with findings from other basins (e.g. Hardenbol et al., 1998; Gély & Lorenz, 2006; Hermoso et al., 2013; Pittet et al., 2014) and thus support a trans-regional, possibly global, character of Early Toarcian sea level changes. Data from the Lorraine Sub-Basin further confirm a significant coupling of 3rd and 4th order sea level cycles and salinity changes, which is indicated by the inverse correlation of tri-/di-MTTC ratio with TAR (Fig. 4-10A) as well as of tri-/di-MTTC ratio with Si/Al ratios (Fig. 4-10B). Stages of high sea level, expressed by low Si/Al and TAR values, were accompanied by significantly reduced SSS as indicated by high tri-/di-MTTC ratios (Fig. 4-10). On the base of these observations it can be concluded that changes in SSS were directly bound to sea level evolution, whereas the scatter in the data might result from other factors, like riverine fresh water discharge, that further contributed to changes in SSS (Fig. 4-10A). Furthermore, lowest SSS were confirmed for the upmost *D. tenuicostatum* zone and the lower *H. elegantulum* subzone that reflect the most pronounced sea level rise, attributed to the Toa1-Toa1a transgression.

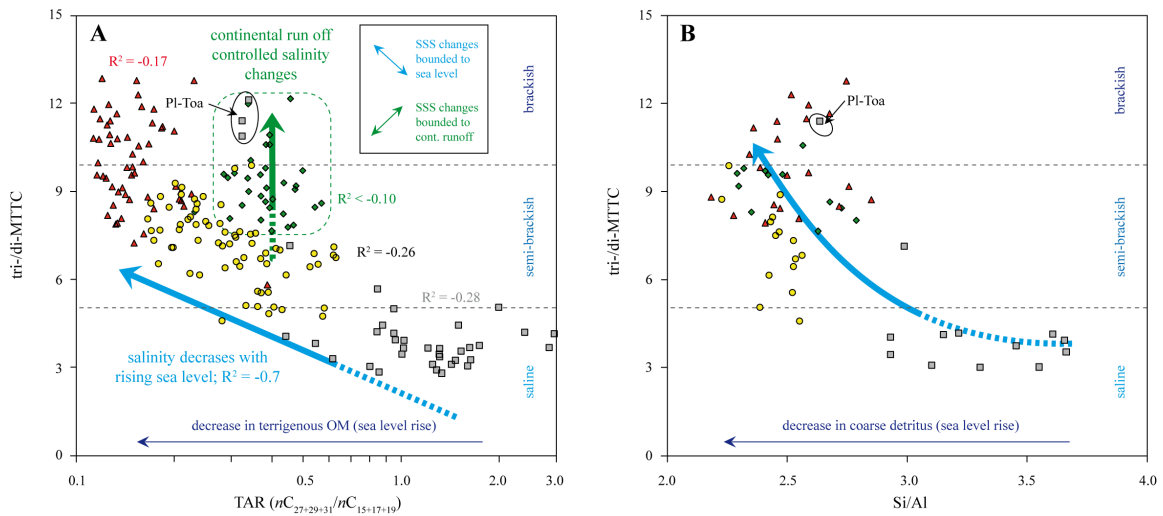


Figure 4-10: A) The inverse correlation observed between the TAR and tri-/di-MTTC ratio indicates that changes in SSS were bound to sea level evolution, whereby stages of high sea level can be associated with decreased SSS. This relation rules out that riverine discharge was the main driver controlling changes in SSS. However, the scatter in data indicates that riverine fresh water discharge contributed to changes in the SSS during certain periods. Riverine fresh water contributions might be of major importance during the *H. falciferum* subzone, which is supported by evolution of Al/K and Al/Na ratios that confirm enhanced chemical weathering during this period, which resulted in enhanced run off rates. **B)** The interpretation is supported by the inverse relation that is documented between Si/Al and tri-/di-MTTC ratios. Low SSS are always bound to low Si/Al ratios, indicating decreased terrigenous contributions during a high sea level. (legend as in figure 4-5)

The stratigraphic extent of 3rd/4th order sea level cycles match those of major salinity changes, which further support a causal relation between sea level evolution and changes in SSS. It is further interesting to note that according to the timescale proposed for Core FR-210-078 (Chapter 2) sea level and salinity changes throughout the upmost *D. tenuicostatum* and *H. serpentinum* zones roughly aligns with 405 kyr eccentricity periods, whereby the long-term trend can be attributed to the 1600 kyr eccentricity period, which is however not clearly confirmed due to the studied sequence being too short in duration (Fig. 4-11) (see Chapter 2). This observation highlights the role of astronomical controls towards oceanographic changes during the Early Toarcian and indicates that sea level and salinity changes throughout the Western Tethyan shelf were controlled by astronomically forced glacio-eustatic mechanism, which has been previously assumed (Brandt, 1986; Korte & Hesselbo, 2010; Pittet et al., 2014). The results further show that Early Toarcian 3rd/4th order eustatic cycles can be linked to long eccentricity periods (405 kyr and possibly 1600 kyr Milankovitch periods), which is in agreement with findings from other periods in the Mesozoic (e.g. Stasser et al., 2000; Gale et al., 2002; Boulila et al., 2011). Additionally, these results support the existence of polar ice caps during the Late Pliensbachian and Early Toarcian, whose existence has been questioned (e.g. Frakes et al., 1992).

On the basis of these findings a detailed model can be developed that explains major sea level and salinity changes in the Lorraine Sub-Basin and possibly throughout the Western Tethyan shelf during the Early Toarcian. During the Late Pliensbachian global cooling, possibly promoted by enhanced carbon burial (Silva & Duarte, 2015), resulted in a major regression due to the expansion of polar ice caps. A pronounced southwards shift of cold climate conditions is also evident from sedimentological observations, comprising glendonites and glacial derived deposits at mid-latitudes (Tchoumatchenco et al., 2008; Teichert & Luppold, 2012; also see Chapter 1.2.3.). Furthermore, sedimentological observations are supported by a southwards migration of cold water-loving ammonites during the Late Pliensbachian (Suan et al., 2008b and references therein).

A minor and brief global warming, proposed for the PI-Toa boundary that was accompanied by a rapid but short-lived transgressive phase (PI8-Toa1 transgression), expressed by the PI-Toa boundary black shale in the Lorraine Sub-Basin. Warming and sea level rise further align with a decrease in SSS, which can be explained by a brief period of enhanced melting of continental ice masses that has formed during the Late Pliensbachian icehouse (e.g. Dera et al., 2011a; Silva & Duarte, 2015). Furthermore, a negative carbon isotope excursion at the PI-Toa boundary (PI-Toa-CIE), which has been documented from several locations (e.g. Hermoso et al., 2000; Bondin et al., 2010; Littler et al., 2010) and which is also evident from the Lorraine Sub-Basin, might reflect the emission of greenhouse gases from climate sensitive reservoirs. The brief warming at the PI-Toa boundary is also expressed by migration patterns of ammonites that show a northwards expansion of warm water-loving Tethyan taxa towards higher latitudes (Suan et al., 2008b and references therein).

The subsequent regressive phase was accompanied by an increase in SSS and can further be associated with a drop in SST (Suan et al., 2010; Dera et al., 2011a), accompanied by a southwards migration of cold-loving ammonites (Suan et al., 2008b and references therein). How far these environmental changes were controlled by astronomical cycles remains unclear as the sedimentation

throughout the Western Tethyan shelf during Late Pliensbachian and the Early Toarcian was affected by significant gaps, which result in an incomplete astrochronology (Ruebsam et al., 2014, 2105; also see Chapter 2). Thus, further studies from more complete sections are necessary to discuss the environmental dynamics during the Pl-Toa boundary. A drastic rise in global SST, placed in the upmost *D. tenuicostatum* zone, is evident from a major decrease in $\delta^{18}\text{O}$ values (Dera et al., 2011a) and can be further associated with a northwards expansion of floral and faunal realms (Vakhrameev, 1991; Suan et al., 2008b; Dera et al., 2009b; 2011b), and an increase in humidity that resulted in enhanced continental weathering (e.g. Cohen et al., 2004; Dera et al., 2009b; Branski, 2012; Montero-Serrano et al., 2015). A detailed overview about the evolution of the climate system is given in Chapter 1.2.3.. Global warming resulted in a rapid melting of polar ice caps causing a major sea level rise that is expressed by the transgressive phase of the Toa1-Toa2 cycles, spanning the upmost *D. tenuicostatum* zone and the lower *H. elegantulum* subzone. This sea level rise was accompanied by massive freshwater discharge to the Arctic Ocean and subsequent to the Western Tethyan shelf (Bjerrum et al., 2001; Dera & Donnadieu, 2012), whereby an Arctic freshwater source is indicated by the evolution of ϵ_{ND} values (Fig. 4-11) (Dera et al., 2015). The coupling of climate, sea level and salinity changes clearly points to glacio-eustatic processes, whereby warming and demise of polar ice sheets might have been controlled by astronomical cycles of different order during a phase of long-term global warming initiated by the emplacement of the Karoo-Ferrar LIP (Burgess et al., 2015; Chapter 1.2.4.). Additionally, melting of polar ice occurred concomitant to release of ^{12}C -enriched carbon from the cryosphere, expressed by the negative Toa-CIE (see Chapter 3). Sea level and salinity fluctuation during the Toa-CIE will be discussed later.

A subsequent increase in SSS in the upper *H. elegantulum* subzone aligns with a regressive phase (Toa1-Toa2 regression). The regressive phase is well expressed in sediments corresponding to the upper *H. elegantulum* subzone (or coeval chronozones) throughout the Western Tethyan shelf and led to the formation of hiatuses (D4 hiatus in Pittet et al., 2014; also see van Breugel et al., 2006; Lezin et al., 2012). An increase in $\delta^{18}\text{O}$ values (Fig. S4-1) might have resulted from a drop in SST but could also have resulted from an increase in SSS due to the reduced freshwater inflow from the Arctic Ocean. The latter is confirmed by biomarker data (C_{30} steroids & tri-di-MTTC ratios) and by the evolution of calcareous nannoplankton (recovery marine communities; e.g. Hermoso et al., 2009b). A drop in global temperatures might have occurred as consequence of widespread organic carbon burial during this period (e.g. Baudin et al., 1990) and enhanced silicate weathering (Cohen et al., 2004; Dera et al., 2009a; Branski, 2012) that resulted in an enhanced removal of CO_2 from the atmosphere. Moreover, global warming itself might have resulted in a negative climate feedback. The demise of polar ice led to sluggish circulation of pole-wards directed ocean currents that transported warm waters towards high latitudes. Sluggish ocean currents occurred as the result of the absence of or the reduced extent of dense deepwater formation in polar regions (Dera & Donnadieu, 2012). Interruption of meridional heat transport would have promoted a cooling at high latitudes, which culminated in the formation of polar ice and led to a glacio-eustatic sea level fall.

The transgressive phase of the Toa2-Toa3 cycle, placed in the *H. falciferum* subzone, was accompanied by a less pronounced decrease in SSS. The lower magnitude of salinity changes might

result from the strongly reduced extent of polar ice caps during the Early Toarcian greenhouse stage (Dera et al., 2011a). However, a decrease in SSS might also have been a consequence of enhanced riverine fresh water supply, which is indicated by the weak correlation of the TAR and tri-/di-MTTC ratios documented for samples from the *H. falciferum* subzone (Fig. 4-10A). A stronger impact of riverine freshwater inflow to the Lorraine Sub-Basin that resulted from enhanced continental weathering is supported by high Al/K and ln(Al/Na) values. The transgressive phase of the Toa2-Toa3 cycle is hard to explain by glacio-eustatic mechanisms alone, when assuming that majority of continental polar ice had disappeared previously. Expansion of polar ice caps during a cooling episode in the upper *H. elegantulum* zone could explain the observation. However, it is also possible that the transgressive phase of the To2-Toa3 cycle corresponds to the upper part of the tectonically driven 2nd order Liassic cycle.

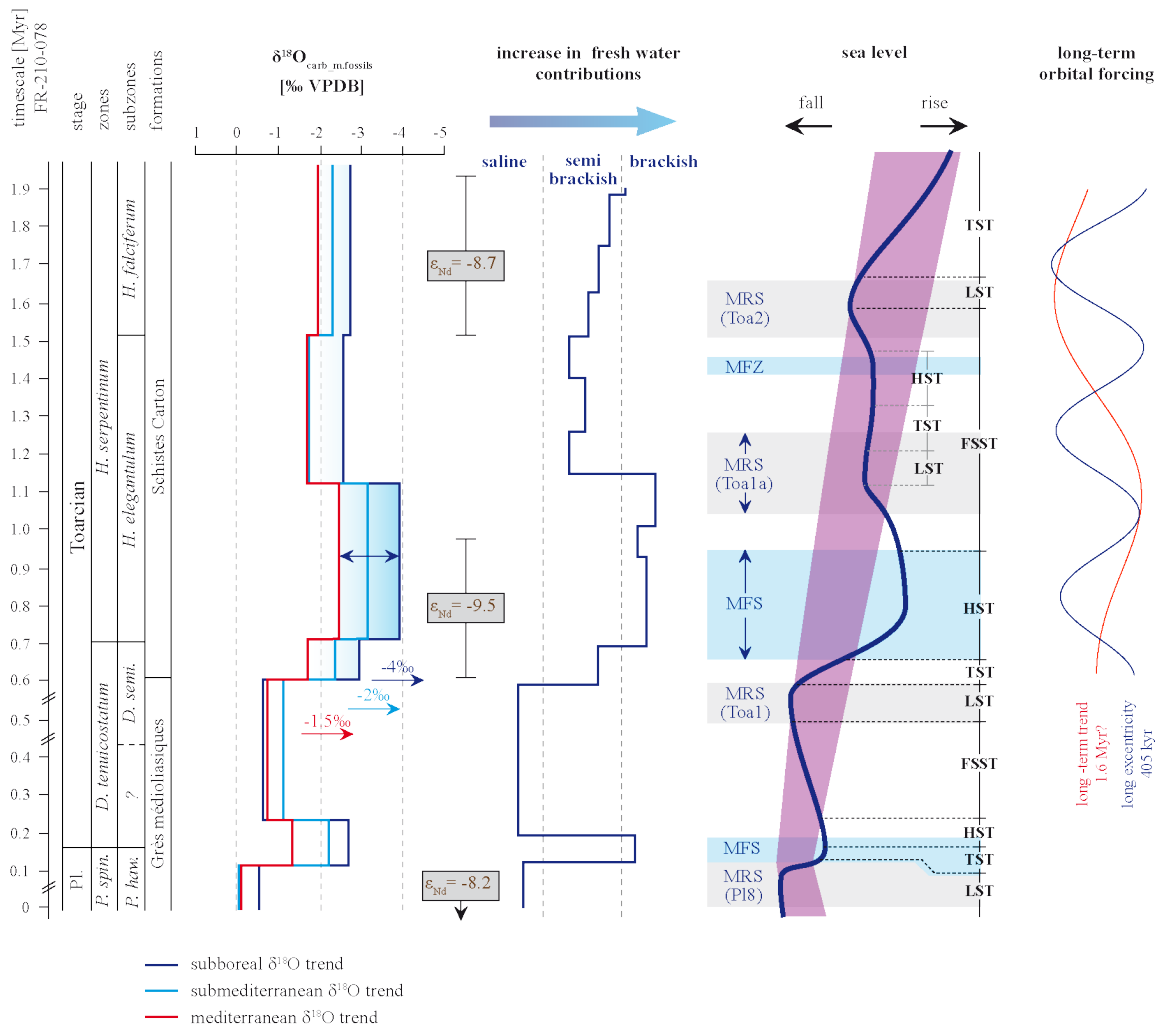


Figure 4-11: Evolution of climate, sea level and sea surface salinity during the latest Pliensbachian and Early Toarcian. The rapid global warming that started within the upper *D. tenuicostatum* zone was accompanied by a rapid sea level rise and a significant decrease in the sea surface salinity. The highest amplitude in $\delta^{18}\text{O}$ values in northern regions of the Western Tethyan shelf resulted from the proximity to the Viking Corridor. Sea level as well as salinity show a close relation with long-term orbital parameters proposed for Core FR-210-078. A negative shift documented in ϵ_{ND} values occurred during the lower *H. elegantulum* subzone and has been attributed to reflect strong southwards directed Arctic currents.

In addition to the long-term sea level and salinity changes that were most likely driven by long-term astronomical cycles (405 kyr and 1600 kyr), significant high-amplitude environmental fluctuations were documented on shorter timescales. The highest variability has been documented in sediments corresponding to the upper *H. elegantulum subzone* (Interval 2). This period corresponds to the regressive phase of the Toa1-Toa2 cycle and possibly represents an additional 4th order T-R cycle (Toa1a-Toa2; Fig. 4-11). The regressive trend resulted in a depositional environment that was highly sensitive towards short-term astronomically forced environmental instabilities (Ruebsam et al., 2014, 2015; also see Chapter 2). During this period changes in the lithology can be directly linked to sea level and salinity changes. Stages representing a high sea level are characterized by distinctly laminated sediments, alginite-dominated OM (Fig. 4-6B), a low TAR (<0.3) and slightly decreased Si/Al ratios, which indicate a reduced impact of terrigenously derived organic matter and detrital contributions. These stages further provide evidence for significantly reduced SSS as indicated by elevated tri-/di-MTTC ratios and decreased $\delta^{18}\text{O}$ values (Fig. 4-12). More brackish conditions are also indicated by the evolution of Sr/Ca ratios that reflect changes in the community structure of the calcareous nannoplankton. A decrease in Sr/Ca ratios during more brackish stages can be attributed to an increasing dominance of *Calyculus*, a coccolithophorid that is tolerant towards reduced SSS (Mattioli et al., 2008; Hermoso et al., 2009b). Moreover, environmental conditions different from normal marine environments are also indicated by low contributions of C₃₀ steroids, indicating a low abundance of *Pelagophyceae* (Fig. 4-12).

Intercalated sediment horizons that show a indistinct lamination and evidence for enhanced benthic activity can be associated with stages of lower sea level, which is also indicated by elevated TAR values (>0.3) and Si/Al ratios as well as by the frequent occurrence of sporinites (Fig. 4-6C, D) that confirmed increased terrigenous contributions. Furthermore, low tri-/di-MTTC ratios and high $\delta^{18}\text{O}$ values, documented in these horizons, provide evidence for increased SSS. An elevation in the Sr/Ca ratios throughout these horizons reflects recovery phases of the deep dwelling coccolithophorid *Crepidolithus* that has been associated with more normal marine conditions (Mattioli et al., 2008; Hermoso et al., 2009b). More normal marine conditions (salinities) are also indicated by increased contributions of C₃₀ steroids that confirm a higher abundance of *Pelagophyceae* (Fig. 4-12).

The coupling of sea level and SSS indicate that these environmental instabilities can be associated with glacio-eustatic mechanisms driven by the extent of polar ice. Waxing and waning of polar ice caps resulted in variable rates of fresh water discharge to the Western Tethyan shelf that therefore experienced drastic variation in the sea level and SSS. According to the timescale proposed for the Core FR-210-078 (see Chapter 2; Ruebsam et al., 2014; 2015) the environmental instabilities in the upper *H. elegantulum subzone* align with ~36 kyr obliquity cycles. The strong impact of the obliquity period can be explained by internal ice sheet forcing during greenhouse climate stage with a reduced extent of polar ice caps (Rudimann, 2006) or by obliquity forcing of polar ice sheets at high latitudes (Berger & Loutre, 1994). Thus, environmental and oceanographic fluctuations in the upper *H. elegantulum subzone* can be attributed to obliquity-driven glacio-eustatic, possibly glacial-interglacial, cycles.

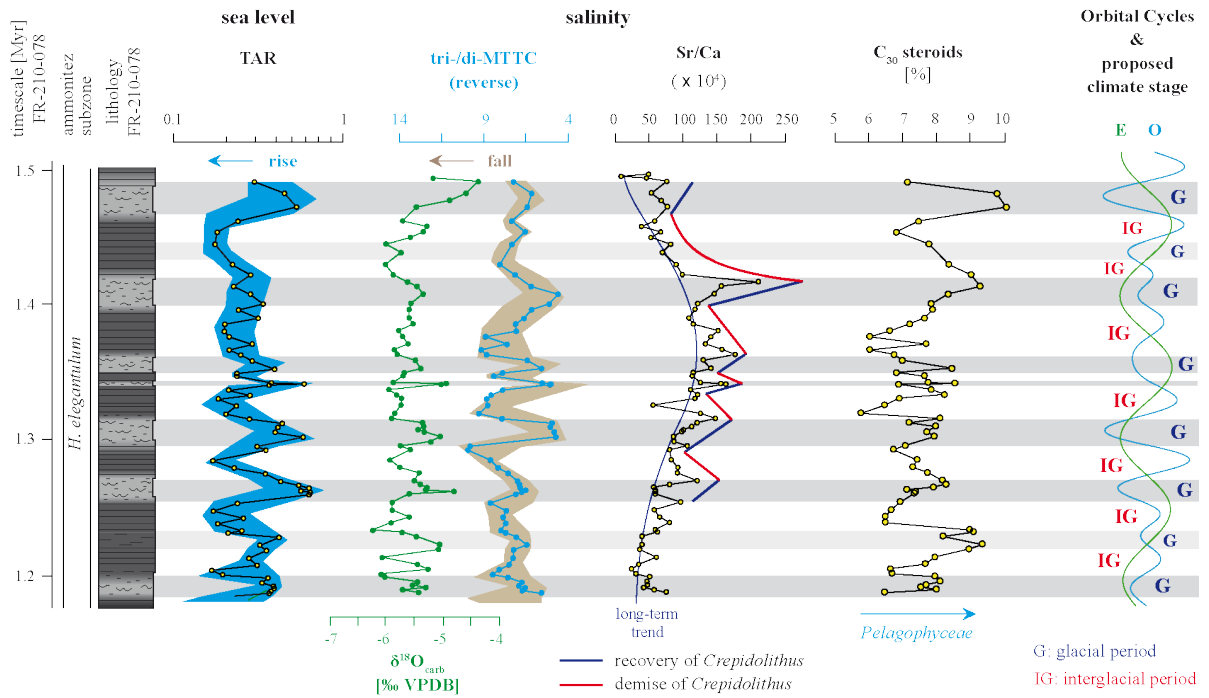


Figure 4-12: The upper *H. elegantulum* subzone (Interval 2) is highlighted by a remarkable variability that is expressed in lithology and sediment composition and can be associated with sea level and salinity related fluctuations. This interval corresponds to the regressive phase of the Toa1-Toa2 sea level cycle and represents a depositional environment that was highly sensitive towards short-term changes in the environmental conditions. Obliquity-forcing, most efficient at high latitudes (Berger & Loutre, 1994) controlled sea level changes and fresh water discharge from the Arctic Ocean to the Western Tethyan shelf due to the waxing and waning of polar ice caps. Brackish stages (high tri-/di-MTTC; low $\delta^{18}O$ values) correspond to episodes of sea level rise (low TAR and Si/Al) represented by sediment horizons that show a distinct lamination and elevated OM content. More saline marine stages (low tri-/di-MTTC; high $\delta^{18}O$ values) were associated with a lower sea level and elevated terrigenous contribution (high TAR and Si/Al). Changes in SSS can be directly linked to changes in the community structure of calcareous nannoplankton, which is indicated by shift in the Sr/Ca ratio. A recovery of deep dwelling *Crepidolithus* is documented during the more marine stages by an increase in the Sr/Ca ratios, whereas brackish stages can be associated with an increased abundance of *Calyculus* as indicated by a drop in the Sr/Ca ratios. A similar trend is documented in the concentrations of C_{30} steroids that can be linked to the abundance of *Pelagophyceae*, an algae class favoring normal marine environments.

4.4.4. Sea level and salinity change during the Toa-CIE

Data presented in this chapter show that the most profound changes in oceanographic conditions, including a rapid rise in sea level and massive freshwater discharge to the Western Tethyan shelf, occurred concomitant to the Early Toarcian carbon cycle perturbation, during a phase of drastic global warming. Results are in agreement with the conceptual model proposed in Chapter 3 and confirm that the release of ^{12}C -enriched carbon from the cryosphere was accompanied by glacio-eustatic sea level rise as well as with a drop in SSS throughout the Western Tethyan shelf sea, both resulting from the melting of polar ice caps. The proposed coupling of carbon cycle and oceanographic changes expressed by the cross-plots of $\delta^{13}\text{C}_{\text{org}}$ values with the TAR as well as with tri-/di-MTTC ratios, whereby lowest $\delta^{13}\text{C}_{\text{org}}$ values are bounded to lowest TAR (Fig 4-13A) and highest tri-/di-MTTC ratios (Fig 4-13B).

The overall trend between TAR and $\delta^{13}\text{C}_{\text{org}}$ values (green arrow in Fig. 4-13A) can be attributed the differences in the isotopic signature of marine and terrigenous originates OM (Tyson, 1995; also see Fig. S3-2). Relative heavy $\delta^{13}\text{C}_{\text{org}}$ values bounded to low TAR values in samples from the upper *H. elegantulum subzone* (brown arrow) might result from a high primary productivity and elevated organic carbon burial rates (Kump & Arthur, 1999) that are expressed by a positive carbon isotope excursion associated with T-OAE (Jenkyns, 1988).

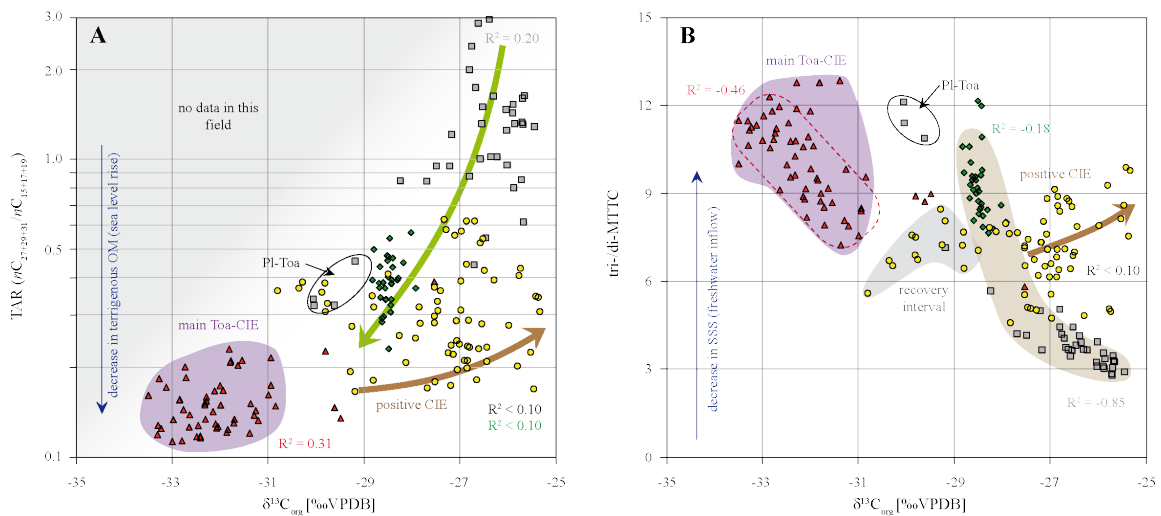


Figure 4-13: A) The Toa-CIE is associated with a rapid sea level rise. Samples from the Toa-CIE interval show the lowest TAR values. The overall scatter in the data shows that $\delta^{13}\text{C}_{\text{org}}$ data are not exclusively bounded to changes in OM composition (green trend) and other factors like $p\text{CO}_2$, primary productivity and OM preservation also affected carbon isotope and TAR values. A) The Toa-CIE interval is further associated with a massive fresh water surge resulting in a strong decreased of SSS. A fair inverse relation between $\delta^{13}\text{C}_{\text{org}}$ data and tri-/di-MTTC ratios ($R^2 = 0.46$) confirm that highest rates of fresh water inflow onto the Western Tethyan shelf were accompanied by massive injection of carbon from ^{13}C -depleted reservoirs. An inverse relation is also evident for samples from Interval 4 (*P. spinatum* and lower *D. tenuicostatum* zones) and from Interval 1 (*H. falciferum subzone*), which can indicate that lower $\delta^{13}\text{C}_{\text{org}}$ values reflect higher $p\text{CO}_2$ or increased contributions of marine OM during a sea level rise. The scatter in the data from the upper *H. elegantulum subzone* indicates fluctuation environmental and depositional conditions. (legend as in figure 4-5)

In the Lorraine Sub-Basin the initial part of the Toa-CIE, comprising the main Toa-CIE shifts (II-A, II-B, II-C), records a drastic decrease in the TAR and the Si/Al ratio (and Zr/Al ratio). The decreases in these proxies occurred in three steps that align with the major Toa-CIE shifts (II-A, II-B, II-C), whereby the decline in TAR values and Si/Al (Zr/Al) ratios is most pronounced during Toa-CIE shift II-A and II-B, but is less significant for shift II-C (Fig. 4-14). The decrease in these proxies can be associated with single transgressive pulses, superimposed onto the 3rd order sea level rise, which resulted in reduced contributions of terrigenous derived OM and coarse-grained siliciclastics. The subsequent increase in these proxies, during the recovery phase of the Toa-CIE shifts II-A and II-B, can be attributed to minor regressive phases. Brief regressive phases possibly resulted from a brief global cooling due enhanced silicate weathering and OM burial (e.g. [Cohen et al., 2004](#); [Montero-Serrano et al., 2015](#)) that drove atmospheric CO₂ concentration towards lower values ([McElwain et al., 2005](#)). Global cooling, during the recovery phase of each hyperthermal, has been proposed as process that promoted a recovery of the cryosphere carbon pool (Chapter 3) and might also contributed to the recovery of polar ice.

The highest sea level (MFZ) is indicated by the lowest TAR and Si/Al ratios (as well as Zr/Al ratios) that are documented from a sediment interval associated with the climax of the Toa-CIE (Fig. 4-14). A high sea level is also indicated by the strong enrichment of pelagic fauna that attest drastically reduced sediment accumulation rates (Fig. A4). The stratigraphic position of the MFZ in the Lorraine Sub-Basin match findings from the Lussitanian Basin, where the MZF is also placed in the lower part of the Toa-CIE ([Pittet et al., 2014](#)). Assuming glacio-eustatic controls, the highest sea level reflects the maximum deglaciation associated with the smallest extent of polar ice. The subsequent regressive phase, taking place during the upper part of the Toa-CIE might result from a global cooling as previously discussed in this chapter. The timing of carbon release and sea level/salinity changes has far reaching consequences for the mechanistic model proposed in this thesis. The offset between the MFZ, representing the highest sea level, and the onset of the Toa-CIE recovery phase that reflects the demise of carbon stored in climate-sensitive reservoirs, indicate that the demise of polar ice caps preceded the demise of carbon by ~300 kyr, with respect to the uncertainties regarding the exact position of the MFZ (Fig. 4-14). This observation is in agreement with modeling results by [Majorowicz et al. \(2014\)](#), which showed that terrestrial hydrates become destabilized over ~400 kyr after full deglaciation.

Moreover, the main Toa-CIE shift (II-A, II-B, II-C) and associated transgressive pulsed occurred synchronously with an increase in tri-/di-MTTC ratios reflecting a stepwise decrease in SSS in the Lorraine Sub-Basin (Fig. 4-14). The decrease in SSS was most pronounced during the major Toa-CIE shifts II-A and II-B, whereas a decrease in SSS of lower magnitude is observed during the Toa-CIE shift II-C. Thus, it can be stated that changes in SSS closely align with the evolution of the sea level.

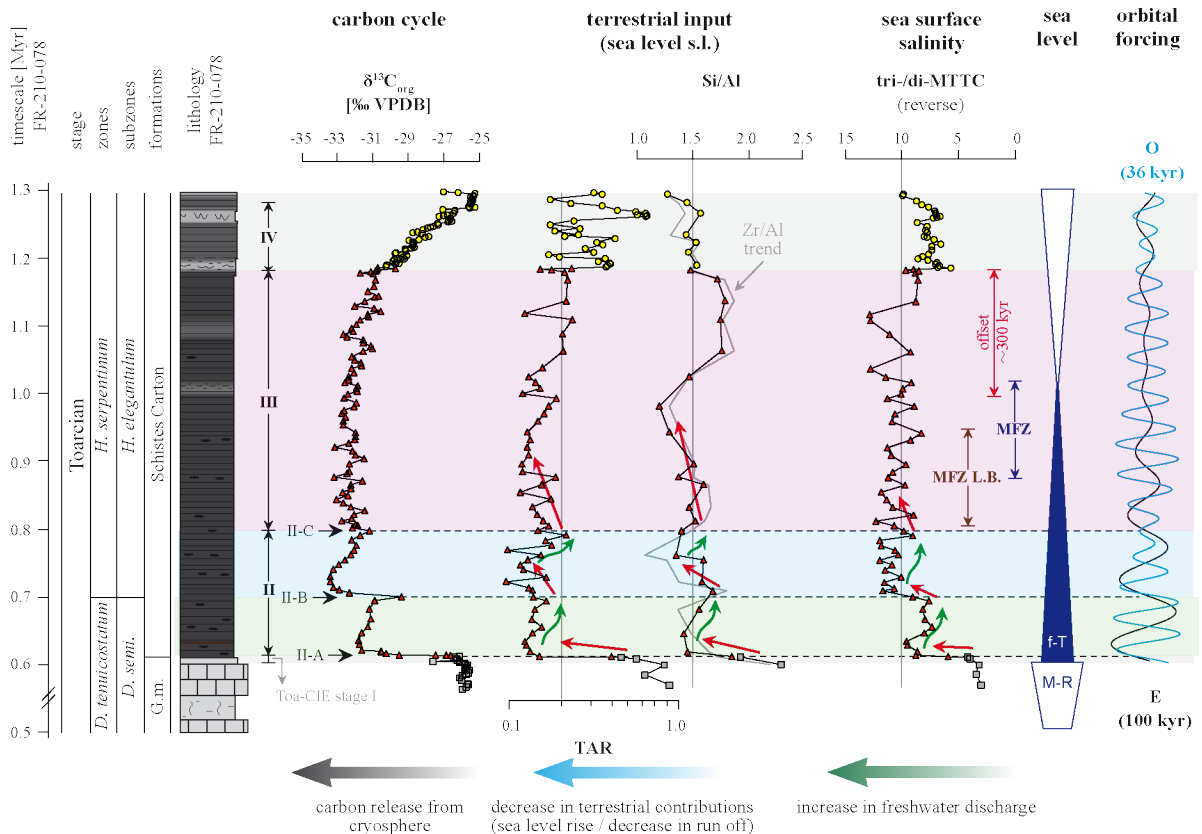


Figure 4-14: The stepwise nature of the Toa-CIE indicates that the release of isotopically light carbon from climate sensitive reservoirs occurred in discrete steps during single hyperthermals (Toa-CIE shifts II-A, II-B, II-C). The Toa-CIE stage I is strongly condensed in the Lorraine Sub-Basin (see Chapter 3). Each negative carbon isotope shift, representing a single hyperthermal, was accompanied by a transgressive pulse as well as by a massive freshwater discharge, both controlled by melting of polar ice paced by astronomical cycles. Oceanographic changes were most pronounced during Toa-CIE shifts II-A and II-B, while oceanographic changes during Toa-CIE shift II-C were of lower magnitude, thus matching the lower magnitude of this carbon isotope shift. Furthermore, the MFS is placed in the climax of the Toa-CIE, at a similar stratigraphic position that has been proposed in the Lusitanian Basin (MFZ L.B.; Pittet et al., 2014). The MFZ can be attributed to the highest sea level, which in regard to the model proposed here, reflect the near total demise of polar ice caps. The timing of sea level and carbon release indicate that declaciation and demise of polar ice caps occurred before all cryosphere stored carbon reservoirs became depleted, which is in agreement with modeling results by Majorowicz et al. (2014).

4.4.5. Ocean circulations pattern on the Western Tethyan Shelf

The role of sea level evolution regarding changes in SSS and reveal that its lowering was most likely bound to freshwater inflow from the Arctic Ocean via the Viking Corridor as previously proposed by Bjerrum et al. (2001), Suan et al. (2010), Dera & Donnadieu (2012), or Dera et al. (2015). Reconstruction of sea level and salinity changes from the Lorraine Sub-Basin in combination with the changes in the spatial $\delta^{18}\text{O}$ pattern allow to reconstruct changes in current systems throughout the Western Tethyan shelf.

Dominant cold climate conditions during the Late Pliensbachian (upper *P. spinatum* zone) and the Earliest Toarcian (lower *D. tenuicostatum* zone) promoted the expansion of polar ice caps, which resulted in a glacio-eustatic sea level fall. According the Bjerrum et al. (2001) the reduced salinity gradient between Arctic Ocean and the Western Tethyan shelf resulted in a weakening of the southwards directed Arctic current systems. Furthermore, a low sea level resulted in a reduced extent of the Viking corridor, which limited the water exchange between Arctic Ocean and Western Tethyan shelf. Weak Arctic current systems caused a strengthening of northwards directed Tethyan counter currents that transported more saline waters onto the Western Tethyan shelf. The geographical pattern of belemnite oxygen isotope values exhibits only a minor, approx. -1‰, difference between low and high latitudinal locations (Fig. 4-15A). Slightly lowered $\delta^{18}\text{O}$ values at high latitudes might indicate a reduced but persistent inflow of low saline Arctic waters, but might also result from riverine fresh water discharge from the surrounding landmasses. This circulation pattern persisted during the Late Pliensbachian and during the lower *D. tenuicostatum* zone and was only interrupted at the PI-Toa boundary event. The later has been associated with a brief warming episode (e.g. Suan et al., 2008b; Dera et al., 2011a), accompanied by a short-lived sea level rise and salinity decrease on the Western Tethyan shelf that is clearly confirmed by this study.

The global warming that started in the upmost *D. tenuicostatum* zone (Dera et al., 2011a) led to the melting of polar ice caps, which resulted in a glacio-eustatic sea level rise and enhanced freshwater inflow to the Arctic Ocean. The high sea level further induced a widening of the Viking Corridor, which favored the southwards discharge of brackish water masses to the Western Tethyan Shelf and led to an weakening of northwards directed Tethyan current systems (Bjerrum et al., 2001; Dera & Donnadieu, 2012). This massive fresh water surge is expressed by a rapid rise in the tri/di-MTTC ratios and can further explain lower $\delta^{18}\text{O}$ values in proximity to the Viking Corridor (Fig. 4-15B). Additionally, freshwater inflow from the Arctic Ocean is supported by a decrease in ϵ_{ND} values (Dera et al., 2015).

During the upper *H. elegantulum* subzone reduced freshwater discharge to the Arctic Ocean resulted from a reduced extent of polar ice caps. A minor cooling during this interval cannot be excluded and could trigger a gentle recovery of polar ice caps, which would explain the regressive trend documented during this period. Regression in combination with reduced freshwater discharge to the Arctic Ocean resulted in a weakening of southwards directed Arctic surface currents and to a strengthening of northwards directed Tethyan deepwater currents. Reduced freshwater inflow is also evidence by a minor increase in $\delta^{18}\text{O}$ values as well as from a reduced latitudinal gradient (Fig. 4-

15). Furthermore, data from the Lorraine Sub-Basin have shown that the *H. elegantulum subzone* reflects a highly dynamic period strongly affected by the interaction of Arctic freshwater and saline Tethyan currents. Astronomically forced glacial-interglacial cycles that align with obliquity periods resulted in significant sea level and salinity fluctuations. Enhanced melting of polar ice during interglacial periods initiated a higher sea level, enhanced freshwater discharge and thus a strengthening of southwards directed Arctic currents. On the contrary, glacial periods were accompanied by the recovery of polar ice caps, which resulted in a lower sea level and a reduced freshwater discharge and thus, in a weakening of Arctic currents.

Lower $\delta^{18}\text{O}$ values and a more pronounced geographical gradients reestablished during the *H. falciferum subzone* and indicate a strengthening of southwards directed Arctic currents that possibly resulted from a wider extent of the Viking Corridor due to a high sea level, promoting an efficient water exchange (Fig. 4-15D). Whether polar ice existed during this period and contributed to the sea level rise and freshwater supply remains unclear. However, the southwards directed Arctic current system possibly originated from density differences of Arctic and Tethyan water masses that persisted even without elevated freshwater inflow from melting polar ice (Bjerrum et al., 2001; Dera & Donnadieu, 2012). Additionally, reduced SSS throughout the Western Tethyan shelf might also have formed via enhanced riverine freshwater discharge that arose from an acceleration of the hydrological cycle during a greenhouse climate. Riverine freshwater contributions during the *H. falciferum subzone* are indicated by the differing pattern in the TAR - tri-/di-MTTC cross plot (Fig. 4-10A).

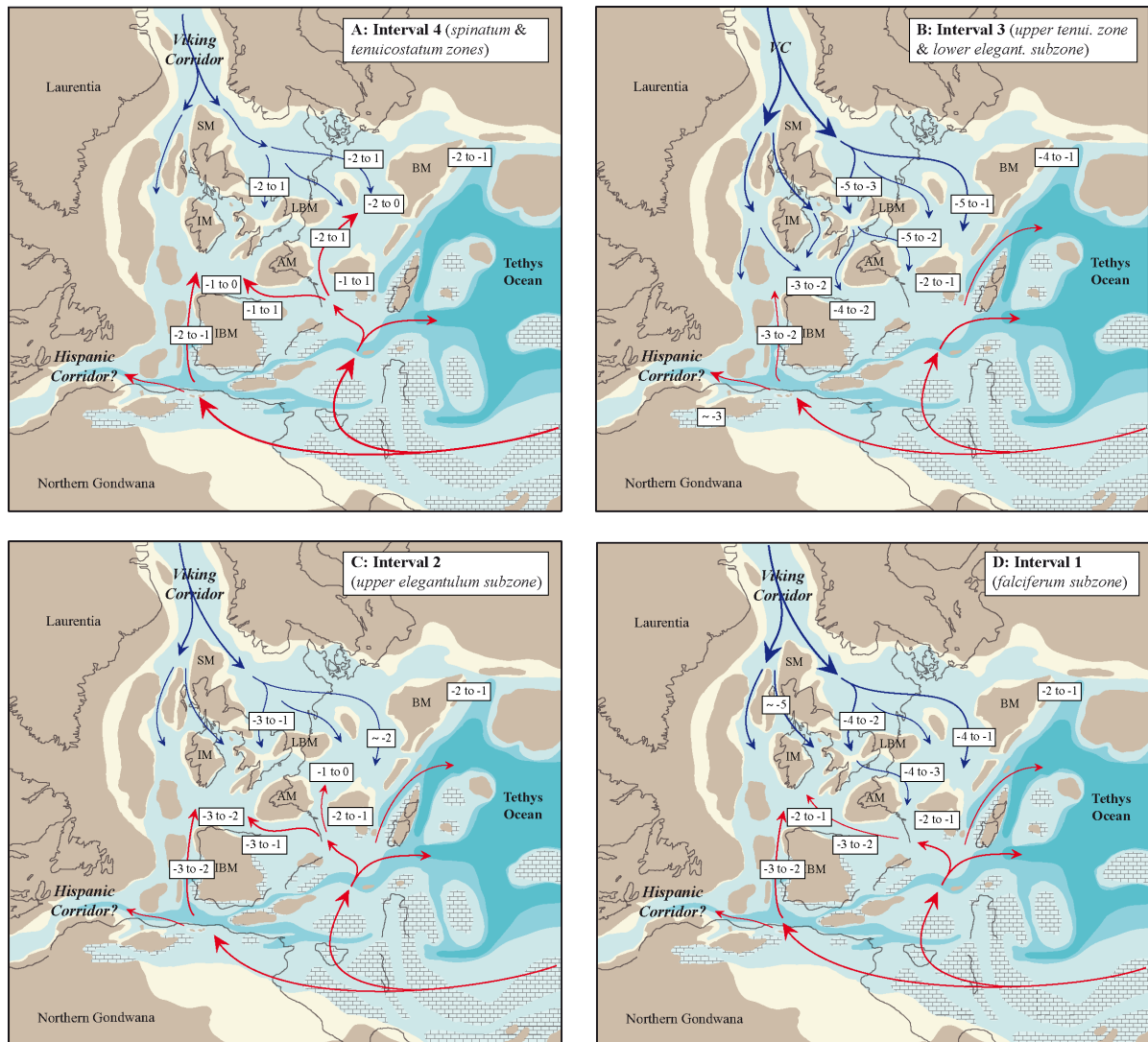


Figure 4-15: Maps showing assumed changes in ocean currents resulting from glacio-eustatic sea level fluctuations and the balance of polar ice accumulation and melting controlling variable rates of fresh water inflow from onto the Western Tethyan shelf from the Arctic Ocean via the Viking Corridor. The spatial pattern of oxygen isotope data confirms a strong NW-SE salinity gradient, whereby lowest $\delta^{18}\text{O}$ values were documented in proximity to the Viking Corridor. Lowest values were confirmed for the Toa-CIE interval (Interval 3) that represents a period of global warming. This warming was associated with a drastic freshening of the Western Tethyan shelf that resulted from the melting of polar ice and led to strong southwards orientated surface currents. The sea level fall taking place during the upper *H. elegantulum* subzone (Interval 2) originated from a decreased fresh water inflow due to the demise of polar ice and led to an increase in the sea surface salinity and possibly to a strengthening of northwards orientated Tethyan currents. A transgression then enhanced connectivity between Arctic and Tethyan Ocean in *H. falciferum* zone. (Oxygen isotope data from: McArthur et al., 2000; Korte & Hesselbo, 2011; Li et al., 2012; Ullmann et al. 2014 (Cleveland Basin), Price, 2010 (Herbrides Basin); Dera et al., 2009b; Hermoso, 2007 (Paris Basin); Harazim et al., 2013 (Grand Causses Basin); Bailey et al., 2003 (Southern German Basin); Teichert & Luppold, 2013 (North German Basin); Metodiev & Koleva-Rekalova, 2008 (Bulgaria); Rosales et al., 2004; Gómez et al., 2008; Gómez et al., 2015 (Spain); Jenkyns et al., 2002; Suan et al., 2008b (Lusitanian Basin); Krecker et al., 2014 (Marocco)).

4.6. Conclusions

Early Toarcian sea level changes, comprising a long-term 2nd order transgression as well as short-term 3rd order sea level cycles, are well expressed in sediments of the Lorraine Sub-Basin and can be inferred from changes in sedimentological and geochemical characteristics (Si/Al, Zr/Al, Ti/Al ratios, TAR). Stratigraphic position as well as extent of transgressive-regressive cycles match findings from the basins (Hardenbol et al., 1998; Gély & Lorenz, 2006; Pittet et al., 2014) and thus support a trans-regional, possibly global, nature of the Early Toarcian sea level changes. The onset of the long-term 2nd order Toarcian transgression is placed in the upmost Pliensbachian (upper *P. spinatum* zone), while the MFZ is placed at the *H. serpentinum* zone – *H. bifrons* zone boundary. Superimposed onto the long-term 2nd order sea level rise three 3rd order transgressive-regressive cycles were identified throughout the lower Toarcian. The Pl8-Toa1 cycle spans the upmost *P. spinatum* and the lower *D. tenuicostatum* zones, the Toa1-Toa2 cycle spans the upmost *D. tenuicostatum* zone and the *H. elegantulum* subzone and the Toa2-Toa3 cycle correspond to the *H. falciferum* subzone. Furthermore, an additional 4th order cycle can be identified within the regressive phase of the Toa1-Toa2 cycle. In the Lorraine Sub-Basin the transgressive phases of the 3rd/4th order cycles align with a significant decrease in the sea surface salinity, whereby the most pronounced freshening of the shelf seas occurred during the Pl8-Toa1 transgression at the Pl-Toa boundary and during the Toa-1-Toa2 transgression in the upmost *D. tenuicostatum* zone and lower *H. elegantulum* subzone. A less pronounced decrease in sea surface salinities can be associated with the transgressive phase of the Toa2-Toa3 cycle in the *H. falciferum* subzone.

According to the astronomical timescale proposed for the studied sediment sequence the 3rd/4th order sea level cycles and salinity changes roughly align with 405 kyr astronomical cycles, which support a glacio-eustatic origin of the Early Toarcian sea level changes and indicate that ice sheet dynamics were the main controlling mechanisms. Environmental changes, including the most rapid transgressive phase and the most pronounced salinity drop can be associated with the Early Toarcian carbon cycle perturbation that aligns with a major global warming, reflecting the demise of polar ice sheets during the transitions from an icehouse to a greenhouse world. This major sea level rise (3rd order Toa1-Toa2 transgressive phase) occurred in distinct transgressive pulses that were accompanied by a stepwise decrease in SSS. These transgressive pulses and changes in SSS occurred synchronically to the Toa-CIE shift and were paced by ~100 kyr eccentricity periods. The coupling of the carbon cycle to oceanographic changes indicates that the release of ¹²C-enriched carbon was directly linked to the melting of polar ice that strongly affected the hydrodynamic regime throughout the Western Tethyan shelf. The MZF of the 3rd order Toa1-Toa2 transgression is placed in the climax of the Toa-CIE, whereas the subsequent regressive phase, possibly resulting from enhanced silicate weathering and organic carbon burial, precedes the recovery phase of the Toa-CIE. This offset indicates that the maximum deglaciation occurred ~300 kyr prior to the last cryosphere stored carbon reservoir to be depleted, which is in agreement with modeling results by Majorowicz et al. (2014).

Subsequent to the long-term changes in climate and oceanographic conditions, sea level of higher order (5th/6th order cycles) matching ~100 kyr eccentricity and ~36 kyr obliquity cycles, were

identified within the upper *H. elegantulum* zone. These sea level fluctuations were paralleled by those in SSS, whereby reduced SSS can be linked to a high sea level. Therefore, these changes in oceanographic conditions possibly reflect glacial-interglacial cycle. The freshwater originated in the Arctic Ocean entered the Western Tethyan shelf via the Viking Corridor that controlled the water exchange between Arctic Ocean and Western Tethyan shelf.

Chapter Five:

Controls on redox conditions in the Lorraine Sub-Basin during the Lower Toarcian

Abstract

During the Early Toarcian widespread organic matter accumulation on shelf settings around the globe has been associated with profound environmental changes, including a drastic rise in global temperatures. Global warming resulted in an intensified continental weathering and in enhanced nutrient supply to the shelf seas that stimulated marine primary productivity. However, diachronous onset and the variable stratigraphic extent of black shale accumulation indicate that local oceanographic conditions also contributed to the accumulation of organic-rich sediments. Moreover, black shale formation has been associated with the expansion of marine oxygen minimum zones, which resulted in an extinction of preferentially benthic communities. The diachronous onset of black shale deposition and the regional character of extinction patterns raise the question whether shelf sea anoxia was dominantly controlled by local or global parameters (Schmidt-Röhl et al., 2002). Distinguishing between local and global factors can help to predict the impact of global climate change onto marine ecosystems and will further allow to discuss the effect of global and local factors controlling the accumulation and preservation of organic matter.

Results of this chapter show that formation and expansion of anoxic/euxinic bottom water in the Lorraine Sub-Basin resulted from global environmental changes. Bottom water anoxia/euxinia and the formation of marine dead zones can be linked to an increased primary productivity that resulted in an elevated organic matter flux to the sea floor, a rise in the sea level that provided low-energetic depositional conditions throughout eutrophic shelf settings and a stratification of the water column as a consequence of enhanced freshwater inflow to the shelf seas. These environmental changes directly resulted from a drastic global warming that was the main driver of this event. The persistence of bottom water anoxia/euxinia was controlled by long-term and short-term glacio-eustatic sea level changes, whereas the expansion of photic zone euxinia into the water column was mediated by the degree of hydrodynamic restriction and water mass stagnation. The degree of hydrodynamic restriction of the Western Tethyan shelf depended on sea level evolution, whereas local paleoceanographic restriction favored the expansion and spatiotemporal extent of photic zone euxinia.

In the Lorraine Sub-Basin prolonged and persistent bottom water anoxia/euxinia, postulated for the Toarcian carbon isotope interval, was not accompanied by the widest extent of euxinia into the water column. The expansion of photic zone euxinia during this period was limited by a high sea level that allowed an efficient mixing of the upper water column and prevented the expansion of euxinic conditions. The widest extent of photic zone euxinia occurred subsequent to the carbon cycle perturbation and can be associated with a regressive phase that resulted in the strongest degree of hydrodynamic restriction. During this phase the low sea level caused high frequent environmental instabilities expressed in significant fluctuation of the redox regime. Findings of this chapter support that Early Toarcian black shales were the local expression of global climate change.

5.1. Introduction

Environmental changes taking place during the Early Toarcian, including a drastic global warming of about 6°C (e.g. [Dera et al., 2011a](#)), were accompanied by widespread OM burial throughout the epicontinental basins of the Western Tethyan shelf (e.g. [Jenkyns, 1988](#); [Bodin et al., 1990](#)) as well as in other shelf settings around the globe (e.g. [Jenkyns, 1988](#); [Jenkyns et al., 2001](#)). Due to the widespread occurrence of organic-rich deposits this period has been termed Toarcian Oceanic Anoxic Event (T-OAE) ([Jenkyns, 1988](#)). Enhanced OM preservation throughout the Western Tethyan shelf was linked to bottom water anoxia, which is evident from sedimentological observations ([Jenkyns, 1988](#); [Röhl et al., 2001](#)), increased rates of pyrite burial (e.g. [Raiswell et al., 1993](#)), as well as from inorganic and organic geochemical proxies (e.g. [Farrimond et al., 1988](#); [McArthur et al., 2008a](#); [Hermoso et al., 2013](#)). Moreover, the occurrence of molecular fossils diagnostic for phototrophic sulfur bacteria indicate that euxinic conditions extended into the photic zone at least during certain periods ([Schouten et al., 2000](#); [Schwark & Frimmel, 2004](#); [van Breugel et al., 2006](#); [French et al., 2014](#)).

Anoxia and the expansion of marine dead zones possibly has been attributed to an elevated primary productivity that was stimulated by increased rates of continental run off and enhanced nutrient supply to the shelf sea during a greenhouse climate (e.g. [Cohen et al., 2004](#); [Montero-Serrano et al., 2015](#)). When reflecting the response of black shale deposition to global climate change during the Early Toarcian a synchronous mode is often inferred but lacks penultimate proof (e.g. [Wignall et al., 2005](#); also see Chapter 1.2.5.). Moreover, formation of anoxic bottom water and the expansion of marine dead zones seems to be bound to local paleogeographic and paleoceanographic conditions, including water mass restriction in silled basins, in which anoxic/euxinic bottom water was separated by a pycnocline from oxic surface water (e.g. [Küspert, 1982](#); [Saalen et al., 1996](#); [Röhl et al., 2001](#); [van de Schootbrugge et al., 2005b](#); [McArthur et al., 2008a](#)). The silled basin model explains the formation of Early Toarcian black shales by local processes, without invoking global factors. Although previous works highlighted the role of sea level changes in the formation of organic rich deposits ([Röhl et al., 2001](#); [Frimmel et al., 2004](#); [Hermoso et al., 2013](#)). However, the impact of sea level changes onto the hydrodynamic regime and its control of extent and persistence of anoxic/euxinic bottom water has so far been investigated on local scale only ([Schwark and Frimmel, 2004](#)).

The diachronous onset and variable stratigraphic extent of black shale deposition as well as the regional character of extinction patterns raise the question whether shelf sea anoxia was controlled by local or global parameters. Distinguishing between local and global factors can help to predict the impact of global climate change towards marine ecosystems and will further allow to discuss the effect of global and local factors controlling the accumulation and preservation of organic matter. This chapter aims to reconstruct the evolution of redox conditions in the Lorraine Sub-Basin and further constrains underlying mechanisms controlling the degree of water column oxygenation. These questions will be addressed by applying an integrated approach, comprising inorganic, organic and isotope geochemical proxies to a single sediment sequence.

5.2. Background – tracing anoxia and euxinia in ancient sediments

5.2.1. Sedimentological evidence

The sediment structure of Recent and Ancient sediments is controlled by depositional processes as well as by benthic activity. Enhanced benthic sediment reworking can result in the removal of former sediment structures and led to the homogenization of the unconsolidated sediment. On the contrary, sedimentation structures can be preserved when benthic activity is significantly reduced or absent. Sediments not affected by benthic activity commonly exhibit a laminated or parallel-textured sedimentation style (e.g. [Wignall, 1994](#)). Abundance and activity of benthic organisms are mainly bound to oxygen availability in bottom waters, as all forms of higher life are aerobic organisms (e.g. [Rhoads & Morse, 1971](#); [Rhoads et al., 1991](#)). Based on this relation the redox classification of sedimentary environments comprises oxic, suboxic and anoxic facies, the last one can further be distinguished into non-sulfidic and sulfidic (euxinic) facies. Studies of Recent benthic environments allowed to estimate oxygen levels for the different redox facies types. Oxygen concentrations of >2 , $2.0 - 0.2$ and >0.2 ml O₂/l H₂O have been estimated for oxic, suboxic and anoxic facies. Sulfidic or euxinic conditions are defined by the presences of free H₂S in the water column ([Tyson & Pearson, 1991](#)). This general scheme includes a variety of special situations, including episodic anoxic and reoxygenation events ([Oschmann, 1991](#)).

5.2.2. TOC-TS-Fe systematic

In normal marine oxic to suboxic environments the extent of sulfate reduction, and thus the extent of sulfur incorporation into the sediment via pyrite formation, is limited by the availability of metabolizable OM. This relation is expressed by a TOC-TS regression line with a slope of about 0.4, commonly attributed to a normal marine trend or “Normal Marine Line” ([Bernier & Raiswell, 1983](#); [1984](#)). A parallel trend with a TS intercept at about 1 to 1.5 wt.% has been identified in sediments from the Black Sea, which represents an euxinic environment where syngenetic sulfur precipitation in the water column induces an elevated sulfur (pyrite) burial flux ([Leventhal, 1983](#); [1987](#); [1993](#)). However, even this TOC-TS relation derives from the limitation of labile OM that controlled the extent of sulfate reduction and thus the sulfur burial flux. In other words, in both systems the amount of H₂S produced by sulfur bacteria covaries with the amount of metabolizable OM. Furthermore, [Raiswell & Bernier \(1985\)](#) found that reactive iron can be limited in anoxic/euxinic environments, which can be expressed by a weak TOC-TS covariation accompanied by relative constant Fe/TS ratios. The amount of reduced iron species hosted by sulfides is expressed by the degree of pyritisation (DOP), whereby ratios < 0.45 , $0.45 - 0.75$ and >0.75 reflect oxic, suboxic and anoxic environments, respectively ([Canfield et al., 1996](#)).

5.2.3. Trace elements

The enrichment pattern of redox sensitive trace elements (TEs) in sediments is widely used to reconstruct redox conditions in modern and ancient environments (Calvert & Pedersen, 1993; Algeo & Maynard, 2004; Tribovillard et al., 2006). Applicability of TE as redox proxies base on the solubility of these elements that vary as a function of the redox regime. Redox sensitive TEs are more soluble under oxic condition but become insoluble under anoxic condition where they get enriched in sediments. A detailed overview about behavior and reaction pathways of redox sensitive TEs is given by Algeo & Maynard (2004) and Tribovillard et al. (2006). These authors distinguish two groups of redox-sensitive TEs based on their enrichment characteristics. Trace elements that show only a weak sulfidic affinity and that are delivered to the sediment in association with the OM flux (Ni, Cu, Zn, Cd). These TEs are not significantly affected by presence of free H₂S. Trace elements that show a strong sulfidic affinity (e.g. Mo, V, U) can become highly enriched in sediments when free H₂S is available. These TEs can be directly precipitate from the seawater as sulfides, can be incorporated into Fe-sulfides, or can involved in reactions catalyzed by free H₂S. Enrichment of these elements can be partly decoupled from OM acumulation. The resulting enrichment pattern of the abovementioned redox-sensitive TEs can be thus used to assess the redox facies and further allows to distinguish anoxic and sulfidic conditions. Geochemical data of selected redox-sensitive TEs, discussed in this chapter, are shown in table 5-1.

Table 5-1: Geochemical data of selected trace elements discussed in this chapter (from Tribovillard et al., 2006 and references therein).

Element	Main species in oxic seawater/ oxidation state	Average concentration in seawater [nmol/kg]	Residence time in seawater [kyr]	Specification in reducing conditions	Average abundance in upper crust [μg/g]	Average shale [μg/g]
Cu	CuCl ⁺ /Cu(II)	2.36	5	CuS, CuS ₂ /Cu(I)	25	45
Ni	NiCl ⁺ , NiCO ₃ , Ni ²⁺ /Ni(II)	8.18	6	NiS/Ni(II)	44	68
V	HVO ²⁻ ₄ , H ₂ VO ⁻ ₄ /V(V)	39.3	50	VO ²⁻ , VO(OH) ⁻ ₃ , VO(OH) ₂ /V(IV); V ₂ O ₃ , V(OH) ₃ /V(III)	107	130
Mo	MoO ²⁻ ₄ /Mo(VI)	105	800	Thiomolybdates	1.5	1.3

5.2.4. Biomarker proxies

Pristane versus Phytane ratio (Pr/Phy)

Pristane (2,6,10,14-tetramethylpentadecane) and phytane (2,6,10,14-tetramethylhexadecane) are common compounds in ancient sediments. They mainly derive from the chlorophyll-a side chain (phytol; (2E,7R,11R)-3,7,11,15-tetramethyl-2-hexadecen-1-ol) and are formed during diagenesis in dependency of the redox environment (Powell & McKirdy, 1973), although other sources including tocopherols and archaea-derived lipids are possible (e.g. Chappe et al., 1982; Goosens et al., 1984; Rowland, 1990; Schwark & Püttmann, 1990). Pristane is formed by oxidation and subsequent decarboxylation of phytol, whereas phytane is formed by dehydration and subsequent hydrogenation of phytol (Powell & McKirdy, 1973; Didyk et al., 1978). The diagenetic pathway of phytol as well as additional sources of pristane and phytane have been summarized in Peters et al. (2005).

Preservation of bacteriohopanes

The C₃₁ to C₃₅ homohopanes originate from C₃₅ hopanoids that are formed during early diagenesis from C₃₅ bacteriohopanetetrols, biosynthesized by prokaryotic organisms (Peters et al., 2005 and references therein). The distribution of the C₃₁ to C₃₅ homohopanes varies as a function of redox conditions, whereby C₃₅ homohopanes are preferentially preserved under anoxic conditions via sulfuration reactions (Sinninghe Damsté et al., 1995). Under oxic conditions, oxidation of the functional groups at the side chain and subsequent decarboxylation result in the formation of C₃₁ to C₃₄ homohopanes. The preservation of the side chain can be expressed as homohopane index (HHI) described as the ratio of C₃₅/C_{Σ(31-35)} homohopanes. Furthermore, the ratio of C₃₂/C₃₁ homohopanes may guide in distinguishing between oxic and suboxic environments. The presence of free oxygen result in the oxidation of bacteriohopanetetrols to a C₃₂ acid that can be preserved as a C₃₂ homohopane if oxygen is limited or can be further oxidized to C₃₁ homohopane if oxygen is available (Peters et al., 2005 and references therein).

Sulfur incorporation into organic matter

The ratio of dibenzothiophene to phenanthrene (DBT/Phen) allows to assess the availability of reduced sulfur for incorporation into OM. Enhanced sulfur incorporation into OM can be promoted by iron limitation in combination with elevated rates of bacterial sulfate reduction. In combination with other redox proxies, the DBT/Phen ratio allows to distinguish different depositional environments (Hughes et al., 1995).

Carotenoid biomarkers as indicator for photic zone euxinia

Sulfidic conditions that extent into the photic zone of the water column (termed: photic zone euxinia, PZE) can be traced by specific pigments (carotenoids) that derive from anaerobic phototrophic prokaryotes, comprising purple sulfur bacteria (*Chromatiaceae*) as well as green and

brown-pigmented sulfur bacteria (*Chlorobiaceae*). Carotenoids synthesized by these strictly anaerobes, which require H₂S and sunlight, act as accessory pigments allowing them to perform photosynthesis in the deeper part of the water column under low light intensities (e.g. Koopmanns et al., 1996; Sinninghe Damsté & Schouten, 2006; Brooks & Schaeffer, 2008). The monoaromatic carotenoid okenane (originating from the precursor okenone), with 2,3,4-trimethyl substitution pattern at the aromatic ring, is highly specific for purple sulfur bacteria (*Chromatiaceae*). These prokaryotes thrive in the upper part of the photic zone, using the shorter wavelengths of the electromagnetic spectrum of sunlight and can thus be attributed to a very shallow chemocline that extends into the upper parts of the photic zone, typically at depth of less than 20 m below water surface (Brooks & Schaeffer, 2008). Chlorobactane, a C₄₀ monoaromatic carotenoid, with 2,3,6-trimethyl substitution pattern at the aromatic ring, can be associated with green-pigmented green sulfur bacteria. These sulfur bacteria inhabit the water layers below the purple sulfur bacteria at depth down to 40 m below water surface. Isorenieratane, a C₄₀ di-aromatic carotenoid, with 2,3,6-trimethyl substitution pattern at both aromatic rings, derived from isorenieratene during early diagenesis, is exclusively biosynthesized by the brown-colored strains of phototrophic green sulfur bacteria (*Chlorobiaceae*). Green sulfur bacteria can grow at lower light intensities and thus inhabit the lower part of the photic zone, below 40 m (Brooks & Schaeffer, 2008).

5.2.5. Isotope systems ($\delta^{34}\text{S}$ and $\delta^{98/95}\text{Mo}$)

Sulfur isotopes ($\delta^{34}\text{S}$)

The sulfur isotope signature of pyrite is controlled by the rate of BSR. Bacterial sulfate reduction results in ³²S-enriched sulfide and ³⁴S-enriched residual aqueous sulfate, whereby the isotope fractionation between sulfide and sulfate can range from 0 to 70‰ (Canfield et al., 2010). Extent of isotope fractionation during BSR is controlled by sulfate reduction rates. Low rates of sulfate reduction result in large fractionation factors, whereby isotopic fractionation decreases with increased rates of sulfate reduction (Habicht & Canfield, 1997; Canfield, 2001). Enhanced pyrite burial thus induces lower isotopic fractionation. Isotopic fractionation due to BSR can be further altered by sulfur redox recycling and microbial disproportionation of sulfur (Habicht & Canfield, 2001). Thus, the isotopic composition of sedimentary sulfur allows to assess changes in the sulfur cycle, which can be associated with modifications of the fluxes to and out of the ocean (Bottrell & Netwon, 2006). However, interpretation of sulfur isotope data can be complicated by the fact that pyrite formation, even in non-disturbed euxinic sediments, occurs over a period of several 10th of thousands of years and measured $\delta^{34}\text{S}$ values may integrate syngenetic and epigenetic pyrite formation (Rickard, 2012).

Molybdenum isotopes ($\delta^{98/95}\text{Mo}$)

Molybdenum isotope ratios have been established as a paleoredox proxy (Siebert et al., 2003; Poulson et al., 2006; 2009; Pearce et al., 2008; Dickson et al., 2012; 2014; Proemse et al., 2013). In oxic to suboxic environments Mo is preferentially adsorbed onto Fe- and Mn-oxides, which is associated with an isotopic fractionation of about 1 to 3‰ and result in $\delta^{98/95}\text{Mo}_{\text{SED}}$ values of about -1 to +1‰, significantly lower than that of the Mo dissolved in the seawater ($\delta^{98/95}\text{Mo}_{\text{SW}} = 2.3 \pm 0.1\%$; Siebert et al., 2003; Poulson Brucker et al., 2009). Under anoxic conditions Mo removal rates from seawater significantly increases (Mo scavenging by OM and sulfides; Scholz et al., 2013) and isotope fractionation results in sedimentary $\delta^{98/95}\text{Mo}$ values of about +1.5‰, which is +0.7‰ heavier than $\delta^{98/95}\text{Mo}_{\text{SW}}$ values (Poulson et al., 2006). In euxinic settings Mo can be nearly or even completely removed from the water column without any isotopic fractionation. Then the isotopic signature of Mo_{SW} is transferred into the sedimentary Mo and $\delta^{98/95}\text{Mo}_{\text{SED}} = \delta^{98/95}\text{Mo}_{\text{SW}} = 2.3\%$. (Siebert et al., 2003; Poulson Brucker et al., 2009).

5.3. Results

5.3.1. Lithological observations, OM and pyrite burial

A detailed sedimentological description of Core FR-210-078 is given in Chapter 4 (4.2.1.). High OM concentrations (or TOC, respectively) accompanied by high sulfur (TS) concentrations are documented in laminated and partly parallel-textured sediments of the Schistes Carton Fm (Intervals 3, 2, 1; upmost *D. tenuicostatum* and *H. serpentinum* zones). Changes in TOC and TS closely align with facies changes, whereby periodically changing depositional conditions throughout Interval 2 are well expressed in the evolution of TOC and TS values that show the highest variability within this interval. TOC and TS values throughout the Schistes Carton Fm mainly vary between 5 and 15 wt.% and 2 and 6 wt.%, respectively (Fig. 5-1).

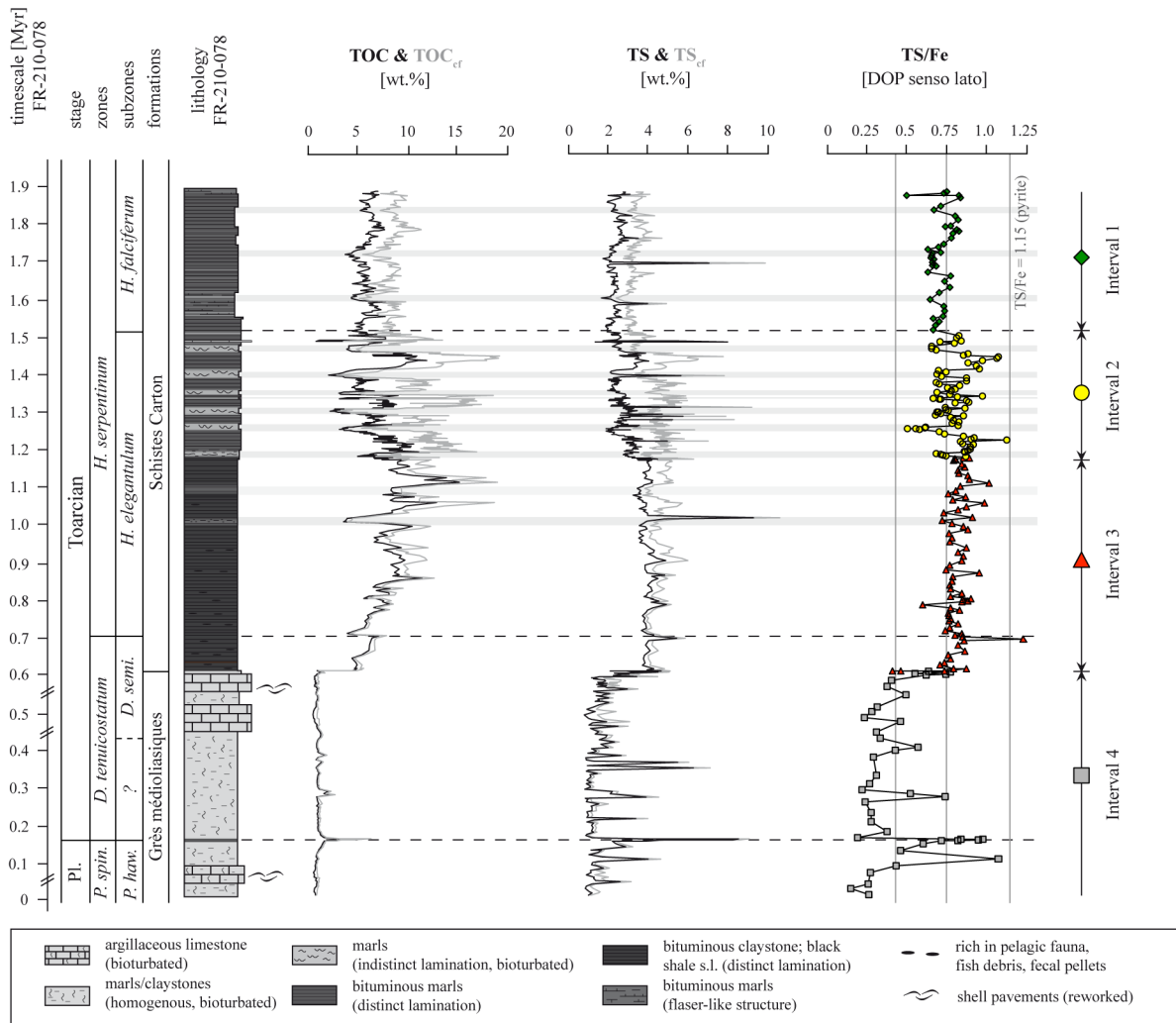


Figure 5-1: Stratigraphic evolution of TOC, TS values (as well as TOC_{cf} and TS_{cf}) and the TS/Fe ratio that reflect the degree of pyritisation (DOP; senso lato). All parameters align with lithological changes, whereas positive spikes in TS and TS/Fe in samples from the Grés médioliasiques Fm (Interval 4) are bound to epigenetic euhedral pyrite. The highest DOP > 0.75 is observed throughout the Interval 3.

High TOC and TS values that reach 3 wt.% and 8 wt.%, respectively, were also documented for the PI-Toa boundary black shale. In contrast, low TOC and TS values <1 wt.% and <2 wt.%, respectively, occur in the bioturbated sediments of the Grés médioliasiques Fm. Higher TS values (up to 7 wt.%) are bound to thin horizons strongly enriched in euhedral pyrite (Fig. 5-1). Similar trends were observed for TOC_{cf} and TS_{cf} values, indicating that rather changes in primary productivity and preservation of OM than variable carbonate dilution controlled the content of OM and pyrite in the sediments.

Changes in pyrite burial can be estimated by calculating the ratio of TS/Fe that reflects the DOP (degree of pyritisation, *sensu lato*), assuming that Fe is mainly bound to pyrite (Canfield et al., 1996). However, it must be mentioned that the reliability of this approach is limited without performing an iron specification analysis (Rickard, 2012), which was not conducted in this study. Highest DOP that varied between 0.6 and 1.0 were documented for samples from Intervals 3 and 2 (upmost *D. tenuicostatum* zone and *H. elegantulum* subzone), whereas the highest variability in the DOP is documented for samples from Interval 2 (upper *H. elegantulum* subzone). Changes in DOP further align with facies changes, whereas a higher DOP is restricted to for samples from horizons with high TOC values and distinct lamination (Fig. 5-1). Slightly decreased and less variable values, ranging from 0.6 and 0.8, were documented for Interval 1 (*H. falciferum* subzone) (Fig. 5-1).

5.3.2. Trace element-based redox proxies

TEs associated with OM flux and weak sulfidic affinity (Cu, Ni)

Cu and Ni are preferentially associated with the OM flux and have been thus attributed to be productivity-related proxies (Tribovillard et al., 2006). In oxic environments Cu (Cu(II)) is mainly present as organo-metal ligand, whereby Ni exists as Ni²⁺, Ni-carbonate (NiCO₃), or is adsorbed on macromolecular OM. Both TEs are transported to the seafloor in association with the OM flux. After OM decay elements are liberated and may form sulfides (NiS, CuS, CuS₂) under anoxic conditions.

Low Ni/Al and Cu/Al ratios of ~10 and ~7, respectively, were observed throughout Interval 4 (upper *P. spiantum* and the lower *D. tenuicostatum* zones), whereby these values match those of average shale (Wedepohl, 1971, 1991). Higher ratios were only found in laminated sediments at the Pliensbachian-Toarican boundary, where Ni/Al and Cu/Al ratios reach ~25 and ~15, respectively (Fig. 5-2). Additionally, high Ni/Al ratios occur in a single sample from the uppermost *P. spinatum* zone. High Ni/Al and Cu/Al ratios of about ~15 and ~13 were determined for Interval 3 (upmost *D. tenuicostatum* zone and lower *H. elegantulum* subzone), whereby both TEs exhibit similar trends throughout this interval (Fig. 5-2). The Ni/Al and Cu/Al ratios remain high throughout the Intervals 2 and 1 (upper *H. elegantulum* subzone and *H. falciferum* subzone), whereby Ni/Al ratios vary between 8 and 25 and Cu/Al ratios between 6 and 18. Both ratios show periodically fluctuations that align with facies changes.

TEs with sulfidic affinity (Mo, V)

Vanadium: Under oxic conditions vanadium is present as dissolved vanadate (V(V)) ionic species (HVO_4^{2-} or H_2VO_4^-). Under suboxic to anoxic conditions V(V) is reduced to V(IV) that forms insoluble hydroxyls ($\text{VO}(\text{OH})_3^-$) or hydroxides ($\text{VO}(\text{OH})_2$). V(IV) hydroxyls can be removed from the water column by adsorption onto OM particles or by the formation of organometallic ligands. Thus, under mildly anoxic conditions V is mainly bound to the OM fraction. Under sulfidic conditions V is reduced to V(III), which may form vanadyl porphyrins or is precipitated as solid oxide (V_2O_3) or hydroxide ($\text{V}(\text{OH})_3$).

Low V/Al ratios of ~ 7 occurred in samples from Interval 4 (upper *P. spinatum* and lower *D. tenuicostatum* zones), whereby values are significantly lower than those of average shale (Wedepohl, 1971, 1991). Significantly increased ratios were measured in samples from Interval 3 (upmost *D. tenuicostatum* zone and lower *H. elegantulum* subzone), where values vary between ~ 15 and ~ 25 . A drop to ratios of ~ 7 is seen at the base of Interval 2 (upper *H. elegantulum* subzone), before values again increase in the uppermost part of this interval. Ratios between ~ 10 and ~ 15 were observed in samples from Interval 1 (*H. falciferum* subzone). The same periodicity documented in Ni/Al and Cu/Al ratios within the Intervals 2 and 1 is also evident from V/Al ratios (Fig. 5-2).

Molybdenum: In oxic environments Mo is present as Mo(VI) that forms MoO_4^{2-} . Reaction pathways of Mo under anoxic or sulfidic conditions are complex and will not be described in detail at this point. For further details I refer to e.g. Algeo & Maynard (2004) and to Tribouillard et al. (2006) as well as to the reference therein. Under anoxic conditions Mo(VI) is reduced to Mo(V), forming MoO_2^+ , or to Mo(IV), forming thiomolybdates ($\text{MoO}_x\text{S}_{4-x}^{2-}$). Further reduction of thiomolybdates can form solid MoS_4^{2-} species that precipitate together with Fe-sulfides. Mo precipitation by uptake in syngenetic Fe-sulfides can be accelerated when H_2S is present in the water column. Thus, in euxinic environments the removal of Mo from the seawater can be exceptionally efficient, despite of the high concentration and residence time in seawater (Algeo, 2004; Algeo & Maynard, 2004).

Throughout Interval 4 (upper *P. spinatum* and lower *D. tenuicostatum* zones) the concentration of Mo stay below the limit of detection of the applied method ($\text{Mo} < 2\text{ppm}$). High Mo concentrations were only noted for the Pl-Toa boundary black shale, where Mo/Al ratios increase to ~ 4 . Mo/Al ratios that vary between ~ 0.5 and ~ 4 were determined for Interval 3 (upmost *D. tenuicostatum* zone and lower *D. elegantulum* subzone), whereby a decreasing trend was noted for the upper part of this interval. The decreasing trend continues in the lower part of Interval 2 (upper *H. elegantulum* subzone). Lowest Mo/Al ratios are limited to the middle part of Interval 2, whereas an increasing trend to Mo/Al ratios of about 4 is seen in the upper part of this interval before a second minimum occurs in the uppermost part of this interval (Fig. 5-2). Mo/Al ratios show an increasing trend throughout Interval 1 (*H. falciferum* subzone), where the highest values of ~ 10 are restricted to the top of this interval. A pronounced periodicity that has been documented for the other TEs is also evident from Mo/Al ratios.

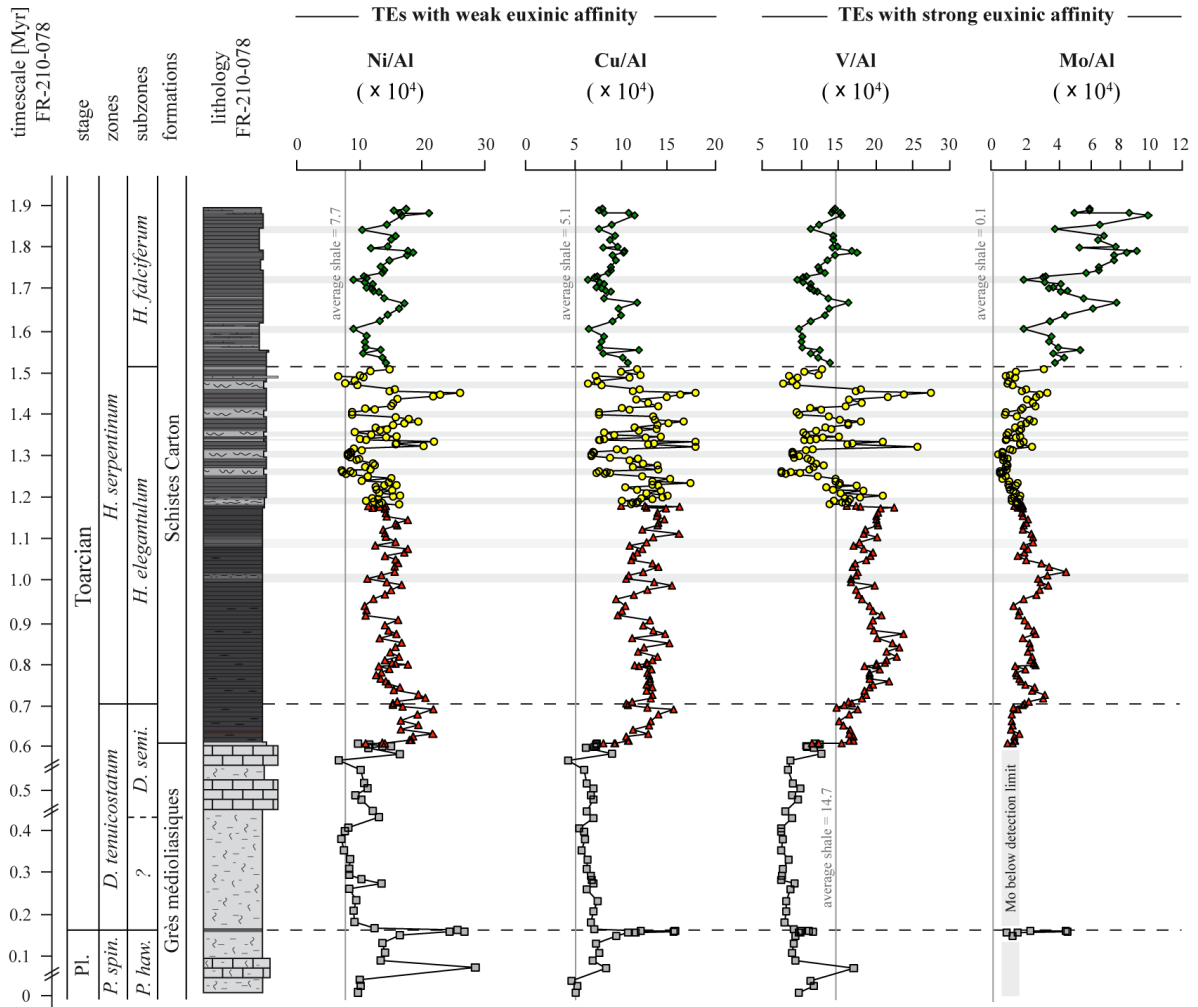


Figure 5-2: Stratigraphic evolution of redox-sensitive trace element data (elements normalized to Al). Average shale values after Wedepohl (1971, 1991). Ni and Cu are TEs with only a weak euxinic affinity and concentrations are mainly bound to the OM flux. V and Mo are preferentially enriched in anoxic and euxinic environments. Similar TE enrichment patterns are documented for all TEs throughout the Intervals 1 and 2, whereby Mo is significantly depleted in Interval 2. Throughout Interval 3 different trends were observed for TEs with weak and strong sulfidic affinity.

5.3.3. Biomarker-based proxies

Pristane/Phytane ratio (Pr/Phy)

Pristane and Phytane, present in the aliphatic hydrocarbon fraction, were quantified from the total ion current chromatogram. High Pr/Phy ratios that vary between 2 and 3 were observed in samples from Interval 4 (upper *P. spinatum* and lower *D. tenuicostatum* zones), whereby a slightly decreasing trend is observed throughout the upper part of this interval. A significant drop in the ratio to values of about 1.2 marks the Pl-Toa boundary (Fig. 5-3). A drastic decrease in Pr/Phy ratios to values <1, which occurred in two steps, has been found within the lower part of Interval 3 (upmost *D. tenuicostatum* and lower *H. elegantulum* subzone), whereby ratios remain low throughout the entire interval. Low but less variable Pr/Phy ratios ranging from 0.8 to 1.3 were

observed in Intervals 2 and 1 (upper *H. elegantulum* and *H. falciferum* subzones). However, throughout the Schistes Carton Fm minor changes in the Pr/Phy ratios cannot be associated with lithological changes (Fig. 5-3).

Homohopane Index* (HHI*) and C₃₂/C₃₁ hopane ratio

Hopanoids, present in the aliphatic hydrocarbon fraction, were identified from the m/z=191 chromatograms by using the elution order as well as characteristic mass spectra. The m/z=191 chromatograms are dominated by homohopanes in $\alpha\beta R$ and $\beta\beta$ configuration. The $\alpha\beta S$ and $\beta\alpha S+R$ isomers were identified as well but occur only in trace amounts only. Furthermore, unsaturated hopene homologues are present for each homohopane analog. The HHI* (= HHI \times 100) was calculated by using the regular hopanes (C₃₁₋₃₅) in $\alpha\beta R$ and $\beta\beta$ configuration, whereby hopenes were not included as these compounds occurred only in very low concentrations. A representative m/z 191 mass chromatogram including an identification of the single compounds is shown in the appendix (Fig. A11).

Low HHI* values <3 were determined for Interval 4 (upmost *P. spinatum* and lower *D. tenuicostatum* zones), whereby a slightly increasing trend to indices of ~ 4 has been observed throughout the upper part of this interval (Fig. 5-3). Interestingly no increase in the HHI* were found for the Pl-Toa boundary black shale, where indices stay below 4. A rapid increase in the HHI* to indices of ~ 6 has been observed at the base of Interval 3 (upmost *D. tenuicostatum* zone and lower *H. elegantulum* subzone). Afterwards indices increase to values of ~ 10 in the upper part of this interval (Fig. 5-3). Highest HHI* values were documented in Interval 2 (upper *H. elegantulum* subzone), where indices systematically vary between 7 and 12. Variation in the indices align with lithological changes, whereby high HHI* values are indicative of distinctly laminated horizons and lower indices for horizons that show only an indistinct lamination. Furthermore, the base of this interval is marked by a brief horizon where the HHI* reached values of about 14 (Fig. 5-3). Throughout Interval 1 (*H. falciferum* subzone) indices varied between 5 and 10, whereby lower values were confined to the middle part of the interval.

The evolution of the C₃₂/C₃₁ hopane ratios shows a similar trend to those observed in the HHI* (Fig. 5-3). Ratios <0.3 were observed for samples from Interval 4 (upmost *P. spinatum* and lower *D. tenuicostatum* zones). Throughout Interval 3 (upmost *D. tenuicostatum* zone and lower *H. elegantulum* subzone) ratios varied between 0.2 and 0.4, but mainly remained below 0.3. Higher ratios, exceeding 0.4, were limited to the upper part of this interval. Throughout Interval 2 (upper *H. elegantulum* subzone) ratios remained relatively high and predominantly varied between 0.3 and 0.4, whereas local maxima occurred in the lowermost and uppermost part of this interval. Ratios significantly decrease in the lower part of Interval 1 (*H. falciferum* subzone), where they reached a minimum of about 0.2. Afterwards, ratios increased to about values of about 0.3.

DBT/Phen

DBT and Phen were identified and quantified by using the characteristic molecular masses of $M=184$ and $M=178$, respectively (see Fig. A15 in the appendix). DBT/Phen ratios show a steady increasing trend throughout the studied interval that starts in the lower *D. tenuicostatum* zone (Interval 4) and culminates in a maximum of 0.8 that is placed in the upper part of the Interval 2 (upper *H. elegantulum* subzone). Afterwards ratios decline to values of about 0.6 within the lower part of Interval 1 (*H. falciferum* subzone) and remain quite stable throughout the upper part of this interval (Fig. 5-3). This overall long-term trend is further highlighted by a brief horizon within the lower part of the Interval 2 that shows significantly increased ratios of about 1.1.

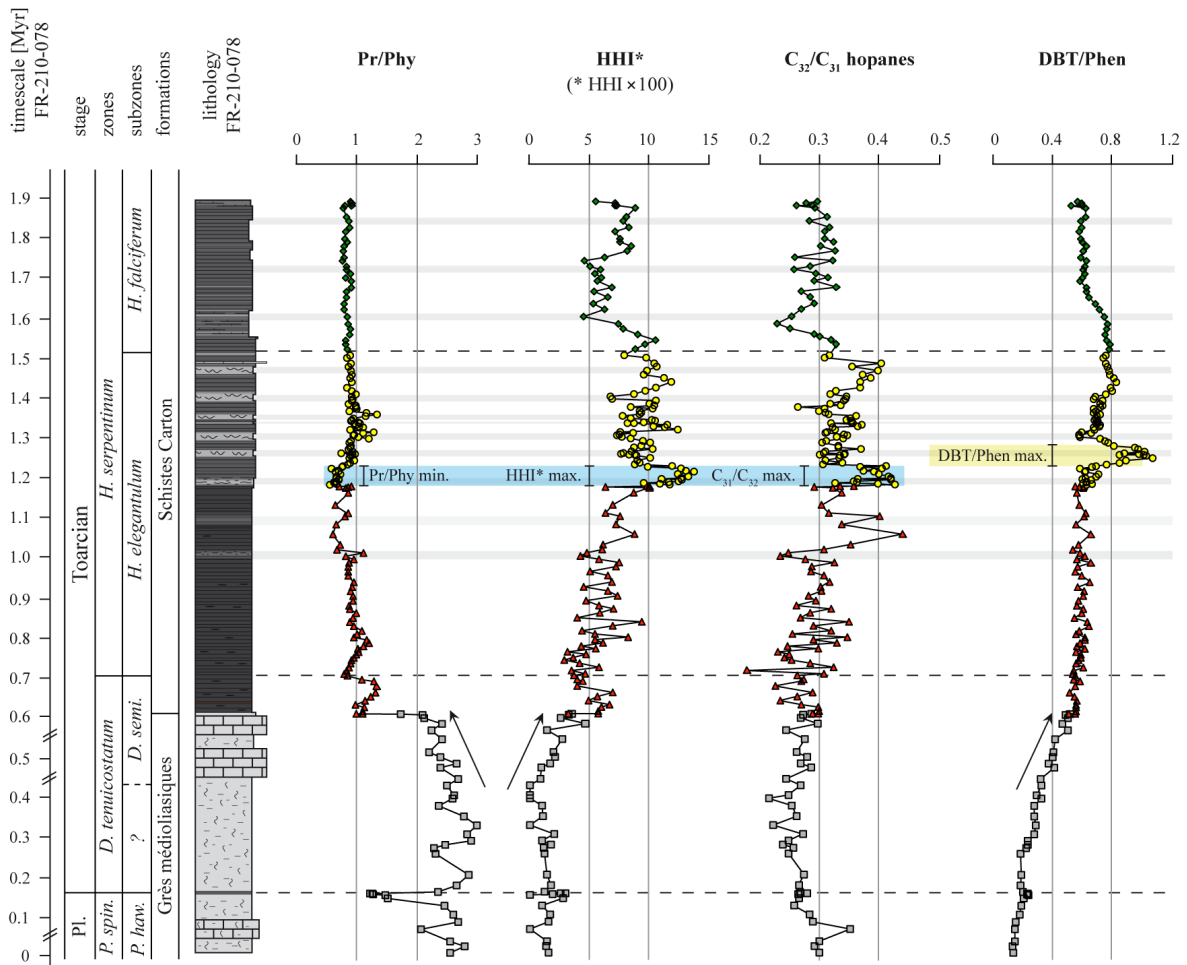


Figure 5-3: Stratigraphic evolution of bio/geo-marker-based redox proxies Pr/Phy, HHI*, C₃₂/C₃₁ hopanes and the ratio of DBT/Phen. All proxies attest to predominantly anoxic conditions for the Schistes Carton Fm, whereby the HHI* shows the highest variability which can be interpreted in terms of a high sensitivity towards redox fluctuations. The Pr/Phy ratio is less sensitive and only allows distinguishing oxic/suboxic conditions during deposition of the Grès médioliasiques Fm and preferentially anoxic conditions during deposition of the Schistes Carton Fm. The DBT/Phen ratio indicates enhanced S-incorporation into OM of the Schistes Carton Fm. All proxies indicate an initial oxygen depletion prior the onset of black shale deposition (arrows). Furthermore, a significant maximum in the HHI* and C₃₂/C₃₁ hopanes values that occurred at the base of Interval 2 is followed by a maximum in DBT/Phen ratios, revealing a substantial offset.

Carotenoid biomarkers as indicator for photic zone euxinia

Carotenoids, present in the aromatic hydrocarbon fraction, were identified by using the characteristic mass fragments m/z 133 and m/z 134, in combination with their molecular masses. Quantification was done by using the mass fragment m/z 133. A representative m/z 133 ion chromatogram is shown in Fig. A16 in the appendix.

Only isorenieratane, exclusively biosynthesized by brown-pigmented green sulfur bacteria, has been identified in samples from the sediment section studied. Chlorobactane and okenone were not found and seems to be absent. Only traces of isorenieratane ($<0.05 \mu\text{g/gTOC}$) were found in the bioturbated sediments from Interval 4 (upper *P. spinatum* and the lower *D. tenuicostatum* zones). The occurrence of isorenieratane in these sediments, however, indicates that brief episodes of PZE reoccurred during this period. Elevated isorenieratane concentrations of about $5.6 \mu\text{g/gTOC}$ were found in laminated sediments that mark the Pl-Toa boundary black shale. Mainly low isorenieratane concentrations that stay below $3 \mu\text{g/gTOC}$ were determined for Interval 3 (upmost *D. tenuicostatum* zone and lower *H. elegantulum* subzone), whereas one horizon in the upper part of this interval shows significantly increased concentrations of $\sim 19.6 \mu\text{g/gTOC}$. Elevated isorenieratane concentrations were also noted for Interval 2 (upper *H. elegantulum* subzone), where values fluctuate between 2.5 and $18.4 \mu\text{g/gTOC}$. Interestingly, high concentrations are not exclusively bound to the distinctively laminated horizons within this interval. High isorenieratane concentrations of $\sim 8 \mu\text{g/gTOC}$ occur in the basal part of Interval 1 (*H. falciferum* subzone), whereas concentrations decrease and stay below $5 \mu\text{g/gTOC}$ in the upper part of this interval (Fig. 5-4).

5.3.4. Sulfur and molybdenum isotopes

$\delta^{34}\text{S}_{\text{bulk}}$

Sulfur isotopes were measured employing bulk sediment that may comprise different sulfur fractions. In marine sediments sulfur is mainly hosted by sulfides. However sulfur can also be associated with the OM fraction as well as with the carbonate fraction (Bottrell & Netwon, 2006). Due to the dominance of the sulfide fraction it can be assumed that $\delta^{34}\text{S}_{\text{bulk}}$ values mainly represent changes in the isotopic composition of sulfur present in sulfides.

Sulfur isotope data (pyrite associated sulfur) from Early Jurassic sediments (Posidonia Shale and Jet Rock) vary between -40 and -15% (Fisher & Hudson, 1987; Raiswell et al., 1993). Similar values were determined for contemporaneous sediments from the Lorraine Sub-Basin (Schistes Carton Fm). $\delta^{34}\text{S}_{\text{bulk}}$ values between -35 and -25% are reported for samples from Interval 3 (upper *P. spinatum* and the lower *D. tenuicostatum* zones). Slightly higher values that vary between -30 and -15% were found in Intervals 2 and 1 (upper *H. elegantulum* and *H. falciferum* subzones) (Fig. 5-4). Background values of about -50% were confined to bioturbated sediments of the Grés médioliasiques Fm (Interval 4; upmost *P. spinatum* and lower *D. tenuicostatum* zones) where some samples that are strongly enriched in ^{34}S show values that reach -30% .

$\delta^{98/95}\text{Mo}$

Molybdenum isotope analysis was performed for samples with Mo >2 ppm, which are mainly restricted to the Schistes Carton Fm (Intervals 3, 2, 1). Only two reference samples from the bioturbated sediments of the Grès médioliasiques Fm (upmost Interval 4) were analyzed. Samples from the PI-Toa boundary black shale were not analyzed. Molybdenum isotope values of about 0.5‰ were documented for the two samples from the upmost Interval 4 (upmost *P. spiantum* and lower *D. tenuicostatum* zones). Isotope values from Interval 3 (upmost *D. tenuicostatum* zone and lower *H. elegantulum* subzone) are relative low and vary between 0.2 and 0.5‰ (Fig. 5-4). Values increase within Interval 2 (upper *H. elegantulum* subzone), where they range between 0.8 and 1.3‰. Slightly higher values approaching 1.5‰ were determined for samples from the lower part of Interval 1 (*H. falciferum* subzone). Molybdenum isotope data throughout this interval mainly vary between 0.8 and 1.5‰ (Fig. 5-4).

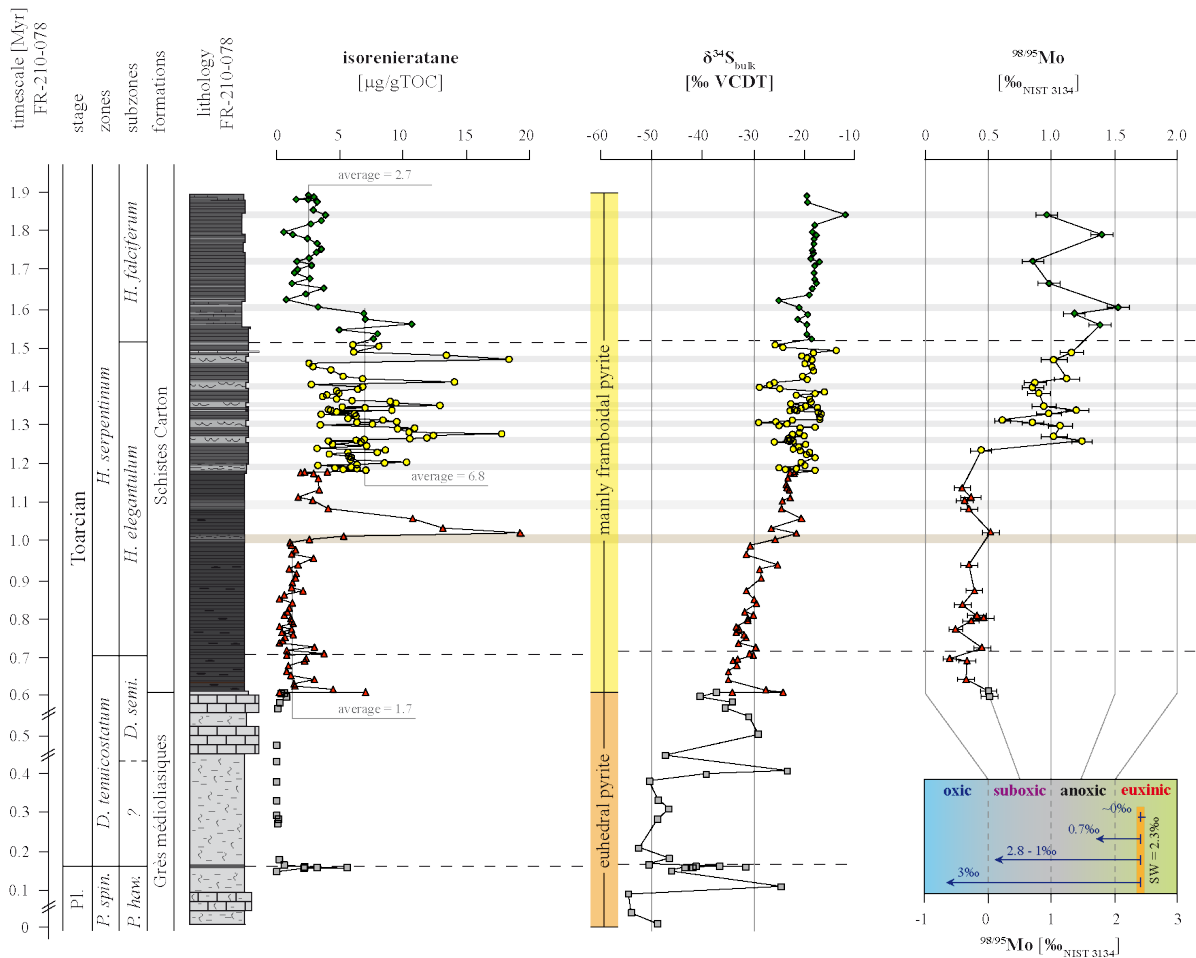


Figure 5-4: Stratigraphic evolution of isorenieratane concentrations, reflecting changes in the abundance of *Chlorobiacea*. The increasing $\delta^{34}\text{S}_{\text{bulk}}$ trend throughout the Schistes Carton Fm can be connected with elevated rates of BSR and pyrite burial. $\delta^{98/95}\text{Mo}$ values have been proposed to reflect changes in redox conditions (redox scale after: Poulson et al., 2006; SW is the isotopic composition of Mo in seawater).

5.4. Discussion

5.4.1. Assessing the redox facies

The redox facies of the different lithological units represented by the Grés médioliasiques and Schistes Carton Fm as well as fluctuations of redox conditions within these lithological units can be inferred from the integrated application of organic and inorganic as well as isotope geochemical proxies. This integrated approach will allow to discuss the overall evolution of redox conditions in the Lorraine Sub-Basin and will further allow to identify mechanisms controlling the extent and persistence of anoxia, euxinia as well as PZE.

Redox facies inferred from trace element enrichment pattern (TOC_{cf} – TE/Al covariation)

Low TE/Al ratios that show no correlation with the TOC_{cf} content have been documented for samples from the organic-poor (TOC_{cf} <2 wt.%) and bioturbated clay-/marl-stones of the Grés médioliasiques Fm (Interval 4) (Fig. 5-5), which is in agreement with the TE behavior proposed for oxic to suboxic sediments (Algeo & Maynard, 2004; Tribovillard et al., 2006). Low productivity rates in combination with a dominantly well-oxygenated water column prohibited a significant enrichment of redox-sensitive TEs in the sediment. Variable TE/Al ratios might result from different detrital sources, which is however not recognizable by Al-TE cross-plots that exhibit no statistical significant correlation for Ni, V and Mo with Al ($R^2 < 0.2$). However, a correlation coefficient of 0.43 confirms a stronger detrital impact onto the enrichment of Cu (Fig. S5-1 in the supplementary). Due to these observations it is most likely that the TEs were enriched in the sediment by a combination of autochthonous and allochthonous sources. Allochthonous TE-enrichment by detrital contributions possibly resulted from a low sea level (see Chapter 4). Autochthonous enrichment resulted from brief anoxic episodes. Subsequent reoxygenation events led to the degradation of OM within the upmost-unconsolidated sediment layers, which resulted in the post-depositional loss of TOC. Redox-sensitive TEs were less affected by post-depositional sediment reworking and remain relatively enriched in the reworked sediments (Tribovillard et al., 2006).

Samples from the laminated PI-Toa boundary black shale are significantly enriched in Ni and Cu, whereby the highest TE/Al ratios relative to TOC_{cf} contents are documented for this horizon (Fig. 5-5A & B). The strong correlation of TOC_{cf} with Ni/Al and Cu/Al ($R^2 = 0.74$ and 0.83 , respectively) indicates that these elements were bounded to the OM flux and were subsequently enriched in the sediment under dominantly anoxic conditions at the sediment-water interface. Slopes of the regression lines calculated match with trends documented for Cretaceous C/T black shales (Cenomanian-Turonian boundary) or Mediterranean sapropels, but plot above the trends documented for Pennsylvanian shales by Algeo & Maynard (2004) (grey fields in Fig. 5-5A & B). A strong correlation has also been observed between TOC_{cf} and V/Al ($R^2 = 0.73$) as well as between TOC_{cf} and Mo/Al ($R^2 = 0.70$), whereas absolute V/Al ratios do not exceed detrital background values from the bioturbated oxic to suboxic sediments of the Grés médioliasiques Fm (Fig. 5-5C & D). The strong correlation of TOC_{cf} with TE/Al ratios that show a strong euxinic affinity (V, Mo) indicate

preferentially anoxic conditions with only mildly euxinic conditions during deposition of the Pl-Toa boundary black shale (Algeo & Maynard, 2004; Tribovillard et al., 2006). Euxinic conditions, if temporarily present, might have been bound to the PP and OM export rates into the bottom water layers. The overall V/Al and Mo/Al ratios, determined for the Pl-Toa boundary black shale, match with trends reported for Pennsylvanian shales (grey fields in Fig. 5-5C & D), but plot significantly below trends known from Recent anoxic settings.

The TEs Ni and Cu, associated with the OM flux (Algeo & Maynard, 2004; Tribovillard et al., 2006), are significantly enriched in the bituminous facies of the Schistes Carton Fm ($\text{TOC}_{\text{cf}} \approx 3$ to 19 wt.%). Trends exposed in the TOC_{cf} -TE/Al cross-plots roughly follow trends reported by Algeo & Maynard (2004) for Pennsylvanian shales (grey areas in Fig. 5-5) and further match with TE/Al ratios from contemporaneous Jurassic sediments of the Southern German Basin, the Cleveland Basin (Yorkshire) as well as with ratios known from Recent anoxic and euxinic settings (Fig. 5-5A & B). However, Ni/Al and Cu/Al ratios are significantly lower than ratios documented for the Pl-Toa boundary black shale (Fig. 5-5A & B). Interestingly, only a weak correlation of TOC_{cf} with TE/Al ratios is observed for samples from the Schistes Carton Fm. The highest degree of correlation is achieved for samples from the *H. falciferum subzone* (Interval 1; $R^2_{\text{Ni/Al}} = 0.59$, $R^2_{\text{Cu/Al}} = 0.43$), whereas no statistically significant correlation is diagnosed for TOC_{cf} -TE/Al patterns in the upmost *D. tenuicostatum zone* and the *H. elegantulum subzone* (Intervals 3 & 2; $R^2 < 0.2$) (Fig. 5-5A & B). Detrital contributions fail to explain these observations as indicated by the lack of a correlation between Al and TE contents (Fig. S5-1 in the supplementary). Post-depositional loss of TOC could explain the absence of a covariation. This process might explain the weak TOC_{cf} -TE/Al covariation within the upper *H. elegantulum subzone* (Interval 2) that shows evidence for frequent reoxygenation events and sediment reworking. However, no evidence for sediment reworking processes have been found within the upmost *D. tenuicostatum zone* and lower *H. elegantulum subzone* (Interval 3), thus, post depositional loss of TOC can not account for the weak TOC_{cf} -TE/Al covariation. Consequently, other processes must be taken into account that affected TE accumulation rates. In this context the hydrodynamic regime that controlled the TE resupply and thus the TE concentrations in the seawater may have played an important role (Algeo & Maynard, 2004; Tribovillard et al., 2006).

Vanadium is enriched in sediments of the Schistes Carton Fm, however, absolute V/Al ratios are significantly lower than ratios documented from contemporaneous sediments from the Southern German Basin, the Cleveland Basin (Yorkshire) as well as from Recent anoxic and euxinic settings (Fig. 5-5C). A statistically significant correlation between TOC_{cf} and V/Al is only achieved for samples from the *H. falciferum subzone* (Interval 1; $R^2 = 0.66$). According to Algeo & Maynard (2004) and Tribovillard et al. (2006) this pattern can be attributed to V-enrichment under preferentially anoxic conditions, without prolonged euxinia. The lack of correlation of TOC_{cf} with V/Al ratios in combination with the strong V-enrichment in samples from the upper *D. tenuicostatum* and lower *H. elegantulum subzone* (Interval 3) can be explained by the presence of free H_2S in the water column that resulted in a decoupling of OM enrichment and vanadium accumulation (Algeo & Maynard, 2004; Tribovillard et al., 2006). On the contrary, variable V/Al

ratios in combination with a poor TE/Al - TOC_{cf} covariation documented for samples from the upper *H. elegantulum subzone* (Interval 2) can be explained by fluctuating redox conditions that shifted between suboxic and euxinic conditions. Furthermore, the resupply of V to the seawater might also affect V concentrations in the seawater and thus the V accumulation into the sediment.

The cross-plot of TOC_{cf} with Mo/Al exhibits two distinct trends for samples from the Schistes Carton Fm. High Mo/Al ratios that show a strong correlation with TOC_{cf} values ($R^2 = 0.66$) were determined for samples from the *H. falciferum subzone* (Interval 1). On the contrary, relative low Mo/Al ratios that show no correlation with TOC_{cf} values were reported from the upmost *D. tenuicostatum zone* and *H. elegantulum subzone* (Intervals 3 and 2), whereby the lowest Mo enrichment is noted for samples from the upper *H. elegantulum subzone* (Interval 2) (Fig. 5-5D). This pattern has been previously documented from contemporaneous sediments (McArthur et al., 2008a; Pearce et al., 2008; Lezin et al., 2012; Hermoso et al., 2013) and has been interpreted to reflect a drawdown of seawater Mo abundance that resulted from prolonged euxinic conditions in a strong restricted hydrodynamic setting (Algeo, 2004; Algeo & Lyons, 2006). Under such conditions the accumulation of redox sensitive trace elements is not primary controlled by the changes in redox conditions, but by the resupply of aqueous trace elements (Algeo, 2004; Algeo & Lyons, 2006; Brumsack, 2006; Algeo & Rowe, 2012). Low Mo/Al ratios in samples from Intervals 3 and 2 thus indicate that free H₂S was present in the water column during certain periods, facilitating a rapid and efficient removal of Mo to the sediment. Thus, euxinia in combination with the restricted setting of the Western Tethyan shelf resulted in a significant decrease of aqueous Mo concentrations.

This process might be most pronounced for Mo as this redox-sensitive TE has the longest residence time in the ocean (~800 kyr). For comparison, residence times for V is ~50 kyr, whereas residence times for Ni and Cu are ~6 and ~5 kyr, respectively (Tab. 5-1). Furthermore, the drawdown effect might be most significant for Mo as this TE can be removed most efficiently from the seawater by Mo uptake in syngenetic pyrite (e.g. Algeo & Maynard, 2004 and references therein). Based on the lowest Mo/Al ratio the strongest degree of restriction in the Lorraine Sub-Basin can be assumed for the upper *H. elegantulum subzone* (Interval 2). Intermediate basin restriction can be assumed for the upper *D. tenuicostatum zone* and the lower *H. elegantulum subzone* (Interval 3). On the contrary, less restricted conditions that allowed a continuous resupply of aqueous TEs are indicated for the *H. falciferum subzone* (Interval 1) by highest Mo/Al ratios (Fig. 5-5D). The degree of restriction might also be reflected by the TE/Al - TOC_{cf} covariation of the other TEs that show the weakest correlation with TOC_{cf} values for intervals reflecting strong hydrodynamic restriction that possibly resulted in overall reduced aqueous TE concentration. Furthermore, Mn redox cycling can significantly affect the downward flux of redox-sensitive elements to the bottom water and might also account for the scatter in the data (e.g. Tribouillard et al., 2006 and references therein).

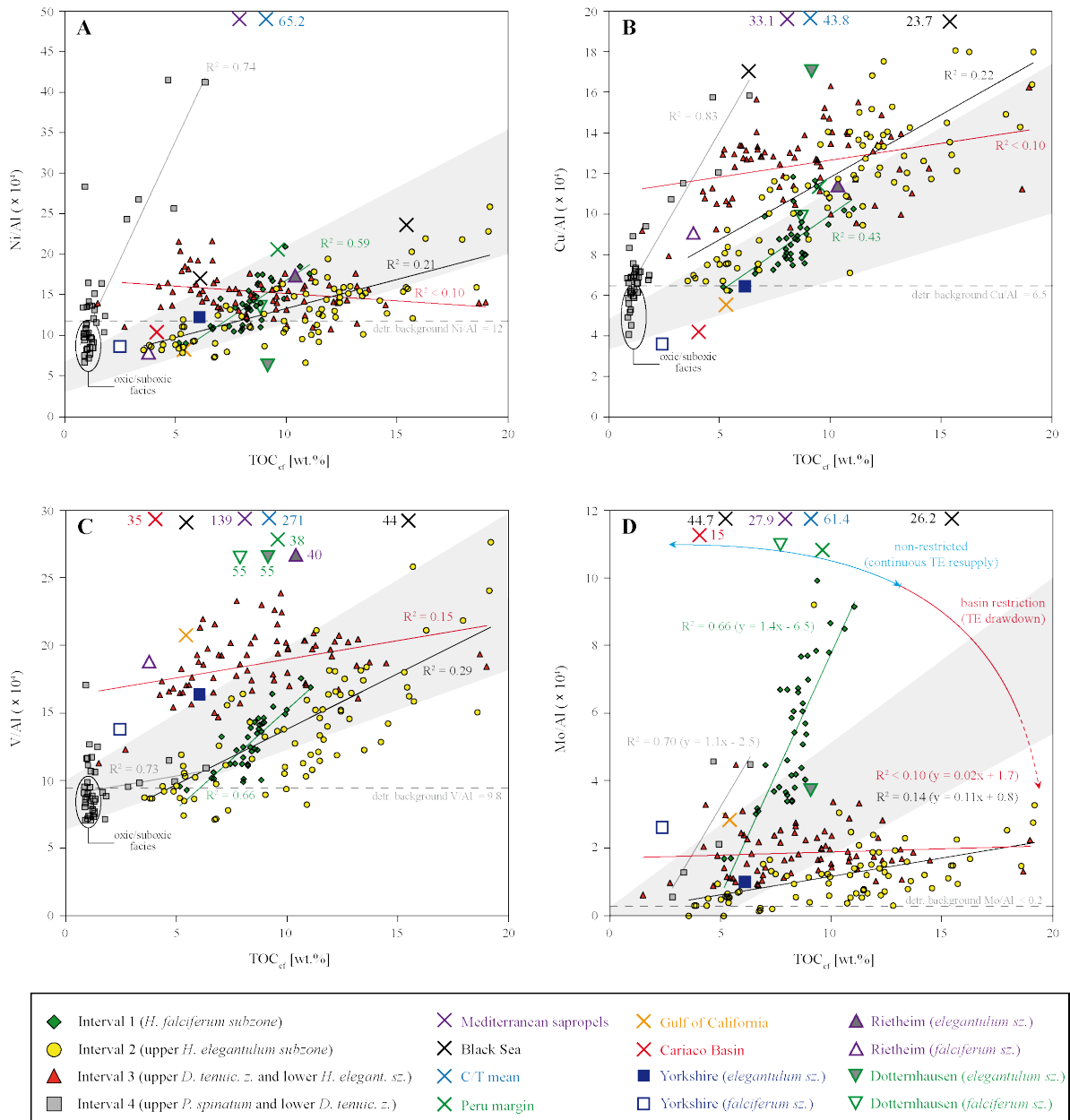


Figure 5-5: Selected Al-normalized redox-sensitive trace elements with weak (Ni, Cu) and strong euxinic affinity (V, Mo) plotted versus TOC_{cf} content. Trace elements of both groups exhibit an overall weak TE-TOC_{cf} co-variation. A statistically significant correlation between TEs and TOC_{cf} content is only noted for the PI-Toa boundary black shale and for the *H. falciferum* subzone (Interval 1). Different slopes of the regression lines for the Mo/Al-TOC_{cf} co-variation point to an element drawdown during the upper *D. tenuicostatum* zone and the *H. elegantulum* subzone. The grey areas mark the anoxic trends documented for Upper Pennsylvanian shales (Algeo & Maynard, 2004). Reference data for Recent Mediterranean sapropels, Black Sea, C/T OAE, Peru margin, and the Gulf of California from Brumsack, 2006; data from the Cariaco Basin from Yarincik et al., 2000b and Little et al., 2015, data from Rietheim from Montero-Serrano et al., 2015, data from Dotternhausen are unpublished and data from Yorkshire are from McArthur et al., 2008a (TE/Al data out of scale are labeled). Detrital background values for the single TEs (TE/Al_{detr.}) are calculated as the average values of the TE/Al ratios from the oxidic/suboxic Grés médioliasiques Fm.

Sulfur burial and TE accumulation pattern (TS_{cf} – TE/Al covariation)

In the sediment redox-sensitive TEs are hosted by pyrite, form own sulfide phases (e.g. Ni, Cu; see Tab. 5-1), or precipitation of these elements directly from seawater is bound to the availability of free H₂S (e.g. V, Mo; see Tab. 5-1), which is produced by BSR. Moreover, sulfate reduction rates are the major factor controlling pyrite burial rates and thus the amount of sulfur accumulated in the sediment (e.g. Leventhal, 1983; Berner & Raiswell, 1983). Therefore, cross-plots of sedimentary sulfur content (TS or TS_{cf}, respectively) with redox-sensitive TE/Al ratios can provide information about the relation of BSR rates, sulfur/pyrite burial and TE accumulation.

The absence of a statistical significant correlation of TE/Al ratios with TS_{cf} values for samples from the non-bituminous Grés médioliasiques Fm (Interval 4) indicate a decoupling of TE and sulfur accumulation in the sediment (Fig. 5-6A-D). The occurrence of euhedral pyrite in sediments of the Grés médioliasiques Fm hints to a diagenetic pyrite formation, which can also have affected the covariation of TS_{cf} with TE/Al ratios. In contrast, a strong correlation of TS_{cf} values with TE/Al ratios is observed for samples from the Pl-Toa boundary black shale ($R^2 > 0.7$) that shows the highest TS_{cf} values (>8 wt.%) (Fig. 5-6A-D). Moreover, this black shale interval shows the highest Ni/Al ratios, which might hint to Ni supply in association with a high OM flux. Furthermore, significant amounts of Ni might be present as Ni-porphyrines (Triboviallard et al., 2006 and references therein). Cu is enriched in the Pl-Toa boundary black shale as well, whereas Cu/Al ratios are significantly lower than Ni/Al ratios (Fig. 5-6A & B). Lower Cu/Al ratios might indicate that the high OM flux that transported Ni to the sediment did not coincide with persistent anoxic/euxinic conditions that controlled the accumulation of Cu. Preferentially anoxic conditions, without prolonged euxinia are also indicated by low V/Al and Mo/Al ratios (Fig. 5-6C & D).

Samples from the Schistes Carton Fm (Intervals 1 to 3) exhibit an overall good correlation between TS_{cf} and Ni/Al ratios as well as between TS_{cf} and Cu/Al ratios ($R^2_{Ni} = 0.4$, $R^2_{Cu} = 0.6$). Highest correlation coefficients, which range from 0.5 to 0.6, were observed for samples from the upper *H. elegantulum* and *H. falciferum* subzones (Intervals 1 & 2) (Fig. 5-6A & B). Regression lines show similar slopes that exhibit a parallel but offset trend, with higher TS_{cf} values documented for samples from the upper *H. elegantulum* subzone (Interval 2). This pattern can be attributed to different sulfur/pyrite burial rates that resulted from different redox conditions, whereby higher TS_{cf} values in samples from the upper *H. elegantulum* subzone indicate stronger reducing, possibly prolonged euxinic, conditions. Euxinic conditions would not affect Ni, as Ni is preferentially bound to the OM flux. The stronger enrichment of Cu in samples from the upper *H. elegantulum* subzone might indicate multiple enrichment processes, comprising the complexation of Cu with OM and the adsorption on particulate Mn-Fe-oxyhydroxides. Moreover, lower enrichment of Ni might result from slower reaction kinetics of Ni incorporation into pyrite (Triboviallard et al., 2006 and references therein). Nevertheless, the overall good correlation of TS_{cf} values with Ni/Al and Cu/Al ratios, in the upper *H. elegantulum* and the *H. falciferum* subzones, indicate that BSR rates and thus the sulfur/pyrite burial rates were controlled by the OM flux to the bottom water and thus to the PP. The absence of a correlation of TS_{cf} values with Ni/Al and Cu/Al ratios in the upmost *D. tenuicostatum* zone and lower *H. elegantulum* subzone (Interval 3), where correlation coefficients for

TS_{cf} -TE/Al patterns do not exceed 0.1 (Fig. 5-6A & B), indicates a decoupling of sulfur burial rates from the OM flux (Algeo & Maynard, 2004; Tribovillard et al., 2006). A decoupling of Ni, Cu and sulfur burial rates hint to preferentially euxinic conditions. The stronger enrichment of Cu when compared with Ni might again result from multiple enrichment processes of Cu as well as from differences in the reaction kinetics (Tribovillard et al., 2006 and references therein).

A good correlation of TS_{cf} values with V/Al ratios ($R^2 > 0.5$) in samples from the upper *H. elegantulum* and *H. falciferum* subzones (Intervals 1 and 2) indicates that the accumulation of V was associated with the sulfur burial flux (Fig. 5-6C). However, elevated sulfur burial rates, indicating more reducing conditions, in the upper *H. elegantulum* subzone (Interval 2) were not accompanied by significantly increased V/Al ratios that are comparable to those from the *H. falciferum* subzone (Interval 1). Thus, regression lines in the cross-plot of TS_{cf} values with V/Al ratios expose parallel trends, with similar slopes of regression (Fig. 5-6C). According to the behavior of V in euxinic systems, elevated pyrite burial should be accompanied by elevated burial rates of V, not observed here. A possible explanation could be the limited availability of aqueous V, which might have resulted from prolonged euxinic conditions in a restricted hydrodynamic regime (McArthur et al., 2008a). A depletion of aqueous V might further explain the overall low V/Al ratios in the lower Toarcian black shale of the Western Tethyan shelf, when compared with other anoxic/euxinic environments (compare with V/Al ratios given in Fig. 5-5C). The strong enrichment of V in samples from the upmost *D. tenuicostatum* zone and lower *H. elegantulum* subzone (Interval 3) is not associated with the highest TS_{cf} values. The absence of a correlation between TS_{cf} values and V/Al ratios ($R^2 > 0.1$) indicates that the enrichment of sulfur/pyrite and V was controlled by different factors (Fig. 5-6C). High V/Al ratios in combination with moderate TS_{cf} values might hint to an iron limitation that resulted in lower pyrite burial rates (Leventhal, 1983; Berner & Raiswell, 1983). The limitation of reactive iron species would affect pyrite burial rates but not the vanadium burial rates, as vanadium is not hosted in the sulfide fraction (Algeo & Maynard, 2004; Tribovillard et al., 2006).

The cross-plot of TS_{cf} values with Mo/Al ratios expose a similar pattern observed in the TOC_{cf} - Mo/Al plot (Figs. 5-5D, 5-6D). The highest degree of regression ($R^2 = 0.55$) is observed for samples from the *H. falciferum* subzone (Interval 1) that also show the highest Mo/Al ratios (Fig. 5-6D). The good correlation of TS_{cf} values and Mo/Al ratios indicates that Mo-enrichment was bounded to the pyrite burial rates and thus to the redox conditions. On the contrary, samples from the upmost *D. tenuicostatum* zone and *H. elegantulum* subzone (Intervals 3 and 2) are characterized by the highest TS_{cf} values and low Mo/Al ratios. This pattern indicates that redox conditions controlling sulfur burial rates were not the main control on Mo burial rates. Thus, Mo-accumulation was decoupled from the redox conditions. As before discussed, this observation can be explained by a Mo-depletion of the seawater that resulted from a strong hydrodynamic restriction of the Western Tethyan shelf (McArthur et al., 2008a). The lowest Mo/Al ratios, indicating the strongest depletion of aqueous Mo, are documented in the upper *H. elegantulum* subzone that also shows lower V/Al ratios, with respect to the high TS_{cf} values. Differences in the enrichment pattern of V and Mo might result from the different residence times of these TEs in the seawater (Tab. 5-1).

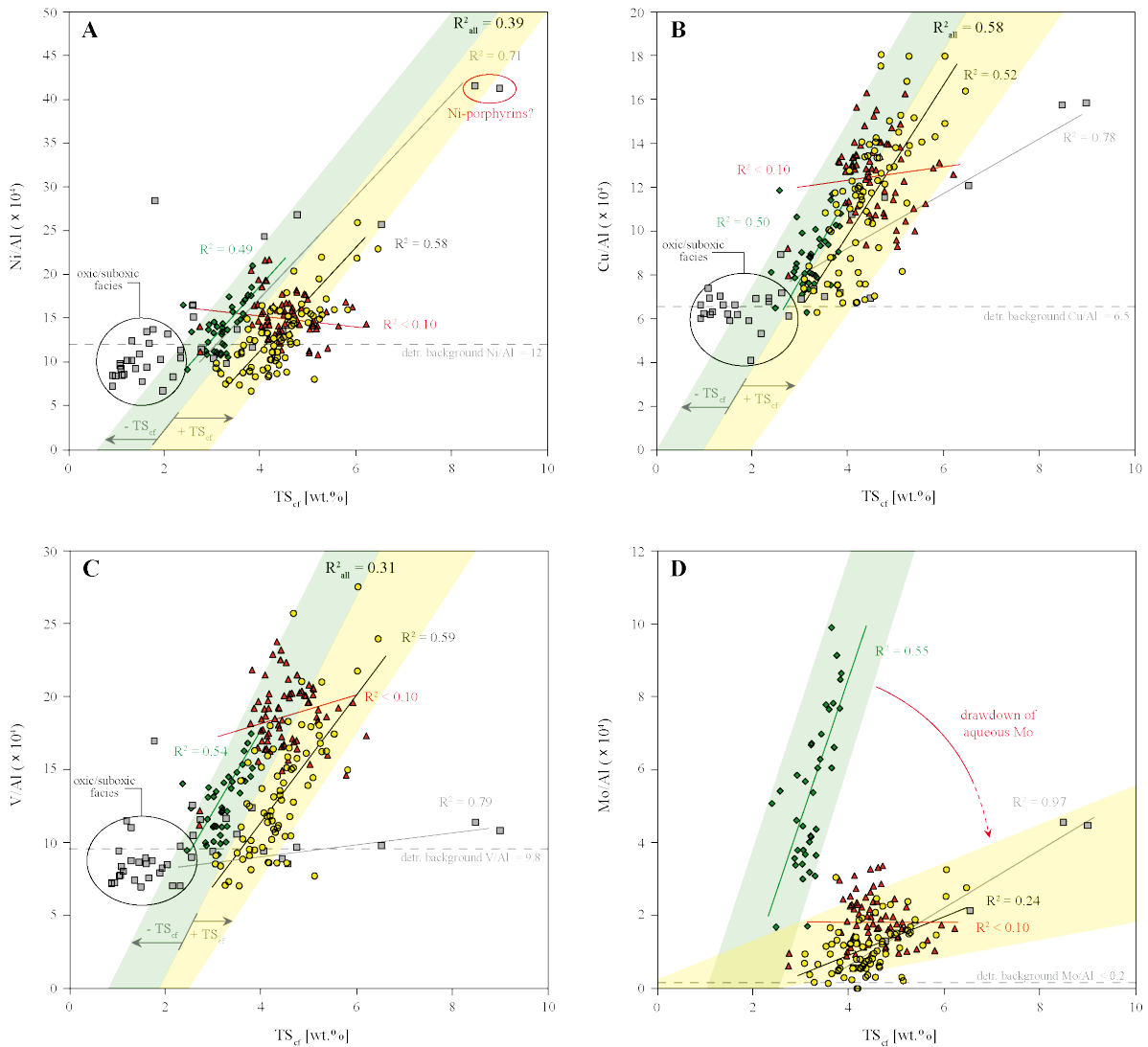


Figure 5-6: Cross-plot of TS_{cr} and selected redox-sensitive TEs yield a higher degree of correlation when compared with TOC_{cr} -TE/Al cross-plots (see Fig. 5-5). A good correlation of TS_{cr} values with Ni/Al, Cu and V/Al ratios is observed for samples from Intervals 1 and 2, whereby the parallel but offset trends in the slopes of regression point to different sulfur/pyrite burial rates. The absence of a correlation of the TS_{cr} values with TE/Al ratio for samples from Interval 3 indicating a decoupling of sulfur/pyrite burial rates from TE accumulation. The effect of a proposed Mo-drawdown, which resulted from a strong hydrodynamic restriction, is well-expressed in the cross-plot of TS_{cr} values with Mo/Al ratios that confirm a decoupling of sulfur/pyrite burial rates and Mo accumulation during Intervals 2 and 3 (legend as in figure 5-5).

TOC-TS-Fe systematic, implications for the sulfur cycle

Some samples from the non-bituminous Grés médioliasiques Fm (Interval 4) are anomalously enriched in sulfur (TS up to 4 wt.%) and thus plot above the “Normal Marine Line” (Fig. 5-7A). However, high TS values are mainly bound to euhedral pyrite indicating epigenetic pyrite formation, which prohibits an interpretation of the TOC-TS systematic in terms of redox conditions (Berner & Raiswell, 1983, 1984). Low TS/Fe ratios indicate a mainly oxic to suboxic depositional environment, which is more consistent with lithological observations (Fig. 5-7B). Sedimentary pyrite is strongly depleted in ^{34}S ($\delta^{34}S < 40\%$) indicating low rates of BSR (Habicht & Canfield, 1997; Canfield, 2001). Low DBT/Phen ratios (< 0.5) support this interpretation and indicate only minor

sulfur incorporation into OM (Hughes et al., 1995), which is consistent with low BSR rates (Fig. 5-7A & B). Samples from the laminated PI-Toa boundary black shale differ from this trend. Samples are enriched in OM and sulfur (TOC up to 6 wt.%; TS up to 9 wt.%), whereby TOC and TS exhibit a strong co-variation ($R^2 = 0.66$) with a TS intercept close to 0, indicating that BSR was controlled by the availability of labile OM (Fig. 5-7A). Highest TS values, indicating extremely high sulfur burial rates, might have resulted from high contributions of reactive iron species that promoted elevated rates of pyrite formation. High TS/Fe ratios (~ 0.75) indicate a higher degree of pyritisation and thus preferentially anoxic/euxinic conditions (Fig. 5-7B). However, elevated rates of BSR, confirmed by increased $\delta^{34}\text{S}$ values up to 30‰, did not result in enhanced sulfur incorporation into OM as indicated by relative low DBT/Phen ratios that do not exceed 0.3 (Fig. 5-7A & B). Low DBT/Phen ratios further support that Fe was not limited and H_2S was preferentially precipitated as pyrite.

Samples from the Schistes Carton Fm are strongly enriched in OM and sulfur (TOC up to 15 wt.%; TS up to 5.5 wt.%) and thus plot exclusively above the “Normal Marine Line”, close to the “Black Sea trend” characteristic for anoxic/euxinic environments (Fig. 5-7A) (Bernier & Raiswell, 1983, 1984). Preferentially anoxic conditions are also indicated by relative high TS/Fe ratios > 0.5 (Fig. 5-7B). The increase in the sulfur burial flux can be attributed to increased rates of BSR, which is supported by ^{32}S -depleted sedimentary sulfur ($\delta^{34}\text{S}$ values up to -15‰). The absence of a covariation of TOC with TS values ($R^2 < 0.1$), documented in the upmost *D. tenuicostatum* zone and lower *H. elegantulum* subzone (Interval 3), indicates that BSR was not limited by the availability of labile OM (Fig. 5-7A). Rates of BSR in the interval were always high, which is indicated by a rise in $\delta^{34}\text{S}$ values from about -40 to -20‰, and the excess supply of OM shifted the BSR zone from the sediment into the water column. Under such conditions pyrite formation occurs within the sulfidic part of the water column and is only limited by the availability of reactive iron species, which is indicated by intercept of regression line with the TS axis at 3.8 wt.% TS (Fig. 5-7A). The significant covariation of Fe with TS ($R^2 = 0.65$), in combination with the highest TS/Fe ratios (~ 0.75), implies that reactive iron might be the limiting factor controlling the sulfur incorporation into the sediment (Fig. 5-7B). The limitation of reactive iron resulted in elevated sulfur incorporation into OM, which is evident from high DBT/Phen ratios that exceed 0.5 (Fig. 5-8A). A similar trend is documented for the upper *H. elegantulum* and *H. falciferum* subzones (Intervals 2 and 1), whereby a stronger correlation between TOC and TS values ($R^2 = \sim 0.4$) indicate that BSR rates were more affected by the availability of metabolizable OM. Regressions approaching the “Normal Marine Line”, with lower TS intercepts of 2.0 and 1.3 for the upper *H. elegantulum* and *H. falciferum* subzone, respectively, point towards a decrease in the sulfur burial flux through these intervals (Fig. 5-7A). However, sulfides strongly depleted in ^{32}S ($\delta^{34}\text{S}$ values range from 30 to 15‰) confirm high BSR rates and sulfate drawdown throughout these intervals. Less persistent anoxic/euxinic conditions are attested by slightly decreased TS/Fe ratios that range from 0.5 to 0.7. Moreover, the lack of a statistically significant correlation between TS and Fe concentration indicated the reduced sulfur/pyrite burial rates not to originate from Fe-limitation (Fig. 5-7B). However, significant amounts of sulfur were incorporated into OM as indicated by DBT/Phen ratios between 0.5 and 0.8 confirming enhanced availability of H_2S or expanded euxinic conditions (Fig. 5-8B).

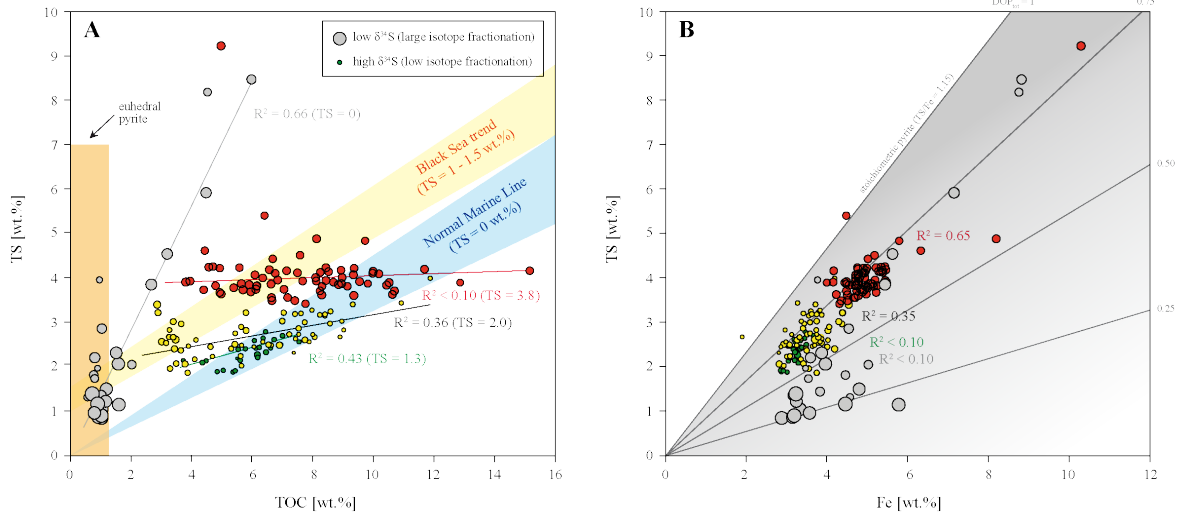


Figure 5-7: A) The TOC/TS plot reveals a poor correlation between sulfur and OM indicating that the sulfate reduction and thus the pyrite formation was not bound to the availability of OM being metabolizable by sulfate reducing bacteria. The weakest correlation of TOC with TS and the highest intercept of the regression line with the TS axis is documented for samples from Interval 3. Samples from Intervals 2 and 1 exhibit a similar trend but plot closer to the field of more normal marine conditions. **B)** A fair correlation between Fe and TS documented in samples from Intervals 3 and 2 indicate that pyrite formation and burial was partly controlled by the availability of iron (Raiswell & Berner, 1985). Prevailing high rates of BSR in these intervals are confirmed by heavy $\delta^{34}\text{S}$ values. A weak correlation of Fe with TS values is noted for Intervals 1 and 4, which indicate that Fe is not exclusively hosted by sulfides. The lowest DOP is documented for Interval 4, reflecting less reducing conditions in this interval. (legend as in figure 5-5)

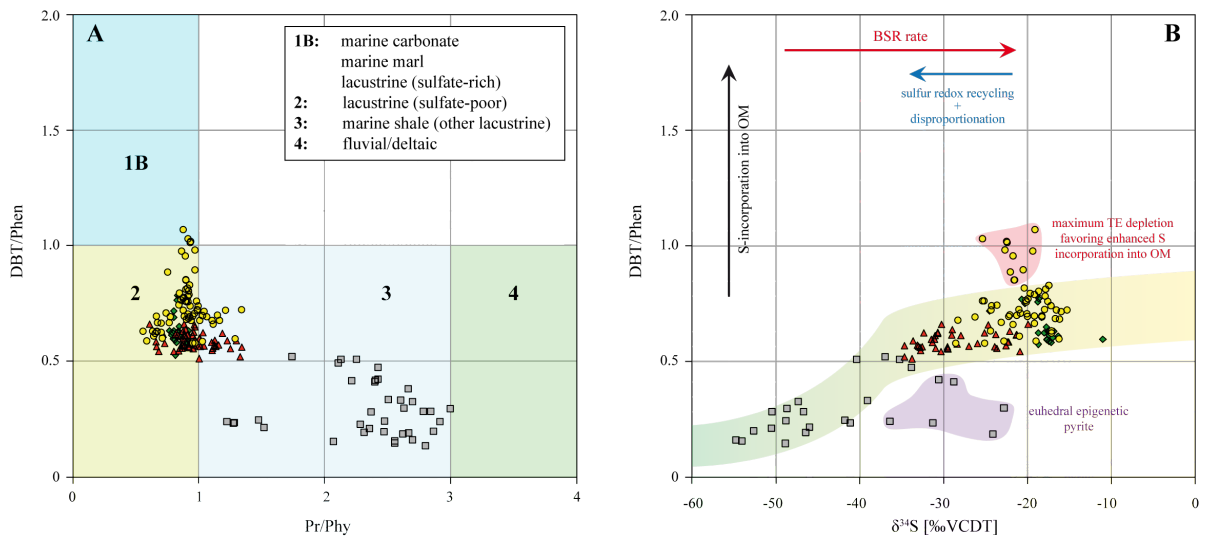


Figure 5-8: A) The plot of Pr/Phy versus DBT/Phen (Hughes et al., 1995) points to increased sulfur incorporation into OM for samples from the uppermost *D. tenuicostatum* zone and the *H. serpentinum* zone. **B)** Light $\delta^{34}\text{S}$ values determined throughout the *P. spinatum* and lower *D. tenuicostatum* zone, in combination with low DBT/Phen ratios can be attributed to low BSR rates. An increase in BSR is confirmed for the upper *D. tenuicostatum* zone and the lower *H. elegantulum* subzone by a significant ^{32}S -depletion and initiated enhanced sulfur incorporation into OM, reflected by an increase in the DBT/Phen ratio. (legend as in figure 5-5)

The overall increasing trend documented in the $\delta^{34}\text{S}$ signature of the sulfides throughout the Schistes Carton Fm (Fig. 5-4) is also evident from carbonate associated sulfur isotope data that reflect the marine sulfate pool (Gill et al., 2011; Newton et al., 2011). These authors showed that high rates of BSR throughout the Western Tethyan shelf induced a decrease in marine sulfate concentrations, whereby estimates range from 1 to 8 mM. A decrease in marine sulfate concentrations resulted from prolonged anoxia/euxinia that are associated with high rates of BSR in combination with the restricted hydrodynamic setting of the Western Tethyan shelf (Gill et al., 2011; Newton et al., 2011). Data from the Lorraine Sub-Basin confirm that the deposition of the Schistes Carton Fm and contemporaneous deposits on the Western Tethyan shelf were associated with the establishment of sulfidic conditions and high rates of pyrite burial into the sediments. Replenishment rates of the sulfate pool did not match the sulfate withdrawal from seawater by BSR, which is expressed by the increase in $\delta^{34}\text{S}$ values of the sulfides and the carbonate associated sulfur (Gill et al., 2011; Newton et al., 2011).

Redox facies inferred from biomarker data

Samples from the OM-poor grey clay/marl-stones of the Grés médioliasiques Fm (Interval 4; TOC < 2 wt.%) show high Pr/Phy ratios (>2) and low HHI* values (<3), indicating preferentially oxic to temporarily suboxic conditions (Fig. 5-9A). However, some samples show slightly increased HHI* values (2.5 to 5.0) and increased $\text{C}_{32}/\text{C}_{31}$ hopane ratios (0.25 to 0.30), which point to brief episodes of decreased bottom water oxygenation that resulted in an enhanced preservation of bacteriohopanes. Furthermore, the presence of isorenieratane in the bioturbated clay-/marl-stones supports periodic short-lived episodes of PZE (Figs. 5-3, 5-9B). Low Pr/Phy ratios of 1.2 to 1.8, documented from the PI-Toa boundary black shale, reflect more reducing conditions. Moreover, isorenieratane concentrations up to 5.6 $\mu\text{g}/\text{gTOC}$ confirm frequent episodes of PZE (Figs. 5-4, 5-9B). Interestingly, anoxic/euxinic conditions did not induce enhanced preservation of bacteriohopanes. The relative low HHI* values and $\text{C}_{32}/\text{C}_{31}$ hopane ratios that do not exceed 4 and 0.3, respectively, might point to the high sensitivity of C_{35} bacteriohopanetetrols towards post-depositional oxidation processes. In contrast, isorenieratane reveals a more recalcitrant nature and seems to be less affected by secondary oxidation processes, possibly due to the absence of functional groups in the molecular structure, which is further stabilized by two benzene rings. Moreover, isorenieratane is biosynthesized by bacteria whose habitat is located in the euxinic part of the water column. Thus, lipids derived from these organisms are less exposed towards aerobic degradation processes. In contrast, bacteriohopanes originate from bacteria that live in the oxic as well in the anoxic and euxinic part of the water column and in the sediment.

Samples from the bituminous Schistes Carton Fm (Intervals 1 - 3; TOC up to 15 wt.%) show overall low Pr/Phy ratios (<1.2), which in combination with elevated HHI* values (ranging from 3 to 10), indicate preferentially anoxic conditions (Figs. 5-3, 5-9A). Furthermore, the presence of significant amounts of isorenieratane (up to 15 $\mu\text{g}/\text{gTOC}$) in all samples from the Schistes Carton Fm confirms reoccurring episodes of PZE (Figs. 5-4, 5-9B). Throughout the Schistes Carton Fm the

Pr/Phy ratios remain rather constant, whereas the HHI* expose a much higher variability that aligns with facies changes. Moderate HHI* between 3 and 10 in combination with variable but conservative C_{32}/C_{31} hopane ratios (0.2 to 0.35) were determined in samples from the upmost *D. tenuicostatum* zone and lower *H. elegantulum* subzone (Interval 3) as well as in samples from the *H. falciferum* subzone (Interval 1), indicating that bacteriohopanes were more prone to aerobic degradation. A longer exposure of bacteriohopanes towards oxygen may be explained by frequent reoxygenation events in the bottom water, e.g. by storm events, or by an expanded zone of oxic surface water that overlaid persistent anoxic bottom water of reduced extent (Fig. 5-9B). The later explanation seems to be more probable as moderate isorenieratane concentrations (Interval 3: 1.7 $\mu\text{g/gTOC}$ on average; Interval 1: 2.7 $\mu\text{g/gTOC}$ on average) indicate a reduced extent of PZE (Figs. 5-4, 5-9B). Throughout the upper *H. elegantulum* subzone (Interval 2) higher HHI* values between 7 and 15, in combination with high C_{32}/C_{31} hopane ratios that range from 0.25 to 0.45, indicate euxinic conditions that extended over a larger part of the water column, which is confirmed by elevated isorenieratane concentrations (on average 6.8 $\mu\text{g/gTOC}$). A highly variable extent of PZE and thus less stable redox conditions are indicated by most variable isorenieratane concentrations ranging from 2.6 to 18.4 $\mu\text{g/gTOC}$ (Figs. 5-4, 5-9B). However, when present during this interval, euxinic conditions extended over large part of the water column and bacteriohopanetetrols were thus better protected from degradation processes. The effect of the relative proportions of oxic versus anoxic/sulfidic zones in the water column on the preservation of bacteriohopanes is expressed in the cross-plot of isorenieratane versus HHI* values that exhibits a positive correlation (Fig. S5-2 in the supplementary). The impact of sulfur and sulfurisation processes towards the preservation of the side chain of bacteriohopanes has been previously discussed by [Simminghe Damsté et al. \(1995\)](#).

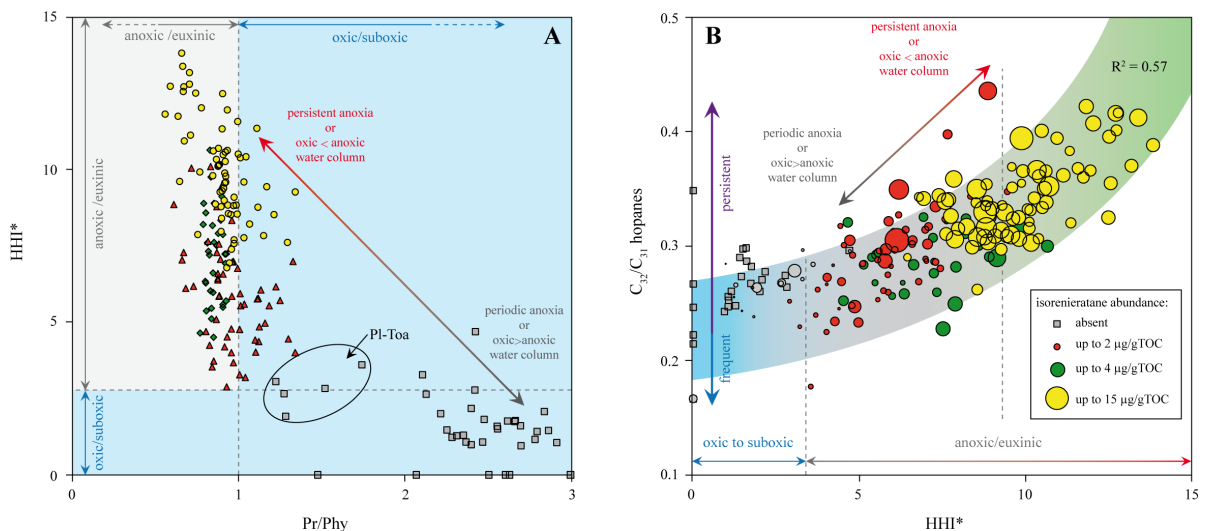


Figure 5-9: A) The cross plot of Pr/Phy versus HHI* allows distinguishing oxic/suboxic facies of the Grés médioliasiques Fm from the preferentially suboxic to anoxic facies of the Schistes Carton Fm. The higher variability of the HHI* can be attributed to differences in the sensitivity of these molecules towards aerobic degradation. **B)** A cross plot of the HHI* versus C_{32}/C_{31} hopane ratios, in combination with isorenieratane concentrations, provides additional information about the extent and/or persistence of water column anoxia. Stages of extended and/or persistent water column anoxia/euxinia show high HHI*, high C_{32}/C_{31} hopane ratios and high isorenieratane concentrations. (legend as in figure 5-5)

5.4.2. Evolution of redox conditions

Lithological observations as well as geochemical proxies attest to significant variations in the redox conditions throughout the interval studied. Redox conditions encompass fully oxic conditions as well as strictly anoxic episodes. Moreover, the presence of isorenieratane, a biomarker diagnostic for brown-pigmented green sulfur bacteria, confirms that euxinic conditions extent into the photic zone during certain periods. However, the absence of okenone and chlorobactane indicate that euxinic conditions were generally limited to the bottom water and the chemocline will have been situated below a water depth of 40 m (Brooks & Schäfer, 2008).

Oxic conditions prevailed during the upper *P. spinatum* zone as indicated by a low HHI* (<3), high Pr/Phy ratios (>2) and a low enrichment of redox-sensitive TEs (Figs. 5-2, 5-3, 5-10). Furthermore, ³²S-enriched sulfides (Fig. 5-4) and the absence of isorenieratane indicate that BSR rates were low and resulted in a redox boundary that was always situated in the sediment (Fig. 5-10). Mainly low TS/Fe ratios of <0.5 support low rates of sulfur/pyrite burial (Figs. 5-1; 5-7B). Overall oxic conditions are in agreement with lithological observations, indicating enhanced benthic activity and sediment reworking.

Preferentially anoxic conditions were documented for the Pl-Toa boundary black shale. Anoxic conditions are confirmed by low Pr/Phy ratios (~1.2) as well as by a significant enrichment of TEs with weak euxinic affinity, whereas TEs with strong euxinic affinity are not significantly enriched (Figs. 5-2, 5-3; 5-10). However, significant amounts of isorenieratane indicate that sulfidic conditions must have extended into the photic zone at least during certain episodes. Moreover, elevated rates of BSR, confirmed by high $\delta^{34}\text{S}$ values (up to -30‰), shifted the redox boundary from the sediment into the water column, which resulted in high sulfur/pyrite burial rates that are confirmed by high TS/Fe ratios (0.75 to 1.00) (Fig. 5-1, 5-7B). Interestingly, no significant response is documented in the HHI* that remain relative low in the Pl-Toa boundary black shale (Fig. 5-10). Low HHI* values (<4) and C₃₂/C₃₁ hopane ratios (<0.3) reflect enhanced degradation of bacteriohopanes during frequent reoxygenation events or might also result from a anoxic/euxinic water column of reduced extent overlain by an expanded layer of oxic surface waters.

A return to preferentially oxic/suboxic conditions in the lower part of the *D. tenuicostatum* zone is indicated by high Pr/Phy ratios (>2), low HHI* values (<3) and low TE/Al ratios (Figs. 5-2, 5-10). However, traces of isorenieratane have been confirmed for several samples from this interval, indicating that brief episodes of PZE must have existed during this preferentially oxic/suboxic episode. Overall low TS/Fe ratios (<0.5) in combination with low $\delta^{34}\text{S}$ values (< -40‰) can be associated with low rates of sulfate removal via BSR and with low rates of sulfur/pyrite burial (Figs. 5-1; 5-7B). Values differing from this trend might result from epigenetic processes that are indicated by the occurrence of euhedral pyrite. During the lower part of the *D. tenuicostatum* zone brief anoxic/euxinic episodes might have been established after episodic algal blooms that resulted in oxygen depletion due to aerobic OM break down. Subsequent reoxygenation of the entire water column allowed the resettlement of the seafloor by benthic communities, which resulted in enhanced reworking of the unconsolidated sediments and OM degradation.

A rapid shift from oxic/suboxic to anoxic conditions occurred in the upmost *D. tenuicostatum* zone and is associated with a major facies change. Throughout the upmost *D. tenuicostatum* zone and the lower *H. elegantulum* subzone the redox boundary is expected to have been positioned in the water column. Sulfidic conditions expanding into the water column are indicated by a strong enrichment of V, when compared with Ni and Cu as well as by the efficient removal of Mo from the water column (Figs. 5-5, 5-10). Furthermore, prolonged high rates of BSR, indicated by a steady increase in $\delta^{34}\text{S}$ values (from -40 to -20‰), resulted in elevated sulfur/pyrite burial rates that are attested to high TS/Fe ratios >0.75 . However, a limited extent of PZE is indicated by the relative low abundance of isorenieratane (on average 1.7 $\mu\text{g/gTOC}$). Intermediate HHI* values that vary between 3 and 10 further confirm that a certain part of the upper water column must be well oxygenated, which resulted in an enhanced degradation of bacteriohopanes (Fig. 5-10). These conditions seem to be relative stable throughout this interval. However, a massive expansion of PZE in the upper part of the interval is indicated by a drastic increase in isorenieratane concentrations to values of about 20 $\mu\text{g/gTOC}$ (Fig. 5-10). This horizon is also highlighted by an increase in the HHI* and in the $\text{C}_{32}/\text{C}_{31}$ hopane ratios that confirm an enhanced preservation of bacteriohopanetetrols due to the reduced extent of the oxygenated part of the water column.

Highest HHI* values (7 - 14) and $\text{C}_{32}/\text{C}_{31}$ hopane ratios (0.30 to 0.45) and elevated isorenieratane concentrations (6.8 $\mu\text{g/gTOC}$ on average), documented in the upper *H. elegantulum* subzone, reflect the expansion of euxinic conditions in the water column and into the photic zone (Fig. 5-10). Elevated BSR rates and pyrite burial rates are supported by high $\delta^{34}\text{S}$ values (-30 to -15‰) and by high TS/Fe ratios (0.6 to 1.1). However, the upper *H. elegantulum* subzone also records the highest variability in redox conditions, whereby fluctuation aligns with subtle facies changes. More persistent reducing conditions were confirmed by high HHI* (>10) and high TE/Al ratios for sediments that show distinct lamination, whereas sediments with a more indistinct lamination show a lower HHI* (<10) and low TE/Al ratios (Fig. 5-10). A similar trend can be observed in $\delta^{34}\text{S}$ values and TS/Fe ratios that attest to elevated rates of BSR and enhanced pyrite burial rates for distinctly laminated horizons (Figs. 5-1, 5-4). Interestingly, the evolution of the isorenieratane abundance differs from this trend and high concentrations were documented from some of the horizons characterized as deposited under less reducing conditions. This observation indicates that the persistence of euxinic conditions might not be the major factor controlling the spatiotemporal abundance of *Chlorobiaceae* and thus of sedimentary isorenieratane contributions. Moreover, the interaction of persistence and extent of euxinic conditions in the photic zone controlled the abundance of these organisms. Thus, short-lived PZE that expanded over a large part of the water column might result in a stronger enrichment of isorenieratane than more persistent PZE of only limited extent.

A slightly lowered HHI* (5 - 10) and lower TE/Al ratios (not valid for Mo/Al) in samples from the *H. falciferum* subzone (Interval 1) attest to an increased oxygen availability over a wider extent in the water column, which is also confirmed by a decrease in isorenieratane concentrations that predominantly stay below 5 $\mu\text{g/gTOC}$ (Fig. 5-10). Slightly decreased TS/Fe ratios (0.6 to 0.8) support this finding. However, $\delta^{34}\text{S}$ values remain relative high (about -20‰), which points to high

rates of BSR and/or a ^{32}S -depleted sulfate pool. However, distinctly laminated sediments confirm preferentially anoxic bottom waters that prevented enhanced benthic activity. On the contrary, some horizons show evidence for enhanced activity of bottom currents and winnowing. Increased strength of current systems possibly prohibited an expansion of euxinic conditions into the upper part of the water column.

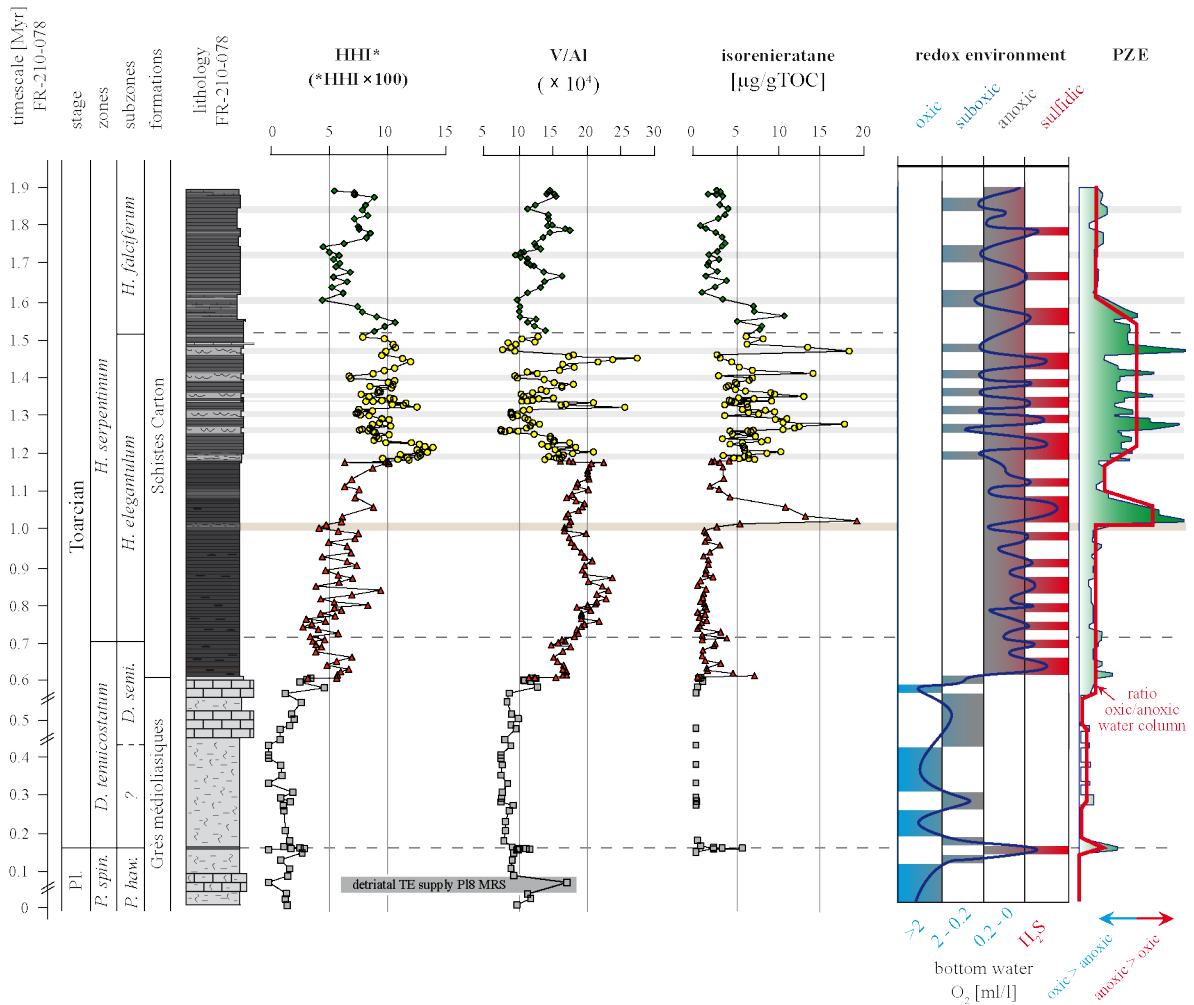


Figure 5-10: The evolution of geochemical redox proxies aligns with lithological changes and attests to strongly reducing conditions throughout the Schistes Carton Fm as well as for the Pl-Toa boundary black shale, whereas the Grés médioliasiques Fm represents mainly oxic to suboxic conditions. Furthermore, the presence of isorenieratane in all samples from anoxic facies of the Schistes Carton Fm indicates reoccurring PZE. The graph at the right illustrates the evolution of redox conditions and the redox state prevailing during the Early Toarcian. The abundance of isorenieratane in combination with the HHI* allow to infer the relative proportions of oxic versus anoxic water column.

5.4.3. Insights into the hydrodynamic regime and extent of shelf sea anoxia

Mo enrichment in sediments is controlled by redox conditions and by aqueous Mo concentrations that vary with Mo burial rates and Mo resupply to the oceans. The latter process varies as a function of the hydrological regime, whereby seawater may become depleted in Mo under persistent euxinic conditions in strongly restricted basins where the Mo resupply from the open ocean reservoir does not match the export rates in the restricted basin (Algeo, 2004; Algeo & Lyons, 2006; Algeo & Rowe, 2012). Changes in Mo accumulation rates can be inferred from regression slopes in the cross-plots of TOC with Mo values as applied for lower Toarcian sediments (McArthur et al., 2008a, Pearce et al., 2008; Lezin et al., 2012; Hermoso et al., 2013). These works confirmed reduced Mo accumulation rates throughout the Western Tethyan shelf in sediments corresponding to the upmost *D. tenuicostatum* zone and *H. elegantulum* subzone. Based on findings by Algeo (2004) and Algeo & Rowe (2006), McArthur et al. (2008a) this pattern can be attributed to low Mo accumulation rates that resulted from a strong hydrodynamic restriction of the Western Tethyan shelf that in combination with persistent shelf sea anoxia that led to an aqueous Mo drawdown. Similar observations were made for the Lorraine Sub-Basin, where lowest regression slopes in the cross-plot of TOC_{cf} with Mo/Al ratios (Fig 5-5D) were also determined for samples from the upmost *D. tenuicostatum* zone and *H. elegantulum* subzone.

Changes in the degree of hydrodynamic restriction can be inferred from the evolution of Mo/TOC trends as applied by McArthur et al. (2008a) for sediment from the Cleveland Basin. The trend documented from the Cleveland Basin is also evident from other basins located on the Western Tethyan shelf and is further confirmed for the Lorraine Sub-Basin (Fig. 5-11). The overall similar evolution of the Mo/TOC ratios indicates a shelf-wide decrease in aqueous Mo concentrations, controlled by regional, at least shelf-wide, processes. In all basins moderate Mo/TOC ratios in the upmost *D. tenuicostatum* zone and the lower *H. elegantulum* subzone (Mo/TOC: 1 - 6) hint to an intermediate hydrodynamic restriction. The lowest Mo/TOC ratios were documented from the upper *H. elegantulum* subzone (Mo/TOC < 2), indicating the strongest hydrodynamic restriction. A significant increase in Mo/TOC ratios in the *H. falciferum* subzone (Mo/TCO: 2 - 30) indicates the termination of the hydrodynamic restriction of the Western Tethyan shelf. The rapid rise in Mo/TOC ratios further indicates that depletion of aqueous Mo was limited to the Western Tethyan shelf and was not a global ocean wide phenomenon, which would have resulted in a much longer replenishment period due to the long residence time of Mo (Tab. 5-1). Differences in absolute values of the Mo/TOC ratio, documented from the different basins, can be attributed to local redox conditions, the activity of Mn-redox cycling and/or the local hydrodynamic regime (e.g. Tribovillard et al., 2006; Algeo & Tribovillard, 2009; Scholz et al., 2013). An alternative explanation for the low Mo concentrations and the absence of a strong Mo enrichment during the onset of shelf sea anoxia (reflecting the draw down phase) might be freshwater contributions from glacial meltdown that protrudes southwards onto the Western Tethyan shelf during the upmost *D. tenuicostatum* zone and the lower *H. elegantulum* subzone (Chapter 4). Glacially derived freshwater contribution might carry lower Mo concentrations than ambient seawater and may have affected the seawater chemistry of the

Western Tethyan shelf. However, this theory is difficult to reconcile, as Mo concentrations of polar ice have not been reported so far.

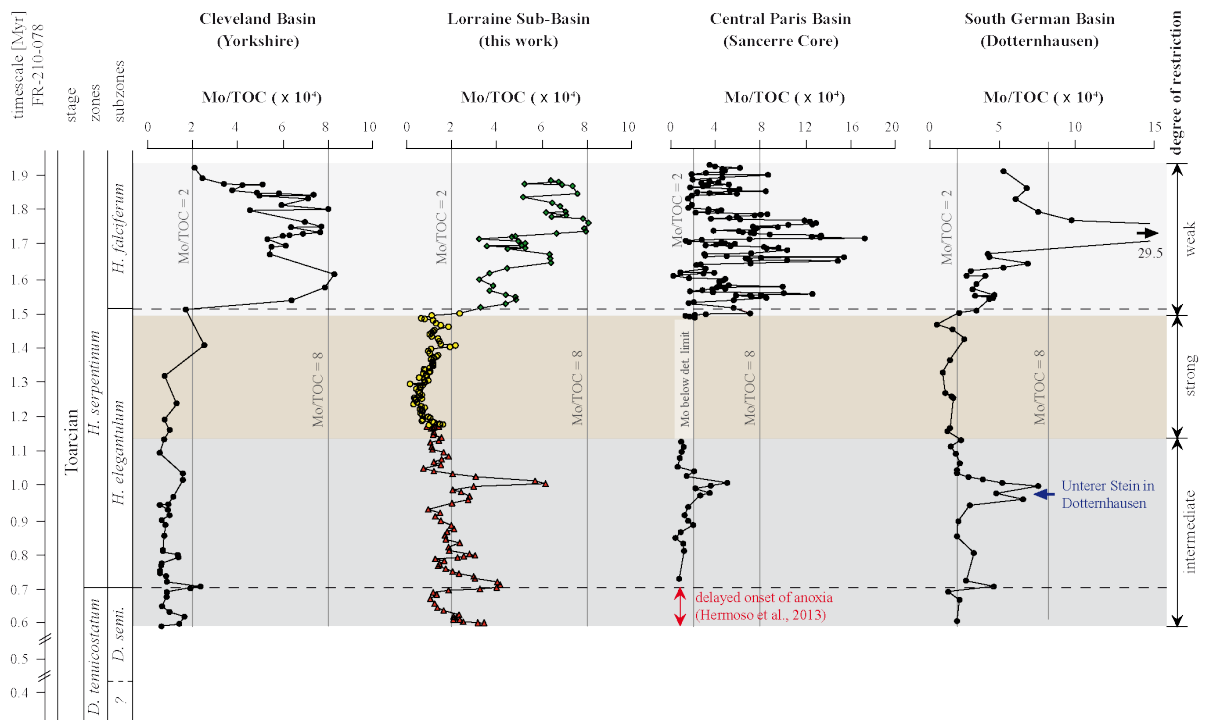


Figure 5-11: Stratigraphic evolution of Mo/TOC trends for different basins situated on the Western Tethyan shelf adapted to the timescale proposed for Core FR-210-078 (see Chapter 2). Similar trends indicate that changes in aqueous Mo concentration were controlled by shelf-wide processes, comprising changes in the hydrodynamical regime and Mo replenishment and/or glacial meltwater contributions with Mo concentration lower than ambient seawater. The last mechanism might explain the relatively low Mo accumulation rates during the onset of shelf sea anoxia. Local mechanisms, like redox conditions, can explain differences in the absolute values of the Mo/TOC ratio. In Dotternhausen the Mo/TOC spike in the lower *H. elegantulum* subzone correspond to the Unterer Stein, a diagenetic limestone bed that can be associated with special oceanographic conditions (Frimmel, 2003) (data sources: McArthur et al., 2008a (Yorkshire); Hermoso et al., 2013 (Sancerre Core); data from Dotternhausen are unpublished).

Further insights into extent of shelf sea anoxia, the hydrological regime and the redox conditions can be obtained from Mo isotope data. Changes in $\delta^{98/95}\text{Mo}_{\text{SED}}$ are commonly used as redox indicator, whereas $\delta^{98/95}\text{Mo}_{\text{SED}}$ data from the Lorraine Sub-Basin exhibit a challenging picture as they are strongly depleted in ^{98}Mo , which becomes commonly enriched in anoxic/euxinic sediments (Poulson et al., 2006). According to the redox scale proposed by Poulson et al. (2006) $\delta^{98/95}\text{Mo}$ values of about 0.5 to 1.5‰, documented from the Lorraine Sub-Basin would reflect mainly suboxic to mildly anoxic conditions, where Mo precipitation occurs under a high fractionation factor of about 0.7 to 2.8‰, when assuming a $\delta^{98/95}\text{Mo}_{\text{SW}}$ value of $\sim 2.3\text{‰}$ (Pearce et al., 2008 and references therein). This is not in full agreement with previous findings that attest to persistent anoxic/euxinic conditions during deposition of the Schistes Carton Fm. Therefore, other factors than exclusively redox conditions must have controlled $\delta^{98/95}\text{Mo}_{\text{SED}}$ values. Pearce et al. (2008) suggested that the areal extent of anoxia has the potential to drive $\delta^{98/95}\text{Mo}_{\text{SW}}$ and thus $\delta^{98/95}\text{Mo}_{\text{SED}}$ towards

lower values, as under widespread prolonged anoxic conditions the seawater may become depleted in ^{98}Mo due to the preferential removal of the heavier isotope from the seawater. A shelf-wide change in aqueous Mo concentration is indicated by the evolution of TOC/Mo ratios (Fig. 5-11) and might be also accompanied by shelf-wide changes in $\delta^{98/95}\text{Mo}_{\text{SW}}$. Shelf-wide changes of the isotopic composition of aqueous Mo are indicated by parallel trends documented in the of $\delta^{98/95}\text{Mo}_{\text{SED}}$ values from the Cleveland Basin (Pearce et al., 2008) and from the Lorraine Sub-Basin (Figs. 5-12A, 5-13). However, shelf-wide changes in the $\delta^{98/95}\text{Mo}_{\text{SW}}$ fail to explain the offset in $\delta^{98/95}\text{Mo}_{\text{SED}}$ values documented between the Lorraine Sub-Basin and the Cleveland Basin, whereby overall lower values were documented in sediments from the Lorraine Basin (Figs. 5-12A, 5-13). Thus, other mechanisms than changes in $\delta^{98/95}\text{Mo}_{\text{SW}}$ must have driven $\delta^{98/95}\text{Mo}_{\text{SED}}$ values.

Differences in the redox conditions fail to explain the values and the offset in the data as euxinic conditions are confirmed for Lorraine Sub-Basin as well as for the Cleveland Basin (French et al., 2014). Spatial differences in $\delta^{98/95}\text{Mo}_{\text{SW}}$ values throughout the Western Tethyan shelf that resulted from an extreme hydrodynamic restriction of the different basin might explain the offset. However, in this case the isotopic difference between different basins should be most significant during the period of strongest restriction, which again is not supported by the data. The strongest hydrodynamic restriction has been proposed for the upper *H. elegantulum subzone*, whereas the strongest offset in $\delta^{98/95}\text{Mo}_{\text{SED}}$ values has been analyzed in samples from the upmost *D. tenuicostatum zone* and the lower *H. elegantulum subzone*. Nevertheless, spatial differences in the $\delta^{98/95}\text{Mo}_{\text{SW}}$ values throughout the Western Tethyan shelf cannot be fully excluded and may have resulted from local riverine Mo supply with a specific isotopic signature.

Interestingly, similar low $\delta^{98/95}\text{Mo}_{\text{SED}}$ values ($\sim 0.6\text{‰}$) were documented for upper Pennsylvanian shales that were deposited under euxinic conditions (Herrmann et al., 2012). These authors suggested that low $\delta^{98/95}\text{Mo}_{\text{SED}}$ values in euxinic sediments can be explained by Mo-enrichment via Mn redox cycling in the water column. They concluded that ^{98}Mo -depleted Mo becomes preferentially adsorbed on particulate Mn oxyhydroxides that form in the oxic part of the water column. When sinking to the anoxic/sulfidic bottom water these Mn particles become dissolved and the ^{98}Mo -depleted Mo is released, buried and thus the isotopically light Mo signature is preserved in the sediment. Contributions of ^{98}Mo -depleted Mo by Mn shuttle processes can thus significantly alter or overprint $\delta^{98/95}\text{Mo}$ values from Mo precipitated from anoxic/sulfidic waters under a low isotope fractionation factor, which reflects local redox conditions (Poulson et al., 2006). The impact of the Mn redox cycling towards $\delta^{98/95}\text{Mo}_{\text{SED}}$ values might depend on the activity of the Mn shuttle processes as well as on the extent of anoxic/sulfidic bottom water from which ^{98}Mo -enriched Mo is precipitated (Fig. 5-12B). An expanded zone of oxic water overlaying the anoxic/sulfidic bottom water of minor extent might result in $\delta^{98/95}\text{Mo}_{\text{SED}}$ values dominated by Mn redox cycling delivered ^{98}Mo -depleted signal. On the contrary, an expanded zone of anoxic/sulfidic bottom water underlying an oxic surface water of reduced extent might result in $\delta^{98/95}\text{Mo}_{\text{SED}}$ values dominated by ^{98}Mo -enriched signature, representing redox conditions in the bottom water.

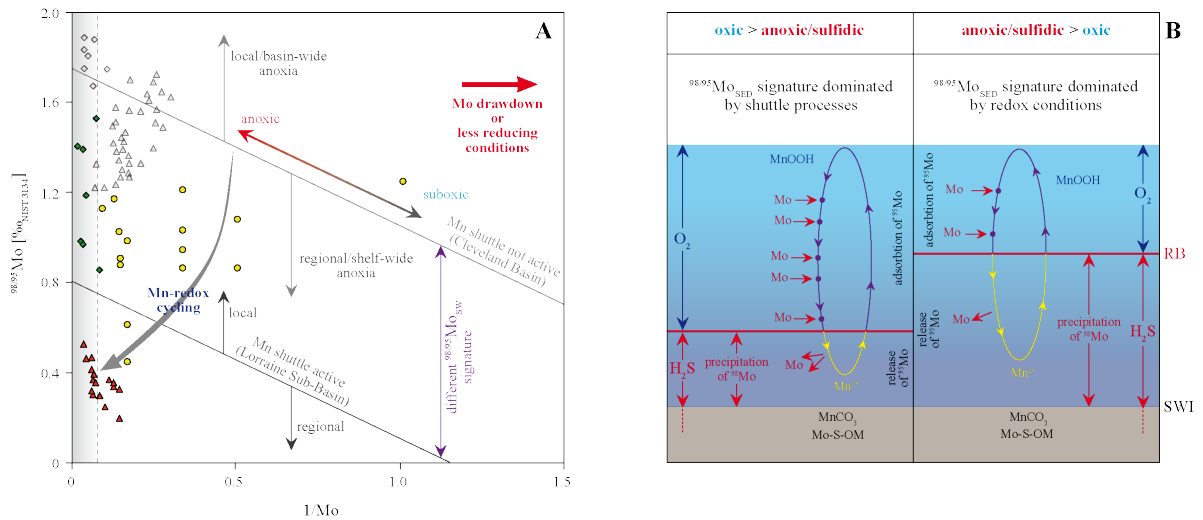


Figure 5-12: A) Cross-plot of $1/Mo$ versus $\delta^{98/95}Mo$ differentiating processes driving molybdenum isotope values. Pearce et al. (2008) used this plot to address changes in the areal extent of marine anoxia (data from Yorkshire are ghosted). In the Cleveland Basin as well as within the Lorraine Sub-Basin lower $\delta^{98/95}Mo$ values were determined for the upmost *D. tenuicostatum* zone and the lower *H. elegantulum* subzone (triangles). Higher $\delta^{98/95}Mo$ values characterize the *H. falciferum* subzone (diamonds) as well as from the upper *H. elegantulum* subzone (circles). This pattern hints to regional (shelf-wide) processes that drove $\delta^{98/95}Mo$ values, which were further modified by local processes, e.g. the activity of Mn-redox shuttle processes. Differences in $\delta^{98/95}Mo_{SW}$ might also contribute to differences in $\delta^{98/95}Mo_{SED}$ signatures. **B)** Impact of Mn-redox cycling onto sedimentary molybdenum isotopes. Mn-redox shuttle processes may promote the export of isotopically-light Mo to the bottom water and thus affect Mo accumulation rates in the sediment (e.g. Algeo & Tribovillard, 2009; Scholz et al., 2013) as well as the Mo isotope signature (Herrmann et al., 2012). The effect of Mn-redox shuttle processes onto sedimentary $\delta^{98/95}Mo$ values might be controlled by the ratio of oxic to anoxic/sulfidic water column as well as by local redox conditions. A detailed discussion of these processes is given in the text (SWI: sediment water interface; RB: redox boundary).

Based on these findings it can be proposed that $\delta^{98/95}Mo_{SED}$ values provide information about the extent of anoxic/sulfidic conditions. Low $\delta^{98/95}Mo_{SED}$ values (<0.5‰) in the upmost *D. tenuicostatum* zone and the lower *H. elegantulum* subzone indicate anoxic/sulfidic bottom water of reduced extent, which is in agreement with low isorenieratane concentrations (1.7 $\mu\text{g/gTOC}$). Low $\delta^{98/95}Mo_{SED}$ values throughout this interval derived from ^{98}Mo -depleted Mo contributions via Mn redox cycling that overprint the anoxic/sulfidic bottom water signal. This finding is also supported by high Mn/Ca ratios, documented in this sediment interval (Fig. S5-3B). An increase in $\delta^{98/95}Mo_{SED}$ values (up to 1.5‰) in sediments from the upper *H. elegantulum* subzone indicates an expansion of anoxic/sulfidic bottom water, which is in agreement with increased isorenieratane concentrations (6.8 $\mu\text{g/gTOC}$). On the contrary, a decrease in $\delta^{98/95}Mo_{SED}$ values (1.2‰ on average) that is accompanied by lower isorenieratane concentrations (2.7 $\mu\text{g/gTOC}$) in the *H. falciferum* zone can be attributed to a reduced extent of anoxic/sulfidic bottom water. Results show that $\delta^{98/95}Mo_{SED}$ values were strongly affected by local mechanisms, including Mn redox cycling or redox conditions (Figs. 5-12, 5-13), but were also driven by changes in $\delta^{98/95}Mo_{SW}$ that resulted from the areal extent of anoxia throughout the Western Tethyan shelf as proposed by Pearce et al. (2008). The later mechanism is well expressed by the parallel trend in $\delta^{98/95}Mo_{SED}$ values from the Cleveland Basin (Pearce et al., 2008) and the Lorraine Sub-Basin, whereas local mechanisms are reflected by the

offset between both records (Fig. 5-13). In combination with the evolution of Mo/TOC ratios it can be stated that areal extent as well as the degree of restriction changed synchronically on regional (shelf-wide) scale (Figs. 5-11, 5-13). With respect to the data from the Lorraine Sub-Basin and the Cleveland Basin it can be proposed that the widest areal extent of shelf sea anoxia can be placed in the lower part of the *H. elegantulum* subzone coinciding with the Toa-CIE interval. Hydrodynamic restriction of the Western Tethyan shelf was most pronounced during the upper *H. elegantulum* subzone (Fig. 5-13).

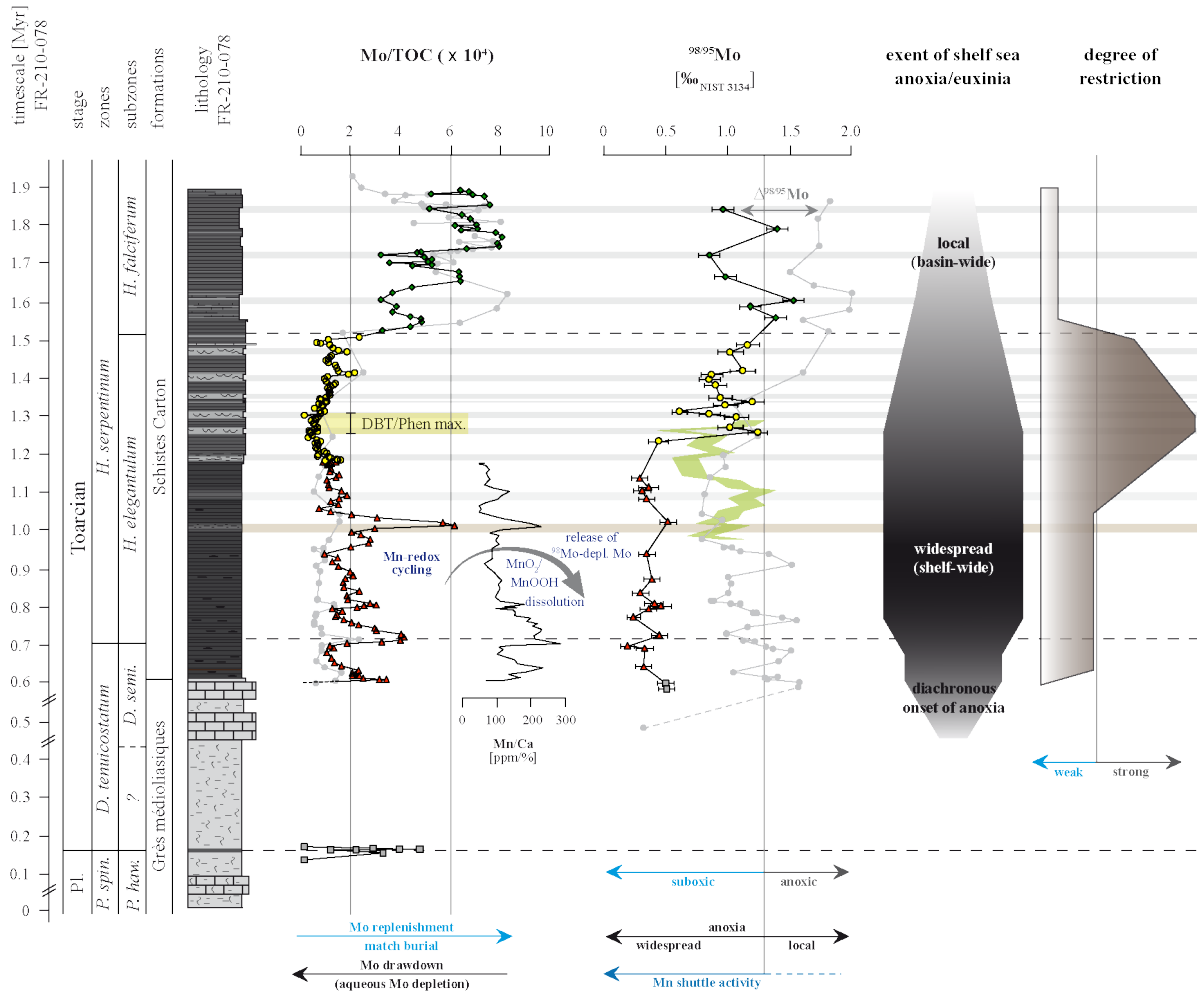


Figure 5-13: Evolution of hydrodynamic conditions and areal extent of shelf sea anoxia inferred from Mo/TOC and $\delta^{98/95}\text{Mo}_{\text{SED}}$ trends. Similar Mo/TOC trends observed throughout the Western Tethyan shelf (see Fig. 5-11) attest to regional, at least shelf-wide processes controlling aqueous Mo concentration. Lowest Mo/TOC ratios in the upper *H. elegantulum* subzone can be attributed to the strongest degree of hydrodynamic restriction. Low aqueous TE concentrations possibly resulted in an enhanced S-incorporation into OM as indicated by highest DBT/Phen ratios. Moreover, the absence of a stron Mo enrichment during the onset of prolonged anoxia might hint to low aqueous Mo concentrations that resulted from the Arctic freshwater inflow. The $\delta^{98/95}\text{Mo}$ values were controlled by regional (shelf-wide) as well as by local (basin-wide) processes (see text for discussion). The $\delta^{98/95}\text{Mo}$ trend from the Cleveland Basin is shown ghosted (data from Pearce et al., 2008), the green area indicates the $\delta^{98/95}\text{Mo}$ trend reported from Dotternhausen (data from Luthardt, 2013). Despite of the high spatial variability in $\delta^{98/95}\text{Mo}$ values, data from the Cleveland and the Lorraine Sub-Basin expose similar long-term trends that might reflect changes in the areal extent of anoxia throughout the Western Tethyan shelf as proposed by Pearce et al. (2008). On the base of these data it can be concluded that shelf sea anoxia reached its widest areal extent during the lower *H. elegantulum* subzone.

5.4.4. Controls on redox conditions and PZE

Works by Röhl et al. (2001) and Frimmel et al. (2004) from the Southern German Basin as well as by Hermoso et al. (2013) from the southern Central Paris Basin highlighted the role of sea level changes towards the evolution of redox conditions and OM preservation during the Early Toarcian. The impact of the sea level evolution is also evident in data from the Lorraine Sub-Basin. According to the sea level curve established for Core FR-210-078 (see Chapter 4) the accumulation of OM as well as long-term changes in the redox conditions align with 3rd and 4th order sea level changes that were controlled by long eccentricity periods. Enhanced preservation of OM coincided with stages of high sea level represented by the bituminous facies of the PI-Toa boundary black shale and the Schistes Carton Fm (Fig. 5-16). Moreover, sea level changes were accompanied by changes in SSS (see Chapter 4), whereby stages of high sea level can be associated with reduced SSS. In contrast, more saline conditions were confirmed for stages of lower sea level. Sea level changes in combination with changes in SSS controlled the overall depositional environment, the hydrodynamic regime and the stability of water column stratification and thus the persistence of the bottom water anoxia/euxinia. These relationships between the sea level evolution, changes in sea surface salinities and redox conditions are expressed in the cross-plots of tri-/di-MTTC ratios with V/Al ratios and of Si/Al ratios with V/Al ratios. Persistent anoxic/euxinic conditions were confined to semi-brackish to brackish conditions during stages of high sea level (Fig. 5-14). Moreover, an overall similar evolution of redox conditions is proposed for the different basins throughout the Western Tethyan shelf, which indicates that regional, at least shelf-wide, factors controlled the persistence of shelf sea anoxia (Fig. S5-4).

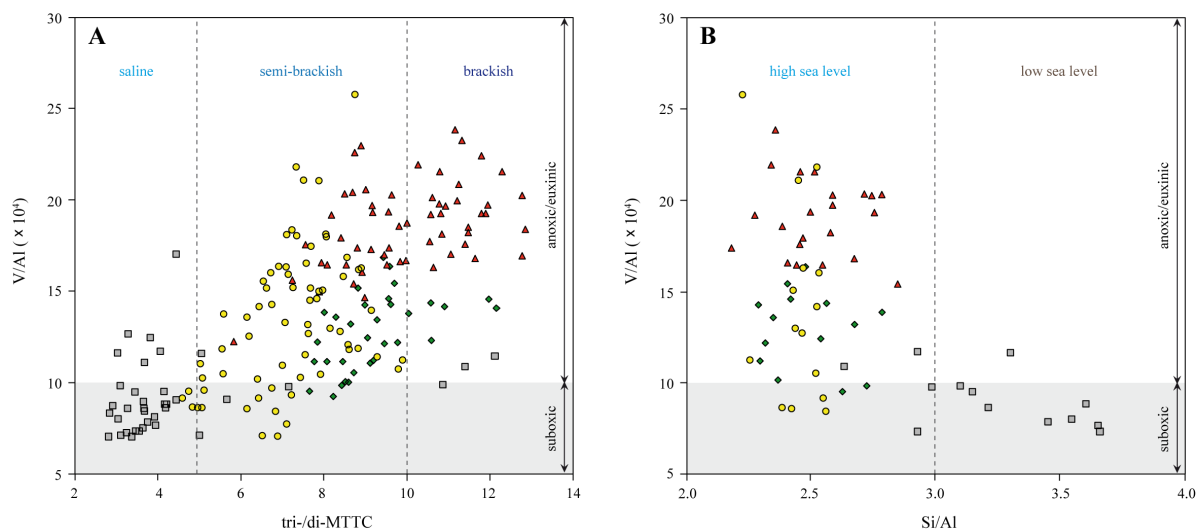


Figure 5-14: A) Cross-plot of tri-/di-MTTCs versus V/Al ratios indicates persistent anoxic/euxinic conditions to have been bound to reduced salinities. B) Cross-plot of Si/Al versus V/Al ratios attest to anoxic/euxinic conditions to stages of high sea level. The scatter in the data indicates that neither salinity nor sea level exclusively controlled redox conditions and rather a combination of both factors contributed to the changes in redox conditions. (legend as in figure 5-5)

High amounts of isorenieratane, reflecting expanded PZE, are exclusively bounded to the bituminous strata of the Schistes Carton Fm, which indicates that a minimum water depth was required to establish persistent euxinic conditions. However, the extent of PZE was not exclusively controlled by the sea level and the stability of water column stratification. In addition, highest isorenieratane concentrations, reflecting the widest extent of PZE, were reported from the upper *H. elegantulum subzone*, a period that reflects an only intermediate sea level during a regressive phase. Moreover, during this period increased SSS can be associated with less stable stratification of the water column. These conditions resulted in highly variable redox conditions and less prolonged bottom water anoxia/euxinia (Figs. 5-15A; 5-16). However, the regressive trend resulted in the strongest degree of hydrodynamic restriction (Fig. 5-13), which prohibited an efficient water exchange between the different basins throughout the Western Tethyan shelf. These conditions formed a shallow marine stagnant environment that provided optimal conditions for the expansion of euxinic conditions in the water column (Fig. 5-15B). The extent of PZE varied between the different basins on the Western Tethyan shelf as deduced from its location-specific evolution, highlighting the role of paleogeographic and paleoceanographic features (Fig. S5-4).

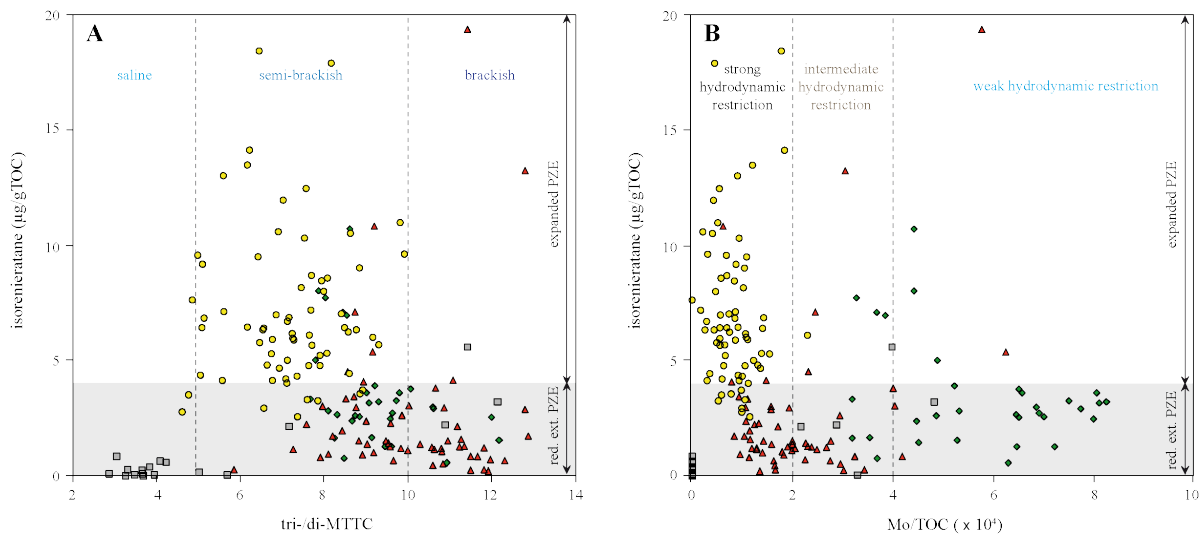


Figure 5-15: A) The cross-plot of tri-/di-MTTC ratios with isorenieratane concentrations suggests reduced SSS to have promoted the expansion of euxinic conditions in the water column. However, freshwater discharge and salinity stratification were not the exclusive drivers on the extent of PZE as highest isorenieratane concentrations were documented during semi-brackish conditions. **B)** The cross-plot of Mo/TOC ratios with isorenieratane concentrations confirms that the degree of hydrodynamic restriction strongly affected the extent of euxinic conditions in the water column, whereby periods of strong hydrodynamic restriction records the highest abundance of isorenieratane, indicating the widest spatiotemporal expansion of PZE in the water column. (red. ext. PZE = reduced extent of PZE; legend as in figure 5-5)

Results confirm that 3rd and 4th order glacio-eustatic sea level changes, driven by 405 kyr eccentricity periods (see Chapters 2 and 4) were the major mechanism controlling shelf sea anoxia during the Early Toarcian. Moreover, high-frequent fluctuations in redox conditions can be associated with astronomical periods of higher order (mainly 100 kyr eccentricity and 37 kyr obliquity periods; see Chapters 2 and 4).

Rapid melting of polar ice during the upmost *D. tenuicostatum* zone and the lower *H. elegantulum* subzone initiated a rapid transgression and was further accompanied by a massive freshwater discharge onto the Western Tethyan shelf. These conditions have resulted in prolonged shelf sea anoxia/euxinia and favored the expansion of marine dead zones that reached their widest areal extent during this period (Fig. 5-16). The vertical expansion of euxinic conditions into the water column was, however, affected by local oceanographic conditions. In the Lorraine Sub-Basin the high sea level during the lower *H. elegantulum* subzone resulted in an intermediate degree of hydrodynamic restriction and prevented the expansion of PZE into the upper part of the water column. Moreover, an intensification of the monsoonal circulation resulted in more frequent and stronger storm events, which led to a better mixing of the surface water (Krencker et al., 2015). These conditions did not favor the expansion of PZE into the upper parts of the water column.

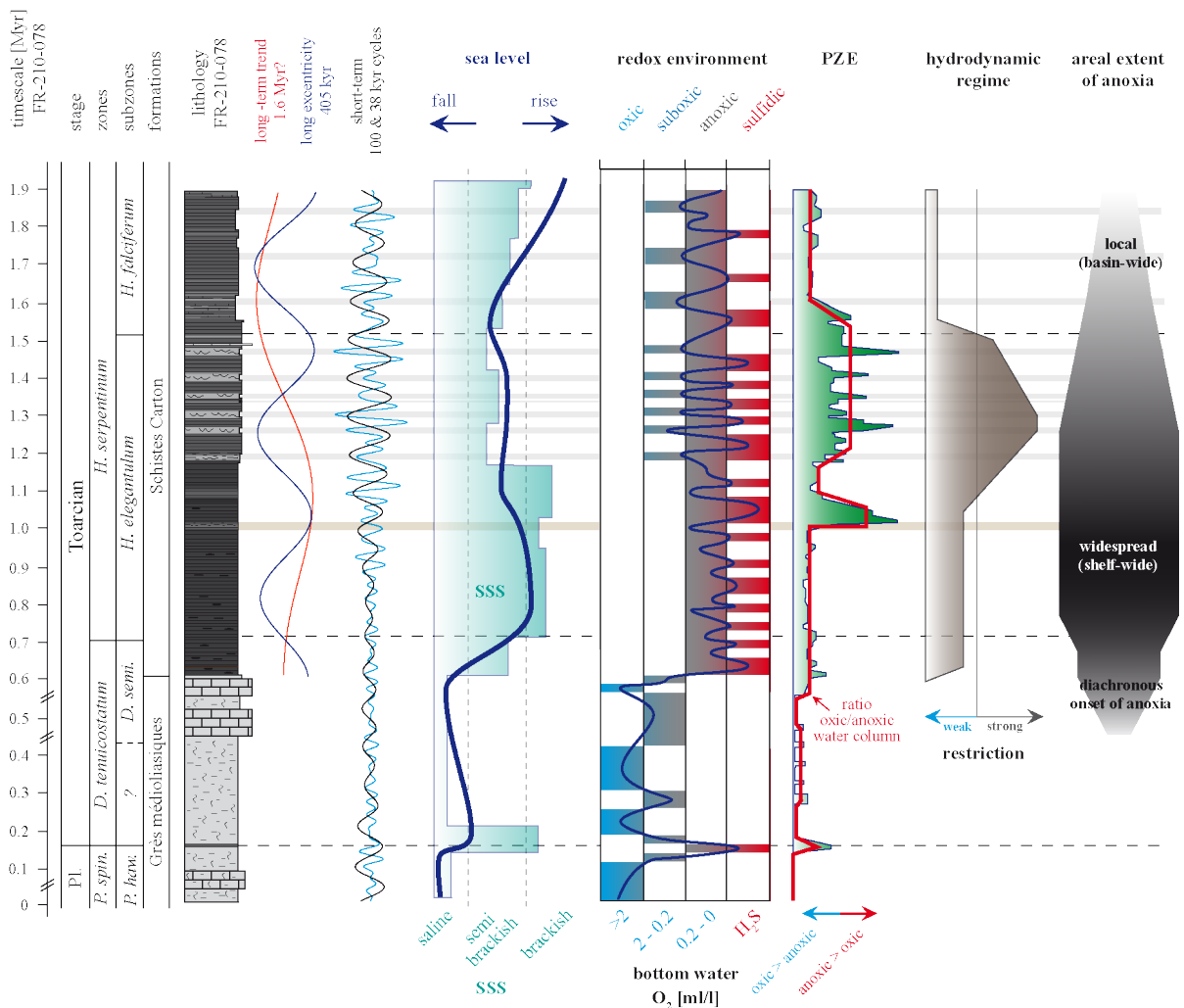


Figure 5-16: Changes in redox conditions during the Late Pliensbachian and the Early Toarcian were driven by changes in sea level and changes in SSS, forced by astronomical cycles of variable frequency. The high sea level stand during the upmost *D. tenuicostatum* zone and the lower *H. elegantulum* subzone account for the widest areal extent of shelf sea anoxia. The subsequent regression during the upper *H. elegantulum* subzone resulted in the maximum restriction of the shelf sea, which favored the expansion of sulfidic/euxinic conditions.

The subsequent regressive trend in the upper *H. elegantulum* subzone promoted a stronger hydrodynamic restriction of the Western Tethyan shelf as indicated by lowest Mo/TOC ratios (Figs. 5-11; 5-16). Moreover, the intermediate sea level created an environment most sensitive towards minor environmental changes as expressed by the high variability of lithology and geochemical proxies. Redox fluctuations during within the upper *H. elegantulum* subzone will be discussed in detail below. Upon low sea level in combination with strong hydrodynamic restriction expanded sulfidic/euxinic conditions into the water column (and into the photic zone) are recognizable by the highest isorenieratane concentrations (Fig. 5-16). However, due to the lower sea level and a less stable stratification of the water column euxinic conditions were less stable and frequently interrupted by reoxygenation events. The sea level rise in the *H. falciferum* subzone led to a better connectivity between the different basins on the Western Tethyan shelf as well as between the shelf sea and the Tethyan Ocean, as indicated by an increase in Mo/TOC ratios (Figs. 5-11, 5-16). The high sea level resulted in preferentially anoxic/sulfidic bottom water of limited extent evident by low isorenieratane concentrations.

5.4.5. Redox fluctuations during the upper *H. elegantulum* subzone

The upper *H. elegantulum* subzone is highlighted by the most significant variability in the studied section that is expressed in the lithology as well as by geochemical proxies associated with sea level and salinity fluctuations. Findings presented in Chapter 2 and 4 allow to attribute these fluctuations to astronomically forced glacial/interglacial cycles on frequency bands corresponding to obliquity cycles. In the Lorraine Sub-Basin glacial/interglacial cycles resulted in significant variations in the redox regime (Figs. 5-16, 5-17). Glacial stages, associated with a lower sea level and increased SSS, are characterized by a lower PP. A reduced PP is inferred from decreased TOC values as well as from low Cu/Al and Ni/Al ratios that reflect a reduced OM flux to the sea floor (e.g. [Tribovillard et al., 2006](#)) and might have resulted from a reduced nutrient supply to the shelf seas during a cooler climate. Lower OM export rates diminished BSR rates, which in combination with a lower sea level resulted in less persistent anoxia/euxinia as indicated by low V/Al ratios (Fig. 5-17). Moreover, increased SSS destabilized the pycnocline, which further promoted an efficient mixing of the water column. Interglacial stages are associated with a higher sea level and enhanced freshwater discharge to the Western Tethyan shelf sea via the Viking Corridor and thus with a more stable water column stratification. Furthermore, more humid climate conditions increased continental weathering and runoff rates that in turn stimulated PP and thus the OM export to the sea floor, which is indicated by high Cu/Al and Ni/Al ratios as well as by high TOC values (Fig. 5-17). Subsequent aerobic OM breakdown drove the oxygen concentrations in the water column towards lower values and promoted elevated rates of BSR. More reducing conditions during interglacial stages are well expressed by high V/Al ratios (Fig. 5-17). The significant coevolution of the TOC content with productivity indicators (Ni/Al, Cu/Al) and redox proxies (V/Al, HHI*) throughout the upper *H. elegantulum* subzone identifies redox conditions to have been driven by the availability of labile OM.

Productivity-driven anoxia/euxinia has also been inferred from the TOC-TS plot, where samples from this interval match well with the salinity stratified “Black Sea trend” (Fig. 5-7).

Throughout the lower part of this interval (from ~1.18 to ~1.32 Myr) the coevolution of isorenieratane concentrations with V/Al ratios propose the abundance of *Chlorobiaceae* to be linked to the persistence of anoxic/euxinic conditions (Fig. 5-17). A decoupling of isorenieratane concentrations and V/Al ratios throughout the upper part of this interval (from ~1.32 to ~1.50 Myr) is taken as evidence that the abundance of *Chlorobiaceae* was not exclusively controlled by the persistence of anoxia/euxinia. Interestingly, the highest concentrations of isorenieratane have been documented in sediments horizons characterized as less reducing. However, these horizons are still rich in TOC (~5 wt.%) indicating that temporal high PP rates (e.g. annual algal blooms) resulted in an oxygen-depletion of the bottom water and promoted the expansion of sulfidic conditions into the water column. If present, PZE expanded throughout a wide part of the water column, which resulted in massive but shortlived blooms of *Chlorobiaceae*, contributing high amounts of isorenieratane to the sediment. Expanded PZE was, however, highly sensitive towards environmental changes and thus less persistent. Annual mixing of the water column resulted in the termination of PZE, in enhanced sediment reworking, water bottom currents and transport of oxygen to the seafloor allowing benthic organisms to resettle the seafloor. However, if rapidly buried (e.g. due to high sedimentation rates) recalcitrant isorenieratane.

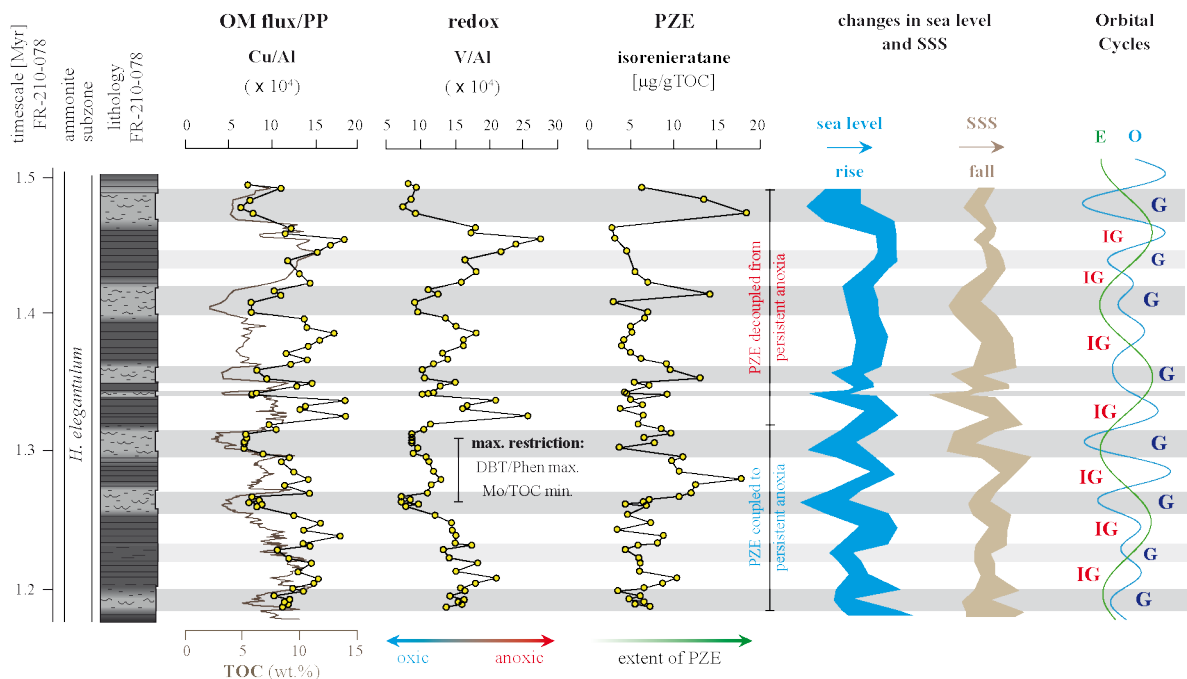


Figure 5-17: Throughout the upper *H. elegantulum* subzone redox-fluctuations can be linked with variation in the PP during glacial/interglacial cycles that were driven by obliquity periods. The strong coupling of PP and redox conditions indicates that anoxia/euxinia was productivity-driven, whereby a higher PP and thus more persistent reducing conditions were confined to interglacial stages. The extent of PZE was, however, not exclusively driven by the persistence of euxinic conditions. Moreover, short-lived but extremely expanded PZE may have contributed to a significant enrichment of isorenieratane in the sediments (G: glacial stage; IG: interglacial stage).

5.4.6. Evolution of redox conditions during the Toa-CIE

In the Lorraine Sub-Basin anoxic/euxinic conditions established rapidly during the initial part of the Toa-CIE and remain persistent throughout this interval. Anoxia established stepwise, whereby each negative carbon isotope shift (II-A; II-B; II-C) was followed by the expansion of anoxia, recognizable in a stepwise increase in V/Al ratios (Fig. 5-18) as well as by a stepwise decrease of Pr/Phy ratios (Fig. 5-3). Persistent anoxia/euxinia was induced by an overall increase in PP and the subsequent OM export to the bottom water, as expressed in elevated TOC values and Cu/Al ratios (Fig. 5-18). However, the detailed inspection of the data reveals that the negative Toa-CIE shifts II-B and II-C can be attributed to a brief decrease in the PP, indicated by a drop in TOC values and in the Cu/Al ratios (Fig. 5-18). A decrease in PP might have resulted from increased environmental stress onto the primary producing communities as a consequence of CO₂ injections into the Earth's ocean/atmosphere system. Carbon injections led to ocean acidification that directly affected the calcareous nannoplankton (e.g. [Mattioli et al., 2008](#); [Hermoso et al., 2009b, 2012](#)). The brief decrease in PP did not significantly affect the redox regime. A minor decrease is documented in the V/Al ratio, but is not documented in the Pr/Phy ratio (Figs. 5-18; 5-3). The decoupling of PP and redox conditions during the Toa-CIE interval is also expressed in the TOC-TS-FE systematic (Fig. 5-7) and attest to changes in redox conditions not driven by the availability of labile OM. Moreover, changes in redox conditions can be attributed to oceanographic conditions. As shown in Chapter 4 each negative carbon isotope shift was accompanied by a rise in sea level and a freshwater pulse (Fig. 5-18). Enhanced freshwater inflow favored a stable stratification of the water column and in combination with a high sea level promoted the formation of anoxic bottom water. Brief regressive intervals during the recovery phases of the individual carbon injections can be associated with a shift to less reducing conditions (Fig. 5-18). A decrease in V/Al ratios can be associated with the MFZ and may have derived from oxic surface water expansions. The return to less reducing conditions during the recovery phase of the Toa-CIE may have been associated with a regressive phase.

Persistent bottom water euxinia during the Toa-CIE interval was not accompanied by a wide expansion of PZE. Rather low isorenieratane concentrations (on average 1.7 µg/gTOC) indicate PZE of reduced extent, i.e. limited to the bottom water. An intensification of the monsoonal circulation and a strengthening of the storm activity might have resulted in an enhanced mixing of the surface water ([Krencker et al., 2015](#)), which prevented the expansion of PZE into the upper water column. Similarly low isorenieratane concentrations (<2 µg/gTOC) were documented for the Toa-CIE interval in core ANDARA HTM 102, also located in the Lorraine Sub-Basin ([van Breugel et al., 2006](#)). These authors concluded that the recycling of ¹³C-depleted CO₂ in a stratified water column as proposed by [Küspert \(1982\)](#) (Küspert model) fails to explain the Toa-CIE as supported by this study.

A drastic increase in isorenieratane concentrations in the upper part of the Toa-CIE interval, subsequent to the MFZ is proposed to be in causal relationship with a decrease in SSS (Fig. 5-18). According to the sea level evolution established for the Lorraine Sub-Basin this stage reflects an early regressive phase. The fall in the sea level might have resulted in a strengthening of local

processes, including riverine freshwater contributions that in combination with a lowered sea level favored the expansion of PZE over a wider part of the water column. Whether this *Chlorobiaceae* bloom is a local or a regional (shelf-wide) phenomena remains to be confirmed. It is however interesting to note that the stratigraphic position of the isorenieratane spike match with the position of the “Unterer Stein” in the South German Basin, diagenetic carbonate horizon that can be associated with exceptional environmental conditions, including prolonged PZE (Schwark & Frimmel, 2004).

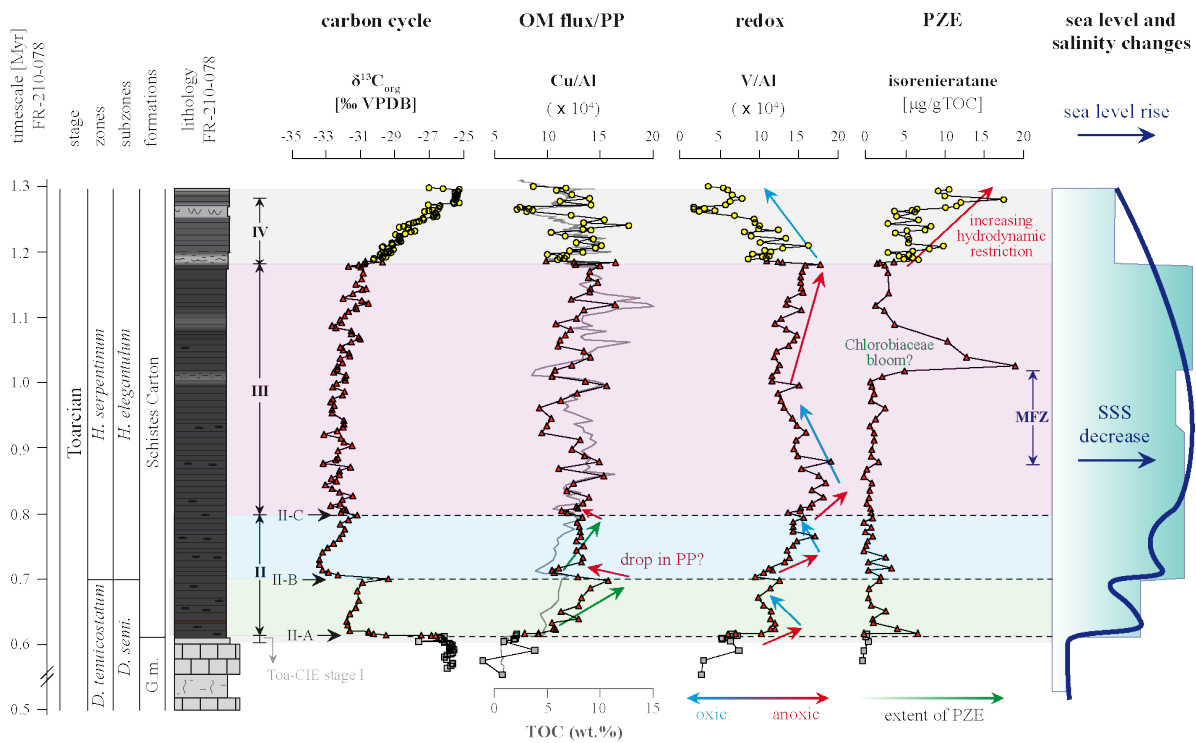


Figure 5-17: The evolution of redox conditions during the Toa-CIE was decoupled from the PP. Redox conditions were primarily controlled by oceanographic factors, including sea level changes and changes in SSS. Shifts to more reducing conditions occurred synchronous with individual large carbon injections (Toa-CIE shifts II-A, II-B, II, C) and can be linked to transgressive pulses and enhanced freshwater inflow. The stage of highest sea level, placed in the climax of the Toa-CIE, may have been connected to less reducing conditions due to enhanced water exchange with adjacent basins. A massive increase in isorenieratane concentrations subsequent to the proposed MFZ might hint to special environmental conditions induced by a decrease in SSS.

5.5. Conclusions

Conclusion concerning paleoceanographic conditions

Expansion of anoxia and euxinia on the Western Tethyan shelf during the Early Toarcian can be linked to profound environmental changes on a global scale. Global warming that started in the upmost *D. tenuicostatum zone* led to an acceleration of the hydrological cycle that resulted in an enhanced nutrient flux and caused an eutrophication of the shelf seas (Cohen et al., 2004; Montero-Serrano et al., 2015). An increase in PP and elevated rates of OM export to the seafloor are expressed by and high TOC values and high Cu/Al and Ni/Al documented in samples from the Schistes Carton Fm. The subsequent aerobic OM degradation drove oxygen concentrations in the bottom water towards lower values and elevated rates of BSR as indicated by the increasing trend in $\delta^{34}\text{S}$ values as well as by the TOC-TS-Fe systematic. Prolonged anoxia and euxinia throughout the Western Tethyan shelf was further promoted by a rise in sea level and enhanced freshwater supply, both resulting from the demise of polar ice caps. These conditions provided a low-energetic depositional environment below the wave and storm base with a stable stratification of the water column, which prevented an efficient mixing of the water column and thus favored the accumulation and preservation of OM.

Results confirm that 3rd and 4th order sea level changes, driven by astronomical parameters (possibly 405 kyr cycles), controlled the redox regime in the Lorraine Sub-Basin as well as in other basins throughout the Western Tethyan shelf. The effect of sea level changes has been previously proposed as the main parameter controlling anoxia (e.g. Röhl et al., 2001; Hermoso et al., 2013) and is reinforced by this work. Moreover, sea level changes in association with lowered SSS controlled the hydrodynamic regime throughout the Western Tethyan shelf. Persistent anoxia seems to coincide with a high sea level and a strong freshwater inflow. However, during stages of a high sea level PZE was limited to the euxinic bottom water, overlain by an expanded well-oxygenated water column. Enhanced basin communication throughout the Western Tethyan shelf might have resulted in strong surface currents, eventually enforced by monsoonal circulation, which prohibited an expansion of PZE into the upper part of the water column. The expansion of PZE over a wide part of the water column was promoted by a strong restriction of the shelf seas that resulted in water mass stagnation. In the Lorraine Sub-Basin the widest extent of PZE occurred in the upper *H. elegantulum subzone* that can be attributed to a regressive phase, subsequent to the high sea level during the Toa-CIE. The overall similar evolution of redox conditions in the different basins throughout the Western Tethyan shelf confirm that glacio-eustatic mechanisms associated with astronomically-forced global climate changes controlled the deposition of black shales during the Early Toarcian. Black shale deposition on the Western Tethyan shelf was favored by paleogeographic and paleoceanographic features that provided an environment most suitable for the accumulation and preservation of organic matter. Local conditions in the different sub-basins, however, controlled the expansion of PZE into the water column.

Conclusion concerning the application of redox proxies

The overall evolution in the redox regime is well expressed by inorganic as well as by organic geochemical redox proxies. Differences remaining in the observed trends can be attributed to the mechanisms that control these proxies. The persistence of anoxia/euxinia in the bottom water can be assessed by inorganic proxies, including the TOC-TS-Fe systematic as well as in V/Al ratios. However, the extent of euxinic conditions and thus the ratio of oxic versus anoxic/euxinic water column controls the concentrations of isorenieratane. Moreover, the extent of euxinic conditions in the water column is expressed by the HHI* and the C₃₂/C₃₁ hopane ratio, as the availability of H₂S is critical for the preservation of bacteriohopanes. Therefore, the combined use of inorganic and organic redox proxies allows discussing persistence as well as extent of anoxic/euxinic conditions.

As shown in previous works by [McArthur et al. \(2008a\)](#) or by [Hermoso et al. \(2013\)](#) the enrichment of Mo in the sediments is controlled by the redox and by the hydrodynamic regime, whereby strong hydrodynamic restriction induced a drawdown of aqueous Mo. Basin restriction and element drawdown might also affect other TEs (Ni, Cu, V) but is most significant for Mo due to the long residence time of this element.

Caution must be taken when interpreting $\delta^{98/95}\text{Mo}_{\text{SED}}$ values in terms of redox conditions ([Poulson et al., 2006](#)). Results indicate that several mechanisms have the potential to affect molybdenum isotope data. Mechanisms that can affect the $\delta^{98/95}\text{Mo}_{\text{SED}}$ values on the Western Tethyan shelf:

- changes in $\delta^{98/95}\text{Mo}_{\text{SW}}$ values due to the areal extent of shelf sea anoxia as proposed by [Pearce et al. \(2008\)](#);
- spatial differences and thus a local evolution of $\delta^{98/95}\text{Mo}_{\text{SW}}$ values due to a strong hydrodynamic restriction of the different basin and a reduced water exchange between those;
- spatial differences in the $\delta^{98/95}\text{Mo}$ signature of Mo contributed by riverine discharge (can result in a local provenance $\delta^{98/95}\text{Mo}_{\text{SW}}$ signature, when mixing throughout was hampered)
- changes in local redox conditions
- Mn-redox cycling (Mn particulate shuttle) in operation as proposed by [Herrmann et al. \(2012\)](#).

Chapter Six:

Phytoplankton community dynamics during the Early Toarcian

Abstract

Detailed information about changes in the community structure of marine primary producers associated with the Early Toarcian environmental crisis mainly base on micropaleontological observations and thus address only a small part of the marine phytoplankton. Moreover, dynamics in the community structure of phytoplankton during the Early Toarcian carbon cycle perturbation remain unknown. However, the response of marine primary producers towards environmental changes, including global warming, acidification of the oceans as well as eutrophication of the shelf seas, is of major interest and may provide information that help to predict the response of marine ecosystems towards the recent climate change.

Biomarkers that can be linked to marine primary producers, mainly algae, provide information about phytoplankton community dynamics and about changes in the phytoplankton assemblages during the Early Toarcian. The period of major environmental change that spans the upmost *D. tenuicostatum zone* and the lower *H. elegantulum subzone* shows a demise of marine algae groups, including red algae, golden algae and *Haptophyceae*. These were replaced by opportunistic green algae groups (e.g. *Prasinophyceae*, *Chlorophyceae*), which experienced a radiation during this period. Biomarker data confirm that lowered sea surface salinities were a major factor contribution to the demise of marine algae groups. Moreover, marine phytoplankton directly suffered from the rise in sea surface temperatures and ocean acidification. Reduced sea surface salinities mainly affected phytoplankton communities in shelf settings, whereas high sea surface temperatures and an increase in ocean acidity affected the phytoplankton globally.

A high-resolution biomarker approach allowed to reconstruct community dynamics that reflect the response of the marine phytoplankton during a time of drastic global warming. Abrupt changes in community structure can be associated with individual carbon isotope shifts and related hyperthermals. Each subsequent recovery phase was accompanied by a recovery of the marine phytoplankton. Thus, changes in the community structure occurred stepwise over a period of >300 kyr. A stepwise change in the phytoplankton community structure, including recovery phases can explain the low extinction rated that have been documented for nektonic ecosystems.

6.1. Introduction

With a rapid rise in global temperatures of about 6°C (Dera et al., 2011a) and a threefold increase in atmospheric $p\text{CO}_2$ (McElwain et al., 2005) the Early Toarcian reflects one of most drastic phases of global warming during the Mesozoic, only exceeded by the warming at the Permian-Triassic boundary (Figs. 6-1, S6-1). Environmental changes were accompanied by a severe biotic crisis that affected mainly marine organisms, comprising benthic as well as nektonic ecosystems. However, extinction preferentially affected benthic communities, whereby extinctions rates show a strong regional character and differ on regional as well as on global scale (e.g. Little & Benton, 1995; Harries & Little, 1999; Caswell et al., 2009; Caruthers et al., 2013; Caswell & Coe, 2014; also see Chapter 1.2.1.). In the European realm extinction of benthic groups has been associated with prolonged shelf sea anoxia and the expansion of marine death zones (Danise et al., 2013; Caswell & Coe, 2014), which explains the strong regional character that has been documented in the extinction pattern. On the contrary, nektonic communities, like belemnites or ammonites, record drastic shifts in their community structure, whereas extinction rates were relative low (Dera et al., 2010; 2011b). The decoupling of benthic and nektonic ecosystems indicate that different environmental factors controlled the evolution of these communities (Danise et al., 2015).

Environmental changes also affected marine primary producers, whereas the response of the marine phytoplankton is less constrained, a fact that results from the limited fossilization and preservation potential of these fragile organisms. A drastic demise in calcareous nannoplankton can be associated with an acidification of the oceans that resulted from increased atmospheric carbon dioxide concentrations (e.g. Erba, 2004; Mattioli et al., 2008, 2009; Hermoso et al., 2009b, 2012; Suan et al., 2010; Clémence, 2014; Clémence et al., 2015). Furthermore, red algae and dinoflagellates that dominated the primary producer community prior to the Early Toarcian environmental change, were replaced by opportunistic taxa, like green algae and here particularly prasinophytes that were better adapted to warm and low saline waters (Bucefalo Palliani et al., 2002; van de Schootbrugge et al., 2005a; 2013) (also see Chapter 1.2.1.).

However, these organism groups represent only a small part of the marine phytoplankton and thus the response of marine primary producers towards the Early Toarcian environmental changes remains unknown. Moreover, the discrepancy between the magnitude of environmental/climatologic changes and the magnitude of the biotic response is still not understood (Fig. S6-1).

In this chapter biomarkers, characteristic for marine phytoplankton, are used to reconstruct dynamics of marine primary producing communities. Previous works have already shown that specific biomarkers have the potential to characterize and to discuss changes in the community structure of the phytoplankton (e.g. Schwark & Empt, 2006). The biomarker approach will allow to discuss the response of the marine phytoplankton towards rapid global warming and changes in oceanographic conditions at high temporal resolution.

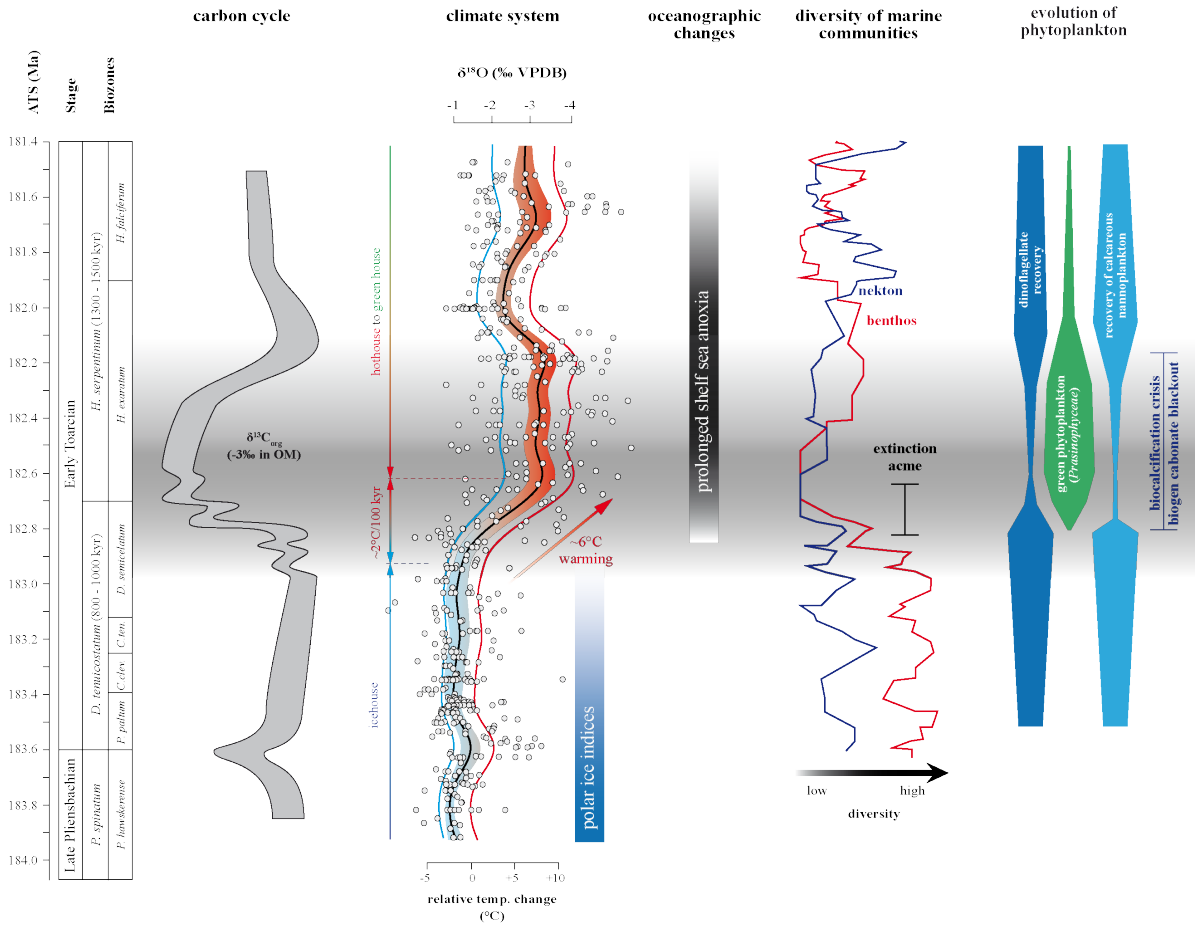


Figure 6-1: The perturbation of the carbon cycle and the drastic global warming, taking place during the Early Toarcian, were accompanied by profound changes in marine ecosystems. Extinction preferentially affected benthic communities and has been linked to the expansion of marine death zones. Nektonic communities document severe shifts in their community structure, whereas extinction rates remain relative low. A drastic demise of calcareous nannoplankton has been associated with a biocalcification crisis that resulted from ocean acidification.

6.2. Background: Biomarkers as indicators of marine phytoplankton

Beside cyanobacteria and acritaches, the phytoplankton in the Early Jurassic oceans was composed of a variety of algae groups (e.g. [Killops & Killops, 2005](#); [Peters et al., 2005](#) and references therein). Only a few of them, including siliceous radiolarians, calcareous coccolithophores and foraminiferans, as well as organic-walled dinoflagellates, are represented in the fossil record. However, the majority of the marine phytoplankton, like *Chlorophyta* (green algae), *Rhodophyta* (red algae), *Chrysophyceae* (golden algae), or *Xanthophyceae* (yellow-green algae), do not form hard parts, which results in a limited fossilization and preservation potential. Thus, these groups are not represented in the fossil record. A possibility to overcome the limited fossilization potential of marine phytoplankton is the use of molecular fossils (biomarkers), which can be linked to former organisms or organism groups (e.g. [Peters et al., 2005](#); [Briggs & Summons, 2014](#)).

A variety of steroidal compounds have been identified in eukaryotic phytoplankton groups (mainly algae) ([Volkman et al., 1990](#); [Kodner et al., 2008](#); [Volkman, 2003, 2006](#)), whereas specific hopanoids can be diagnostic for prokaryotic phytoplankton (mainly cyanobacteria) ([Summons et al., 1999](#)). Some of these biomolecules possess taxonomically specific properties, like the position of double bonds and/or the position of functional groups. These molecules can get preserved in the sediment, whereby diagenetic alteration results in the loss of chemotaxonomic information. In ancient sediments that experienced a certain degree of diagenetic overprint mainly the hydrocarbon skeletons of former functionalized biomolecules are preserved, which limits their diagnostic potential. However, despite of their reduced chemotaxonomic significance diagenetically altered molecules still allow to draw conclusions about changes in the phytoplankton community structure. Moreover, the majority of the algae always synthesize a variety of different steroids, which further complicates the reconstruction of ancient phytoplankton communities ([Volkman et al., 1990](#); [Kodner et al., 2008](#); [Volkman, 2003, 2006](#)).

Desmethyl-steroids in the range from C₂₇ to C₃₀ are biosynthesized by different algae classes (e.g. [Volkman et al., 1998](#); [Volkman, 2003](#)). C₃₀-24-propyl-steroids (C₃₀ steroids) are diagnostic for marine *Sarcinochrysis marina* and *Nematochryopsis roscoffensis* algae ([Volkman, 2003](#) and references therein) that were originally assigned to *Chrysophyceae* but have been reclassified into *Pelagophyceae* (see [Volkman, 2003](#) and references therein). C₂₇ steroids, derived from cholesterol precursors, can be associated with marine red algae and thus can also be indicative for marine environments ([Volkman, 2003](#); [Peters et al., 2005](#)). C₂₈ steroids may originate in ergosterol precursors, which occur in various microalgae, comprising *Chlorophyceae*, *Euglenophyceae*, *Haptophyceae*, *Prasinophyceae*. These algae can be associated with highly contrasting environments, comprising marine and freshwater habitats. Stigmasterols, precursors of C₂₉ steroids, has been found in higher land plants, but occurs also in various marine and freshwater algae, comprising for example *Chlorophyceae*, *Chrysophyceae*, *Euglenophyceae*, *Eustigmatophyceae*, or *Rapidophyceae*. Moreover, the input of cyanophytes can be identified by 2-methylhopanes (2Me-hopanes), whereby not all cyanobacteria must necessarily synthesize bacteriohopanoids with a 2Me substitution (e.g. [Summons et al., 1999](#)). 4-methylsterols (4Me-sterols) with a 23,24-methyl

Chapter Six: Phytoplankton community dynamics

substitution and related diagenetic products can be diagnostic for dinoflagellates that developed during the Triassic (e.g. Wolff et al., 1986; Robinson et al., 1994; Amo et al., 2010). However, 4Me-steroids have been also documented from prymnesiophyte microalgae (*Haptophyceae*) as well as from *Raphidophyceae* confirming that these compounds are not unique to dinoflagellates (Volkman et al., 1990; 1998; Volkman, 2003). Furthermore, not all dinoflagellates contain high concentrations of 4Me-steroids (Volkman, 2006 and references therein). An overview about the molecular composition of the main phytoplankton groups is given in table 6-1.

Table 6-1: Sterol distribution in microalgae, bacteria and fungi (Volkman et al., 1998; Volkman, 2003, 2006). Habitats of the different microalgae (Margulis et al., 1990; Lee, 2008). Algae associated with freshwater can be also common in terrestrial habitats. Algae common for marine habitats highlighted in blue color, freshwater algae in green color and algae from marine, freshwater and terrestrial habitats in purple. Note that the association of the microalgae classes with different habitats base on present day observations, so caution must be taken when transferring these relation to fossil environments.

microorganisms		habitat	major/common sterols
Bangiophyceae	Red algae	mainly marine	$C_{27}\Delta^5$, $C_{27}\Delta^{5,22}$, $C_{28}\Delta^{7,22}$,
Chlorophyceae	Green algae	mainly freshwater	$C_{28}\Delta^5$, $C_{28}\Delta^{5,7,22}$, $C_{28}\Delta^{7,22}$, $C_{29}\Delta^{5,22}$, $C_{29}\Delta^5$
Chrysophyceae	Golden algae	marine & freshwater	$C_{29}\Delta^{5,22}$, $C_{29}\Delta^5$, $C_{28}\Delta^{5,22}$
Cryptophyceae		marine & freshwater	$C_{28}\Delta^{5,22}$
Dinophyceae	Dinoflagellates	mainly marine	4Me- Δ^0 , dinosterol, $C_{27}\Delta^5$, $C_{28}\Delta^{5,24(28)}$
Euglenophyceae		mainly freshwater	$C_{28}\Delta^{5,7,22}$, $C_{29}\Delta^5$, $C_{28}\Delta^7$, $C_{29}\Delta^{5,7}$, $C_{28}\Delta^{7,22}$
Eustigmatophyceae		marine & freshwater	$C_{27}\Delta^5$ (marine), $C_{29}\Delta^5$ (freshwater)
Haptophyceae	e.g. <i>Coccolithophores</i>	mainly marine	$C_{28}\Delta^{5,22}$, $C_{27}\Delta^5$, $C_{29}\Delta^{5,22}$, $C_{29}\Delta^5$, 4Me
Pelagophyceae		mainly marine	$C_{30}\Delta^{5,24(28)}$, $C_{29}\Delta^{5,22}$, $C_{29}\Delta^5$, $C_{28}\Delta^{5,24(28)}$
Prasinophyceae	Green algae	marine & freshwater	$C_{28}\Delta^5$, $C_{28}\Delta^{5,24(28)}$
Raphidophyceae		mainly freshwater	$C_{29}\Delta^5$, $C_{28}\Delta^{5,24(28)}$, 4Me- Δ^8
Rhodophyceae	Red algae	mainly marine	$C_{27}\Delta^5$, $C_{27}\Delta^{5,22}$
Xanthophyceae	Yellow-green algae	mainly freshwater	$C_{29}\Delta^5$, $C_{27}\Delta^5$
Thraustochytrids		mainly marine	$C_{27}\Delta^5$, $C_{29}\Delta^{5,22}$, $C_{28}\Delta^{5,22}$, $C_{29}\Delta^{5,7,22}$
Methylotrophic bacteria		diverse habitats	4Me- Δ^8
Other bacteria		diverse habitats	$C_{27}\Delta^5$
Land plants		terrestrial habitats	C_{29}

6.3. Results

6.3.1. Molecular composition of the aliphatic hydrocarbon fraction

Aliphatic fractions are mainly composed of *n*-alkanes (from nC_{12} to nC_{35}), isoprenoids (mainly farnesane, iC_{16} , norpristane, pristane, phytane), steroids and hopanoids, whereby relative contributions of individual classes of compounds change throughout the studied interval. Samples from Interval 4 (upper *P. spinatum* and lower *D. tenuicostatum* zones) are dominated by *n*-alkanes, whereas samples from the Interval 1 to 3 (upmost *D. tenuicostatum* and *H. serpentinum* zones) show the highest amounts of steroids (Fig. 6-2). Furthermore, samples from Interval 1 to 3 show higher concentrations of isoprenoids (here only the sum of pristane and phytane have been considered) accompanied by lower contributions of hopanoids. On the contrary, higher hopanoid concentrations and lower isoprenoid concentrations are documented in samples from Interval 4 (Fig. 6-2).

n-alkane distribution

The *n*-alkane distribution may provide information about relative contributions of terrigenous and marine derived OM, whereby odd-numbered short-chain *n*-alkanes (nC_{15-19}) predominantly originate from marine organisms and odd-numbered long-chain *n*-alkanes (nC_{27-31}) mainly derive from land plants (Eglinton & Hamilton, 1967; Cranwell, 1973; Cranwell et al., 1987; Meyers, 2003). The *n*-alkanes, present in the aliphatic hydrocarbon fraction, were quantified by using the mass fragment m/z 85. Representative ion chromatograms for Intervals 1 to 4 are shown in the appendix (Fig. A10). Changes in the relative contributions from marine organisms and land plants can be expressed by the TAR (terrestrial-aquatic-ratio; Bourbonniere & Meyers, 1997), which is defined as:

$$TAR = \frac{C_{25} + C_{27} + C_{29}}{C_{15} + C_{17} + C_{19}}$$

High TAR values >1 in samples from Interval 4 (upmost *P. spinatum* zone and lower *D. tenuicostatum* zone) attest to a significant contribution from land plant derived material. In contrast, preferentially marine organic matter sources were confirmed by low TAR values <1 for samples from Intervals 1 to 3 (upmost *D. tenuicostatum* and the *serpentinum* zones) (Fig. 6-2).

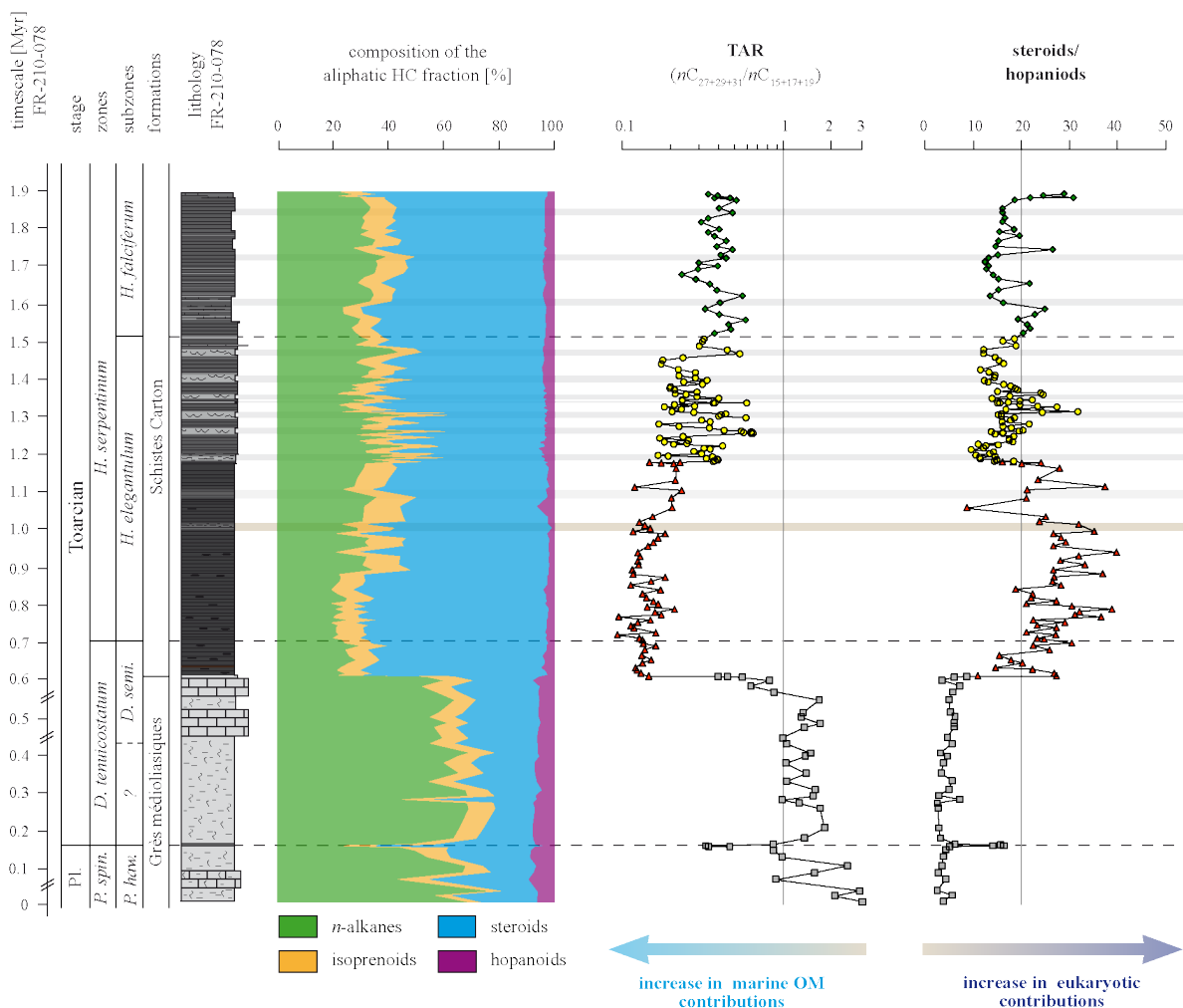


Figure 6-2: Stratigraphic evolution of changes in the composition of the aliphatic hydrocarbon fraction that is mainly composed of *n*-alkanes, steroids, isoprenoids (pristane, phytane) and hopanoids. Highest contributions of preferentially long-chained *n*-alkanes were documented in samples from the Grès médioliasiques Fm (Interval 4). High steroid/hopanoid ratios indicate mainly eukaryotically derived organic matter.

6.3.2. Eukaryotic versus prokaryotic contributions (steroid/hopanoid ratio)

Hopanes and hopenes were identified in the samples from Core FR210-078, whereby regular hopanes occur in $\alpha\beta\text{S}+\text{R}$, $\beta\alpha\text{S}+\text{R}$ as well as in $\beta\beta$ configuration (see Fig. A11 in the appendix for a representative *m/z* 191 ion chromatogram). In this chapter only changes in the overall hopanoid contributions will be addressed to assess the relative contributions of prokaryotes (bacteria) relative to eukaryotic (mainly algae) sources. An important feature of the hopane distribution is the absence of significant concentrations of 2Me- and 3Me-hopanes, indicating that specific classes of cyanobacteria and methanotrophs did not contribute significant amounts to the sedimentary OM. However, caution must be taken when interpreting the absence of 2Me- and 3Me-hopanes as evidence for the absence of these organisms as not all cyanophytes and methanotrophs will synthesize these compounds. Changes in the contributions from eukaryotes and prokaryotes can be

inferred from the evolution of the steroid/hopanoïd ratio, which reflects the sum of all steroidal compounds (here diasterenes, 4Me diasterenes and regular steranes have been considered; see m/z 217, 257, 271 chromatograms: Figs. A12, A13 in the appendix) versus the sum of all hopanoïds (here regular hopanes from C₃₀ to C₃₅ have been considered; see m/z 191 chromatogram: Fig. A11 in the appendix).

Low and less variable steroid/hopanoïd ratios, ranging from 1 to 9, have been determined in samples from Interval 4 (upmost *P. spinatum* zone and lower *D. tenuicostatum* zone). In contrast, samples from the Pl-Toa boundary black shale show ratios of ~15. High ratios that may exceed values of 30, but mainly vary between 15 and 38 occur in samples from Interval 3 (upmost *D. tenuicostatum* zone and lower *H. elegantulum* subzone). One sample in the upper part of this interval shows a very low ratio of about 9. Steroid/hopanoïd ratios in samples from Interval 2 (upper *H. elegantulum* subzone) mainly vary between 10 and 30, whereby an increasing trend from values of ~12 to ~25 is documented through the lower part of this interval. Afterwards ratios decrease to values of about 15. Ratios in samples from Interval 1 (*H. falciferum* subzone) range from 10 to 30, whereby high values > 20 are characteristic for the lower and upper part of this interval (Fig. 6-2).

6.3.3. Distribution of steroidal compounds

Steroidal compounds, almost entirely originating from eukaryotes (see Tab. 6-1), are present as regular steranes, diasterenes, diasteranes and 4Me-diasterenes, whereby diasterenes and 4Me-diasterenes are the dominating compounds. These steroids originate from sterol precursors and are formed during diagenesis (Mackenzie et al., 1982). The 4Me-diasterenes will not be discussed here, as these compounds show a complex distribution pattern, but do not reveal significant trends. The distribution pattern of the 4Me-diasterenes is shown in figure S6-3 in the supplementary.

Desmethyl diasterenes and regular steranes in the range from C₂₇ to C₃₀ and can be associated different algal classes (Tab. 6-1). Diasterenes occur in βββS+R as well as in βαβS+R substitution. Regular steranes occur as αααS+R and αββS+R isomers with some subordinate βαα-isomers, whereby the distribution pattern is clearly dominated by steranes in αααR isomerisation. Representative ion chromatograms and molecular structures of diasterenes and regular steranes are given in the appendix (Figs. A12, A13A). Diasterenes show a strong correlation with regular steranes, whereby correlation coefficients are mainly >0.7 (see supplementary Fig. S6-2). To express changes in the abundance of the different steroid classes it is therefore reasonable to express the abundance as the sum of the diasterene and the corresponding regular sterane. Changes in the contribution are expressed in percentage of total steroids. The steroid distribution is characterized by high concentrations of C₂₉ and C₂₇ steroids that exceed C₂₈ and C₃₀ steroid abundances (C₂₉ > C₂₇ > C₂₈ >> C₃₀). The stratigraphic evolution of each steroid class exhibits a high variability and is shown in figure 6-3.

C₂₇ steroids: The concentration of C₂₇ steroids in samples from Interval 4 (the *P. spinatum* and the lower *D. tenuicostatum* zones) varies between 25 and 32%, whereby a slightly increasing trend is documented throughout this interval. A higher abundance of C₂₇ steroids is found in samples from the PI-Toa boundary interval, where concentrations reach 37% (Fig. 6-3). Low concentrations of C₂₇ steroids, ranging from ~25 to ~35%, occur in samples from Interval 3 (upmost *D. tenuicostatum* zone and lower *H. elegantulum* subzone), whereas C₂₇ steroid concentration exceeds 40% in one sample from the upmost part of this interval. Concentrations of C₂₇ steroids ranging from ~25 to ~40% have been measured in samples from Interval 2 (upper *H. elegantulum* subzone), whereby higher concentrations (>32%) are always bound to the laminated horizons identified within this interval. Throughout Interval 1 (*H. falciferum* subzone) C₂₇ steroid concentrations decline from values of ~32% in the lowermost part to values of ~27% in the upper part (Fig. 6-3).

C₂₈ steroids: Low concentrations of C₂₈ steroids, ranging from ~12 to ~15%, are specific for samples from Interval 4, whereas concentrations exceed 20% in the PI-Toa boundary interval (Fig. 6-3). The abundance of C₂₈ steroids rapidly increases by ~5% at the base of the Interval 3. Throughout this interval the concentration of C₂₈ steroids remains high and varies between 17% and 20%, with only one sample reaching a higher concentration of 24%. The abundance of C₂₈ steroids remains high in samples from Interval 2, whereby values are variable and range from ~15 to ~22%. Similar concentrations in C₂₈ steroids are present in samples from Interval 1, whereby a slightly increasing trend is observed through this interval (Fig. 6-3).

C₂₉ steroids: The highest abundance of C₂₉ steroids is noted for samples from Interval 4, where concentrations vary between ~45% and ~55%. A drastic drop in the C₂₉ steroid concentration is observed in samples from the PI-Toa boundary interval, where values decline to ~38%. A decrease from 50 to 40% in the lowermost part of Interval 3 is followed by a return to concentrations of ~50%. Afterwards, values remain relative high and vary around 45%, whereby the upper part of this interval exposes a high variability in C₂₉ steroid concentration (Fig. 6-3). Relative proportions of C₂₉ steroids in samples from Interval 2 vary between 35% and 48%. Highest C₂₉ steroid concentrations (>44%) are documented in bioturbated and less distinctively laminated horizons, whereas laminated horizons show lower C₂₉ steroid concentrations (Fig. 6-3). Throughout Interval 1 concentration of C₂₉ steroids increase from ~40% to ~47% (Fig. 6-3).

C₃₀ steroids: Low C₃₀ steroid concentrations, ranging from 6% to 7%, are reported for samples from Interval 4, whereas samples from the PI-Toa boundary interval show lower values of about 4.2%. Concentrations remain low throughout Interval 3 and do not exceed 8% (Fig. 6-3). A gentle increase in C₃₀ steroid concentration is documented throughout the lower part of Interval 3, whereas a decreasing trend is noted throughout the upper part. Samples from the Interval 2 and 1 show significantly increased but highly variable concentrations of C₃₀ steroids, ranging from ~6% to ~10% (Fig. 6-3). Throughout Interval 2, high C₃₀ contributions are bound to the bioturbated horizons showing a more indistinct lamination, whereas lower C₃₀ steroid concentrations are observed in samples from laminated horizons (Fig. 6-3).

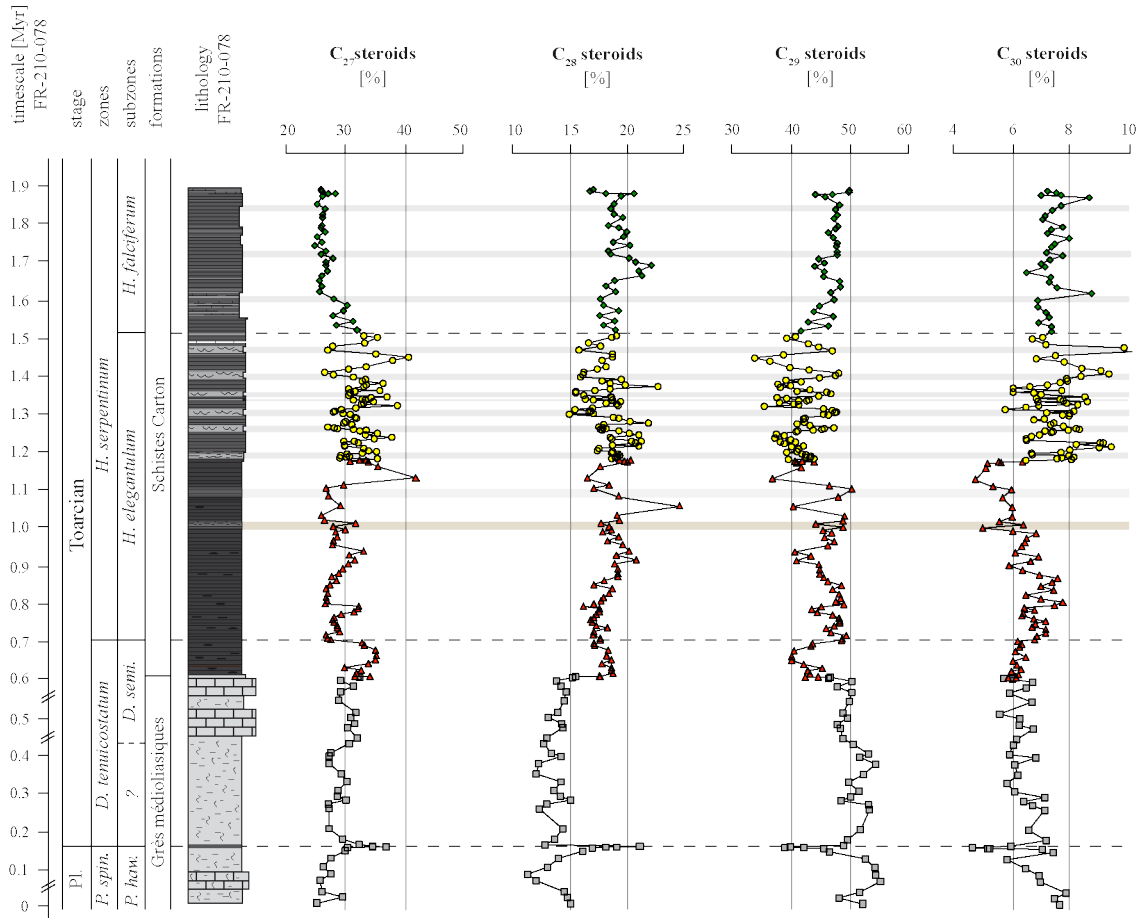


Figure 6-3: Stratigraphic evolution of steroid biomarkers reflecting changes in the eukaryotic input. Changes can be linked to shifts in the algal community structure, whereby C_{29} -steroids can also reflect contributions from land plants. The highest variability in the steroid input has been documented throughout the upper *H. elegantulum* subzone (Interval 2) that is also highlighted by pronounced facies changes. Bioturbated horizons in the upper *H. elegantulum* subzone are highlighted grey.

6.4. Discussion

6.4.1. Assessing the steroid sources

Steroid distribution pattern

The relative distribution of C_{27} to C_{29} steroids can be associated with different biological sources that vary in dependence of environmental and oceanographic conditions. According to the classical approach established by Huang & Meinschein (1979) the steroid distribution in the Lorraine Sub-Basin reflects input from algae communities that are common for estuarine to partly open marine environments, thus environmental conditions differing from normal marine settings (Fig. 6-4). However, significant input of terrigenous derived OM, characteristic for estuarine environments, is only documented for the Grés médioliasiques Fm (Interval 4), which is supported by high TAR values (>1) and the overall high abundance of n -alkanes (Fig. 6-2).

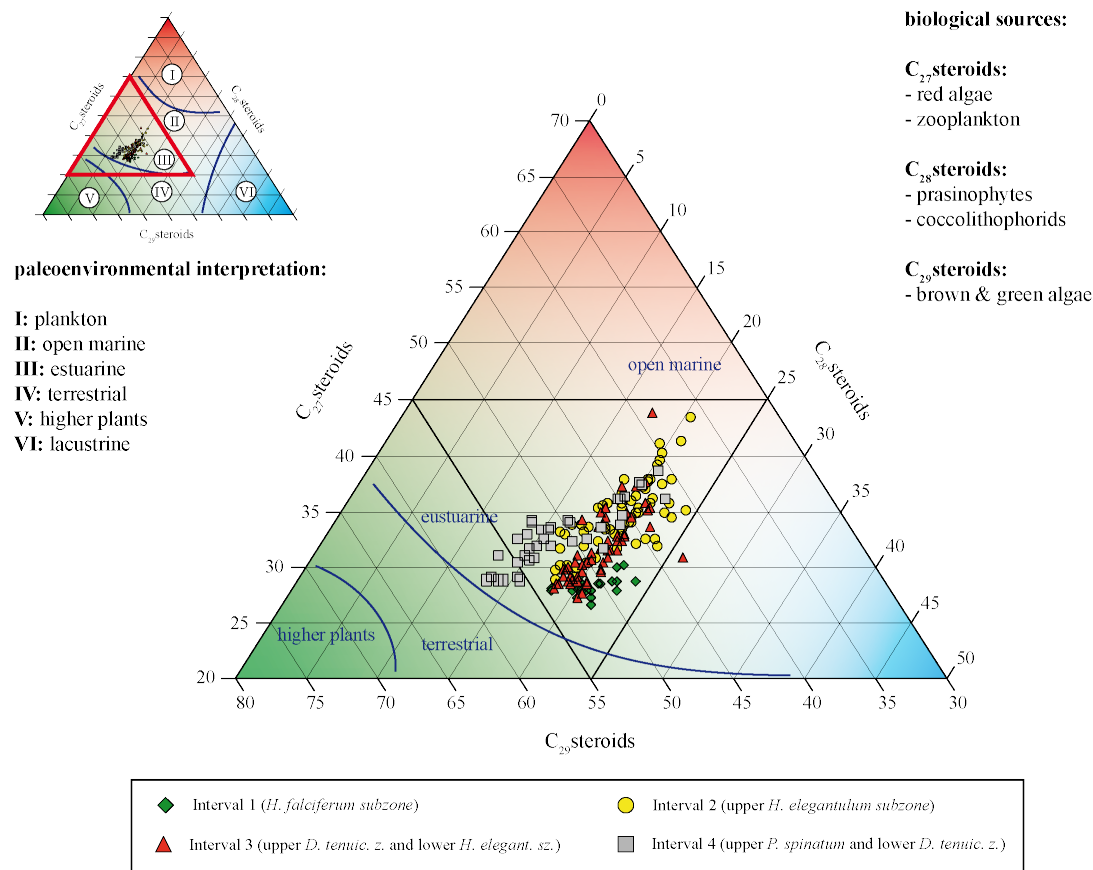


Figure 6-4: A ternary-plot for steroids in the range from C_{27} to C_{29} (Huang & Meinschein, 1979) reveals increased contributions of C_{29} steroid attributed to land plants as well as reduced contributions of C_{28} steroids for samples from the Grés médioliasiques Fm. Samples from the Schistes Carton Fm exhibit elevated but relative uniform proportions of C_{28} steroids, but highly variable contributions of C_{27} and C_{29} steroids. C_{29} steroids of this formation, however, are not expected to derive from higher land plants but rather from aquatic sources. The overall distribution of steroids indicates contributions from algae communities that differ from normal marine communities, supporting the prevalence of special oceanographic conditions.

Elevated contributions of C₂₉ steroids might therefore reflect input of higher land plants. On the contrary, low TAR values (<0.7) and a drastically reduced abundance of *n*-alkanes, documented from the Schistes Carton Fm does not support significant contribution of land plant derived OM. Almost exclusively marine derived organic matter is also supported by microscopic observations that confirm a figured OM mainly composed present of alginites (see Fig. 4-6 in Chapter 4). Therefore, high concentrations of C₂₉ steroids in samples from the Schistes Carton Fm (Intervals 1 - 3) are expected to originate from brown or green algae (Huang & Meinschein, 1979), which is in agreement with findings from contemporaneous sediments (Song et al., 2014 and references therein). It can thus concluded that the steroid distribution in the Lorraine Sub-Basin reflects input from algae communities differing from those of normal marine ecosystems, which hints to special oceanographic and environmental conditions.

Covariation of steroids with environmental parameters (TAR and tri-/di-MTTC ratio)

Linking the different steroids in the range from C₂₇ to C₂₉ to specific algal sources is complicated by the fact that algae taxa, characteristic for specific environments, synthesize a suite of steroids (Tab. 6-1). To assess possible biological sources of steroids cross-plots of different steroid proportions with the TAR and the tri-/di-MTTC ratios can be employed (Fig. 6-5). Such discrimination diagrams may guide in distinguishing steroid contribution from marine algae from those of algae adapted to conditions deviating from normal marine environments. Hereby, changes in the TAR reflect variable contributions from land plant derived organic matter and changes in the tri-/di-MTTC ratios can be associated with changes in SSS.

C₂₇ steroids: Contributions of C₂₇ steroids can be associated with algae common for full marine environments, including *Bangiophyceae* and *Rhodophyceae* (red algae) (Tab. 6-1). A negative trend between the TAR and C₂₇ steroids documented within Intervals 4 and 2 indicates that C₂₇ steroids to be associated with preferentially marine (red) algae, whose abundance oppose that of terrigenous input. Low concentrations of C₂₇ steroids in the Intervals 3 and 1, characterized by low TAR values as well, indicate that the reduced contribution from terrigenous sources were not accompanied by a high abundance of marine C₂₇ steroid synthesizing (red) algae (Fig. 6-5A). Thus, these stages must represent environmental conditions that were not favorable for these full marine organisms. Furthermore, this pattern indicates that changes in the abundance of marine algae were not exclusively controlled by the sea level. The cross-plot of tri-/di-MTTCs ratios with C₂₇ steroid concentrations reveals low concentrations of C₂₇ steroids in Intervals 3 and 1 to coincide with high tri-/di-MTTC ratios indicating reduced SSS, thus, conditions not favorable for fully marine algae (Fig. 6-5B).

C₂₈ steroids: C₂₈ steroids can be occur in a variety of algae associated with freshwater environments (e.g. *Chlorophyceae*, *Cryptophyceae*, *Euglenophyceae*, *Prasinophyceae*), but can also be derived from algae associated with normal marine conditions (e.g. *Bangiophyceae*, *Haptophyceae/Coccolithophores*) (Tab. 6-1). The origin of C₂₈ steroids in algal classes associated with highly contrasting environments generates a more complex pattern exposed in the cross-plot of the TAR with C₂₈ steroids (Fig. 6-5C). Samples from Intervals 4, 2 and 1 follow an overall negative

background trend (negative regression), indicative of contributions of C₂₈ steroids of marine algae origin to correlate with stages of high sea level and reduced contribution from terrigenous sources. Significant contributions of C₂₈ steroids in the Intervals 2 and 1 might be derived from *Coccolithophores* (*Haptophyceae*) known to be important primary producers during the Lower Toarcian, but which experienced a recovery in these intervals subsequent to a previous biocalcification crisis (Hermoso et al., 2009b; Clémence, 2015). Samples from Interval 3 slightly differ from this trend and are highlighted by a reduced abundance of C₂₈ steroids, which might indicate the impact of the biocalcification crisis that caused a demise of calcareous nannoplankton, including *Coccolithophores* (e.g. Hermoso et al., 2009b; Clémence, 2015). However, despite of a biogenic carbonate blackout throughout Interval 3 the concentration of C₂₈ steroids do not decline dramatically, indicating that significant contributions of these compounds were delivered by other algae classes, like *Chlorophyceae*, *Cryptophyceae*, *Euglenophyceae*, *Prasinophyceae*. A cross-plot of the tri-/di-MTTC ratio with C₂₈ steroids also indicates that normal marine C₂₈ synthesizing algae were replaced by those members tolerant towards reduced SSS (Fig. 6-5D).

C₂₉ steroids: Samples from Intervals 4 and 2 reveal an overall positive trend between TAR and C₂₉ steroids supporting the assignment of these steroids to land plant sources (Fig. 6-5E). Significant influx of higher plants is in agreement with an overall low sea level during this period (see Chapter 4). A different pattern is observed for samples from the Intervals 3 and 1 that show low TAR values and relatively high contributions of C₂₉ steroids (Fig. 6-5E). Due to the lack of allochthonous terrigenous input, this pattern can be explained a C₂₉ steroid source from fully marine algae, like *Haptophyceae* or *Pelagophyceae*. However, C₂₉ steroids can also be derived from algae tolerant towards reduced SSS, comprising *Chlorophyceae*, *Euglenophyceae*, *Eustigmatophyceae*, *Prasinophyceae*, or *Raphidophyceae* (Tab. 6-1). A C₂₉ steroid origin from freshwater tolerant algae in Intervals 3 and 1 agree well with a positive correlation of tri-/di-MTTC ratios with C₂₉ steroids (Fig. 6-5F).

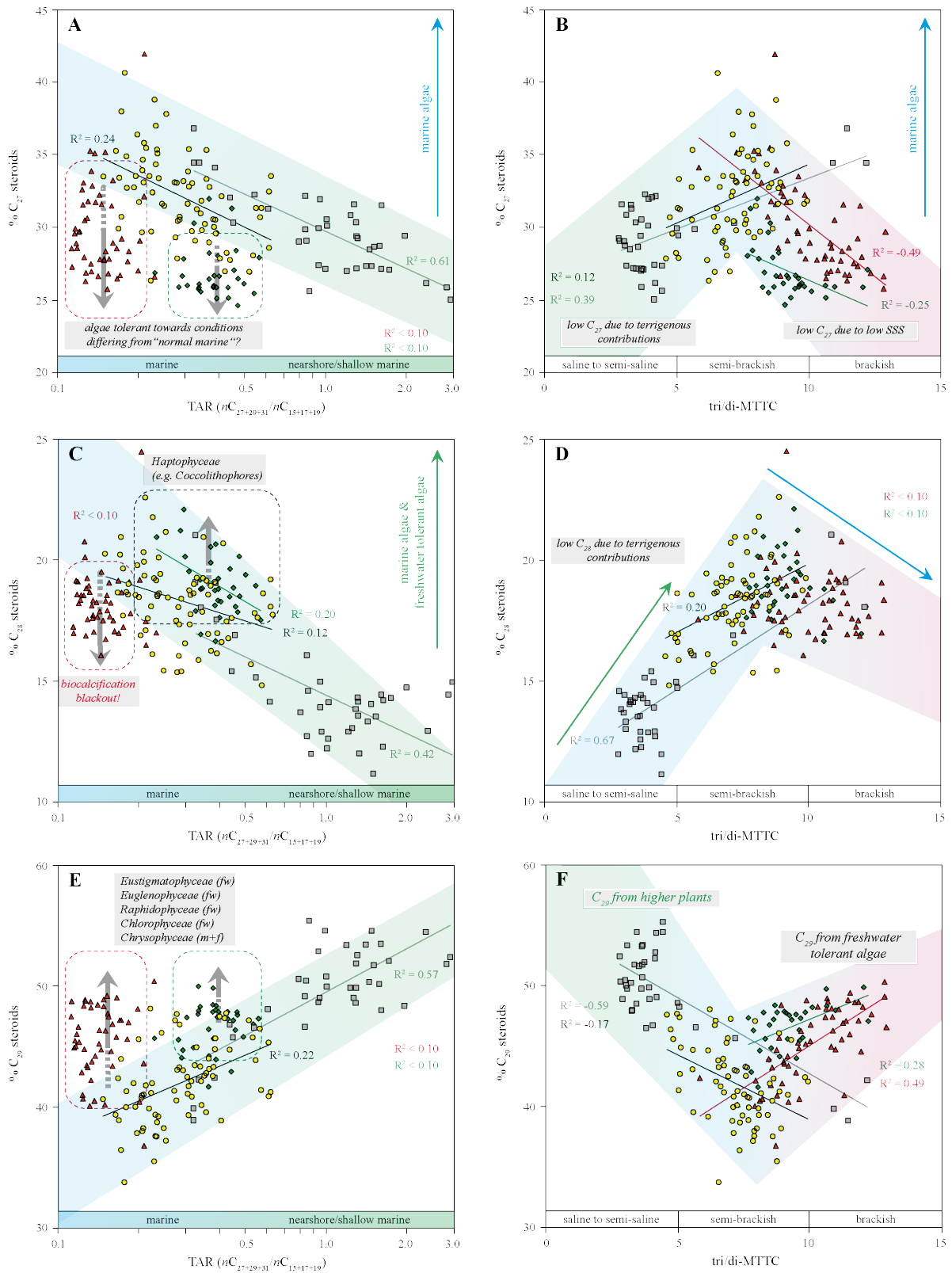


Figure 6-5: Cross-plots of steroids in the range from C_{27} to C_{29} with the TAR and the ratio of tri/di-MTTC provide information about environmental conditions and allow to disentangle enhanced influx of terrigenous lipids upon low sea level stands from that of freshwater adapted algae upon sea level high stand. Significant terrigenous fluxes are limited to the Grés médioliasiques Fm (Interval 4) and freshwater stratification characterized by hyposalinity-tolerant algae is confined to Interval 3 (upmost *D. tenuicostatum* zone and lower *H. elegantulum* subzone).

Abundance of C₃₀ steroids as indicator for *Pelagophyceae* input

Specific C₃₀ steroids (C₃₀ desmethylsteroids) are diagnostic for *Pelagophyceae* (Volkman et al., 1998; Volkman, 2003), an algae class restricted to marine environments (Peters et al., 2005). The relative low abundance of these compounds (<10%) indicates that *Pelagophyceae* did not belong to the most important primary producers, possibly due to oceanographic conditions that were not favorable for these algae. The affinity of C₃₀ synthesizing *Pelagophyceae* towards fully marine environments is well expressed by the negative regression documented between TAR values and the abundance of C₃₀ steroids. Low contributions of C₃₀ steroids in the upmost *P. spinatum* and lower *D. tenuicostatum* zones (Interval 4) are thought to be associated with a low sea level and significant contributions of terrigenous derived OM (Fig. 6-6A; also see Chapter 4). In contrast, elevated proportions of C₃₀ steroids in samples from the upper *H. elegantulum* and *H. falciferum* subzones (Intervals 1 & 2) are due to more marine conditions upon high sea level and reduced input of higher land plant lipids, as indicated by low TAR values (Fig. 6-6A). Interestingly, samples from the upmost *D. tenuicostatum* zone and lower *H. elegantulum* subzone (Interval 3) differ from this trend. The cross-plot of TAR values versus the abundance of C₃₀ steroids indicates that the rapid transgression, starting in the upmost *D. tenuicostatum* zone was not accompanied by a radiation of *Pelagophyceae*. The low abundance of C₃₀ steroids and thus of *Pelagophyceae* in Interval 3 is related to drastically decreased SSS as indicated by high tri-/di-MTTC ratios (Fig. 6-6B; also see Chapter 4). The overall negative regression documented in the cross-plot of tri-/di-MTTC ratio with the abundance of C₃₀ steroids, confirm *Pelagophyceae* to be intolerant towards surface water freshening (Fig. 6-6B). This plot further demonstrates that the abundance of *Pelagophyceae* was controlled by the interaction of sea level and SSS changes.

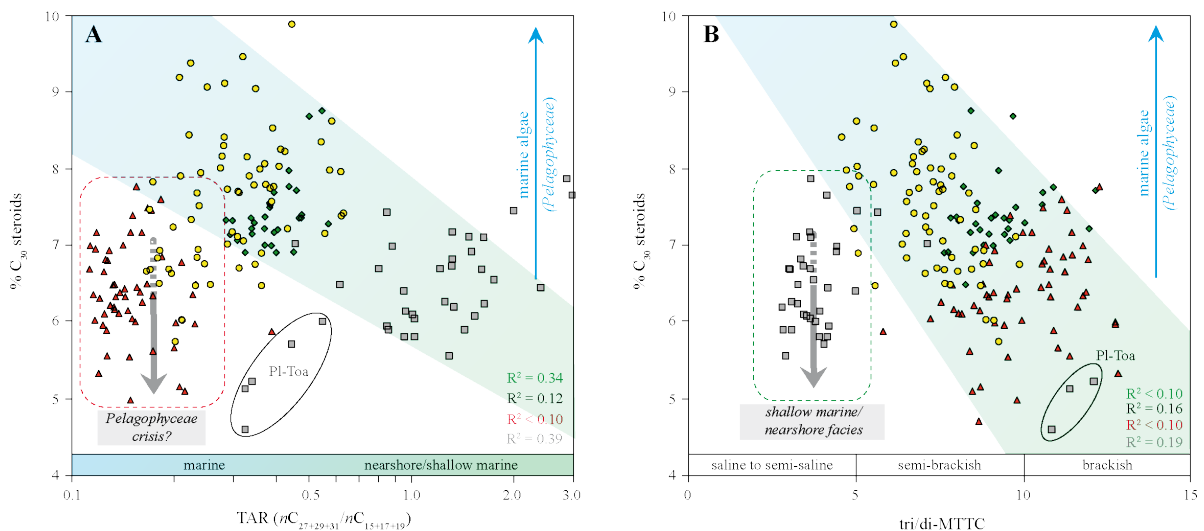


Figure 6-6: **A)** The cross-plot of the TAR versus the abundance of C₃₀ steroids exhibits a negative correlation, indicating that the abundance of *Pelagophyceae* was bound to marine conditions during stages of high sea level. Samples from the Intervals 4, 2 and 1 follow this trend, whereas samples from the Interval 3 significantly differ, pointing to other factors than sea level controlling abundances of *Pelagophyceae*. **B)** The cross-plot of tri-/di-MTTCs versus C₃₀ steroids shows an overall negative correlation, indicating that *Pelagophyceae* were most abundant during phases of normal marine salinity. The low abundance of C₃₀ steroids in samples from Interval 3 can be explained by drastically reduced SSS inferred from high tri-/di-MTTC ratios.

Inferred steroid sources

During the Early Toarcian the phytoplankton in the Lorraine Sub-Basin was dominated by eukaryotes (algae), whereas prokaryotes (cyanobacteria) did not play a major role and contributed only a small fraction to the sedimentary organic matter. The preponderance of eukaryotes is well expressed by the high steroid/hopanoid ratios (Fig. 6-2). Changes in the community structure of eukaryotes are reflected by variations in the abundance of the different steroids, which is however complicated by variations in the sources of single steroid compounds. Thus, interpretation of steroid ratios must always be discussed in the context of other environmental data. C₂₇ steroids can be linked to red algae (*Bangiophyceae*, *Rhodophyceae*) as well as to *Eustigmatophyceae*, algae groups that are most common in marine environments (Tab. 6-1). C₃₀ n-propylsteroids can be solely linked to *Pelagophyceae*, an algae group that exclusively occurs in fully marine environments. It can be assumed that the abovementioned sources of C₂₇ and C₃₀ steroids did not change significantly through the interval studied and that these steroids reflect input from algae adapted to fully marine conditions (Tab. 6-2). Sources of C₂₈ steroids are more variable and significantly change throughout the sections investigated. C₂₈ steroids can be attributed to both, marine algae (e.g. *Haptophyceae*, *Chrysophyceae*, *Pelagophyceae*), as well as freshwater tolerant algae groups (e.g. *Prasinophyceae*, *Chlorophyceae*, *Euglenophyceae*) (Tab. 6-1). A high source variability can also be attested to C₂₉ steroids that can originate from marine algae (e.g. *Haptophyceae*, *Chrysophyceae*, *Pelagophyceae*), from freshwater tolerant algae (e.g. *Chlorophyceae*, *Euglenophyceae*, *Eustigmatophyceae*, *Xanthophyceae*) and also from higher land plants (Tabs. 6-1, 6-2).

Chapter Six: Phytoplankton community dynamics

Table 6-2: Assumed steroid sources for the different intervals distinguished on the base of lithological and geochemical parameters. C₂₇ and C₃₀ steroids can be linked to fully marine algae. Sources of C₂₈ steroids are more variable and change throughout the different intervals. In Intervals 4 and 2 C₂₈ steroids are thought to preferentially derive from marine algae, whereas in the Intervals 3 and 1 freshwater tolerant algae contribute significant amounts to the C₂₈ steroids. Contributions of C₂₉ steroids can be linked to marine algae and to the freshwater tolerant algae, but might also be derived from higher land plants. Significant influx from terrigenous sources must be considered for the Interval 4. The relative abundance of the different steroid proportions from C₂₇ to C₃₀ is shown in the right column (average abundance given for each interval).

steroid Interval	C ₂₇ steroids	C ₂₈ steroids	C ₂₉ steroids	abundance [%]			
				C ₂₇	C ₂₈	C ₂₉	
Interval 1 (<i>H. falciferum</i> subzone)	<div style="display: flex; align-items: center; justify-content: center;"> <div style="border: 1px solid blue; padding: 2px; margin: 0 5px;">fully marine algae: - <i>Bangiophyceae</i> (red algae) - <i>Eustigmatophyceae</i> - <i>Rhodophyceae</i> (red algae)</div> <div style="flex-grow: 1; border-left: 1px solid blue; border-right: 1px solid blue; position: relative;"> <div style="position: absolute; top: -10px; left: 50%; transform: translate(-50%, -100%);">↑</div> <div style="position: absolute; bottom: -10px; left: 50%; transform: translate(-50%, 100%);">↓</div> </div> </div>	freshwater tolerant & marine algae: - <i>Chlorophyceae</i> (green algae) - <i>Euglenophyceae</i> - <i>Eustigmatophyceae</i> - <i>Xanthophyceae</i>	- <i>Haptophyceae</i> (Coccoliths) - <i>Chrysophyceae</i> (golden algae) - <i>Pelagophyceae</i>	10 40 60 80	C ₂₇	C ₂₈	C ₂₉
Interval 2 (upper <i>H. elegantulum</i> subzone)		marine algae: - <i>Haptophyceae</i> (Coccoliths) - <i>Bangiophyceae</i> (red algae) - <i>Chrysophyceae</i> (golden algae) - <i>Pelagophyceae</i>	marine algae (& land plants): - <i>Haptophyceae</i> (Coccoliths) - <i>Chrysophyceae</i> (golden algae) - <i>Pelagophyceae</i>	34.7	19.8	45.5	
Interval 3 (upmost <i>D. tenuicostatum</i> zone and lower <i>H. elegantulum</i> subzone)		freshwater tolerant algae: - <i>Chlorophyceae</i> (green algae) - <i>Euglenophyceae</i> - <i>Prasinophyceae</i> - <i>Rapidophyceae</i>	freshwater tolerant algae: - <i>Chlorophyceae</i> (green algae) - <i>Euglenophyceae</i> - <i>Eustigmatophyceae</i> - <i>Xanthophyceae</i>	31.9	19.4	48.7	
Interval 4 (upmost <i>P. spinatum</i> and lower <i>D. tenuicostatum</i> zones)		mainly marine algae: - <i>Haptophyceae</i> (Coccoliths) - <i>Bangiophyceae</i> (red algae) - <i>Chrysophyceae</i> (golden algae) - <i>Pelagophyceae</i>	land plants & marine algae: - <i>Chrysophyceae</i> (golden algae) - <i>Haptophyceae</i> (Coccoliths) - <i>Pelagophyceae</i>	31.7	15.4	52.9	

Pelagophyceae/ (fully marine) → 6.5 6.7 6.9 7.1 7.3 7.5
C₂₇ steroids [%]

6.4.2. Changes in the phytoplankton community structure

Steroid distribution patterns support an evolution of the marine phytoplankton linked to changes in environmental conditions, whereby sea level as well as the SSS played a critical role. Moreover, changes in nutrient supply, ocean acidity and SST strongly affected the marine primary producers (Danise et al., 2015), hence also contributing to changes in steroid input and composition. Ocean acidification preferentially affected the calcareous nannoplankton (e.g. *Haptophyceae*), which has been demonstrated by micropaleontological investigations (e.g. Erba, 2004; Mattioli et al., 2008, 2009; Hermoso et al., 2009b, 2012; Suan et al., 2010; Clémence et al., 2015). The interaction of these environmental parameters resulted in complex steroid distribution pattern. Moreover, data highlight the role of multiple biological sources of single steroid species that change throughout the studied interval. Therefore, steroid-based ratios as proxies for changes in the phytoplankton community structure cannot be applied unambiguously, when discussing its changes throughout the entire section characterized by contrasting oceanographic conditions. The evolution of selected steroids ratios over the entire sediment succession is show in the supplementary (Fig. S6-4). Here the evolution of the phytoplankton community structure is discussed by interpreting the relative abundance of individual steroid species with respect to changes in environmental parameters.

During the upmost *P. spinatum* and lower *D. tenuicostatum* zones (Interval 4), a period that reflects a low sea level with normal SSS (see Chapter 4), the phytoplankton assemblage was dominated by algae groups adapted to shallow though fully marine environments, comprising red algae (*Bangiophyceae*, *Rhodophyceae*) and *Eustigmatophyceae* as well as *Pelagophyceae* and *Haptophyceae* (Fig. 6-7; Tab. 6-2). However, significant contributions of C₂₉ steroids were derived from higher land plants, as confirmed by the high abundance of long-chain odd-numbered *n*-alkanes (Fig. 6-2; Tab. 6-2).

The upmost *D. tenuicostatum* zone and the lower *H. elegantulum* subzone (Interval 3) are associated with severe environmental changes, including global warming and a rise in atmospheric CO₂ concentration that caused a biocalcification crisis. Global warming led to the melting of polar ice caps, which resulted in a glacio-eustatic sea level rise and a massive freshwater discharge to the Western Tethyan shelf (Chapter 4). Paleontological observations confirmed that these environmental changes led to a reorganization of the marine phytoplankton community structure, including a radiation of *Prasinophyceae* (e.g. Bucefalo Palliani et al., 2002; van de Schootbrugge et al., 2005a, 2013) and a demise of calcareous nannoplankton (e.g. Suan et al., 2010; Clémence et al., 2015). However, profound changes in the phytoplankton community structure are not reflected by significant changes in the relative distribution of steroids (Fig. 6-7; Tab. 6-2). Nevertheless, in the context of environmental changes it can be shown that steroid sources shifted during this interval. Biomarker data attest to a marine phytoplankton that was dominated by freshwater tolerant algae groups, like *Prasinophyceae*, *Chlorophyceae*, or *Euglenophyceae* that contributed significant amounts of C₂₈ and C₂₉ steroids (Fig. 6-7; Tab. 6-2). Significant contributions of C₂₈ steroids from *Haptophyceae* can be excluded as the calcareous nannoplankton experienced a biocalcification crisis, which is proven by the very low carbonate content during this interval (mainly <10 wt.%).

Concentrations of C₂₇ and C₃₀ steroids show no significant increase, which indicates that the sea level rise was not accompanied by a radiation of marine algae, like *Pelagophyceae* and red algae. Low contributions from marine algae groups can be explained by low SSS that has not been favorable for these algae groups (Fig. 6-7; Tab. 6-2). Results reinforce findings by [Bucefalo Palliani et al. \(2002\)](#) and [van de Schootbrugge et al. \(2005a; 2013\)](#), who showed that during the Toa-CIE interval and the associated environmental perturbation normal marine phytoplankton was replaced by opportunistic taxa, including a radiation of green algae.

In the upper *H. elegantulum* subzone (Interval 2) the calcareous nannoplankton (*Haptophyceae*) experienced a recovery and a new radiation (e.g. [Bucefalo Palliani et al., 2002](#); [Suan et al., 2010](#); [Clémence et al., 2015](#)). Increased contribution from calcareous nannoplankton can be inferred from an increase in the biogenic carbonate content and might also have contributed to significant amounts of C₂₈ steroids (Fig. 6-7; Tab. 6-2). Moreover, contributions of C₂₇ and C₂₉ steroids might also derive from *Haptophyceae* (Tab. 6-1). A regressive phase, confirmed for this interval, was associated with increased contributions of land plant derived biomass as indicated by elevated TAR values as well as by the occurrence of abundant sporinities (Fig. 4-6 in Chapter 4). Consequently, C₂₉ contribution from terrigenous sources cannot be excluded. Despite the regressive trend fully marine algae groups comprising red algae (*Bangiophyceae*, *Rhodophyceae*), *Eustigmatophyceae*, *Chrysophyceae* and *Pelagophyceae* experienced a new radiation, which is indicated by a drastic increase in C₂₇ and C₃₀ steroids (Fig. 6-7; Tab. 6-2).

The transgressive phase during the *H. falciferum* subzone was associated with a decrease in SSS (Chapter 4), which resulted in a decrease of marine red algae (*Bangiophyceae*, *Rhodophyceae*) and *Pelagophyceae*, as expressed by a slight decrease in the concentrations of C₂₇ and C₃₀ steroids (Fig. 6-7; Tab. 6-2). High proportions of C₂₈ and C₂₉ steroids in this interval might be associated with contributions from *Haptophyceae* as supported by the high abundance of calcareous nannoplankton during this period (e.g. [Clémence et al., 2015](#)). The reduced abundance of fully marine algae (*Bangiophyceae*, *Rhodophyceae*, *Pelagophyceae*) suggests that of C₂₈ and C₂₉ steroids might also have originated in algae groups tolerant towards lowered SSS (e.g. *Prasinophyceae*, *Chlorophyceae*, *Euglenophyceae*) (Fig. 6-7; Tab. 6-2).

Chapter Six: Phytoplankton community dynamics

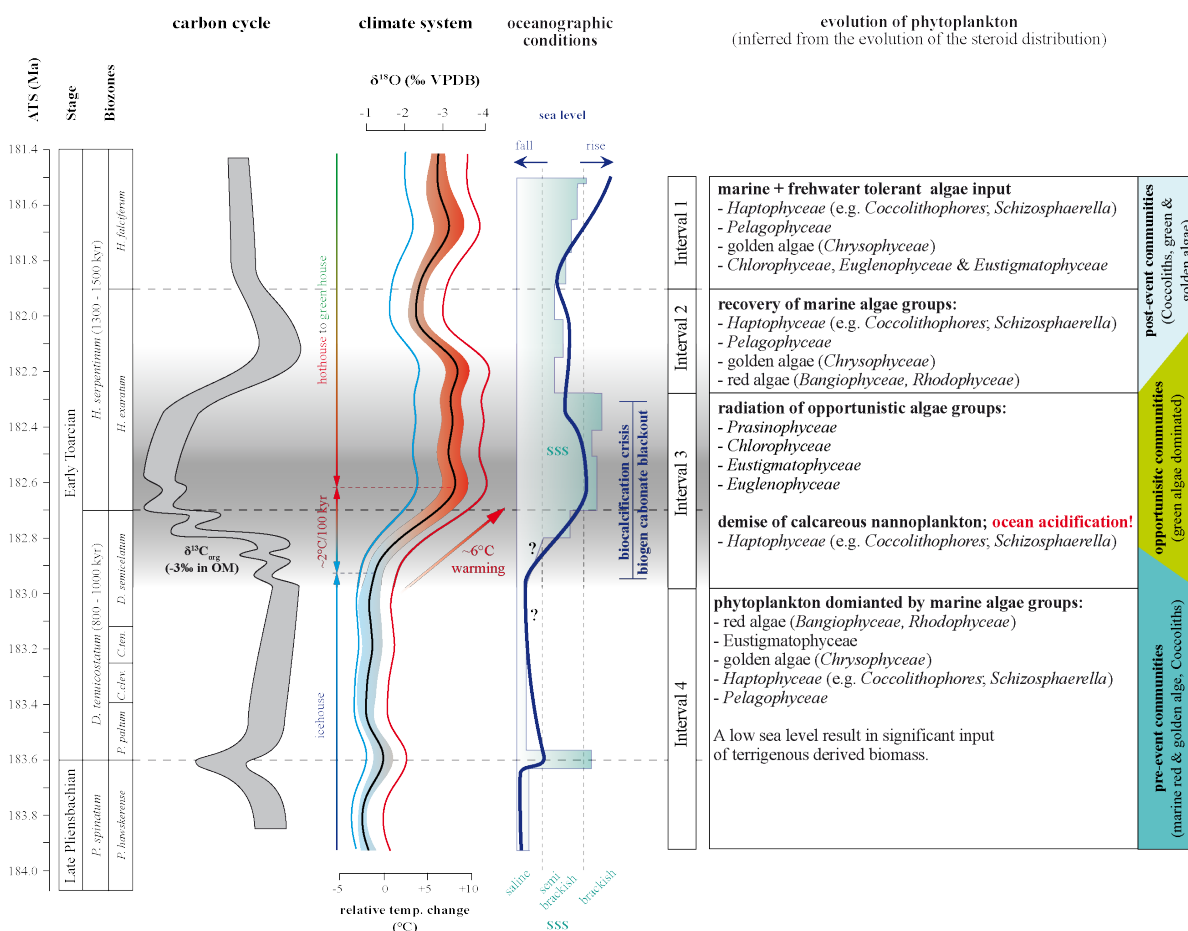


Fig. 6-7: The evolution of marine phytoplankton during the Early Toarcian environmental crisis inferred from the steroid distribution pattern, in the context of environmental changes. During the acme of the Early Toarcian environmental crisis (Interval 3) that is associated with a negative CIE, global warming, sea level rise and a drop in SSS, normal marine algae groups (e.g. red algae, golden algae, *Pelagophyceae*, *Haptophyceae*) were replaced by opportunistic algae taxa (*Prasinophyceae*, *Chlorophyceae*, *Euglenophyceae*). Changes in the Phytoplankton community structure can be associated with the acidification of the oceans (*Haptophyceae*) and with the freshening of the shelf seas (e.g. radiation of freshwater tolerant *Prasinophyceae*). Radiations of freshwater-tolerant algae taxa might be however most pronounced for near shore shelf settings. Nannoplankton in the pelagic setting might have been mainly affected by global warming (rise in SST) and ocean acidification that resulted from elevated atmospheric CO₂ concentration.

6.4.3. Phytoplankton response towards the Toa-CIE

The biotic crisis that is associated with the environmental changes during the Early Toarcian resulted in a shift in the primary producer community structure. According to Danise et al. (2015) or Clémence et al. (2015) nektonic communities suffered from increases SST, an acidification of the ocean and from the eutrophication of the shelf seas. Moreover, results of this chapter highlight the role of reduced SSS that has previously proposed as factor controlling changes in the community structure of calcareous nannoplankton (Hermoso et al., 2009b, 2012). In contrast, the extinction of benthic communities can be linked to prolonged anoxia that lasted for several millennia (Danise et al., 2013; Caswell & Coe, 2014), whereas the low extinction rates of nektonic communities, including marine phytoplankton, remain challenging (Dera et al., 2010; 2011b).

Significant changes in the community structure of primary producing phytoplankton are also expressed by changes in the distribution of steroid biomarkers. High-resolution biomarker data confirm that significant shifts in the community structure of marine phytoplankton can be linked to separate carbon injections, represented by the negative carbon isotope shifts (II-A, II-B, II-C) (Fig. 6-8, 6-9). Overall high steroid/hopanoid ratios indicate that algae dominated the phytoplankton community structure (Fig. 6-8). Cyanobacteria did not play an important role as primary producer, which is reinforced by the absence of 2Me-hopanoids that indicate cyanobacteria input (Summons et al., 1999). Low steroid/hopanoid ratios in the sediments of the Grés médioliasiques Fm resulted from enhanced biodegradation (Peters et al., 2005), which is confirmed by sedimentological observations. However, the single injections of ^{12}C -enriched carbon were accompanied by a short-lived decrease in the steroid/hopanoid ratio that cannot be explained by enhanced OM reworking, as sedimentological observations provide no evidence for enhanced bioturbation processes. Therefore, the decrease in the steroid/hopanoid ratio can be interpreted to reflect brief episodes of enhanced prokaryotic biomass input (cyanobacteria blooms?) and/or result from a decrease in contributions from algae. A decrease in eukaryotic contribution can be attributed to increased environmental stress caused the injection of CO_2 into the Earth ocean atmosphere system and rise in SST. Carbon isotope recovery phases were accompanied by an increase in the steroid/hopanoid ratio, indicating a radiation of eukaryotic primary producers (Fig. 6-8).

As previously discussed, the rapid rise in the sea level that accompanied the Toa-CIE, did not trigger a radiation of marine phytoplankton, like red algae or *Pelagophyceae*. Moreover, this period can be associated with a *Pelagophyceae* crisis, as indicated by low abundance of C_{30} steroids. Only a slightly increase in C_{30} steroids is noted upon the transgressive phase during the initial part of the Toa-CIE (Fig. 6-8). Overall low contributions from fully marine algae taxa can be associated with significantly decreased SSS that were not favorable for e.g. *Pelagophyceae* (see Chapter 4). This dual relation resulted in a complex pattern. The CIE shift II-A is associated with a transgressive pulse as well as with a massive freshwater discharge to the Western Tethyan shelf. The drastic freshening of the surface water initiated a decrease in the abundance of *Pelagophyceae*. The second negative carbon isotope shift (II-B) is also associated with a freshwater pulse and a transgression. Both resulted in a delayed radiation of *Pelagophyceae* that is indicated by the offset between carbon

isotope shift and increasing C_{30} steroid abundances (Fig. 6-8). The CIE shift II-C was also accompanied by a transgression that was, however, accompanied by an only moderate seawater freshening (see Chapter 4). The stronger impact of the sea level rise is seen to have triggered an instantaneous increase in the abundance of *Pelagophyceae* as indicated by a rise in the abundance C_{30} steroids concomitant to the carbon injection (Fig. 6-8). The decrease *Pelagophyceae* abundance throughout upper part of the Toa-CIE (stage III) can be attributed to a regressive trend and an increased impact of lowered SSS, possibly due to additional riverine freshwater inflow.

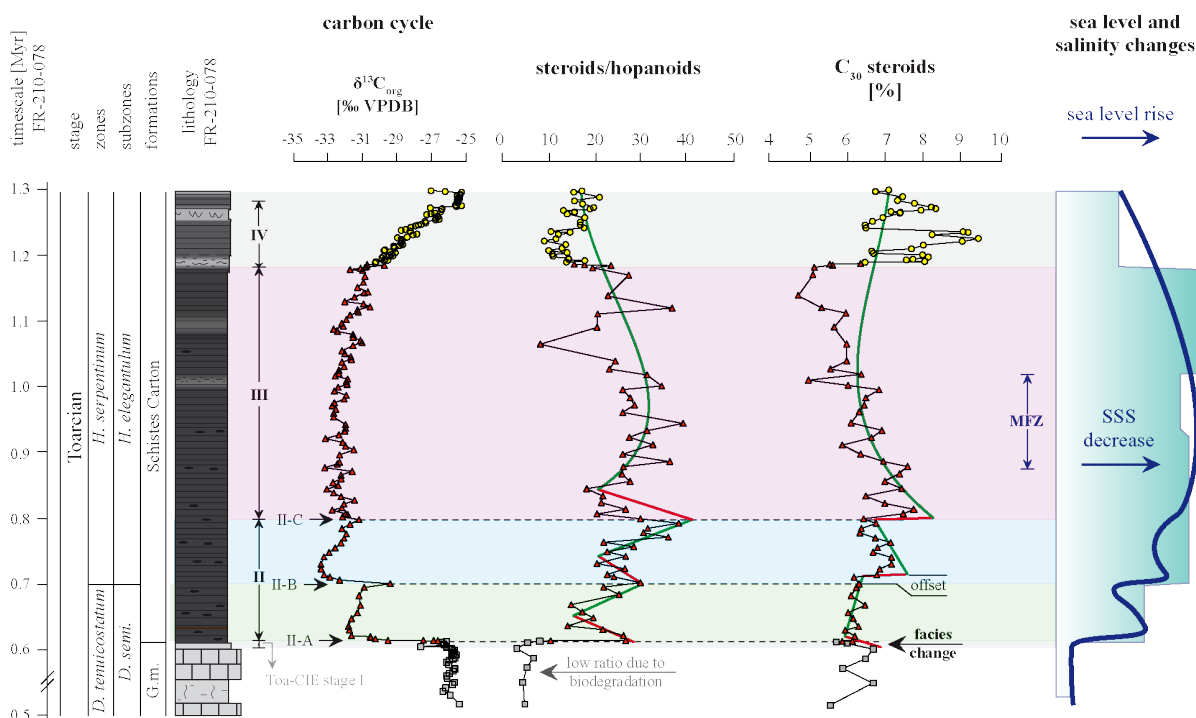


Fig. 6-8: The evolution of the steroid/hopanoid ratio confirm that eukaryotes dominated the phytoplankton during the carbon cycle perturbation. However, each negative CIE shift (II-A, II-B, II-C) is accompanied by a drop in the ratio and is followed by a recovery phase. The increase in prokaryotic contributions during the individual carbon injection might hint to enhanced environmental stress onto the eukaryotic primary producer community. Changes in C_{30} steroids indicate the response of marine *Pelagophyceae* towards the stepwise decrease in SSS, whereby the rise in sea level does not contribute to a radiation of marine algae taxa.

Moreover, the main Toa-CIE steps (II-A, II-B, II-C) were accompanied by significant changes in the C_{28}/C_{27} and C_{27}/C_{29} steroids ratios that indicate an instantaneous response of the phytoplankton community towards the individual carbon injections (Fig. 6-9). Both ratios indicate a relative decrease in the abundance of C_{27} steroid synthesizing algae (mainly marine red algae). The relative increase of C_{28} and C_{29} steroids can be attributed to a radiation of opportunistic green algae groups (e.g. *Prasinophyceae*, *Chlorophyceae*). Interestingly, each abrupt change in the steroid ratios was followed by a recovery phase, where values return towards pre-excursion values (Fig. 6-9). Such a trend can be associated with a recovery of algae taxa that dominated before the carbon injections and the associated hyperthermals (see Chapter 3). These results are in agreement with findings by

Hermoso et al. (2012), who reported a stepwise decrease of calcareous nannoplankton synchronous with individual carbon injections. Moreover, these authors documented a gentle recovery of calcareous nannoplankton during the recovery phases following each negative carbon isotope shifts. The stepwise change might explain the low extinction rates documented in nektonic ecosystems, as these communities had time to adapt to the new environmental conditions. Interestingly, each carbon isotope shift that is associated with a freshwater pulse and a rise in the sea level of different magnitude was accompanied by shift in the steroid ratios that show no significant different in the amplitude. This discrepancy might result from differences in the sensitivity of the proxies that were used to address changes in sea level and SSS, but might also indicate that these parameters were not the exclusive driver of changes in the phytoplankton community structure. Rise in SST and a stepwise acidification of the ocean might directly have affected the primary producing community structure.

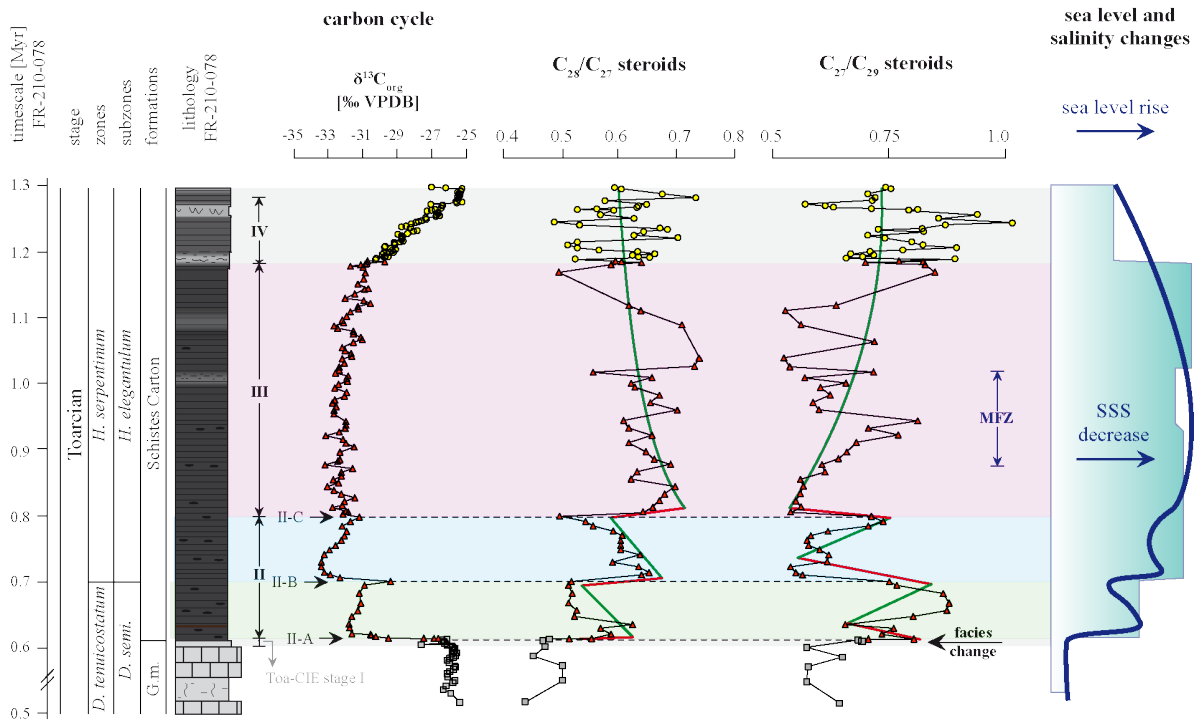


Fig. 6-9: The evolution of the C_{28}/C_{27} and the C_{27}/C_{29} steroid ratios indicates that each negative CIE shift was accompanied by a rapid change in the community structure of eukaryotic phytoplankton followed by a recovery phase. A stepwise change in the primary producer assemblage over a period of about >300 kyr might explain the low extinction rates.

6.4.4. Phytoplankton community dynamics during the upper *H. elegantulum* subzone

Beside changes in the phytoplankton community structure that are associated with Early Toarcian carbon cycle perturbation and the associated environmental changes, significant fluctuations in the phytoplankton community structure were also observed for the upper *H. elegantulum* subzone (Interval 2). These shifts may have been associated with environmental changes that could be attributed to glacial/interglacial cycles (see Chapter 4). The overall high contributions of C₂₇ and C₃₀ steroids in this interval can be attributed to a recovery of marine algae taxa, including red algae (*Bangiophyceae*, *Rhodophyceae*), *Pelagophyceae* and *Haptophyceae*. The recovery of these algae groups may have been induced by increases in SSS towards more normal marine conditions as well as by increases in ocean alkalinity. However, oceanographic instabilities in this interval linked to obliquity-forced ice sheet dynamics strongly affected the phytoplankton community structure. Interglacial stages can be associated with a high sea level and lowered SSS, whereas glacial stages are characterized by a lower sea level and increased SSS due to the reduced freshwater inflow from the Arctic Ocean (see Chapter 4).

The reduced SSS during interglacial stages resulted in a *Pelagophyceae* decline, as indicated by relative low contributions of C₃₀ steroids that are comparable to those in the Interval 3 (Fig. 6-10). High ratios of C₂₇/C₂₉ and C₂₈/C₂₉ indicate significant contributions from e.g. *Haptophyceae*, *Chrysophyceae*, whereas contributions from freshwater tolerant algae groups (e.g. *Prasinophyceae*, *Cryptophyceae*, *Chlorophyceae*) cannot be excluded, as reduced SSS are confirmed for the interglacial stages. Moreover, within the upper *H. elegantulum* subzone C₂₉ steroids may partly have been contributed by higher land plants, as indicated by significant abundances of long-chain odd-numbered *n*-alkanes (Fig. 6-2). Reduced fluxes of C₂₉ steroids from land upon high sea level will have raised the C₂₇/C₂₉ and C₂₈/C₂₉ ratios. The C₂₈/C₂₇ ratio shows no clear trend, as within this interval both steroid species were associated with marine algae. It can be assumed that the ratio reflects proportional abundances of C₂₇ synthesizing red algae versus C₂₈ synthesizing *Haptophyceae*, *Chrysophyceae* (Tabs. 6-1, 6-2). Glacial stages of lower sea level and increased SSS represent fully marine conditions, expressed by increased abundance of C₃₀ steroids reflecting *Pelagophyceae* input (Fig. 6-10). Low ratios of C₂₇/C₂₉ and C₂₈/C₂₉ during glacial stages most likely resulted from enhanced C₂₉ contributions from land plants. Preferentially high C₂₈/C₂₇ steroids may have been induced by C₂₈ contribution from *Pelagophyceae* and/or *Chrysophyceae*.

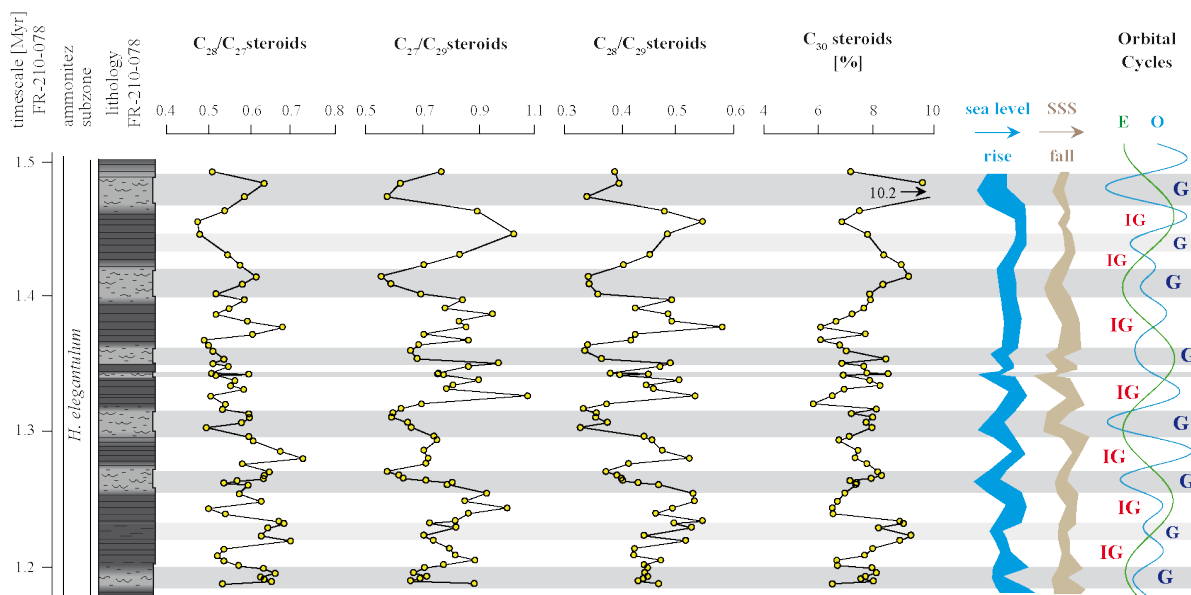


Figure 6-10: The upper *H. elegantulum* subzone (Interval 2) shows the highest variability in steroid ratios that can be associated with astronomically introduced changes in oceanographic conditions, comprising changes in sea level, SSS and nutrient availability (see Chapter 5). The dominance of C_{27} and C_{28} steroids during interglacial stages (high sea level, lowered SSS) can be linked to increased contributions from red algae (*Bangiophyceae*, *Rhodophyceae*), *Pelagophyceae* and *Haptophyceae*. On the contrary, increased contributions of C_{29} steroids during glacial stages might result from increased land plant derived OM as testified to high TAR values. However, more marine conditions are supported by elevated C_{30} steroid abundances that indicate increased input from *Pelagophyceae*. No clear trend is documented in the C_{28}/C_{27} steroid ratios.

6.5. Conclusions

Conclusions concerning the Early Toarcian phytoplankton community structure

The distribution of biomarkers, associated with marine phytoplankton, allowed to discuss changes in the community structure of the primary producing community at a high temporal resolution. Data confirm that environmental changes, associated with Early Toarcian CIE that spans the upmost *D. tenuicostatum zone* and the lower *H. elegantulum subzone*, resulted in a drastic shift in the phytoplankton community structure. Marine algae groups, like red algae, golden algae or *Haptophyceae*, which dominated the algae assemblage prior the Toarcian carbon cycle perturbation, were replaced by opportunistic green algae groups (e.g. *Prasinophyceae*, *Chlorophyceae*). The shift in the phytoplankton community structure occurred in discrete steps, each associated with a hyperthermal and an injection of carbon into the Earth ocean atmosphere system. Moreover, recovery phases of individual isotope events were accompanied by recovery of the phytoplankton community structure. The stepwise shift in the phytoplankton community structure that occurred over a period of > 300 kyr can explain the low extinction rates that have been documented for nektonic ecosystems. In the Lorraine Sub-Basin as well as throughout the Western Tethyan shelf phytoplankton suffered from a freshening of the surface water. This mechanism can explain changes in the phytoplankton community structure throughout the Western Tethyan shelf as well as in other near shore environments around the globe. However, marine phytoplankton also suffered directly from the rise in SST and an acidification of the ocean that was not limited to shelf settings. These processes affected the phytoplankton on a global scale.

Beside the shift in the phytoplankton community structure that can be associated with the Early Toarcian environmental crisis, fluctuations in the phytoplankton assemblage were also documented in the upper *H. elegantulum subzone*, subsequent to the global event. During this period phytoplankton instability can be associated with glacial/interglacial cycles that resulted in contrasting oceanographic conditions in the Lorraine Sub-Basin. These changes were induced by global mechanisms (astronomically-forced ice sheet dynamics), but shifts in the phytoplankton community structure can be causally linked to a high sensitivity of the shelf setting towards these climate cycles. Thus, local or possibly regional (shelf-wide) conditions promoted drastic changes in the phytoplankton community structure.

Conclusions concerning the applicability of steroid based ratios as paleoenvironmental proxies

Results of this chapter emphasize the role of source variability for individual steroid species. Especially C₂₈ and C₂₉ steroids characterize algae groups that inhabit contrasting environments. Thus, steroid-based ratios that are widely used to reconstruct changes in oceanographic conditions (sea level changes, freshwater inflow) must be interpreted with caution and cannot be applied without additional information about the environmental condition.

Chapter Seven:

Conclusions and Summary

7.1. Environmental and biotic changes during the Toarcian: A unifying model

Results of this thesis allow to propose a new unifying model for the environmental changes documented during the Early Toarcian (Early Jurassic; ~183 Ma BP). The key features of the Early Toarcian, comprising a global warming, increasing sea level, rise in atmospheric CO₂ concentrations, ocean acidification, enhanced hydrological cycling and weathering, elevated nutrient flux to the ocean, establishment of oxygen minimum zones in shelf areas and the perturbation of the global carbon cycle can be explained by the response of the Earth's sensitive cryosphere (polar ice caps and cryosphere stored carbon) towards a moderate global warming that was externally triggered by the eruption of the Karoo-Ferrar LIP. The formation of a persistent cryosphere during the late Pliensbachian cold snap was associated with an increase of the cryosphere-stored carbon pool and with the formation of persistent polar ice caps. The size of this carbon pool is difficult to estimate. However, warm climate conditions during the lower Pliensbachian that promoted northwards biome expansion might have contributed to the formation of a large biogenic carbon-reservoir at high and mid latitudes. This biogenic carbon pool was transferred into the cryosphere during the Late Pliensbachian cooling. The cryosphere-associated carbon pool reacted very sensitive to and became destabilized by a rise in global temperature that was initiated by the emplacement of the Karoo-Ferrar LIP (Burgess et al., 2015).

Melting of polar ice caps during the Early Toarcian global warming can explain the rapid transgression that occurred synchronically with the increase in SST. Moreover, the demise of cryosphere-stored carbon and the release of ¹²C-enriched carbon into the Earth's ocean-atmosphere system can explain the Toarcian carbon cycle perturbation. Both, transgression and carbon release occurred synchronically in discrete steps and were paced by changes in the Earth's solar orbit. Warming and carbon cycle perturbation were of global extent and lasted for about 900 kyr (Fig. 7-1). Different durations previously calculated can be attributed to high variable sedimentations rates in the different basins on the Western Tethyan shelf. The stepwise nature of this event can be associated with single hyperthermals, whereby each hyperthermal was connected with a single methane gun of less than 100 kyr in duration (Dickens, 1999). Each hyperthermal and the associated methane injection were followed by a recovery phase that was tied to decrease in atmospheric CO₂ concentration (McElwain et al., 2005) and a recovery of the cryosphere, including the cryosphere-stored carbon pool. A similar pulsed pattern has also been proposed for the Paleocene-Eocene Thermal Maximum and the subsequent hyperthermals and carbon cycle perturbations of smaller magnitude that occurred over a period of about 5 Myr (DeConto et al., 2012; Kirtland Turner et al., 2014). The shorter time span of the Early Toarcian carbon cycle perturbation resulted from a more rapid global warming of about 6°C within less than 0.5 Myr. An offset of about 300 kyr, documented between the stage of the highest sea level reflecting the demise of polar ice caps and the recovery of the Toa-CIE, indicates that the cryosphere carbon pool became depleted some kyr after full deglaciation (Fig. 7-1), which is in agreement with modeling results by Majorowicz et al. (2014). It can be assumed that the effects of global warming, elevated SST and a rise in atmospheric CO₂ concentration causing ocean acidification affected marine ecosystems at global scale.

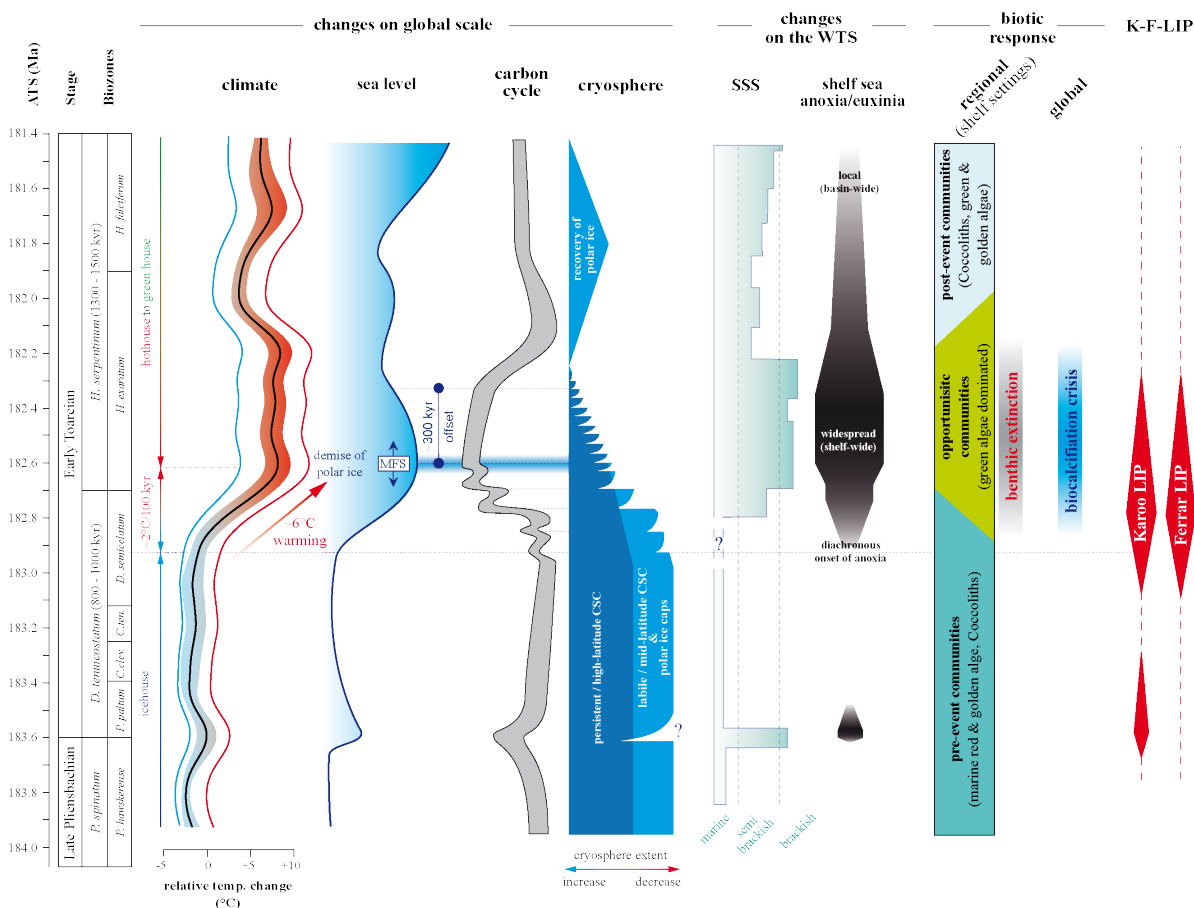


Fig. 7-1: Chronology of the Early Toarcian environmental crisis and the associated OAE. The key features of the Early Toarcian environmental crisis, comprising, a rise in SST and atmospheric CO₂ concentration, rapid transgression and the perturbation of the carbon cycle can be explained by astronomically-forced demise of the cryosphere (polar ice caps and cryosphere-stored carbon). The demise the polar ice caps explains the rise in the sea level as well as the freshening of the Western Tethyan shelf via meltwater inflow through the Viking Corridor. Astronomically-forced demise of cryosphere-stored isotopically light carbon (permafrost soil carbon & gas hydrates) is intrinsically connected to the Toa-CIE. Oceanographic changes (freshening, formation of euxinic bottom waters) on the Western Tethyan shelf resulted from the paleogeographic setting and the connection of the shelf with the Arctic Ocean via the Viking Corridor. All these environmental changes were externally initiated by the eruption of the Karoo-Ferrar LIP. The subsequent release of carbon from the cryosphere accelerated global warming in a runaway mode.

Moreover, oceanographic conditions on shelf settings, especially on the Western Tethyan shelf, were affected by a massive freshwater discharge that resulted from the melting of polar ice caps. Freshening of the shelf seas might be most significant for the Western Tethyan shelf, a fact that can be explained by the paleogeographic setting and the connection the this shelf with the Arctic Ocean via the Viking Corridor (Fig. 7-1). It can be thus concluded that the widespread deposition of black shale throughout the Western Tethyan shelf that were attributed to the T-OAE (Jenkyns, 1988) reflect the local response of this shelf environment towards global warming, acceleration of the hydrological cycle, nutrient fluxes to the shelf and the associated eutrophication of the shelf sea. Similar conditions might also have persisted on other shelf settings throughout the globe as indicated by the global occurrence of organic-rich deposits during the Early Toarcian. However, onset and duration of black shale deposition varied even throughout the Western Tethyan shelf and can therefore assumed to be non-synchronous (Fig. 7-1). Diachronous onset of shelf sea anoxia and thus

of black shale deposition was induced by paleogeographic features, like water depth or hydrodynamic restriction. Nektonic ecosystems on shelf settings suffered from rising SST, the acidification of the Ocean as well as from the freshening of the shelf seas that resulted in a bloom of opportunistic algae groups that tolerated reduced SSS. Low extinction rates documented for nektonic ecosystems possibly resulted from a stepwise change in the community structure that allowed the nekton to adapt to changing environmental conditions. High but variable extinction rates documented for benthic ecosystems can be associated with prolonged shelf sea anoxia and the expansion of marine death zone (Fig. 7-1).

7.2. Facies model for the Lorraine Sub-Basin

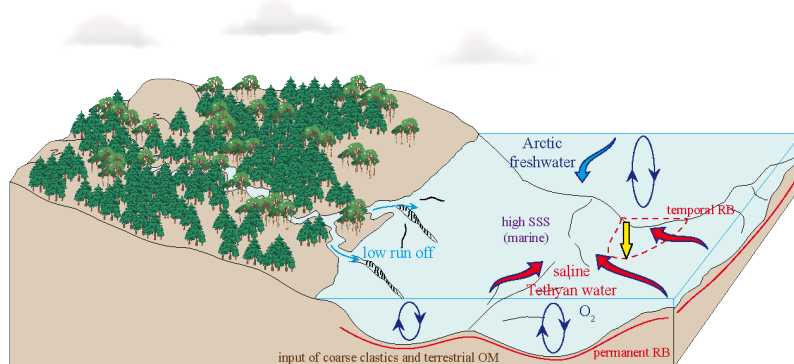
The Lorraine Sub-Basin represents the northeastern part of the Paris Basin. Beside the central part of the Paris Basin, the Lorraine Sub-Basin was one of the major subsiding areas as indicated by high sediment accumulation rates (A2 in the appendix). To the southwest and the southeast it was bordered by shallow marine shoals (sills, swells). To the northeast and the northwest the basin was bordered by the Rhenish Massif and the London-Brabant Massif, respectively (see Fig. 1-5 in Chapter 1.1.3.). The distances to these emergent landmasses that represent the nearby coastlines were > 100 km, possibly in a lower distance during stages of a low sea level and progradating coastlines (Ziegler et al., 1990).

upmost *P. spinatum* and lower *D. tenuicostatum* zones (Interval 4)

Cold and preferentially arid climate conditions dominated during the upmost *P. spinatum* and the lower *D. tenuicostatum* zones. These conditions were associated with low continental weathering rates and a reduced run off to the shelf seas, which resulted in preferentially mesotrophic conditions and in a moderate primary productivity (Fig. 7-2). The phytoplankton community in the shelf sea was dominated by dinoflagellates (Bucefalo Palliani et al., 2002; van de Schootbrugge et al., 2005a; 2013), calcareous nannoplankton (e.g. Erba, 2004; Mattioli et al., 2008; Hermoso et al., 2009b; Clémence et al., 2015) as well as by red algae and golden algae. The sea level during this period was relative low (<<50 m water depth), which resulted in elevated contributions of coarse clastics (silt) and land plant derived OM throughout the Lorraine Sub-Basin. Moreover, the overall low sea level allowed a mixing of the entire water column, which in combination with a moderate downward flux of OM prevented the formation of prolonged bottom water anoxia (Fig. 7-2). The redox boundary was preferentially situated in the sediment. Oxidic to temporary suboxic bottom water favored enhanced sediment reworking by benthic epi- and infauna, which is expressed by a homogenous sediment structure and the frequent occurrence of bioturbation traces. Bioturbation processes resulted in an efficient degradation of OM as testified by preferentially low TOC values (<1 wt.%) in the sediments that have been accumulated during this period. These conditions were only rarely disturbed by brief episodes of bottom water anoxia that possibly resulted from episodic algal blooms. However, periods of anoxic and partly euxinic bottom waters are confirmed by the occurrence of biomarkers characteristic for *Chlorobiaceae*.

Oceanographic conditions during this period were controlled by the impact of northwards directed saline Tethyan bottom currents and the weak southwards directed Arctic surface current system that together resulted in preferentially saline to semi-saline conditions. Salinities lower than normal marine might also have been induced by riverine derived freshwater inflow as indicated by terrigenous derived OM and coarse siliciclastics (Fig. 7-2).

upmost *P. spinatum* and lower *D. tenuicostatum* zones
(mesotrophic shallow marine shelf)



key features:

climate system:

- cold and arid (low SST)
- low weathering rates and low run off

oceanographic conditions:

- low sea level
- low Arctic freshwater inflow
- enhanced inflow of saline Tethyan water
- well-mixed water column
- saline/marine conditions (high SSS)

phytoplankton community:

- red algae, golden algae, *Haptophyceae* (dinoflagellates)

redox regime:

- oxic water column (oxic >> anoxic)
- RB preferentially situated in the sediment

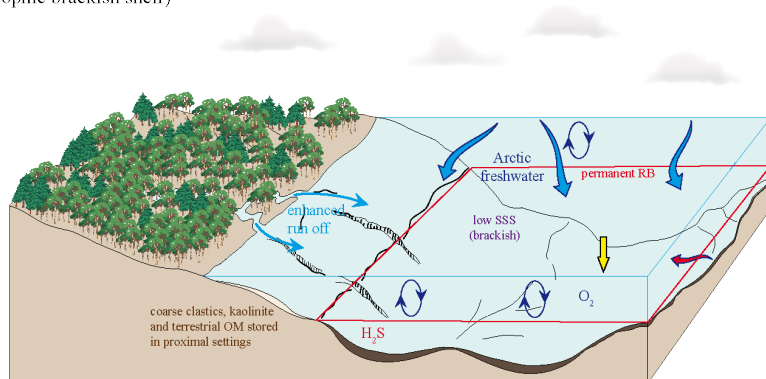
Fig. 7-2: Facies model for the upmost *P. spinatum* and the lower *D. tenuicostatum* zones, representing a shallow marine mesotrophic shelf with a predominantly well-oxygenated water column (RB: redox boundary; the yellow arrow marks the position of the study site).

upmost *D. tenuicostatum* zones and lower *H. elegantulum* subzone (Interval 3)

During the upmost *D. tenuicostatum* zone and the lower *H. elegantulum* subzone a drastic global warming that was accompanied by a rise in SST (e.g. Dera et al., 2011a). Moreover, global warming resulted in an intensification of the monsoonal circulation (Krencker et al., 2015), an acceleration of the hydrological cycle, which in turn caused an increase in continental weathering and elevated run off rates (e.g. Cohen et al., 2004; Montero-Serrano et al., 2015). Increased continental run off rates transported huge amounts of nutrients to the shelf seas, which stimulated the PP and caused an eutrophication. The rapid rise in the sea level led to sediment starvation (very low sediment accumulation rates) and a massive freshwater discharge to the Western Tethyan shelf via melting of polar ice caps as an effect of global warming. The strengthening of the southwards directed Arctic freshwater current that entered the Western Tethyan shelf via the Viking Corridor and the weakening of the northwards directed saline Tethyan countercurrent resulted in a surface layer freshening of the shelf seas (Fig. 7-3). Prolonged brackish condition on the shelf, in combination with elevated SST and ocean acidification caused a drastic shift in the phytoplankton community structure. During this period, marine phytoplankton, mainly composed of red algae groups, golden algae, *Haptophyceae* and dinoflagellates, was replaced by opportunistic algae groups, like *Prasinophyceae* or *Chlorophyceae* (mainly green algae groups). Algae adapted to marine conditions mainly suffered from brackish surface waters, whereas calcareous nannoplankton suffered from ocean acidification. A high sea level in combination with high PP and the establishment of a stable pycnocline promoted the formation of euxinic bottom waters and the expansion of marine

death zones culminating in the extinction of benthic ecosystems. However, in the Lorraine Sub-Basin euxinic conditions were limited to the bottom water, whereby an expansion into the upper part of the water column was possibly prohibited by the high sea level that promoted enhanced basin communication and strong surface water current. Moreover, enhanced mixing of the surface water might have been a consequence of an intensification of monsoonal circulation and an increasing storm activity (Krencker et al., 2015). Nevertheless, persistent and prolonged bottom water euxinia was promoted by a stable stratification of the water column due to the massive freshwater discharge.

upmost *D. tenuicostum* zone and lower *H. elegantulum* subzone
(eutrophic brackish shelf)



key features:

climate system:

- warm/hot and humid (high SST)
- high weathering rates and elevated run off

oceanographic conditions:

- high sea level
- massive Arctic freshwater inflow
- reduced inflow of saline Tethyan water
- stratified water column
- brackish surface water (low SSS)

phytoplankton community:

- bloom of opportunistic green algae
(e.g. *Prasinophyceae*, *Chlorophyceae*)

redox regime:

- euxinic bottom water overlain by oxic surface water (oxic > anoxic)
- persistent RB situated in the bottom water

Fig. 7-3: Facies model for the upmost *D. tenuicostatum* zone and the lower *H. elegantulum* subzone, representing an eutrophic and brackish self setting. This stage represents the acme of the Early Toarcian environmental crisis and is associated with a drastic global warming that resulted in profound environmental changes (RB: redox boundary; the yellow arrow marks the position of the study site).

upper *H. elegantulum* subzone (Interval 2)

The upper *H. elegantulum* subzone reflects a regressive phase that resulted in an intermediate sea level and thus in a depositional environment more sensitive towards environmental instabilities. The regressive trend can be associated with an increase in land plant derived OM contributions but was not accompanied by a significant increase in silt-sized detritus contributions. However, lithological observations attest to reoccurring high energetic depositional conditions. In shallow settings, on swell or in near coastal environments, the regressive phase is well documented by erosional events and hiatuses in sediments corresponding to the *H. elegantulum* subzone (e.g. van Breugel et al., 2006; Lezin et al., 2012). In these settings mud that had been deposited previously was eroded and transported to deeper parts of the basin (Fig. 7-4A). Redeposition processes and elevated terrestrial contribution drastically enhanced the sediment accumulation rate. An overall increase in ocean alkalinity and an increase in SSS resulted in a recovery of marine algae groups, comprising red algae, golden algae, *Haptophyceae* and *Pelagophyceae*. The overall lower sea level resulted in a maximum hydrodynamic restriction of the Western Tethyan shelf, which promoted an expansion of euxinic conditions into the upper parts of the water column.

However, the intermediate sea level induced a high variability in depositional conditions that were controlled by obliquity-forced changes in sea level and SSS. These fluctuations can be

explained by glacial/interglacial cycles coupled to ice sheet dynamics. During glacial stages, the growth of polar ice caps was paralleled by a sea level drop and in a reduced freshwater discharge to the Western Tethyan shelf (Fig. 7-4A). The low sea level allowed a periodically expansion of euxinic condition throughout a wide part of the water column. However, these conditions were not stable and episodically reoccurring reoxygenation events enabled a mixing of the entire water column and the sea floor became resettled by benthic organisms. Thus, during glacial stages the permanent redox boundary was situated in the sediment and expanded into the water column during brief episodes, possibly during episodic algal blooms. Anoxia/euxinia during this period was driven by the PP. During interglacial stages a higher sea level in combination with the enhanced inflow of Arctic freshwater promoted the formation of a stable pycnocline. Oceanographic conditions in combination with an elevated productivity, due to enhanced continental run off and nutrient supply, promoted the formation of persistent euxinic bottom water. During interglacial stages the redox boundary was preferentially situated in the lower part of the water column.

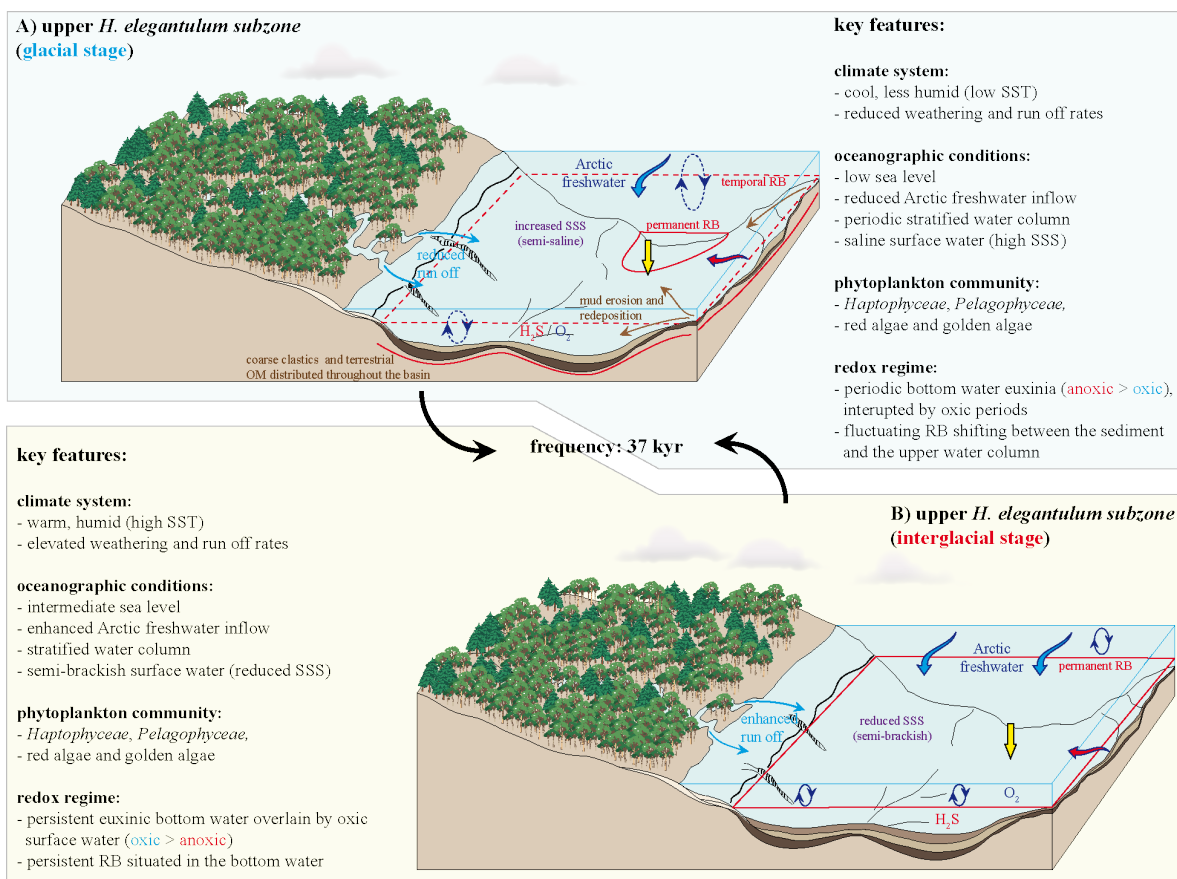
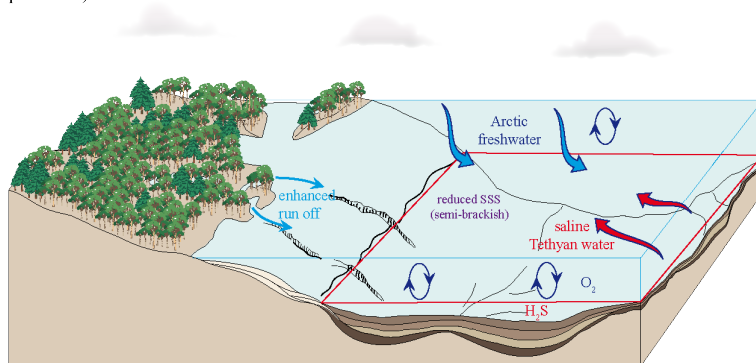


Fig. 7-4: Facies model for the upper *H. elegantulum* subzone, which is characterized by a high variability in oceanographic conditions (RB: redox boundary; the yellow arrow marks the position of the study site). Variations in the oceanographic conditions controlled the depositional conditions and can be associated with glacial/interglacial cycles. The high variability of the depositional conditions can be explained by the intermediate sea level that provided an environment most sensitive towards minor environmental changes.

***H. falciferum* subzone (Interval 1)**

The sea level rise throughout the *H. falciferum* subzone culminated in a sea level highstand that is placed in the upmost part of this biochronozone. The high sea level resulted in the termination of the hydrodynamic restriction of the Western Tethyan shelf and allowed an efficient water exchange between the shelf sea and the Tethyan Ocean. Moreover, the high sea level promoted the communication between Arctic Ocean and Western Tethyan shelf, which allowed an enhanced inflow of low saline Arctic freshwater onto the Western Tethyan shelf, driven by a salinity gradient (Bjerrum et al., 2010; Dera & Donnadieu, 2012). The interaction of the southwards directed freshwater surface current and the strong northwards directed saline Tethyan bottom water current resulted in semi-brackish conditions. Moreover, a stronger impact of riverine derived freshwater supply is indicated by increased contributions of land plant derived OM. Furthermore, changes in current systems that resulted from the rearrangement of the hydrodynamic regime might also have contributed to the distribution of terrestrial OM through the basin. The freshwater inflow promoted a stratification of the water column, which in combination with a high PP, induced the formation of euxinic bottom water. The semi-brackish conditions in the surface water resulted in diverse phytoplankton assemblage, comprising marine *Pelagophyceae*, *Haptophyceae* or golden algae, as well as green algae groups that were better adapted to reduced SSS.

H. falciferum subzone
(the open shelf)



key features:

climate system:

- warm and humid (high SST)
- high weathering rates and elevated run off

oceanographic conditions:

- highest sea level
- enhanced Arctic freshwater inflow
- enhanced inflow of saline Tethyan water
- stratified water column
- semi-brackish surface water (low SSS)

phytoplankton community:

- *Haptophyceae*, *Pelagophyceae*
- golden algae as well as green algae

redox regime:

- euxinic bottom water overlain by oxic surface water (oxic > anoxic)
- persistent RB situated in the bottom water

Fig. 7-5: Facies model for the *H. falciferum* subzone, representing an open shelf setting (RB: redox boundary; the yellow arrow marks the position of the study site). The very high sea level during the *H. falciferum* subzone resulted in a termination of the hydrodynamic restriction of the Western Tethyan shelf. Moreover, the high sea level resulted in a low energetic depositional environment. The redox boundary was situated in the bottom water, whereas an expansion of euxinic conditions into the upper part of the water column was prevented by enhanced mixing of the surface water.

7.3. Outlook

The age model developed for Core FR-210-078 allows to explain the discrepancy between the durations previously calculated for the Toa-CIE and shows that differences in time assignment can be related to highly variable sedimentation rates throughout the highly dynamic Western Tethyan shelf. Further works should focus on pelagic sections that experienced less variable sedimentation rates. A first step has been undertaken by [Gröcke et al. \(2011\)](#) and [Ikeda & Hori \(2014\)](#), which investigated pelagic sediment sequences from the Panthalassa Ocean. However, the poor biostratigraphy and the missing carbon isotope stratigraphy raise questions about the comparability of this sediment sequence with records from the Western Tethyan shelf. Moreover, floating chronologies must be calibrated by independent dating techniques to confirm timing and duration of the Toa-CIE and the link to the emplacement of the Karoo-Ferrar LIP.

The model proposed here bases on the assumption that the Toa-CIE reflects oceanic as well as atmospheric signals resulting from the release of ^{12}C -enriched carbon from the cryosphere, which has been proposed based on $\delta^{13}\text{C}$ data from fossil wood ([Hesselbo et al., 2000, 2007](#); [Hesselbo & Pieńkowski, 2011](#)). However, a potential alteration of the primary wood $\delta^{13}\text{C}$ signature by diagenetic processes in the marine realm raises questions on the reliability of these atmospheric CO_2 proxies. Therefore, an independent proof of the atmospheric carbon isotope signal, by the compound-specific $\delta^{13}\text{C}$ analysis of land plant derived biomarkers, is considered necessary to reinforce a carbon injection into the atmosphere system.

Additionally, a numerical modeling approach may allow to test various scenarios of cryosphere demise and associated amounts of CO_2 and CH_4 released in the wake of the T-OAE. As reliable estimation of the Jurassic cryosphere dimension by geological/geochemical proxies does not appear feasible, a modelling approach may be suitable for cryosphere carbon reservoir assessment.

In this work, the reconstruction of changes in SSS relied on the interpretation of MTTCs a geomarker, whose origin is still unknown ([Sinninghe Damsté et al., 1987](#); [Li et al., 1995](#); [Tulipani et al., 2013](#)). Result of this work reinforces the applicability of this empirical facies parameter as a salinity proxy. However, underlying mechanisms as well as origin or the formation pathway(s) of these compounds remain unknown and must be addressed by future research. A solution could be found in the application of compound specific δD measurements at biomarkers (MTTCS itself, steroids) from sediments that experienced only a very low degree of thermal overprint, which allow to exclude hydrogen exchange reactions.

Results of this thesis indicated that multiple processes affect the $\delta^{98/95}\text{Mo}$ signature that has been commonly attributed to vary as a function of the redox regime. Particulate shuttle processes, the proportional extent of oxic versus euxinic water column as well as spatial variation in the $\delta^{98/95}\text{Mo}$ signature of seawater may strongly impact on the $\delta^{98/95}\text{Mo}$ ratio of sediments. These processes and their impact onto the $\delta^{98/95}\text{Mo}$ signature of recent and ancient sediments must be addressed by further investigations. The enhanced understanding of $\delta^{98/95}\text{Mo}$ dynamics in combination with biomarkers diagnostic for photoautotrophic sulfur bacteria can provide detailed information about redox conditions in the water column and the extent of euxinic conditions.

Appendix and Supplementary Material

A1. Study Site and Stratigraphy

A1.1. Geology of the Paris Basin

The study site is located in the northeastern Paris Basin, an intracratonic semicircular basin of about 200 km in radius, bounded by the Armorican Massif in the west, the Massif Central in the south, the Vosges in the east and the Ardennes and the Rhenish Massif in the north and northeast (e.g. [McCann, 2008](#)). The Paris Basin contains about 3500 m of Mesozoic sedimentary rocks, mainly shallow water shelf sediments, which unconformably overlie the Variscian basement and locally Permian clastics ([Perrodon & Zabeck, 1990](#)). The Mesozoic sediments record the major tectonic events of the western Eurasian plate, including opening and closing of the Tethyan Ocean as well as opening of the Atlantic Ocean (e.g. [McCann, 2008](#)). From the Early Triassic to the Jurassic the Paris Basin was a widespread subsiding area in an extensional tectonic framework ([Guillocheau et al., 2000](#)). Sedimentation was controlled by variable subsidence controlled by local tectonic features in combination with global transgressive and regressive events ([McCann, 2008](#)). Mesozoic sediments show a synclinal structure, gently dipping towards the centre of the Basin. Thus, the oldest Triassic and Jurassic sediments are located at the basin margins, younger Cretaceous and Tertiary sediments are situated in the central part of the basin. Jurassic sediments crop out in a large continuous belt in the east and northeast. Less extensive outcrops of Jurassic sediments can be found in the southern and southwestern part of the basin (Fig. A1A). Slowing of the subsidence and uplift during the Cenozoic resulted in the exposure and erosion of Mesozoic sedimentary rocks, whereby the present day shape of the Paris Basin evolved during Miocene tectonic events ([Guillocheau et al., 2000](#)).

A1.2. Study site and drill location

The Thesis presented here base on investigations performed on Core FR-210-078 drilled in 2008 during a tunnel construction campaign in southern Luxembourg, near the city of Esch-sur-Alzette (Fig. A1B). The study area is located in the northeastern part of the Paris Basin, also termed Gulf of Luxembourg or Lorraine Sub-Basin. Preliminary investigation, mainly focusing on maturity reconstruction and low-resolution geochemical investigations, were performed on Core FR-207-142 ([Wagner, 2010](#); [Ruebsam, 2010](#)) that recovered about 60 m of upper Pliensbachian and lower Toarcian strata. This core and was also investigated for their fossil content in order to establish a reliable ammonite biostratigraphy ([Guérin-Franiette et al., 2010](#)). The distance in field between both drill cores is about 1.5 km (Fig. A1B).

Core FR-207-142: 49.509730 / 5.950763 (preliminary investigations, biostratigraphy framework)

Core FR-210-078: 49.507402 / 5.930132 (this study)

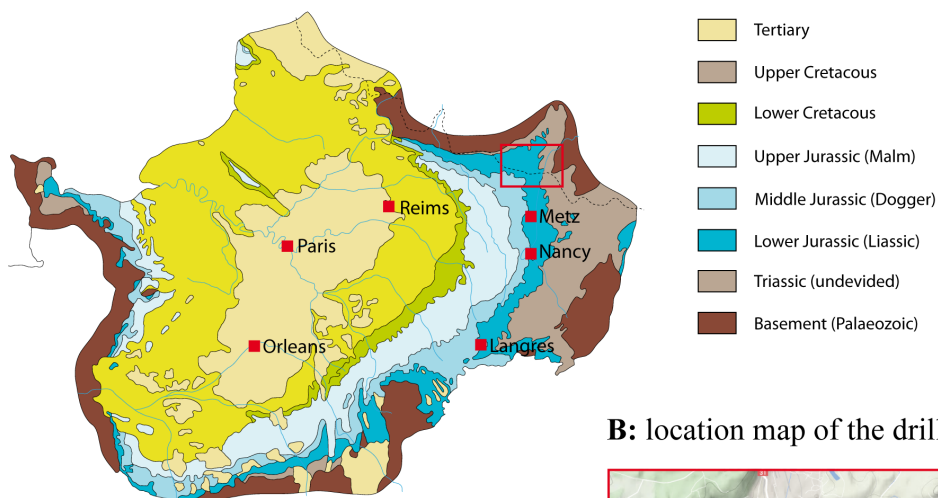
A: geological map of the Paris Basin**B:** location map of the drill sites

Figure A1: A) B) Geological map of the Paris Basin. The study site is located in the northeastern Paris Basin, in southern Luxembourg (red square). **B)** Location of drill sites of Core FR-210-078 and Core FR-207-142. This work base on sedimentological and geochemical investigations of Core FR-210-078. Core FR-207-142 was subjected to palaeontological investigations (Guérin-Franiatte et al., 2010) and was further subjected to low-resolution preliminary geochemical analysis (Wagner, 2010; Ruebsam, 2010).

A1.3. Biostratigraphy and core correlation

Cores FR-207-142 (preliminary investigations) and FR-210-078 (this study) penetrate lower Jurassic sediments spanning the uppermost Pliensbachian to middle Toarcian, mainly represented by the Grès médioliasiques formation (upper Pliensbachian and lowermost Toarcian), the Schistes Carton Fm (lower Toarcian) and the Marnes à Bifrons Fm (lower middle Toarcian). The Marnes à Bifrons Fm is only recovered in Core FR-207-142. Detailed biostratigraphic investigations carried out at Core FR-207-142 by Guérin-Franiatte et al. (2010) provide a robust biostratigraphic framework at ammonite subzone scale (Fig. A2).

The Grès médioliasiques Fm corresponds to the upper *P. spinatum* zone (uppermost Pliensbachian, lm3, Fig. A2) and to the lower *D. tenuicostatum* zone (lower Toarcian), whereby the *D. tenuicostatum* zone reaches a thickness of about 6 m (lo1a, Fig. A2). The boundary between *D. tenuicostatum* and *H. serpentinum* zone is located within the lowermost Schistes Carton formation (lo1, Fig. A2). The boundary between *H. serpentinum* and *H. bifrons* zones is place in the uppermost Schistes Carton Fm (lo2, Fig. A2). In Core FR-207-142 the *H. serpentinum* zone reaches a thickness

of 26.2 m. Furthermore, ammonite assemblages in Core FR-207-142 allowed to place the boundary between *H. elegantulum* and *H. falciferum* subzones at about 42.30 m (Fig. A2).

In the Lorraine Sub-Basin the total thickness of organic-rich sediments of the Schistes Carton facies can reach a thickness of up to 50 m and spread over the uppermost *D. tenuicostatum* zone, *H. serpentinum* zone and the lower *H. bifrons* zone (Binz et al., 1984). In Core FR-207-142 the Schistes Carton Fm spans a sediment succession of about 31.80 m (lo1 + lower lo2 in Fig. A2). The boundary between Schistes Carton Fm and Marnes à Bifrons Fm is not very precise but can be placed at core depth of approximately 23.80 m (Münzberger, pers. comm.).

Core FR-207-142 was used as reference core and biostratigraphic boundaries were transferred to Core FR-210-078 using lithological and geochemical data (e.g. gamma ray, carbonate content). The core correlation is shown in figure A2. Details on the biostratigraphy are given by Guérin-Franiatte et al. (2010).

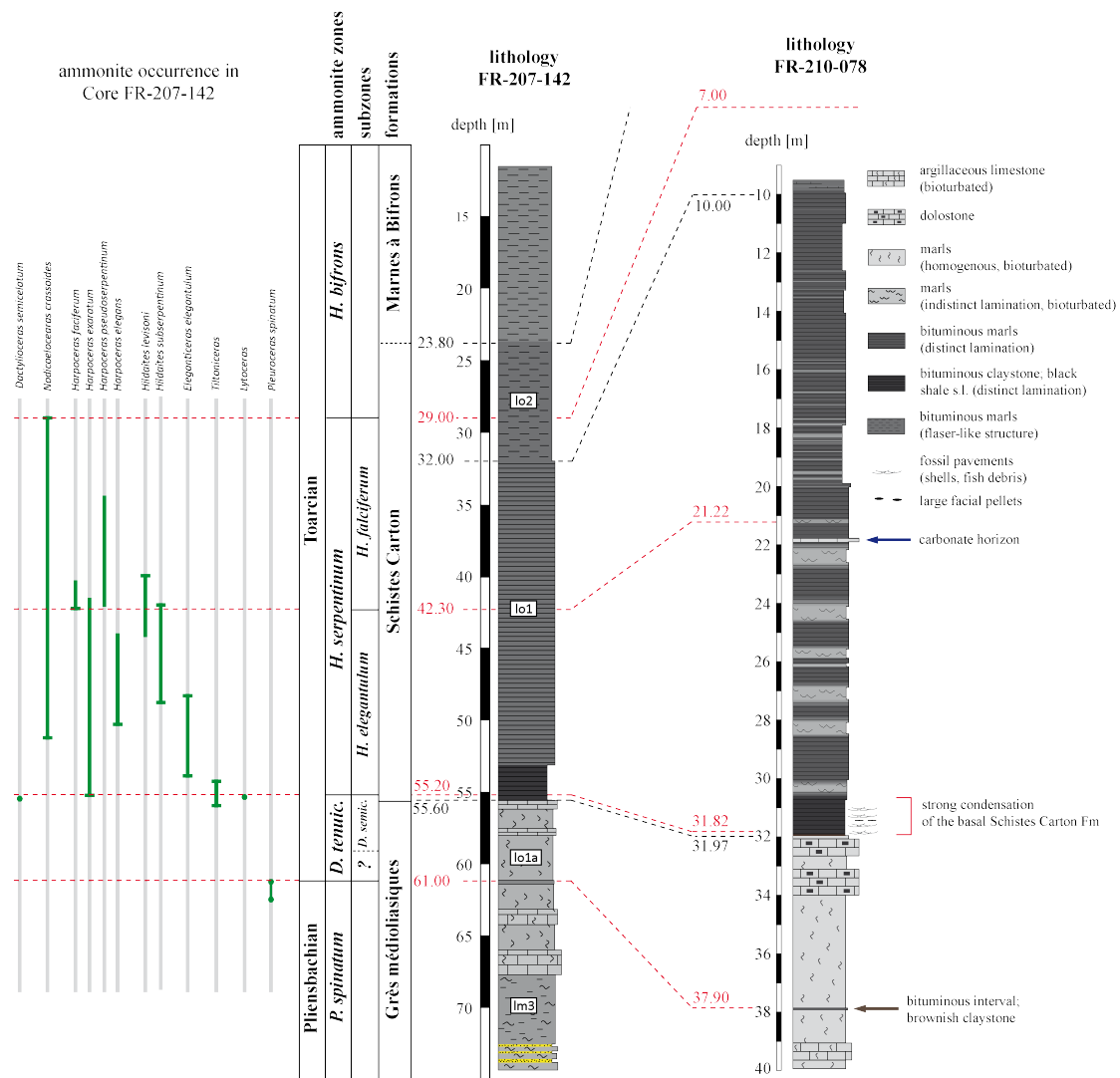


Figure A2: Occurrence of ammonites in Core FR-207-142 and inferred biostratigraphy (Guérin-Franiatte et al., 2010). Biostratigraphy of Core Fr-210-078 (this study) is adapted from Core FR-207-142 (Guérin-Franiatte et al., 2010 and Münzberger, pers. comm.). Both cores cover middle Liassic (lm3) and upper Liassic (lo1 and lo2) sediments, mainly claystones and marlstones. Biostratigraphic boundaries shown are in red, lithological boundaries in black.

In Core FR-210-078 (this study) the Pliensbachian-Toarcian boundary is placed in a thin dark-grey to brownish claystone at 37.90 m. The boundary between the *D. tenuicostatum* zone and *H. serpentinum* zone is placed within the lowermost Schistes Carton Fm at 31.82 m. Furthermore, the boundary between the *H. elegantulum* and *H. falciferum* subzones is placed at 21.22 m. The boundary between the *H. serpentinum* and *H. bifrons* boundary is placed at around 7 m, indicating that about 2.5 m of the uppermost *H. serpentinum* zone are missing.

A1.4. Lithology of Core FR-210-078

Core FR-210-078 provided about 30 m of continuously and exceptionally well-preserved sediments spanning the uppermost Pliensbachian and lower Toarcian, represented by the Grès médioliasiques and Schistes Carton Fm. Lithological inspection of the core indicates significant differences in sedimentation style and sediment composition between the formations (Figs. A3, A4). The Grès médioliasiques Fm (31.97 - 39.92 m) consists of homogenous light-grey to grey slightly calcareous mudstones with minor contributions of silt, strongly affected by bioturbation and sediment reworking (Fig A3; A – C). Intervals ranging from 39.80 to 39.00 m, 33.90 to 33.30 m and 32.40 to 32.15 m are enriched in carbonate and can be attributed to argillaceous marlstones/dolostones. Irregular shaped diagenetic pyrites (size up to 0.5 cm) occur frequently in sediments of the Grès médioliasiques Fm. A thin interval from 37.95 to 37.87 m, which marks the Pliensbachian-Toarcian boundary, consists of dark-grey bituminous laminated mudstone or claystones. The occurrence of thin horizons strongly enriched in reworked shell fragments at about 39.80 m and at 32.20 and 32.05 m might indicate potential erosional events (Fig. A3; A, C).

The Schistes Carton Fm (9.55 - 31.97 m) mainly consists of grey to dark-grey marlstones that show a distinct lamination (parallel-textured sedimentation style), indicating strongly reduced or the absence of benthic activity and sediment reworking (Fig. A3; D – N and Fig. A4). However, detailed inspection reveals that these laminated sediments were frequently interrupted by intercalated horizons that show an indistinct lamination and a partly homogenous sedimentation style, which indicate enhanced bioturbation and sediment reworking (Fig. A3; G, I, J and Fig. A4B). Horizons with indistinct lamination are most pronounced in the lower part of the Schistes Carton Fm (22.00 – 30.50 m). Furthermore, the basal Schistes Carton Fm (30.75 - 31.97 m) significantly differs from the upper part, as this interval is less cemented (due to low carbonate content) and thus rather represents bituminous mudstones/claystones (black shale, *sensu lato*) than bituminous marlstones (Fig. A3; E, F). Within this interval several lenses of amorphous solid bitumen were observed between 31.55 and 31.25 m (Fig. A3; E – red arrow). The transition between Grès médioliasiques Fm and Schistes Carton Fm is marked by a condensed interval that is enriched in fish debirs, indicating a strongly reduced sediment supply or sediment starvation (Fig. A3; D – red arrow and Fig. A4A). Strong reduced sediment supply during deposition of the basal Schistes Carton Fm is also indicated by the general increased fossil abundance within this interval. Sediment below this condensed horizons show evidence for strong sediment reworking. The upper part of Core FR-210-078 (22.00 – 9.55)

shows a less variable sedimentation style. Sediments are generally indistinctly laminated with a partly turbulent sedimentation structures and sharp-based erosive surfaces, possibly representing winnowing (Fig. A3; M, N, O and Fig. A4D). A carbonate bank (21.79 to 21.88 m) is intercalated into the marlstones (Fig A3, L).

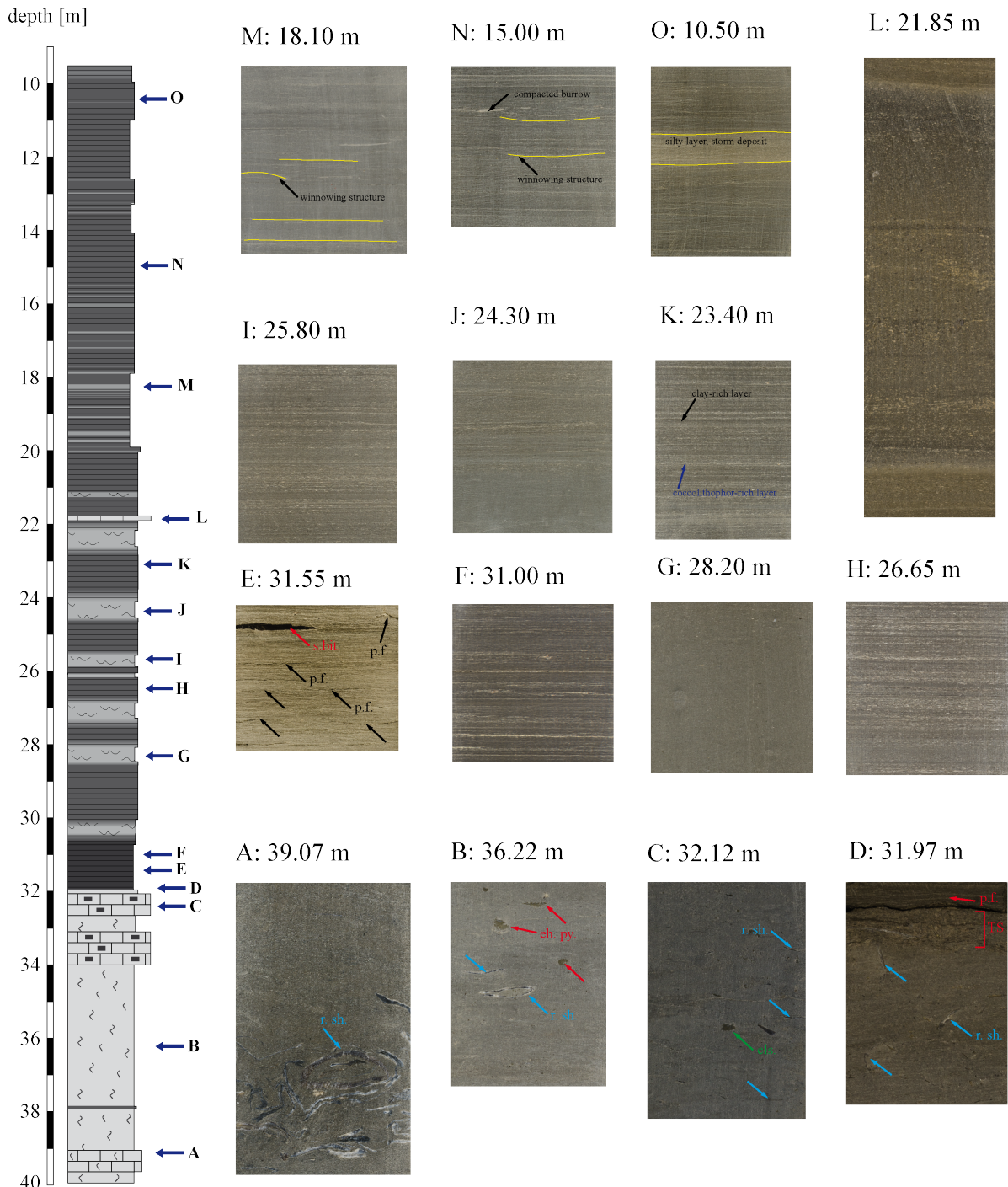


Figure A3: Photographs taken from selected core intervals show significant differences in lithology (width of each photograph is about 7 cm). The sediment color might be obscured as the contrast of the photographs was increased in order to highlight sediment structures. Lithological signatures as shown in figure A2 (cls.: allochthonous clasts; r.sh.: reworked shells; biot.: bioturbation traces; eh.p.: euhedral pyrite; s.bit.: solid bitumen; TS: transgressive surface; p.f.: pelagic fauna).

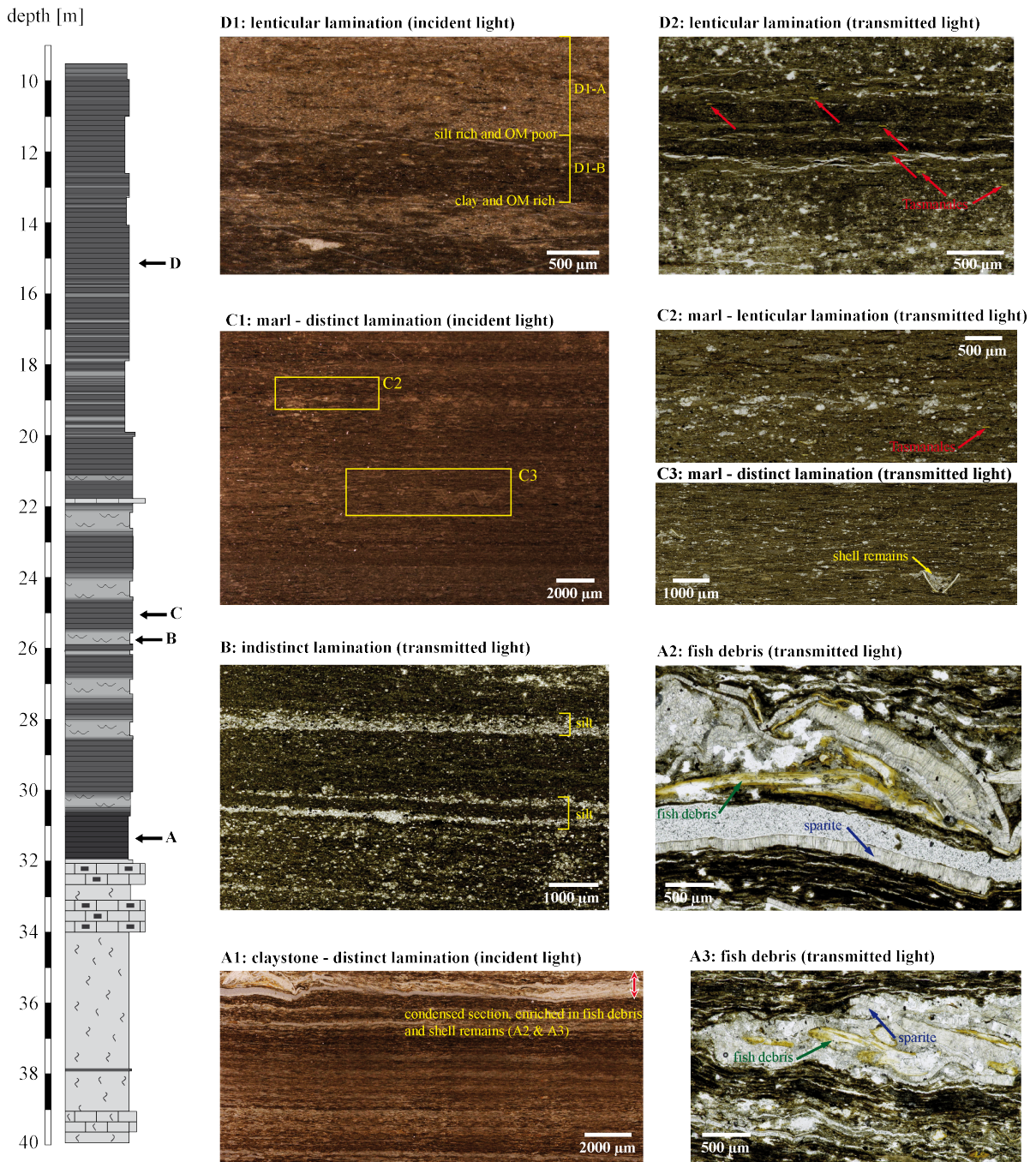


Figure A4: Photographs of thin section (incident and transmitted light) representative for different lithological units of Core FR-210-078. **A:** Microfacies of the basal Schistes Carton Fm showing a distinct to partly lenticular type of lamination (A1). Horizons strongly enriched in fish debris and shell remains hint to condensation and sediment starvation (A2 & A3). **B:** Microfacies of the indistinct laminated horizons intercalated into the upper *H. elegantulum* subzone. Silt-rich intervals might result from more frequent turbidite currents the transported more coarse-grained siliciclastics into the deeper parts of the basin.

A2. Paleogeographic reconstruction of the Western Tethyan shelf

Shelf settings represent dynamical and highly variable sedimentation regimes, which are extremely sensitive towards environmental and oceanographic changes (e.g. [Nittrour, 1981](#); [Einsele, 2000](#); [Coe, 2003](#)). The expression of global environmental changes in marine sediment sequences can be, however, significantly modified by the local paleogeographic conditions, like water depth, distance to land masses and basin/shelf morphology that control water mass exchanges and basin restriction. Therefore, a detailed paleogeographic reconstruction is of interest to understand processes controlling oceanographic conditions throughout shelf settings. Previous works by [Ziegler \(1990\)](#), [Bassoulet et al. \(1993\)](#) and [Thierry et al. \(2000\)](#) already indicated that the Western Tethyan shelf was a heavily structured epicontinental shelf setting, subdivided into different sub-basin that were separated by shallow sills and swells (Fig. A5).

Reconstruction of the shelf morphology of the Western Tethyan shelf presented here (Fig. A6) base on the analysis of lithological and sedimentological information extracted from the references given in figure A5. Shelf morphology and thus the water depth can be inferred from sedimentation style and sediment composition of contemporaneous sediments, which can be associated with different depositional environments (e.g. [Sahagian et al., 1996](#)). Marginal, near coastal areas are characterized by elevated contributions of terrigenous contributions, including sand and silt-sized clastics as well as high concentrations of land plant derived organic matter. Shallow settings, like swells and sills, can be highlighted by sedimentation gaps and hiatuses, which can however also be characteristic for marginal areas as these environments represent high-energetic depositional environments. Deeper basin settings, situated below the wave and storm base, represent low energetic depositional environments. Sediments deposited in such environments are commonly dominated by clay-sized clastics and low contributions of land plant derived organic matter, less affected by erosional events. Furthermore, differences in the stratigraphic thickness of ammonite zones and subzone, which represent the same time spans, can provide information about the spatial variability in accommodation space through the Western Tethyan shelf, which can be associated with different rates of subsidence and differences in water depth.



Figure A5: Paleogeographic reconstruction of the Western Tethyan shelf after Ziegler (1990), Bassoulet et al. (1993) and Thierry et al. (2000) showing the distribution of landmasses (brownish areas) and marine basins (blue areas). Marginal areas are shown in yellow. Areas for which detailed data are available are marked by squares. Further data used for the more detailed paleogeographic reconstruction shown in figure A6 are indicated by numbers 1 to 30 (1: Nøttvedt et al., 2008; 2: Vajda & Wigforss-Lange, 2009; 3: Hesselbo & Coe, 2000; 4: Jenkyns & Clayton, 1997; 5: Caswell & Coe, 2012; 6: Trabucho-Alexandre et al., 2012; 7: Ainsworth & Riley, 2010; 8: Underhill & Stoneley, 1998; 9: Ansonge, 1996; 10: Hesselbo et al., 2011; 11: Baldschun et al., 2001; 12: Sundararaman et al., 1993; 13: Franke, 2014; 14: Gräfe, 2005; 15: Gómez & Goy, 2005; 16: Lorenz & Gely, 1994; 17: Lézin et al., 2001; 18: Bécaud, 2002; 19: Emmanuel et al., 2006; 20: Suan et al., 2013; 21: Mailliot et al., 2009; 22: Léonide et al., 2007; 23: Reisdorf, 2001; 24: Reisdorf et al., 2011; 25: Brigaud et al., 2014; 26: Hermoso et al., 2014; 27: Blaise et al., 2011; 28: van Breugel et al., 2006; 29: Lézin et al., 2013; 30: Röhl & Schmid-Röhl, 2005). (SM: Scottish Massif; FS: Fennosarmantia; IM: Irish Massif; WM: Wales Massif; CH: Cornubia High; LBM: London-Brabant Massif; RM: Rhenish Massif; AM: American Massif; IBM: Iberian Massif; MC: Massif Central; VS: Vindeleceian Swell; BM: Bohemian Massif).

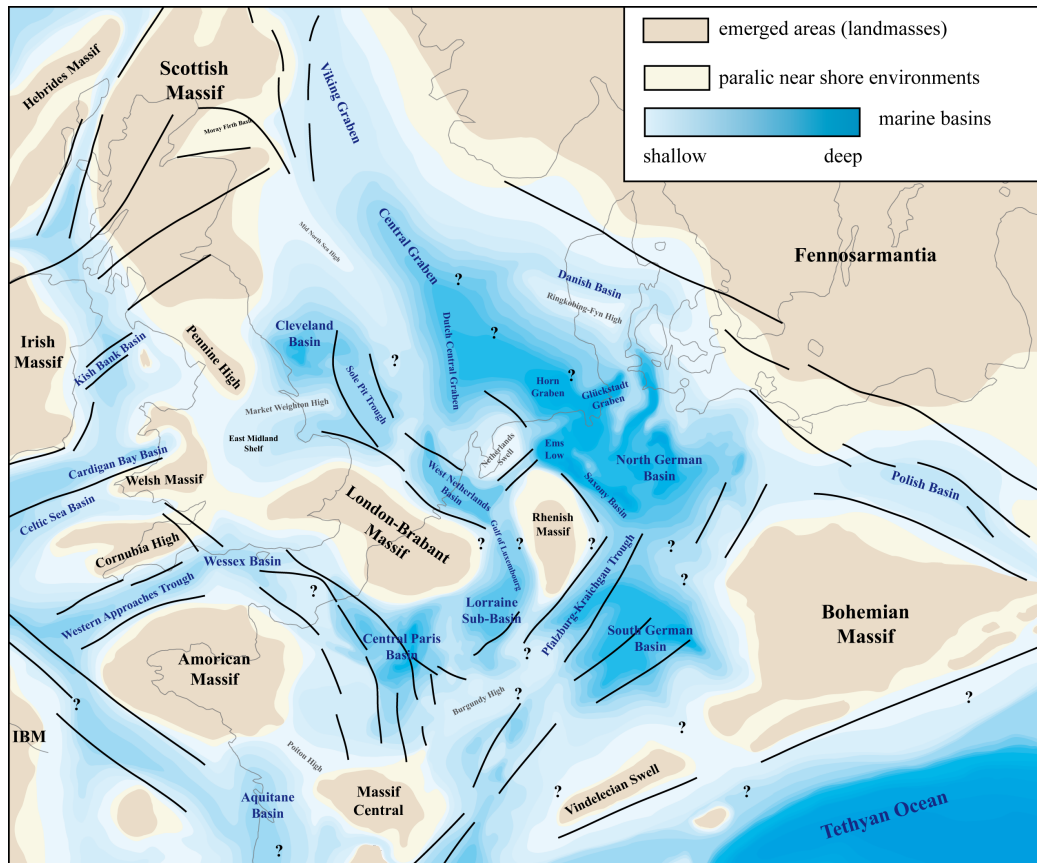


Figure A6: Detailed construction of the Western Tethyan shelf on base of references listed in figure A5. The light-grey line indicates the present-day coastline, black lines indicate major faults active during the lower Jurassic, question marks indicate areas with high uncertainty due to missing Lower Jurassic strata or poor data density.

A3. Methodology and analytical procedures

A multi-proxy approach, comprising continuous measurements and discrete sample analysis, was applied to sediment Core FR-210-078 in order to obtain a comprehensive data set that provide information about changes in sediment composition on a high temporal resolution. Continuous analysis, comprising spectrophotometry and magnetic susceptibility measurements, were performed to obtain a continuous record of changes in sediment features. These records were subjected to spectral analysis in order to identify sediment cycles and to establish a floating chronology for Core FR-210-078. Discrete samples analysis, comprising inorganic, organic and isotope geochemical analysis, were performed for selected samples that were chosen on the base of lithological observations and results from continuous core scanning techniques. Furthermore, selected samples were investigated by microscopic inspection of polished thin sections. An overview about the analytical procedures applied in this work is shown in figure A7.

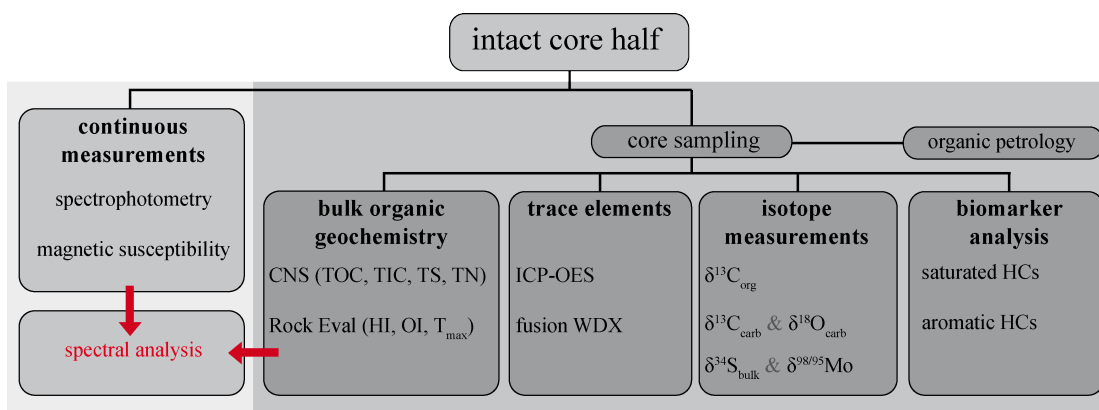


Figure A7: Generalized analytical flow chart showing the different techniques applied to sediment core FR-210-078. High-resolution data obtained from continuous measurements were subjected to spectral analysis. Bulk organic, inorganic and isotope geochemical analysis were performed at discrete samples taken from the core.

A3.1. Continuous measurements

In order to obtain a continuous record of the variability observed in the lithology of Core FR-210-078 different continuous and non-destructive techniques, including spectrophotometry and magnetic susceptibility measurements, were applied to the sediment core. All measurements were taken directly on the cleaned core halves parallel to the strata at fixed steps of 1 cm.

A3.1.1. Magnetic Susceptibility (MagS) measurement

The magnetic susceptibility of a sediment measures the ability of the mineral constituents to acquire magnetization when an external magnetic field is applied (Evans & Heller, 2003). In marine sediments strong positive MagS can be associated with e.g. ferromagnetic iron oxides, whereby paramagnetic clay minerals and pyrite have a weak positive MagS. On the contrary, calcium carbonate and quartz are diamagnetic and characterized by a weak negative MagS. Thus, MagS measurements of marine sediment sequences provide information about changes in sediment composition that can be associated with variable allochthonous and autochthonous contributions. Magnetic susceptibility measurements were performed using a Bartington MS3 device equipped with a MS2E spot reading sensor (sensitivity 2×10^{-6} SI). During data acquisition, blank readings against air were obtained every 10 measurements in order to correct the data for shifts in the sensor's background due to temperature drift.

A3.1.2. Spectrophotometry

Spectrophotometric measurements allow quantify changes in sediment color, resulting from changes in sediment composition, like variation in carbonate and organic matter content as well as variable composition of the detrital sediment fraction (e.g. Balsam et al., 1997). Spectrophotometric parameters were measured using a hand held Konica Minolta CM-700d spectrometer operating in a simultaneous SCI and SCE mode, with an aperture set to 2 mm (SCI: specular component included; SCE: specular component excluded). Results are recorded in the CIE L*a*b*chromaticity space relative to a white standard. Additionally spectrophotometric measurements at a higher resolution of 70 μm were archived for the basal black shale interval of the Schistes Carton Fm (30.75 - 31.97 m) as this interval provide evidence for strong sediment condensation. Ultra-high resolution L*a*b* data sets (resolution 70 μm) for the basal Schistes Carton Fm (30.75 – 31.97 m; Core Interval 3) were obtained from line camera scanning using a JAI 3CCD Line Scan Camera (model CV L107CL).

A3.2. Discrete sample analysis

Subsequent to continuous core scanning, core halves were cut into three parts as shown in figure A8. The stratigraphic high (h) combined in one sample was set to 0.5 to 1.0 cm in order to minimize time-averaging effects. The base of the Schistes Carton Fm was sampled in a higher resolution (~3 mm steps). Furthermore, some samples taken from non-bituminous facies comprise up to 1.5 cm of strata to obtain a sufficient amount of sample material especially for solvent extraction. Samples were selected with respect to the high-resolution data achieved continuous measurements in order to get a representative dataset representing the variability of the sediment succession. Samples taken from the core were crushed and powdered in order to get a homogenous and representative sample material for further analysis. Afterwards the powdered samples were dried in an oven at 40°C for 48 hours. Samples taken from the outer part (I) were subjected to bulk geochemical analysis, including trace metal measurements, CNS, Rock Eval and isotope geochemistry, as these procedures are less sensitive towards possible contaminations. Samples subjected to detailed biomarker investigation were taken from the inner part (II).

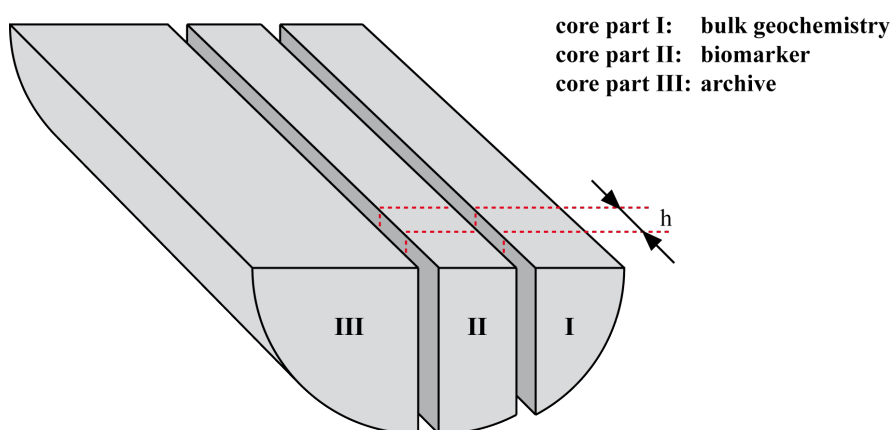


Figure A8: Sampling scheme used to obtain discrete core samples from Core FR-210-078. The sample high (h) was 0.5 - 1.0 cm in order to minimize time-averaging effects. Samples taken from core part I were subjected to bulk-geochemical analysis (CNS, Rock Eval Pyrolysis, trace metal analysis) and isotope measurements that are less sensitive towards contaminations. Solvent extraction and subsequent biomarker analysis was performed on samples taken from the inner core part II.

A3.2.1. Bulk Geochemistry

CNS Analysis

Total carbon (TC), total nitrogen (TN) and total sulfur (TS) contents were directly measured on powdered sample material using a Vario CNS Elemental Analyzer EL III (Elementar®). Total organic carbon (TOC) content was determined on decalcified samples. Decalcification was achieved by treating samples with HCl (10% and 25%) to remove calcium carbonate and dolomite. Subsequently the samples were washed and neutralized with deionized water and dried in an oven at 40°C for 48 h. Values determined on decalcified samples were corrected for their carbonate loss to yield original TOC concentrations. The total inorganic carbon (TIC) was calculated by subtracting corrected TOC from TC. Reproducibility and accuracy were checked by running replicate analysis of laboratory standards and duplicate analysis of samples and is better than 0.01 wt.% for nitrogen, 0.1 wt.% for carbon and sulfur (1 σ). The carbonate content was calculated by multiplying the TIC by 8.33 (stoichiometry of CaCO₃). The amount of organic matter (OM) has been calculated by multiplying the TOC by 1.3, based on the elemental analysis of [Küspert \(1983\)](#) of the Posidonia Shale organic matter. The pyrite/sulfide content has been calculated by multiplying the TS by 1.7, assuming that 90% of the TS is incorporated into sulfides.

Rock Eval Pyrolysis

Rock Eval Pyrolysis is a common technique to characterize organic matter present in a sample in terms of organic matter source, the state of preservation and thermal maturity. Rock Eval pyrolysis was carried out at the original sample material using a VINCI Rock Eval II Analyzer. The amount of free bitumen present in a sample is recorded as S1 (mgHC/gTOC) and the amount of kerogen as S2 (mgHC/gTOC). The pyrolytically released amount of CO₂ is recorded as S3 (mgCO₂/gTOC). The temperature at which the maximum amount of pyrolyzate yields is released is recorded as T_{max} (°C). Reproducibility and accuracy were checked by running replicate analysis of laboratory standards and duplicate analysis of samples and is better than 0.2 mgHC/gRock for the S1 value, 2 mgHC/gRock for the S2 values, 0.3 for S3 mgCO₂/gRock and 1.5°C for T_{max} (1 σ). A detailed description of the methodology is given by [Espitalié et al. \(1977\)](#) and [Bordenave et al. \(1993\)](#). HI and OI values were calculated from S2 and S3 values, respectively by using the formulas:

$$HI = \frac{(S2 * 100)}{TOC} [mgHC/gTOC]$$

$$OI = \frac{(S3 * 100)}{TOC} [mgCO_2/gTOC].$$

A3.2.2. Element concentrations

Aqua Regia ICP-OES

Major and minor trace elements (metals) contents were determined via ICP-OES analysis (Inductively coupled plasma atomic emission spectroscopy) at Activation Laboratories Ltd. (Canada). Powdered samples were digested with Aqua Regia, a partial digestion that uses a mixture of hydrochloric and nitric acid to dissolve sulfides. Oxides and silicates are only partially dissolved. Therefore 0.5 g of powdered sample material was digested with aqua regia for two hours at 95°C. Afterwards the samples was cooled down and diluted with deionized water. Dissolved elements were analyzed via ICP-OES using a Varian Vista 735 ICP-OES. Accuracy and reproducibility of the analysis were monitored by running replicate analysis of laboratory standards and duplicate analysis of samples.

Lithium metaborate/tetraborate fusion - ICP-OES

Quantitative determination of elements bound to refractory minerals (zircon, spherene, monazite, chromite, gahnite, quartz) was done by lithium metaborate/tetraborate fusion – ICP-OES. Analysis was done at Activation Laboratories Ltd. (Canada). For analysis, 3 g of powdered rock sample is mixed with a flux of lithium metaborate and lithium tetraborate and fused in an induction furnace afterwards. The melt is then immediately poured in a weak nitric acid (5%) containing an internal standard, and mixed continuously until completely dissolved. Dissolved elements were then analyzed using a Thermo Jarrel-Ash ENVIRO II ICP-OES. Calibration was performed using prepared USGS and GANMET certified reference materials. In addition certified standards and blanks analysis were done for every batch of ten samples.

A3.2.3. Stable Isotope Geochemistry

Isotopic composition of the carbonate ($\delta^{18}\text{O}$ and $\delta^{13}\text{C}$)

Stable oxygen and carbon isotope measurements at the carbonate fraction were performed at the University Erlangen-Nürnberg. Powdered rock samples were treated with 103% phosphoric acid at 70°C using a Gasbench II connected to a ThermoFinnigan Five Plus mass spectrometer. Isotope values were reported in per mil relative to V-PDB by assigning a $\delta^{13}\text{C}$ and a $\delta^{18}\text{O}$ to NBS19 and -49.6‰ and -26.7‰ to LSVEC, respectively. Reproducibility and accuracy were monitored by replicate analysis of laboratory standards calibrated to NBS19 and LSVEC and is better than 0.1‰. A detailed description of the methodology is given by [Rosenbaum & Sheppard \(1986\)](#) and [Kim et al. \(2007\)](#). Results were reported in standard δ notation (in ‰) using the equations:

$$\delta^{13}\text{C} = \left[\frac{{}^{13/12}\text{C}_{\text{sample}} - {}^{13/12}\text{C}_{\text{standard}}}{{}^{13/12}\text{C}_{\text{standard}}} \right] \times 1000$$

$$\delta^{18}O = \left[\frac{{}^{18/16}O_{sample} - {}^{18/16}O_{standard}}{{}^{18/16}O_{standard}} \right] \times 1000$$

Organic carbon isotopes ($\delta^{13}C_{org}$)

Stable carbon isotope measurements for the bulk organic carbon were performed at the decalcified sample material. Carbonate was removed from the sample by acid leaching as described under point 3.2.3.. Stable isotope analysis was performed using a Thermo Finnigan Delta^{PLUS}XL (aka Alaska) coupled to a Costech EA at the Isotope Science Lab (University of Calgary, Alberta, Canada). Isotope ratios are expressed in conventional delta notation: $\delta_{sample} (\text{‰}) = [(R_{sample} - R_{standard}) / R_{standard} - 1] \times 1000$, where R is the ratio of $^{13}C/^{12}C$ of the sample and the standards V-PDB for carbon. Reproducibility and accuracy were monitored by replicate standard and sample analysis and are better than 0.2‰ for $\delta^{13}C_{org}$.

Sulfur isotopes ($\delta^{34}S_{bulk}$)

Stable sulfur isotopes ($^{34/32}S$) were measured via combustion of the untreated powdered bulk-sample using a Thermo Finnigan Delta V (aka Vathi) with Elementar Vario ISOTOPE cube at the Isotope Science Lab (University of Calgary, Alberta, Canada). The mass spectrometer is equipped with a collector array for simultaneous analysis of SO_2 and SO , which allows for oxygen isotope effects to be corrected for during analysis. Sulfur isotope values were reported in conventional delta notation relative to VCDT (Vienna Canyon Diablo Troilite). Reproducibility of the analysis is better than 0.3‰. This method allows to determine the $^{32}S/^{34}S$ isotopic ratio of the bulk sulfur, consisting of carbonate associated and pyrite bounded sulfur. Distinguishing between both sulfur species is not possible by using this method.

$$\delta^{34}S = \left[\frac{{}^{34/32}S_{sample} - {}^{34/32}S_{standard}}{{}^{34/32}S_{standard}} \right] \times 1000$$

Molybdenum isotopes ($\delta^{98/95}Mo_{bulk}$)

Stable isotope analysis of molybdenum (Mo) was performed in the isotope laboratory of the Department of Physics and Astronomy, University of Calgary, Canada. Powdered samples (~200 mg) were weighed into teflon beakers or acid digestion using a combination of $HF+HNO_3$, $HCl+HNO_3$ and HCl . Afterwards samples were subjected to an ion exchange procedure in order to extract Mo (Wieser et al., 2007). Molybdenum concentrations and isotope ratios were determined by “double spiking” (Wieser and De Laeter, 2007). The samples were doped with a known quantity of $^{98}Mo/^{92}Mo$ spike Mo before any sample preparation step to monitor mass fractionation during sample preparation (Siebert et al., 2001). Molybdenum isotope measurements were performed on a

Thermo Scientific multi-collector inductively coupled plasma mass spectrometry (MC-ICP-MS) and are reported as:

$$\delta^{98}\text{Mo} = \left[\frac{{}^{98/95}\text{Mo}_{\text{sample}}}{{}^{98/95}\text{Mo}_{\text{standard}}} - 1 \right] \times 1000$$

Samples were measured against an in-house standard and stable molybdenum isotope ratios are referenced to NIST SRM-3134 (Greber et al., 2012). Analytical uncertainty was assessed by running replicate analysis and was better than $\pm 0.20\%$.

A3.2.5. Molecular Geochemistry

Solvent Extraction

Extractable organic compounds (bitumen) were obtained from solvent extraction using an ASE® 200 (Accelerated Solvent Extraction; Dionex). Powdered samples were extracted using a mixture of dichloromethane (DCM) and methanol (MeOH) (93:7, v/v) at 75°C and 50 bar. Heating time was set to 5 min and the static extraction time to 20 min. A detailed description of the method is given by Richter et al. (1996). After extraction the solvent volume was reduced to less than 1 ml using a Büchi parallel evaporator and total lipid extracts (TLE) were transferred into pre-weight glass vials. Afterwards, complete solvent evaporation was achieved under atmospheric conditions under a fume hood. Extract yields were archived from balancing the glass vials including dry extracts and subtracting the weight of the empty glass vials.

Column chromatography

Total lipid extracts (TLE) were separated into aliphatic (saturated), aromatic and NSO compounds using column chromatography that was performed by a FREESTYLE® SPE robot system (LCTech). Therefore, a small amount of silica 60 mesh (63 – 200 µm) was filed in a glass vial and impregnated with an extract aliquot of about 10 mg dissolved in 200 µl DCM. The glass vial was placed under a fume hood until all DCM was evaporated. The impregnated (and solvent-free) silica was loaded on a 8 ml SPE column that was filled with 2.8 g Silica 60 mesh (25 – 40 µm). Afterwards, the prepared SPE columns were placed on the autosampler rack of the FREESTYLE® SPE robot system. Aliphatic hydrocarbons were eluted by flushing the SPE column with 6 ml *n*-pentane, aromatic hydrocarbons were eluted by flushing with 6 ml *n*-pentane/DCM (3/2; v/v) and hetero compounds were eluted by flushing with 16 ml DCM/MeOH (1/1; v/v) and the hydrocarbon fractions were collected in different glass vials.

After column chromatography the aliphatic hydrocarbon fractions were treated with activated copper in order to remove elemental sulfur. Copper was activated by acid treatment (HCl 25%) on a heating plate for 15 min and neutralization with distilled water afterwards. Before adding

to the aliphatic hydrocarbon fraction copper was treated with 2-propanol and DCM in order to remove residual water and to avoid contamination, respectively. Copper and formed sulfides were removed from the aliphatic fraction by filtration. Aliphatic and aromatic hydrocarbon fractions were concentrated to a volume of about 1 ml and transferred to a 2 ml auto-sampler vial. To allow a quantification of single compounds internal standard compounds were added to the saturated and aromatic fractions. Therefore, d_{50} tetracosane and d_4 cholestane were added to the aliphatic fractions and d_{10} pyrene was added to the aromatic fraction.

GC-MS Measurement

Aliphatic and aromatic fractions were analyzed by gas chromatography-mass spectrometry (GC-MS) in order to investigate the biomarker distribution. Measurements were performed on an Agilent 7890A Gaschromatograph equipped with a Chromech Evolution MS/MS (built upon an Agilent 5975B MSD; www.chromtech.de). Compound mixtures were separated on a fused silica column (Agilent DB1HT; 30 m length, 0.25 mm inner diameter, 25 μ m film thickness). Helium was used as carrier gas at a flow rate of 1 ml/min. Samples were injected into an Agilent Multimode-Inlet (MMI) in splitless mode, equipped with a bottom hole liner. The temperature program of the MMI was: 50°C (0 min) to 400 at 400°C/min (held for 4 min), then to 280°C at 10°C/min. The over program was: 50°C (5 min iso.) to 140°C at 10°C/min, then to 325°C at 2°C/min (held for 10 min). The quadrupol mass spectrometer operating in scan mode in the mass-charge range from 50 to 750.

A3.3. Organic petrology and microscopy of thin sections

Organic petrography is widely used in the field of organic geochemistry and can provide information about composition of organic matter and microlithotype. Investigation base on the microscopic inspection of polished blocks with a size of 2 – 3 cm². Therefore, whole-rock samples were taken from the core and prepared following the international standard procedure ISO7404-2: 2009 (E). Petrographic analyzes were performed by Walter Pickel at the Coal & Organic Petrology Services Pty Ltd..

The microscopic inspection of thin sections can provided detailed insights into the microstructure of sediments and thus into sedimentation processes. Polished thin sections were prepared from selected sample in bedding-normal orientations (Trabucho-Alexandre et al., 2012 and references therein). Microscopic photographs were taken by using a Keyence digital microscope VHX-700F.

A3.4. Spectral Analysis

High-resolution data sets obtained from continuous core scanning as well as high-resolution bulk geochemical data ($\delta^{13}C_{org}$ data) were subjected to spectral analysis in order to identify periodic signals. Spectral analysis was performed using the multi-taper method (MTM, [Thomson, 1982](#)) as

implanted in the KSpecra toolkit V3.4.1. (Ghil et al., 2002). Power spectra were calculated with 3 tapers and a resolution of 2. Confidence levels were calculated using the robust red-noise modeling method (Mann & Lees, 1996). Prior analysis long-term trend, if present, were removed using 3rd order polynomial regressions. In order to reduce the impact of variations in sedimentation rate spectral analysis was performed separately for different core intervals that were distinguished on the base of lithological parameters. To convert the depth domain to the time domain a*-records of all intervals were time-calibrated separately. The ultra-high resolution a*-data for Interval 3 were incorporated into the 1 cm scaled a*-data set (Intervals 1, 2 and 4) and a composite time-scale was built. The tuned a*-data set was analyzed by the MTM method again. Results are compared with the Milankovitch parameters for the Toarcian (according to Laskar et al., 2004).

A4. GC-MS traces

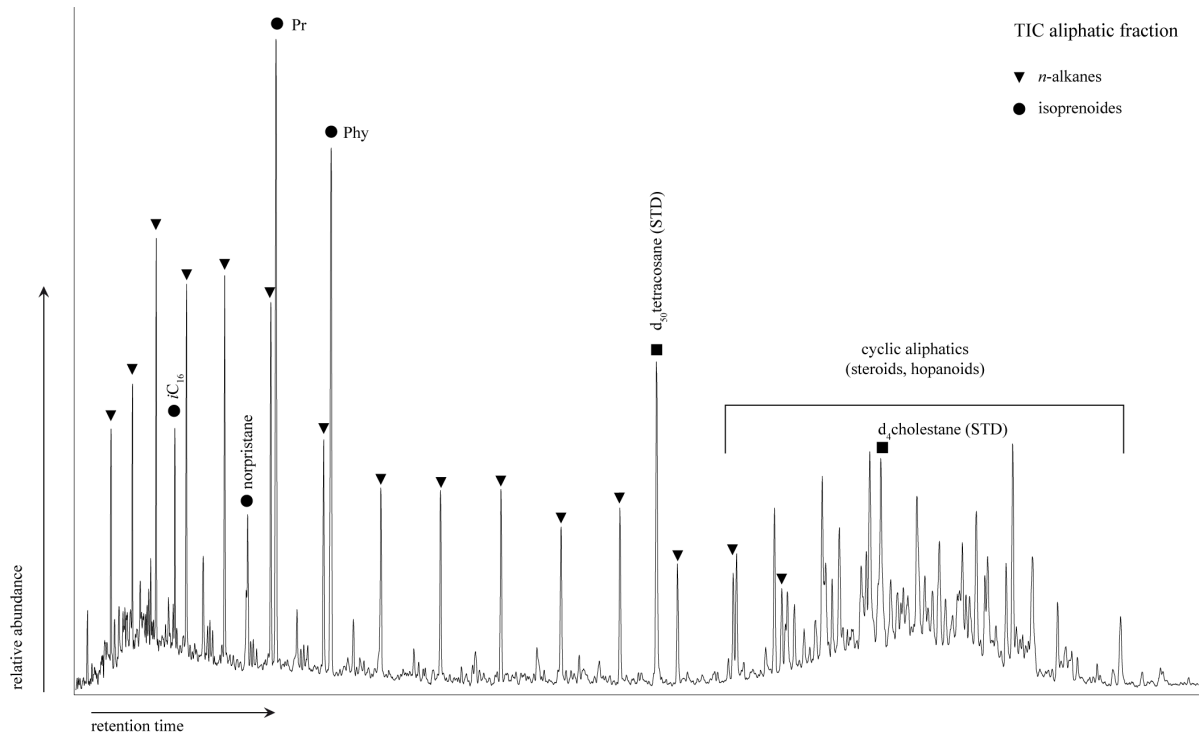


Figure A9: Total ion current chromatogram of an aliphatic fraction from a sample from the Schistes Carton Fm (*H. serpentinum* zone). Aliphatic hydrocarbon fractions are dominated by *n*-alkanes, the isoprenoids pristane and phytane and by cyclic compounds, comprising regular steranes, diasterenes 4Me-diasterenes, regular hopanes and hopenes.

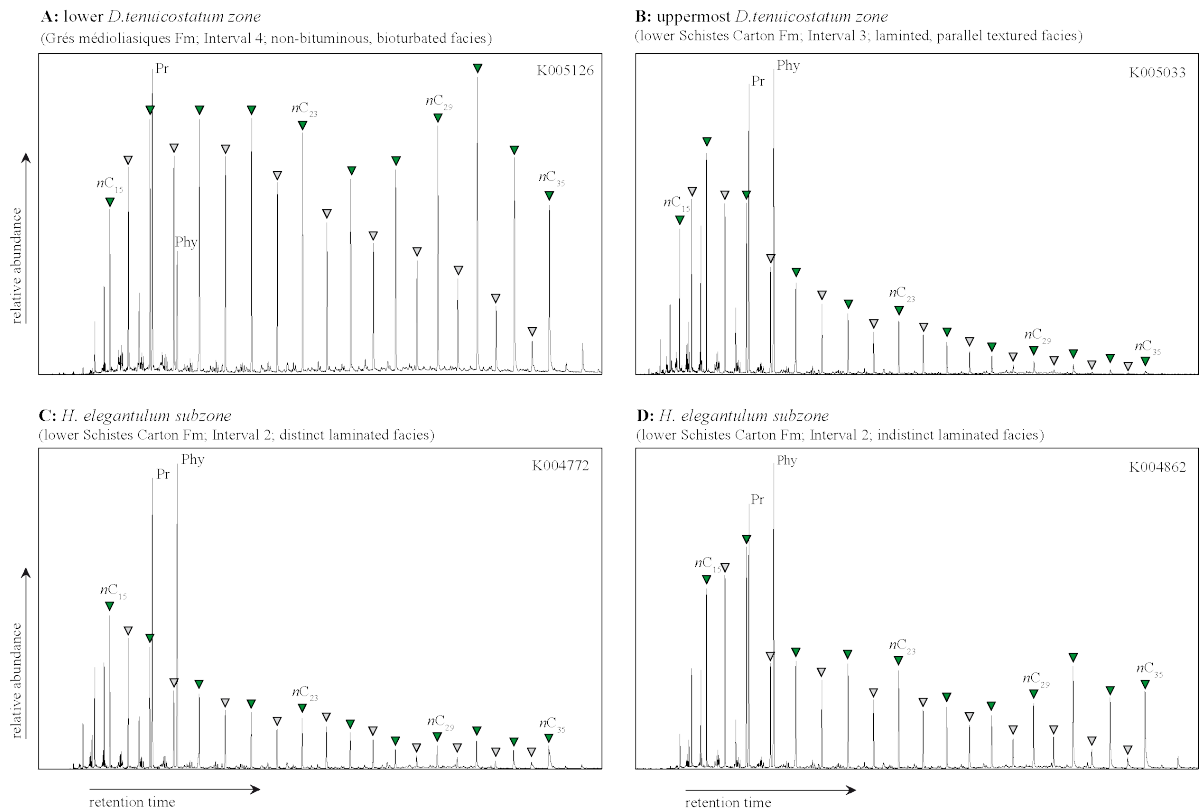


Figure A10: Representative ion chromatograms (m/z 85) of an aliphatic hydrocarbon fraction showing the n -alkane distribution for the different facies types identified throughout Core FR-210-078.

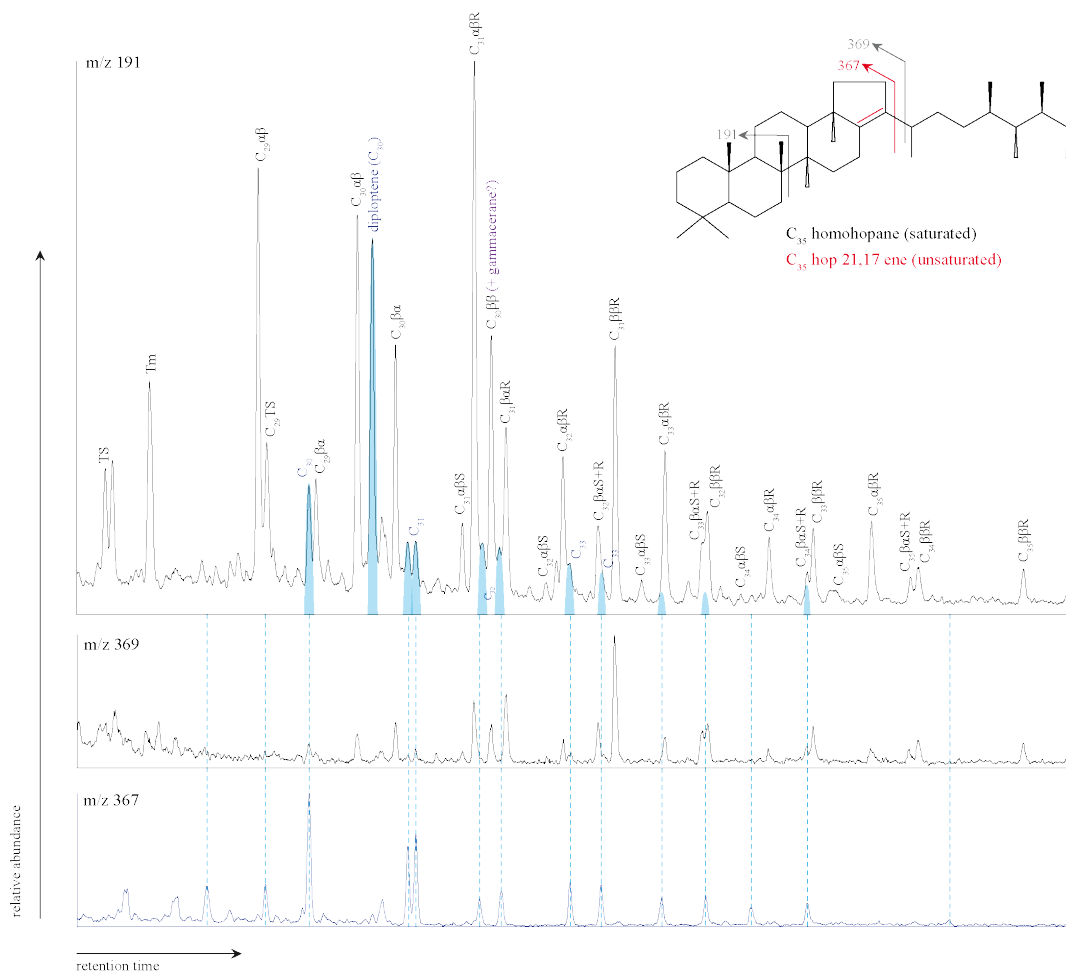


Figure A11: Ion chromatograms m/z 191, 369, 367 of an aliphatic hydrocarbon fraction showing the distribution of regular hopanes (homohopanes) and hopenes (highlighted blue).

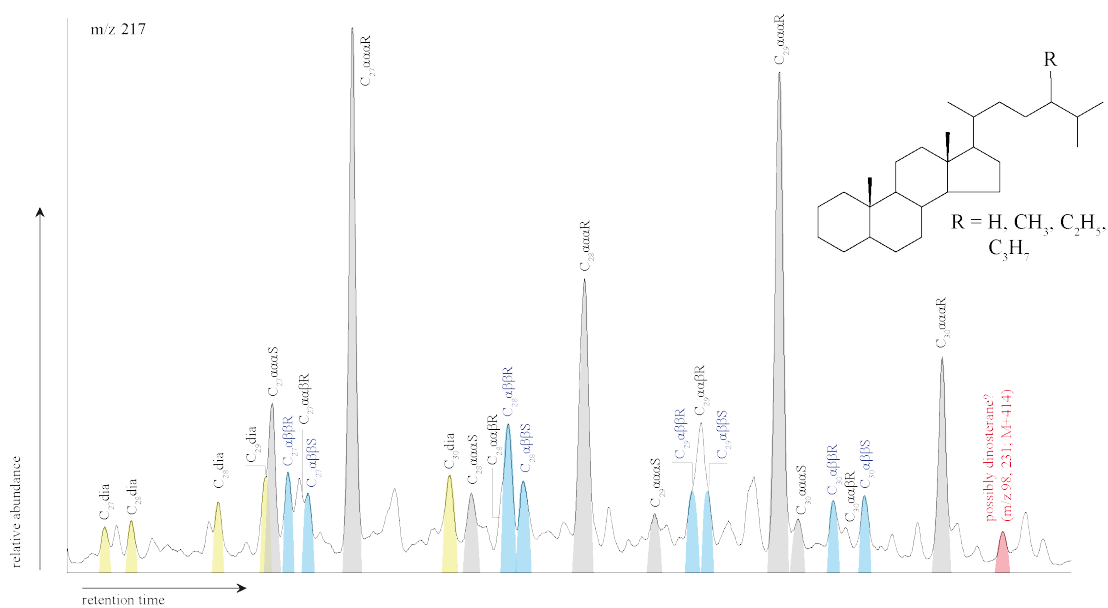


Figure A12: Ion chromatogram m/z 217 of an aliphatic hydrocarbon fraction showing the distribution of regular steranes in the range from C_{27} to C_{30} . The C_{27} cholestanes, C_{28} methylcholestanes, C_{29} ethylcholestanes and C_{30} propylcholestanes occur in $\alpha\alpha\alpha S+R$, $\alpha\beta\beta S+R$ as well as in $\alpha\alpha\beta S+R$ configuration. Furthermore, corresponding diasteranes were observed for each sterane species.

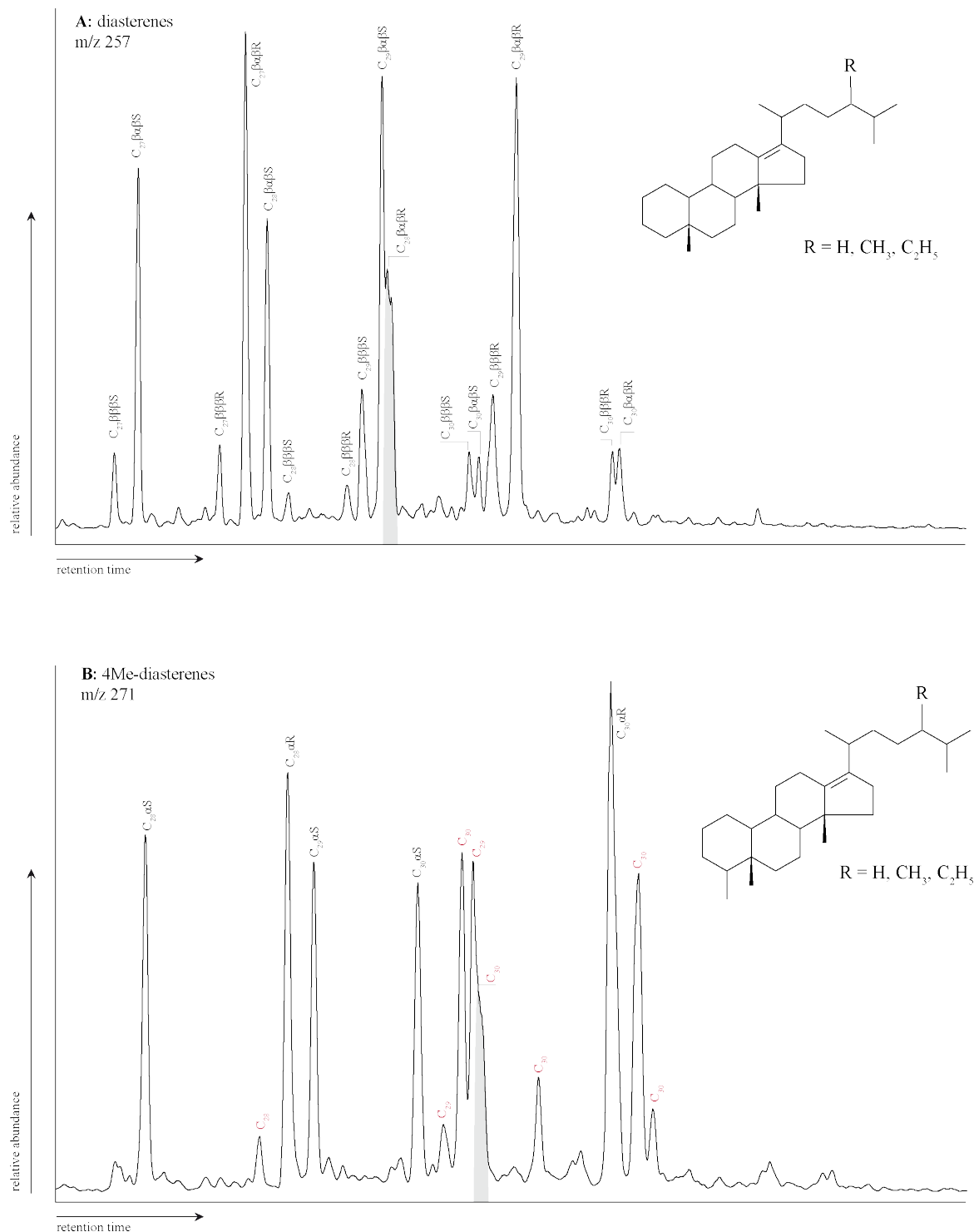


Figure A13: A) Ion chromatogram m/z 257 of an aliphatic hydrocarbon fraction showing the distribution of diasterens in the range from C_{27} to C_{30} , which are the dominating steroidal compounds. Each diasterene occur in $\beta\beta\beta S+R$ and $\beta\alpha\beta S+R$ substitution. **B)** Ion chromatogram m/z 271 of an aliphatic hydrocarbon fraction showing the distribution of 4Me-diasterens, which occur in the range from C_{28} to C_{30} . The exact elution order of the different isomers is not fully

established. The C₃₀ 4Me-diasterenes have either a 24-ethyl or a 23, 24-dimethyl substitution, which couldn't be distinguished on the base of the mass spectrums.

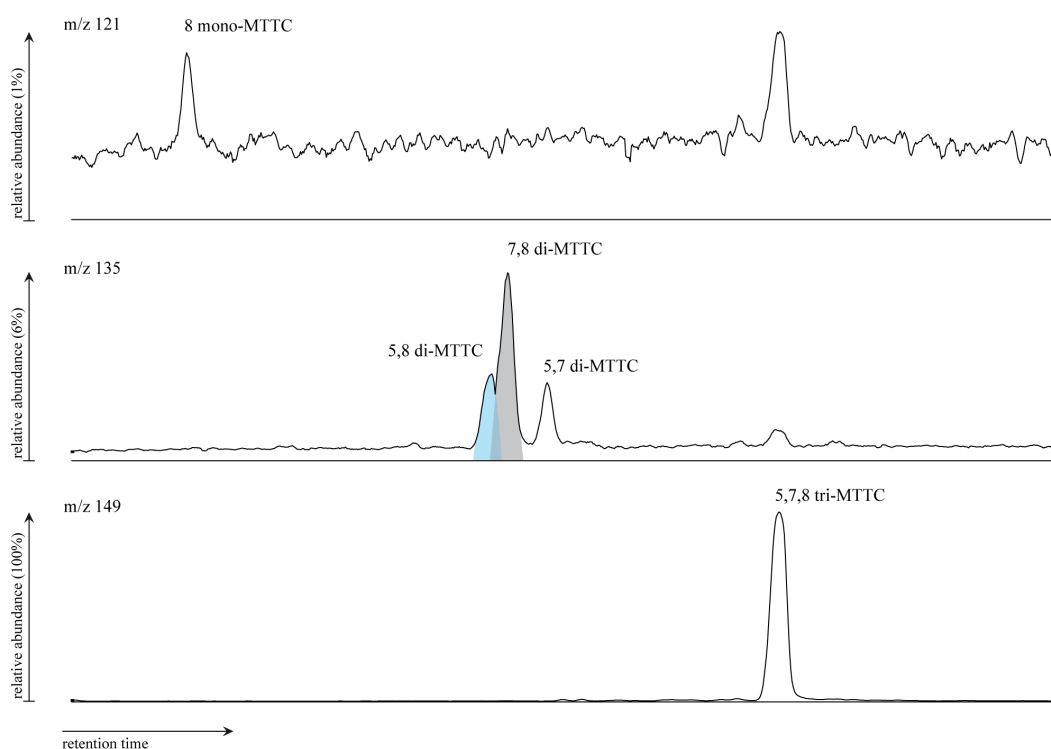


Figure A14: Ion chromatograms m/z 121, 135 and 149 of an aromatic hydrocarbon fraction showing the distribution of mono-, di, and tri-MTTCs (methyltrimethyltridecylchromanes). All samples are dominated by tri-MTTCs, whereas mono-MTTCs occur only in traces. The abundance of the tri-MTTCs has been set to 100%, the relative abundance of the di- and mono-MTTCs is given for comparison. For molecular structures the reader is referred to [Sinninghe Damsté et al. \(1987\)](#).

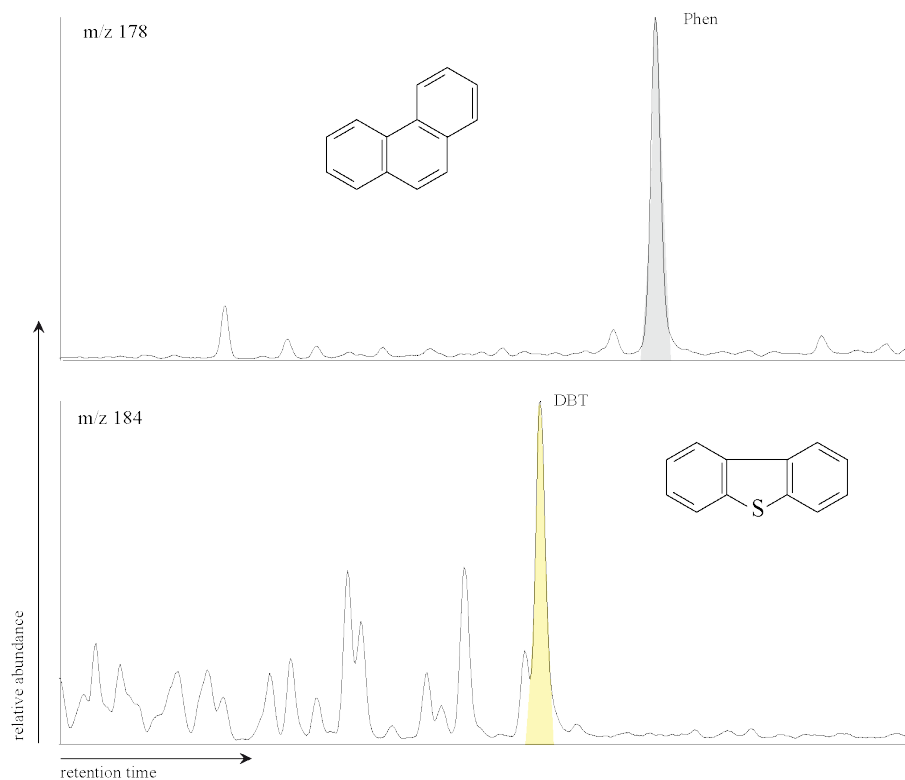


Figure A15: Ion chromatograms of m/z 178 and of m/z 184 of an aromatic hydrocarbon fraction showing phenanthrene (Phen) and dibenzophenanthrene (DBT).

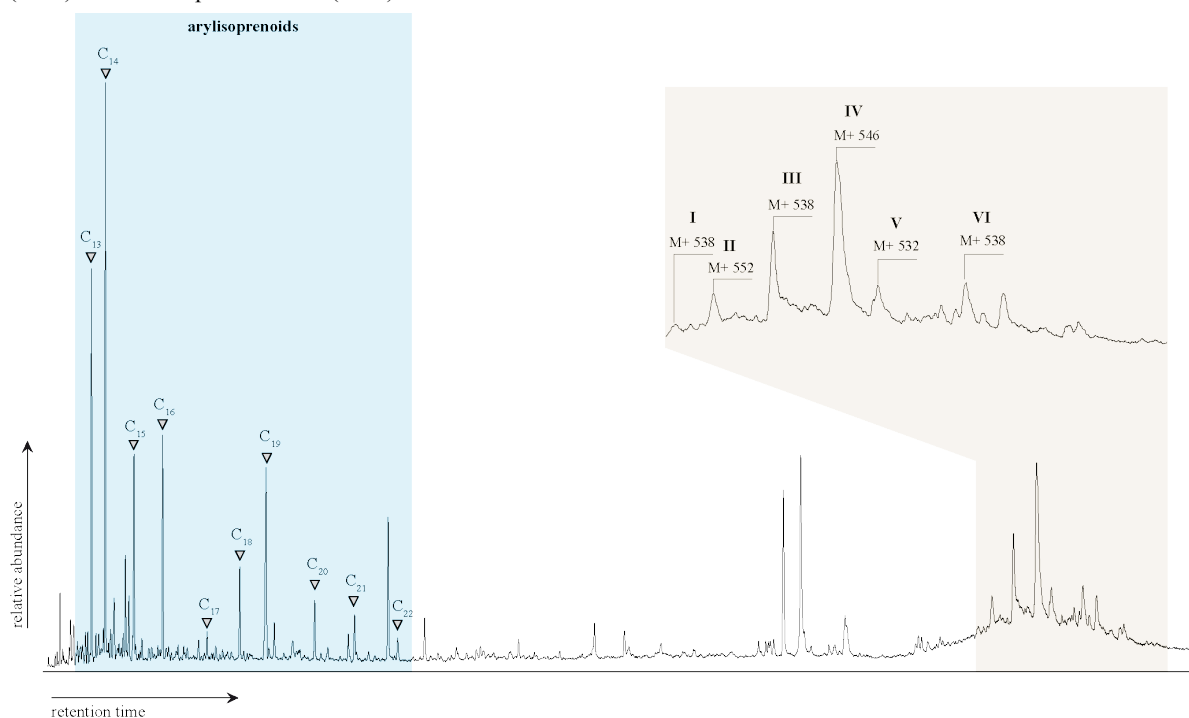


Figure A16: Ion chromatograms m/z 133 of an aromatic hydrocarbon fraction showing the distribution aryl isoprenoids (from C_{13} to C_{22}) as well as aromatic carotenoid biomarkers (II: β -isorenieratane; IV: isorenieratane) and diagenetic products (I, II, V, VI).

Supplementary information

S1. Supplementary information: Chapter One

Table S1-1: Summary of magnitudes documented for the Toa-CIE from different locations and different depositional environments. The magnitude documented in OM varies between -4 and -6‰. High higher variability is documented in the magnitude of carbonate carbon isotope values that range from -2 to -6‰ (-12‰). Extreme low $\delta^{13}\text{C}_{\text{carb}}$ values are documented from anoxic settings. Data from anoxic settings are marked in red, data from suboxic setting in green and data from oxic settings in blue.

data source	location	facies	type of analysis	magnitude Toa-CIE [‰]
Küspert, 1986	Southern German Basin, Ger	Anoxic	OM	-4 to -5
			Carbonate	-10
Jenkyns, 1985	Dogan, Italy	Oxic	Carbonate	-3
Jenkyns & Clayton, 1986	Italy	Suboxic	Carbonate	-3 to -5
Jiménez et al., 1996	Basque Basin, Spain	Oxic	Carbonate	-2
Jenkyns & Clayton, 1997	Cardigan Bay Basin, UK	Anoxic	OM	-7
			Carbonate	-6
			Carbonate	-3
Morettini & Bartolini, 1999	Winterborne Kingstone, UK	suboxic	Carbonate	-3
	Italy	Oxic	Carbonate	-3
Hesselbo et al., 2000	Hawsker Bottoms, UK	Anoxic	OM	-6
			Carbonate	-5
Jenkyns et al., 2001	Dogna, Italy	Suboxic	OM	-8
Röhl et al., 2001	Southern German Basin, Ger	Anoxic	OM	-6
			Carbonate	-6
Duarte et al., 2003	Lusitanian Basin, P	oxic	Carbonate	-3
Kemp et al., 2005	Hawsker Bottoms, UK	Anoxic	OM	-7
Emmanuel et al., 2006	Aquitane Basin, Fr	Anoxic	Carbonate	-6
Van Breugel et al., 2006	NE Paris Basin, Fr	Anoxic	OM	-6
Hesselbo et al., 2007	Lusitanian Basin, P	Oxic	Carbonate	-3
Sabatino et al., 2009	Valdorbina, Italy	Suboxic	OM	-6
			Carbonate	-4
			OM	-7
Bodin et al., 2010	N-Africa	Oxic	Carbonate	-3
Caruthers et al., 2011	N-America, Can	Anoxic	OM	-6
Gröcke et al., 2011	Inuyama, Japan	Suboxic?	OM	-6
Kafousia et al., 2011	Greece	Oxic	OM	-4
			Carbonate	-2
Suan et al., 2011	Arctic	Anoxic	OM	-4 to -6
Hermoso et al., 2012	Southern Paris Basin, Fr	Anoxic	OM	-7
			Carbonate	-6
Tabucho-Alexandre et al., 2012	Dutch Central Graben, NI	Anoxic	OM	-6
Sabation et al., 2013	Adriatic Platform, Croatia	Oxic	Carbonate	-2 to -3
Kemp & Izumi, 2014	Japan	Suboxic	OM	-3
Krencker et al., 2015	N-Africa	Oxic	OM	-4
			Carbonate-	-5
Monte-Serrano et al., 2015	Southern German Basin, Ger	Anoxic	OM	-4
			Carbonate	-6
Suan et al., 2015	Southern German Basin, Ger	Anoxic	OM	-6
			Carbonate	-6 (-12)

Table S1-2: Data sources for oxygen isotope data available for the Pliensbachian and Toarcian presented in figure 1-10.

Data source	Material	location	Period covered
Hesselbo et al., 2000b	Belemnites	Cleveland Basin, UK	PI
McArthur et al., 2000	Belemnites	Cleveland Basin, UK	upper PI to lower Toa
Jenkyns et al., 2002	Belemnites	Cleveland Basin, UK	PI to Toa
Baily et al., 2003	Belemnites	Southern German Basin, Ger	upper PI to lower Toa
Rosales et al., 2004	Belemnites	Basque-Cantabrian Basin, Es	PI to lower Toa
Van de Schootbrugge et al., 2005	Belemnites	Basque-Cantabrian Basin, Es	PI to lowermost Toa
Gomez et al., 2008	Belemnites	Basque-Cantabrian Basin, Es	upper PI to lower Toa
Metodiev & Koleva-Rekalova, 2008	Belemnites	Western Balkan, Bulgaria	Toa
Dera et al., 2009b	Belemnites & fish	Paris Basin, Fr	Toa
Nunn et al., 2009	Belemnites	West Herbrides Basin, UK	PI
Gomez & Arias, 2010	Belemnites	Es	Lower Toa
Price et al., 2010	Belemnites	West Herbrides Basin, UK	Toa
Suan et al., 2010	Brachiopodes	Lusitanian Basin, P	PI to lower Toa
Dera et al., 2011a	Belemnites	Paris Basin, Fr	Toa
Korte & Hesselbo, 2011	div. biocalcifiers	Cleveland Basin, UK	PI to lowermost Toa
Li et al., 2012	Belemnites	Cleveland Basin, UK	Toa
Harazim et al., 2013	Belemnites	Grands Causses Basin, Fr	upper PI to Toa
Aremdariz et al., 2014	Belemnites	Asturian Basin, Es	PI
Krencker et al., 2014	Brachiopodes	Oran Meseta, Marocco	Toarican
Ullmann et al., 2014	Belemnites	Cleveland Basin, UK	upper PI to lower Toa

S2. Supplementary information: Chapter Two

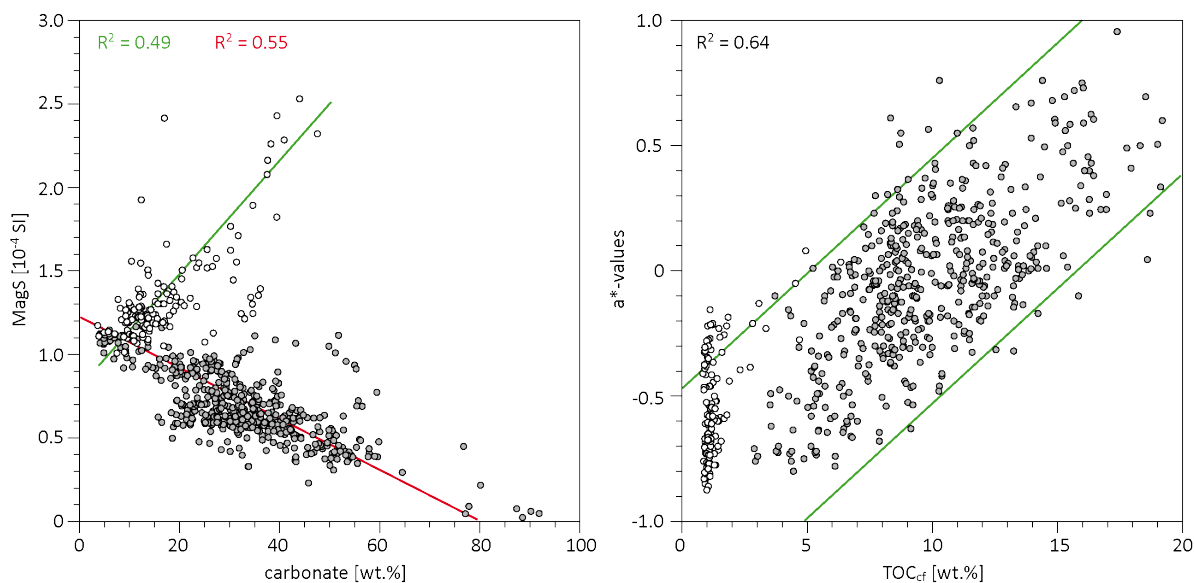


Figure S2-1: Cross-plot of carbonate content with MagS-values (left) shows a positive correlation for samples corresponding the Grès médioliasiques Fm and a negative correlation for samples corresponding the Schistes Carton Fm. The positive correlation between carbonate and MS-values might indicate contributions of Fe-bearing carbonates such as ankerite or siderite. The negative correlation between carbonate and MS-values in sediments of the Schistes Carton Fm indicates variable degrees of dilution of terrigenous-derived clay minerals by marine carbonate. The positive correlation observed between a*-values and TOCcf (total organic carbonate on carbonate-free base) indicate that changes in organic matter abundance (and possible associated sulfides) have a strong impact on this parameter.

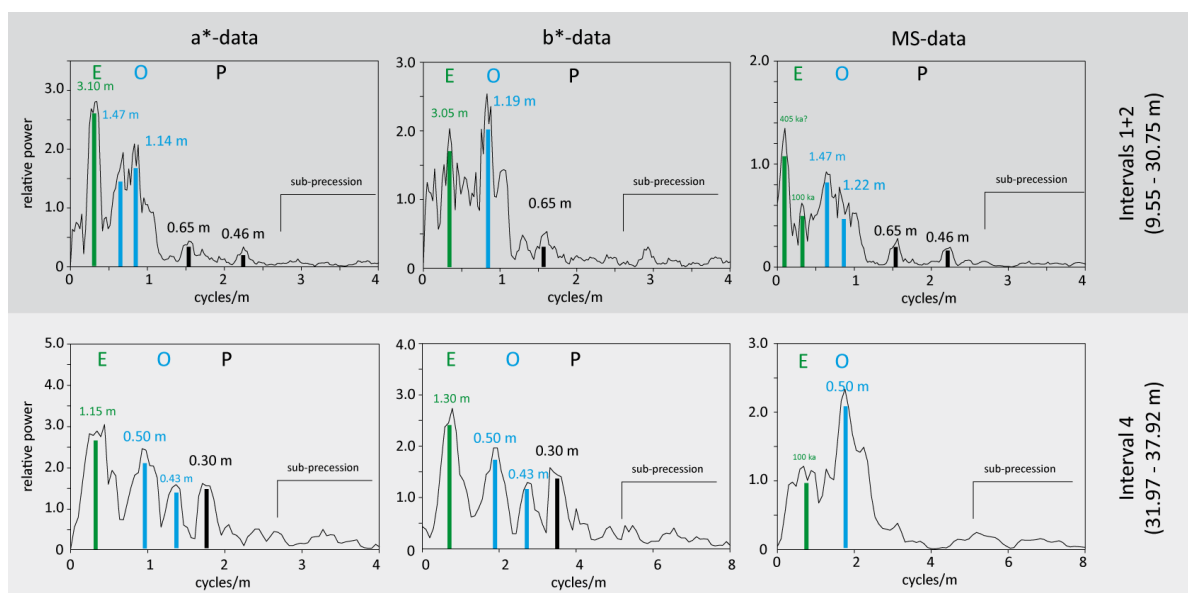


Figure S2-2: 2π -MTM power spectrum for Intervals 1+2 (top) and for Interval 4 (bottom) of a*-, b*-, and MS-data (MS-data within Interval 4 analyzed from 34.00 – 38.00 m). Throughout Intervals 1+2 (top) the presence of regular cycles with a mean wavelength of around 3.10 m, 1.47 m, 1.20 m, 0.65 and 0.46 m is confirmed. The presence of regular cycles with a mean wavelength of around 1.20 m, 0.50 m, 0.43 m and 0.30 m is confirmed for Interval 4. In Interval 4 slightly different wavelengths of the low-frequency compounds are observed between a*- and b*-data. This discrepancy can be attributed to the incomplete removal of preferentially low-frequency cycles by erosional events. On the base of their cycle hierarchy we attribute those cycles to short eccentricity (E), obliquity (O) and precession (P) based cycles.

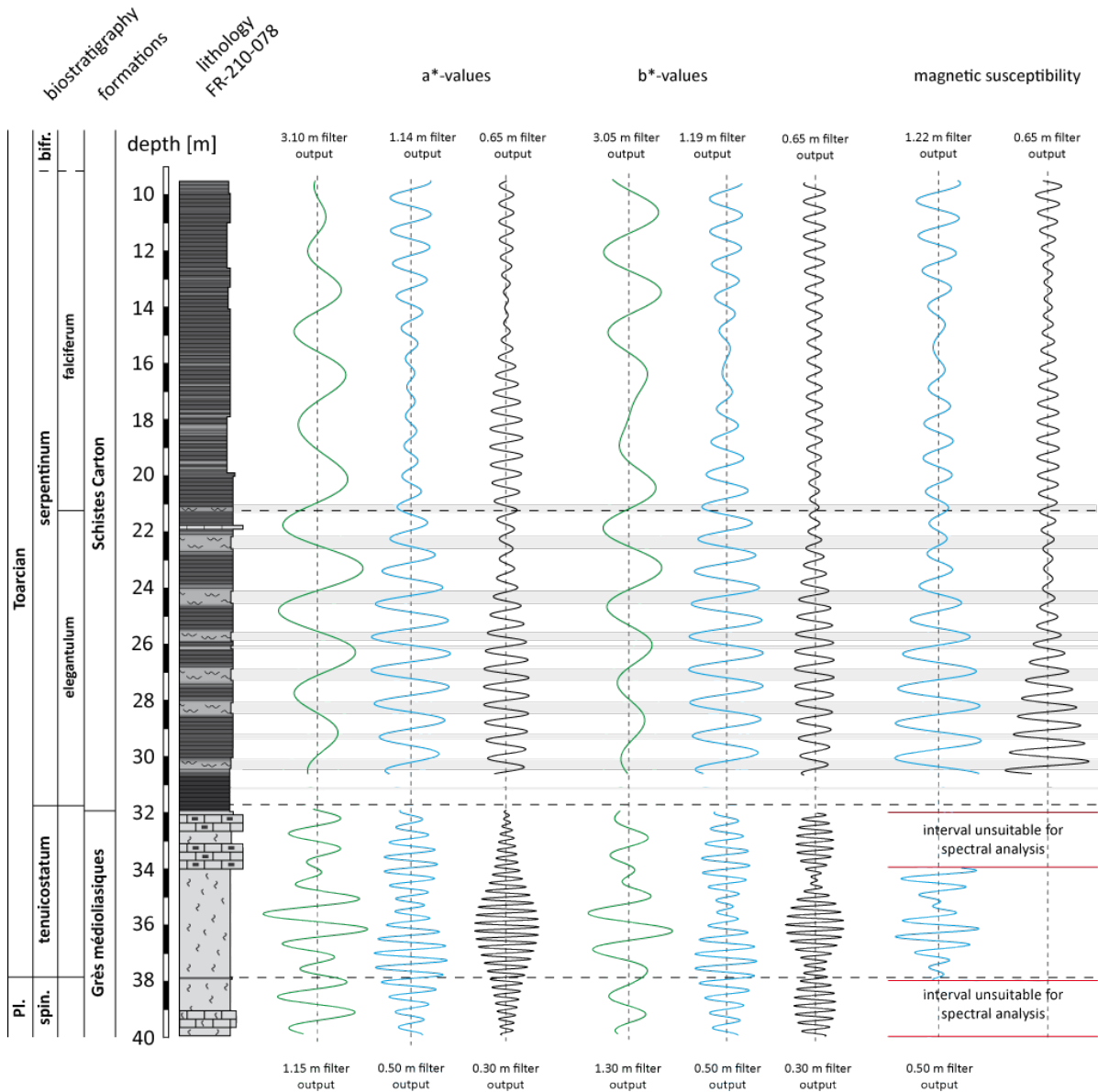


Figure S2-3: Filter output for a^{*}-, b^{*}- and MagS-values of significant spectral peaks (see Fig S3A). The 100 kyr eccentricity, 35 kyr obliquity and 21 kyr precession components are well expressed in the parameters investigated. The 100 kyr eccentricity component is always very weak in MS-data, whereas sediment color seems to be more sensitive towards this frequency component. By analyzing Intervals 1 + 2 the presence of a 100 kyr eccentricity component is confirmed for Interval 2 and the 1.10 m cycle within this interval can be clearly attributed to the obliquity component. The 100 kyr eccentricity component might be weak in Interval 2 as this interval represents only a short period of time (around 290 to 315 kyr) and thus cover only 3 short eccentricity cycles. Cycles were extracted using the Gaussian filter with a bandwidth of 0.2 for Intervals 1 and 2. A bandwidth of 0.25 was used to extract cycles in the Interval 4.

S3. Supplementary information: Chapter Three

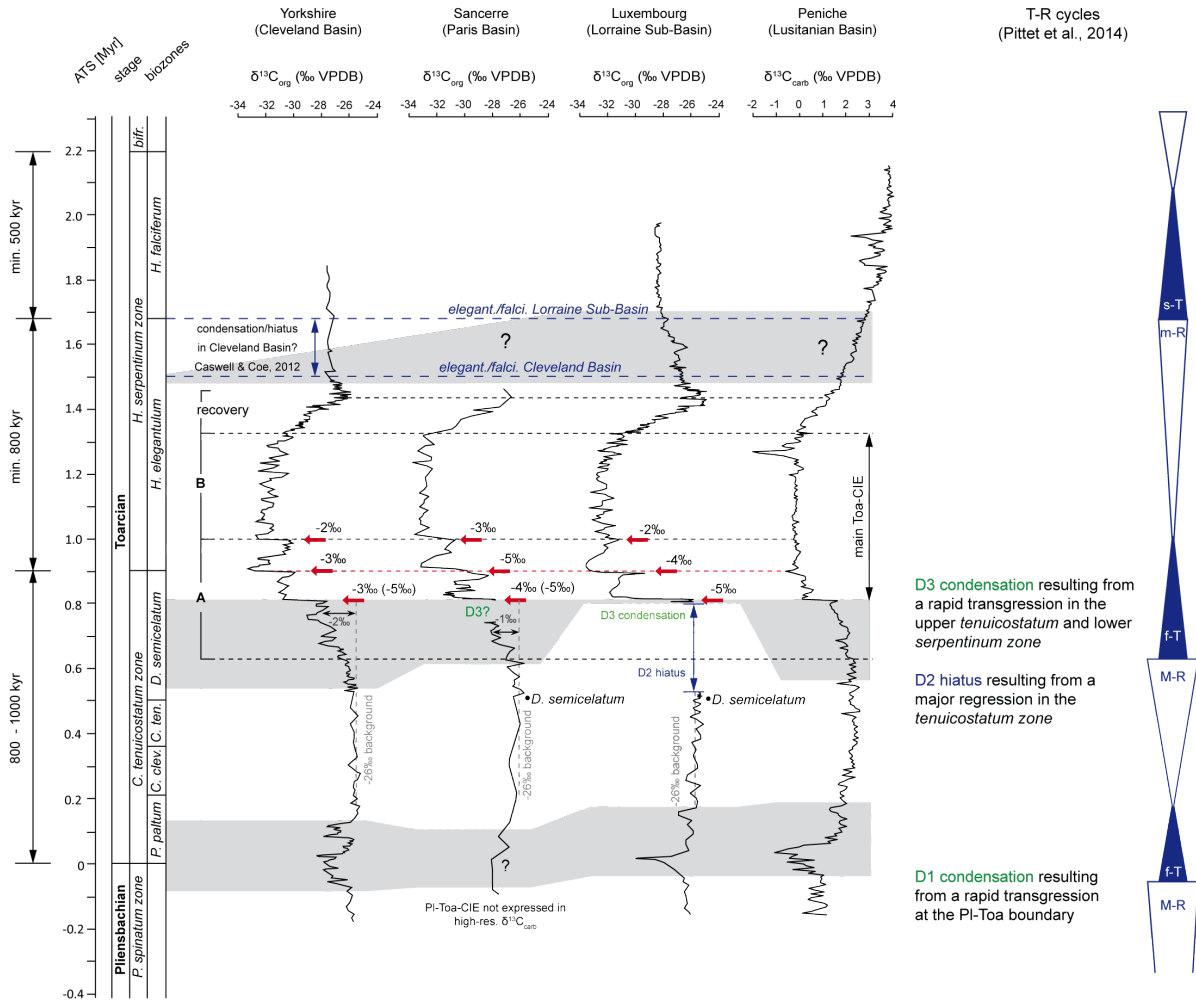


Figure S3-1: Carbon isotope records from the Cleveland Basin (Kemp et al., 2005; 2011), the southern Paris Basin (Sancerre, Hermoso et al., 2012), from the Lorraine Sub-Basin (this study) and from the Lusitanian Basin (Hesselbo et al., 2007) allow to establish a robust carbon isotope stratigraphy for the Late Pliensbachian and Early Toarcian. The PI-Toa-CIE is not expressed in the Sancerre Core (even not in the high-resolution $\delta^{13}\text{C}_{\text{carb}}$ -record; see Hermoso et al., 2012). In all records, the main negative Toa-CIE exhibits a tripartite nature, whereby slightly differences in the amplitude observed for the first negative shift might result from differences in the chosen baseline. The astronomical timescale (ATS) as well as durations given for the ammonite zones and subzones base on floating chronologies proposed by Suan et al. (2008), Huang & Hesselbo (2014) and by this work (Chapter 2; also see Ruebsam et al. (2014; 2015)).

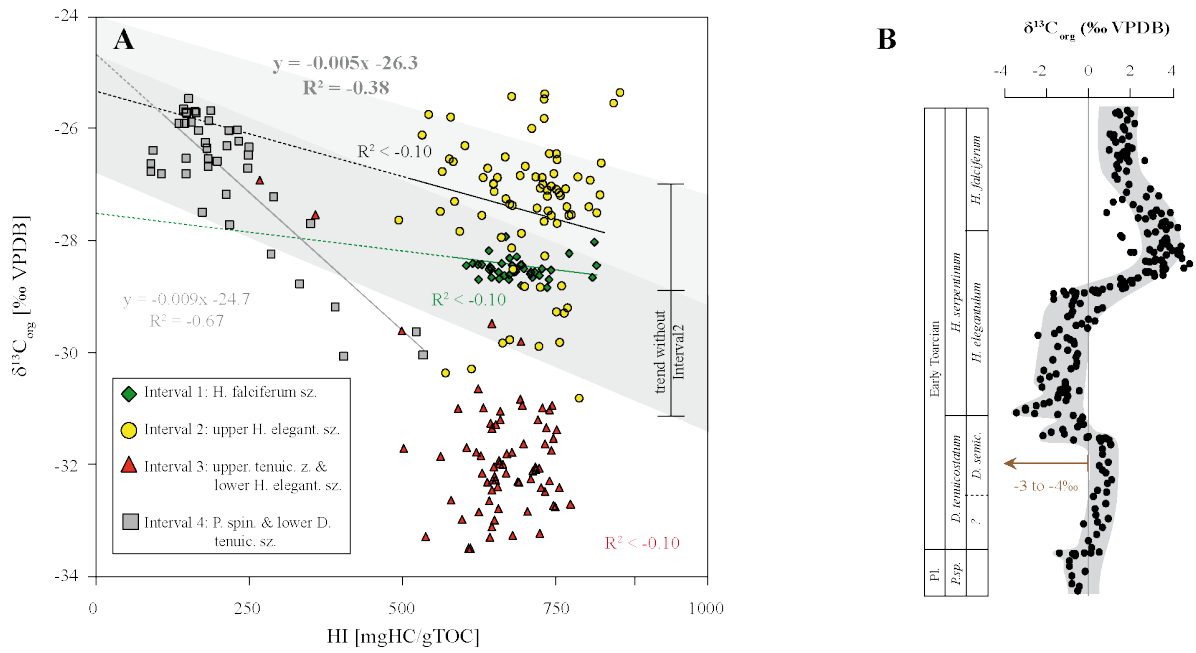


Figure S3-2: A) Cross-plot of HI values with organic carbon isotope values has been used by [Suan et al. \(2015\)](#) and [Montero-Serrano et al. \(2015\)](#) to correct organic carbon isotope values for different organic matter sources. According to these authors $\delta^{13}C_{org}$ values slightly decrease with increasing HI values (samples from the Toa-CIE are excluded). Such a relation is not well expressed in the cross plot of HI values and $\delta^{13}C_{org}$ values for Core FR-210-078. However, when excluding samples from Interval 2 that show relative heavy organic carbon isotope values and high HI values a weak negative regression can also be documented between HI and $\delta^{13}C_{org}$ values. The resulting equation for the regression line is $y = -0.005x - 26.3$ ($R^2 = -0.38$). This trend rough match the overall trend documented between HI and $\delta^{13}C_{org}$ in Jurassic sediments ([Tyson, 1995](#)). The poor correlation documented fro samples from Interval 2 might result from high OM burial rates affecting dissolved CO_2 and thus $\delta^{13}C_{org}$ values of OM (e.g. [Kump & Arthur, 1999](#)). Furthermore, differenced in the degree of OM preservation can alter HI values ([Bordenave et al., 1993](#)). **B)** Organic carbon isotope trend corrected for different organic matter sources, calculated following the approach by [Suan et al. \(2015\)](#). Correction of organic carbon isotope data result in a magnitude of about -3 to -4‰, which is in agreement with findings by [Suan et al. \(2015\)](#) and [Montero-Serrano et al. \(2015\)](#).

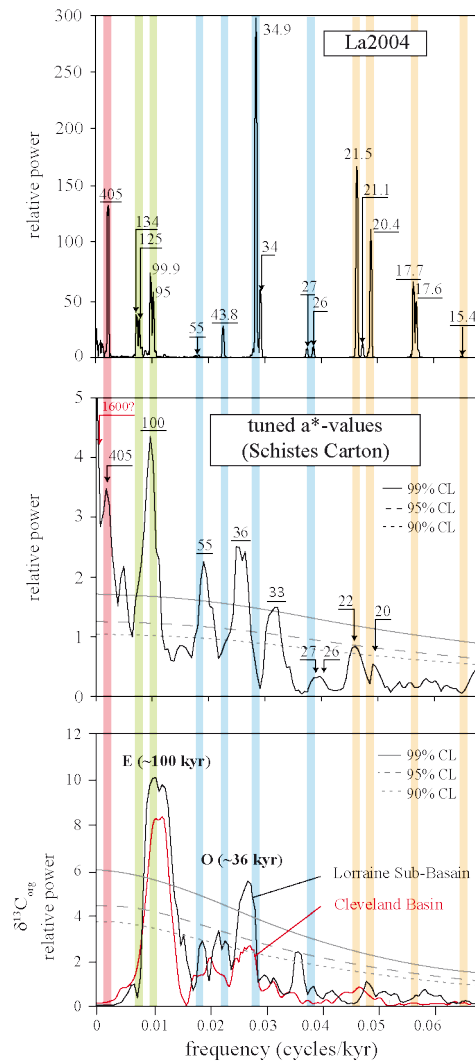


Figure S3-3: MTM power spectra for tuned a^* -values (see Chapter 2) and for the organic carbon isotope data sets from the Lorraine Sub-Basin and the Cleveland Basin compared with the astronomical model La2004 (Laskar et al., 2004). Periodicities documented in organic carbon isotope data match periodicities expressed in sedimentological parameters of Core FR-210-078 and further aligns with the frequency spectrum proposed by La2004.

S4. Supplementary information: Chapter Four

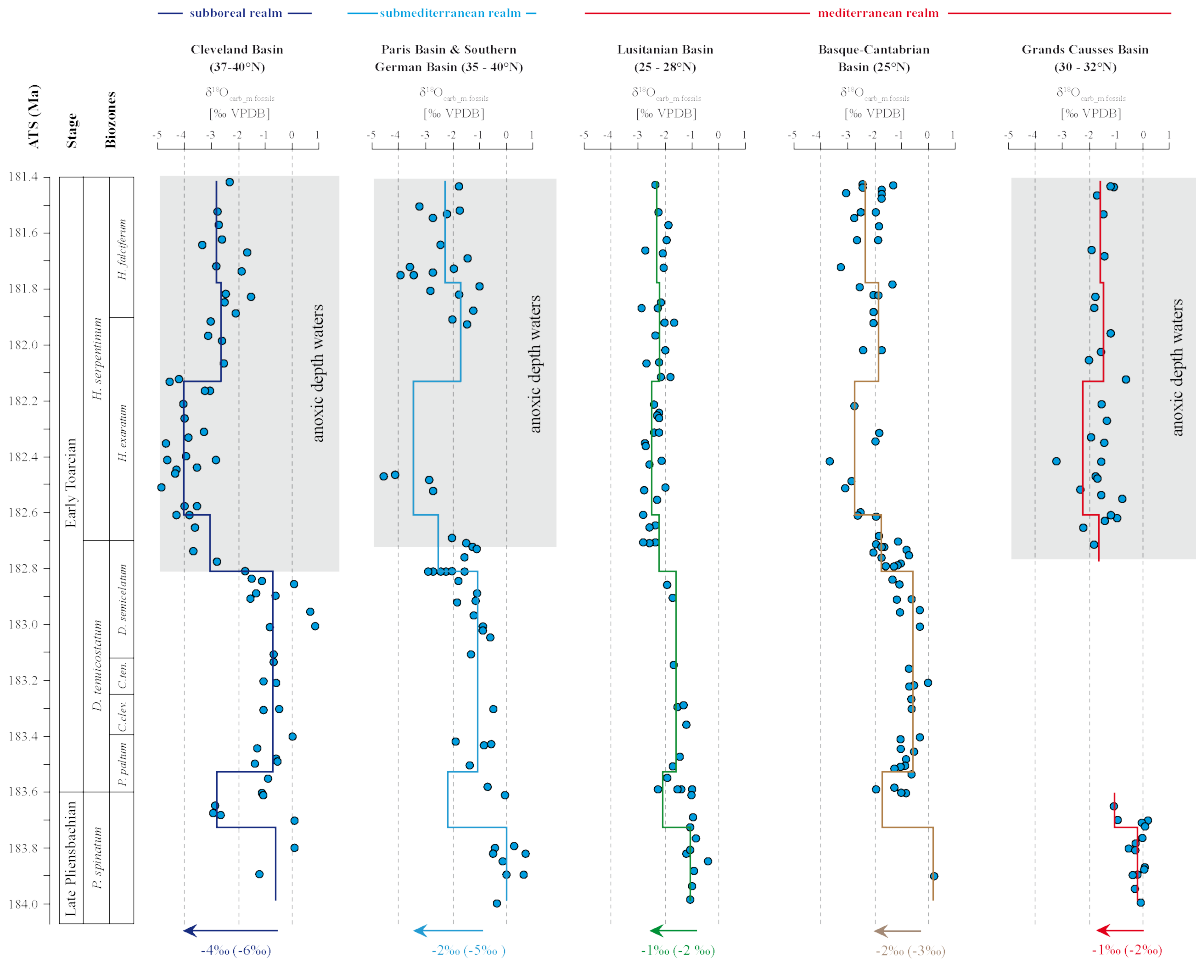


Figure S4-1: Stratigraphic evolution of oxygen isotope data from location situated at different latitudes. Data are from references listed in table S2 (appendix 4.1.). Overall lower $\delta^{18}\text{O}$ values and a stronger decrease in the values have been documented from locations at high latitudes, like the Cleveland Basin, the Paris Basin and the Southern German Basin. In contrast, lower amplitudes have been documented from the Mediterranean sector. Amplitudes are given as average values and as absolute value. According to the e.g. [McArthur et al. \(2008a\)](#) or [Dera & Donnadieu \(2012\)](#) geographical differences most likely reflect a latitudinal dependent salinity gradient throughout the NW Tethyan shelf. Stratigraphic extent of bottom water anoxia mainly based on the stratigraphic extent of organic-rich deposits as well as on redox proxies, if those are available (Cleveland Basin: [McArthur et al., 2008a](#); Paris Basin: [Hermoso et al., 2013](#); Southern German Basin: [Röhl et al., 2001](#); [Frimmel et al., 2004](#); Lusitanian Basin: [Hesselbo et al., 2000](#); Basque-Cantabrian Basin: [van de Schootbrugge, 2005a](#); [Gomez & Arias, 2010](#); Grands Causses Basin: [Harazim et al., 2013](#)).

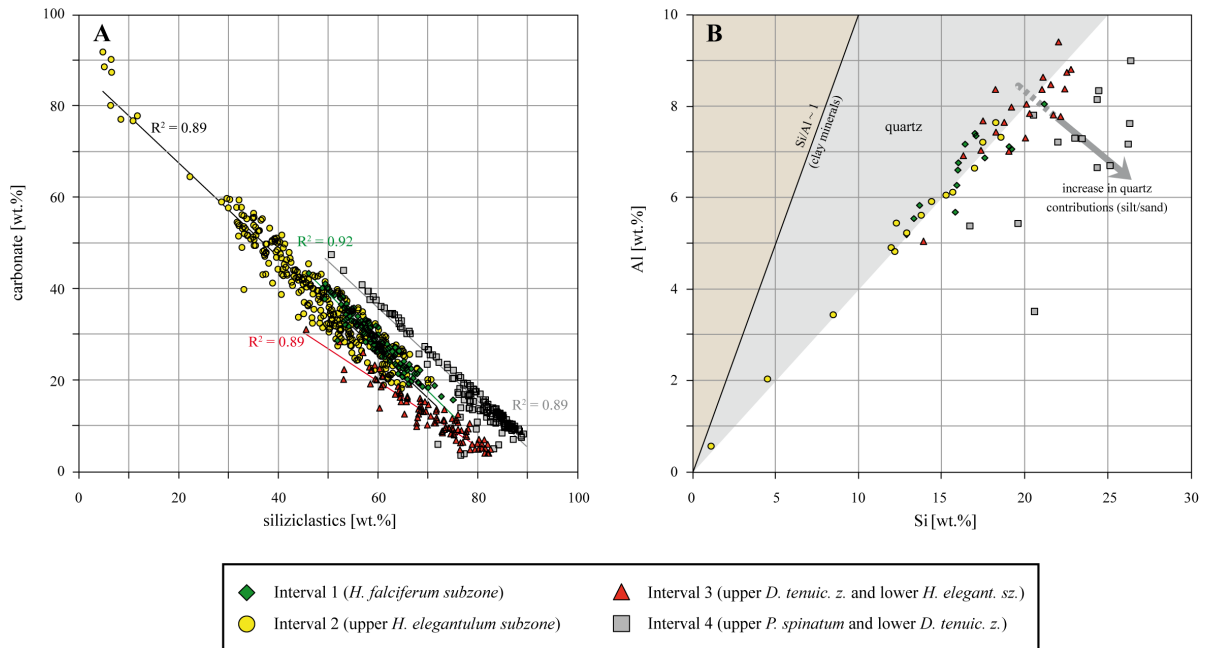


Figure S4-2: **A)** The inverse relation observed between siliciclastics and carbonate indicate variable contributions of allochthonous siliciclastics and autochthonous carbonate. **B)** The Si versus Al plot allows a qualitative estimate of quartz contributions. The Si/Al atomic ratio of about 1 for of clay minerals (kaolinite, muscovite) is shown.

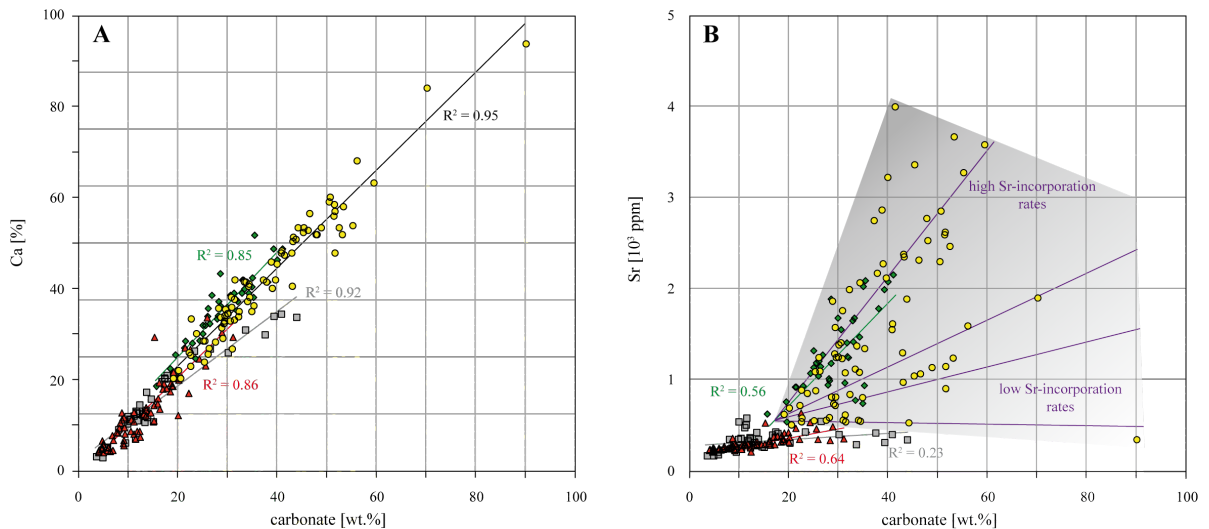


Figure S4-3: **A)** The linear regression observed between carbonate content and Ca concentrations confirm that Ca is mainly bound to the carbonate fraction. Minor differences in the slope of the regression line result from variations in the carbonate compositions, may due to Mg or Fe incorporation (review Hermoso et al., 2009). **B)** The cross-plot of carbonate with Sr content expose different slopes for intervals. A weak correlation of carbonate with Sr has been documented for Interval that represents a stage of increased terrigenous contribution. Thus, significant amounts of Sr might be bounded to the detrital sediment fraction. A good correlation of carbonate with Sr has been documented for the Interval 3, whereby the flat slope of the regression line indicate low Sr incorporation rates into the carbonate lattice. High Sr concentration were documented for samples from Interval 2, whereby the scatter in the data result from highly variable Sr incorporation rates into the carbonate lattice. The step slope of the regression line calculated for samples from Interval 1 indicate high Sr incorporation rates that were less variable.

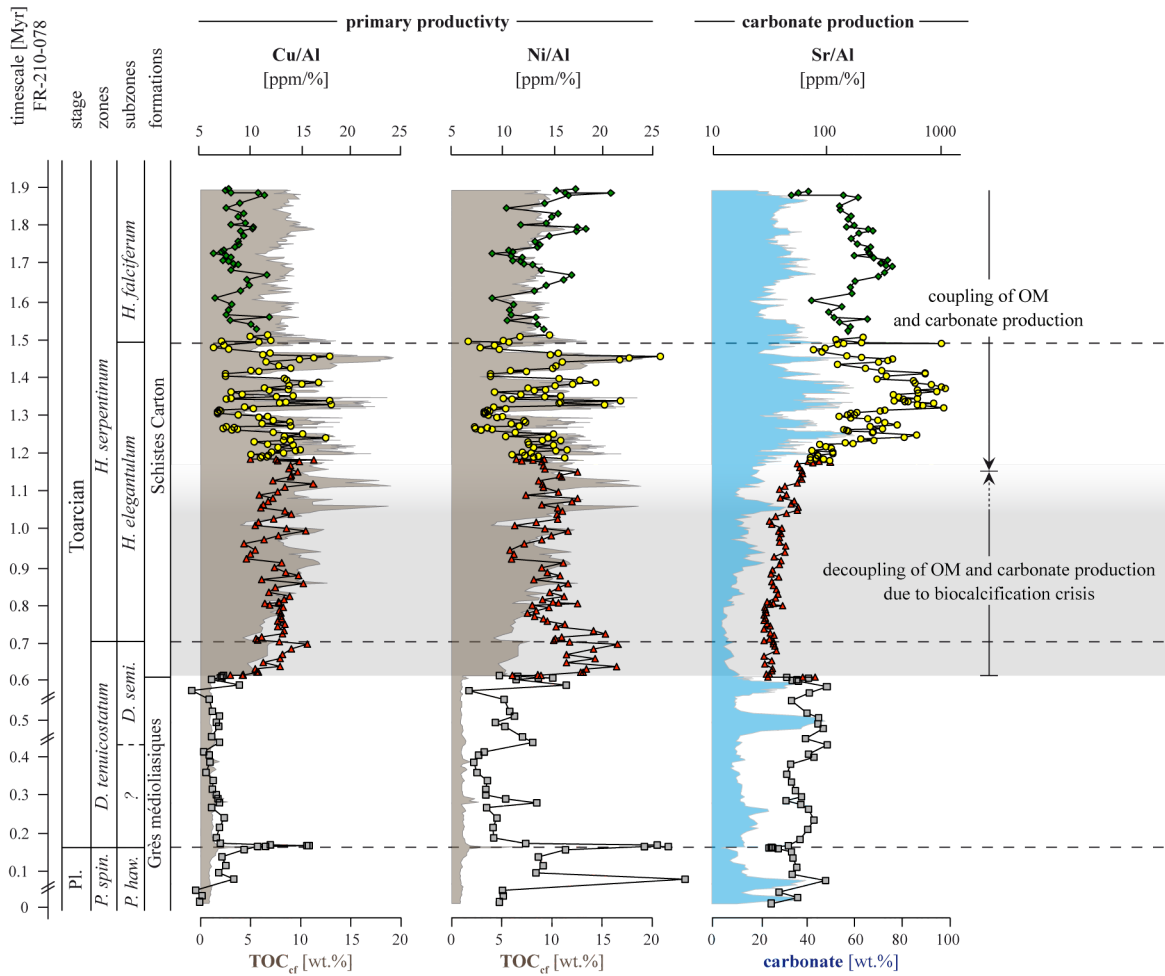


Figure S4-4: Stratigraphic evolution of TOC_{cf} and the primary productivity indicators Cu/Al and Ni/Al indicate high OM export rated during the Schistes Carton Fm. The base of the Schistes Carton Fm, corresponding to the Toa-CIE interval, show extreme low carbonate and Sr concentrations indicating reduced carbonate production and thus a decoupling of organic matter and carbonate export. Low carbonate concentrations result from a biocalcification crisis as carbonate concentrations are bound to the abundance of calcareous nannoplankton (e.g. [Hermoso et al., 2009](#)). A fair co-variation between OM and carbonate production is observed throughout the upper *elegantulum* subzone and the *falciferum* subzone indicating a coupling of OM and carbonate production.

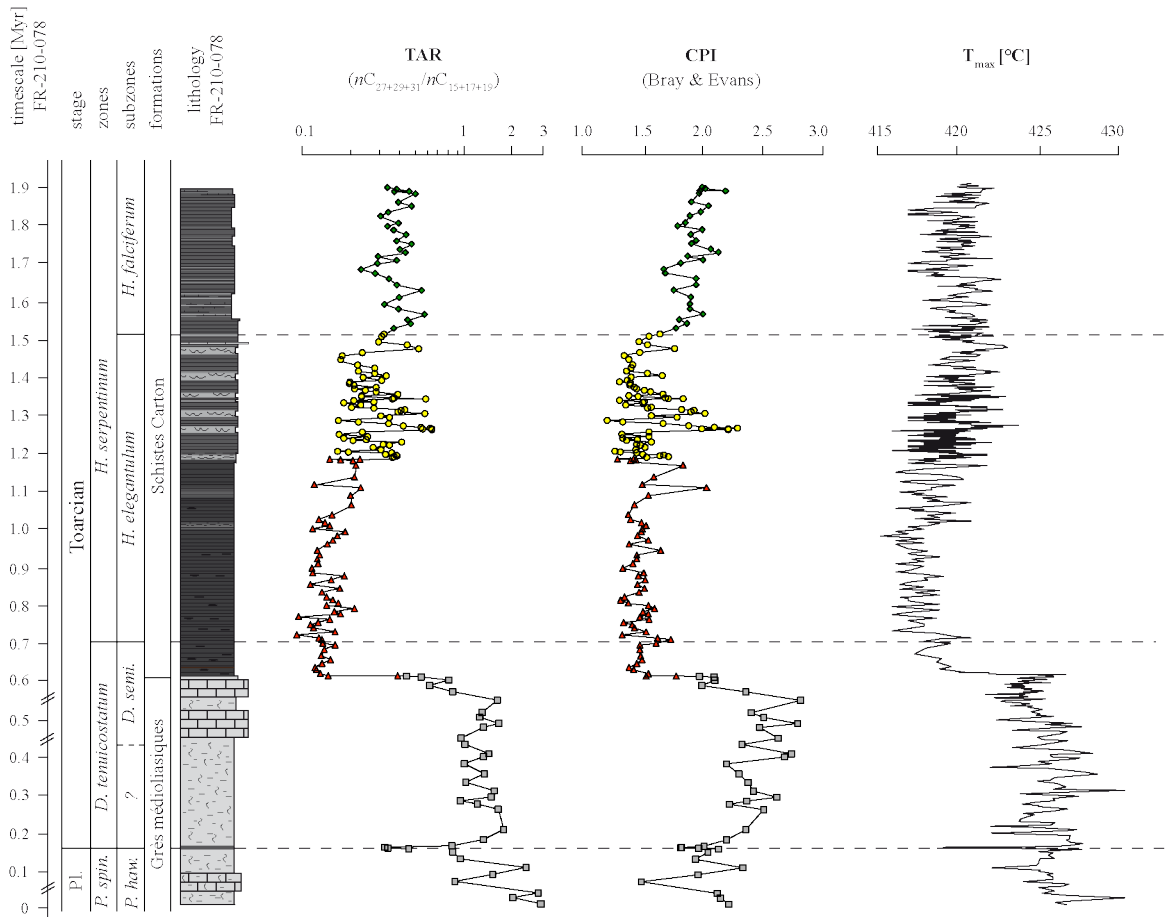


Figure S4-5: Changes in TAR, CPI and T_{max} values align with facies changes, whereby low T_{max} values confirm a low thermal maturity for OM in Core FR-210-078, which was indicated by previous works (Ruebsam, 2010; Wagner, 2010).

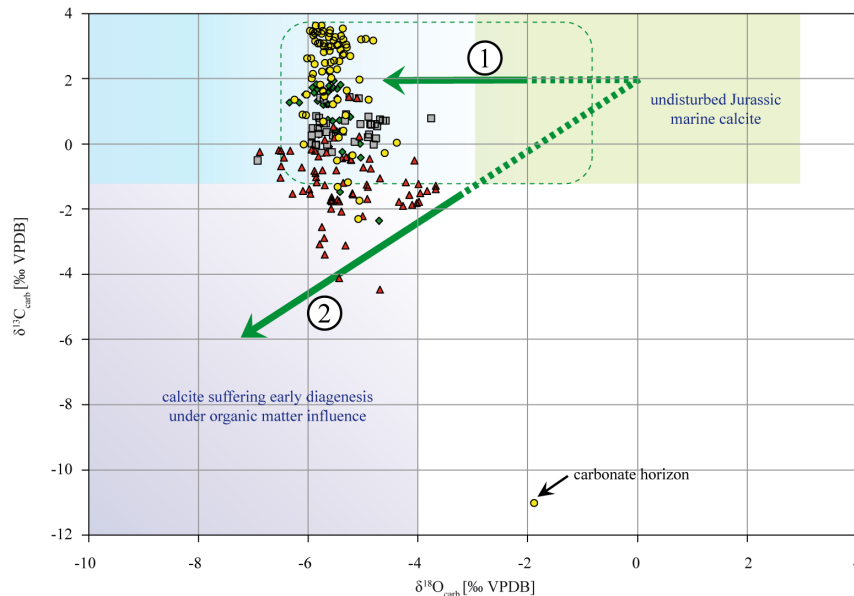


Figure S4-6: The cross-plot of bulk (micritic) carbonate $\delta^{18}\text{O}$ with $\delta^{13}\text{C}$ values allow to estimate diagenetic alterations of the carbonate fraction and thus of the isotope values. Trend 1 represents the evolution of marine calcite during slightly meteoric diagenesis, while trend 2 represents the evolution during intensive meteoric diagenesis and/or marine calcite affected by early diagenesis (see Lavastre et al., 2011 for details). Bulk carbonate values, representing micritic and biogenic carbonates, are commonly lower (dark-green box) than values from unaltered carbonate shells (light-green field).

S5. Supplementary information: Chapter Five

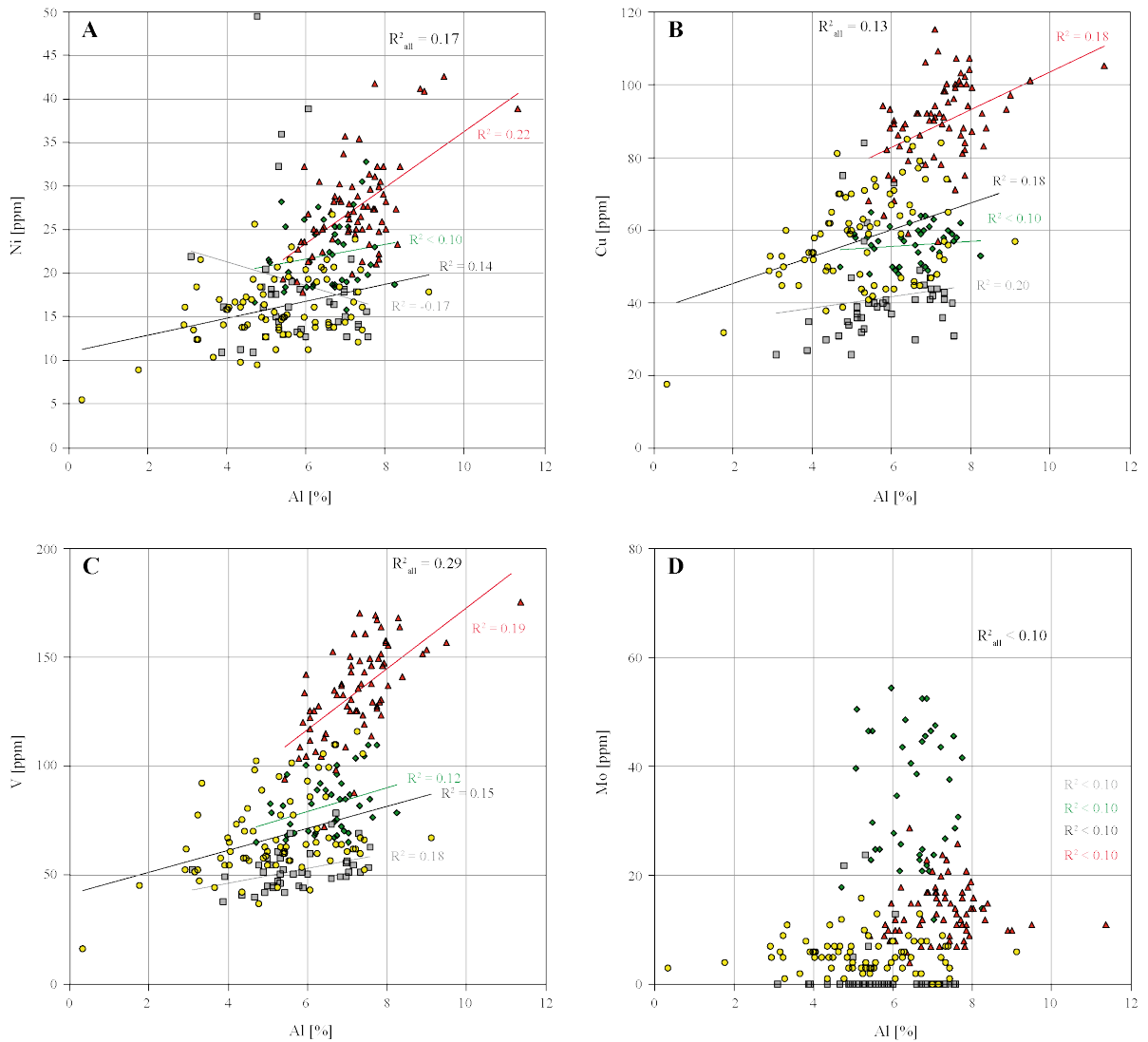


Figure S5-1: Cross-plot of Al content with redox-sensitive elements associated with the OM flux (Ni, Cu) and elements with strong euxinic affinity. The absence of a statistically significant correlation indicates that TE enrichment was mainly controlled by autochthonous mechanisms and detrital contribution played only a minor role. However, a minor detrital contribution of Ni, Cu, V and Mo cannot be ruled out.

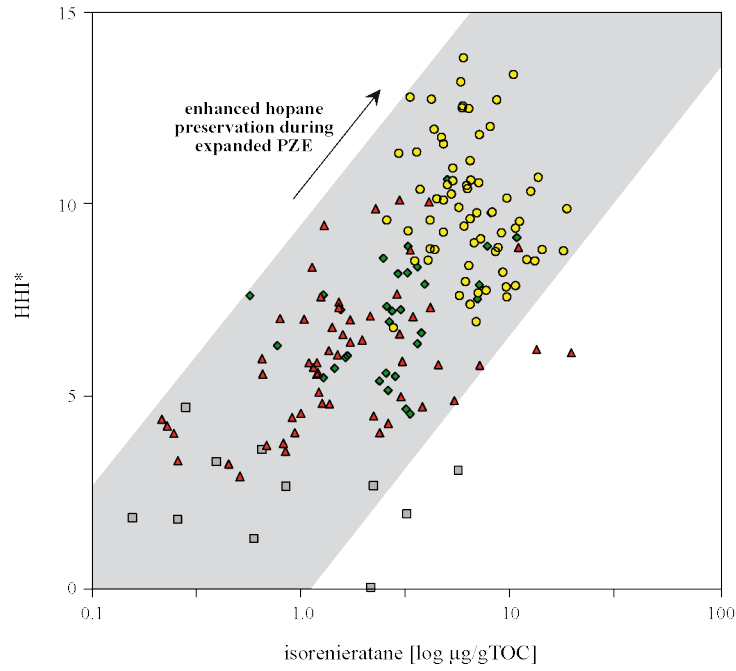


Figure S5-2: The cross-plot of isorenieratane concentration (logarithmic scale) with HHI* values expose a positive correlation, which indicate an enhanced preservation of bacteriohopanes during periods of expanded euxinic conditions.

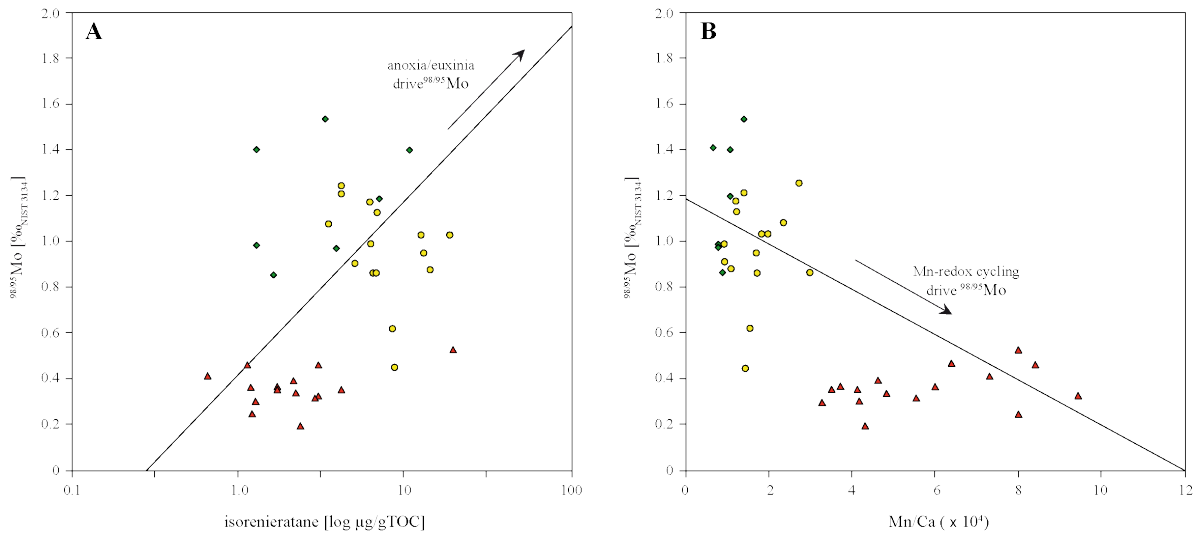


Figure S5-3: A) The cross-plot of isorenieratane concentrations with molybdenum isotope values can be used to determine the relation between extent of euxinia and $\delta^{98/95}\text{Mo}_{\text{SED}}$ values. A positive trend can be associated with the preferential removal of ^{98}Mo under anoxic/euxinic conditions. **B)** Adsorption of isotopically-light Mo onto Mn particles in the oxic part of the water column can alter $\delta^{98/95}\text{Mo}_{\text{SED}}$ values. A high Mn downwards-flux to the euxinic bottom water can be indicated by high Mn/Ca ratios (Mn present in the sediment as rhodochrosite).

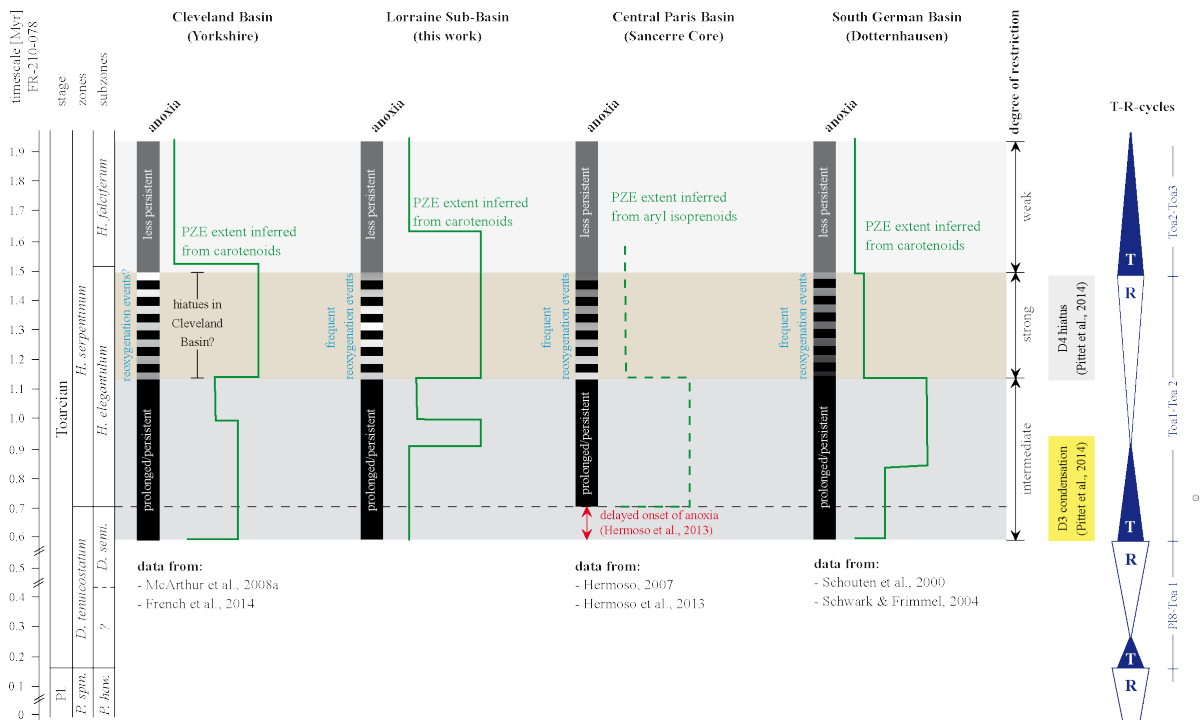


Figure S5-4: Evolution of redox conditions and PZE for different basins throughout the Western Tethyan Shelf. A similar evolution of anoxia in all basins can be associated with eustatic sea level changes, whereby a regressive phase throughout the upper *H. elegantulum* subzone resulted in a more frequent bottom water reoxygenation that is evident from all locations. The extent of PZE, inferred from the abundance of carotenoid biomarkers (aryl isoprenoid ratios for Sancerre), expose a different pattern and different trends were observed. Moreover, okenane and chlorobactane were documented from the Cleveland Basin (French et al., 2014) and the South German Basin (Schouten et al., 2000), but are absent in the samples from the Lorraine Sub-Basin. The absence of these biomarkers indicate that the redox boundary in the Lorraine Sub-Basin was situated in a water depth >40 m (e.g. Sinninghe Damsté & Schouten, 2006).

S6. Supplementary information: Chapter Six

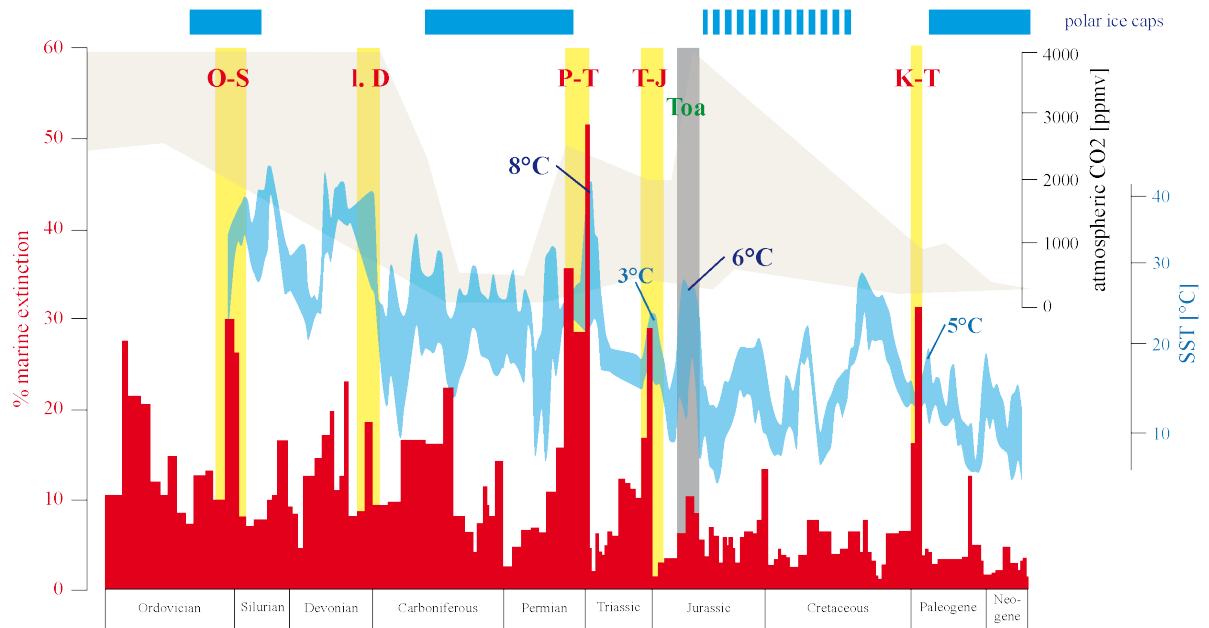


Figure S6-1: Marine extinction from the Ordovician to the Neogene (Peters, 2008) in comparison with the evolution of the Earth climate. Shown are the evolution of atmospheric carbon dioxide concentration (Berner, 2001) and SST (Grossmann, 2012).

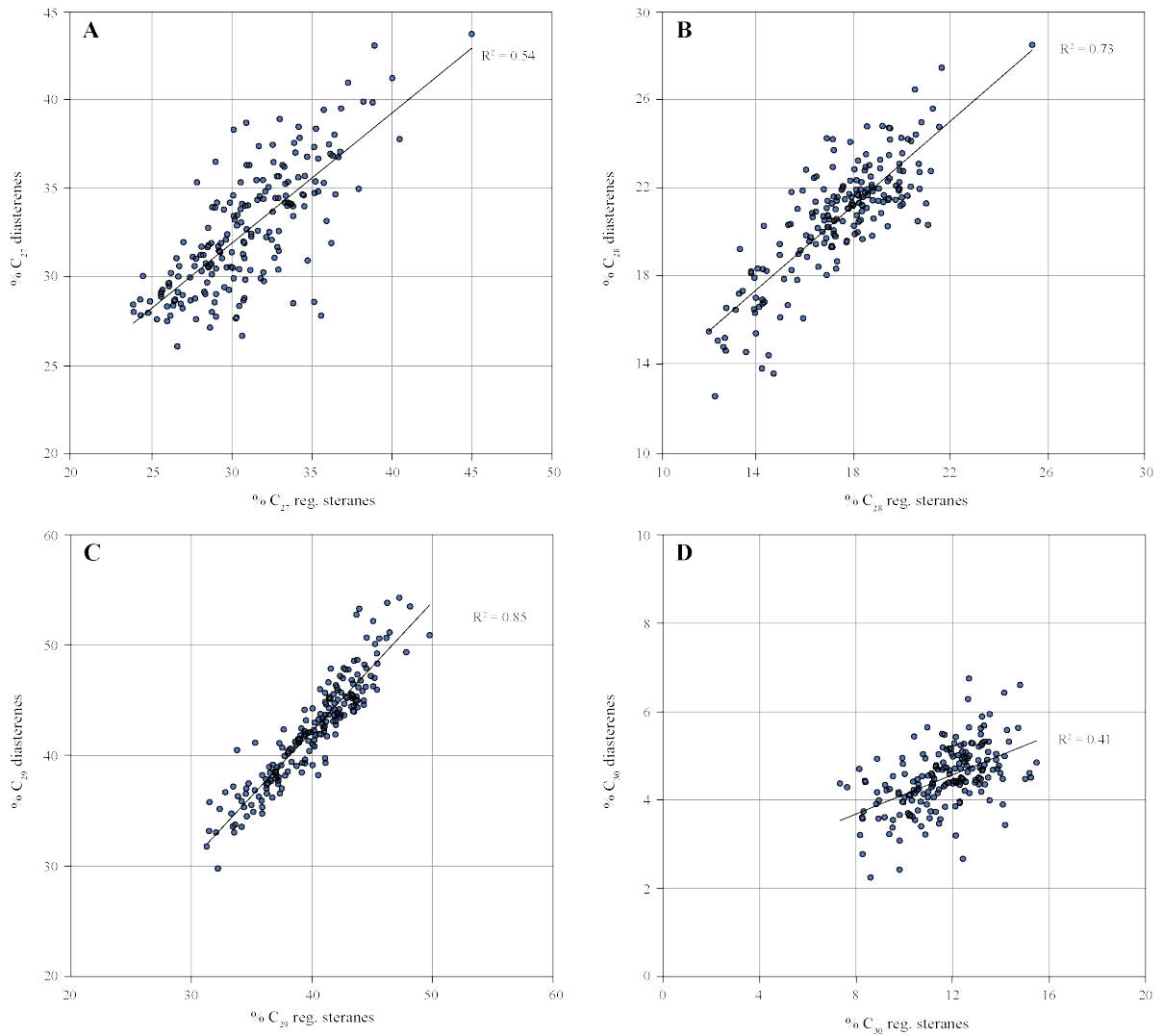


Figure S6-2: Cross-plots of regular steranes with diasterenes from C_{27} to C_{30} show an overall strong positive covariation, confirming similar distribution patterns for both steroid species.

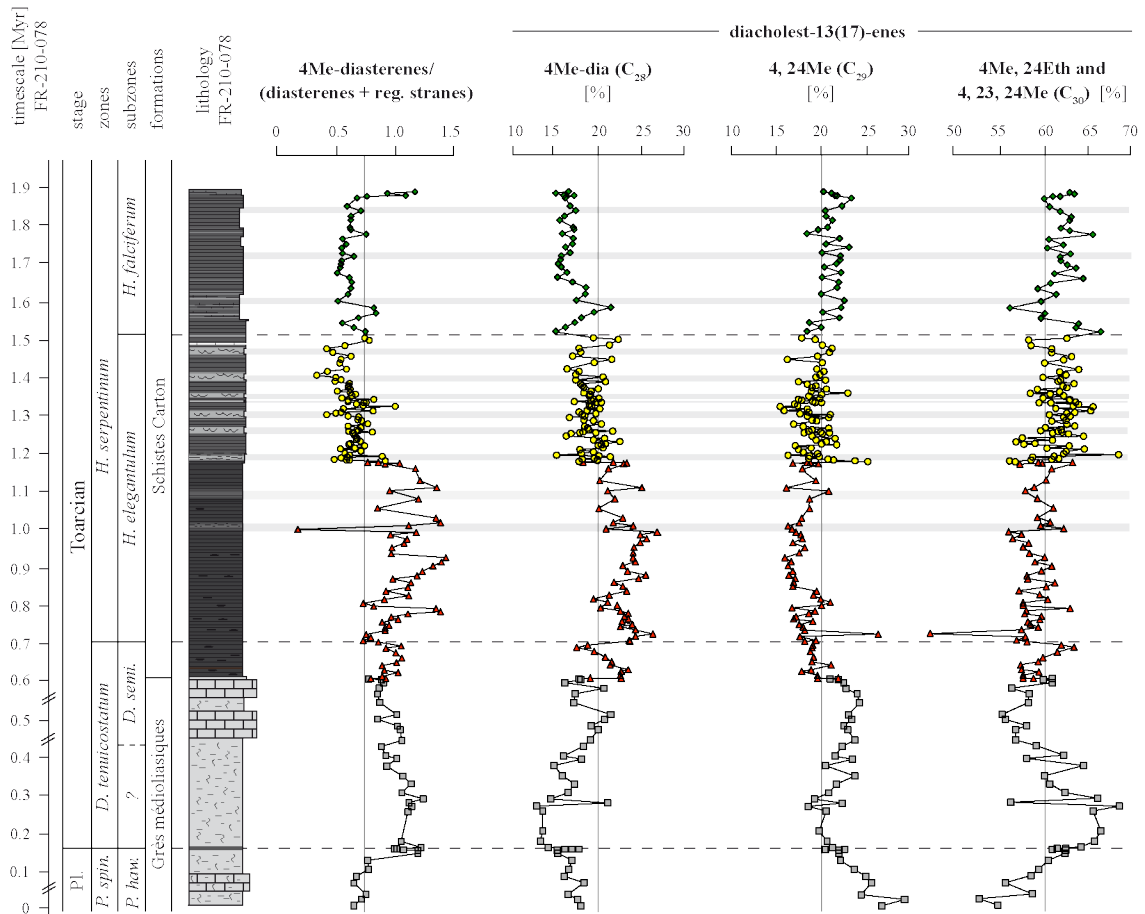


Figure S6-3: Stratigraphic evolution of 4Me-diasterenes expressed as ratio with des-methyl-steroids and as percentage of the different 4Me-diasterenes that has been identified. The C_{28} compound can be ascribed to 4-methyl-diacholest-13(17)-enes and the C_{29} compounds to 4, 24-methyl-diacholest-13(17)-enes. The C_{30} compounds can either be ascribed to 4-methyl, 24-ethyl-diacholest-13(17)-enes or to 2, 23, 24-methyl-diacholest-13(17)-enes, which could not be distinguished on the base of the mass spectrums.

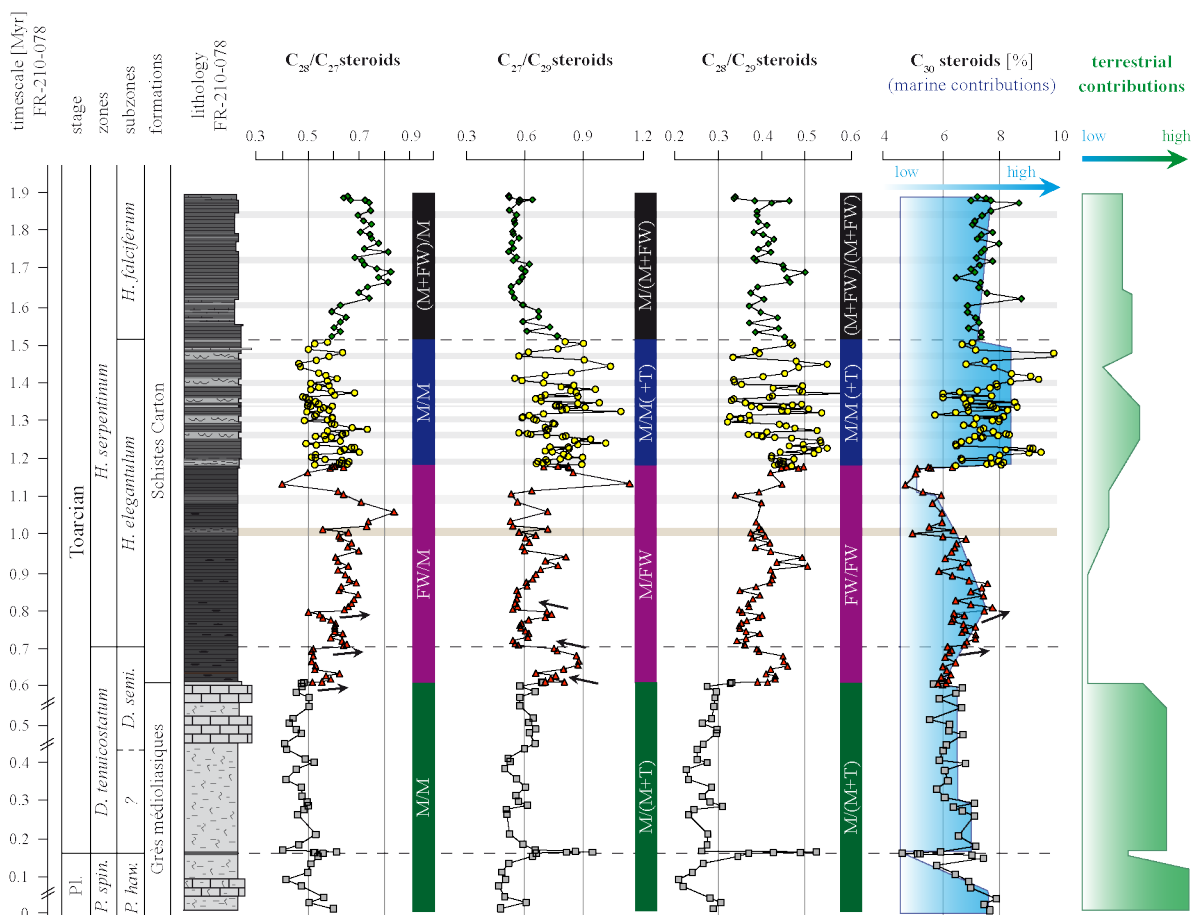


Figure S6-4: Changes in steroids ratios allow to document shifts in eukaryotic communities, mainly algae, which were the dominating primary producers during the Early Toarcian. However, the significance of steroid-based ratios as source indicator is limited as sources of single steroids change throughout the profile. Especially ratios that include C_{29} steroids might be misleading as C_{29} -steroids are originated in land plants as well as in marine algae, whereas relative contributions from these sources change throughout the profile. Relative changes in land plant derived biomass can be inferred from the evolution of the TAR. Within intervals, characterized by a high TAR, significant amounts of the C_{29} steroids can be originated in higher land plants. Changes in the relative abundance of C_{30} steroids can be associated with contributions from *Pelagohyceae* and thus represent input from exclusively marine algae. High contribution of C_{30} can be associated with marine conditions (high sea level, normal marine SSS). Steroid ratios (C_{29} to C_{29}) provide further information about changes in the phytoplankton community structure. However, interpretation of these ratios must be done for each interval separately as the biological sourced of the steroids change throughout the intervals. Inferred biological sourced of the different steroid species and thus the underlying prediction of the ratios are given as well (M: marine algae input; FW: freshwater tolerant algae; T: terrestrial contributions).

**Information about the digital data sheet
(data_table_Diss_WR_Core-FR-210-078)**

Data discussed in this thesis are available as excel data sheet that is attached to the thesis.

Date data sheet contains the following sub-sheets:

- 1- Master sheet: comprising merged data from organic, inorganic and isotope geochemical analysis
- 2- MagS data: high-resolution magnetic susceptibility measurements
- 3- Lab: com: high-resolution spectrophotometry measurements
- 4- ultra-high-res_a: a*-values from line scanning of the basal Schistes Carton Fm
- 5- bulk data: bulk geochemical data (TC, TS, TN, TOC, TIC, Rock Eval)
- 6- elements_1: element data measured via Aqua Regia ICP-OES
- 7- elements_2: element data measured via Lithium metaborate/tetraborate fusion - ICP-OES
- 8- 13Corg: $\delta^{13}\text{C}_{\text{org}}$ data
- 9- 18O & 13Ccarb: $\delta^{18}\text{O}_{\text{carb}}$ data and $\delta^{13}\text{C}_{\text{carb}}$ data
- 10- 34S: $\delta^{34}\text{C}$ data of the sediment
- 11- dMo: $\delta^{198/95}\text{Mo}$ data
- 12- biomarker data: selected biomarker data

References

- A -

- Aberhan, M., 2001. Bivalve palaeobiogeography and the Hispanic Corridor: time of opening and effectiveness of a proto-Atlantic seaway. *Palaeogeography, Palaeoclimatology, Palaeoecology* 165, 375 – 394.
- Ainsworth, N.R., Riley, L.A., 2010. Triassic to Middle Jurassic stratigraphy of Kerr McGee 97/12-1 exploration well, offshore southern England. *Marine and Petroleum Geology* 27, 853 – 894.
- Algeo, T.J., 2004. Can marine anoxic events draw down the trace element inventory of seawater? *Geology* 32, 107 – 1060.
- Algeo, T.J., Maynard, J.B., 2004. Trace-element behavior and redox facies in core shales of the Upper Pennsylvanian Kansas-type cyclotherms. *Chemical Geology* 206, 289 – 318.
- Algeo, T.J., Lyons, T.W., 2006. Mo–total organic carbon covariation in modern anoxic marine environments: Implications for analysis of paleoredox and paleohydrographic conditions. *Paleoceanography* 21, doi: 10.1029/2004PA001112.
- Algeo, T.J., Tribovillard, N., 2009. Environmental analysis of paleoceanographic systems based on molybdenum–uranium covariation. *Chemical Geology* 268, 211 – 225.
- Algeo, T.J., Rowe, H., 2012. Paleoceanographic applications of trace-metal concentration data. *Chemical Geology* 324 – 325, 6 – 18.
- Al-Suwaidi, A.H., Angelozzi, G.N., Baudin, F., Damborenea, S.E., Hesselbo, S.P., Jenkyns, H.C., Mancenido, M.O., Riccardi, A.C., 2010. First record of the Early Toarcian Oceanic Anoxic Event from the Southern Hemisphere, Neuquen Basin, Argentina. *Journal of the Geological Society* 167, 633 – 636.
- Amo, M., Suzuki, N., Kawamura, H., Yamaguchi, A., Takano, Y., Horiguchi, T., 2010. Sterol composition of dinoflagellates: Different abundance and composition in heterotrophic species and resting cysts. *Geochemical Journal* 44, 225 – 231.
- Ansorge, J., 1996. Insekten aus dem oberen Lias von Grimmen (Vorpommern, Norddeutschland). *Neue Paläontologische Abhandlungen* 2, 1 – 132.
- Anthony, K.M.W., Anthony, P., Grosse, G., Chanton, J., 2012. Geological methane seeps along boundaries of Arctic permafrost thaw and melting glaciers. *Nature Geoscience* 5, 419 – 424.
- Antonov, J. I., Seidov, D., Boyer, T.P., Locarnini, R.A., Mishonov, A.V., Garcia, H.E., Baranova, O.K., Zweng, M.M., Johnson, D.R., 2010. World Ocean Atlas 2009, Volume 2: Salinity. S. Levitus, Ed. NOAA Atlas NESDIS 69, U.S. Government Printing Office, Washington, D.C., 184 pp.
- Arias, C., 2006. Northern and Southern Hemispheres ostracod palaeobiogeography during the Early Jurassic: Possible migration routes. *Palaeogeography, Palaeoclimatology, Palaeoecology* 233, 63 – 95.
- Armendáriz, M., Rosales, I., Bádenas, B., Aurell, M., Garcia-Ramos, J.C., Piñuela, L., 2014. High-resolution chemostratigraphic records from Lower Pliensbachian belemnites: Palaeoclimatic perturbations, organic facies and water mass exchange (Asturian basin, northern Spain). *Palaeogeography, Palaeoclimatology, Palaeoecology* 333 – 334, 178 – 191.
- Arp, G., Seppelt, S., 2011. The bipolar bivalve *Oxytoma* (*Palmoxytoma*) *cygnipes* (Young & Bird,

1822) in the Upper Pliensbachian of Germany. *Paläontologische Zeitschrift* 86, 43 – 57.

- B -

- Bachtadse, V., Rolf, C., 2012. Paleo- and Rockmagnetic Studies on the Kirkpatrick Basalts of Early Jurassic Age, Northern Victoria Land, Antarctica. *GU Research Abstracts* 14, EGU2012-10948.
- Bailey, T.R., Rosenthal, Y., McArthur, J.M., van de Schootbrugge, B., 2003. Paleooceanographic changes of the Late Pliensbachian-Early Toarcian interval: A possible link to the genesis of an Oceanic Anoxic Event, *Earth and Planetary Science Letters* 212, 307 – 320.
- Baldschun, R., Binot, F., Fleig, S., Kockel, F., 2001. *Geotektonischer Atlas von Nordwest-Deutschland und dem deutschen Nordsee-Sektor – Strukturen, Strukturentwicklung, Paläogeographie*. *Geologisches Jahrbuch Reihe A, Band A 153*, 88 pp.
- Balsam W L, Damuth J E, Schneider, R. 1997. Comparison of shipboard vs. shore-based spectral data from Amazon Fan cores: implications for interpreting sediment composition. *Proceedings of the Ocean Drilling Program, Scientific Results* 155, 193 – 215.
- Barakat, A., Rullkötter, J., 1997. A comparative study of molecular paleosalinity indicators: chromanes, tocopherols and C20 isoprenoid thiophenesin Miocene lake sediments (Nördlinger Ries, southern Germany). *Aquatic Geochemistry* 3, 169 – 190.
- Bassoulet, J.P., Baudin, F., 1994. Le Toarcian Inférieur: Une période de crise les bassins et sur les plate-formes carbonates de l'Europe du nord-ouest et de la Téthys. *Geobios* 17, 645 – 654.
- Bassoulet, J. P., Elmi, S., A. Poisson, Cecca, F., Bellion, Y., Guiraud, R., Baudin, F., 1993. Mid-Toarcian. In: Dercourt, J., Ricou, L. E., Vrielynck, B. (Eds.), *Atlas Tethys paleoenvironmental maps*, BEICIP — FRANLAB, Rueil-Malmaison, 63–84.
- Baudin, F., Herbin, J.P., Bassoulet, J.P., Dercourt, J., Lachkar, G., Manivit, H., Renard, M., 1990. Distribution of organic matter during the Toarcian in the Mediterranean Tethys and Middle East. In: Huc, Y. (Ed.), *Deposition of Organic Facies. AAPG Studies in Geology*, pp. 73 – 92.
- Bécaud, M., 2002. Le Toarcien de la bordure sud et sud-est du Massif armoricain (Deux-Sèvres et Vendée). *Le Naturaliste Vendéen* 2, 3 – 33.
- Bechtel, A., Gawlick, H.J., Gratzer, R., Tomaselli, M., Püttmann, W., 2007. Molecular indicators of palaeosalinity and depositional environment of small-scale basins within carbonate platforms: The Late Triassic Hauptdolomite Wiestalstausee section near Hallein (Northern Calcareous Alps, Austria). *Organic Geochemistry* 38, 92 – 111.
- Berling, D.J., Brentnall, S.J., 2007. Numerical evaluation of mechanisms driving Early Jurassic changes in global carbon cycling. *Geology* 35, 247 – 250.
- Berger, A., Loutre, M.F., 1994. Precession, eccentricity, obliquity, insolation and paleoclimates, In: Duplessy, J.C., Spyridakis, M.T. (Eds.), *Long Term Climatic Variations, Data and Modelling: Nato ASI series, Serie I: Global Environmental Change*, Springer-Verlag, Berlin, 22, 107 – 151.
- Berner, R.A., Raiswell, R., 1983. Burial of organic carbon and pyrite sulfur in sediments over Phanerozoic time: a new theory. *Geochimica et Cosmochimica Acta* 47, 855 – 862.
- Berner, R.A., Raiswell, R., 1984. C/S method for distinguishing freshwater from marine sedimentary rocks. *Geology* 12, 365 – 368.

- Berner, R.A., Kothavala, Z., 2001. GEOCARB III: A revised model of atmospheric CO₂ over Phanerozoic time. *American Journal of Science* 301, 182 – 204.
- Benton, M.J., 1995. Diversification and extinction in the history of life. *Science* 268, 52 – 58.
- Blaise, T., Izart, A., Michels, R., Suarez-Ruiz, I., Cathelineau, M., Landrein, P., 2011. Vertical and lateral changes in organic matter from the Mesozoic, eastern Paris Basin (France): Variability of sources and burial history. *International Journal of Coal Geology* 88, 163 – 178.
- Bintz J., Pixius R., Wagner A., 1984. Géologie, Géochimie et possibilités d'exploitation des schistes bitumineux luxembourgeois. *Revue technique* 4, 132 – 145.
- Bjerrum C.J., Surlyk, F., Callomon, J.H., Slingerland, R.L., 2001. Numerical paleoceanographic study of the Early Jurassic transcontinental Laurasian Seaway. *Paleoceanography* 16, 390 – 404.
- Bodin, S., E. Mattioli, E., S. Fröhlich, S., Marshall, J.D., Boutib, L., Lahsini, S., Redfern, J., 2010. Toarcian carbon isotope shifts and nutrient changes from the Northern margin of Gondwana (High Atlas, Morocco, Jurassic): Palaeoenvironmental implications. *Palaeogeography, Palaeoclimatology, Palaeoecology* 297, 377 – 390.
- Bond, D.P.G., Wignall, P.B., 2014. Large igneous provinces and mass extinctions: An update. In: Keller, G., Kerr, C. (Eds.), *Volcanism, impacts and mass extinctions: causes and effects*. The Geological Society of America, Special Publications 505, pp. 29 – 56.
- Bottrell, S.H., Newton, R.J., 2006. Reconstruction of changes in global sulfur cycling from marine sulfate isotopes. *Earth Science Reviews* 75, 59 – 83.
- Bordenave, M.L., Espitalié, J., Leplat, P., Oudin, J.L., Vandenbroucke, M., 1993. Screening Techniques for Source Rock Evaluation. In: Bordenave, M.L. (Ed.), *Applied Petroleum Geochemistry*. Éditions Technip, Paris, 217 – 278.
- Bour, Y., Mattioli, E., Pittet, B., 2007. Nannofacies analysis as a tool to reconstruct paleoenvironmental changes during the Early Toarcian anoxic event. *Palaeogeography, Palaeoclimatology, Palaeoecology* 249, 58 – 79.
- Bourbonniere, R. A., Meyers, P. A., 1997. Sedimentary geolipid records of historical changes in the watersheds and productivities of Lakes Ontario and Erie, *Limnology and Oceanography* 41, 352 – 359.
- Boulila, S., Galbrun, B., Miller, K.G., Pekar, S.F., Browning, J.V., Laskar, J., Wright, J., 2011. On the origin of Cenozoic and Mesozoic “third-order” eustatic sequences. *Earth-Science Reviews* 109, 94 – 112.
- Boulila, S., Galbrun, B., Huret, E., Hinnov, L.A., Rouget, I., Gardin, S., Bartolini, A., 2014. Astronomical calibration of the Toarcain Stage: Implications for sequence stratigraphy and the duration of the early Toarcain OAE. *Earth and Planetary Science Letters* 386, 98 – 111.
- Brandt, K., 1986. Glacioeustatic cycles in the Early Jurassic. *Neues Jahrbuch für Geologie und Paläontologie* 5, 257 – 274.
- Branski, P., 2012. The mineralogical record of the Early Toarcain stepwise climate changes and other environmental variations (Ciechocinek Formation, Polish Basin). *Volumina Jurassica* 10, 1 – 24.
- Brazier, J.M., Suan, G., Tacail, T., Simon, L., Martin, J.E., Mattioli, E., Balter, V., 2015. Calcium

- isotope evidence for dramatic increase of continental weathering during the Toarcian oceanic anoxic event (Early Jurassic). *Earth and Planetary Science Letters* 411, 164 – 176.
- Bray, E.E., Evans, E.D., 1961. Distribution of *n*-paraffins as a clue to recognition of source beds. *Geochimica et Cosmochimica Acta* 22, 2 – 15.
- Brigaud, B., Vincent, B., Carpentier, C., Robin, C., Guillocheau, F., Yven, B., Huret, E., 2013. Growth and demise of the Jurassic carbonate platform in the intracratonic Paris Basin (France): interplay of climate change, eustasy and tectonics. *Marine and Petroleum Geology* 53, 3 – 29.
- Briggs, D.E.G., Summons, R., 2014. Ancient biomolecules: Their origins, fossilization, and role in revealing the history of life. *Bioessays* 36, 482 – 490.
- Brocks J.J., Schaeffer, P., 2008. Okenane, a biomarker for purple sulfur bacteria (Chromatiaceae), and other new carotenoid derivatives from the 1640 Ma Barney Creek Formation. *Geochimica et Cosmochimica Acta* 72, 1396 – 1414.
- Brown, J., Ferrians, O.J., Heginbottom, J.A., Melnikov, E.S., 1997. Circum-Arctic map of permafrost and ground-ice conditions. Washington, DC: U.S. Geological Survey in Cooperation with the Circum-Pacific Council for Energy and Mineral Resources. Circum-Pacific Map Series CP-45, scale 1:10,000,000, 1 sheet.
- Brumsack, H.J., 2006. The trace metal content of recent organic-rich sediments: Implications for Cretaceous black shale formation. *Palaeogeography, Palaeoclimatology, Palaeoecology* 232, 344 – 361.
- Bucefalo Palliani, R.B., Mattioli, E., Ridinng, J.B., 2002. The response of marine phytoplankton and sedimentary organic matter to the early Toarcian (Lower Jurassic) oceanic anoxic event in northern England. *Marine Micropaleontology* 46, 223 – 245.
- Buchardt, B., Seaman, P., Stockmann, G., Voss, M., Wilken, U., Düwel, L., Kristiansen, A., Jenner, C., Whiticar, M.J., Kristensen, R.M., Petersen, G.H., Thorjörn, L., 1997. Submarine columns of ikaite tufa. *Nature* 390, 129 – 130.
- Buckman, S.S., 1910. Certain Jurassic (Lias-Oolite) strata of South Dorset. *Quarterly Journal of the Geological Society of London* 66, 52 – 89.
- Burdige, D.J., 2007. Preservation of Organic Matter in Marine Sediments: Controls, Mechanisms, and an Imbalance in Sediment Organic Carbon Budget. *Chemical Review* 107, 467 – 485.
- Burgess, S.D., Bowring, S.A., Fleming, T.H., Elliot, D.H., 2015. High-precision geochronology links the Ferrar large igneous province with early-Jurassic ocean anoxia and biotic crisis. *Earth and Planetary Science Letters* 415, 90 – 99.

- C -

- Calvert, S.E., Pedersen, T.F., 1993. Geochemistry of Recent oxic and anoxic marine sediments: implications for the geological record. *Marine Geology* 113, 67 – 88.
- Calvert, S.E., Pedersen, T.F., 2007. Elemental proxies for palaeoclimatic and palaeoceanographic variability in marine sediments: interpretation and application. In: Hillaire-Marcel, C., Vernal, A.D. (Eds.), *Proxies in Late Cenozoic Paleooceanography*, Elsevier, Amsterdam (2007), pp. 567 – 644.

- Canfield, D.E., 2001. Isotopic fractionation by natural populations of sulfate-reducing bacteria. *Geochimica et Cosmochimica Acta* 65, 1117 – 1124.
- Canfield, D.E., Lyons, T.W., Raiswell, R., 1996. A model for iron deposition to euxinic Black Sea sediments. *American Journal of Science* 296, 818 – 834.
- Canfield, D.E., Farquhar, J., Zerkle, A., 2010. High isotope fractionations during sulfate reduction in a low-sulfate euxinic ocean analog. *Geology* 38, 415 – 418.
- Caruthers, A.H., Gröcke, D.R., Smith, P.L., 2011. The significance of the Early Jurassic (Toarcian) carbon-isotope excursion in Haida Gwaii (Queen Charlotte Islands), British Columbia, Canada. *Earth and Planetary Science Letters* 307, 19 – 26.
- Caruthers, A.H., Smith, P.L., Gröcke, D.R., 2014. The Pliensbachian-Toarcian (Early Jurassic) extinction: A North American perspective. In: Keller, G., Kerr, C. (Eds.), *Volcanism, impacts and mass extinctions: causes and effects*. The Geological Society of America, Special Publications 505, pp. 225 – 244.
- Caswell, B.A., Coe, A.L., 2012. A high-resolution shallow marine record of the Toarcian (Early Jurassic) Oceanic Anoxic Event from the East Midlands Shelf, UK. *Palaeogeography, Palaeoclimatology, Palaeoecology* 365, 124 – 135.
- Caswell, B.A., Coe, A.L., 2014. The impact of anoxia on pelagic macrofauna during the Toarcian Oceanic Anoxic Event (Early Jurassic). *Proceedings of the Geologists Association* 125, 383 – 391.
- Caswell, B.A., Coe, A.L., Cohen, A.S., 2009. New range data for marine invertebrate species across the Early Toarcian (Early Jurassic) mass extinction. *Journal of Geological Society* 166, 859 – 872.
- Ceballos, G., Ehrlich, P.R., Barnosky, A.D., Garcia, A., Pringle, R.M., Palmer, T.M., 2015. Accelerated modern human-induced species losses: entering the sixth mass extinction. *Science Advances* 1, e1400253, doi: 10.1126/sciadv.1400253.
- Chandler, M.A., Rind, D., Ruedy, R., 1992. Pangaeon climate during the Early Jurassic: GCM simulations and the sedimentary record of paleoclimate. *Geological Society of America Bulletin* 104, 543 – 559.
- Chappe, B., Albrecht, P., Michaelis, W., 1982. Polar lipids of archeobacteria in sediments and petroleum. *Science* 217, 65 – 66.
- Clémence, M.E., Huret, E., Bartolini, A., Galbrun, B., Gardin, S., Hinnov, L., Beaumont, V., 2006. Micropalaeontologic, geochemical and cyclostratigraphic approach for the timing of the early Toarcian Oceanic Anoxic Event in the Paris Basin (GPF-Sancerre borehole). *Volumina Jurassica* 4, 154 – 155.
- Clémence, M.E., 2014. Pattern and timing of the Early Jurassic calcareous nannofossil crisis. *Palaeogeography, Palaeoclimatology, Palaeoecology* 411, 56 – 64.
- Clémence, M.E., Gardin, S., Bartolini, A., 2015. New insights in the pattern and timing of the Early Jurassic calcareous nannofossil crisis. *Palaeogeography, Palaeoclimatology, Palaeoecology* 427, 100 – 108.
- Coe, A.L., 2003. *The sedimentary Record of Sea-Level Change*. Cambridge University Press, 287 pp.

- Cohen, A.S., Coe, A.L., Harding, S.M., Schwark, L., 2004. Osmium isotope evidence for the regulation of atmospheric CO₂ by continental weathering. *Geology* 32, 157 – 160.
- Comas-Rengifo, M.J., Arias, C., Gómez, A., Herrero, C., Osete, M.L., Palencia, A., 2010. A Complementary Section for the Proposed Toarcian (Lower Jurassic) Global Stratotype: the Almonacid De La Cuba Section (Spain). *Stratigraphy and Geological Correlation* 18, 133 – 152.
- Cope, J.C.W., 2006. Jurassic: The returning seas. In: Brenchley, P.J., Rawson, P.F. (Eds.), *The Geology of England and Wales. Second Edition*, The Geological Society, 325 – 364.
- Cúeno, R., Ramezani, J., Scasso, R., Pol, D., Escapa, I., Zavattieri, A.M., Bowring, S.A., 2013. High-precision U–Pb geochronology and a new chronostratigraphy for the Cañadón Asfalto Basin, Chubut, central Patagonia: Implications for terrestrial faunal and floral evolution in Jurassic. *Gondwana Research* 24, 1267 – 1275.
- Cranwell, P. A., 1973. Chain length distribution of *n*-alkanes from lake sediments in relation to post-glacial environmental change. *Freshwater Biology* 3, 259 – 265.
- Cranwell, P. A., Eglinton, G., Robinson, N., 1987. Lipids of aquatic organisms as potential contributors to lacustrine sediments – II, *Organic Geochemistry* 11, 513 – 527.

- D -

- Damborenea, S.E., Echevarria, J., Ros-Frach, S., 2013. Southern Hemisphere Paleobiogeography of Triassic-Jurassic Marine Bivalves. Springer. doi: 10.1007/978-94-007-5098-2.
- Danise, S., Twitchett, R.J., Littöe, C.T.S., Clémence, M. E., 2013. The Impact of Global Warming and Anoxia on Marine Benthic Community Dynamics: an Example from the Toarcian (Early Jurassic). *PLoS ONE* 8(2): e56255. doi: 10.1371/journal.pone.0056255.
- Danise, S., Twitchett, R.J., Little, C.T.S., 2015. Environmental controls on Jurassic marine ecosystems during global warming. *Geology* 43, 263 – 266.
- DeConto, R.M., Galeotti, S., Pagani, M., Schaefer, K., Zhang, T., Pollard, D., Beerling, D.J., 2012. Past extreme warming events linked to massive carbon release from thawing permafrost. *Nature* 484, 87 – 92.
- de Graciansky, P.C., Dardeau, G., Dumont, T., Jacquin, T., Marchand, D., Mouterde, R., Vail, P.R., 1993. Depositional sequence cycles, transgressive/regressive facies cycles and extensional tectonics: example from the Southern Sub-Alpine Jurassic basin. *Bulletin de la Société Géologique de France* 164, 709 – 718.
- Dera, G., Donnadiou, Y., 2012. Modeling evidences for global warming, Arctic seawater freshening, and sluggish oceanic circulation during the Early Toarcian anoxic event. *Paleoceanography* 27, doi: 10.1029/2012PA002283.
- Dera, G., Pellenard, P., Neige, P., Deconinck, J.F., Pucéat, E., Dommergues, J.-L., 2009a. Distribution of clay minerals in Early Jurassic Peritethyan seas: Palaeoclimatic significance inferred from multiproxy comparisons. *Palaeogeography, Palaeoclimatology, Palaeoecology* 271, 39 – 51.
- Dera, G., Pucéat, E., Pellenard, P., Neige, P., Delsate, D., Joachimski, M., Reisberg, L., Martinez, M., 2009b. Water mass exchange and variations in seawater temperature in the NW Tethys

- during the Early Jurassic: Evidence from neodymium and oxygen isotopes of fish teeth and belemnites. *Earth and Planetary Science Letters* 286, 198 – 207.
- Dera, G., Neige, P., Dommergues, J.L., Fara, D., Laffont, R., Pellenard, P., 2010. High-resolution dynamics of Early Jurassic marine extinctions: the case of Pliensbachian-Toarcian ammonites (Cephalopoda). *Journal of the Geological Society* 167, 21 – 33.
- Dera, G., Brigaud, B., Monna, F., Laffont, R., Pucéat, E., Deconinck, J.-F., Pellenard, P., Joachimski, M.M., Durlet, C., 2011a. Climatic ups and downs in a disturbed Jurassic world. *Geology* 39, 215 – 218.
- Dera, G., Neige, P., Dommergues, J.L., Brayard, A., 2011b. Ammonite paleobiogeography during the Pliensbachian–Toarcian crisis (Early Jurassic) reflecting paleoclimate, eustasy, and extinctions. *Global and Planetary Change* 78, 92 – 105.
- Dera, G., Prunier, J., Smith, P., Haggart, J.W., Popov, E., Guzhov, A., Rogov, M., Delsate, D., Thies, D., Cuny, G., Puéat, E., Charbonnier, G., Bayon, G., 2015. Nd isotope constrains on ocean circulation, paleoclimate, and continental drainage during the Jurassic breakup of Pangaea. *Gondwana Research* 27, 1599 – 1615.
- Dickens, R.D., 1999. The blast in the past. *Nature* 401, 752 – 755.
- Dickson, A.J., Cohen, A.S., Coe, A.L., 2012. Seawater oxygenation during the Paleocene-Eocene Thermal Maximum. *Geology* 40, 639 – 642.
- Dickson, A.J., Cohen, A.S., Coe, A.L., 2014. Continental margin molybdenum isotope signatures from the Early Eocene. *Earth and Planetary Science Letters* 404, 389 – 395.
- Didyk, B.M., Simoneit, B.R.T., Brassell, S.C., Eglinton, G., 1978. Organic geochemical indicators of paleoenvironmental conditions of sedimentation. *Nature* 272, 216 – 222.
- Dromart, G., Allemand, P., Garcia, J.P., Robin, C., 1996. Variation cyclique de la production carbonatée au Jurassique le long d'un transect Bourgogne-Ardèche, Est France. *Bulletin de la Société Géologique de France* 167, 423 – 433.
- d'Orbigny, A., 1842 – 1851. *Paléontologie Française. Description zoologique et géologique de tous les animaux mollusques et rayonnés fossiles de France. Terrains oolitiques ou jurassiques. I céphalopodes.* Masson, Paris. 642 pp.
- d'Orbigny, A., 1852. *Cours élémentaire de paléontologie et de géologie stratigraphique, Vol. 2,* Masson, Paris, pp. 383 – 847.
- Duarte, L.V., Rodrigues, R., Dino, R. 2003. Carbon stable isotope analysis as a sequence stratigraphy tool. Case study from Lower Jurassic marly limestones of Portugal. IV South American Symposium of Isotope Geology, Salvador, 341 – 344.
- Duncan, R.A., Hooper, P.R., Rehacek, J., Marsch, J.S., Duncan, A.R., 1997. The timing and duration of Karoo igneous event, southern Gondwana. *Journal of Geophysical Research* 102, 127 – 138.

- E -

- Eglinton, G. and Hamilton, R. J., 1967. Leaf epicuticular waxes. *Science* 156, 1322 – 1335.
- Enay, R., Mangold, C., Cariou, E., Debrand-Passard, S., Donze, P., Gabilli, J., Lafavrais-Raymond, A., Mouterde, R., Thierry, J., 1980. Synthèse paléogéographique du Jurassique français.

- Villeurbanne. Dép. des sciences de la terre, Université Claude-Bernard, 210 pp.
- Encarnación, J., Fleming, T.H., Elliot, D.H., Eales, H.V., 1996. Synchronous emplacement of Ferrar and Karoo dolerites and the early breakup of Gondwana. *Geology* 24, 535 – 538.
- Einsele, G., 2000. *Sedimentary basins*. Springer Verlag, 792 pp.
- Elmi, S., 1999. Report of the Pliensbachian-Toarcian Boundary Working Group. International Subcommission on Jurassic Stratigraphy. *Newsletter* 26, 43 – 46.
- Elmi, S., 2006. Pliensbachian-Toarcian boundary: the proposed GSSP of Peniche (Portugal). *Volumina Jurassica* 4, 5 – 16.
- Elmi, S., Gabilly, R., Mouterde, R., Rulleau, L., Rocha, R.B., 1994. L'étage Toarcien de l'Europe et de la Téthys; divisions et corrélation. *Geobios* 17, 149 – 159.
- Elmi, S., Rulleau, L., Gabilly, J. et Mouterde, R., 1997. 4. Toarcien. In: Cariou, E., Hantzpergue, P. (Eds.), *Biostratigraphie du Jurassique ouest-européen et méditerranéen: zonations parallèles et distribution des invertébrés et microfossiles*. Bulletin des Centres de recherches exploration-production Elf-Aquitaine, Pau, Mémoire 17, pp. 25 – 36.
- Ellwood, B.B., Crick, R.E., Hassani, A.E., Benoist, S.L., Young, R.H., 2000. Magnetostratigraphy event and cyclostratigraphy method applied to marine rocks: Detrital versus carbonate productivity. *Geology* 28, 1135 – 1138.
- Emmanuel, L., Renard, M., Cubaynes, R., de Rafelis, M., Hermoso, M., Lecallonnec, L., le Solleuz, A., Rey, J., 2006. The “Schistes Carton” of Quercy (Tarn, France): a lithological signature of a methane hydrate dissociation event in the early Toarcian. Implications for correlations between Boreal and Tethyan realms. *Bulletin de la Société Géologique de France* 177, 239 – 249.
- Encarnación, J., Fleming, T.H., Elliot, D.H., Eales, H.V., 1996. Synchronous emplacement of Ferrar and Karoo dolerites and the early breakup of Gondwana. *Geology* 24, 535 – 538.
- Epshteyn, O.G., 1978. Mesozoic–Cenozoic climates of northern Asia and glacial–marine deposits. *International Geology Review* 20, 49 – 58.
- Erba, E., 2004. Calcareous nannofossils and Mesozoic oceanic anoxic events. *Marine Micropaleontology* 52, 85 – 106.
- Espitalié, J., Laporte, J.L., Madec, M., Marquis, F., Leplat, P., Paulet, J., Boutefeu, A., 1977. Rapid method for source rocks characterization and for determination of petroleum potential and degree of evolution. *Revue de l'Institut Français du Pétrole* 32, 23 – 42.
- Evans, M.E., Heller, F., 2003. *Environmental magnetism - principles and applications of enviromagnetics*. International Geophysics Series 86. Academic Press, 299 pp.

- F -

- Farrimond, P., Eglinton, G., Brassel, S.C., 1988. Toarcian Anoxic Event in Europe: an organic geochemical study. *Marine Petroleum Geology* 6, 136 – 147.
- Farrimond, P., Stoddart, D.P., Jenkyns, H.C., 1994. An organic geochemical profile of the Toarcian Anoxic Event in northern Italy. *Chemical Geology* 111, 17 – 33.
- Faugères, J.C., Stow, D.A.V., 1993. Bottom-current-controlled sedimentation: a synthesis of the contourite problem. *Sedimentary Geology* 82, 287 – 297.

- Filho, J.G.M., Menezes, T.R., de Oliveira Mendonca, J., de Oliveira, A.D., da Silva, T.F., Rondon, N.F., da Silva, F.S., 2012. Organic Facies: Palynofacies and Organic Geochemistry Approaches. In: Panagiotaras, D. (Ed.), *Geochemistry – Earth's System Processes*. InTech, pp. 211 – 248.
- Fisher, I.St.J., Hudson, J.D., 1987. Pyrite formation in Jurassic shales of contrasting biofacies. In: Brooks, J., Fleet, A.J. (Eds.), *Marine Petroleum Source Rocks*. Geological Society, London, Special Publications 26, pp. 69 – 78.
- Fleet, A.J., Clayton, C.J., Jenkyns, H.C., Parkinson, D.,N., 1987. Liassic source rock deposition in western Europe. In: Brooks, J., Glennie, K. (Eds.), *Petroleum geology of northwest Europe*. Graham & Trotman, London, pp. 59 – 70.
- Fraguas, A., Comas-Rengifo, M.J., Gómez, J.J., Goy, A., 2012. The calcareous nannofossil crisis in Northern Spain (Asturias province) linked to the Early Toarcian warming-driven mass extinction. *Marine Micropaleontology* 94 – 95, 58 – 71.
- Frakes, L.A., Francis, J.E., Syktus, J.I., 1992. *Climate Modes of the Phanerozoic*. Cambridge University Press, Cambridge. 274 pp.
- Franke, D., 2014. *Regionale Geologie von Ostdeutschland – Ein Wörterbuch*. www.regionalgeologie-ost.de
- French, K. L., Sepúlveda, J., Trabucho-Alexandre, J., Gröcke, D. R., Summons, R. E., 2014. Organic geochemistry of the early Toarcian oceanic anoxic event in Hawsker Bottoms, Yorkshire, England. *Earth and Planetary Science Letters* 390, 116 – 127.
- Frimmel, A., 2003. *Hochauflösende Untersuchungen von Biomarkern an epikontinentalen Schwarzschiefern des Unteren Toarciums (Posidonienschiefer, Lias ε) von SW-Deutschland*. Dissertation, University of Tübingen, 108 pp.
- Frimmel, A., Oschmann, W., Schwark, L., 2004. Chemostratigraphy of the Posidonia Black Shale, SW Germany I. Influence of sea level variations on organic matter facies evolution. *Chemical Geology* 206, 199 – 230.

- G -

- Gabily, J., 1976. Le Toarcien á Thouars et dans le centre-ouest de la France: biostratigraphie, evolution de la faune (Harpoceratinae – Hildoceratine). *Les Stratotypes Français* 3. Centre National Recherche Scientifique, Paris, 217 pp.
- Gale, A.S., Hardenbol, J., Hathway, B., Kennedy, W.J., Young, J.R., Phansalkar, V., 2002. Global correlation of Cenomanian (Upper Cretaceous) sequences: Evidence for Milankovitch control on sea level. *Geology* 30, 291 – 294.
- Gradstein, F.M., Ogg, J.G., Schmitz, K., Ogg, G., 2012. *The Geological Time Scale 2012*, vol. 2. Elsevier. 1144 pp.
- Graham, L., Wong, T., Dusa, M., Andsbjerg, J., Mönning, E., Feldmann-Olszewska, Verreussel, R., 2010. Jurassic. In: Doornenbal, J.C., Stevenson, A.G. (Eds.), *Petroleum Geological Atlas of the Southern Permian Basin Area*. EAGE Publications b.v. (Houten), pp. 175 – 194.

- Gély, J.P., Lorenz, J., 2006. Lias and Odgger series of the Paris Basin (France): syn-sedimentary tectonic and paleogeographic reconstructions for each ammonite biozonation level. *Geobios* 39, 631 – 649.
- Ghil M., R. M. Allen, M. D. Dettinger, K. Ide, D., Kondrashov, M. E. Mann, A. Robertson, A. Saunders, Y. Tian, F. Varadi, and P. Yiou, 2002. Advanced spectral methods for climatic time series: *Reviews of Geophysics* 40, 1 – 41.
- Gill, B.C., Lyons, T.W., Jenkyns, H.C., 2011. A global perturbation to the sulfur cycle during the Toarcian Oceanic Anoxic Event. *Earth and Planetary Science Letters* 312, 484 – 496.
- Goldberg, K., Humayun, M., 2010. The applicability of the chemical index of alteration as a paleoclimatic indicator: An example from the Permian of the Paraná Basin, Brazil. *Palaeogeography Palaeoclimatology Palaeoecology* 293, 175 – 183.
- Golonka, J., Ross, M.I., Scotese, R.C., 1994. Phanerozoic Paleogeography and paleoclimate Modeling Maps. In: Embry, A.F., Beauchamp, B., Glass, D. (Eds.), *Pangea: Global Environments and Resources*. Canadian Society of Petroleum Geologist Memoir 17, pp. 1 – 48.
- Golonka, J., 2007. Late Triassic and Early Jurassic palaeogeography of the world. *Palaeogeography, Palaeoclimatology, Palaeoecology* 244, 297 – 307.
- Golonka, J., 2011. Phanerozoic paleoenvironment and paleolithofacies maps, In: Spencer, A.M., Embry, A.F., Gautier, A.V., Stoupakova, A.V., Sørensen, K. (Eds.), *Arctic Petroleum Geology*. Geological Society Memoir No. 35, pp. 79 – 130.
- Gómez, J.J., Goy, A., 2005. Late Triassic and Early Jurassic palaeogeographic evolution and depositional cycles of the Western Tethys Iberian platform system (Eastern Spain). *Palaeogeography, Palaeoclimatology, Palaeoecology* 222, 77 – 94.
- Gómez, J.J., Goy, A., Canales, M.L., 2008. Seawater temperature and carbon iso- tope variations in belemnites linked to mass extinction during the Toarcian (Early Jurassic) in Central and Northern Spain. Comparison with other European sections. *Palaeogeography, Palaeoclimatology, Palaeoecology* 258, 28 – 58.
- Gómez, J.J., Arias, C., 2010. Rapid warming and ostracods mass extinction at the Lower Toarcian (Jurassic) of central Spain. *Marine Micropaleontology* 74, 119 – 15.
- Gómez, J.J., Comas-Rengifo, M.J., Goy, A., 2015. Palaeoclimatic oscillations in the Pliensbachian (Lower Jurassic) of the Asturian Basin (Northern Spain). *Climate of the Past* 11, 4039 – 476.
- Goossens, H., de Leeuw, J.W., Schenk, P.A., Brassel, S.C., 1984. Tocopherols as likely precursors of pristane in ancient sediments and crude oils *Nature* 312, 440 – 442.
- Gourtillet, V., Fluteau, F., 2014. A review of the embedded time scales of flood basalt volcanism with special emphasis on dramatically short magmatic pulses. In: Keller, G., Kerr, C. (Eds.), *Volcanism, impacts and mass extinctions: causes and effects*. The Geological Society of America, Special Publications 505, pp. 301 – 318.
- Goy, A., Ureta, M.S., Arias, C., Canales, M.L., Gracia Joral, F., Herrero, C., Martinez, G., Perilli, N., 1996. Die Toarcium/Aalenium-Grenze im Profil Fuentalsaz (Iberische Kette, Spanien). In: Ohmert, W. (Ed.), *Die Grenzziehung Unter/Mitteljura (Toarcium/Aalenium) bei Wittenau und Fuentalsaz*. Beispiele interdisziplinärer geowissenschaftlicher Zusammenarbeit. Geologisches

- Landesamt Baden-Württemberg, Informationen 8, pp. 43 – 52.
- Gradstein, F.M., Ogg, J.G., Schmitz, M., Ogg, G., 2012. The Geological Timescale 2012. Elsevier, 1144 pp.
- Gräfe, K.U., 2005. Benthic foraminifers and palaeoenvironment in the Lower and Middle Jurassic of the Western Basque-Cantabrian Basin (Northern Spain). *Journal of Iberian Geology* 31, 217 – 233.
- Greber, N.D., Siebert, C., Nägler, T.F., Pettke, T., 2012. $\delta^{98/95}\text{Mo}$ values and molybdenum concentration data for NIST SRM 610, 612 and 3134: Towards a common protocol for reporting Mo data. *Geostandards and Geoanalytical Research* 36, 291 – 300.
- Gröcke, D.R., Hori, R.S., Trabucho-Alexandre, J., Kemp, D.B., Schwark, L., 2011. An open ocean record of the Toarcian oceanic anoxic event. *Solid Earth* 2, 245 – 257.
- Grossmann, E.L., 2012. Chapter 10: Oxygen isotope stratigraphy. In: Gradstein, F.M., Schmitz, M., Ogg, G. (Eds.), *The Geological Time Scale 2012*, Vol. 1. Elsevier, pp. 181 – 206.
- Guérin-Franiatte, S., Maquil, R., Münzberger, P., 2010. Le Toarcian au Grand-Duché de Luxembourg: Biostratigraphie dans la région de Belvaux, in Weis, R., Guérin-Franiatte, S., eds., *Le Jurassiques inférieur et moyen au Luxembourg: Nouvelles données paléontologiques et biostratigraphiques: Ferrantia*, 62, 19 – 34.
- Guex, J., Bartolini, A., Spangenberg, J., Vicente, J.-C., Schaltegger, U., 2012a. Ammonoid multi-extinction crises during the Late Pliensbachian–Toarcian and carbon cycle instabilities. *Solid Earth Discussions* 4, 1205 – 1228.
- Guillocheau, F., Robin, C., Allemand, P., Bourquin, S., Brault, N., Dromart, G., Friedenber, R., Gracia, J.P., Gaulier, J.M., Gaumet, F., Grosdoy, B., Hanot, F., Le Strat, P., Mettraux, M., Nalpas, T., Prijac, C., Rigollet, C., Serrano, O., Grandjean, G., 2001. Meso-Cenozoic geodynamic evolution of the Paris Basin: 3D stratigraphic constraints. *Geodinamica Acta* 13, 189 – 245.

- H -

- Habicht, K.S., Canfield, D.E., 1997. Sulfur isotope fractionation during bacterial sulfate reduction in organic-rich sediments. *Geochimica et Cosmochimica Acta* 61, 5351 – 5361.
- Habicht, K.S., Canfield, D.E., 2001. Isotope fractionation by sulfate-reducing natural populations and the isotopic composition of sulfide in marine sediments. *Geology* 29, 555 – 558.
- Hallam, A., 1986. The Pliensbachian and Tithonian extinction events. *Nature* 319, 765 – 768.
- Hallam, A., 1994. Jurassic Climates as inferred from the sedimentary and fossil record. In: Allen, J.R.L., Hoskins, B.J., Sellwood, B.W., Spicer, R.A., Valdes, P.J. (Eds.), *Paleoclimates and their modelling*. The Royal Society, pp. 79 – 87.
- Hallam, A., 1997. Estimates of the amount and rate of sea-level change across the Rhaetian–Hettangian and Pliensbachian–Toarcian boundaries (latest Triassic to early Jurassic). *Journal of the Geological Society* 154, 773 – 779.
- Hallam, A., 2001. A review of the broad pattern of Jurassic sea level changes and their possible causes in the light of current knowledge. *Palaeogeography, Palaeoclimatology, Palaeoecology* 167, 23 – 37.
- Hanzo, M., Espitalié, J., 1994. Relationship between Organic Matter and Sedimentation in the Lias

- of Lorraine (France). In: Mascle, A. (Ed.), *Hydrocarbon and Petroleum Geology of France*. Special Publication EAPG No. 4, pp. 121 – 136.
- Harazim, D., van de Schootbrugge, B., Sorichter, K., Fiebig, J., Weug, A., Suan, G., Oschmann, W., 2013. Spatial variability of water mass conditions within the European Epicontinental Seaway during the Early Jurassic (Pliensbachian–Toarcian). *Sedimentology* 60, 359 – 390.
- Hardenbol, J., Thierry, J., Farley, M.B., Jacquin, T., de Graciansky, P.C., Vail, P.R., 1998. Mesozoic and Cenozoic sequence chronostratigraphic framework of European basins. In: de Graciansky, P.C., Hardenbol, J., Jacquin, T., Vail, P.R. (Eds.), *Mesozoic and Cenozoic Sequence Stratigraphy of European Basins*. SEPM Special Publication 60. Tulsa, OK, pp. 3 – 13.
- Hargreaves, R.B., Rehacek, J., Hooper, P.R. 1997. Paleomagnetism of the Karoo igneous rocks in South Africa. *South African Journal of Geology* 100, 195 – 212.
- Harries, P.J., Little, C.T.S., 1999. The early Toarcian (Early Jurassic) and Cenomanian-Turonian (Late Cretaceous) mass extinctions: similarities and contrasts. *Palaeogeography, Palaeoclimatology, Palaeoecology* 154, 39 – 66.
- Hastie, W.W., Watkeys, M.K., Aubourg, C., 2014. Magma flow in dyke swarms of the Karoo LIP: Implications for the mantle plume hypothesis. *Gondwana Research* 25, 736 – 795.
- Hermoso, M., F. Minoletti, F., 2008. Nannofloral assemblage change during the Early Toarcian anoxic event in the Paris Basin and biogeochemical insights, paper presented at Foraminifera and Nannofossil Groups Joint Spring Meeting, Micropalaeontological Society, Tübingen, Germany.
- Hermoso, M., 2007. Les perturbations environnementales au cours du Toarcien inférieur. Apport de l'étude sédimentologique et géochimique de séries boréales et Ouest-Téthysiennes. PhD Thesis Marie Curie University, Paris, 326 pp.
- Hermoso, M., Le Callonnec, L., Minoletti, F., Renard, M., Hesselbo, S.P., 2009a. Expression of the Early Toarcian negative carbon-isotope excursion in separated carbonate microfractions. *Earth and Planetary Science Letters* 277, 194 – 203.
- Hermoso, M., Minoletti, F., Le Callonnec, L., Jenkyns, H.C., Hesselbo, S.P., Rickaby, R.E.M., Renard, M., de Refélis, M., Emmanuel, L., 2009b. Global and local forcing of Early Toarcian seawater chemistry: A comparative study of different paleoceanographic settings (Paris and Lusitanian basins). *Paleoceanography* 24, PA4208, doi: 10.1029/2009PA001764.
- Hermoso, M., Minoletti, F., Rickaby, R.E.M., Hesselbo, S.P., Baudin, F., Jenkyns, H.C., 2012. Dynamics of a stepped carbon-isotope excursion: Ultra high-resolution study of early Toarcian environmental change. *Earth and Planetary Science Letters* 319, 45 – 54.
- Hermoso, M., Minoletti, F., Pellenard, P., 2013. Black shale deposition during Toarcian super-greenhouse driven by sea level. *Climate Past Discussions* 9, 4365 – 4384.
- Hermoso, M., Pellenard, P., 2014. Continental weathering and climatic changes inferred from clay mineralogy and paired carbon isotopes across the early to middle Toarcian in the Paris Basin. *Palaeogeography, Palaeoclimatology, Palaeoecology* 399, 385 – 393.
- Hermoso, M., Delsate, D., Baudin, F., Le Callonnec, L., Minoletti, F., Renard, M., Faber, A., 2014. Record of Early Toarcian carbon cycle perturbations in a nearshore environment: Bascharage section (easternmost Paris Basin). *Solid Earth Discussions* 6, 1073 – 1100.

- Herrmann, A.D., Kendall, B., Algeo, T.J., Gordon, G.W., Wasylenki, L.E., Anbar, A.D., 2012. Anomalous molybdenum isotope trends in Upper Pennsylvanian euxinic facies: Significance for use of $\delta^{98}\text{Mo}$ as a global marine redox proxy. *Chemical Geology* 324 – 325, 87 – 98.
- Hesselbo, S.P., 2008. Sequence stratigraphy and inferred relative sea-level change from the onshore British Jurassic. *Proceedings of the Geologists' Association* 119, 19 – 34.
- Hesselbo, S.P., Jenkyns, H.C., 1998. British Lower Jurassic sequence stratigraphy. In: de Graciansky, P.C., Hardenbol, J., Jacquin, Th., Vail, P.R. (Eds.), *Mesozoic–Cenozoic Sequence Stratigraphy of European Basins*. SEPM Special Publication 60, pp. 562 – 581.
- Hesselbo, S.P., Coe, A., 2000. Jurassic sequences of the Herbrides Basin, Isle of Skye, Scotland. In: Graham J.R., Ryan, A. (Eds.), *Field Trip Guidebook, International Sedimentologists Association Meeting, Dublin, 2000*, pp. 41-58.
- Hesselbo, S.P., Pieńkowski, G., 2011. Stepwise atmospheric carbon-isotope excursion during the Toarcian Oceanic Anoxic Event (Early Jurassic, Polish Basin). *Earth and Planetary Science Letters* 301, 365 – 372.
- Hesselbo, S.P., Gröcke, D.R., Jenkyns, H.C., Bjerrum, C.J., Farrimod, P., Morgenas Bell, H.S., Green, O.R., 2000a. Massive dissociation of gas hydrate during the Jurassic oceanic anoxic event. *Nature* 406, 392 – 395.
- Hesselbo, S.P., Meister, C., Gröcke, D.R., 2000b. A potential global stratotype for the Sinemurian–Pliensbachian boundary (Lower Jurassic), Robin Hood's Bay, UK: ammonite faunas and isotope stratigraphy. *Geol. Mag.* 137, 601 – 607.
- Hesselbo, S.P., Jenkyns, H.C., Duarte, L.V., Oliveira, L.C.V., 2007. Carbon-isotope record of the Early Jurassic (Toarcian) Oceanic Anoxic Event from fossil wood and marine carbonate (Lusitanian Basin, Portugal). *Earth and Planetary Science Letters* 253, 455 – 470.
- Hinnov, L.A., Park, J.J., 1999. Strategies for assessing Early-Middle (Pliensbachian–Aalenian) Jurassic cyclochronologies. *Philosophical Transactions of the Royal Society of London* 357, 1831 – 1859.
- Hinnov, L.A., Park, J., Erba, E., 2000. Lower-Middle Jurassic rhythmites from the Lombard Basin, Italy: a record of orbitally forced carbonate cycles modulated by secular environmental changes in West Tethys, In: Hall, R.L., Smith, P.L. (Eds.), *Advances in Jurassic Research 2000*, Trans Tech Publications, pp. 437 – 454.
- Howarth, M.K., 1980. The Toarcian age of the upper part of the Marlstone Rock bed in England. *Paleontology* 23, 637 – 656.
- Howarth, M.K. 1992a. The ammonite family *Hildoceratidae* in the Lower Jurassic of Britain. Part 1. Monograph of the Palaeontographical Society London, pp. 1 – 106.
- Howarth, M.K. 1992b. The ammonite family *Hildoceratidae* in the Lower Jurassic of Britain. Part 2. Monograph of the Palaeontographical Society London, pp. 107 – 200.
- Huang, W.Y., Meinschein, W. G., 1979. Sterols as ecological indicators. *Geochimica et Cosmochimica Acta*, 43, 739 – 745.
- Huang, C., Hesselbo, S.P., 2014. Pacing of the Toarcian Oceanic Anoxic Event (Early Jurassic) from astronomical correlation of marine sections. *Gondwana Research* 25, 1348 – 1356.

- Hughes, W.B., Holba, A.G., Dzou, L.I.P., 1995. The ratio of dibenzothiophene to phenanthrene and pristane to phytane as indicator of depositional environment and lithology of petroleum source rocks. *Geochimica et Cosmochimica Acta* 59, 3581 – 3598.
- Hulme, M., Barrow, E.M., Arnell, N.W., Harrison, P.A., John, T.C., Downing, T.E., 1999. Relative impacts of human-induced climate change and natural variability. *Nature* 397, 688 – 691.
- Husmo, T., Hamar, G., Høiland, Johannessen, E.P., Rømuld, A., Spencer, A., Titterton, R., 2002. Lower and Middle Jurassic. In: Evans, D., Graham, C., Armour, A., Bathurst, P. (Eds.), *The Millennium Atlas: petroleum geology of the central and northern North Sea*. The Geological Society, London, pp. 314 – 371.

- I -

- IFP Report, 2002, Estimating the Ultimate Recoverable Reserves of the Paris Basin, France: Oil and Gas Science and Technology – Rev. IFP, v. 57/6, 621-629.
- Ikeda, M., Hori, R.S., 2014. Effects of the Karoo-Ferrar volcanism and astronomical cycles on the Toarcian Oceanic Anoxic Events (Early Jurassic). *Palaeogeography, Palaeoclimatology, Palaeoecology* 410, 134 – 142.
- Immenhauser, A., 2005. High-rate sea-level change during the Mesozoic: New approaches to an old problem. *Sedimentary Geology* 175, 277 – 296.
- Ineson, J.R., Surlyk, F., *The Jurassic of Denmark and Greenland*. The Geological Survey of Denmark and Greenland, 948 pp.
- Irwin, H., Curtis, C., Coleman, M., 1977. Isotopic evidence for source of diagenetic carbonates formed during burial of organic-rich sediments. *Nature* 269, 209 – 213.
- ISO7404-2: 2009 (E). *Methods for the petrographic analysis of coals – part 2: methods of preparing coal samples*.

- J -

- Jarvis, I., Murphy, A.M., Gale, A.S., 2001. Geochemistry of pelagic and hemipelagic carbonates: Criteria for identifying systems tracts and sea-level change. *Journal of the Geological Society of London* 158, 685 – 696.
- Jenkyns, H.C., 1985. The Early Toarcian and Cenomanian-Turonian anoxic events in Europe: comparison and contrasts. *Geologische Rundschau* 74, 505 – 518.
- Jenkyns, H.C., 1988. The Early Toarcian (Jurassic) Anoxic Event – stratigraphic, sedimentary, and geochemical evidence. *American Journal of Science*, 288, 101 – 151.
- Jenkyns, H.C., Clayton, C.J., 1986. Black Shales and carbon isotopes in pelagic sediments from the Tethyan Lower Jurassic. *Sedimentology* 33, 87 – 106.
- Jenkyns, H.C., Clayton, C.J., 1997. Lower Jurassic epicontinental carbonates and mudstones from England and Wales: chemostratigraphic signals and the early Toarcian anoxic event. *Sedimentology* 44, 687 – 706.

- Jenkyns, H.C., Gröcke, D., Hesselbo, S.P., 2001. Nitrogen isotope evidence for water mass denitrification during the early Toarcian oceanic anoxic event. *Paleoceanography* 16, 593 – 603.
- Jenkyns, H.C., Jones, C.E., Gröcke, D.R., Hesselbo, S.P., Parkinson, D.N., 2002. Chemostratigraphy of the Jurassic System: applications, limitations and implications for paleoceanography. *Journal of the Geological Society* 159, 351 – 378.
- Jiménez, A. P., Jiménez de Cisneros, C., Rivas, P., Vera, J.A., 1996. The early Toarcien anoxic event in the westernmost Tethys (Subbetic): Paleogeographic and paleobiogeographic significance. *The Journal of Geology* 104, 399 – 416.
- Jourdan, F., Féraud, G., Bertrand, H., Watkeys, M.K., Renne, P.R., 2007. Distinct brief major events in the Karoo large igneous province clarified by new $^{40}\text{Ar}/^{39}\text{Ar}$ ages on the Lesotho basalts. *Lithos* 98, 195 – 209.
- Jourdan, F., Féraud, G., Bertrand, H., Watkeys, M.K., Renne, P.R., 2008. The $^{40}\text{Ar}/^{39}\text{Ar}$ ages of the sill complex of the Karoo large igneous province: Implications for the Pliensbachian-Toarcian climate change. *Geochemistry Geophysics Geosystems* 9, doi: 10.1029/2008GC001994.

- K -

- Kafousia, N., Karakitsios, V., Jenkyns, H.C., Mattioli, E., 2011. A global event with regional character: the Early Toarcian Oceanic Anoxic Event in the Pindos Ocean (northern Peloponnese, Greece). *Geological Magazine* 0, 1 – 13.
- Kaplan, M.E., 1978. Calcite pseudomorphoses in Jurassic and Lower Cretaceous deposits of the Northern Area of Eastern Siberia. *Geologiya i Geofizika* 19, 62 – 70.
- Kemp, D.B., Izumi, K., 2014. Multiproxy geochemical analysis of a Panthalassic margin record of the early Toarcian oceanic anoxic event (Toyora area, Japan). *Palaeogeography, Palaeoclimatology, Palaeoecology* 414, 332 – 341.
- Kemp, D.B., Coe, A.L., Cohen, A.S., Schwark, L., 2005. Astronomical pacing of methane release in the Early Jurassic period. *Nature* 437, 396 – 399.
- Kemp, D.B., Coe, A.L., Cohen, A.S., Weedon, G.P., 2011. Astronomical forcing and chronology of the early Toarcian (Early Jurassic) Oceanic Anoxic Event in Yorkshire, UK. *Paleoceanography* 26, doi: 10.1029/2011PA002122.
- Killops, S., Killops, V., 2005. *Introduction into Organic Geochemistry*. Blackwell Science, 393 pp.
- Kim, S.T., Mucci, A., Taylor, B.E., 2007. Phosphoric acid fractionation factors for calcite and aragonite between 25 and 75° C: Revisited. *Chemical Geology* 246, 135 – 146.
- Kirtland Turner, S., Sexton, P.F., Charles, C.D., Norris, R.D., 2014. Persistence of carbon release events through the peak of early Eocene global warmth. *Nature Geoscience* 7, 748 – 751.
- Knies, J., Matthissen, J., Vogt, C., Laberg, J.S., Hjelstuen, B.O., Smelror, M., Larsen, E., Andreassen, K., Eidvin, T., Vorren, T.O., 2009. The Plio-Pleistocene glaciation of the Barents Sea–Svalbard region: a new model based on revised chronostratigraphy. *Quaternary Science Reviews* 28, 812 – 829.

- Knyazev, V.G., Devyatov, V.P., Kutugin, R.V., Nikitenko, B.L., Schurygin, B.N., 2003. Zonal Standard of the Toarcian Stage of the North-East Part of Asia. YB of the SD RAS Publishing House, Yakutsk, pp. 103.
- Kodner, R.B., Pearson, A., Summons, R.E., Knoll, A.H., 2008. Sterols in red and green algae: quantification, phylogeny, and relevance for the interpretation of geologic steranes. *Geobiology* 6, 411 – 420.
- Koopmans M. P., Köster J., van Kaam-Peters H. M. E., Kenig F., Schouten S., Hartgers W.A., de Leeuw J. W., Sinninghe Damsté, J.S., 1996. Diagenetic and catagenetic products of isorenieratene: Molecular indicators for photic zone anoxia. *Geochim. Cosmochim. Acta* 60, 4467 – 4496.
- Korte, C., Hesselbo, S.P., 2011. Shallow marine carbon and oxygen isotope and elemental records indicate icehouse-greenhouse cycles during the Early Jurassic. *Paleoceanography* 26, doi: 10.1029/2011PA002160.
- Krencker, F.N., Bodin, S., Hoffmann, R., Suan, G., Mattioli, E., Kabiri, L., Föllmi, K.B., Immenhauser, A., 2014. The middle Toarcian cold snap: Trigger of mass extinction and carbonate factory demise. *Global and Planetary Change* 117, 64 – 78.
- Krencker, F.N., Bodin, S., Suan, G., Heimhofer, U., Kabiri, L., Immenhauser, A., 2015. Toarcian extreme warmth led to tropical cyclone intensification. *Earth and Planetary Science Letters* 425, 12 – 130.
- Kump, L.R., Arthur, M.A., 1999. Interpreting carbon-isotope excursions: carbonates and organic matter. *Chemical Geology* 161, 181 – 198.
- Küspert, W.G., 1982. Environmental changes during oil shale deposition as deduced from stable isotope ratios. In: Einsele, G., Seilacher, A. (Eds.), *Cyclic and Event Stratification* 482–501. Springer, Berlin, Germany. pp. 482 –501.

- L -

- Laepfle, T., Lohmann, G., 2009. Seasonal cycle as template for climate variability on astronomical timescales. *Paleoceanography* 24, doi: 10.1029/2008PA001674.
- Laskar, J., Robutel, P., Joutel, F., Gastineau, M., Correia, A.C.M., Levrard, B., 2004. A long-term numerical solution for the insolation quantities of the Earth. *Astronomy and Astrophysics* 428, 261 – 285.
- Lavastre, V., Ader, M., Buschaert, S., Petit, E., Javoy, M., 2011. Water circulation control on carbonate- $\delta^{18}\text{O}$ records in a low permeability clay formation and surrounding limestones: the Upper Dogger-Oxfordian sequence from the eastern Paris basin, France. *Applied Geochemistry* 26, 818 – 827.
- Lea, D.W., Pak, D.K., Spero, H.J., 2000. Climate impact of late Quaternary equatorial Pacific sea surface temperature variations. *Science* 289, 1719 – 1724.
- Leanza, H.A., Mazzini, A., Corfu, F., Llambías, E.J., Svensen, H., Planke, S., Galland, O., 2013. The Chachil Limestone (Pliensbachian-earliest Toarcian) Neuquén Basin, Argentina: U-Pb age

- calibration and its significance on the Early Jurassic evolution of southwestern Gondana. *Journal of South American Earth Sciences* 42, 171 – 185.
- Lee, R.E., 2008. *Phycology* 4th Edition. Cambridge University Press. Cambridge Books Online.
- Lemna, O.S., Bachtadse, V., Kirscher, U., Rolf, C., Petersen, N., 2015. Paleomagnetism of the Jurassic Transantarctic Mountains revisited — Evidence for large dispersion of apparent polar wander within less than 3 Myr. *Gondwana Research* (in press), doi: 10.1016/j.gr.2015.01.002.
- Léonide, P., Floquet, M., Villir, L., 2007. Interaction of tectonics, eustasy, climate and carbonate production on the sedimentary evolution of an early/middle Jurassic extensional basin (Southern Provence Sub-Basin, SE France). *Basin Research* 19, 125 – 152.
- Léonide, P., Floquet, M., Durllet, C., Baudin, B., Lécuyer, C., 2012. Drowning of a carbonate platform as a precursor stage of the Early Toarcian global anoxic event (southern Provence Sub-Basin; South-east France). *Sedimentology* 59, 156 – 184.
- Leventhal, J.S., 1983. An interpretation of carbon and sulfur relationships in Black Sea sediments as indicators of environments of deposition. *Geochimica et Cosmochimica Acta* 47, 133–138.
- Leventhal, J.S., 1987. Carbon and sulfur relationships in Devonian shales from the Appalachian Basin as an indicator of environment of deposition. *American Journal of Science* 287, 33 – 49.
- Leventhal, J., 1993. Metals in black shales. In: Engel, M.H., Macko, S.A. (Eds.), *Organic Geochemistry: Principles and applications*. Plenum Press, New York, pp. 581 – 592.
- Lézin, C., Rey, J., Cubaynes, R., Péglise, T., 2001. Les événements du passage Lias–Dogger dans le Quercy (France). *Earth and Planetary Sciences* 332, 161 – 168.
- Lézin, C., Andreu, B., Pellenard, P., Bouchez, J.-L., Emmanuel, L., Fauré, P., Landrein, P., 2012. Geochemical disturbance and paleoenvironmental changes during the Early Toarcian in NW Europe. *Chemical Geology* 341, 1 – 15.
- Lorenz, J., Gely, J.P., 1994. Sequence analysis from Lower and Middle Jurassic of the South of Paris Basin well-log correlated to the Couy borehole (Cher, France). *Geobios* 17, 597 – 604.
- Li, M., Larter, S.R., Taylor, P., Jones, D.M., Bowler, B., Malvin, B., 1995. Biomarkers or not biomarkers? A new hypothesis for the origin of pristane involving derivation from methyltrimethyltridecylchromans (MTTCs) formed during diagenesis from chlorophyll and alkylphenols. *Organic Geochemistry* 23, 159 – 167.
- Li, Q., McArthur, J.M., Atkinson, T.C., 2012. Lower Jurassic belemnites as indicators of paleo-temperature. *Palaeogeography, Palaeoclimatology, Palaeoecology* 315 – 316, 38 – 45.
- Li, Q., McArthur, J.M., Doyle, P., Janssen, N., Leng, M.J., Müller, W., Reboulet, S., 2013. Evaluating Mg/Ca in belemnite calcite as a paleo-proxy. *Palaeogeography, Palaeoclimatology, Palaeoecology* 388, 98 – 108.
- Littke, R., Baker, D.R., Leythaeuser, D., 1988. Microscopic and sedimentologic evidence for the generation and migration of hydrocarbons in Toarcian source rocks of different maturities. *Organic Geochemistry* 13, 549 – 559.
- Little, C.T.S., Benton, M.J., 1995. Early Jurassic mass extinction: A global long-term event. *Geology* 23, 495 – 498.

- Little, S.H., Vance, D., Lyons, T.W., McManus, J., 2015. Controls on trace metal authigenic enrichment in reducing sediments: Insights from modern oxygen-deficient settings. *American Journal of Science* 315, 77 – 119.
- Littler, K., Hesselbo, S.P., Jenkyns, H.C., 2010. A carbon-isotope perturbation at the Pliensbachian-Toarcian boundary: evidence from the Lias Group, NE England. *Geological Magazine* 147, 181 – 192.
- Luthardt, C., 2013. Molybdenum Isotopes of Black Shales and the Toarcian Oceanic Anoxic Event. MSc Thesis, Eberhard Karls University Tübingen.

- M -

- Macchioni, F., 2002. Myths and legends in the correlation between the Boreal and Tethyan Realms. Implications on the dating of the Early Toarcian mass extinctions and the Oceanic Anoxic Event. *Geobios* 35, 150 – 163.
- Mackenzie, A. S., Lamb, N. A., Maxwell, J. R., 1982 Steroid hydrocarbons and the thermal history of sediments. *Nature* 295, 223 – 226.
- Macquaker, J. H. S., Howell, J. K. 1999. Small-scale (<5.0 m) vertical heterogeneity in mudstones: implications for high-resolution stratigraphy in siliciclastic mudstone successions. *Journal of the Geological Society* 156, 105 – 112.
- Majorowicz, J., Grasby, S.E., Safanda, J., Beauchamp, B., 2014. Gas hydrate contribution to Late Permian global warming. *Earth and Planetary Science Letters* 393, 243 – 253.
- Mailliot, S., Mattioli, E., Bartolini, A., Baudin, F., Pittet, B., Guex, J., 2009. Late Pliensbachian–Early Toarcian (Early Jurassic) environmental changes in an epicontinental basin of NW Europe (Causses area, central France): A micropaleontological and geochemical approach. *Palaeogeography, Palaeoclimatology, Palaeoecology* 273, 346 – 364.
- Mancenido, M.O., 2002. Paleobiogeography of Mesozoic brachiopod faunas from Andean-Patagonian areas in a global context. *Geobios* 35, 176 - 192.
- Mann, M.E., Lees, J.M., 1996. Robust estimation of background noise and signal detection in climatic time series. *Climate change* 33, 409 – 445.
- Margulis, L., Corliss, J.O., Melkonian, M., Chapman, D.J. (Eds.), 1990. *Handbook of Protoctista: the Structure, Cultivation, Habitats and Life Histories of the Eukaryotic Microorganisms and their Descendants Exclusive of Animals, Plants and Fungi*. Jones & Bartlett Publication, Boston 1012 pp.
- Markwick, P. J., 2007. The palaeogeographic and palaeoclimatic significance of climate proxies for data-model comparisons. In: Williams, M., Haywood, A. M., Gregory, J., Schmidt, D. N. (Eds.), *Deep-Time Perspectives on Climate Change: Marrying the Signal from Computer Models and Biological Proxies*, Geological Society Special Publication, pp. 251 – 312.
- Marzoli, A., Bertrand, H., Knight, K.B., Cirilli, S., Buratti, N., Verati, C., Nomade, S., Renne, P.R., Youbi, N., Martini, R., Allerbach, K., Neuwerth, R., Rapaille, C., Zaninetti, L., Bellieni, G., 2004. Synchrony of the Central Atlantic Magmatic Province and the Triassic-Jurassic boundary climatic and biotic crisis. *Geology* 32, 973 – 976.

- Masclé, A. (Ed.), 1994. Hydrocarbon and petroleum geology of France. EAPG Spec. Publ. 4, 446 pp.
- Mailliot, S., Mattioli, E., Bratolini, A., Baudoin, F., Pittet, B., Guex, J., 2009. Late Pliensbachian–Early Toarcian (Early Jurassic) environmental changes in an epicontinental basin of NW Europe (Causses area, central France): A micropaleontological and geochemical approach. *Palaeogeography, Palaeoclimatology, Palaeoecology* 273, 346–364.
- Mattioli, E., Pittet, B., 2002. Contribution of calcareous nannoplankton to carbonate deposition: a new approach applied to the Lower Jurassic of central Italy. *Marine Micropaleontology* 45, 175 – 190.
- Mattioli, E., Pittet, B., 2004. Spatial and temporal distribution of calcareous nanofossils along a proximal-distal transect in the Umbria–Marche basin (Lower Jurassic, Italy). *Palaeogeography, Palaeoclimatology, Palaeoecology* 205, 295 – 316.
- Mattioli, E., Pittet, B., Suan, G., Mailliot, S., 2008. Calcareous nannoplankton across the Early Toarcian Anoxic Event: implications for paleoceanography within the western Tethys. *Paleoceanography* 23, doi: 10.1029/2007PA001435.
- Mattioli, E., Pittet, B., Petitpierre, L., Mailliot, S., 2009. Dramatic decrease of pelagic carbonate production by nannoplankton across the Early Toarcian Anoxic Event (T-OAE). *Global and Planetary Change* 65, 134 – 145.
- Mazzini, A., Svensen, H., Leanza, H.A., Corfu, F., Planke, S., 2010. Early Jurassic shale chemostratigraphy and U-Pb ages from the Neuquén Basin (Argentina): Implications for the Toarcian Oceanic Anoxic Event. *Earth and Planetary Science Letters* 297, 633 – 645.
- McArthur, J.M., Donovan, D.T., Thirlwall, M.F., Fouke, B.W., Matthey, D., 2000. Strontium isotope profile of the early Toarcian (Jurassic) oceanic anoxic event, the duration of ammonite biozones, and belemnite palaeotemperatures. *Earth and Planetary Science Letters* 179, 269 – 285.
- McArthur, J.M., 2007. Comment on “Carbon isotope record of the Early Jurassic (Toarcian) oceanic anoxic event from fossil wood and marine carbonate (Lusitanian Basin, Portugal)” by Hesselbo S., Jenkyns H. C., Duarte L. V. and Oliveira L. C. V., *Earth and Planetary Science Letters* 259, 634 – 639.
- McArthur, J.M., Wignall, P.B., 2007. Comment on “Non-uniqueness and interpretation of the seawater $^{87}\text{Sr}/^{86}\text{Sr}$ curve” by Dave Waltham and Darren R. Gröcke (*GCA* 70, 2006, 384 – 394). *Geochimica et Cosmochimica Acta* 71, 3382 – 3386.
- McArthur, J. M., Algeo, T.J., van de Schootbrugge, B., Li, Q., Howarth, R.J., 2008a. Basinal restriction, black shales, Re-Os dating, and the Early Toarcian (Jurassic) oceanic anoxic event. *Paleoceanography* 23, PA4217, doi: 10.1029/2008PA001607.
- McArthur, J. M., Cohen, A.S., Coe, A.L., Kemp, D.B., Bailey, R.J., Smith, D.G., 2008b. Discussion on the Late Paleocene – Early Eocene and Toarcian (Early Jurassic) carbon isotope excursions: A comparison of their time scales, associated environmental change, causes and consequences. *Journal of the Geological Society* 164, 1093 – 1108.
- McCann, T., 2008. *The Geology of Central Europe, Volume 2: Mesozoic and Cenozoic*, The Geological Society, London, 1449 pp.

- McElwain, J.C., Wade-Murphy, J., Hesselbo, S.P., 2005. Changes in carbon dioxide during an oceanic anoxic event linked to intrusion into Gondwana coals. *Nature* 435, 479 – 482.
- Mégnién, C., 1981. Synthèse géologique du bassin de Paris. *Mémoire BRGM n°101*, 102, 103.
- Meier, H.E.M., Kjellström, E., Graham, L.P., 2006. Estimating uncertainties of projected Baltic Sea salinity in the late 21st century. *Geophysical Research Letters* 33, L15705.
- Melinte, M.C., 2004. Calcareous nannoplankton, a tool to assign environmental changes. *Geo-Eco-Marina* 9 – 10.
- Mertens, K.N., Bradley, L.R., Takano, Y., Mudie, P.J., Marret, F., Aksu, A.E., Hiscott, R.N., Verleye, T.J., Mousing, E.A., Smyrnova, L.L., Bagheri, S., Mansor, M., Pospelova, V., Matsuoka, K., 2012. Quantitative estimation of Holocene surface salinity variation in the Black Sea using dinoflagellate cyst process length. *Quaternary Science Reviews* 39, 45 – 59.
- Metodiev, L., Koleva-Rekalova, E., 2008. Stable isotope records ($\delta^{18}\text{O}$ and $\delta^{13}\text{C}$) of Lower-Middle Jurassic belemnites from the Western Balkan mountains (Bulgaria): Paleoenvironmental application, *Applied Geochemistry* 23, 2845 – 2856.
- Meyers, P.A., 2003. Applications of organic geochemistry to paleolimnological reconstructions: a summary of examples from the Laurentian Great Lakes, *Organic Geochemistry* 34, 261 – 289.
- Meyers, P.A., Ishiwatari, R., 1993. Lacustrine organic geochemistry – an overview of indicators of organic matter sources and diagenesis in lake sediments. *Organic Geochemistry* 20, 867 – 900.
- Minoletti, F., Hermoso, M., Gressier, V., 2009. Separation of sedimentary micron-sized particles for palaeoceanography and calcareous nannoplankton biogeochemistry. *Nature Protocols* 4, 14 – 24.
- Montero-Serrano, J.C., Föllmi, K.B., Adtte, T., Spangenberg, J.E., Tribovillard, N., Fantasia, A., Suan, G., 2015. Continental weathering and redox conditions during the early Toarcian Oceanic Anoxic Event in the northwestern Tethys: insight from the Posidonia Shale section in the Swiss Jura Mountains. *Palaeogeography, Palaeoclimatology, Palaeoecology* 429, 83 – 99.
- Moretini, E., Bartolini, A. 1999. Stable carbon isotope stratigraphy in the Umbria-Marche and Sabatina realm. *Palaeopelagos Special Publications* 3, 131 – 135.
- Moulin, M., 2012. The “van Zijl” Jurassic geomagnetic reversal revisited. *Geochemistry, Geophysics, Geosystems* 13, doi: 10.1029/2011GC003910.
- Moulin, M., Fluteau, F., Courtillot, V., Marsh, J., Delpech, G., Quidelleur, X., Gérard, M., Jay, A.E., 2011. An attempt to constrain the age, duration, and eruptive history of the Karoo flood basalt: Naude’s Nek section (South Africa). *Journal of Geophysical Research* 116, doi: 10.1029/2011JB008210.
- Mundil, R., Renne, P.R., Min, K.K., Ludwig, K.R., 2006. Resolvable miscalibration of the $^{40}\text{Ar}/^{39}\text{Ar}$ geochronometer. *Eos Trans. AGU*, 87(52), Fall Meet. Suppl., Abstract V21A-0543.
- Mussard, M., Le Hir, G., Fluteau, F., Lefebvre, V., Goddérès, Y., 2014. Modeling carbon-sulfur interplays in climate changes related to the emplacement of continental flood basalts. In: Keller, G., Kerr, C. (Eds.), *Volcanism, impacts and mass extinctions: causes and effects*. The Geological Society of America, Special Publications 505, pp. 339 – 352.

- Nägler, T.F., Siebert, C., Lüschen, H., Böttcher, M.E., 2005. Sedimentary Mo isotope record across the Holocene fresh-brackish water transition of the Black Sea. *Chemical Geology* 219, 283 – 295.
- Nesbitt, H.W., Young, G.M., 1982. Early Proterozoic climates and plate motions inferred from major element chemistry of latitudes. *Nature* 299, 715 – 717.
- Newton, R.J., Reeves, E.P., Kafousia, N., Wignall, P.B., Bottrell, S.H., Sha, J.G., 2011. Low marine sulfate concentrations and the isolation of the European epicontinental sea during the Early Jurassic. *Geology* 39, 7 – 10.
- Nittrouer, C.A., 1981. Sedimentary dynamics of continental shelves. *Developments in Sedimentology* 32, 449 pp.
- Nikitenko, B., Shurygin, B., Mickey, M., 2008. High resolution stratigraphy of the Lower Jurassic and Aalenian of Arctic regions as the basis of detailed paleobiogeographic reconstructions. *Norwegian Journal of Geology* 88, 267 – 277.
- Nøttvedt, A., Johannessen, E., Surlyk, F., 2008. The Mesozoic of western Scandinavia and eastern Greenland. *Episodes* 31, 1 – 7.

- O -

- Ogg, J.G., Hinnov, L.A., 2012. Jurassic. In: Gradstein, F.M., Ogg, J.G., Schmitz, M.D., Ogg, G.M. (Eds.), *The Geological Timescale 2012*. Elsevier, pp. 731 – 792.
- Oschmann, W., 1991. Anaerobic – poikiloaerobic – aerobic: a new facies zonation for modern and ancient neritic redox facies. In: Einsele, G., Ricken, W., Seilacher, A. (Eds.), *Cycles and Events in Stratigraphy*. Springer, Berlin, pp. 565 – 571.

- P -

- Page, K.N., 2003. The Lower Jurassic of Europe: its subdivision and correlation. *Geological Survey of Denmark and Greenland Bulletin* 1, 23 – 59.
- Page, K.N., 2008. The evolution and geography of Jurassic ammonites. *Proceedings of the Geologists Association* 119, 35 – 57.
- Palfy, J., 2008. The quest for refined calibration of the Jurassic timescale. *Proceedings of the Geologists Association* 119, 85 – 95.
- Palfy, J., Smith, P.L., 2000. Synchrony between Early Jurassic extinction, oceanic anoxic event, and the Karoo-Ferrar flood basalt volcanism. *Geology* 28, 747 – 750.
- Pálfy, J., Smith, P.L., Mortensen, J.K., 2000. A U–Pb and $^{40}\text{Ar}/^{39}\text{Ar}$ time scale for the Jurassic. *Canadian Journal of Earth Science* 37, 923 – 944.
- Pálfy, J., Smith, P.L., Mortensen, J.K., 2002. Dating the end-Triassic and Early Jurassic mass extinctions, correlative large igneous provinces, and isotopic events, In: Koeberl, C., MacLeod, K.G. (Eds.), *Catastrophic Events and Mass Extinctions: Impacts and Beyond*. Geological Society of America Special Paper 356, 523 – 532.
- Parrish, J.T., Ziegler, A.M., Scortese, C.R., 1982. Rainfall patterns and the distribution of coals and evaporites in the Mesozoic and Cenozoic. *Palaeogeography, Palaeoclimatology, Palaeoecology* 40, 67 – 101.

- Patterson, M.O., McKay, R., Naish, T., Escutia, C., Jimenez-Espejo, F.J., Raymo, M.E., Meyers, S.R., Tauxe, L., Brinkhuis, H., and IODP Expedition 318 Scientists, 2014. Orbital forcing of the East Antarctic ice sheet during the Pliocene and Early Pleistocene. *Nature Geoscience* 7, 841 – 847.
- Pearce, C.R., Cohen, A.S., Coe, A.L., Burton, K.W., 2008. Molybdenum isotope evidence for global ocean anoxia coupled with perturbations to the carbon cycle during the Early Jurassic. *Geology* 36, 231 – 234.
- Pellenard, P., Deconinck, J.-F., 2006. Mineralogical variability of Callovo–Oxfordian clays from the Paris Basin and the Subalpine Basin. *Comptes Rendus Geoscience* 338, 854 – 866.
- Perrodon, A., Zabbeck, J., 1990. Paris Basin. In: Leighton, M.W., Kolata, D.F., Oltz, J., Eidl, J., (Eds.), *Interior cratonic basins*. American Association of Petroleum Geologists Memoir 51, 633 – 679.
- Peters, S.E., 2008. Environmental determinants of extinction selectivity in the fossil record. *Nature*, 454, 626 – 630.
- Peters, K.E., Walters, C.C., Moldowan, J.M., 2005. *The Biomarker Guide: Volume 2, Biomarkers and Isotopes in Petroleum Systems and Earth History*. Cambridge University Press, 1132 pp.
- Pienkowski, G., Schudack, M.E., Bosak, P., Enay, R., Feldmann-Olszewska, A., Golonka, J., Gutowski, J., Hengreen, G.F.W., Jordan, P., Krobicki, M., Lathuiliere, B., Leinfelder, R.R., Michalik, J., Mönning, E., Noe-Nygaard, N., Palfy, J., Pint, A., Rasser, M.W., Reisdorf, A.G., Schmidt, D.U., Schweigert, G., Surlyk, F., Wetzel, A., Wong, T.E., 2008. Jurassic. In: McCann, T. (Ed.), *The Geology of Central Europe*. The Geological Society, pp. 823 – 923.
- Pitman, W.C., and Golovchenko, X., 1983. The effect of sea-level change on the shelf edge and slope of passive margins. *Society of Economic Paleontology and Mineralogy (SEPM) Special publication* 33, 41– 58.
- Pittet, B., Suan, G., Lenoir, F., Duarte, L.V., Mattioli, E., 2014. Carbon isotope evidence for sedimentary discontinuities in the lower Toarcian of the Lusitanian Vasin (Portugal): Sea-Level change at the onset of the Oceanic Anoxic Event. *Sedimentary Geology* 303, 1 – 14.
- Ponsot, C.M., 1994. Sequence stratigraphy of the Jurassic Series of the Paris-London Basin. In: Mascle (Ed.), *Hydrocarbon and Petroleum Geology of France*. Springer, pp. 77 – 105.
- Poulson, R.L., Siebert, C., McManus, J., Berelson, W.M., 2006. Authigenic molybdenum isotope signatures in marine sediments. *Geology* 34, 617 – 620.
- Poulson Brucker, R.L., McManus, J., Severmann, S., Berelson, W.M., 2009. Molybdenum behavior during early diagenesis: Insights from Mo isotopes. *Geochemistry, Geophysics, Geosystems* 10, Q01010, doi: 10.1029/2008GC002180.
- Powell, T.G., McKirdy, D.M., 1973. Relationship between Ratio of Pristane to Phytane, Crude Oil Composition and Geological Environment in Australia. *Nature* 243, 37 – 39.
- Powell, J.H., 2010. Jurassic sedimentation in the Cleveland Basin: a review. *Proceedings of the Geological Society* 58, 21 – 72.
- Price, G.D., 1999. The evidence and implications of polar ice during the Mesozoic. *Earth-Science Reviews* 48, 183 – 210.

- Price, G.D. 2010. Carbon-isotope stratigraphy and temperature change during the Early-Middle Jurassic (Toarcian-Aalenian), Raasay, Scotland, UK. *Palaeogeography, Palaeoclimatology, Palaeoecology* 285, 255 – 263.
- Proemse, B.C., Grasby, S.E., Wieser, M.E., Mayer, B., Beauchamp, B., 2013. Molybdenum isotopic evidence for oxic marine conditions during the latest Permian extinction. *Geology*, G34466.1, doi: 10.1130/G34466.1.
- R -
- Raiswell, R., Berner, R.A., 1985. Pyrite formation in euxinic and semi-euxinic sediments. *American Journal of Science* 285, 710 – 724.
- Raiswell, R., Bottrell, S.H., Al-Biatty, H.J., Tan, M.M.D., 1993. The influence of bottom water oxygenation and reactive iron content on sulfur incorporation into bitumens from Jurassic marine shales. *American Journal of Science* 293, 569 – 596.
- Rees, P.M., Ziegler, A.M., Valdes, P.J., 2000. Jurassic phytogeography and climates: new data and model comparisons. In: Huber, B.T., Macleod, K.G., Wing, S.L. (Eds.), *Warm climates in Earth history*. Cambridge University Press, pp. 297 – 318.
- Reisdorf, A., 2001. Mind the Gaps: Evidence for Early Toarcian regression and tectonic activity in N-Switzerland. 2nd EUCOR-URGENT WORKSHOP 2001, Mont Saint-Odile, Strasbourg, France, 7-11 Octobre 2001.
- Reisdorf, A., Wetzel, A., Schlatter, R., Jordan, P., 2011. The Staffelegg Formation: a new stratigraphic scheme for the Early Jurassic of northern Switzerland. *Swiss journal of Geoscience* 104, 97 – 146.
- Rey, J., Cubaynes, R., 1991. Séquences lithoclinales et sequences genetiques de depot dans le Lias moyendu Basin aquitaine. *Comptes rendus de l'Académie des Science* 312, 1447 – 1463.
- Rhoads, D.C., Morse, J.W., 1971. Evolutionary and ecologic significance of oxygen-deficient marine basins. *Lethaia* 4, 413 – 428.
- Rhoads, D.C., Mulslow, S.G., Gutschik, R., Baldwin, C.T., Stolz, J.F., 1991. The dysaerobic zone revisited: a magnetic facies? In: Tyson, R.V., Pearson, T.H. (Eds.), *Modern and Ancient Continental Shelf Anoxia*. Special Publications of the Geological Society of London, vol. 58, pp. 187 – 199.
- Richter, B.E., Jones, B.A., Ezzell, J.L., Porter, N.L., Avdalovic, N., Pohl, C., 1996. Accelerated Solvent Extraction: A Technique for Sample Preparation. – *Analytical Geochemistry* 68, 1033 – 1039.
- Rickaby, R.E.M., et al., 2006. Potential of ikaite to record the evolution of oceanic $\delta^{18}\text{O}$. *Geological Society of America* 34, 497 – 500.
- Rickard, D., 2012. Sulfidic sediments and sedimentary rocks. *Developments in Sedimentology* 65, 801 pp.
- Riegraf, W., 1985. Mikrofauna, Biostratigraphie und Fazies im Unteren Toarcium Südwestdeutschlands und Vergleiche mit benachbarten Gebieten. *Tübinger Mikropaläontologische Mitteilungen* 3, 232 pp.

- Riley, T.R., Knight, K.B., 2001. Age of pre-break-up Gondwana magmatism. *American Science* 13, 99 – 110.
- Riley, T.R., Millar, I.L., Watkeys, M.K., Curtis, M.L., Leat, P.T., Klausen, M.B., Fanning, C.M., 2004. U-Pb zircon (SHRIMP) ages for the Lebombo rhyolites, South Africa: refining the duration of Karoo volcanism. *Journal of the Geological Society* 161, 547 – 550.
- Riley T.R., Curtis, M.L., Leat, P.T., Watkeys, M.K., Duncan, R.A., Millar, I.L., Owens, W.H., 2006. Overlap of Karoo and Ferrar Magma Types in Kwa Zulu-Natal, South Africa. *Journal of Petrology* 47, 541 – 566.
- Robinson, N., Eglinton, G., Brassel, S.C., Cranwell, P.A., Dinoflagellate origin for sedimentary 4 α -methylsteroids and 5 α (H)-stanols. *Nature* 308, 439 – 442.
- Robock, A., 2000. Volcanic eruptions and climate. *Review of Geophysics* 38, 191 – 219.
- Röhl, H.J., Schmid-Röhl, A., 2005. Lower Toarcian (Upper Liassic) black shales of the Central European Epicontinental Basin: a sequence stratigraphic case study from the SW German Posidonia Shale. *SEPM Special Publications* 82, 165 – 189.
- Röhl, H.J., Schmidt-Röhl, A., Oschmann, W., Frimmel, A., Schwark, L., 2001. The Posidonia Shale (Lower Toarcian) of SW-Germany: an oxygen-depleted ecosystem controlled by sea level and palaeoclimate. *Palaeogeography, Palaeoclimatology, Palaeoecology* 165, 27 – 52.
- Rosales, I., Quesada, S., Robles, S., 2004. Paleotemperature variations of Early Jurassic seawater recorded in geochemical trends of belemnites from the Basque-Cantabrian basin, northern Spain. *Palaeogeography, Palaeoclimatology, Palaeoecology* 203, 253 – 275.
- Rosenbaum, J., Sheppard, S.M., 1986, An isotopic study of siderites, dolomites and ankerites at high temperatures.- *Geochimica et Cosmochimica Acta*, 50, 1147 – 1150.
- Rowland, S.J., 1990. Production of acyclic isoprenoid hydrocarbons by laboratory maturation of methanogenic bacteria. *Organic Geochemistry* 15, 9 – 16.
- Ruddiman, W.F., 2006. Orbital changes and climate. *Quaternary Science Reviews* 25, 3092 – 3112.
- Ruebsam, W., 2010. Organic facies development during the Toarcian Ocean Anoxic Event in Luxembourg. Diploma Thesis, University of Cologne.
- Ruebsam, W., Münzberger, P., Schwark, L., 2014. Chronology of the Early Toarcian environmental crisis in the Lorraine Sub-Basin (NE Paris Basin). *Earth and Planetary Science Letters* 404, 273 – 282.
- Ruebsam, W., Münzberger, P., Schwark, L., 2015. Reply to the comment by Boulila and Hinnov towards “Chronology of the Early Toarcian environmental crisis in the Lorraine Sub-Basin (NE Paris Basin)” by W. Ruebsam, P. Münzberger, and L. Schwark [*Earth and Planetary Science Letters* 404 (2014) 273–282]. *Earth and Planetary Science Letters* 416, 147 – 150.

- S -

- Sabatino, N., Neri, R., Bellanca, A., Jenkyns, H.C., Baudin, F., Parisi, G., Masetti, D., 2009. Carbon-isotope records of the Early Jurassic (Toarcian) oceanic anoxic event from the Valdorbia (Umbria-Marche Apennines) and Monte Mangart (Julian Alps) sections: paleoceanographic and stratigraphic implications. *Sedimentology* 56, 1307 – 1328.

- Sabatino, N., Vlahovic, I., Jenkyns, H.C., Scopelliti, G., Neri, R., Prtoljan, B., Velic, I., 2013. Carbon-isotope record and palaeoenvironmental changes during the early Toarcian oceanic anoxic event in shallow-marine carbonates of the Adriatic Carbonate Platform in Croatia. *Geological Magazine* 150, 1085 – 1102.
- Saelen, G., Doyle, P., Talbot, M.R., 1996. Stable-isotope analyses of belemnite rostra from the Whitby Mudstone Fm, England: surfacewater conditions during deposition of a marine black shale. *Palaios* 11, 97–117.
- Sahagian D, Pinous O, Olfieriev A, Zakharov V., 1996. Eustatic curve for the Middle Jurassic–Cretaceous based on Russian platform and Siberian stratigraphy: zonal resolution. *AAPG Bulletin* 80, 1433 – 1458.
- Schlische, R.W., Withjack, M.O., Olsen, P.E., 2003. Relative timing of CAMP, rifting, continental breakup, and basin invasion: tectonic significance. In: Hames, W.E., McHone, J.G., Renne, P.R., Ruppel, C. (Eds.), *The Central Atlantic Magmatic Province: Insights from fragments of Pangaea*. American Geophysical Union Geophysical Monograph 136, pp. 33 – 59.
- Schmidt-Röhl, A., Röhl, H.J., Oschmann, W., Frimmel, A., Schwark, L., 2002. Paleoenvironmental reconstruction of Lower Toarcian black shales (Posidonia shale, SW Germany): Global versus regional control. *Geobios* 35, 13 – 20.
- Scholz, F., McManus, J., Sommer, S., 2013. The manganese and iron shuttle in a modern euxinic basin and implications for molybdenum cycling at euxinic ocean margins. *Chemical Geology* 355, 56 – 68.
- Schouten, S., van de Kaam-Peters, H.M.E., Rijpstra, W.I.C., Schoell, M., Sinninghe Damste, J.S., 2000. Effects of an oceanic anoxic event on the stable carbon isotope composition of Early Toarcian carbon. *American Journal of Science* 300, 1 – 22.
- Schuur, E.A.G., McGuire, A.D., Schädel, C., Grosse, G., Harden, J.W., Hayes, D.J., Hugelius, G., Koven, C.D., Kuhry, P., Lawrence, D.M., Natali, S.M., Olefeldt, D., Romanovsky, V.E., Schaefer, K., Turetsky, M.R., Treat, C.C., Vonk, J.E., 2015. Climate change and the permafrost carbon feedback. *Nature* 520, 171 – 179.
- Schwark, L., Püttmann, W., 1990. Aromatic hydrocarbon composition of the Permian Kupferschiefer in the Lower Rhine Basin, NW Germany. *Organic Geochemistry* 16, 749 – 761.
- Schwark, L., Frimmel, A., 2004. Chemostratigraphy of the Posidonia Black Shale, SW-Germany II. Assessment of extent and persistence of photic-zone anoxia using aryl isoprenoid distributions. *Chemical Geology* 206, 231 – 248.
- Schwark, L., Empt, P., 2006. Sterane biomarkers as indicators of palaeozoic algal evolution and extinction events. *Palaeogeography, Palaeoclimatology, Palaeoecology* 240, 225 – 236.
- Schwark, L., Vliex, M., Schaeffer, P., 1998. Geochemical characterization of Malm Zeta laminated carbonates from the Franconian Alb, SW-Germany (II). *Organic Geochemistry* 29, 1921 – 1952.
- Scott, R.A., and Turton, M.A.K., 2001. Mesozoic tectonic events in the North Atlantic and Arctic: Stratigraphic response in an adjacent rift-flank basin (Sverdrup Basin, Arctic Canada). *Polarforschung* 69, 73 – 83.

- Scortese, C., 2014. Atlas of Jurassic Paleogeographic Maps, PALEOMAP Atlas for ArcGis, Volume 4, The Jurassic and Triassic, Maps 32 – 42, Mollwide Projection, PALEOMAP Project, Evanston.
- Self, S., Schmidt, A., Mather, T.A., 2014. Emplacement characteristics, time scales and volcanic gas release rates of continental flood basalt eruptions on Earth. In: Keller, G., Kerr, C. (Eds.), *Volcanism, impacts and mass extinctions: causes and effects*. The Geological Society of America, Special Publications 505, pp. 319 – 338.
- Sell, B., Ovtcharova, M., Guex, J., Bartolini, A., Jourdan, F., Spangenberg, J.E., Vicente, J.C., Schaltegger, U., 2014. Evaluating the temporal link between the Karoo LIP and climatic-biotic events of the Toarcian stage with high precession U-Pb geochronology. *Earth and Planetary Science Letters* 408, 48 – 56.
- Shannon, P.M., Haugthon, P.D.W., Corcoran, D.V., 2001. The petroleum exploration of Ireland's Offshore Basin. Geological Society Special Publications 188, 410 pp.
- Siebert, C., Nägler, T.F., and Kramers, J.D., 2001, Determination of molybdenum isotope fractionation by double- spike multicollector inductively coupled plasma mass spectrometry. *Geochemistry Geophysics Geosystems* 2, doi: 10.1029/2000GC000124.
- Siebert, C., Nägler, T.F., von Blanckenburg, F., Kramers, J.D., 2003. Molybdenum isotope records as a potential new proxy for paleoceanography. *Earth and Planetary Science Letters* 211, 159 – 171.
- Silva, R.L., Duarte, L.V., 2015. Organic matter production and preservation in the Lusitanian Basin (Portugal) and Pliensbachian climate hot snaps. *Global and Planetary Change* 131, 24 – 34.
- Simms, M.J., 2004. British Lower Jurassic stratigraphy: an introduction. In: Simms, M.J., Chidlaw, N., Morton, N., Page, K.N. (Eds.), *British Lower Jurassic Stratigraphy*. Geological Conservation Review Series 30, Joint Nature Conservation Committee, Peterborough, pp. 1 – 25.
- Sinninghe Damsté, J.S., Schouten, S., 2006. Biological markers for anoxia in the photic zone of the water column. In: Volkman, J.K., (Ed.), *Marine Organic Matter: Biomarkers, Isotopes and DNA*. Springer, pp. 127 – 163.
- Sinninghe Damsté, J.S., Keely, B.J., Betts, S.E., Baas, M., Maxwell, J.R., de Leeuw, J.W., 1993. Variations in abundances and distributions of isoprenoid chromans and long-chain alkylbenzenes in sediments of the Mulhouse Basin: a molecular sedimentary record of palaeosalinity. *Organic Geochemistry* 20, 1201 – 1215.
- Sinninghe Damsté, J.S., Van Duin, A.C.T., Hollander, D., Kohnen, M.E.L., De Leeuw, J.W., 1995. Early diagenesis of bacteriohopanepolyol derivatives: Formation of fossil homohopanoids. *Geochimica et Cosmochimica Acta* 59, 5141 – 5155.
- Smith, A.G., Smith, D.G., Funnel, B.M., 1994. *Atlas of Mesozoic and Cenozoic coastlines*. Cambridge University Press, 99 pp.
- Song, J., Littke, R., Maquil, R., Weniger, P., 2014. Organic facies variability in the Posidonia Black Shale from Luxembourg: Implications for thermal maturation and depositional environment. *Palaeogeography, Palaeoclimatology, Palaeoecology* 410, 316 – 336.

- Steinthorsdottir, M., Vajda, V., 2013. Early Jurassic (late Pliensbachian) CO₂ concentrations based on stomatal analysis of fossil conifer leaves from eastern Australia. *Gondwana Research* 27, 932 – 939.
- Stoll, H.M., Schrag, D.P., 2001. Sr/Ca variations in Cretaceous carbonates: relation to productivity and sea level changes. *Palaeogeography, Palaeoclimatology, Palaeoecology* 168, 311 – 336.
- Strasser, A., Hillgärtner, H., Hug, W., Pittet, B., 2000. Third-order depositional sequences reflecting Milankovitch cyclicity. *Terra Nova* 12, 303 – 311.
- Suan, G., Pittet, B., Bour, I., Mattioli, E., Duarte, L.V., Mailliot, S., 2008a. Duration of the Early Toarcian carbon isotope excursion deduced from spectral analysis: consequence for its possible causes. *Earth and Planetary Science Letters* 267, 666 – 679.
- Suan, G., Mattioli, E., Pittet, B., Mailliot, S., Lécuyer, C., 2008b. Evidence for major environmental perturbation prior to and during the Toarcian (Early Jurassic) oceanic anoxic event from the Lusitanian Basin, Portugal. *Paleoceanography* 23, doi: 10.1029/2007/PA001459.
- Suan, G., Mattioli, E., Pittet, B., Lécuyer, C., Suchéras-Marx, B., Duarte, L.V., Philippe, M., Geggiani, L., Martineu, F., 2010. Secular environmental precursors to the Early Toarcian (Jurassic) extreme climate changes. *Earth and Planetary Science Letters* 290, 448 – 458.
- Suan, G., Nikitenko, B.L., Rogov, M.A., Baudin, F., Jorge E. Spangenberg, J.E., Knyazev, V.G., Glinskikh, L.A., Goryacheva, A.A., Adatte, T., Riding, J.B., Föllmi, K.B., Pittet, B., Mattioli, E., Lécuyer, C., 2011a. Polar record of Early Jurassic massive carbon injection. *Earth and Planetary Science Letters* 312, 102 – 113.
- Suan, G., Oschmann, W., Fiebig, J., van de Schootbrugge, B., 2011b. New astronomical timescale for the Toarcian carbon isotope excursions from Dotternhausen, SW Germany. *Geophysical Research Abstracts* 13, EGU2011-11894.
- Suan, G., Brazier, J.M., Nikitenko, B.L., Simon, L., 2013a. Evidence for continental and sea ice in Siberian Arctic during the Pliensbachian-Toarcian (Early Jurassic). *Strata* 2013, series 1, vol. 14. Pre-Cenozoic climates Workshop.
- Suan, G., Rulleau, L., Mattioli, E., Suchéras-Marx, B., Rousselle, B., Pittet, B., Vincent, P., Martin, J.E., Léna, A., Spangenberg, J.E., Föllmi, K.B., 2013b. Palaeoenvironmental significance of Toarcian black shales and event deposits from southern Beaujolais. *Geological Magazine* 150, 728 – 742.
- Suan, G., van de Schootbrugge, B., Adatte, T., Fiebig, J., Oschmann, W., 2015. Calibrating the magnitude of the Toarcian Carbon cycle perturbation. *Paleoceanography* 30. doi: 10.1002/2014PA002758.
- Summons, R.E., Volkman, J.K., Boreham, C.J., 1987. Dinosterane and other steroidal hydrocarbons of dinoflagellate origin in sediments and petroleum. *Geochimica et Cosmochimica Acta* 51, 3075 – 3082.
- Summons, R.E., Jahnke, L.L., Hope, J.M., Logan, G.A., 1999. 2-Methylhopanoids as biomarkers for cyanobacterial oxygenic photosynthesis. *Nature* 400, 554 – 557.

- Sundararaman, P., Schoell, M., Littke, R., Baker, D.R., Leythaeuser, D., Rullkötter, J., 1993. Depositional environment of Toarcian shales from northern Germany as monitored with porphyrins. *Geochimica et Cosmochimica Acta* 57, 4213 – 4218.
- Surlyk, F., 1991. Sequence stratigraphy of the Jurassic lowermost Cretaceous of East Greenland. *Aapg Bulletin-American Association of Petroleum Geologists*, 75, 1468 – 1488.
- Svensen, H., Planke, S., Chevallier, L., Malthe-Sørensen, A., Corfu, F., Jamtveit, B., 2007. Hydrothermal venting of greenhouse gasses triggering Early Jurassic global warming. *Earth and Planetary Science Letters* 256, 554 – 566.
- Svensen, H., Corfu, F., Polteau, S., Hammer, O., Planke, S. 2012. Rapid magma emplacement in the Karoo Large Igneous Province. *Earth and Planetary Science Letters* 325, 1 – 9.

- T -

- Taylor, D.G., Callomon, J.H., Hall, R., Smith, P.L., Tipper, H.W., Westermann, G.E.G., 1984. Jurassic Cretaceous ammonite biogeography of western North America: the tectonic implications. In: Westermann, G.E.G. (Ed.), *Jurassic Cretaceous biochronology and paleogeography of North America*. I.G.C.P. Project 171, Geol. Assoc. Canada Spec. Paper, pp. 121 – 141.
- Tchoumatchenco, P., Philippe, M., Yaneva, M., 2008. Did glaciation occurred during the Toarcian (Early Jurassic) in the east Strata Planina Mts. (East Bulgaria)? *Comptes rendus de l'Académie bulgare des Sciences* 61, 1301 – 1308.
- Teichert, B.M.A., Luppold, F.W., 2012. Glendonites from an Early Jurassic methane seep – Climate or methane indicators? *Palaeogeography, Palaeoclimatology, Palaeoecology* 390, 81 – 93.
- Tessin, R., 2010. Lias – Mächtigkeit und Lithofazies. In: Freytag, K., Stackebrand, W. (Eds.), *Atlas zur Geologie von Brandenburg*, 4. aktualisierte Auflage 2010.
- Thierry, J., 2000. Middle Toarcian. In: Dercourt, J., Geatini, M., Vrielynck, B., Barrier, E., Biju-Duval, B., Brunet, M.F., Cadet, J.P., Crasquin, S., Sandulescu, M. (Eds.), *Atlas Peri-tethys, Paleogeographical Maps*. Map. 8, pp. 61 – 70.
- Thomson, D.J., 1982. Spectrum estimation and harmonic analysis. *Proceedings of the IEEE* 70, 1055 – 1096.
- Trabucho-Alexandre, J., 2014. More gaps than shale: erosion of mud and its effect on preserved geochemical and palaeobiological signals. In: Smith, D. G., Bailey, R. J., Burgess, P.M., Fraser, A. J. (Eds.), *Strata and Time: Probing the Gaps in Our Understanding*. Geological Society, London, Special Publications 404, 251 – 270.
- Trabucho-Alexandre, J., Dirkx, R., Veld, H., Klaver, G., de Boer, P.L., 2012. Toarcian black shales in the Dutch Central Graben: record of energetic, variable depositional conditions during an Oceanic Anoxic Event. *Journal of Sedimentary Research* 82, 104 – 120.
- Trecalli, A., Spangenberg, J., Adette, T., Föllmi, K.B., Parente, M., 2012. Carbonate platform evidence of ocean acidification at the onset of the early Toarcian oceanic anoxic event. *Earth and Planetary Science Letters* 357 – 358, 214 – 225.
- Tremolada, F., van de Schootbrugge, B., Erba, E., 2005. Early Jurassic schizosphaerellid crisis in

- Cantabria, Spain: implications for calcification rates and phytoplankton evolution across the Toarcian oceanic anoxic event. *Paleoceanography* 20, doi: 10.1029/2004PA001120.
- Trenberth, K.E., Fasullo, J.T., Shepherd, T.G., 2015. Attribution of climate extreme events. *Nature Climate Change*. doi: 10.1038/nclimate2657.
- Tribovillard, N., Algeo, T.J., Lyons, T., Riboulleau, A., 2006 Trace metals as paleoredox and paleoproductivity proxies: An update. *Chemical Geology* 232, 12 – 32.
- Tulipani, S., Grice, K., Greenwood, P.F., Schwark, L., 2013. A pyrolysis and stable isotopic approach to investigate the origin of methyltrimethyltridecylchromans (MTTCs). *Organic Geochemistry* 61, 1 – 5.
- Tulipani, S., Grice, K., Greenwood, P.F. Schwark, L., Bötcher, M.E., Summons, R.E., Foster, C.B., 2015. Molecular proxies as indicators of freshwater incursion-driven salinity stratification. *Chemical Geology* 409, 61 – 68.
- Tyson, R.V., 1995. *Sedimentary Organic Matter*. Chapman & Hall. 615 pp.
- Tyson, R.V., Pearson, T.H., 1991. Modern and ancient continental shelf anoxia: an overview. In: Tyson, R.V., Pearson, T.H. (Eds.), *Modern and Ancient Continental Shelf Anoxia*. Geological Society, London, Special Publications 58, 1 – 26.

- U -

- Ullmann, C.V., Thibault, N., Ruhl, M., Hesselbo, S.P., Korte, C., 2014. Effect of a Jurassic oceanic anoxic event on belemnite ecology and evolution. *PNAS* 111, 10073 – 10076.
- Underhill, J.R., Stoneley, R., 1998. Introduction into the development, evolution and petroleum geology of the Wessex Basin. *Geological Society London Special Publications* 133, 1 – 18.

- V -

- Vail, P.R., Audemart, F., Bowman, S.A., Eisner, P.N., 1991. The stratigraphic signatures of tectonics, eustasy and sedimentology – an overview. In: Einsele, G., Ricken, W., Seilacher, A. (Eds.), *Cycles and Events in stratigraphy*. Springer, pp. 617 – 659.
- Vajda, V., Wigforss-Lange, J., 2009. Onshore Jurassic of Scandinavia and related areas. *GFF* 131, 5 – 23.
- Vakhrameev, V.A., 1991. *Jurassic and Cretaceous floras and climates of the Earth*. Cambridge University Press, 318 pp.
- van Breugel, Y., Bass, M., Schouten, S., Mattioli, E., Sinninghe Damste, J.S., 2006. isorenieratane record in black shales from the Paris Basin, France: Constraints on recycling of respired CO₂ as a mechanism for negative carbon isotope shifts during the Toarcian oceanic anoxic event. *Paleoceanography* 21, doi: 10.1029/2006PA001305.
- van de Schootbrugge, Bailey, B., Rosenthal, T., Katz, Y., Wright, M., Feist-Burkhardt, J.D., Miller, S., 2005a. Early Jurassic climate change and the radiation of organic-walled phytoplankton in the Tethys Ocean. *Paleobiology* 31, 73 – 97.

- van de Schootbrugge, B., McArthur, J.M., Bailey, T.R., Rosenthal, Y., Wright, J.D., Miller, K.G., 2005b. Toarcian Oceanic Anoxic Event: An assessment of global causes using belemnite C isotope records. *Paleoceanography* 20, doi: 10.1029/2004PA001102.
- Van de Schootbrugge, B., Bachan, A., Suan, G., Richoz, S.R., Payne, J.L., 2013. Microbes, mud and methane: cause and consequence of reoccurrent Early Jurassic anoxia following the End-Triassic mass extinction. *Paleontology* 56, 1 – 25.
- Vaughan, A.P.M., 2007. Climate and Geology – a Phanerozoic perspective. In: Williams, M., Haywood, A.M., Gregory, F.J., Schmidt, D.N. (Eds.), *Deep-Time perspectives on climate change: Marrying the signal from computer models and biological proxies*. The Geological Society, London, pp. 5 – 59.
- Vaughan, S., Bailey, R.J., Smith, D.G., 2014. Cyclostratigraphy: data filtering as a source of spurious spectral peaks. In: Smith, D. G., Bailey, R. J., Burgess, P.M., Fraser, A. J. (Eds.), *Strata and Time: Probing the Gaps in Our Understanding*. Geological Society, London, Special Publications, 404, 151 – 156.
- Vincent, B., Rambeau, C., Emmanuel, L., Loreau, J.P., 2006. Sedimentology and trace element geochemistry of shallow-marine carbonates: an approach to paleoenvironmental analysis along the Pagny-sur-Meuse Section (Upper Jurassic, France). *Facies* 52, 69 – 84.
- Volkman, J.K., 2003. Sterols in microorganisms. *Applied Microbiology and Biotechnology* 60, 495 – 506.
- Volkman, J.K., 2006. *Marine Organic Matter: Biomarkers, Isotopes and DNA*. Springer, 374 pp.
- Volkman, J.K., Kearney, P., Jeffrey, S.W., 1990. New source of 4-methyl sterols and 5 α (H)-stanols in sediments: prymnesiophyte microalgae of the genus *Pavlova*. *Organic Geochemistry* 15, 489 – 497.
- Volkman, J.K., Barrett, S.M., Blackburn, S.I., Mansour, M.P., Sikes, E.L., Gelin, F., 1998. Microalgal biomarkers: A review of recent research developments. *Organic Geochemistry* 29, 1163 – 1179.
- von Eynatten, H., Barcelo-Vidal, C., Pawlowsky-Glahn, V., 2003. Modelling compositional change: the example of chemical weathering of granitoid rocks. *Math. Geol.* 35, 231 – 251.
- Vonk, J.E., Sánchez-García, L., van Dongen, B.E., Alling, V., Kosmach, D., Charkin, A., Semiletov, I.P., Dudarev, O.V., Shakhova, N., Roos, P., Eglinton, T.I., Andersson, A., Gustafsson, O., 2014. Activation of old carbon by erosion of coastal and subsea permafrost in Arctic Siberia. *Nature* 489, 137 – 140.

- W -

- Wade-Murphy, J., Kuerschner, W.M., Hesselbo, S.P., 2006. Abrupt and gradual vegetation changes associated with Toarcian global change inferred from high resolution palynological study of the Korsodde section on Bornholm (DK). *Geophysical Research Abstracts*. 8.
- Wadham, J.L., Arndt, S., Tulaczyk, S., Stiball, S.M., Tranter, M., Telling, J., Lis, J.G.P., Lawson, E., Ridgwell, A., Dubnick, A., Sharp, M.J., Anesio, A.M., Butler, C.E.H., 2012. Potential methane reservoirs beneath Antarctica. *Nature* 488, 633 – 637.

- Wagner, A., 2010. Organo-facies and maturity-reconstruction of Toarcian bituminous shales in Luxembourg. Diploma Thesis, University of Cologne.
- Wakeham, S.G., Lee, C., 1993. Production, transport and alteration of particulate organic matter in the marine water column. In: Engel, M.H, Macko, A. (Eds.), *Organic Geochemistry – Principles and applications*. Plenum Press, pp. 145 – 170.
- Wang, Y, Mosbrugger, V., Zeng, H., 2005. Early to Middle Jurassic Vegetation and climate events in the Qaidam Basin, Northwest China. *Palaeogeography, Palaeoclimatology, Palaeoecology* 224, 200 – 216.
- Wang, L., Song, Z., Yin, Q., George, S.C., 2011. Paleosalinity significance of occurrence and distribution of methyltrimethyltridecyl chromans in the Upper Cretaceous Nenjiang Formation, Songliao Basin, China. *Organic Geochemistry* 42, 1411 – 1419.
- Wedepohl, K.H., 1971. Environmental influences on the chemical composition of shales and clays. In: Ahrens, L.H., Press, F., Runcorn, S.K., Urey, H.C. (Eds.), *Physics and Chemistry of the Earth*, vol. 8. Pergamon, Oxford, pp. 305 – 333.
- Wedepohl, K.H., 1991. The composition of the upper earth's crust and the natural cycles of selected metals. *Metals in natural raw materials. Natural Resources*. In: Merian, E. (Ed.), *Metals and their Compounds in the Environment*. VCH, Weinheim, pp. 3 – 17.
- Weedon, G., 2003. *Time-series analysis and cyclostratigraphy*: Cambridge, 247 pp.
- Wien, K., Kölling, M., Schulz, H.D., 2005. Close correlation between Sr/Ca ratios in bulk sediments from the southern Cape Basin and the SPECMAP record. *Geo-Marine Letters* 25, 265 – 271.
- Wieser, M.E., De Laeter, J.R., and Varner, M.D., 2007. Isotope fractionation studies of molybdenum: *International Journal of Mass Spectrometry* 265, 40 – 48.
- Wieser, M.E., and De Laeter, J.R., 2007. Absolute isotopic composition of molybdenum and the solar abundances of the p-process nuclides $^{92,94}\text{Mo}$: *Physical Review C* 75, doi: 10.1103/PhysRevC.75.055802.
- Wignall, P.B., 1994. *Black Shales*. Oxford University Press, 130 pp.
- Wignall, P.B., 2001. Large igneous provinces and mass extinctions. *Earth Science Reviews* 53, 1 – 33.
- Wignall, P.B., 2005. The link between large igneous province eruptions and mass extinctions. *Elements* 1, 293 – 297.
- Wignall, P. B., Newton, R. J., Little, C. T. S., 2005. The timing of paleoenvironmental change and cause-and-effect relationships during the early Jurassic mass extinction in Europe, *American Journal of Science* 305, 1014 – 1032.
- Williams, R.G., Hesselbo, S.P., Jenkyns, H.C., Morgans-Bell, H.S., 2001. Quartz silt in mudrocks as a key to sequence stratigraphy (Kimmeridge Clay Formation, Late Jurassic, Wessex Basin, UK). *Terra Nova* 13, 449 – 455.
- Wolff, G.A., Lamb, N.A., Maxwell, J.R., 1986. The origin and fate of 4-methyl steroids – II. Dehydration of stanols and occurrence of C_{30} 4-methyl steranes. *Organic Geochemistry* 10, 965 – 974.

- Y -

- Yarincik, K. M., Murray, R. W., Peterson, L. C., 2000a. Climatically sensitive eolian and hemipelagic deposition in the Cariaco Basin, Venezuela, over the past 578,000 years: Results from Al/Ti and K/Al. *Paleoceanography* 15, 210 – 228.
- Yarincik, K. M., Murray, R.W., Lyons, T.W., Peterson, L.C., Haug, G.H., 2000b. Oxygenation history of bottom waters in the Cariaco Basin, Venezuela, over the past 578,000 years: Results from redox-sensitive metals (Mo, V, Mn and Fe). *Paleoceanography* 15, 593 – 604.

- Z -

- Zhao, N., Xu, X., Yu, H., Yao, J., Su, Q., Peng, S., 2011. The color reflectance of marine-terrigenous deposits in LZ908 borehole in south coastal plain of Laizhou Bay: *Acta Oceanologica Sinica* 30, 53–59.
- Ziegler, P.A., 1990. *Geological Atlas of Western and Central Europe*. Shell International Petrology. Maatschappij B.V. Geological Society Publishing House, Bath, pp. 1 – 239.
- Ziegler, A.M., Parrish, J.M., Jiping, Y., Gyllenhaal, E.D., Rowley, D.B., Parrish, J.T., Shangyou, N., Bekker, A., Hulver, M.L., 1994. Early Mesozoic phytogeography and climate. In: Allen, J.R.L., Hoskins, B.J., Sellwood, B.W., Spicer, R.A., Valdes, P.J. (Eds.), *Paleoclimates and their modeling*. The Royal Society, pp. 89 – 98.
- Ziegler, P.A., Eshel, G., Rees, P.M, Rothfus, T.A., Rowley, D.B., Sunderlin, D., 2003. Tracing the tropics across land and sea: Permian to present. *Lethaia* 36, 227 – 254.
- Zonneveld, K.A.F., Versteegh, G.J.M., Kasten, S., Eglinton, T.I., Emeis, K.C., Huguet, C., Koch, B.P., de Lange, G.J., de Leeuw, J.W., Middelburg, J.J., Mollenhauer, G., Prahl, F.G., Retheneyer, J., Wakeham, S.G., 2010. Selective preservation of organic matter in marine environments; processes and impact on the sedimentary record. *Biogeoscience* 7, 483 – 511.